

Transactions of the ASME®

Technical Editor,
G. K. SEROVY
Associate Technical Editors
Advanced Energy Systems
M. J. MORAN
Environmental Control
H. E. HESKETH (1995)
Fuels and Combustion Technologies
D. W. PACER (1994)
Gas Turbine
L. S. LANGSTON (1993)
Internal Combustion Engine
H. H. CHUNG (1995)
Nuclear Engineering
S. M. CHO (1992)
Power
R. W. PORTER (1993)

**BOARD ON
COMMUNICATIONS**
Chairman and Vice-President
R. D. ROCKE

Members-at-Large
**T. BARLOW, W. BEGELL, T. F. CONRY,
T. DEAR, J. KITTO, R. MATES,
W. MORGAN, E. M. PATTON,
S. PATULSKI, R. E. REDER,
A. VAN DER SLUYS, F. M. WHITE**

President, **J. A. FALCON**
Executive Director,
D. L. BELDEN
Treasurer, **ROBERT A. BENNETT**

PUBLISHING STAFF
Mng. Dir., Publ.
CHARLES W. BEARDSLEY
Managing Editor,
CORNELIA MONAHAN
Sr. Production Editor,
VALERIE WINTERS
Production Assistant,
MARISOL ANDINO

Transactions of the ASME, Journal of Engineering
for Gas Turbines and Power (ISSN 0742-4795) is
published quarterly (Jan., Apr., July, Oct.) for \$130.00
per year by The American Society of Mechanical
Engineers, 345 East 47th Street, New York, NY
10017. Second class postage paid at New York, NY
and additional mailing offices. POSTMASTER: Send
address changes to Transactions of the ASME,

Journal of Engineering for
Gas Turbines and Power, c/o THE AMERICAN
SOCIETY OF MECHANICAL ENGINEERS, 22 Law
Drive, Box 2300, Fairfield, NJ 07007-2300.

CHANGES OF ADDRESS must be received at Society
headquarters seven weeks before they are to be
effective. Please send old label and new address.

PRICES: To members, \$40.00, annually, to
nonmembers, \$136.00.

Add \$24.00 for postage to countries outside the
United States and Canada.

STATEMENT from By-Laws: The Society shall not be
responsible for statements or opinions advanced in
papers or . . . printed in its publications (B 7.1, para. 3).

COPYRIGHT © 1993 by The American Society of
Mechanical Engineers. Authorization to photocopy material
for internal or personal use under circumstances not falling
within the fair use provisions of the Copyright Act is granted
by ASME to libraries and other users registered with the
Copyright Clearance Center (CCC) Transactional Reporting
Service provided that the base fee of \$3.00 per article plus
\$.30 per page is paid directly to CCC, 27 Congress St., Salem,
MA 01970. Request for special permission or bulk copying
should be addressed to Reprints/Permission Department.

INDEXED by Applied Mechanics Reviews and
Engineering Information, Inc.
Canadian Goods & Services
Tax Registration #126148048

Journal of Engineering for Gas Turbines and Power

Published Quarterly by The American Society of Mechanical Engineers

VOLUME 115 • NUMBER 1 • JANUARY 1993

TECHNICAL PAPERS

- 1 Ceramic Component Processing Development for Advanced Gas Turbine Engines (91-GT-120)
B. J. McEntire, R. R. Hengst, W. T. Collins, A. P. Tagliavere, and R. L. Yeckley
- 9 Application of Ceramics to Turbocharger Rotors for Passenger Cars (91-GT-264)
Y. Katano, M. Ando, T. Itoh, and M. Sasaki
- 17 Design and Evaluation of Silicon Nitride Turbocharger Rotors (91-GT-258)
K. Takama, S. Sasaki, T. Shimizu, and N. Kamiya
- 23 Development of Ceramic Turbocharger Rotors for High-Temperature Use (91-GT-270)
H. Kawase, K. Kato, T. Matsuhisa, and T. Mizuno
- 30 Fabrication and Testing of Ceramic Turbine Wheels (91-GT-142)
K. Takatori, T. Honma, N. Kamiya, H. Masaki, S. Sasaki, and S. Wada
- 36 Research and Development of Ceramic Turbine Wheels (92-GT-295)
K. Watanabe, M. Masuda, T. Ozawa, M. Matsui, and K. Matsuhira
- 42 Status of the Automotive Ceramic Gas Turbine Development Program (92-GT-2)
T. Itoh and H. Kimura
- 51 Current Status of 300 kW Industrial Ceramic Gas Turbine R&D in Japan (92-GT-3)
K. Honjo, R. Hashimoto, and H. Ogiyama
- 58 Ceramic Matrix Composite Applications in Advanced Liquid Fuel Rocket Engine Turbomachinery (92-GT-316)
J. W. Brockmeyer
- 64 Ceramic Matrix Composites for Rocket Engine Turbine Applications (92-GT-394)
T. P. Herbell and A. J. Eckel
- 70 Lifetime Prediction for Ceramic Gas Turbine Components (91-GT-96)
G. Stürmer, A. Schulz, and S. Wittig
- 76 High-Temperature Oxidation and Corrosion of Engineering Ceramics (92-GT-434)
K. G. Nickel, Z. Fu, and P. Quirnbach
- 83 Impact Design Methods for Ceramic Components in Gas Turbine Engines (91-GT-115)
J. Song, J. Cuccio, and H. Kington
- 91 Mechanical Behavior of Fiber-Reinforced SiC/RBSN Ceramic Matrix Composites: Theory and Experiment (91-GT-209)
A. Chulya, J. P. Gyekenyesi, and R. T. Bhatt
- 103 Structural Reliability Analysis of Laminated CMC Components (91-GT-210)
S. F. Duffy, J. L. Palko, and J. P. Gyekenyesi
- 109 Reliability Analysis of Structural Ceramic Components Using a Three-Parameter Weibull Distribution (92-GT-296)
S. F. Duffy, L. M. Powers, and A. Starlinger
- 117 Reliability Analysis of Ceramic Matrix Composite Laminates (91-GT-211)
D. J. Thomas and R. C. Wetherhold
- 122 Micromechanical Analysis of the Failure Process in Ceramic Matrix Composites (91-GT-95)
A. A. Rubinstein
- 127 Stability Analysis of Bridged Cracks in Brittle Matrix Composites (91-GT-94)
R. Ballarini and S. Muji
- 139 Ceramic Oxide Coatings for the Corrosion Protection of Silicon Carbide (91-GT-38)
M. van Roode, J. R. Price, and C. Stala
- 148 Precision Drilling of Ceramic-Coated Components With Abrasive-Waterjets (91-GT-232)
M. Hashish and J. Whalen
- 155 Nickel-Base Alloy GTD-222, a New Gas Turbine Nozzle Alloy (91-GT-73)
D. W. Seaver and A. M. Beltran
- 160 Effect of Cold Work and Aging Upon the Properties of a Ni-Mo-Cr Fastener Alloy (91-GT-14)
M. F. Rothman and S. K. Srivastava
- 165 Extending the Fatigue Life of Aircraft Engine Components by Hole Cold Expansion Technology (92-GT-77)
A. C. Rufin
- 172 Multikilowatt Lasers in Manufacturing (91-GT-233)
C. M. Banas
- 177 Application of Flash Welding to a Titanium Aluminide Alloy—Microstructural Evaluations (91-GT-231)
J. E. Gould and T. V. Stotler

(Contents continued on page 16)

Contents (continued)

184 Finite Element Simulation of the Upset Welding Process (91-GT-230)
H. A. Nied

193 Developments in Magnesium-Based Materials and Processes (91-GT-15)
P. Lyon, J. F. King, and G. A. Fowler

200 The In-Process Dressing Characteristics of Vitrified Bonded CBN Grinding Wheels
J. Williams and H. Yazdzik

TECHNICAL BRIEFS

205 Extension of a Noninteractive Reliability Model for Ceramic Matrix Composites
S. F. Duffy, R. C. Wetherhold, and L. K. Jain

ANNOUNCEMENTS

22 Change of address form for subscribers

208 Information for authors

Ceramic Component Processing Development for Advanced Gas Turbine Engines

B. J. McEntire

R. R. Hengst

W. T. Collins

A. P. Tagliaiavore

R. L. Yeckley

Norton/TRW Ceramics,
Northboro, MA 01532-1545

Norton/TRW Ceramics (NTC) is developing ceramic components as part of the DOE-sponsored Advanced Turbine Technology Applications Project (ATTAP). NTC's work is directed at developing manufacturing technologies for rotors, stators, vane-seat platforms, and scrolls. The first three components are being produced from a HIPed Si_3N_4 , designated NT154. Scrolls were prepared from a series of siliconized silicon-carbide (Si-SiC) materials designated NT235 and NT230. Efforts during the first three years of this five-year program are reported. Developmental work has been conducted on all aspects of the fabrication process using Taguchi experimental design techniques. Appropriate materials and processing conditions were selected for power beneficiation, densification, and heat-treatment operations. Component forming has been conducted using thermal-plastic-based injection molding (IM), pressure slip-casting (PSC), and Quick-SetTM injection molding.¹ An assessment of material properties for various components from each material and process were made. For NT154, characteristic room-temperature strengths and Weibull Moduli were found to range between ≈ 920 MPa to ≈ 1 GPa and ≈ 10 to ≈ 19 , respectively. Process-induced inclusions proved to be the dominant strength-limiting defect regardless of the chosen forming method. Correction of the lower observed values is being addressed through equipment changes and upgrades. For the NT230 and NT235 Si-SiC, characteristic room-temperature strengths and Weibull Moduli ranged from ≈ 240 to ≈ 420 MPa, and 8 to 10, respectively. At 1370°C , strength values for both the HIPed Si_3N_4 and the Si-SiC materials ranged from ≈ 480 MPa to ≈ 690 MPa. The durability of these materials as engine components is currently being evaluated.

Introduction

Efficient automotive gas turbine engines require the incorporation of high-reliability advanced ceramic components. The Advanced Turbine Technology Applications Project (ATTAP) addresses this requirement. The ATTAP is a DOE-sponsored five-year ceramic component development and demonstration program that utilizes the AGT101 and AGT5 gas-turbine engines as functional test-beds. The goals of this program include: (1) the development and demonstration of reliable ceramic fabrication processes, (2) production of the required ceramic components, and (3) evaluation of these components in actual engine tests. Under the ATTAP, Norton/TRW Ceramics (NTC) is a subcontractor to both Garrett Auxiliary Power Division (GAPD) of Allied Signal Aerospace Co., and Allison Gas Turbine, a Division of General Motors. As a participant with these companies, NTC has been assigned component proc-

essing development work on the rotors, stators, vane-seat platforms, and scrolls. NTC's effort centers on the development of controlled manufacturing processes for each component. To achieve this goal, NTC has developed an integrated approach to process optimization using Taguchi experiment design techniques. Taguchi methods were selected because they provide an efficient means for experimentation, while allowing linking to occur between many of the process operations. Described below are process and component development work for both the Si_3N_4 and Si-SiC materials.

NT154 Process Development

The Si_3N_4 material selected for use within the program, NT154, is a 4 percent Y_2O_3 -doped composition densified by hot-isostatic pressing (HIP). HIPing is accomplished using glass encapsulation techniques. Assessment and characterization of this material have been conducted both at NTC, GAPD, GM/Allison and by a number of additional laboratories [1-3]. Typical physical, thermal, and mechanical properties are given in Table 1. NT154 possesses excellent flexural fast-fracture behavior up to 1370°C , accompanied by an ac-

¹Quick-SetTM injection molding is a proprietary forming technique developed by Ceramics Process Systems, Milford, MA 01757.

Contributed by the International Gas Turbine Institute and presented at the 36th International Gas Turbine and Aeroengine Congress and Exposition, Orlando, Florida, June 3-6, 1991. Manuscript received at ASME Headquarters February 20, 1991. Paper No. 91-GT-120. Associate Technical Editor: L. A. Riekert.

Table 1 Properties of NT154 Si₃N₄

Properties	Values
1. Density (g/cc)	3.232 ± 0.004
2. Elastic Modulus (GPa)	310 - 320
3. Shear Modulus (GPa)	126
4. Poisson's Ratio	0.273
5. Hardness (Kg/mm ²)	1620
6. Thermal Expansion Coefficient	3.93 × 10 ⁻⁶ /°C
7. Thermal Conductivity (W/m·K)	
(25°C)	37.6
(900°C)	20.7
(1400°C)	15.8
8. Typical 22°C Mechanical Properties	
Flexural Strength (MPa)	896 ± 55
Characteristic Strength (MPa)	917
Weibull Modulus	19
Fracture Toughness (MPa·m ^{1/2})	4.7 - 5.5*
Tensile Strength (MPa)	900 - 920**
9. Typical 1370°C Mechanical Properties	
Flexural Strength (MPa)	579 ± 48
Characteristic Strength (MPa)	600
Weibull Modulus	11.4
Fracture Toughness (1300°C MPa·m ^{1/2})	4.1*
Tensile Strength (MPa)	240 - 520***

* Chevron Notch or Controlled Flaw Methods.

** Includes CIP and Cast Samples, (ORNL Data).

*** Loading Rate Dependent, (ORNL Data).

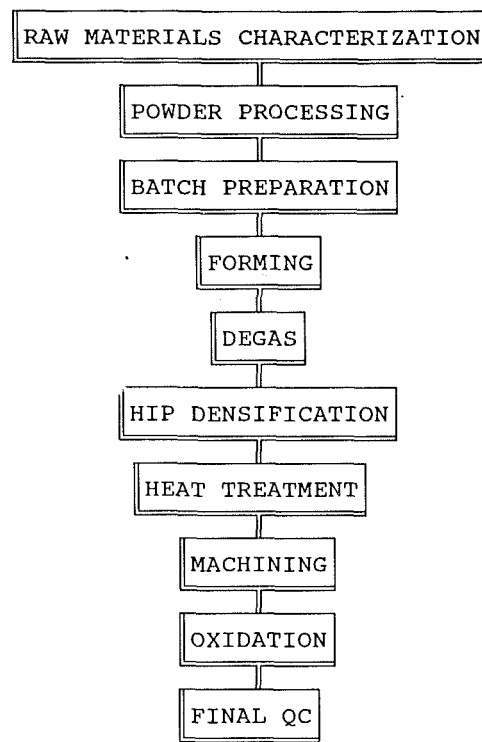


Fig. 1 NT154 process flow chart

ceptable Weibull Modulus. Failure origins have been dominantly associated with surface related machining flaws and occasional minor impurities. Reported tensile strengths under fast-loading conditions parallel flexural tests [4]. Principal failure origins in tension were volume inclusions, particularly iron impurities. Under slow-loading conditions, slow crack growth and creep rupture have been noted [1, 5]; although stress-rupture tests have consistently demonstrated life in excess of 200 h at 300 MPa under static loads.

An experimental plan was developed to cover the entire NT154 process including: (1) powder beneficiation; (2) component forming by pressure slip casting and injection molding; (3) binder removal and degassing; (4) HIP densification; and (5) post-HIP heat treatments. Each sequential process operation was evaluated both independently, and in consort with other fabrication steps. In this way, the influence and interaction between both upstream and downstream process steps was effectively evaluated. A process flow chart for component fabrication is shown in Fig. 1.

One of the key experiments used to characterize the process was an L9 × L4 linked Taguchi array. Within this design, the effects of various powder blends, milling procedures, and HIP densification schedules were compared and optimized. The design of this experiment is shown in Fig. 2. The experiment

uses an L9 power processing array coupled to an L4 HIP design. Powder blend (PB), milling time (MT), and solids concentration (SC) were the factors selected for study within the L9 array. Temperature (TP), time (TM), and cooling rate (CR) were the HIP factors. Components for the experiment were formed both by cold isostatic pressing (CIP) and slip casting. The CIP process was used only as a comparison standard for slip casting. The experiment required 72 separate trials, and therefore represents one-sixth of a full-factorial array. The purpose of the experiment was to: (1) select appropriate powder processing parameters that optimize forming, and (2) evaluate suitable process conditions that maintain required physical and mechanical properties. A discussion of processing conditions as they relate to forming was presented previously. [6]. It was found that the Si₃N₄ blend source was the controlling factor for forming. Coarser blends, possessing a broad size distribution of particles, were easiest to form, and provided the highest level of green density.

Subsequent to the evaluation of this experiment for forming, selected physical and mechanical property data were obtained and correlated to powder beneficiation process factors. Analysis of Variance (ANOVA) results implied that the prime focus for process control in powder beneficiation should be on the

Nomenclature

ANOVA = Analysis of Variance
 ATTAP = Advanced Turbine
 Technology Applications
 Project
 CIP = Cold Isostatic Press-
 ing
 CR = Cooling Rate
 GAPD = Garrett Auxiliary
 Power Division, Al-

lied Signal Aero-
 space Company
 GM = General Motors
 HIP = Hot Isostatic Press-
 ing
 IM = Injection Molding
 MT = Milling Time
 NT154 Si₃N₄ = HIPed Silicon Ni-
 tride

NT235, NT230,
 NC430 Si-SiC = Siliconized Silicon
 Carbides
 NTC = Norton/TRW Ce-
 ramics
 PB = Power Blend
 PSC = Pressure Slip Casting
 SC = Solids Content

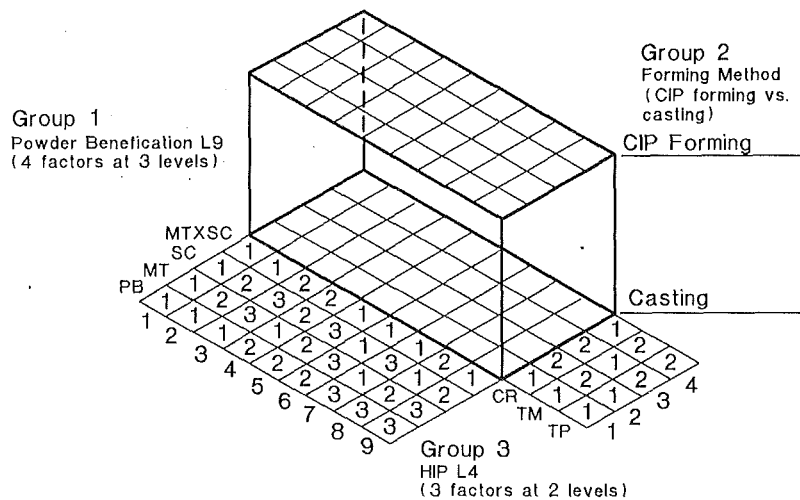


Fig. 2 Taguchi L9 x L4 powder beneficiation experiment design

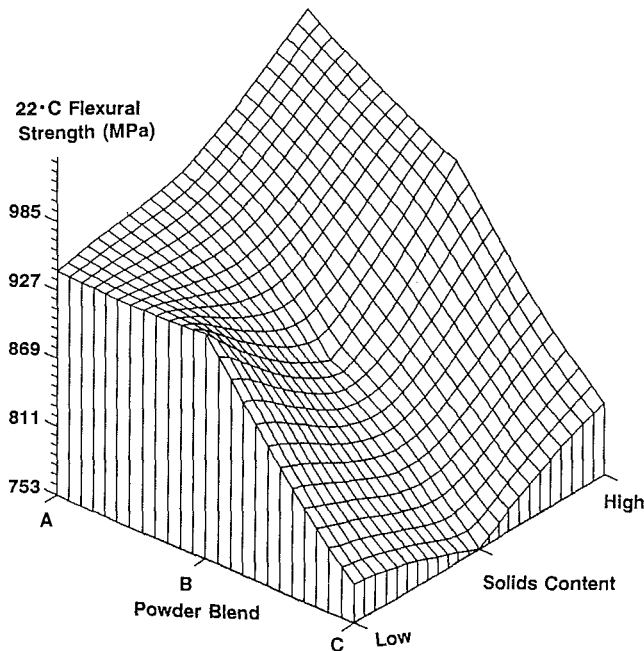


Fig. 3 Effect of powder blend and solids content on 22°C flexural strength

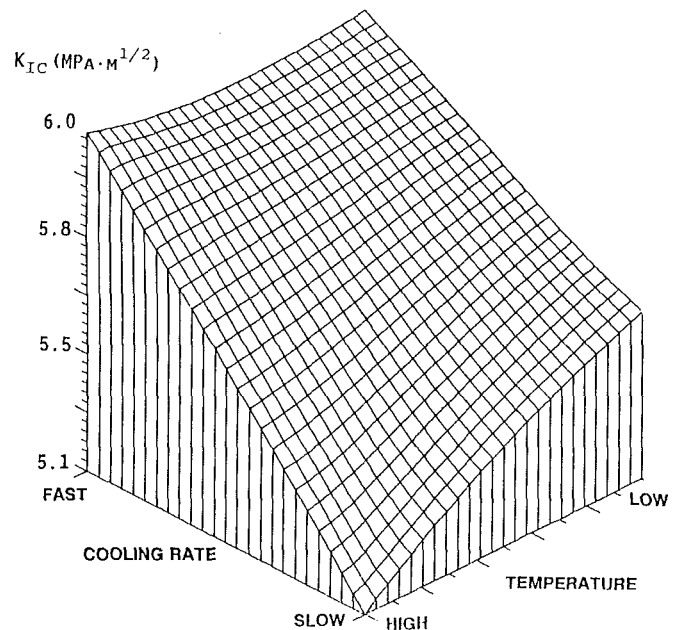


Fig. 4 Effect of HIP Temperature and cooling rate on fracture toughness

powder blend. Data suggested that the selected powder blend was the dominant factor for every response variable. Using level average data from the experiment, response surface plots were prepared for significant variables. An example is presented in Fig. 3. This plot indicates that blend is the major determinant of mechanical properties. Finer powders provided the highest strength components, but a broad size distribution was necessary for acceptable forming behavior. Similar analyses and plots were generated for all response variables. By specific selection of optimum conditions, strength both at room temperature and 1370°C were pushed to in excess of 1 GPa (145 Ksi) and 620 MPa (90 Ksi), respectively. Optimum fracture toughness values ($> 6 \text{ MPa}\cdot\text{m}^{1/2}$) corresponded to conditions that also gave the highest strengths. These results confirmed that preferred conditions for component forming were also conducive to the attainment of acceptable mechanical properties. Specific process conditions included: (1) short mix/mill times, (2) high solids contents; and (3) an intermediate to broad particle size.

In a similar fashion, the L4 portion of the experiment for

HIP conditions was also evaluated. Figure 4 shows the response surface plot for the HIP array. Based on the ANOVA for this portion of the experiment, all three process factors (time, temperature, and cooling rate) were critically important. However, it was surprising and interesting to note that cooling rate played a significant role in microstructure development and consequently fracture toughness. Improvements of up to ≈ 20 percent (from 5.1 to 6.1 $\text{MPa}\cdot\text{m}^{1/2}$) were observed. Overall results suggested that preferred HIP conditions included: (1) lower soak temperature; (2) shorter time; and (3) faster cooling rate.

From ANOVA and response surface plots, additional supplemental HIP conditions were selected and evaluated. These results were combined with the L9 x L4 data to provide a broad perspective of the effects of powder processing and HIP densification conditions on material properties. To link the two arrays fully, data analysis was subsequently conducted using intrinsic powder properties as opposed to specific processing conditions. Examples of data obtained from these analyses are given in Figs. 5–7.

Figures 5 and 6 show trends for fracture toughness and

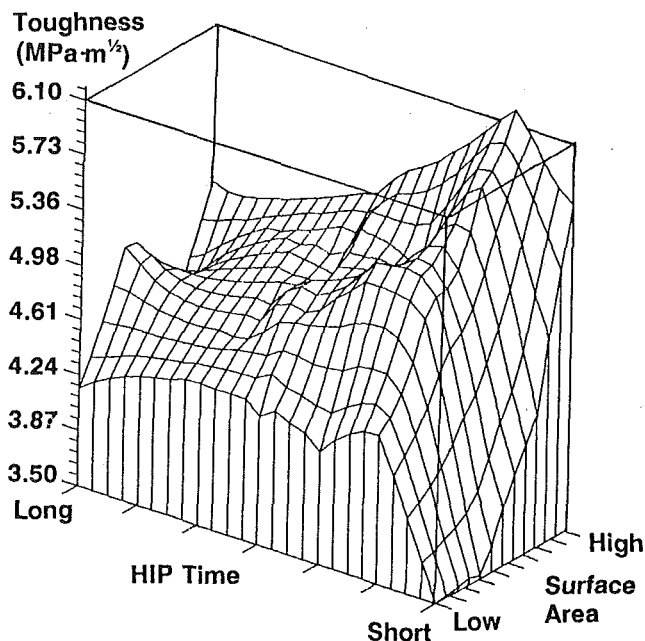


Fig. 5 L9 x L4 response surface diagram for fracture toughness

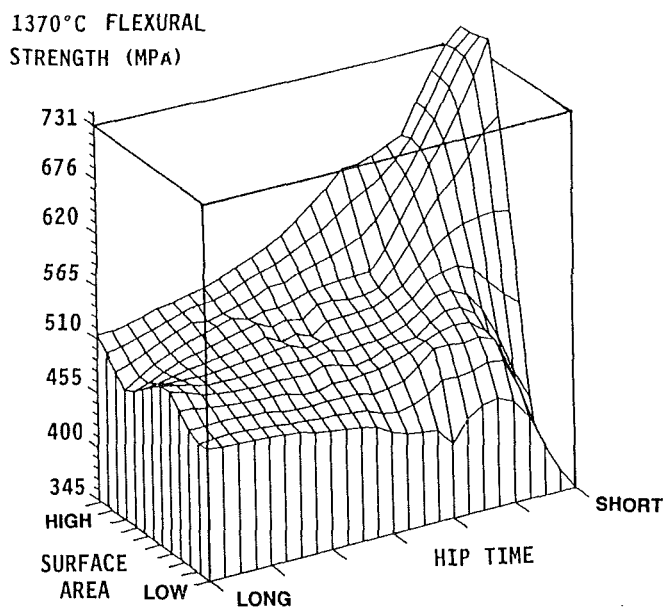


Fig. 6 The effect of HIP time and powder surface area on 1370°C flexural strength

1370°C fast-fracture strength. A modest improvement in toughness led to marked improvement in flexural strength. The best values (i.e., $> 6.1 \text{ MPa}\cdot\text{m}^{1/2}$ and $\sim 740 \text{ MPa}$) were achieved with finer powders of high surface area. However, at these conditions, the response surface shows high variability, indicating that slight changes in processing conditions could result in significant alterations in properties. It is also worth pointing out that the range of conditions studied within the experiment resulted in over 100 percent change in these two response variables. The data demonstrate the role and overriding effect HIP conditions have on mechanical properties. For high-surface area powders, 1370°C strengths in excess of 690 MPa (100 Ksi) were observed for the shortest HIP time.

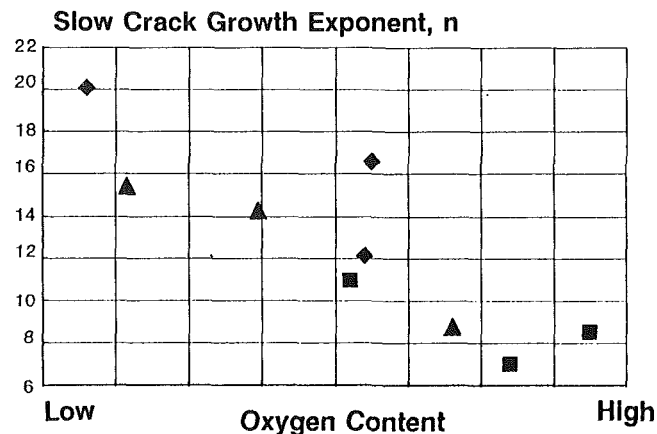


Fig. 7 The effect of oxygen content on time-dependent mechanical properties

Figure 7 presents results from dynamic fatigue tests conducted to determine slow crack growth behavior. The slow crack growth exponent for each powder of the L9 experiment is plotted against powder oxygen content. The data demonstrate that high oxygen content materials resulted in poorer durability. Powder batches possessing high oxygen content were derived from narrow size distribution powder blends of high surface area. Intermediate blends, of moderate surface area and a broad size distribution, are therefore preferred despite the fact that these powders give lower fast fracture strengths. This result presents an interesting engineering paradox. Selected conditions that favor fast fracture strength do not coincide with optimum conditions for time-dependent strength. As a compromise, an intermediate set of powder processing and HIP conditions is preferred.

With the acquisition of this broad data base on powders and HIP operations, a clear understanding of the roles for specific process variables on component properties was achieved. Conclusions from this experiment are as follows:

- An acceptable powder blend was identified. This blend possesses a broad particle size distribution and intermediate surface area. Because of these characteristics, the powder exhibits good forming behavior. When densified at preferred conditions, excellent fast fracture and high-temperature durability are achieved. The selected blend represents a compromise between fast-fracture strength and slow crack growth behavior. Ultra-high fast-fracture strengths were sacrificed in favor of improved high-temperature time-dependent mechanical properties.

- An appropriate HIP schedule was defined and selected. Intermediate temperature and time conditions maximize density, fracture toughness, and strength.

- Based on the response surface plots from the experiment, as well as on-going SPC, specifications and appropriate control ranges for powders (i.e., particle size, surface area, and chemistry) and the HIP schedule have been finalized and implemented.

Following forming, components are subjected to a high-temperature inert atmosphere heat treatment. This operation, known as degassing, is performed prior to encapsulation HIPing. Its purpose is to remove water and carbonaceous residue from components. Several key Taguchi experiments were conducted in this area. The most significant of these, an L9 array, was used to set basic conditions. The experiment correlated time, temperature, atmosphere, and forming method (CIP, cast, and injection molding) with physical and mechanical properties. ANOVA and level average results for the array indicated that temperature and the interaction of time and temperature were critical controlling parameters. Excellent

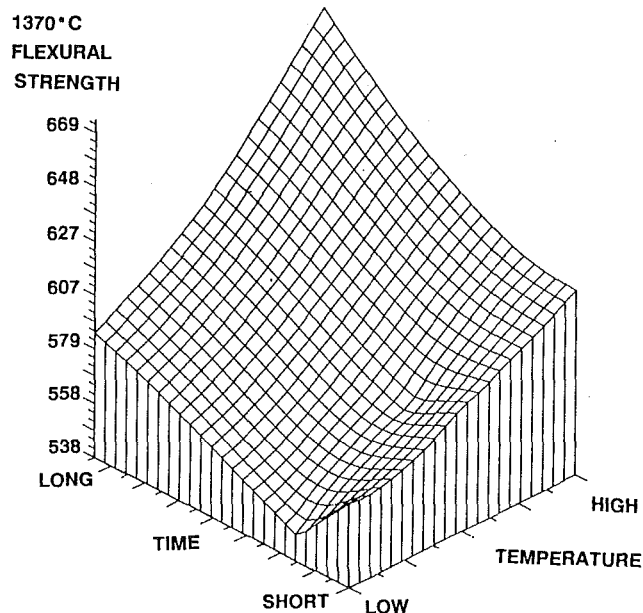


Fig. 8 1370°C flexural strength of NT154 versus degas heat-treatment conditions

high-temperature strengths were observed (> 700 MPa or 102 Ksi) for specific degas schedules, refer to Fig. 8. The results demonstrated that longer hold times at higher temperatures improved mechanical properties. Dynamic fatigue tests were completed in an attempt to discern the effect of degas operations on high-temperature durability. Tests were performed by loading samples to failure at 1370°C under three different loading rate conditions. ANOVA data for these tests showed that both temperature and time were critical factors in determining high-temperature durability. Level average values for slow-crack-growth exponents are presented in Table 2. From these results, preferred conditions for improved durability were identified. They included a low-temperature, short-to-intermediate time schedule. This conclusion is at variance with the conclusion drawn from fast-fracture data. Preferred conditions for achieving optimum high-temperature fast-fracture strengths included a high-temperature, long-time schedule; while the converse appears true for optimum time-dependent properties. With the understanding that improved time-dependent properties are perhaps more critical, NTC selected schedule conditions for the degas operation that optimized 1370°C time-dependent behavior.

After HIP densification, NTC developed two heat-treatment steps to improve the uniformity of crystalline phases within the material, and repair surface damage associated with decapsulation or machining. It was reasoned that improvements in both bulk and surface properties could be obtained by crystallization of the intergranular glass phase and by oxidation of the surface. Under the crystallization operation, components are heated to a high-temperature in an inert environment. The oxidation step is performed in air, after crystallization and subsequent to any machining operations. To optimize these operations, two Taguchi designed experiments were employed. Under the first experiment, an L16 array, seven treatment factors were studied. Four time-temperature schedules were coupled with different inert atmospheres. Oxidation was applied to half of the array; and component properties were assessed for as-fired and bulk-ground surfaces. Work was also conducted on these forming methods: cold isostatic pressing (CIP), injection molding (IM) and pressure slip casting (PSC). Results are presented in Table 3. These data serve to highlight differences between the various forming methods and offer a

Table 2 Degass L9 experiment—level average slow-crack growth exponents

Temperature			Time			Atmosphere	
T_1	T_2	T_3	t_1	t_2	t_3	N_2	N_2/H_2
13.0	8.5	10.4	12.6	11.6	7.6	10.7	10.4

Table 3 Mechanical properties for CIP, slip-cast, and injection-molded processes from the component L16 experiment

Process and Properties	CIP	Slip-Cast	Injection Molding
I. Bulk-Ground Test Bars - 22°C			
Modulus of Rupture (MPa)	834 \pm 103	893 \pm 56	876 \pm 119
(Ksi)	121 \pm 15	130 \pm 8	127 \pm 17
Weibull Modulus	8.2	18.4	5.6
K_{IC} (MPa·m ^{1/2})	5.5 \pm 0.1	5.6 \pm 0.2	5.1 \pm 0.5
II. Bulk-Ground Test Bars - 1370°C			
Modulus of Rupture (MPa)	525 \pm 39	578 \pm 50	573 \pm 58
(Ksi)	76 \pm 6	84 \pm 7	83 \pm 8
Weibull Modulus	14.7	12.7	10.5
III. As-Fired Test Bars - 22°C			
Modulus Of Rupture (MPa)	531 \pm 39	583 \pm 25	540 \pm 52
(Ksi)	77 \pm 6	85 \pm 4	78 \pm 8
Weibull Modulus	15.5	27.3	11.1
K_{IC} (MPa·m ^{1/2})	6.7 \pm 1.1	7.3 \pm 0.6	7.7 \pm 0.8
IV. As-Fired Test Bars - 1370°C			
Modulus of Rupture (MPa)	394 \pm 34	368 \pm 35	395 \pm 34
(Ksi)	57 \pm 5	53 \pm 5	57 \pm 5
Weibull Modulus	12.7	11.5	12.7

Strength and Weibull data are for 20 - 30 samples for each forming method. Fracture Toughness values were compiled for 3 - 5 samples each.

comparison standard for work conducted on the process itself. Overall, the casting process produced the highest strengths and Weibull Moduli, regardless of surface condition. Injection-molding components showed acceptable strengths, but lower Weibull Moduli. In general, the CIP process fell in between the IM and PSC processes. As-fired surfaces showed ≈ 35 –37 percent reduction in 22°C flexural strength for each forming technique. This difference was ≈ 25 –35 percent at 1370°C. The reduction in strength is attributable to surface roughness and the HIP reaction layer. For mechanical properties, the most significant result from the experiment was a marked improvement in 1370°C as-fired surface strength. For either type of test bar, all heat treatments improved strengths to above the nontreated baseline values. It is particularly noteworthy that strengths > 551 MPa (80 Ksi) were achieved with as-fired test bars. Crystallization appeared to affect the strength of bulk-ground samples adversely; but the subsequent application of an oxidation heat treatment aided in strength recovery.

Due to the observed results from the L16 design, a follow-up L4 array was conducted to confirm the effects of selected crystallization and oxidation conditions. Experimental factors included crystallization (on or off); and oxidation temperature and time, each at two levels. The impact of selected conditions on high-temperature strength was of particular interest. Substantial improvements were noted in 1370°C strength with the crystallization heat treatment. Figure 9 shows a dramatic rise in "as-fired" surface strengths through application of a post-HIP crystallization heat treatment. Regardless of subsequent

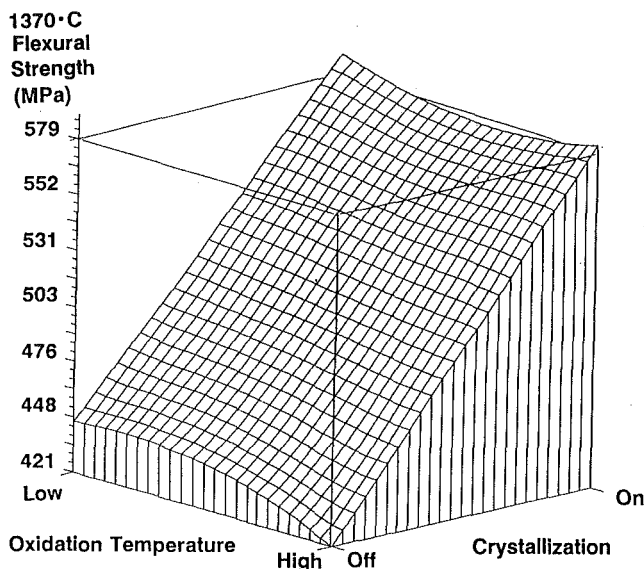


Fig. 9 Component integrity L4 experiment 1370°C strength for "as-fired" surfaces

oxidation conditions, 1370°C flexural strength improved to > 580 MPa (84 Ksi) for "as-fired" surfaces when the crystallization heat treatment was employed.

Collectively, both crystallization and oxidation tend to optimize both room-temperature and 1370°C flexural properties. Respective bulk-material strengths of approximately 1 GPa (145 Ksi) and 620 MPa (90 Ksi) can be expected. Utilization of the crystallization treatment also significantly improves "as-fired" surface strengths. Strengths for "as-fired" surfaces were demonstrated to be insensitive to test-temperature. Values of + 550 MPa (+ 80 Ksi) were observed from 22°C to 1370°C.

NT154 Component Development

Component fabrication was performed using three forming processes: injection molding, pressure slip casting, and Quick-Set™, injection molding.

For AGT101 stators, injection molding was initially selected. However, due to process control and impurity problems, the IM process was abandoned in favor of pressure slip casting. The PSC process has been utilized for forming both the AGT101 stator and rotor as well as the AGT5 gasifier rotor. Pressure slip casting was initially developed in the laboratory using plaster molds. The process utilizes external pressure to force filtration of the ceramic particles against porous plaster. To produce complex-shaped components in a crack-free state, several casting modifications were developed and employed. These included: (1) modification of the size distribution of the NT154 powder through agglomeration to increase casting rates; (2) the incorporation of novel mold designs possessing both porous and nonporous segments; and (3) the development of a freezing step subsequent to pressure casting followed by sublimation drying. The combination of these forming methods led to adequate feature definition and the production of crack-free components. AGT101 demonstration rotors and stators have been prepared by the PSC process and delivered to GAPD for evaluation. Minor problems have been encountered in maintaining powder purity during the sequence of casting operations. Iron impurities, primarily introduced during the agglomeration step, resulted in a slight reduction in flexural properties. Correction of this problem is being addressed by equipment modification.

For AGT5 rotors, spin-testing of fully machined components has been completed. Several passed an 80 Krpm proof speed.

Table 4 Physical, thermal, and mechanical properties of NT235 and NT 230 Si-SiC

Properties	NT235 Values	NT230 Values
1. Density (g/cc)	3.10 - 3.15	3.05
2. Elastic Modulus (GPa)	383	395
3. Shear Modulus (GPa)	187	165
4. Poisson's Ratio	0.24	0.17
5. Hardness (Kg/mm ²)	1620	-
6. Thermal Expansion Coefficient	$4.8 \times 10^{-6}/^{\circ}\text{C}$	$4.7 \times 10^{-6}/^{\circ}\text{C}$
7. Thermal Conductivity (W/m ² K)		
(25°C)	135	-
(1000°C)	36	-
8. Flexural Strength		
(25°C)	245	410
(1260°C)	274	540
(1370°C)	251	500
Weibull Modulus	10	8
9. Fracture Toughness (MPa·m ^{1/2})	3.5 - 4.4*	-

* Controlled Flaw Method at 25°C and 1370°C, respectively.

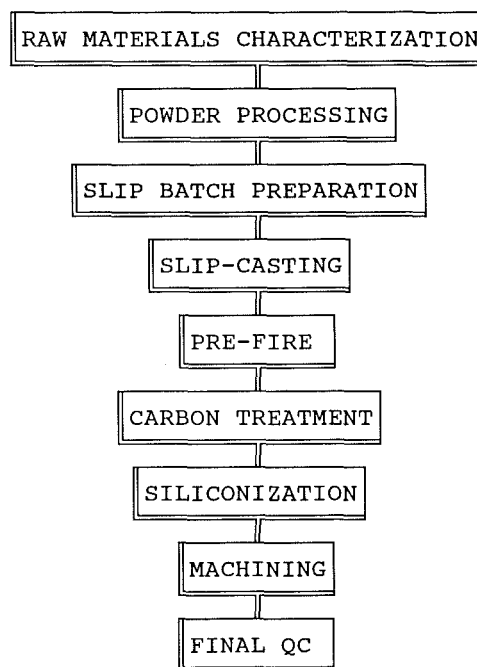


Fig. 10 NT230 process flow chart

Of those that failed, origins have been determined and corrective action taken. Successful components have been built into rig tests at GM/Allison, and are currently being evaluated for durability.

Under a cooperative program with Ceramic Process Systems, Quick-Set™ injection molding was utilized to prepare vane-seat platforms. Within this endeavor, NTC supplied NT154 Si₃N₄ powder to CPS. CPS formed components using their proprietary injection-molding process and returned them to NTC. NTC then completed densification, and assessed mechanical properties. In general, form and feature definition for these components was excellent; and mechanical properties were found to be equivalent to the best NT154 material prepared by the forming methods.

NT230 Process Development

During the ATTAP, NTC began developmental work on an

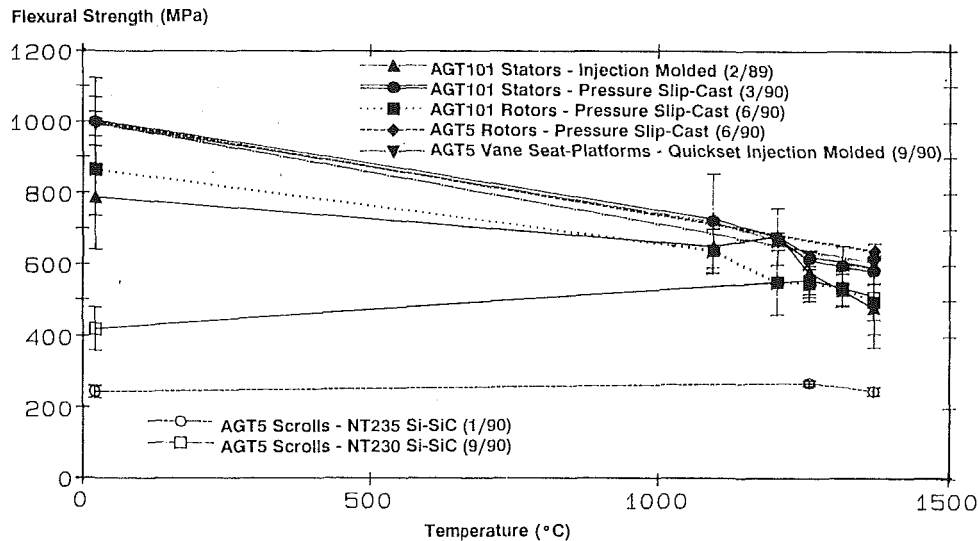


Fig. 11 Flexural strengths of advanced gas turbine components

existing siliconized silicon-carbide for potential use as static-structural components within advanced gas turbine engines. Initial work utilized an existing Si-SiC, designated NT235. This material has been previously examined for heat-engine applications [7, 8], and is commonly known as NC430. NC430 is a Norton designation for a variation on a better-known material currently produced and marketed under the name Crystar™ [9, 10]. These materials represent a class of densified, reaction-sintered silicon-carbides featuring a bimodal distribution of silicon-carbide grains and metallic silicon. Compositionally, they contain between 5 and 15 percent silicon, and extremely low levels of trace impurities. In connection with the ATTAP, NTC conducted an internal research and development program directed at improving the mechanical behavior of these Si-SiC materials. By modification of the grain-size distribution, and through selective changes to the fabrication process, NTC was able essentially to double the strength of these materials. A new material resulted from this effort, designated NT230. Typical material properties for both NT235 and NT230, along with the process utilized in producing components, are shown in Table 4 and Fig. 10, respectively. The high-temperature durability of this material is being evaluated by several organizations. For either material, components were generally prepared by gravity or pressure casting. In comparison with NT154 Si₃N₄, these Si-SiC materials are readily castable, and easily formed into complex shapes with little or no process optimization. Because they exhibit no shrinkage, iterations on tooling and shape development are generally minimal. Scroll components for the Allison AGT5 gas turbine engine have been produced using NT230 and NT235. These components are fairly large (≈ 25.4 cm, 10 in) in overall diameter and contain an intricate overlapping swirl design, which make them difficult to produce from any material except a shrink-free ceramic.

Material and Process Comparison

For each component and process, mechanical properties were assessed by either destructive evaluation of the component itself, or from co-processed tile. Presented in Fig. 11 is a summary of flexural data. In general, the strength behavior of components is representative of the optimized process and numerous batches. Room-temperature and 1370°C values of between 827 MPa (120 Ksi) and 1070 MPa (155 Ksi), and 483 MPa (70 Ksi) and 655 MPa (95 Ksi) were obtained. The highest overall strengths were observed from either the pressure-casting

or Quick-Set™ injection-molding processes. Lower strengths from either the IM or PSC were identified and traced to impurity problems associated with batch preparation. Correction of this limitation for the PSC process is an ongoing effort. Shown also in this figure are data for the Si-SiC materials. Strength characteristics of the newly developed NT230 Si-SiC approach NT154 at high temperatures.

Summary and Conclusions

Norton/TRW Ceramics has successfully completed its third year effort of the ATTAP program. Process and component development work are continuing for advanced gas turbine components. Accomplishments are summarized below:

- NTC's NT154 Si₃N₄ has been extensively developed and characterized. A significant data base now exists for this material. Excellent strength characteristics at room and elevated temperatures are observed along with adequate static stress rupture behavior. Power beneficiation, degas, HIP crystallization, and oxidation operations have been optimized. Appropriate material, comminution methods, atmosphere, time, and temperature schedules were selected. Paradoxically, it was found that conditions that resulted in improvements in high-temperature durability were opposite those required for enhanced fast-fracture strength. Preference was given to conditions that optimized durability. Further improvements in material properties require iterative changes to the forming process to remove impurities. Increased durability to elevated temperatures is also expected as a result of full implementation of process optimization efforts.

- NT154 forming development utilized several techniques. Injection molding was initially used to form the stator, but later dropped from the program in favor of pressure slip casting. Demonstration rotors and stators for the AGT101 engine have been delivered to GAPD. Rotors for the Allison AGT5 engine have also been successfully prepared and spin-tested. These parts were delivered to Allison for rig and engine testing. Under a cooperative program with Ceramic Process Systems, NTC fabricated AGT5 vane-seat platforms. CPS's Quick-Set™ injection molding operation was used to form these components. Densification and material property assessment were completed by NTC.

- By building on existing Norton technology, NTC has developed a new siliconized silicon carbide, which has approximately twice the fracture strength of existing Si-SiC materials. Designated NT230, this material's high-temperature

strength and durability appear to be nearly equivalent to NT154 Si_3N_4 . Using Si-SiC, NTC has fabricated and delivered scrolls for the AGT5 engine. These components are being evaluated in rig and engine tests.

Continued effort in each of the above areas is scheduled for the 1991 program year. Work will emphasize component specific fabrication challenges, and the attainment of improved mechanical properties.

Acknowledgments

Work accomplished during the past three years under the ATTAP represents the combined efforts of a number of individuals. G. Janulewicz, D. Moylan, J. Gulcius, G. Manoo-gian, B. McGeary, W. Hackett, D. Karsberg, S. FitzGerald, J. Mullaney, A. Johnson, L. Russell, K. Mitchell, P. Reed, S. Sherman, and G. Watson are acknowledged and appreciated for detailed performance of the technical plan. Appreciation is expressed to T. J. Woods, G. A. Fryburg, T. G. Kalamasz, P. K. Caneen, C. Brown, and L. Lynch for their management and technical support; and services in consultation, machine tooling, experiment design, drawing and documentation control, and graphics. Special thanks go to J. Johnson and J. Holowczak for injection-molding development. The Characterization and Analysis Groups of Norton Company are acknowledged for their work in chemical analysis, x-ray diffraction, microfocus x-ray characterization, mechanical property testing, and electron microscopy. A. M. S. Smith, E. M. MacKinnon, G. D. Roberts, R. T. Foy, D. L. Sterner, and M. J. Sweeney are appreciated for cost analysis, accounting, and secretarial services. Appreciation is given to Drs. C. L. Quackenbush and R. R. Willis who constructively reviewed program objectives, plans, and reports; and to J. M. Garwood, and F. P. Teta for government contract administration review and support. J. Smyth, D. Carruthers, B. Morey, J. Schienle, J. Minter, and L. Lindberg of GPAD; and H. Helms, P. Haley,

S. Hilpisch, and L. Groseclose of Allison are acknowledged and thanked for technical guidance, analyses, program direction and support. Finally, appreciation is expressed to Norton Company, TWR Inc. GAPD, Allison, NASA, and DOE for financial support.

References

- 1 Liu, K. C., and Brinkman, C. R., "Cyclic Fatigue of Toughened Ceramics, *Ceramic Technology for Advanced Heat Engines Project*, Semiannual Progress Report for Oct. 1988-Mar. 1989, Oak Ridge, TN; ORNL Publication No. ORNL/TM-11239, pp.351-360.
- 2 Richerson, D. W., "Fractography of Advanced Silicon Nitride Materials for Turbine Applications," Final Report, submitted to Naval Sea Systems Command, Contract No. N00024-88-C-5112, Washington, DC; Salt Lake City, UT, Ceramtec Report No. 8963201, Apr. 1989.
- 3 Hecht, N. L., McCullum D. E., Goodrich, S., and Chuck, L., "Mechanical Properties Characterization of High Performance Ceramics," *27th Automotive Technology Development Contractors' Coordination Meeting*, Dearborn, MI, Oct. 23-26, 1989.
- 4 Hecht, N. L., Goodrich, S. M., Chuck, L., and McCullum, D. E., "Effects of the Environment on the Mechanical Behavior of Ceramics," *Proceedings of the Annual Automotive Technology Development Contractors' Coordination Meeting*, Dearborn, MI, Oct. 22-25, 1990.
- 5 Liu, K. C., Pih, H., Stevens, C. O., and Brinkman, C. R., "Tensile Creep Behavior and Cyclic Fatigue/Creep Interaction of Hot-Isostatically-Pressed Si_3N_4 ," *Proceedings of the Annual Automotive Technology Development Contractors' Coordination Meeting*, Dearborn, MI, Oct. 22-25, 1990.
- 6 McEntire B. J., Tagliavere, A. P., Heichel, D. N., Johnson, J. W., Bright E., and Yeckley R. L., "ATTAP Ceramic Component Development Using Taguchi Methods," *Proceedings of the Twenty-Sixth Automotive Technology Development Contractors' Coordination Meeting P-219*, Dearborn, MI, Oct. 24-27, 1988, pp. 289-300.
- 7 Torti, M. L., Lucek, J. W., and Weaver, G. Q., "Densified Silicon Carbide—An Interesting Material for Diesel Applications," SAE Paper No. 780071, 1978.
- 8 Advanced Gas Turbine (AGT) Technology Project," Final Report, Allison Gas Turbine Division, General Motors Corporation, Report No. DOE/NASA 0168-11, NASA CR-182127, EDR 13295, Aug. 1988.
- 9 Weaver, G. Q., "Process for Forming High Density Silicon Carbide," U.S. Patent No. 3,998,646, Dec. 21, 1976.
- 10 Weaver, G. Q., and Olson, B. A., "Process for Fabricating Silicon Carbide Articles," U.S. Patent No. 4,019,913, Apr. 26, 1977.

Y. Katano

M. Ando

T. Itoh

M. Sasaki

Nissan Research Center,
Nissan Motor Co., Ltd.,
1, Natsuhima-cho, Yokosuka, 237 Japan

Application of Ceramics to Turbocharger Rotors for Passenger Cars

Nissan has been developing and marketing ceramic turbocharger rotors for five years. This paper outlines the major theories and techniques used in ceramic fabrication, joining of ceramic and metal components, and machining of ceramics. It also presents a dynamic stress analysis using DYNA3D and describes techniques used in performing impact damage experiments, reliability evaluation, and lifetime prediction.

Introduction

The adoption of stringent emission standards in Japan in the latter half of the 1970s led to a reduction in power output for many Japanese passenger car engines. To recover lost engine power, there was a strong need to maximize the efficiencies of small engines while minimizing price increases. Another factor that had to be considered was the hefty tax assessed at that time on engines having a displacement over 2.0 liters.

One answer to that situation was the use of a turbocharging system, which is a rather common means of increasing engine output and can be applied without making many modifications to main engine components and systems. Metal turbochargers were first applied to various classes of Nissan cars beginning around 1978. However, there was a growing demand to improve the acceleration response of the turbocharger, which is one of the main demerits of turbocharging. One effective method for overcoming this problem of turbo lag is to reduce the moment of inertia of the turbocharger rotor, which can be accomplished through the use of ceramics.

Nissan has conducted research on experimental turbine rotors for use in ceramic gas turbines since the company started spin tests of ceramic disks toward the end of the 1970s. A high-efficiency ceramic turbocharged engine was released in 1985 and has been used in more than 400,000 passenger cars to date (Fig. 1). In connection with the redesign and modification of the turbocharger, three types of ceramic rotors have been developed so far (Fig. 2).

The CN-1 type [1] was produced between 1985 and 1987 and was used with 2.0-liter in-line six-cylinder DOHC engines. The CNR-1 type [2, 3] has been in production since 1987. This ceramic rotor is a redesigned, low-stress version of the CN-1 and is used with 2.0 liter in-line six-cylinder or V-6 DOHC engines and 3.0-liter V-6 DOHC engines [4]. It features water passages provided in the bearing housing and ball bearings instead of plain journal bearings. A thrust bearing was also

subsequently adopted [5]. The T-25 type has been in production since 1989 and was developed for use with 2.6-liter twin-turbocharged in-line six-cylinder DOHC engines [6]. The design details of this ceramic rotor are explained in [1, 2], and the engine performance obtained is described in [1, 3, 4, 6].

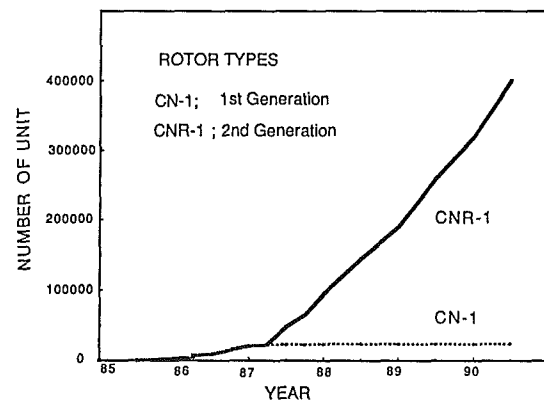


Fig. 1 Number of vehicles equipped with ceramic turbocharger rotors

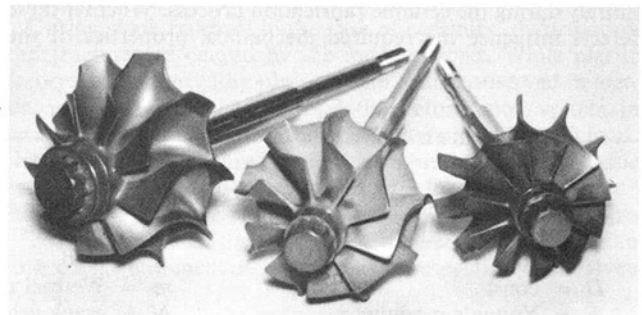


Fig. 2 Three types of ceramic turbocharger rotors: left: CN-1, center: CNR-1, right: T-25

Contributed by the International Gas Turbine Institute and presented at the 36th International Gas Turbine and Aeroengine Congress and Exposition, Orlando, Florida, June 3-6, 1991. Manuscript received at ASME Headquarters March 4, 1991. Paper No. 91-GT-264. Associate Technical Editor: L. A. Riekert.

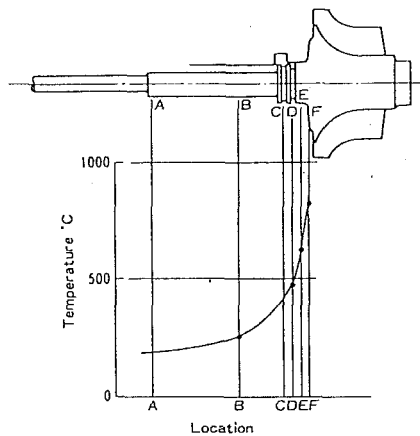


Fig. 3 Temperature distribution in turbine rotor shaft during heat soak-back

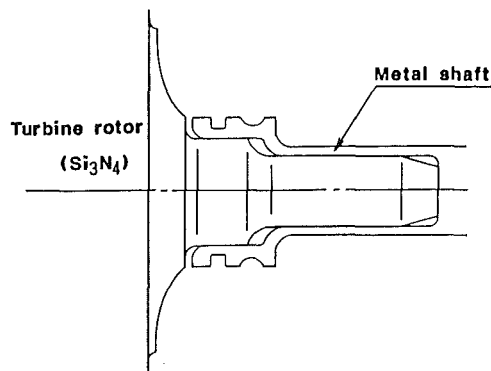


Fig. 4 Design of bonding method (double shrink-fitting)

A turbocharger rotor must be capable of withstanding long periods of use in automobile exhaust gas, which can reach temperatures as high as approximately 900°C. Ceramic materials, which are inherently brittle, have been applied to automobile structural parts that require high reliability and durability. This paper describes some of the techniques for applying ceramics to structural components, using the turbocharger rotor as an example.

Ceramic Materials and Fabrication Process

Ceramic Materials. Silicon nitride was chosen as the rotor material because of its strength, fracture toughness, thermal shock resistance, and thermal expansion coefficient [1, 2]. Generally, covalent silicon nitride is not interable, but is rendered so through the use of common sintering aids such as Y_2O_3 and Al_2O_3 .

Raw Materials—Silicon Nitride and Sintering Aids. It is impossible to avoid the occurrence of pores and other defects entirely during the ceramic fabrication process. Whether these defects influence the required mechanical properties of the

ceramic depends on the stress conditions. Nonetheless, defects must be eliminated as much as possible.

Molding Methods. Molding methods are limited to injection molding and slip casting for a complex geometry like that of a turbine blade. Voids are generally spherical in slip-cast ceramic bodies, but have a sharp form in injection molded bodies. Slip casting has the advantage that stress concentrations, which are caused by spherical voids, are less likely to occur. However, at Nissan we had selected injection molding because it is better suited to mass production.

The injection molding process consists of several operations, including the mixing of the ceramic powder and organic binder, injection molding and binder removal. Mutsuddy and Shetty have presented a detailed report of the injection molding process [7].

Sintering Methods. Densification methods for silicon nitride include reaction sintering, normal sintering, hot pressing, and gas pressure sintering.

In reaction sintering, the silicon powder compacted body is densified by nitridation (reaction of Si with N_2 to Si_3N_4). The sintered body does not have sufficient strength, but dimensional accuracy is maintained during sintering. With hot pressing, the compact body is densified with the help of mechanical pressure applied along one axis. This method, however, is unsuitable for a complex geometry like that of turbine blades. Normal sintering is performed under 1 atm pressure in a nitrogen gas atmosphere. It is thought that thermal decomposition occurs around the sintering temperature, which is usually above 1800°C. Gas pressure sintering is performed under high pressure in a nitrogen gas atmosphere. This method is most suitable for fabrication of a high-density sintered ceramic body.

Gas pressure sintering and normal sintering under well-controlled conditions are thought to be the best sintering methods for ceramic turbocharger rotors.

Joining Technology

The technology for joining the ceramic rotor and steel shaft was a key element in the development of ceramic turbochargers. The two components are joined just under the ring seal pit, where the temperature rises to 450°C for an uncooled housing during heat soak-back, which causes the highest temperatures. An example of the temperature distribution during heat soak-back is shown in Fig. 3. The position for the soak-back is shown in Fig. 3. The position for the ceramic-steel joint was selected for the following reasons: (1) to reduce the possibility of lubricating oil leakage from the bearing to the exhaust pipe; (2) to increase rotor reliability by reducing the effective rotor volume; (3) to reduce production cost. The location chosen, however, presents the severest conditions for joining. For the turbochargers developed to date, mechanical joining has been accomplished using a shrink-fitting method and chemical joining has been effected through an active brazing technique.

A cross section of the steel shaft and ceramic rotor joint formed by shrink-fitting is illustrated in Fig. 4. In an earlier design, a double shrink-fitting method was employed to assure

Nomenclature

A = premultiplier in crack velocity
 a = crack length
 B = const
 D = const
 E = Young's modulus
 F = failure probability
 H = hardness

Kc = fracture toughness
 K_{IC} = critical stress intensity factor
 L = load
 m = Weibull modulus
 N = crack velocity exponent
 P = survival probability
 r = radius

S = material strength
 t = time
 V = velocity
 v_e = effective volume
 Y = shape factor
 ρ = density
 σ = stress

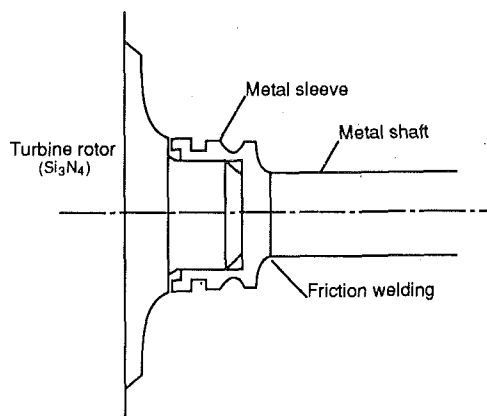


Fig. 5 Design of bonding method (shrink-fitting)

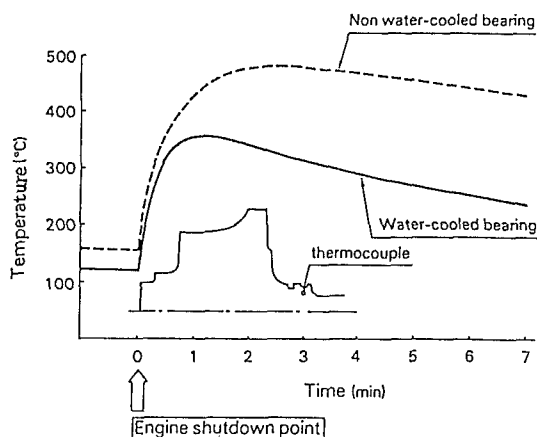


Fig. 6 Temperature of ceramic-to-metal joint during heat soak-back

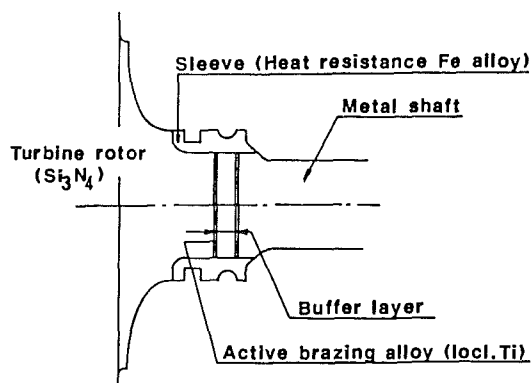


Fig. 7 Design of bonding method (active brazing)

reliability by enhancing the bonding strength. With a more recent design, a simpler shrink-fitting technique has been adopted to facilitate the use of a water-cooled bearing [8], which is shown in Fig. 5. The temperature distributions during heat soak-back for a turbocharger rotor equipped with a water-cooled bearing and one without are given in Fig. 6 [3]. While this shrink-fitting method is simple, it requires micron-order machining accuracy to maintain the bonding strength between the steel shaft and ceramic rotor.

A cross-sectional view of a joint formed by active brazing is shown in Fig. 7. This method employs an active brazing alloy containing titanium. A buffer layer, composed of Ni and W, is also provided between the ceramic rotor and steel shaft. Brazing is performed in only one heating process. A finite element analysis of a joint formed by active brazing indicates

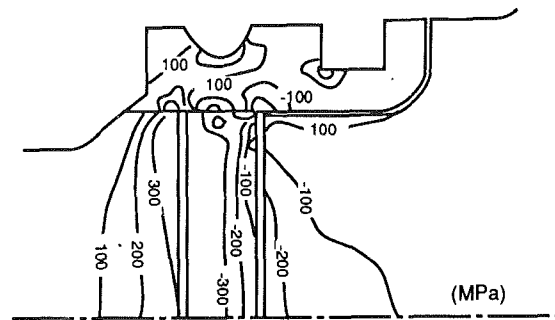


Fig. 8 Residual stress distribution in ceramic rotor

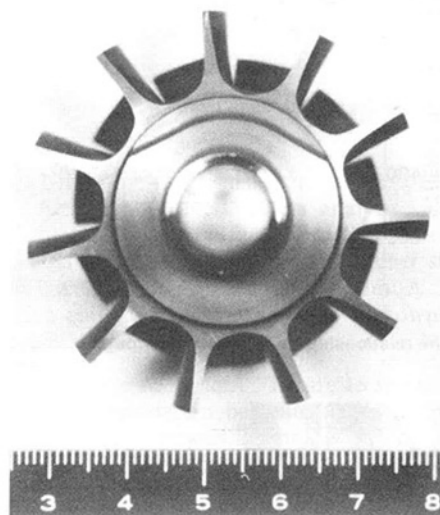


Fig. 9 Ceramic back hub plate after machining for balance

that the provision of a buffer layer reduces the residual stresses as compared with the direct brazing of silicon nitride and steel. Figure 8 shows the stress analysis results obtained with an elastic/plastic model for a joint formed by a silicon nitride rotor with a buffer layer and a steel shaft overlaid with a heat resistant steel having a low thermal expansion coefficient [9].

Machining Techniques for Ceramics

There are two reasons why it is important to study the machining techniques for ceramics. The first is that the machining process for the turbocharger rotor accounts for the greatest position of the total rotor production cost. This is also true for other ceramic components. The second reason is that the residual damage induced during machining degrades the mechanical strength of ceramics. One of the most commonly used machining processes for ceramics to date has been grinding, which is utilized to correct the rotational balance of the turbocharger rotor (Fig. 9) and will be discussed in this section.

During stock removal in the case of ceramics, deformation and fracture are caused by the indenter load. While plastic deformation induced by plastic strain is also observed in metals, regardless of other factors, the deformation system in ceramics differs depending on the indenter radius and load. Hertzian cracks [10] are initiated by a blunt indenter, plastic deformation is caused by a low indenter load, and a median/radial crack system is induced by a high indenter load [11].

The critical loads (Le and Lp) for the initiation of Hertzian cone cracks and median/radial cracks, respectively, are given as [10, 12]

$$Le = De \cdot r \cdot Kc^2 / E \quad (1)$$

$$Lp = Dp \cdot Kc^4 / H^3 \quad (2)$$

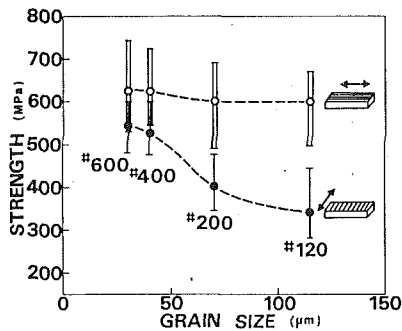


Fig. 10 The relationship between grain size and strength

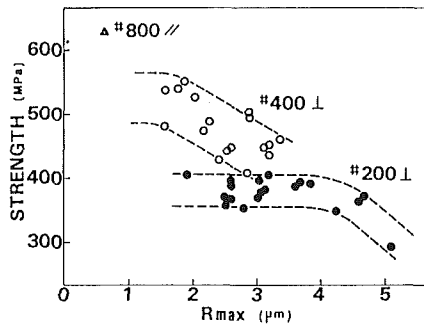


Fig. 11 The relationship between surface roughness and strength

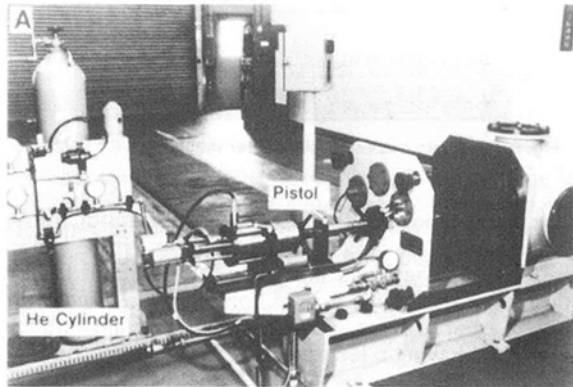


Fig. 12 Experimental apparatus

where De and Dp are dimensionless constants, r is the indenter radius, Kc is the material fracture toughness, E is the Young's modulus, and H is the hardness. In the case of machining, where the indenter is assumed to be a grain of a diamond grinding wheel and Lp is much smaller than Le [10], the median/radial crack size becomes the important factor. The relationship between the indenter load and material fracture toughness is given as [11]

$$L/a^{3/2} = B \cdot Kc \quad (3)$$

where a is the crack length and B is a dimensionless constant, which becomes smaller with a narrower indenter tip radius [13]. Equation (3) indicates that lower fracture toughness and lower indenter loads result in larger cracks.

It is generally acknowledged that the machinability of a material is related to its fracture toughness, hardness, and strength. Evans et al. [14] reported that the stock removal speed, V , varies according to the material parameters Hv and Kc , and proposed the following equation:

$$V \propto L^{5/4} \cdot H^{-1/2} \cdot Kc^{-3/4} \quad (4)$$

where L is the load applied perpendicular to the wheel radius.

Stored elastic strain energy, used as an index of machinability, becomes larger for materials with low E and large σ , resulting in lower machinability. This suggests that commercially available silicon nitride has low machinability [15].

As noted earlier, surface cracks induced in ceramics during machining are a major cause of strength degradation. It is essential to understand the effect of machining damage on strength degradation of ceramics in structural applications requiring high reliability. Experiments were conducted to examine the relationship between machining and material strength. Silicon nitride specimens were ground along their longitudinal and lateral axes using diamond grinding wheels of different grain size. After grinding, the surface roughness and strength of 20 specimens were measured. In Fig. 10, residual strength is shown as a function of grain size for both grinding directions. The results clearly show that strength degradation increased with a larger grain size for grinding in the lateral direction. The fracture origin is thought to be the grinding track and/or cracks generated just below the grinding track. As strength degradation increased with a larger grain size, the track length became larger [16].

The results in Fig. 11 show residual strength as a function of surface roughness. There is some correlation between surface roughness and residual strength resulting from the grain size of the grinding wheel used. In reality, residual strength is determined by the crack size just below the grinding track and so the relationship between surface roughness and strength is thought to be provisional. While residual strength is an important factor in stress simulation, the effect of residual strength on reliability is also considerable.

Impact Damage to Silicon Nitride

Ceramics are inherently brittle and cracks caused by point indentations have been reported to lead to catastrophic failure [17]. In-service examples of this behavior include the failure of aircraft turbine blades caused by ingestion of solid particles [18] and Hertzian cone cracks in helicopter windshields resulting from flotation of solid particles [19]. Results of a model analysis also indicate impact damage to the glassy coating of the heat shield tiles used on the space shuttles [20]. These phenomena have been studied and analyzed using Hertzian cone-fracture theory [21]. In the case of turbine blades in automotive turbochargers, it is thought that oxide scale, particles of welding beads, and residual particles of casting sand can become the cause of catastrophic failure.

Extensive studies have been made of the impact damage to silicon nitride for the purpose of assuring durability of automotive turbocharger rotors made of this ceramic [22]. In the course of developing ceramic rotors at Nissan, impact damage behavior was examined in basic model tests and durability testing was done. The results were then used in designing the turbocharger rotors. Analyses were made of the blade thickness and damage effects of different impactors were also examined in developing practical silicon nitride ceramics for rotor application [22]. Computer simulations were also performed to analyze the stress level [23] and finally the fabricated rotors were subjected to durability tests.

Model Impact Test. Commercially available gas-pressure-sintered silicon nitride was obtained from NGK Spark Plug CO., Ltd. Partially stabilized zirconia (PSZ) spheres 1.0 mm in diameter were obtained from Toso Co., Ltd. and used in impact tests to represent oxide scale, casting sand, and steel particles of welding beads. The silicon nitride specimens, measuring $50 \times 8 \times 3$ mm, $50 \times 8 \times 2$ mm, and $50 \times 8 \times 1$ mm, were polished with two grades of diamond paste ($6 \mu\text{m}$ and $3 \mu\text{m}$) to eliminate surface machining damage. The specimens were oriented perpendicularly to the approach direction. A helium gas gun (Fig. 12) was used to fire the particles at velocities ranging from 100–330 m/s. After the impact tests,

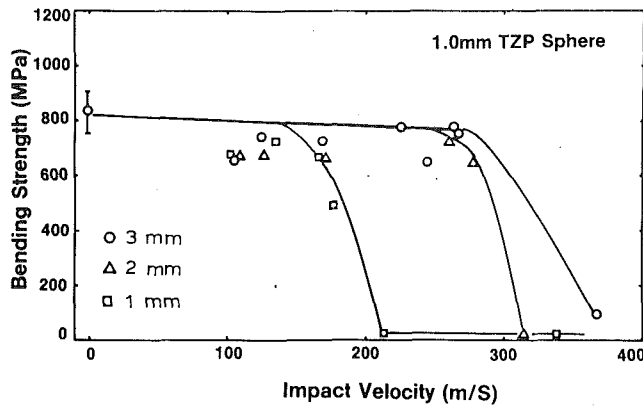


Fig. 13 Post-impact bending strength showing different strength degradation trends for different blade thicknesses

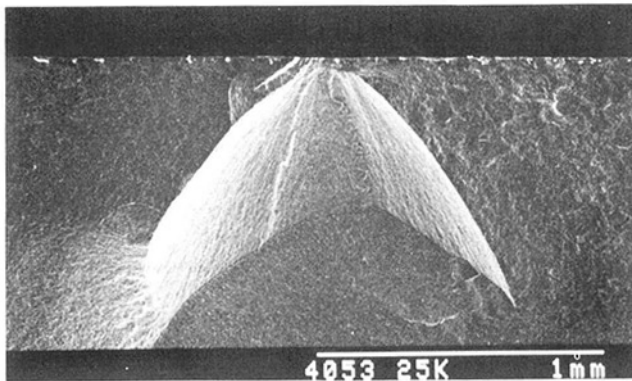


Fig. 14 Hertzian cone crack initiated at the fractured surface

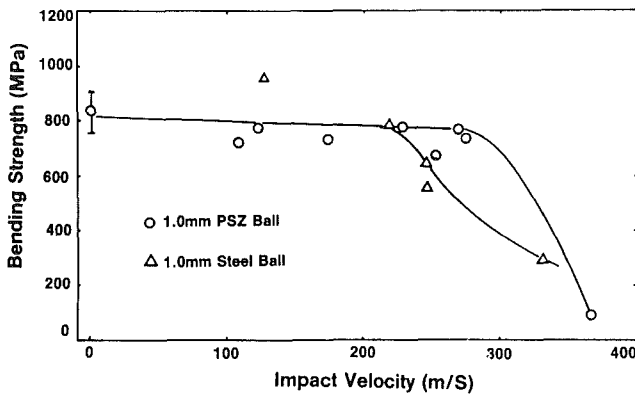


Fig. 15 Post-impact bending strength showing different strength degradation trends for different impactors (specimen thickness = 3 mm)

the residual strength was measured in a four-point bending test (inner span: 10 mm, outer span: 30 mm) at a crosshead speed of 0.5 mm/min. Fractured surfaces were examined by scanning electron microscopy (SEM).

Effect of Turbine Blade Thickness. The postimpact bending strength of the silicon nitrides specimens is shown in Fig. 13 as a function of the impact velocity for three blade thicknesses. For the 2- and 3-mm-thick blades, strength was maintained nearly up to an impact velocity of 290 m/s, when a sudden drop occurred. The PSZ spheres were crushed at a speed of 200 m/s. The bending strength of the 1-mm-thick blade decreased rapidly below 200 m/s. A Hertzian cone crack [21] connected to a surface ring crack was generated in the specimen resulting in strength degradation. This result suggested that impact damage initiated Hertzian cone cracks more

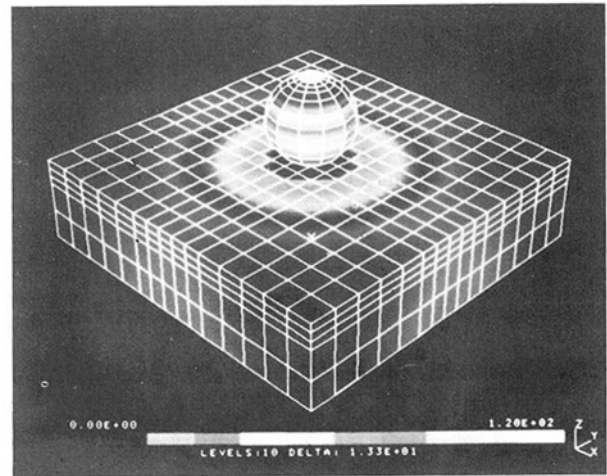


Fig. 16 FEM stress analysis using DYNA3D

easily in the 1-mm-thick specimen than in the 2- or 3-mm-thick specimens. Although a precise stress analysis was not conducted, it is thought that the effect of crack initiation, in terms of the reflected stress wave, caused much higher stress in the 1-mm-thick specimen than in the thicker ones. A micrograph of a Hertzian cone crack in the GPSSN is shown in Fig. 14 for a 3-mm-thick specimen.

Effect of Impactor Materials. Figure 15 shows the difference in strength degradation behavior for two different impactors. With the PSZ spheres, strength degradation occurred at 290 m/s, similar to the results seen in Fig. 13. With the metal impactors, a Hertzian cone crack was initiated in the specimens, although only slight damage was observed on the surface. The crack initiation velocity was lower than in the case of the PSZ spheres. In this case, plastic deformation on the target was not observed. It is presumed that the sphere was probably deformed when the impact load was fully translated to the target, resulting in the generation of a Hertzian stress field. The critical impact velocity of the two types of sphere was accurately compared using the following equation proposed by Wiederhorn and Lawn [24]:

$$Vc_1/Vc_2 = (\rho_2/\rho_1)^{1/2} \quad (5)$$

The subscripts 1 and 2 denote ceramics and metal, respectively. The calculation and experimental results agreed well in a ratio of 1.14.

Dynamic Stress Analysis using DYNA3D. The Hertzian cone crack theory [21] is usually applied to an analysis of fracture behavior resulting from a spherical particle impact. In this work, a dynamic stress analysis was performed using DYNA3D developed by Halloquist [23]. The FEM model was structured with a target size of $4 \times 4 \times 1$ mm, using 1125 hexagonal solid elements to express the target, and a sphere diameter of 1 mm, using 816 pentagonal and hexagonal elements to represent the sphere.

The location of maximum principal stress at $0.6 \mu\text{s}$ after impact is shown in Fig. 16. The maximum stress level (ring shape) is equivalent to the material strength level at a 90-deg impact angle. Its direction is the same as σ_{22} and it is caused by σ_{11} . It corresponds to a ring crack at the top of a Hertzian cone crack. The Hertzian cone crack is thought to extend inward along the σ_{33} direction from a surface ring crack. The results of a computer simulation indicated that the stress level generated at the target surface became the strength level of the material and that the shape coincided with that of the surface ring crack formed at the time of impact [25].

Durability Test [1]. A durability test was conducted under

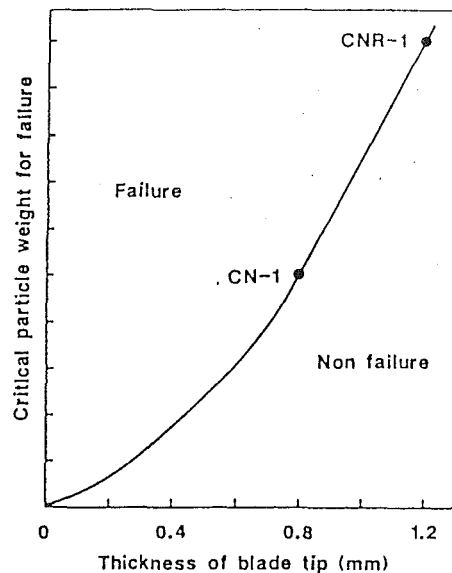


Fig. 17 Effect of blade tip thickness on dynamic strength

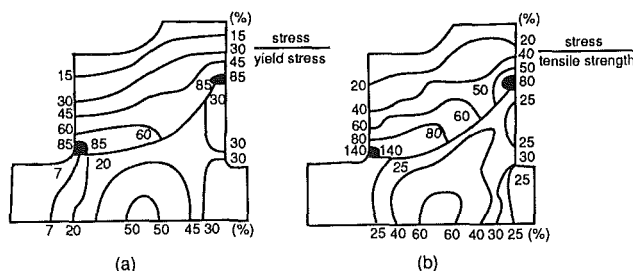


Fig. 18 Stress distributions for same rotor design: (a) metal (INCO 713C); (b) old ceramics (Si_3N_4); rotational speed: 145,000 rpm

real-world conditions using a spin impact tester. The relationship between the blade thickness at the turbine inlet and the particle load causing blade fracture is shown in Fig. 17. The dynamic strength of the turbine blade was determined by its thickness. Following these experiments, it was decided to make the thickness of the CNR-1 type turbocharger rotor 1.2 mm.

The following discussion describes some of the theories and techniques used in evaluating ceramic rotor reliability and in carrying out lifetime prediction and proof tests. Further details may be found in [1] and [27].

Reliability

According to Weibull's fracture theory, the failure probability of a ceramic component under a given stress can be found as

$$F = 1 - \exp[-(\sigma_r/\sigma_o)^m \cdot v_e] \quad (6)$$

where σ_r is the maximum stress in the ceramic component, σ_o is the characteristic strength, m is the Weibull modulus, and v_e is the effective volume. To lower the failure probability, it is necessary to reduce the stress that occurs in a ceramic component. This involves (1) reducing the level of maximum stress σ_r , (2) enhancing the material strength, i.e., increasing σ_o , and (3) reducing the variability in material strength, i.e., increasing the Weibull modulus, m . The work of developing a highly reliable turbocharger rotor was carried out on the basis of this concept.

The application of ceramics of structural components does not involve just a simple one-for-one replacement of metal materials. Figure 18 shows the results of a stress distribution

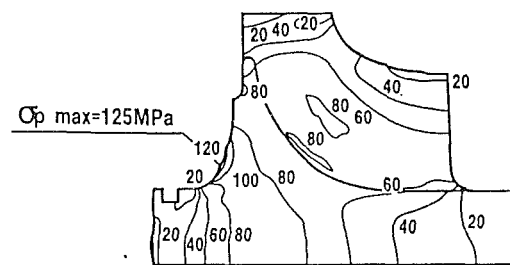


Fig. 19 Combined stress contours of rotor at steady state; rotational speed: 130,00 rpm, turbine inlet temperature: 900°C

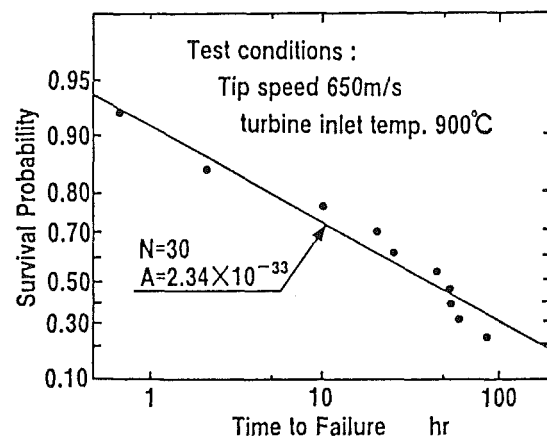


Fig. 20 Survival probability as a function of fatigue life

analysis when a ceramic material was used in place of a metal without changing the rotor design [26]. The results indicated that the shape should be changed in order to lower the maximum stress. This required a very detailed stress analysis. A three-dimensional finite element analysis technique was used in an effort to reduce stress in the ceramic rotor (Fig. 19) [28].

Lifetime Prediction

Slow crack growth under the temperature conditions of actual rotor usage is the dominant mechanism of static fatigue or delayed failure in ceramics. In general, it is thought that a crack in a ceramic component grows to critical crack length under the occurrence of stress, thereby giving rise to fracture. The lifetime of a component until an initial crack length a_i reaches the critical crack length a_c is given as

$$t_c = I[a_i^{(2-N)/2} - a_c^{(2-N)/2}] \quad (7)$$

where I is expressed as

$$I = 2/[A \cdot (N-2) \cdot Y^N \cdot \sigma_i^N] \quad (8)$$

and A and N are material constants determined by the conditions of component use, Y is shape factor, and σ_i is the stress generated under the conditions of use.

It is seen from these equations that component lifetime is determined by the initial crack length, critical crack length, applied stress, and the slow crack growth parameters A and N . However, as these values are also affected by the initial crack size and strength distribution under a condition of equal stress, it is necessary to apply statistical techniques to determine fracture probability in relation to applied stress and expected lifetime. The fracture probability of ceramic components exhibiting static fatigue can be calculated according to Weibull's theory. The initial strength distribution is correlated with the strength distribution of a fatigued material. The strength distribution of a fatigued component can be given by

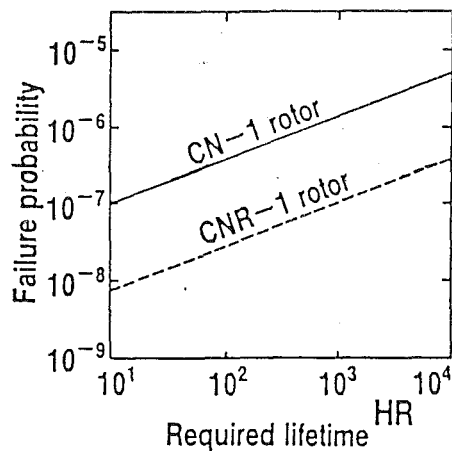


Fig. 21 Failure probability versus required lifetime

$$\ln(-\ln P) = \{m/(N-2)\} \ln t_c + \{mN/(N-2)\} \ln \sigma + \{m/(N-2)\} \ln \left[\{(N-2)/2\} Y^2 \cdot A \cdot (K_{IC}/\sigma_0)^{N-2} \right] \quad (9)$$

where P is the survival probability and is equal to $1 - F$. The values of A and N can be found from this equation. This is accomplished by carrying out a test under a given stress level up to the point where failure occurs. The length of time to failure, t_c , is represented along the horizontal axis, while the survival probability is represented along the vertical axis. The value of N can be found from the slope of the characteristic curves and the value of A from their point of intersection.

Based on this approach, a test was conducted on an actual rotor at a turbine inlet temperature of 900°C and a constant tip speed of 650 m/s . The values of A and N found from experimental results are presented in Fig. 20. The same test was conducted on another rotor of the same shape but from a separated production lot having a different mean strength. Values of $N = 33$ and $A = 4.9 \times 10^{-34}$ were obtained. Since both experiments yielded rather close values, it was verified that the values of A and N could be found from the results of rotational fatigue test conducted with actual rotors.

Using these values of A and N , the relationship between lifetime and cumulative failure probability was calculated from Eq. (9). The results are shown in Fig. 21. The data indicate that the low-stress design of the CNR-1 type rotor has lowered the failure probability by a factor of ten as compared with that of the CN-1 type rotor provides high reliability with respect to component lifetime.

Proof Testing

Sintered ceramic bodies generally show a wide variety of initial defect size, and some cannot satisfy the failure probability requirement due to their initial crack length. At present, nondestructive evaluation to detect defects in complex shapes such as turbocharger rotors. An advance proof test is conducted by putting all sintered bodies under a momentary overloading condition exceeding the design stress. This approach is effective in excluding rotors whose initial defects are so large that they could not satisfy the lifetime and failure probability requirements.

The predicted minimum guaranteed lifetime is expressed as follows:

$$t_{\min} = 2 / [(N-2) \cdot A - Y^2 \cdot K_{IC}^{N-2} \cdot \sigma^2 \cdot (\sigma/\sigma_p)^{N-2}] \quad (10)$$

where σ is the design stress and σ_p is proof stress. Figure 22 shows the results of rotational endurance experiments conducted on rotors that survived the proof test. The proof test results indicated that each rotor has a longer lifetime than the predicted minimum guaranteed lifetime and that the lifetime

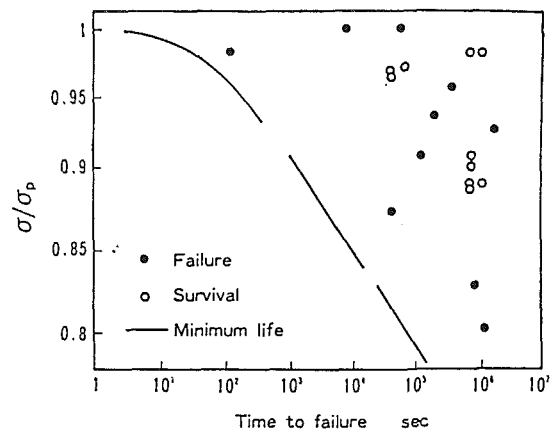


Fig. 22 Fatigue life after proof testing

prediction method, based on the values of A and N obtained with actual rotors, was a valid approach. There were no cases where the proof test itself caused initial defects to exceed the allowable limits.

Conclusions

Techniques for applying for applying ceramics to turbocharger rotor were described with reference to investigations done by other researches. Since the mechanical properties of ceramics are sensitive to defects, it is essential to eliminate defects in the fabrication process as much as possible. The technology for joining ceramics and metals is a key factor is applying ceramics to structural components. It is known that residual machining damage degrades the mechanical strength of ceramics. This makes it necessary to determine the most suitable machining conditions for ceramics. Impact damage experiments provide useful information for determining design factors and assuring the durability of turbocharger materials. Reliability evaluation, lifetime prediction, and proof test evaluation are indispensable methodologies in the application of brittle ceramics to automotive turbocharger rotors.

References

- 1 Katayama, K., Watanabe, Y., Matoba, K., and Katoh, N., "Development of Nissan High Response Ceramic Turbocharger Rotor," Society of Automotive Engineers, Technical Paper No. 861128, 1986.
- 2 Matoba, K., Katayama, K., Kawamura, M., and Mizuno, T., "The Development of Second Generation Ceramic Turbocharger Rotor—Further Improvements in Reliability," Society of Automotive Engineers, Technical Paper No. 880702, 1987.
- 3 Matsuo, I., and Nishiguchi, F., "The Development of Second Generation Ceramic Turbocharger," Society of Automotive Engineers, Technical Paper No. 880703, 1987.
- 4 Ishida, T., Noguchi, M., Ura, S., Orita, M., Enomoto, M., and Hiasa, K., "The Development of New VG30 Twin Cam Ceramic Turbo Engine for CIMA," *Nissan-Gihou (Japan)*, Vol. 24, 1989, pp. 40-45 (s63-12).
- 5 Aida, M., Nakashima, M., Kawanishi, K., Ushigima, Y., Komatsu, H., and Goto, T., "Development of a Ball-Bearing Turbocharger," *ibid.*, Vol. 25, 1989, pp. 48-54.
- 6 Ura, S., Nakamura, K., Fujita, H., Etoh, T., and Yamanaka, J., "The Development of the New RB26DETT Engine," *ibid.*, Vol. 26, 1989, pp. 44-51.
- 7 Mutsuddy, B. C., and Shetty, D. K., "Injection Molding Ceramic Parts for High-Temperature Applications," *Technical Aspects of Critical Materials Used by the Steel Industry*, Vol. II-B, 1982, National Bureau of Standards.
- 8 Nikkei New Materials, No. 68, 1989, pp. 64-71.
- 9 Ito, M., Ishida, N., and Katoh, N., "Development of Brazing Technology for Ceramics Turbocharger Rotors," Society of Automotive Engineers, Technical Paper No. 880704, 1988.
- 10 Frank, F. C., et al., "On the Theory of Hertzian Fracture," *Proc. Roy. Soc. Ser. A*, Vol. 299, 1967, p.291.
- 11 Lawn, B. R., et al., "Indentation Fracture and Strength Degradation in Ceramics," *Fracture Mechanics of Ceramics*, Vol. 3, 1978, pp. 205-229.
- 12 Lawn, B. R., et al., "A Model for Crack Initiation in Elastic/Plastic Indentation Field," *J. Mat. Sci.*, Vol. 12, 1977, p.2195.
- 13 Kirchner, H. P., et al., "Fragmentation and Damage Penetration During

Abrasive Machining of Ceramics," *The Science of Ceramics Machining and Surface Finishing II*, N. B. S Special publication, Vol. 562, 1979, pp. 23-42.

14 Evans, A. G., et al., "Quasi-Static Solid Particle Damage in Brittle Solids I," *Acta Metallurgica*, Vol. 24, 1976, pp. 939-956.

15 Ratterman, E., *Ceramic Industry*, Feb. 1986.

16 Ohta, M., et al., "The Effect of Machining Condition to the Strength," *Proc. Autumn Meeting, Japan Engineering Society*.

17 Evans, A. G., "Strength Degradation by Projectile Impacts," *J. Am. Ceram. Soc.*, Vol. 56, 1973, pp. 405-409.

18 Dao, K. C., Shockey, D. A., Seaman, L., Curran, D. R., and Rowcliffe, D. J., "Particle Impact Damage in Silicon Nitride," Annual Reports, Part III, Office of Naval Research, Contract No. 0001476-057, May 1979.

19 Abou el-leil, M., Cammaratta, F., and Digenova, R. R., "Impact Fracture of Thermally Tempered Glass Helicopter Windshields," *J. Am. Ceram. Soc.*, Vol. 68, 1985, pp. c18-c21.

20 Liaw, B. M., Kobayashi, A. S., Emery, A. F., and Du, J. J., "An Impact Damage Model of Ceramic Coating," in: *Fracture Mechanics of Ceramics*, Vol. 7, R. C. Bradt, A. G. Evans, D. P. H. Hasselman, and F. F. Lange, eds., Plenum Press, New York, 1986.

21 Hertz, H. R., *Hertz's Miscellaneous Papers*, Chaps. 5 and 6, McMillan, London, 1896.

22 Akimune, Y., Katano, Y., and Matoba, K., "Spherical Impact Damage and Strength Degradation in Silicon Nitride for Automobile Turbocharger Rotors," *J. Am. Ceram. Soc.*, Vol. 72, 1989, pp. 1422-1428.

23 Hallquist, J. O., "Theoretical Manual for DYNA3D," Lawrence Livermore Lab., W-7405-Eng-48, 1983.

24 Wiederhorn, S. M., and Lawn, B. R., "Strength Degradation of Glass Resulting From Impact With Spheres," *J. Am. Ceram. Soc.*, Vol. 60, 1977, pp. 451-458.

25 Akimune, Y., Izumi, T., Watanabe, S., and Tajima, Y., "Spherical Impact Damage in Sialon Ceramics for Turbine," *Proc. Annual Conference of Japan Ceramic Society High Temperature Division*, 1988, pp. 61-65.

26 Okazaki, Y., *Fine Ceramics Report*, Vol. 3, 1985, pp.16-23.

27 Sasaki, M., and Itoh, T., "Evaluation of Rotational Strength of Ceramic Gas Turbine Rotors and Development of Ceramic Turbocharger Rotors," *Journal of the Ceramic Society of Japan*, International Edition Vol. 97, R-1-12.

28 Itoh, T., "Reliability of Ceramic Turbocharger Rotor," *Ceramics*, Vol. 23, 1988, pp. 638-641, published by the Ceramic Society of Japan.

K. Takama

S. Sasaki

T. Shimizu

N. Kamiya

Toyota Motor Corporation,
1, Toyota-Cho Toyota Aichi,
471 Japan

Design and Evaluation of Silicon Nitride Turbocharger Rotors

Two types of silicon nitride ceramic rotor have been introduced into the Japanese market by Toyota Motor Corporation, named CT26 and CT12A, to improve engine acceleration response by the reduction in moment of inertia. In order to design a suitable blade shape for a ceramic rotor, the critical stress of the blade was determined by the results obtained experimentally from correlating the fracture origin over spin-tested rotors with centrifugal stress at fracture. A suitable blade shape has been determined for the CT26 turbocharger rotor type, which is identical to the metal rotor except for the disk diameter of hub back face and the blade thickness. The CT12A type is of similar design to the CT26 type; all dimensions could be reduced except for the inlet blade thickness, which is determined by foreign object damage (FOD) resistance.

Introduction

Toyota Motor Corporation has introduced two types of silicon nitride ceramic rotor into the Japanese market, named CT26 and CT12A. The CT26 type has been in use for the 2.0 l in-line four-cylinder engine, 3S-GTE type, maximum power output 165 kW since Oct. 1989, and the CT12A type for 2.5 l in-line six-cylinder engine with adopted twin turbochargers, 1JZ-GTE type, maximum power output 206 kW, since Aug. 1990. The CT26 type is the large-sized rotor and CT12A type is the small-sized rotor in the turbocharger series of Toyota. We have already been in mass production of ceramic parts for the ceramic swirl lower chamber of 2L-T type diesel engine since Aug. 1984 [1]. The technology in this development was applied to mass production of the ceramic rotor. The objectives of this paper are to describe the design and evaluation methods of these ceramic rotors.

In the development of the CT26 type, three typical models for ceramic rotors were studied in order to determine the most suitable blade design capable of reducing the moment of inertia without loss of turbine efficiency, and of ensuring high strength and reliability [2]. In the case of the CT12A type, two models of ceramic rotors were studied in order to determine the most suitable blade shape for the performance inertia described above.

We came to the conclusion that the most suitable blade shape for the CT26 type should be identical to the metal rotor except for the disk diameter (D) of the hub back face and the blade thickness (t). The disk diameter is $0.7D$ and the blade thickness is $1.7t$. (D and t refer to the size of the metal rotor.) The CT12A type rotor is of similar design to the CT26 type, with all dimensions reduced except the inlet blade thickness. The blade thickness is the same size as the CT26 type because the

thickness is determined by foreign object damage (FOD) resistance [3–5].

The ceramic rotor turbocharger efficiency was almost the same as that of the metal rotor in both the CT26 and CT12A types, while the moment of inertia was reduced by about 60 percent over that of metal turbine rotor assembly [2].

Design of the CT26 Type Ceramic Rotor

The ceramic turbine rotor has been developed to reduce the rotor moment of inertia without loss of turbine efficiency. Generally, the ceramic strength is lower than that of the metal. Therefore, for the ceramic turbine rotor, it is necessary to change the blade shape to reduce centrifugal stress and increase the blade thickness to improve the damage resistance of the blades. However, these improvement factors prevent reduction of the rotor moment of inertia. In consequence, the optimum rotor shape was studied by FEA stress analysis. Three typical models for the ceramic rotor were used in order to determine


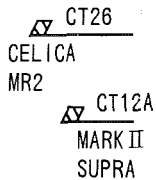
Years	1985	1990
Ceramic Swirl Lower-Chamber		
Ceramic Rotor		

Fig. 1 Introduction year of ceramic swirl lower chamber and ceramic rotor

Contributed by the International Gas Turbine Institute and presented at the 36th International Gas Turbine and Aeroengine Congress and Exposition, Orlando, Florida, June 3–6, 1991. Manuscript received at ASME Headquarters March 4, 1991. Paper No. 91-GT-258. Associate Technical Editor: L. A. Riekert.

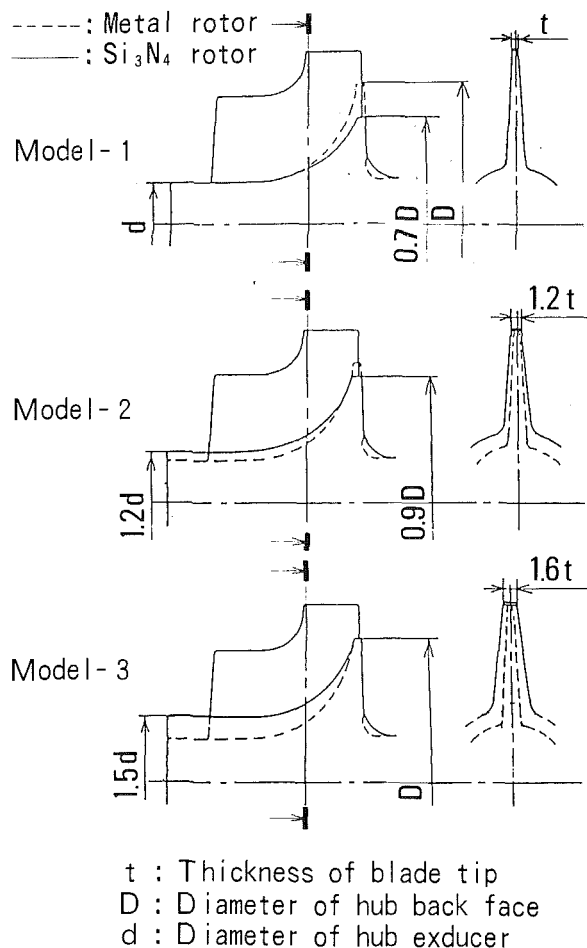


Fig. 2 Typical models for ceramic rotor; t , D , and d are thickness of blade tip, diameter of hub back face, and diameter of hub exducer of conventional metal rotor, respectively

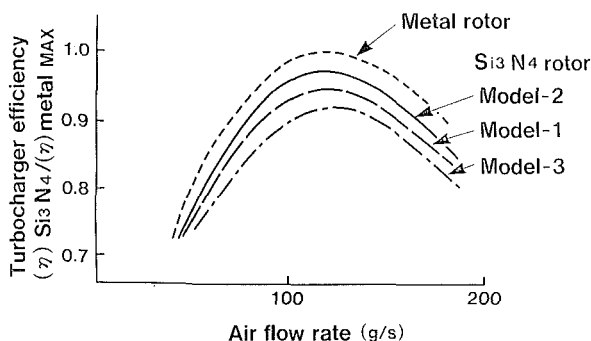


Fig. 3 Turbocharger efficiency versus air flow rate for each model

the most suitable design capable of reducing the moment of inertia, as well as ensuring good aerodynamic characteristics and high strength and reliability. Figure 2 shows three typical models for the ceramic rotor.

Model 1. Modifications to the metal rotor shape include:

- 1 Small-sized disk diameter of the hub back face.
- 2 Enlarged R portion of the blade root.

The objective of this model is to reduce the rotor moment of inertia as much as possible.

Model 2. Modifications to the metal rotor shape include:

- 1 Increased blade thickness.
- 2 Increased hub diameter.
- 3 Small-sized disk diameter of the hub back face. The disk

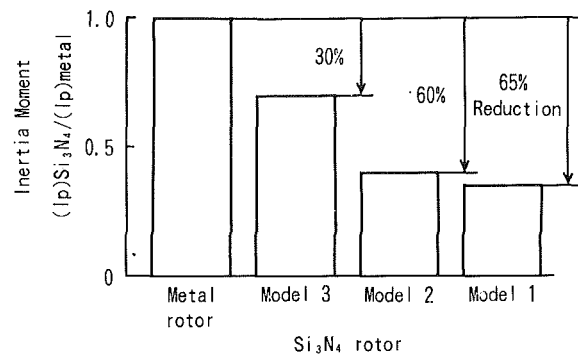
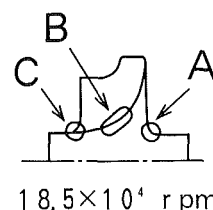


Fig. 4 Comparison of moment of inertia

Table 1 Centrifugal stress calculated by finite element analysis
(Unit: MPa)

Region	A	B	C
Model 1-1	310	250	250
Model 1-2	390	280	220
Model 1-3	310	390	170



size in this case is between that of Model 1 and the metal rotors.

The objective of this model is to improve the damage resistance of the blades and to reduce the stress at the hub exducer root.

Model 3. Modifications to the metal rotor shape include:

- 1 Increased blade thickness compared with 2.
- 2 Increased hub diameter compared with 2.
- 3 Decrease in the number of blades from 10 to 9 to maintain the throat area of the turbine rotor.

The objective of this model is to improve the damage resistance of the blade and the centrifugal stress.

Centrifugal Stress Calculated by Finite Element Analysis. Table 1 shows the maximum stress of three models calculated by FEA stress analysis. The stress at A in Model 2 is 26 percent higher than that of Model 1. This shows that the disk diameter of the hub back face should be small as long as there is no decrease in turbocharger efficiency for each model. The stress at C in Model 2 is lower than that of Model 1. This shows that the stress of the hub exducer root can be reduced by increasing the hub exducer diameter. The disk diameter of the hub back face is the same as that of the metal rotor to prevent a loss of turbocharger efficiency caused by the increase in blade thickness and hub exducer diameter. The stress at A in Model 3 is decreased remarkably by increasing the hub diameter.

Turbocharger Efficiency and Moment of Inertia. Figure 3 shows the efficiency of the ceramic turbocharger for three models, compared with that of the metal rotor. Model 3 has the lowest efficiency among the three models, because the main objective of this model was to improve the FOD and centrifugal stress resistance. It is presumed that the small diameter of the hub back face contributed to the loss of turbocharger efficiency in Model 1.

Figure 4 compares the moment of inertia between metal and ceramic rotors. Model 1 achieves about a 65 percent reduction in the moment of inertia compared with the metal rotor. The

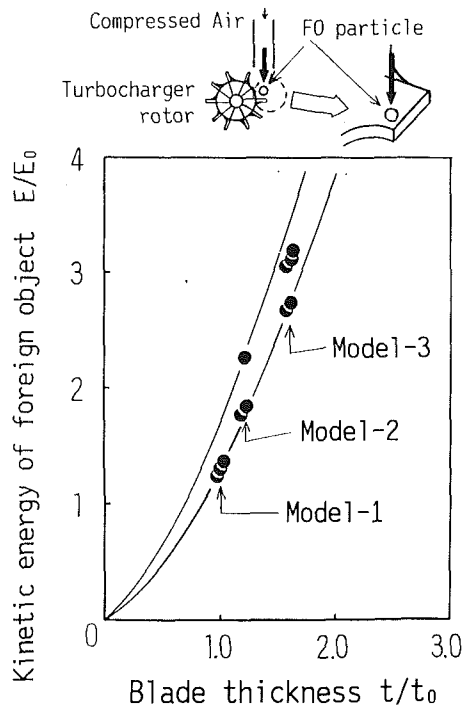


Fig. 5 FOD resistance for three models by the static FOD method

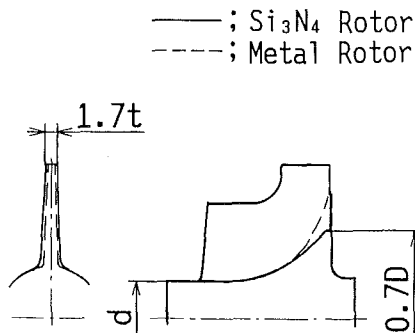


Fig. 6 Final shape of the ceramic rotor for mass production

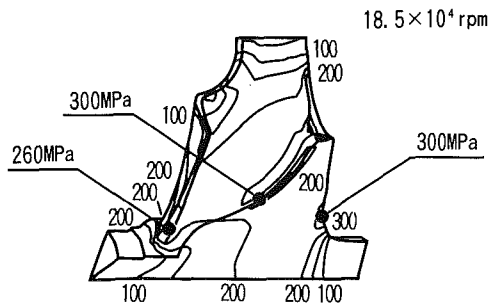


Fig. 7 Calculated centrifugal stress distribution at room temperature

moment of inertia increased by improving FOD and centrifugal stress resistance in Model 3.

FOD Resistance of Blade Inlet Tips. FOD evaluation was carried out using the static collision method (particles were impacted on the rotor under static condition) and the dynamic method (particles were impacted under dynamic conditions). Figure 5 shows FOD resistance for the three models by the static FOD method. The FOD resistance was defined as the point at which the particle's kinetic energy caused cracking on the blade tips. The thickness of the blades in Model 3 was

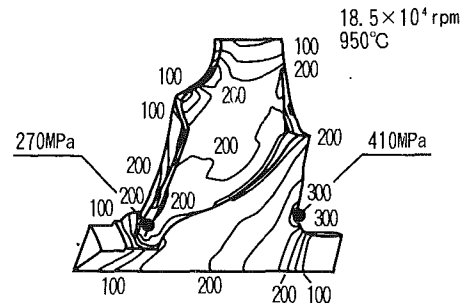


Fig. 8 Calculated stress distribution due to both thermal and centrifugal stress

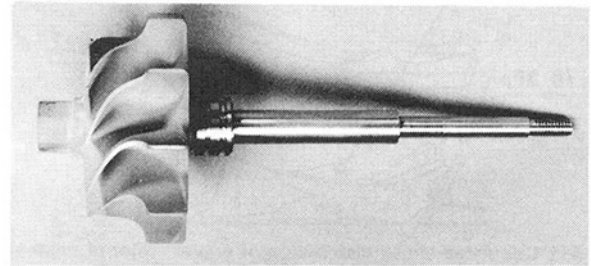


Fig. 9 Mass-produced ceramic rotor

Table 2 Summary of preliminary evaluation of ceramic rotors with different models

	Strength	Inertia Moment	Turbocharger Efficiency	FOD Resistance
Model-1	Excellent	Excellent	Good	Poor
Model-2	Good	Excellent	Good	Good
Model-3	Excellent	Good	Poor	Excellent

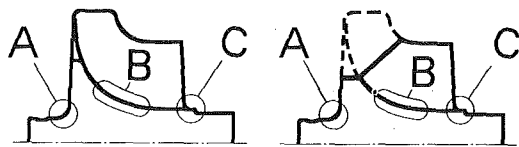
increased by 60 percent over that of Model 1, thus increasing the critical kinetic energy of the particles by 2 to 2.5 times [6].

Final Design for Mass Production. Table 2 shows the pre-evaluation results of the ceramic rotor for the three models. The advantages of each model were incorporated into the final design in order to reduce moment of inertia and centrifugal stress as well as improve FOD resistance and turbocharger efficiency. A suitable design was determined on the basis of Model 1, with the blade thickness similar to that of a Model 3. The centrifugal stress was reduced by the modification of the disk diameter of hub back face and the enlarged R portion of the blade root. Figure 6 shows the final dimensions of the ceramic rotor for mass production.

Figures 7 and 8 show the calculated centrifugal stress distribution of the final ceramic rotor model under room temperature and 950°C, respectively. In the case of this rotor, the fracture was estimated to start from the hub back face under over spin condition. This portion has the highest centrifugal stress. There is a good correlation between the fracture origin of the rotor and the centrifugal stress distribution. A mass-produced silicon nitride ceramic rotor is shown in Fig. 9.

Design of the CT12A Type Ceramic Rotor

In the case of design for the CT12A type, a similar design to the CT26 type was used. All dimensions were reduced except for the inlet blade thickness. The blade thickness is the same as the CT26 type, because the thickness is determined by FOD



Original Rotor Model 6 Rotor

Fig. 10 Blade shape used to obtain the correlation between the fracture origin of the rotor and the centrifugal stress at the fracture speed

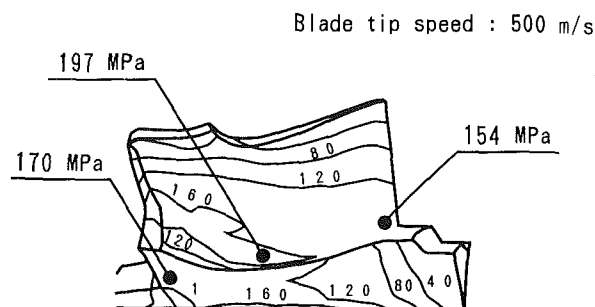


Fig. 11 Calculated stress distribution of original rotor at room temperature

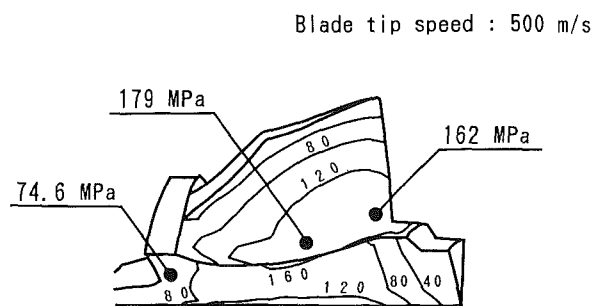


Fig. 12 Calculated stress distribution of Model 6 rotor at room temperature

resistance. Therefore, the centrifugal stress distribution was different from that of the CT26 type, and the centrifugal stress became higher than that of the CT26 type, in which the critical stress for the ceramic material is found.

Therefore, we designed and evaluated two typical models for ceramic rotors with different blade shapes. Model 4 has a blade shape in which the stress distribution meets the large-sized (the CT26 type) ceramic rotor design standard. Model 5 has a blade shape in which the stress distribution is the critical stress for hub back face, center blade root, and hub exducer root, respectively [7, 8].

Model 4: The stress distribution of the blade meets the large-sized ceramic rotor design standard.

Model 5: The stress distribution of the blade is the critical stress. This new blade design is based on results obtained experimentally by correlating the fracture origin of spin-tested rotors with centrifugal stress at fracture.

Experimental Verification of the Fracture Origin. Figure 10 shows the blade shape that was used to obtain the correlation between the fracture origin of the rotor and the centrifugal stress at the fracture speed. The blade inlet tip portion of the model ceramic rotor was eliminated in order to reduce the centrifugal stress of the hub back face. The portions designated

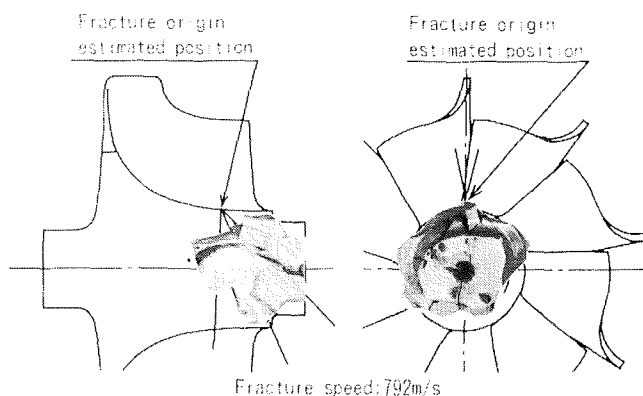


Fig. 13 Experimental verification of the fracture origin



Fig. 14 Photograph of typical rotor failure

A, B, C indicate hub back face, center blade root, and hub exducer, respectively.

Figures 11 and 12 show the FEA stress analysis for the original rotor and the model rotor. The original rotor stress distribution is almost equal to that of the CT26 type. The centrifugal stress of hub back face in the model rotor was reduced by the elimination of the inlet tip portion of the blades.

Table 3 shows the stress distribution for the original rotor and the model rotor under over spin conditions. The original rotor fractured when the rotor tip speed was 713 m/s. The origin of fracture was estimated to be on the hub back face by experimental verification. From this fact, the allowable level of centrifugal stress of A portion became 344 MPa. The model rotor fractured when the rotor tip speed was 756 m/s. The origin of fracture was estimated to be on the center of the blade root. Consequently, the allowable level of centrifugal stress of the B portion became 408 MPa. As the centrifugal stress of portion C is not affected by thermal stress, the allowable level of centrifugal stress of the C portion was able to be determined to be within 372 MPa to 408 MPa. The new allowable levels of centrifugal stress of blade are indicated by a single underline in Table 3.

Figure 13 shows one method of experimental verification of the fracture origin for Model 6. The experimental verification of the fracture origin was carried out by restoring the fragments of the ceramic rotor. The fracture origin was estimated to be the B portion of the rotor [7].

The other experimental method was also used in order to estimate the fracture origin of the rotor, which was carried out by taking photographs at fracture. Figure 14 shows this other method. This work was carried out by Kamiya et al. [9].

Determination of the Blade Profile. Figure 15 shows the rotor cross section for Models 4 and 5. The hub exducer diameter of Model 4 is larger than that of Model 5 in order to reduce the stress at the center of the hub root and the hub

Table 3 Stress distribution for the original rotor and the model rotor under over spin condition

	m/s Fracture speed	Centrifugal stress at fracture speed MPa		
		A	B	C
*Model 6	7 5 6	1 7 1	4 0 8	3 7 2
Original	7 1 3	3 4 4	4 0 0	3 1 4

* blade tips portion of ceramic rotor is eliminated

Table 4 Comparison of the moment of inertia and the turbocharger efficiency

		Model 4	Model 5	Metal
	Rotor+Compressor Wheel etc.	6 5	6 0	1 0 0
Moment of Inertia	Rotor	4 9	4 0	1 0 0
Turbocharger Efficiency		9 5	9 8	1 0 0

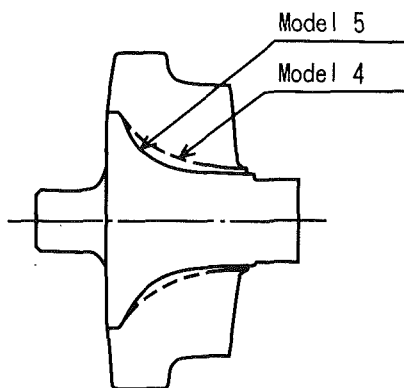


Fig. 15 Rotor cross section for Models 4 and 5

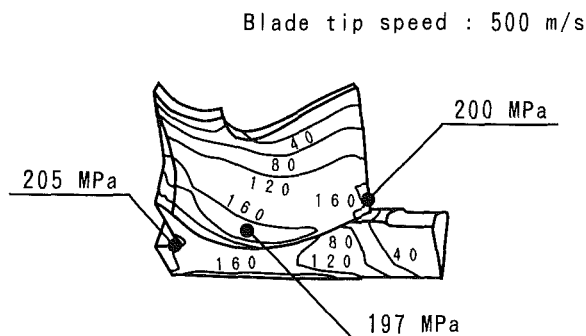


Fig. 16 Calculated centrifugal stress distribution for Model 4 at room temperature

exducer root. The profile of Model 5 became almost the same as that of the metal rotor except for the blade thickness. Figures 16 and 17 show the results of FEA stress analysis. The target stress for each model was achieved.

Table 4 compares the moment of inertia and the turbocharger efficiency of the metal and ceramic rotors. Model 5 has better performance in terms of the moment of inertia and turbocharger efficiency than the Model 4 rotor.

Blade tip speed : 500 m/s

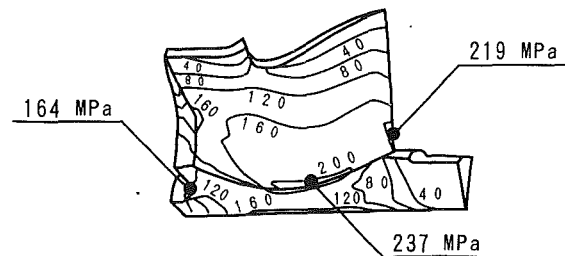


Fig. 17 Calculated centrifugal stress distribution for Model 5 at room temperature

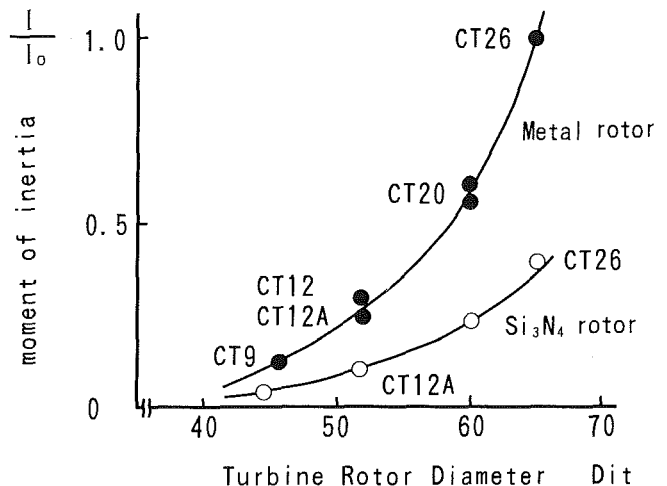


Fig. 18 Comparison of the moment of inertia between metal and ceramic rotors

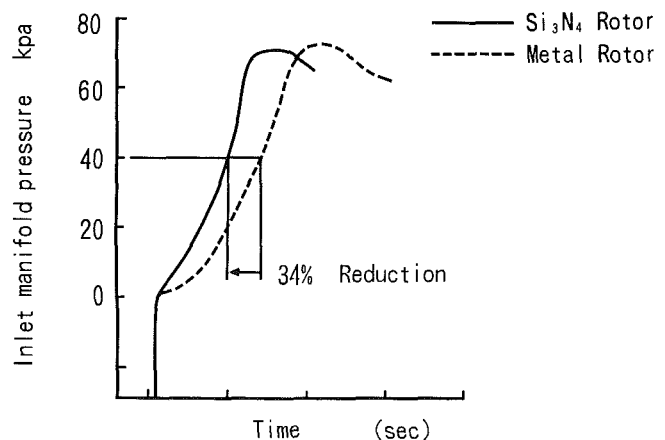


Fig. 19 Acceleration response for the ceramic rotor

Reduction in Moment of Inertia of the Turbine Rotor Assembly. Figure 18 shows a comparison of the moment of inertia between metal and ceramic rotors of the Toyota turbocharger series. Ceramic rotors enable a reduction in moment of inertia of 60 percent compared with metal rotors for both the CT26 and CT12A types. These results could be achieved with the work of the most suitable blade design capable of reducing the moment of inertia without loss of efficiency, and of ensuring high strength and reliability. Ceramic rotors of CT20 and CT9 types are the experimental models.

Acceleration Response. Figure 19 shows the acceleration response for the ceramic rotor. The boost pressure was meas-

ured under the condition of WOT acceleration and initial vehicle speed of 20 km/h. The response time to boost pressure up to kPa was decreased by about 34 percent. This improvement in response can be easily recognized in actual driving conditions.

Conclusions

1 Toyota Motor Corporation has introduced two types of silicon nitride ceramic rotor into the Japanese markets, designated the CT26 type, which is a large-sized rotor, and the CT12A type, which is the small-sized rotor.

2 In the case of ceramic rotor design, it is difficult to use the same concept as in metal rotor design, because the ceramic strength is lower than that of metal, and the inlet blade thickness is determined by FOD resistance. In other words, applying the large-sized ceramic rotor design to the small-sized one negated the effect of ceramic rotor from the standpoint of weight. To overcome this problem, in the case of the small-sized rotor design, the blade shape was redesigned based on results obtained experimentally by correlating the fracture origin of the spin-tested rotors with the centrifugal stress at fracture. From these developments, we could establish the design method for ceramic rotor from the large-sized rotor to the small-sized one.

3 The most suitable blade shape has been determined for the CT26 type, which is identical to the metal rotor except for the disk diameter of hub back face and the blade thickness. The CT12A type is of similar shape to the CT26 type but reduced in all dimensions except for the inlet blade thickness.

The blade thickness is the same size as the CT26 type, because this thickness is determined by FOD resistance, regardless of the size of the rotor.

4 Ceramic rotors enabled a reduction in moment of inertia by about 60 percent compared to metal rotors for both CT26 and CT12A types. The engine acceleration response was improved noticeably by the reduced moment of inertia.

References

- 1 Kamiya, S., Murachi, M., Kawamoto, H., Kawakami, S., and Suzuki, Y., "Silicon Nitride Swirl Lower-Chamber for High Power Turbocharger Diesel Engines," *SAE Transactions*, 850523, 1985, pp. 3.894-3.906.
- 2 Shimizu, T., Takama, K., Enokishima, H., Mikame, K., Tsuji, S., and Kamiya, N., "Silicon Nitride Turbocharger Rotor for High Performance Automotive Engines," SAE Paper No. 900656, 1990.
- 3 Hamano, Y., Sagawa, N., and Miyata, H., "Reliability Evaluation of Ceramic Rotor for Passenger-Car Turbochargers," *ASME JOURNAL OF ENGINEERING FOR GAS TURBINES AND POWER*, Vol. 108, pp. 531-535.
- 4 Matsui, M., Soma, T., Ishida, Y., and Oda, I., "Life Time Prediction of Ceramic Turbocharger Rotor," SAE Paper No. 860443, 1986.
- 5 Toft, G. B., Coy, R. C., Krumm, H., and Muennighoff, H. W., "The Development of a Severe Turbocharger Bench Engine Test," SAE Paper No. 880258, 1988.
- 6 Matoba, K., Katayama, K., Kawamura, M., and Mizuno, T., "The Development of Second Generation Ceramic Turbocharger Rotor—Further Improvements in Reliability," SAE Paper No. 880702, 1988.
- 7 Sasaki, S., Akai, W., Hiei, M., and Okano, H., "Design and Test of Silicon Nitride Radial Turbine Wheel," submitted to the International Gas Turbine Conference, 1991.
- 8 Ozawa, T., Matsuhisa, T., Kobayashi, Y., Matsuo, E., and Inagaki, T., "Hot-Gas Spin Testing of Ceramic Turbine Rotor at TIT 1300°C," SAE Paper No. 890427, 1989.
- 9 Kamiya, N., Asai, M., Bessho, A., and Wada, S., "Determination of Fracture Origin in Ceramic Radial Rotor by Taking Photographs at Failure From Two or Three Directions," ASME Paper No. 90-GT-383, 1990.

H. Kawase

K. Kato

T. Matsuhisa

T. Mizuno

NGK Insulators, Ltd.,
Nagoya, Japan

Development of Ceramic Turbocharger Rotors for High-Temperature Use

A ceramic turbocharger rotor (CTR) for high-temperature use has been developed. The features of this rotor are the use of silicon nitride, which maintains high mechanical strength up to 1200°C, and a new joining technique between the ceramic rotor and its metal shaft. The CTR is expected to cope with stoichiometric mixture burning engines, which produce a higher exhaust gas temperature for fuel economy, and the impact resistance of the rotor against foreign object damage (FOD) has been markedly increased, over that of earlier rotors, resulting in higher reliability. This paper describes the development of ceramic turbocharger rotors for high-temperature use, focusing on the mechanical strength of silicon nitride and the joining of the ceramic rotor and its metal shaft.

Introduction

Turbochargers adopting ceramic turbine wheels for improving vehicle acceleration response have been successfully introduced to the market. Recent turbochargers adopt ball bearings [1] and VGS (Variable Geometry Systems) [2] to improve response to acceleration sufficiently.

Demand for automotive engines with high power and low fuel consumption is increasing year by year. New CAFE regulations will especially intensify the need for fuel economy. One of the approaches to achieve low fuel consumption is stoichiometric mixture burning engines, which produce a high exhaust gas temperature [3]. At present the exhaust gas temperature is around a maximum of 900°C because of the heat resistance of the engine system. The application of high mechanical strength, heat-resistant ceramic parts is expected to cope with rising exhaust gas temperatures.

NGK developed a CTR made of silicon nitride (material code: SN-60) in its first generation in 1986. Recently we have developed a second generation of CTR for use at high temperatures, adopting a silicon nitride (material code: SN-84EC) featuring high mechanical strength up to 1200°C and newly developed joining of the ceramic rotor and its metal shaft. This CTR has been successfully demonstrated in IHI's turbocharger for Honda Formula-1 race cars, which require rotors to withstand high exhaust gas temperatures of around 1030°C [4]. This second generation of CTR is commercially mass produced for Nissan Motor Co.

Development of Ceramic Material

Silicon nitride is one of the best structural materials because of its high mechanical strength and high fracture toughness

compared with other ceramic materials. Generally, the microstructure of interlocked elongated silicon nitride crystals features high mechanical strength and high fracture toughness [5, 6]. The amount and softening point of the intergranular glassy phase greatly affect high-temperature strength in the sintered body. In view of these points, we studied the types and component ratios of the sintering additives and also investigated the production process to develop a new silicon nitride (SN-84EC) material featuring high mechanical strength up to 1200°C.

High mechanical strength at high temperatures is required for the turbine wheel of the automotive turbocharger because it is subjected not only to a high centrifugal force resulting from the high rotating speed (generally around 100,000 rpm or more), but also to a high thermal stress caused by exposure to high exhaust gas temperatures. It is also important to consider slow crack growth (SCG) caused by the growth of initial internal flaws, which result in fatigue failure, and creep failure caused under high stress at high temperature [7]. Another important CTR characteristic is the impact resistance against foreign object damage (FOD), such as particles of oxide peeled off from the interior of the exhaust manifold. The results of our evaluating each characteristic are explained below. Each evaluation was made using specimens cut out from actual ceramic rotors.

1 Mechanical Strength at Elevated Temperature. Figure 1 shows the flexural strength versus temperature characteristics of newly developed SN-84EC and conventional SN-60. The SN-84EC maintains high strength up to 1200°C. Figure 2 shows the comparison of high-temperature tensile strength of SN-84EC and nickel base Inconel 713C, which is widely used for metal turbocharger rotors, and super-heat-resistant alloy Mar-M-247 used for high-temperature exhaust gas racing cars [4]. The strength of metals drops sharply at around 800°C, while

Contributed by the International Gas Turbine Institute and presented at the 36th International Gas Turbine and Aeroengine Congress and Exposition, Orlando, Florida, June 3-6, 1991. Manuscript received at ASME Headquarters March 4, 1991. Paper No. 91-GT-270. Associate Technical Editor: L. A. Riekert.

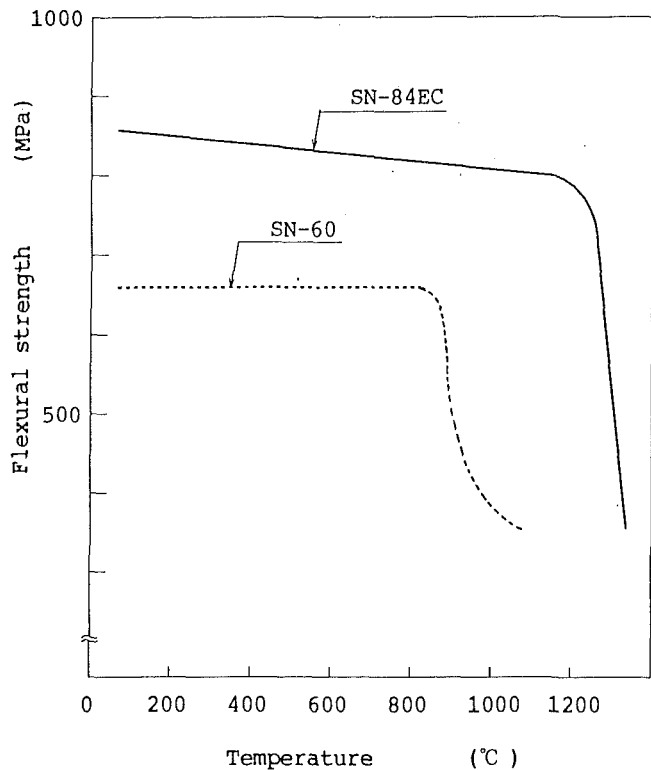


Fig. 1 Flexural strength (four-point bending) of SN-84EC and SN-60

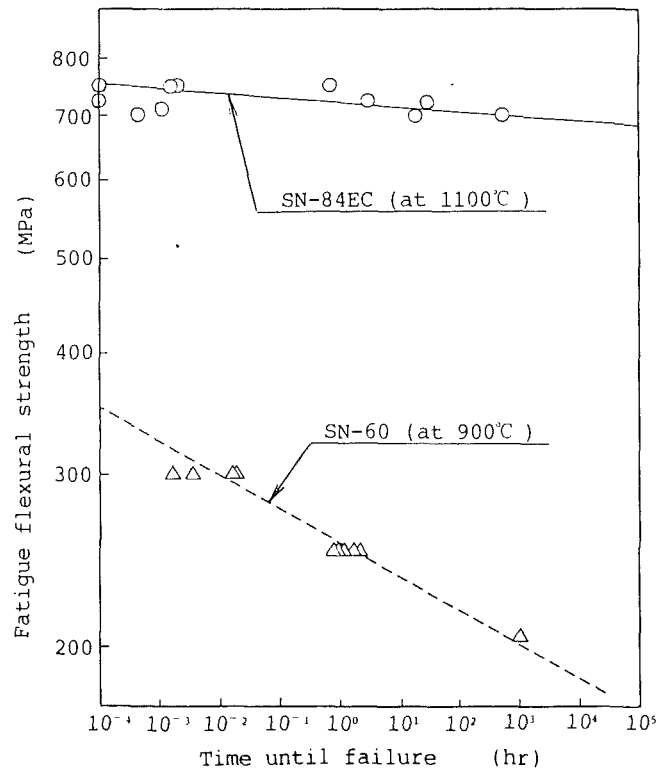


Fig. 3 Fatigue flexural strength (four-point bending)

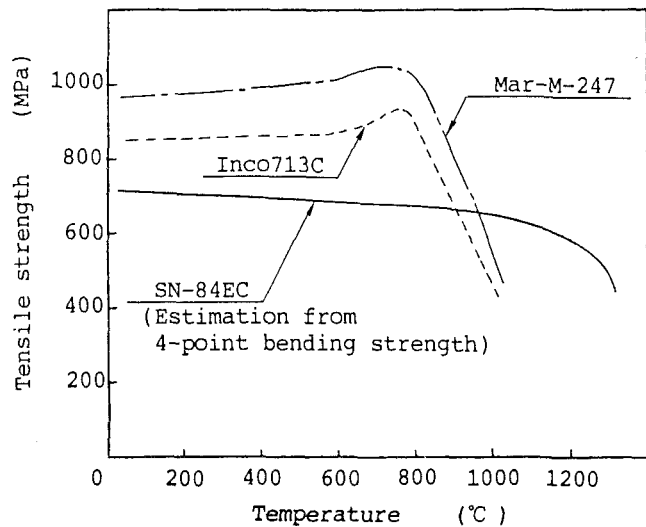


Fig. 2 Tensile strength of SN-84EC and metals

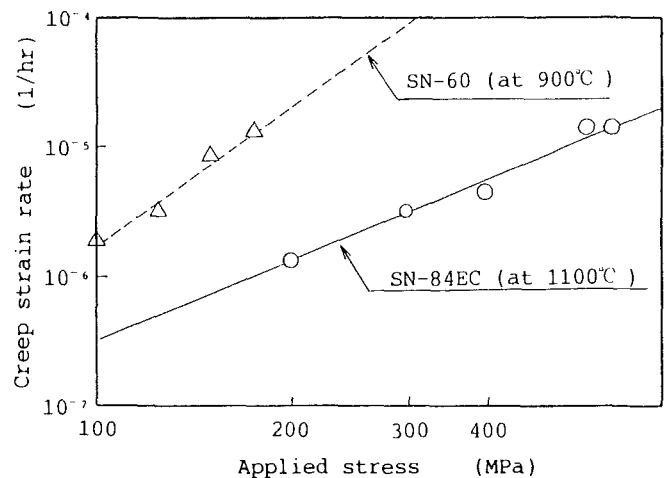


Fig. 4 Creep strain rate versus applied flexural stress (four-point bending)

SN-84EC is superior to these metals up to about 900°C and maintains high strength up to 1200°C. In view of these high use temperatures, SN-84EC is expected to have much better reliability than conventional heat-resistant metals.

2 Static Fatigue and Creep. SN-60 was evaluated at the present maximum exhaust gas temperature of 900°C and SN-84EC was evaluated at 1100°C, because the target temperature of the exhaust gas is expected to be around 1050°C [8]. Figure 3 shows static fatigue test data, and Fig. 4 shows creep strain rate versus flexural stress of SN-84EC and SN-60. Both results for SN-84EC are superior to those for SN-60, which has been successfully used in commercial production.

3 Resistance Against FOD. In order to ensure the reli-

ability of the CTR, it is essential to maintain high resistance against foreign object damage (FOD). It is known that the resistance against FOD depends on the mechanical strength and fracture toughness of the material [9]. The mechanical strength of SN-84EC is superior to that of SN-60 as stated previously. Table 1 shows the K_{IC} values of SN-84EC and SN-60 at various temperatures. The K_{IC} value of SN-84EC remains high at even 1200°C.

FOD can occur in several fracture modes, including: chipping fracture, cantilever beam fracture, flexural fracture, and hertzian fracture [9]. Based on our experience in CTR studies, the chipping fracture is one of the most important modes. To evaluate the resistance against chipping fracture of SN-84EC and SN-60, the critical velocity of chipping fracture caused by foreign objects was measured using the experimental device

Table 1 Fracture toughness K_{IC} (MN/m^{3/2})

Temp.	SN	SN-84EC	SN-60
R.T.		6	6
700 °C		6	6
900 °C		6	5
1,000 °C		6	—
1,200 °C		7	—

Table 2 Comparison of critical velocity for chipping fracture

Si ₃ N ₄	SN-84EC	SN-60
Critical velocity	2.2 Vo	Vo

Table 3 Material properties of SN-84EC

Property	Material	SN-84EC
Density (g/cc)		3.2
Flexural strength (4-point bending)		
R.T. (MPa)		860
800°C		810
1,000°C		800
1,200°C		760
1,400°C		150
Young's modulus, R.T. (GPa)		280
Poisson's ratio, R.T.		0.27
Fracture toughness K_{IC}		
R.T. (MN/m ^{3/2})		6
1,000°C		6
Hardness (Knoop 300g load)		
R.T. (GPa)		15
Thermal expansion coefficient		
40~1,000 °C ($\times 10^{-6}$ / °C)		3.7
Thermal conductivity		
R.T. (W/m·K)		30
1,000°C		17
Heat capacity (KJ/kg·K)		0.7
Oxidation resistance		
1,000°C 1000hr (mg/cm ²)		less than 0.1
Thermal shock resistance (°C)		1,000

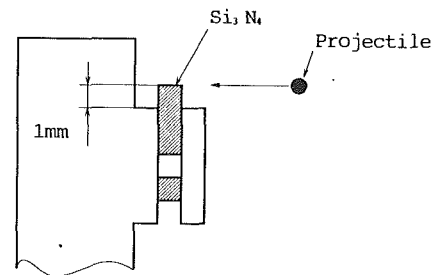
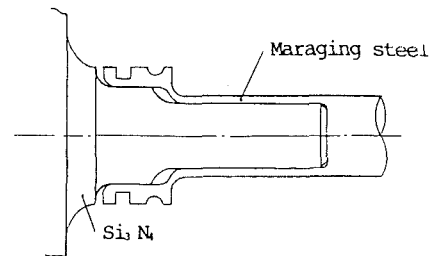
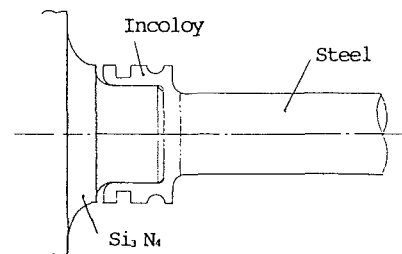


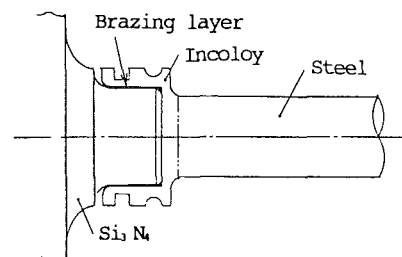
Fig. 5 Schematic of experimental device for chipping fracture test



(a) Type I (Shrink fit)



(b) Type II (Shrink fit)



(c) Type III (Brazing)

Fig. 6 Joint configuration of each method

shown in Fig. 5. The critical speed using SN-84EC is about twice that for SN-60 as shown in Table 2.

The other material properties are shown in Table 3.

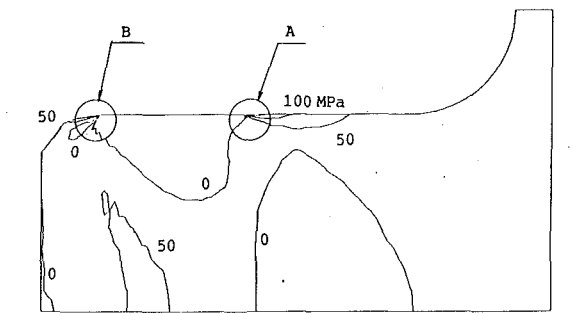
Development of Ceramic-Metal Joining

Three ceramic-metal joining methods have been investigated to obtain high joint strength. Figure 6 shows the types studied.

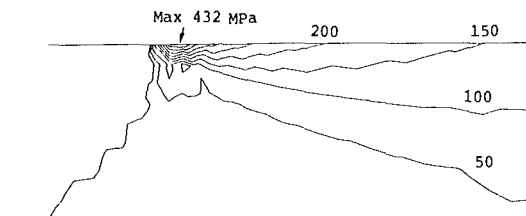
Type I: This type was adopted for the first generation of CTR using shrink fitting at two places on large and small-diameter shafts [10, 11]. It was confirmed that the necessary

specification of the turbocharger can be met by using maraging steel [12] shaft and optimizing the interference and joint length at each of the two places.

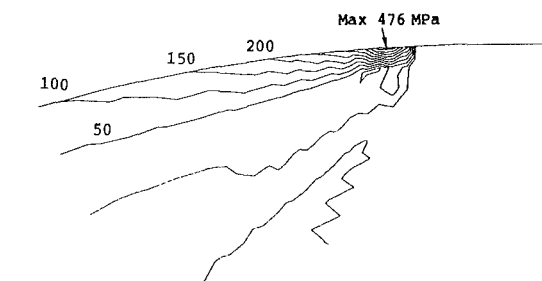
Type II: This type has been newly developed using Incoloy [13] as the low thermal expansion metal, but shrink fitted at only one point on the large diameter. Residual stress reduction and joint strength at high temperatures contradict in the shrink fit design. Design parameters such as the ceramic shaft diameter, metal wall thickness, interference, and joint length have been optimized by means of FEM stress analysis and various experiments. Figure 7 shows typical FEM results with



(a) Maximum principal stress distribution

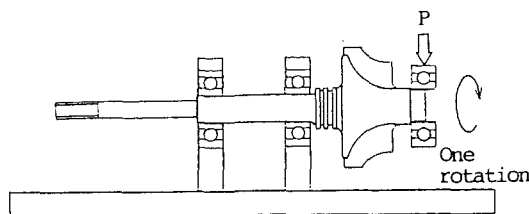


(b) Magnification A

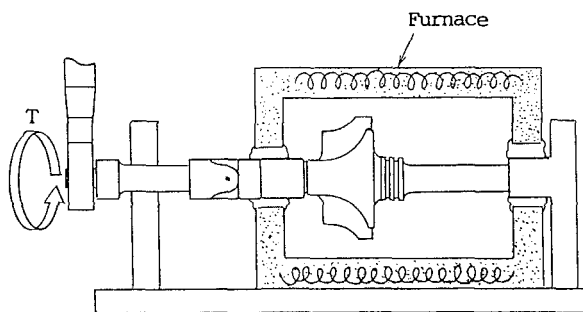


(c) Magnification B

Fig. 7 Result of FEM stress analysis



Bending test



Torsional test

Fig. 8 Method of testing joint

the maximum principal stress generated in the ceramic materials.

Type III: This method has also been newly developed using

Table 4 Joint strength for each joining method

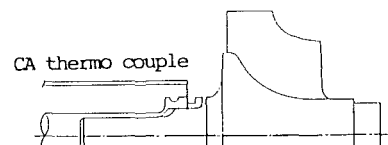
(a) Bending strength

Type	I	II	III
P/Po	2 1	1 1 1 1	1 1 1 1
P : Bending strength Po: Mean bending strength of type I			
		○ : Clear ● : Fracture of ceramic	

(b) Torsional strength

Type	I	II	III
Temperature (°C)	450	450 500 550	450 500 550
T/To	2 1	1 1 1	1 1 1
T : Torsional strength To: Mean torsional strength of type I			
		○ : Clear ● : Rotational slippage	

Table 5 Temperature of joining portion



	TIT	Steady state	Heat soak-back
Result of experiment (°C)	860	305	395
Estimation from experiment (°C)	900	320	410
	1,100	390	510

brazing between ceramic shaft surface and the metal bore, with the ceramic shaft diameter and joint length the same as for Type II.

For a basic evaluation of the three types of joints, the bending and torsional strengths have been evaluated using the method shown in Fig. 8.

1 Bending Strength. The bending strength was evaluated at room temperature because the residual stress at the joined portion is at a maximum. During the bending test, the CTR was rotated once using bearings. The results are shown in Table 4(a). The bending strength is represented as a ratio to the mean bending strength of Type I. Compared with Type I, which has been successfully used in commercial production, Types II and III ensure sufficiently high strength.

(2) Torsional Strength. In order to establish test conditions, the temperature of the joined portion was measured in the engine under conditions of steady engine speed and heat soak-back. Table 5 shows the results of temperature measurement with a water-cooled bearing housing. The temperature of the joint under heat soak-back was 395°C when the turbine

Table 6 Joint strength after each durability test for Type II

(a) Bending strength

Durability test	Before test	Exposure at high temperature	Heat cycle	Vibration
P/Po	3	3	3	3
P : Bending strength Po: Mean bending strength of type before durability test	2	2	2	2
	1	1	1	1

○ : Clear (Using method in Fig.8)
● : Fracture of ceramic (Using method in Fig.9)

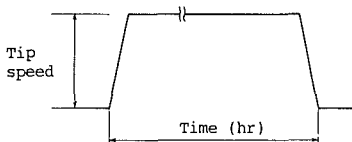
(b) Torsional strength

Durability test	Before test	Exposure at high temperature	Heat cycle	Vibration
Temperature (°C)	550	550	550	550
T/To	2	2	2	2
T : Torsional strength To: Mean torsional strength of type before durability test	1	1	1	1

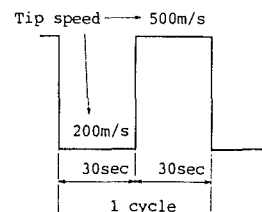
○ : Clear
● : Rotational slippage

Table 7 Hot spin test results

(a) Continuous durability test

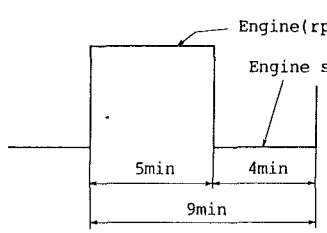
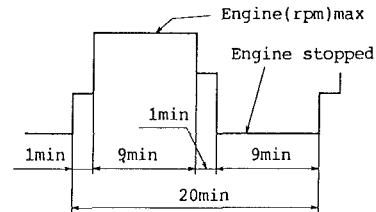
Test condition	Test result																								
	No failure (n=1 at each condition)																								
<table><tr><th>Condition</th><th>A</th><th>B</th><th>C</th><th>D</th><th>E</th></tr><tr><td>TIT(°C)</td><td>950</td><td>1050</td><td>1100</td><td>1100</td><td>1200</td></tr><tr><td>Tip speed(m/s)</td><td>500</td><td>500</td><td>500</td><td>600</td><td>550</td></tr><tr><td>Time(hr)</td><td>200</td><td>100</td><td>100</td><td>0.5</td><td>0.5</td></tr></table>	Condition	A	B	C	D	E	TIT(°C)	950	1050	1100	1100	1200	Tip speed(m/s)	500	500	500	600	550	Time(hr)	200	100	100	0.5	0.5	
Condition	A	B	C	D	E																				
TIT(°C)	950	1050	1100	1100	1200																				
Tip speed(m/s)	500	500	500	600	550																				
Time(hr)	200	100	100	0.5	0.5																				

(b) Cyclic durability test

Test condition	Test result
TIT(°C) : 950 Number of cycles : 3000 	No failure (n=2)

inlet temperature (hereinafter called TIT) was 860°C. Assuming that the shaft temperature is proportional to the TIT [8], the temperatures under heat soak-back conditions were estimated as 410°C and 510°C for TIT values of 900°C and 1100°C, respectively.

Table 8 Engine durability test results

Test condition	Test result
TIT(°C) : 900 Time(hr) : 200 	No failure (n=2)
TIT(°C) : 900 Time(hr) : 200 	No failure (n=1)

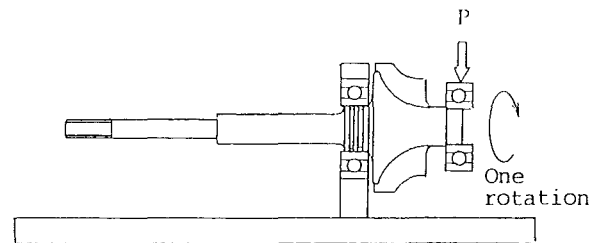


Fig. 9 Bending test method for evaluating fracture strength of joining ceramic

Table 4(b) shows the result of torsional strength evaluation. The torsional strength is represented as a ratio to the mean torsional strength of Type I at 450°C. For Types II and III, evaluation was carried out at 500°C and 550°C exceeding the estimated joint temperature of 510°C for TIT of 1100°C. All results for Types II and III were higher than the torsional strength for Type I.

As stated in the above, Types II and III ensure sufficiently high strength compared with the field proven Type I, and are applicable at high temperatures. Type II was selected for durability tests because of its lower production cost. Various durability tests were conducted for Type II, and the joint strength after the durability test was evaluated. Tests involving exposure at high-temperature heat cycles and vibration were selected in view of the actual operating conditions of the turbocharger. Table 6 shows the joint strength after each durability test. Bending strength, indicated by black dots in Table 6, was measured using the method shown in Fig. 9 to evaluate the fracture strength of the joining ceramic. After each durability test, no degradation in strength was observed, confirming sufficient joint strength.

CTR Evaluation

1 Hot Spin Test. A hot spin tester was used to evaluate the durability of the CTR at high temperature, as follows:

(a) *Continuous Durability Test.* The CTRs were evaluated under conditions A to E shown in Table 7(a), and no failure was experienced [14, 15]. The combined thermal and

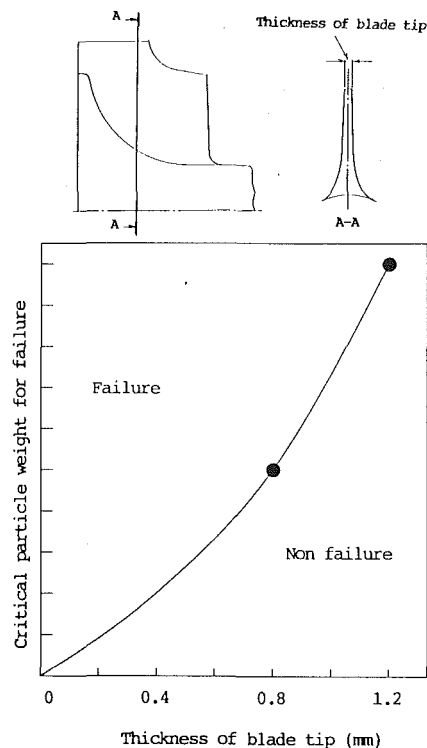


Fig. 10 Effect of blade tip thickness on dynamic strength

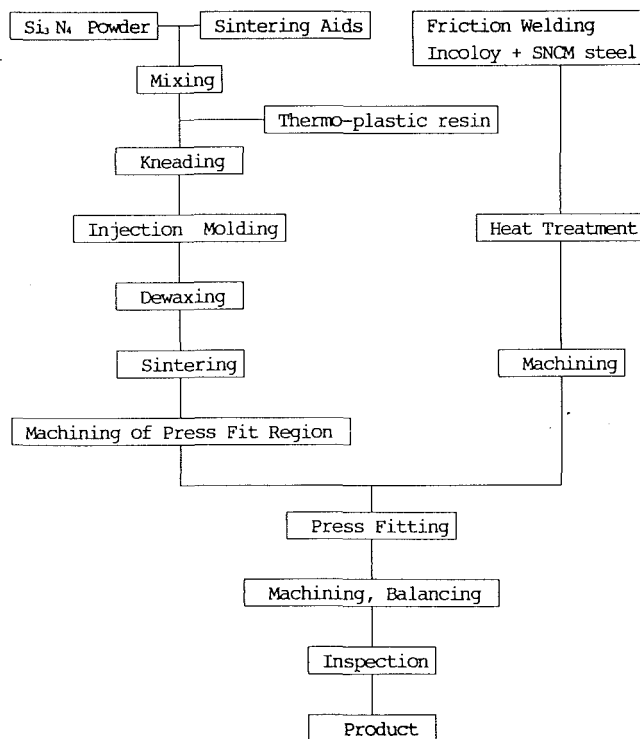


Fig. 11 Process for fabricating the newly developed CTR

centrifugal stresses of Types D and E increase by 21 and 31 percent at a tip speed of 500 m/s and at 1050°C, respectively, and the testing modes correspond to 340 to 4200 hours [15].

(b) *Cyclic Durability Test.* Cyclic durability testing was also carried out up to 3000 cycles under the condition shown in Table 7(b), and no failure was experienced.

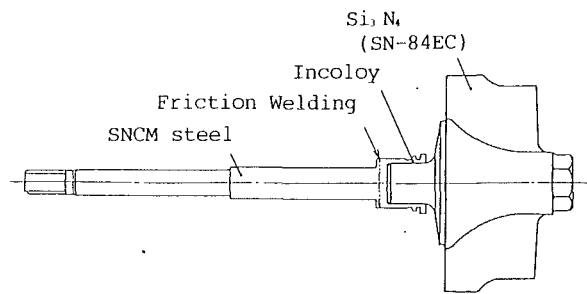


Fig. 12 Structure of completed product

Table 9 Comparison of critical particle weight

TIT : 900 °C

Thickness of blade tip : 1.2 mm

Si ₃ N ₄	critical particle weight
SN-60	W
SN-84EC	2 W

2 Engine Durability Test. This evaluation was conducted at a TIT of 900°C as shown in Table 8 because of the heat resistance of the engine used. Both tests were carried out for 200 hours under the go-stop conditions shown in the table, and no failure was experienced.

3 FOD Test. As described in the previous paragraph, the resistance to FOD depends on the mechanical strength and K_{IC} of the ceramics. It also has a strong relationship with the thickness of the blade tip (Fig. 10) [10]. Table 9 shows the result of the resistance against FOD of CTR's made of SN-84EC and SN-60 having tip thickness of 1.2 mm. The CTR made of SN-84EC had a critical particle weight 2.5 times higher than that of the CTR made of SN-60. This evaluation was made at a TIT of 900°C. Since SN-84EC has high strength and high fracture toughness up to 1200°C, FOD resistance is considered to be maintained up to that temperature.

Fabrication Process

Figure 11 shows the process for fabricating the newly developed CTR. Silicon nitride powder and sintering aids are mixed, then thermoplastic resin for forming is added. The mixture is kneaded and then formed by injection molding. The key feature of NGK's forming method is that the wheel and shaft can be uniformly molded by optimally controlling the material and die temperatures, injection pressure, injection speed, and dewaxing conditions. Incoloy having low thermal expansion and nickel-chromium-molybdenum steel (SNCM steel) are friction welded to form the metal shaft, which is then subjected to heat treatment and machining, followed by press fitting with the ceramic shaft. Machining, balancing, and inspection are carried out to complete the product after joining. Figure 12 shows the structure of the completed product.

Conclusion

The CTR for high-temperature use has been accomplished by developing silicon nitride (SN-84EC), which withstands high temperatures, and a new ceramic-metal joint. It is expected that this CTR will be able to cope with stoichiometric mixture burning engines, which produce a higher exhaust gas temperature for fuel economy. The reliability of the CTR was certified by its success in Formula-1 racing cars, which require rotors

to withstand high exhaust gas temperatures of over 1000°C. The resistance of the new rotors to FOD has also been markedly increased over that of the previous production ones, hence greatly improving reliability in mass-produced CTR's for commercial production automobiles.

Acknowledgments

The authors would like to acknowledge Nissan Motor Co., Ltd., and Ishikawajima-Harima Heavy Industries Co., Ltd., for their cooperation in this research and development.

References

- 1 Miyashita, K., Kurasawa, M., Matsuoka, H., and Ikeya, N., "Development of High Efficiency Ball-Bearing Turbocharger," SAE Paper No. 870354, 1987.
- 2 Matsubara, H., Miyashita, K., Iguchi, Y., Tanaka, S., Akiyama, K., and Nakamura, F., "Superior Charging Technology by Screw Supercharger and High Technology Turbocharger for Automotive Use," SAE Paper No. 890455, 1989.
- 3 Yoritaka, M., Yamamoto, Y., Hasegawa, Y., and Hokari, T., "Automotive Application of Advanced Superalloys," *Journal of Metals*, Dec. 1986.
- 4 Koike, T., "Turbocharger for F1-Race Adopting Ceramic Impeller and Ball Bearing," *Turbomachinery*, Vol. 18, No. 6, June 1990.
- 5 Faber, K. T., and Evans, A. G., "Crack Deflection Processes: I. Theory," *Acta Metall.*, Vol. 31, No. 4, 1983.
- 6 Suzuki, K., "Relation Between Microstructure and Fracture Toughness of Ceramics," *Ceramics*, Vol. 21, No. 7, 1986.
- 7 Matsui, M., Soma, T., Ishida, Y., and Oda, I., "Life Time Prediction of Ceramic Turbocharger Rotor," SAE Paper No. 860443, 1986.
- 8 Miyagi, Y., Miyashita, K., Sugihara, H., and Tomita, T., "Study of Ceramic Rotor and Turbine Housing Material of a Turbocharger up to the Turbine Inlet Gas Temperature 1050°C," *I Mech E*, May 22-24, 1990.
- 9 Tsuruta, H., Masuda, M., Soma, T., and Matsui, M., "Foreign Object Damage Resistance of Silicon Nitride and Silicon Carbide," *Journal of the American Ceramic Society*, Vol. 73, No. 6, June 1990.
- 10 Matoba, K., Katayama, K., Kawamura, M., and Mizuno, T., "The Development of Second Generation Ceramic Turbocharger Rotor—Further Improvements in Reliability," SAE Paper No. 880702, 1988.
- 11 Ito, T., "Application to Turbocharger Rotor," *Machinery Design*, Vol. 32, No. 13, Oct. 1988.
- 12 Kawabe, Y., "Maraging Steel," *Fine Ceramics*, Vol. 5, 1984.
- 13 Smith, D. F., and Clatworthy, E. F., "The Development of High Strength, Low Expansion Alloys," *Metal Progress*, Mar. 1981.
- 14 Miyashita, K., Kitazawa, T., Sakakida, M., Ikeya, N., and Mizuno, T., "RHB5 High Efficiency Ceramic Turbocharger," presented at the JSAE Conference, Paper No. 882132, Oct. 1988.
- 15 Miyashita, K., Miyagi, Y., Sugihara, H., and Kitagawa, M., "Study of High Temperature Ceramic Turbocharger," presented at the JSAE Conference, Paper No. 901088, May 1990.

K. Takatori

T. Honma

N. Kamiya

H. Masaki

Toyota Central R&D Labs. Inc.
Nagakute, Aichi, Japan

S. Sasaki

Toyota Motor Corporation,
Susono, Shizuoka, Japan

S. Wada

Toyota Central R&D Labs., Inc.
Nagakute, Aichi, Japan

Fabrication and Testing of Ceramic Turbine Wheels

A silicon nitride (Si_3N_4) radial inflow turbine wheel was fabricated by injection molding at Toyota Central R&D Labs. The wheel was 142 mm in outer diameter and had 14 blades. The radial wheel was too bulky to manufacture as a homogeneous and defect-free body in one piece. It was divided into two pieces for injection molding and put together into one body by a cold isostatic pressing step after binder removal. Spin testing was executed at room temperature and the resulting photographs, taken from three directions, provided useful information about the fraction mode of the wheels. The maximum burst speed of the wheels at room temperature was 98,900 rpm, which corresponded to 145 percent of the design speed. In a hot rig test, one of the wheels survived 75,000 rpm for ten minutes at a turbine inlet temperature of 1050°C.

Introduction

The development of ceramic materials for high-temperature application began in the end of the 1960s at Toyota Central R&D Labs, emphasizing Si_3N_4 -based materials. The discovery of the solid solution of Al_2O_3 in Si_3N_4 [1], which corresponded to the SIALON synthesis, and pressureless sintering of Si_3N_4 with spinel an additive [2] were the principal results.

Research on the fabrication process of ceramic components for automobiles engine was begun in 1979. Both Si_3N_4 and SiC were evaluated [3] and Si_3N_4 was chosen from the viewpoint of mechanical strength and fracture toughness. Since 1987, ceramic components for gas turbines have been fabricated in the laboratory to prove the applicability of ceramics to the gas turbine engine under development at Toyota Motor Corporation. The gas turbine, named GT-41, is a two-shaft type and its maximum power is designed to be 150 PS. Table 1 shows the major specifications of the GT-41 engine [4]. Figure 1 shows several ceramic components made of SiC for the GT-41 engine, which were fabricated at Toyota Central R&D Labs. Three forming methods were used to fabricate these components: (1) injection molding, (2) slip casting, and (3) cold isostatic pressing.

One of the most difficult components to form was a radial power turbine wheel. The sintered ceramic wheel is 142 mm in outer diameter. It is such a complicated and bulky structure that it is difficult to form by conventional ceramic forming processes. It also requires both high refractoriness and high

strength, which are difficult to satisfy using ordinary ceramic materials. Therefore, most of the radial turbine wheel fabrication efforts utilized an injection molding technique.

As mentioned above, this required both (1) the development of a forming technique for a large, complex-shaped component, and, (2) the development of a high-strength, refractory material to achieve a turbine inlet temperature (TIT) of 1350°C. This paper describes the first step in the development of an injection molding forming process for radial wheels. The results of cold spin tests and hot rig tests are also described.

Fabrication of Si_3N_4 Radial Wheels

Material Properties. In the first step of the development, the major effort was devoted to determining whether the large wheel could be fabricated without serious defects by the injection molding process. An excellent high-temperature property was not required for this step. Si_3N_4 -based ceramic with 5 wt% Y_2O_3 and 5 wt% MgAl_2O_4 (spinel) additives was chosen to fabricate the wheel. Using this ceramic, several small components for reciprocating engines were fabricated by injection molding, and our laboratory accumulated much experience of ceramics injection molding.

Mechanical properties of the Si_3N_4 ceramics used are listed in Table 2. Commercially available powders were used for starting materials in this study. Si_3N_4 powder (SN-9S, Denki Kagaku Kogyo Co., Ltd., Japan) with broad particle size distribution was chosen because it could be injection molded in high ceramic volume fraction using organic binders. At higher ceramic volume fractions, the binder removal process becomes easier. High purity and fine grain size Y_2O_3 (Mitsubishi Chemical Industry Ltd., Japan) and MgAl_2O_4 (Sumitomo Chemical

Contributed by the International Gas Turbine Institute and presented at the 36th International Gas Turbine and Aeroengine Congress and Exposition, Orlando, Florida, June 3-6, 1991. Manuscript received at ASME Headquarters February 20, 1991. Paper No. 91-GT-142. Associate Technical Editor: L. A. Riekert.

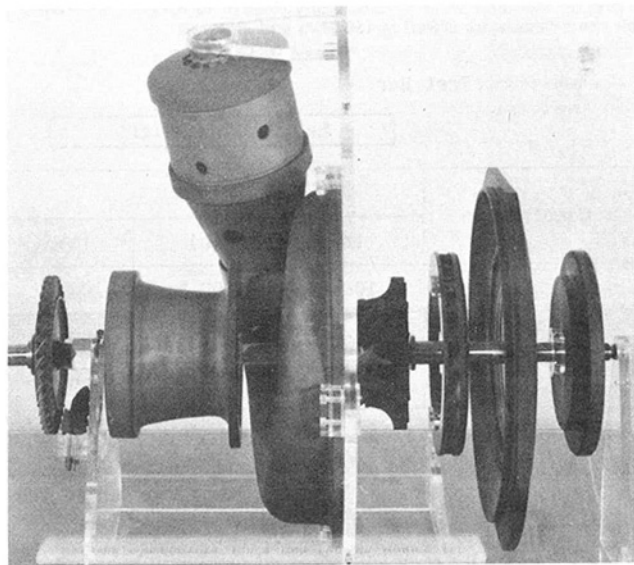


Fig. 1 SiC components for the GT-41 engine fabricated at Toyota Central R&D Labs.

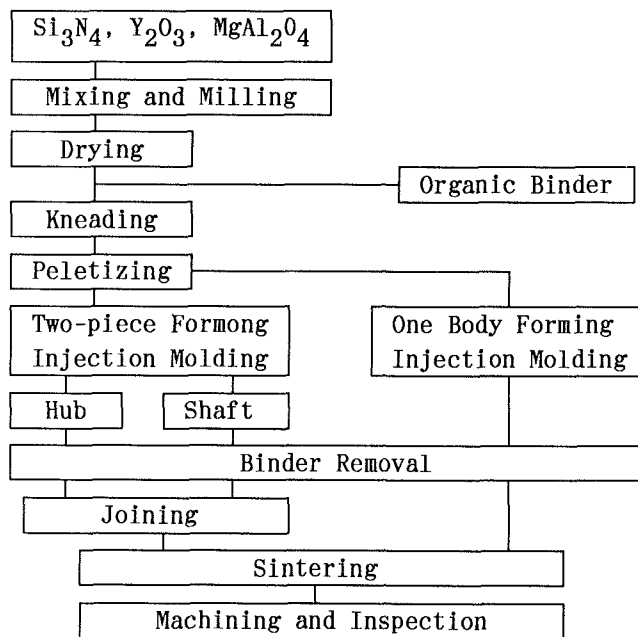


Fig. 2 Flow chart for the Si₃N₄ radial wheel fabrication process

Co., Ltd., Japan) were chosen as additives. Ceramic powders suitable for injection molding were discussed in detail by Honma et al. [6]. The ceramics could be easily densified to a high-strength sintered body. The average four-point flexural strength was found to be over 1100 MPa when fine and mono-size starting powders, such as SN-E10 (Ube Industries Co., Ltd., Japan), are mixed homogeneously and sintered at an optimized condition. But the mono-size powder was not used for injection molding because the ceramic volume fraction was limited to less than 50 percent, compared with the value of 58 percent in the case of SN-9S.

The ceramics used in the first step had good mechanical properties at moderate temperatures, but the high-temperature strength of the ceramics was not satisfactory for gas turbine components which would operate at 1350°C. In the second step, the high-temperature strength of the ceramics was chosen as the target for improvement.

Table 1 Major specifications of GT-41 engine [4]

Type	Two-shaft
Gas Generator Compressor Turbine Rated Speed	Radial Radial Inflow 68,000 rpm
Power Turbine Turbine	Axial with Variable Nozzle
Heat Exchanger	Regenerator Type
Reduction Gear Ratio	10.13
Max. Power	150 PS / 5,300 rpm
Max. Torque	34 kgm / 1,000 rpm

Table 2 Mechanical properties of Si₃N₄ ceramics with Y₂O₃ and MgAl₂O₄ additives

Property	Measured value
Density	3.21 g/cc
Strength R.T.	1000 MPa
1,000°C	600 MPa
Young's modulus	294 GPa
Vickers hardness	15 GPa
Fracture toughness*	7 MPa · m ^{1/2}

* Fracture toughness was measured by indentation microfracture method using Niihara's equation[5].

Fabrication Process. The injection molding of ceramics has both advantages and disadvantages for forming large radial turbine wheels. These include:

Advantages:

- (a) Capable of forming complex shapes.
- (b) Easy to form to near-net shape.
- (c) Surface smoothness of the product.
- (d) Suitable for mass production.

Disadvantages:

- (a) Difficult to form bulky structures.
- (b) Long binder removal times.
- (c) Requires expensive tooling and equipment.

Considering the facts mentioned above, the injection molding of ceramics is suitable for a small, complex shape such as a turbocharger rotor [7].

The outer diameter of the injection molded radial wheel was about 170 mm, which became 142 mm after sintering (about 700 g in weight). It was quite difficult to form such a bulky wheel without serious defects by the current injection molding technology. Two methods for injection molding the wheel were attempted: one-body forming and two-piece forming. One-body forming means that the whole body of the wheel was injection molded at one time. Two-piece forming means that the wheel was divided into two pieces that were injection molded separately. A flow chart of the fabrication processes is shown

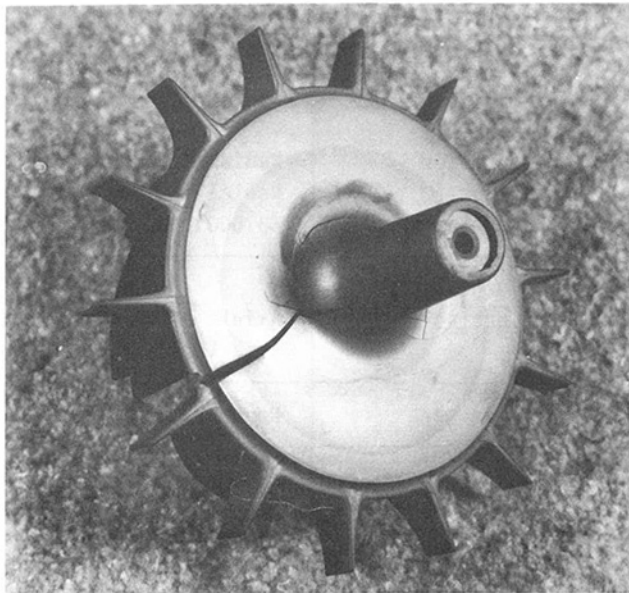


Fig. 3 Cracked Si_3N_4 radial wheel fabricated by one body forming

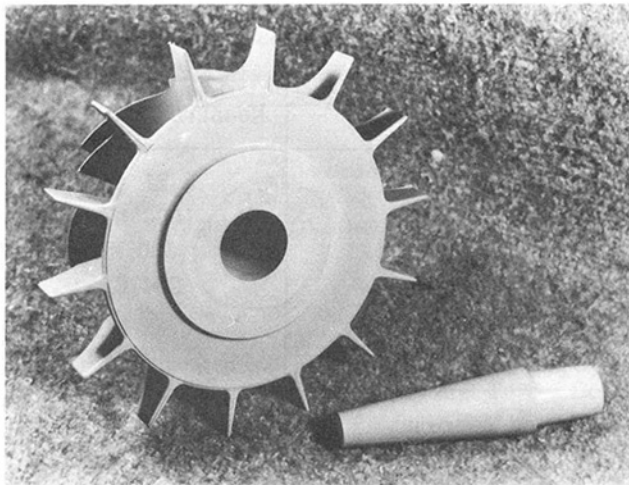


Fig. 4 Two pieces of the Si_3N_4 radial turbine wheel separately injection molded

in Fig. 2. A 360 ton injection molding machine, by which a maximum of 1000 cc could be injected at a time, was utilized for forming the wheel. The proprietary organic binder system was mainly composed of thermoplastic polymers and paraffin waxes.

One-Body Forming. The large wheel was formed by injection molding at one time. There were some defects in all of the wheels. Some wheels had an internal crack detectable by x-radiography, which was associated with thermal contraction of the organic binder. Others were damaged by surface crack generation and broke down during binder removal. The few wheels surviving binder removal failed during sintering. Figure 3 shows a typical crack in the sintered body. The crack was thought to be caused by small internal defects or residual stress in the formed body. It was concluded that one-body forming of the large radial wheel was not practical using the current injection molding technology.

Two-Piece Forming. In this process, the hub of the wheel, the thickest section, was divided into two axially symmetric pieces to reduce the thickness about in half [8]. The pieces were injection molded separately. Figure 4 shows the two pieces of the formed body of the wheel. Survival probability of the

Table 3 Strength of joint specimens relative to nonjoined reference; all specimens were CIPed at 150 MPa and sintered

Test Bar		Joint Plane		
		↓		
		Left	Right	
Combination		Right		
		(a)	(b)	(c)
Left	(a)	100 %	100 %	100 %
	(b)	-	80 %	90 %
	(c)	-	-	60 %

(a): Die pressed at 50 MPa.

(b): ↑ 100 MPa.

(c): ↑ 150 MPa.

wheel after binder removal increased markedly by using two-piece forming. The pieces were consolidated by cold isostatic pressing (CIP) after the binder removal step was completed.

Binder removal was one of the most difficult process steps in the ceramic injection molding [9]. Even for the divided two-piece process, an 11-day heat schedule was required to obtain a sound binderless body. Unless the time for binder removal can be shortened, ceramic injection molding might not be viable as an industrial technique.

A preliminary study was conducted to join the die-pressed specimens by CIP treatment. Disks ($40^{\circ} \times 20^{\circ}$ mm) were die pressed at (a) 50, (b) 100, and (c) 150 MPa and the flat surfaces were joined by CIP at 150 MPa to produce a series of specimens of about 40 mm in thickness. Six combinations of the specimens from (a)-(a) to (c)-(c) were examined. A specimen without a joint was also produced as a reference. These were sintered and cut into flexural test bars ($3 \times 4 \times 36$ mm) in which the joint planes were perpendicular to the longitudinal direction. The results of four-point flexure testing are expressed relative to the reference value in Table 3. The average strength of the combinations (a)-(a), (a)-(b), and (a)-(c) was the same as that of the reference. The combinations (b)-(b), (b)-(c), and (c)-(c) exhibited lower strength than the reference. All specimens of the latter three combinations had broken along the joint plane. These results indicated that the CIP joining pressure should be more than three times higher than the forming pressure of the constituents. For an injection molded green body having a green density of 58 percent of theoretical, this corresponds to the compact, which was die pressed at 150 MPa. Considering the above results, the CIP pressure was set at 500 MPa for the joining of the hub and the shaft to form the radial wheel.

The wheel joined by CIP was sintered under a nitrogen gas pressure less than 1 MPa. The wheel was heated at $1^{\circ}\text{C}/\text{min}$ up to 1100°C , $0.5^{\circ}\text{C}/\text{min}$ up to 1700°C , and kept four hours at 1700°C . The heating rate was carefully chosen so as not to break the wheel by the internal stress generated during sintering.

Fluorescent penetrant inspection (FPI) and x-radiography were conducted as a nondestructive inspection for both injection molded and sintered wheels. To detect cracks and inclusions just below the back surface of the sintered wheel, where the finite-element method (FEM) analysis of stress distribution suggest that high stress might exist, ultrasonic inspection was also performed on the machined surface.

Metal inclusions frequently become the fracture origin of a sintered body in the case of injection molding. These cause degradation of strength, and exceptionally low strength is recorded when the inclusion is located in a high stress position.

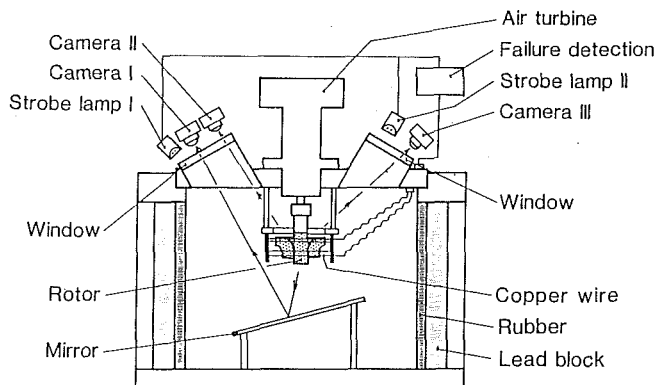
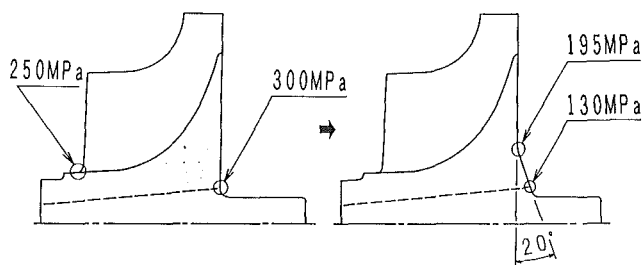


Fig. 5 Schematic diagram of apparatus for cold spin testing [10]



(a) Initial Design (b) Modified Design
Fig. 6 FEM analysis of high stress areas and modified structure

The high-pressure injection molding process used in this study cannot avoid contamination from metal inclusions, because of the use of metal equipment. A large number of strength-controlling metal inclusions was found to be introduced during the mixing of ceramic powders and organic binders by a kneading machine. A new forming technology of ceramics is required to fabricate large completed-shaped components with high reliability.

Spin Testing

Cold Spin Testing. Cold spin testing of the radial turbine wheel was performed at room temperature at Toyota Central R&D Labs. [10]. Figure 5 shows the schematic diagram of the apparatus. The chamber of the tester was evacuated to 0.1 Torr to reduce air drag. The testing wheel was surrounded by copper wires 0.1 mm in diameter, which were sustained by steel rods. The burst of the wheel was detected by the electrical signal caused by the cut-off of the wire. Three cameras and two strobe lamps were located on the cover of the tester to take pictures from three directions at the instant of wheel burst. In this way, two photographs give back views of the wheel, and one gives a front view reflected by the mirror mounted in the chamber. Preliminary cold spin testing was conducted using artificially precracked wheels, and photographs of the burst wheels featured a fracture mode that could be used to trace back to the precracked position.

FEM analysis of stress distribution indicated that very high stresses were exerted in two areas of the initially designed wheel. As shown in Fig. 6(a), one was at the top of the blade fillets, and the other was at the shaft fillet on the back surface of the hub. High stress at the former area could not be reduced while the number of blades was kept at 14 because the curvature of that area could not be increased. An increase of curvature frequently reduces stress concentration. The latter area corresponds to the joint of two pieces, which is shown by a broken line in Fig. 6(a). The joined part sometimes contained defects

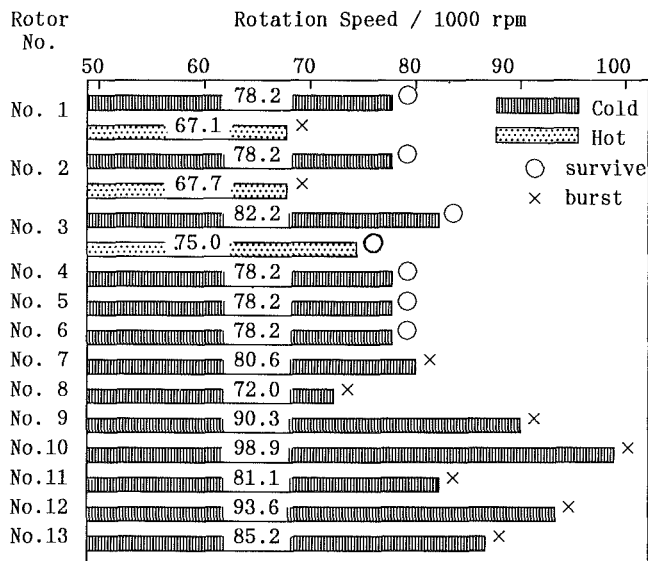


Fig. 7 Results of cold spin testing and hot rig testing of Si_3N_4 radial wheel

caused by the inadequacy of joining. Therefore, the strength of the joint area was expected to be lower than in the other position. High stress at this area could be reduced by a simple modification of the structure, i.e., the addition of a slope on the back surface of the hub. The addition of a 20 deg slope reduced the maximum stress at the back surface to 65 percent and the stress at the joint to only 43 percent of the initial design. High stress areas in the modified structure are indicated in Fig. 6(b).

Cold spin testings were conducted for 13 wheels without the artificial precrack. A threshold speed was tentatively decided at 78,200 rpm for six wheels, and the wheels were withdrawn without fracture; 78,200 rpm corresponded to 581 m/s tip speed and 115 percent of the design speed. Three of these were examined by hot rig testing, as mentioned below. Burst testings were conducted for seven wheels. Figure 7 shows the results of the spin testing. The average burst speed was calculated as 86,000 rpm, which was 125 percent of the design speed. Broken pieces of the burst wheel were collected to examine the fracture origin. It was found that metal inclusions and the inadequacy of joining below the back surface of the hub were the main fracture origins.

Figure 8 shows photographs at the instant of burst from three directions of the wheel, for a burst speed of 98,300 rpm. They clearly indicate the position of the fracture origin near the fillet of the shaft. Fractured species were collected and the fracture origin was micro-analyzed by scanning electron microscopy (SEM). Figure 9 shows the SEM photograph of the metal inclusion, which was the fracture origin of the wheel shown in Fig. 8. This metal inclusion was identified as steel co-existing with cobalt by an elemental analysis. It was concluded that the inclusion originated from an agitation shaft in the mixing process of the ceramics and organic binder.

Hot Rig Testing. The wheels that passed the threshold speed were prepared for hot rig testing, which needed joining of a metal shaft to the ceramic wheel. A proprietary modified shrink fitting was used for the joining. Three wheels were examined by hot rig testing at Toyota Motor Corporation. The maximum turbine inlet temperature was restricted to 1050°C by strength degradation of the ceramics at high temperature. Both temperature and rotation speed were raised stepwise up to the ultimate test condition of 75,000 rpm at 1050°C for ten minutes.

The results of the hot rig testing are shown in Fig. 7. Only one wheel survived the ultimate condition. Two wheels burst

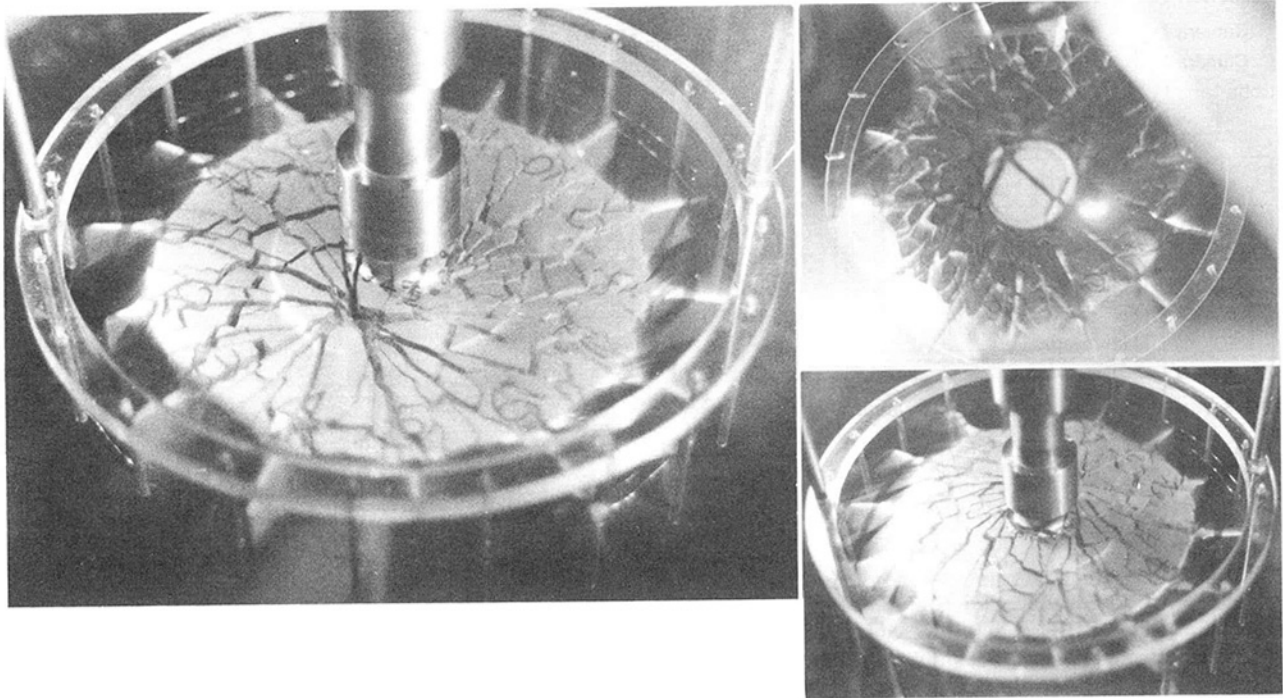


Fig. 8 Fracture photographs of Si_3N_4 radial wheel from three directions at 90,300 rpm

at 67,000 rpm when the temperature was raised from 900°C to 1000°C. From the fractographic investigation of burst fragments, the fracture origin of one wheel was considered to be a metal inclusion near the shaft fillet. No fracture origin could be identified for the other wheel. These results indicated that the wheels fabricated in this study had little margin over the designed working condition of the GT-41, even though some of them had passed the threshold conditions of cold spin testing and hot rig testing. Improvements of both material and forming process were required.

Improvements

Improvements of high-temperature strength of Si_3N_4 ceramics and that of forming process have been studied as the second step of development.

It is well known that the high-temperature strength of Si_3N_4 ceramics is dominated by the properties and amount of glassy phase existing as an intergranular phase in the sintered body. Glassy phase should be decreased by decreasing sintering additives and/or devitrifying. A concept of devitrification was adopted in the improvement study using high-purity Si_3N_4 powder made by the imide decomposition method. At present, Si_3N_4 -based material with flexural strength over 700 MPa at 1200°C has been developed by a gas pressure sintering process.

Post-HIP treatment was also studied as one of the most reliable processes to heal an internal defect within the sintered body.

A new process for mixing and forming is under development, which is expected to prevent metal contamination, and for which the duration of binder removal is greatly reduced.

Those results will be combined to fabricate high-performance ceramic components for a high-temperature operation gas turbine.

Summary

A preliminary development study was performed on the fabrication and testing of ceramic gas turbine components at

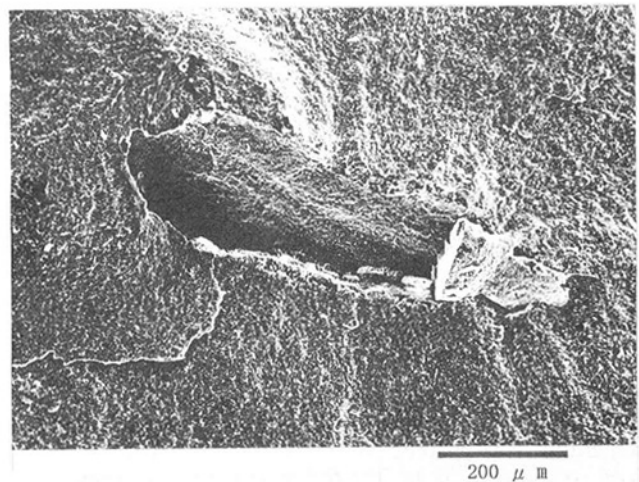


Fig. 9 SEM image of metal inclusion corresponding to the fracture origin of Fig. 8

Toyota Central R&D Labs. and Toyota Motor Corporation. Conclusions are:

1 Optimum conditions were found to fabricate Si_3N_4 radial turbine wheel for the GT-41 engine without flaws by injection molding.

2 The wheel was divided into two pieces in the forming process so as not to generate defects. These were joined by CIP treatment after binder removal.

3 All of the wheels examined by cold spin testing exceeded the design speed, 68,000 rpm, and the average burst speed was 86,000 rpm at room temperature.

4 Hot rig testing was conducted for three wheels and one of them survived the ultimate condition; 75,000 rpm at 1050°C for ten minutes.

5 Metal inclusions were found at the fracture origins of wheels and these controlled the burst speed. The problem of the inclusions still remains in the current ceramic injection molding technology.

Acknowledgments

The authors gratefully acknowledge Dr. S. Kobayashi and co-workers of Toyota Central R&D Labs. for their help and support at various stages of this study.

References

- 1 Oyama, Y., and Kamigaito, O., "Sintered Body of Silicon Nitride and Alumina System," *Yogyo-Kyokai-Shi*, Vol. 80, 1972, pp. 327-336.
- 2 Masaki, H., and Kamigaito, O., "Pressureless Sintering of Silicon Nitride With Addition of MgO, Al₂O₃ and/or Spinel," *Yogyo-Kyokai-Shi*, Vol. 84, 1976, pp. 508-512.
- 3 Wada, S., Masaki, H., Honma, T., and Tani, T., "Injection Molding of SiC Turbocharger Rotor," *1987 Tokyo International Gas Turbine Congress*, 1987, pp. 1143-1147.
- 4 Watanabe, A., Morishita, T., and Sohma, T., "A Development of Control System for Gas Turbine Powered Vehicle," *JSAE Review*, Vol. 10, No. 3, 1989, pp. 16-21.
- 5 Niihara, K., "A Fracture Mechanics Analysis of Indentation-Induced Palmqvist Crack in Ceramics," *J. Mater. Sci. Lett.*, Vol. 2, 1983, pp. 221-223.
- 6 Honma, T., Masaki, H., and Wada, S., "Characterization of Silicon Nitride Power for Injection Molding," *Third International Symposium on Ceramic Materials & Components for Engines (Las Vegas)*, V. J. Tennery, ed., 1988, pp. 42-53.
- 7 Shimizu, T., Takama, K., Enokishima, H., Mikame, K., Tsuji, S., and Kamiya, N., "Silicon Nitride Turbocharger Rotor for High Performance Automotive Engines," SAE Paper No. 900656, 1990.
- 8 Katayama, K., Watanabe, T., Matoba, K., and Katoh, N., "Development of Nissan High Response Ceramic Turbocharger Rotor," SAE Paper No. 861128, 1986.
- 9 Wada, S., and Oyama, Y., "Thermal Extraction of Binder Components From Injection-Molded Bodies," *Proceedings of the Second International Symposium on Ceramic Materials and Components for Engines (Lubeck-Travemunde)*, W. Bunk and H. Hausner, eds., Verlag Deutsche Keramische Gesellschaft, 1986, pp. 225-233.
- 10 Kamiya, N., Asai, M., Bessho, A., and Wada, S., "Determination of Fracture Origin in Ceramic Radial Rotor by Taking Photographs at Failure From Two or Three Directions," ASME Paper No. 90-GT-383, 1990.

K. Watanabe

M. Masuda

T. Ozawa

M. Matsui

NGK Insulators, Ltd.,
Nagoya, Japan

K. Matsuihiro

NGK EUROPE GmbH,
Eschborn, Germany

Research and Development of Ceramic Turbine Wheels

The bending strength of specimens of various sizes, some of which were cut from a turbine wheel, was compared with predictions using Weibull statistical theory. The stress distribution of a ceramic turbine wheel in spin testing was determined with finite elements and the results were used to analyze a wheel that was spun until it burst. The cause of the burst of the ceramic radial turbine wheel at elevated temperature is discussed and based on the tensile rupture data. A design methodology using the Larson-Miller parameter was found to be applicable to the ceramic components at elevated temperatures.

1 Introduction

Advanced ceramics are currently being developed for automotive gas turbine components [1-5]. To design the turbine wheels and utilize ceramic components successfully, an understanding of fracture criteria for ceramics is required. For such purposes, the Weibull statistical theory is commonly used in component design. At elevated temperatures, the slow crack growth and creep characteristics of silicon nitride were studied using tensile specimen experiments. The static fatigue strength degraded with increasing temperature due to slow crack growth and creep deformation. In slow crack growth failure without creep deformation, the power law for crack growth rate controlled the strength degradation. The modified Larson-Miller parameter was applicable to life prediction under static stress in the creep deformation regime.

In this paper, a newly developed heat-resistant high-strength ceramic material and its component fabrication technique were introduced from the viewpoint of the ceramic maker. To evaluate the turbine wheel, MOR bars were cut from the wheel and the flexural strength was measured. The results were compared with the strength data of the specimen with various geometries using Weibull statistical theory. In order to confirm the life prediction for the ceramic turbine wheel, static fatigue test and hot-gas spin tests were carried out.

2 Experimental Procedure

2-1 Silicon Nitride Ceramics for Turbine Wheels. The radial turbine wheels were made from NGK Insulators SN-88 silicon nitride, whose four-point flexural strength exceeds 700 MPa and which has good oxidation resistance at high tem-

Table 1 Properties of turbine wheel material (SN-88)

Material code No.	SN-88
Density	3.5 g/cc
Flexural Strength(4-point, $3 \times 4 \times 40$ mm)	
(RT)	790 \pm 50 (32*) MPa
(1000°C)	770 \pm 20 (5*) MPa
(1200°C)	770 \pm 50 (5*) MPa
(1400°C)	760 \pm 20 (10*) MPa
Young's Modulus	
(RT)	300 GPa
Poisson's Ratio	
(RT)	0.26
Fracture Toughness, K_{Ic}	
(RT)	7 MN/m ^{3/2}
Thermal Expansion Coefficient	
(40-1000°C)	3.4 $\times 10^{-6}/^{\circ}\text{C}$
Oxidation Resistance	
(1000 °C, 1000h)	< 0.1 mg/cm ²
(1200 °C, 1000h)	0.3 mg/cm ²
(1400 °C, 1000h)	0.5 mg/cm ²

* the number of specimens

peratures comparable to that of silicon carbide. The material properties of pressed SN-88 are listed in Table 1. Figure 1 shows the Weibull plot of flexural strength at room temperature. The Weibull modulus of the two-parameter Weibull distribution function is approximately 20.

2-2 Static Fatigue Test Under Tensile Stress. To investigate the lifetime for a hot component, static fatigue tests under tensile stress were carried out using 6-mm-dia button head type specimens made from SN-88 [6]. The button head specimens were loaded with both the lever type and the electromechanical type tensile creep rupture testing apparatus. The specimens were heated in air either by an infrared image fur-

Contributed by the International Gas Turbine Institute and presented at the 37th International Gas Turbine and Aeroengine Congress and Exposition, Cologne, Germany, June 1-4, 1992. Manuscript received by the International Gas Turbine Institute February 24, 1992. Paper No. 92-GT-295. Associate Technical Editor: L. S. Langston.

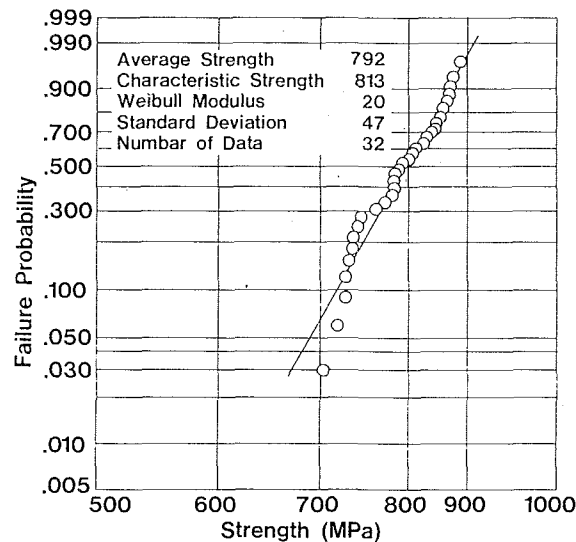


Fig. 1 Four-point flexural strength distribution of SN-88 at room temperature

nance or an electroresistance heating furnace using molybdenum disilicide elements [7].

2-3 Fabrication Process for Radial Turbine Wheel. The radial turbine wheel had an outer diameter of 83.5 mm and 12 blades (Fig. 2). Figure 3 shows the fabrication process. First, the silicon nitride raw material was mixed with sintering aids. The blade section was injection molded and machined for connection with the shaft after dewaxing. In the meantime, the shaft section was produced by pressing first, and machining was carried out for connection in the same manner as for the blade section. The blade section and the shaft section were combined into one, and then sintering was carried out to obtain a sintered body consisting of a unitary radial turbine wheel. The sintered materials thus produced were further machined, their balance was corrected, and nondestructive tests were performed.

2-4 Cold Spin Test. The schematic diagram of the cold spin testing rig is shown in Fig. 4. The maximum spin speed is 200,000 rpm. The air turbine was mounted above the circular plate that seals the vacuum test chamber. Fracture was detected by a coil of fine wire surrounding the turbine wheel. When fracture occurs, the broken pieces interrupt the electrical continuity of the circuit, thus providing a positive external signal that failure has occurred.

2-5 Hot-Gas Spin Test. Hot-gas spin tests were conducted by Mitsubishi Heavy Industries, Ltd., and Mitsubishi Motors Corporation. They used a test rig they had developed. The test rig withstands the turbine inlet temperature up to 1450°C. The hot section is constructed of heat-resistant alloy with air cooling. The testing apparatus has been improved to carry out the hot spin test with accuracy of measurement and safety at high temperature and higher rotational speed.

3 Results and Discussion

3-1 MOR Bar Strength Cut From the Turbine Wheel. In the evaluation of the turbine wheel, MOR (Modulus of Rup-

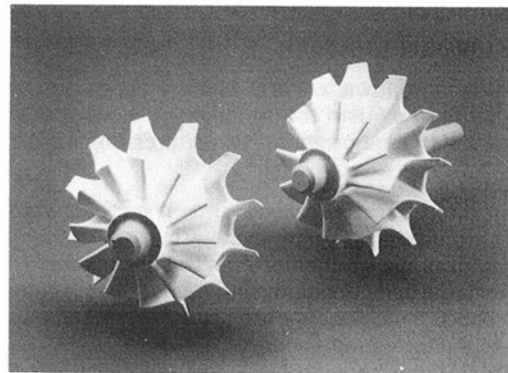


Fig. 2 Radial turbine wheel

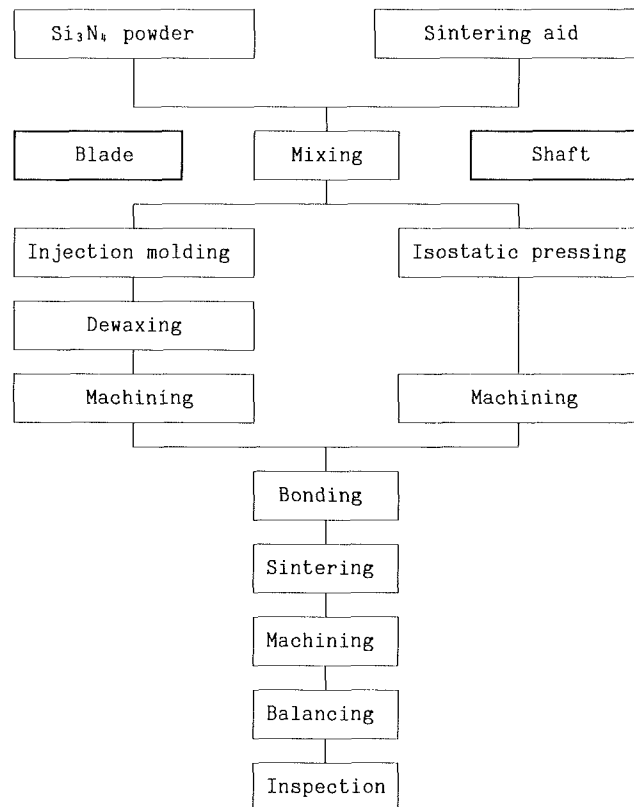


Fig. 3 Fabrication process of the ceramic turbine wheel

ture) bars were cut out and finished longitudinally by a #800 diamond wheel. Before the bending test, all the MOR bars were annealed in air to avoid the machining damage. Figure 5 shows the sections for the cutout. MOR bars were cut out from shaft A, shaft B, and shaft C sections, as

- (i) a specimen of the shaft segment by injection molding,
- (ii) a specimen produced by pressing and
- (iii) a specimen of the junction section between injection-molded and press-formed sections, respectively.

The curvature of the blade prevented the cutting of specimens that would test the as-fired surface strength. So, MOR bars

Nomenclature

A = const
 C = const
 K_I = stress intensity factor, $\text{MN}/\text{m}^{3/2}$
 K_{Ic} = critical stress intensity factor, $\text{MN}/\text{m}^{3/2}$
 P = Larson-Miller parameter

T = absolute temperature, K
 V_e = effective volume, mm^3
 V_{e1} = effective volume of specimen 1, mm^3
 a = crack length
 m = Weibull modulus

t = time, h
 t_r = time to creep rupture, h
 t_s = lifetime under static stress, h
 σ = stress, MPa
 σ_1 = mean strength of specimen 1, MPa

with as-fired surface were cut out from a 7-mm-thick plate fabricated by the injection molding process similar to the turbine wheel.

The results are shown in Table 2. For comparison, we also show the mean strength of the standard test pieces, which were obtained from a plate produced by die pressing (the last row in Table 2).

3-2 Effect of Volume on Strength. It was confirmed that the mean strength of the SN-88 material decreased with increasing size of the specimen. The fracture strength under uniaxial stress was predicted from the effective volume based on the Weibull statistical theory. The relationship between strength and effective volume is given by

$$\frac{\sigma_1}{\sigma_2} = \left(\frac{V_{e2}}{V_{e1}} \right)^{1/m} \quad (1)$$

where σ_1 and σ_2 are mean strength, and V_{e1} and V_{e2} are the effective volume of each specimen, respectively [8].

Bending strength (four-point and three-point using 3 by 4 by 40 mm and four-point using 6 by 8 by 80 mm MOR bars) and tensile strength were measured using SN-88 specimens

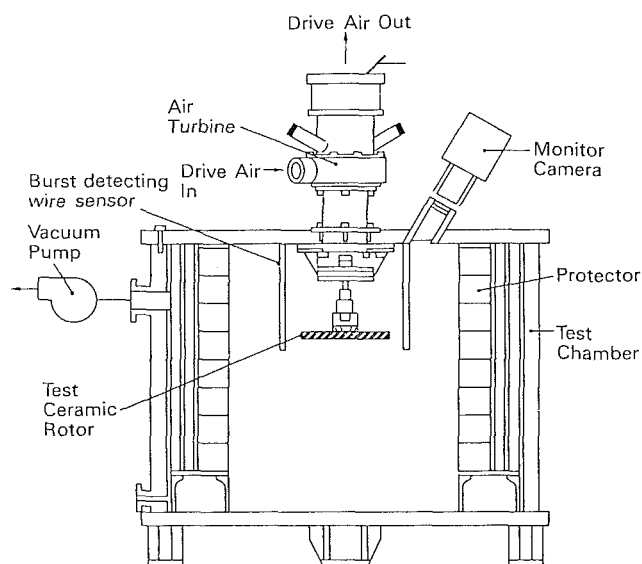


Fig. 4 Schematic diagram of cold spin testing rig

formed by pressing. The effect of volume on the strength of SN-88 and the MOR bar data of the specimens cut from the turbine wheel is shown in Fig. 6. The Weibull modulus calculated based on Eq. (1) is 22, and this value is nearly equivalent to that estimated by the distribution of four-point bending strength of standard specimen (3 by 4 by 40 mm). It was found that the MOR bars cut out of a turbine wheel had a flexural strength approximately 10 percent less than those of the standard specimen. From these results, it was confirmed that the manufacturing process to produce turbine wheels of complex shapes did not strongly affect strength. Essentially the rotor strength was comparable to that of the MOR bars, which were produced from a simple plate by pressing. Also, since the strength at high temperature is identical to that at room temperature, it was concluded that problems due to the difference in the fabrication processes, such as the contamination by foreign material, which could have resulted in the deterioration of high-temperature strength, did not occur.

3-3 Cold Spin Test. A burst test by cold spinning is effective in evaluating the strength of the turbine wheel, which is a rotating component. Three wheels were evaluated in terms of the burst test. Two of the turbine wheels burst at 777 m/s (181,000 rpm) of the turbine tip speed fortuitously, and one of the turbine wheels burst at 751 m/s (175,000 rpm). From the results of analysis of stress distribution of turbine wheels, the maximum stress in the wheel was estimated to be 557 and 519 MPa for tip speeds of 777 m/s and 751 m/s, respectively.

Figure 7 shows the stress distribution in the turbine wheel

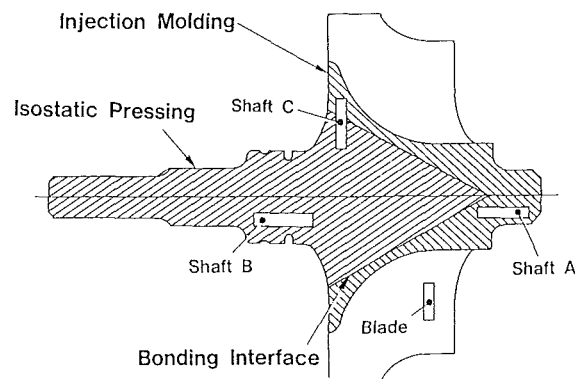


Fig. 5 MOR bar cut out locations

Table 2 Average flexural strength of MOR bars cut from the rotor

MOR Bar						4-Point Flexural Strength(MPa)	
Portion		Process	Surface	Size (mm)	Span(mm) outer/inner		
						RT	1400℃
Turbine Wheel	Shaft A	Injection Molding	#800 ground	1.5x 4x20	15 / 5	760±10 (3*)	760±10 (4*)
	Shaft B	Press	#800 ground	1.5x 4x20	15 / 5	850±30 (6*)	760±60 (4*)
	Shaft C	Injection Molding +Press	#800 ground	1.5x 4x20	15 / 5	780±80 (4*)	790±10 (2*)
Plate (Blade)		Injection Molding	as-fired	3x4 x40	30 /10	710±40 (14*)	720±30 (9*)
Plate (Reference)		Press	#800 ground	3x4 x40	30 /10	790±50 (32*)	760±20 (10*)

* the number of specimens

for a turbine tip speed 750 m/s [12]. Note that the blade of the wheel for the cold spin test was larger than that of the hot-gas spin test wheel. This was done so as to generate higher stresses for the cold spin test.

3-4 Static Fatigue Test Under Tensile Stress. Figure 8 shows static fatigue characteristics of SN-88 under tensile stress. The temperature was set between 1200°C and 1400°C, and the testing time ranged past 1000 h.

The SN-88 specimen showed delayed fracture and creep deformation at temperatures over 1200°C. From Fig. 8, the static fatigue strengths for 1000 h under tensile stress at 1200, 1300, and 1400°C, are estimated to be 300, 200, and 100 MPa, respectively. The rate of static fatigue strength degradation increased with higher temperature.

3-5 Fractographic Analysis of Fracture Surface. The results of the static fatigue test under tensile stress shown in Fig. 8 are divided in two stress regions, that is, the higher stress region and the lower stress region. It is considered that the strength degradation was caused by slow crack growth from pre-existing flaws in the higher stress region; on the other hand,

in the lower stress region, the strength degradation was contributed by creep deformation.

To confirm the fracture mechanisms in the static fatigue under tensile stress, the fractographic analysis of the fracture surfaces was conducted. The results are shown in Table 3. It is recognized, Table 3, that the fracture origins of the specimens

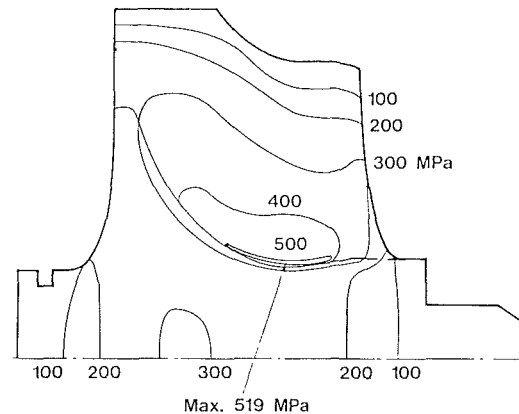


Fig. 7 Stress distribution in turbine wheel; turbine tip speed: 750 m/s

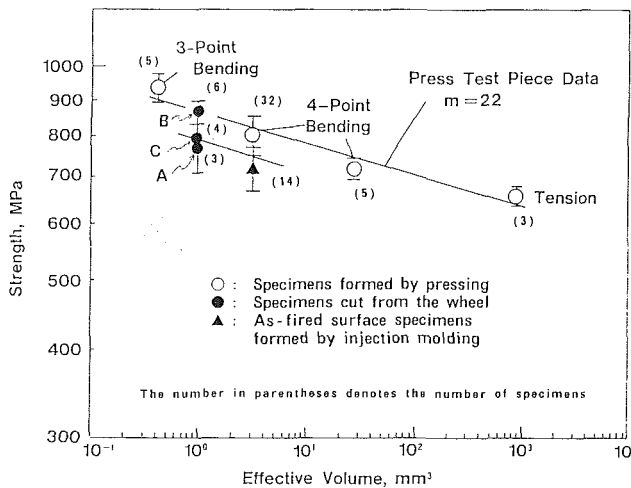


Fig. 6 Size effect on strength of SN-88

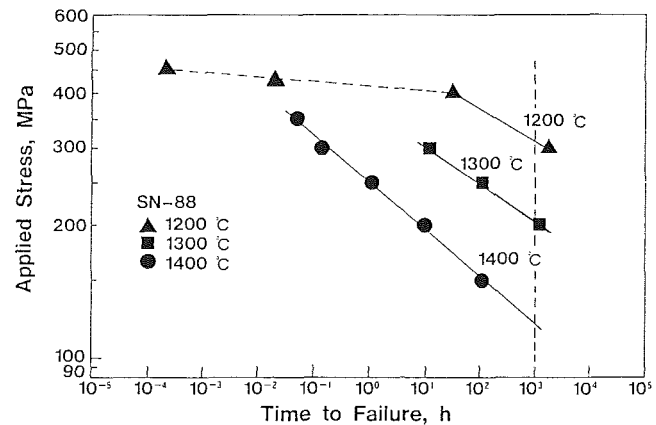


Fig. 8 Results of static fatigue test under tensile stress

Table 3 Fractographic analysis of fracture surface after static fatigue test

Static fatigue testing conditions			Fracture origin characterization	
Temperature (°C)	Stress (MPa)	Rupture Time (hour)	Identity	Location
1200	300	1640	C.G.R.C	Surface
1200	400	29	L.G./Micro crack	Surface
1200	450	1x10 ⁻⁴	Machining damage	Surface
1300	200	1234	C.G.R.C	Surface
1300	250	103	C.G.R.C	Surface
1300	300	11	C.G.R.C	Surface
1400	150	104	C.G.R.C	Surface
1400	200	9	C.G.R.C	Surface
1400	250	1	C.G.R.C	Surface
1400	300	1x10 ⁻¹	C.G.R.C	Surface
1400	350	5x10 ⁻²	Pore	Volume
Ref. RT	674	Fast fracture	Large grain	Volume
RT	646	Fast fracture	Large grain	Volume
RT	627	Fast fracture	Pore	Volume

C.G.R.C : Crack growth region by creep
L.G.: Large grain

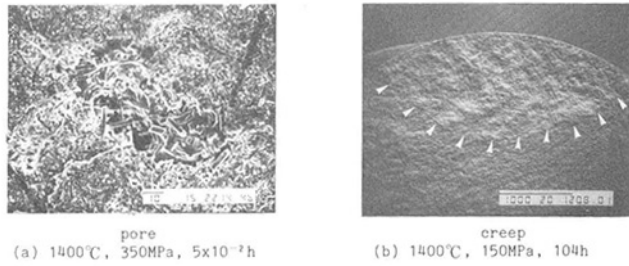


Fig. 9 Fracture origins of the specimen after static fatigue test under tensile stress

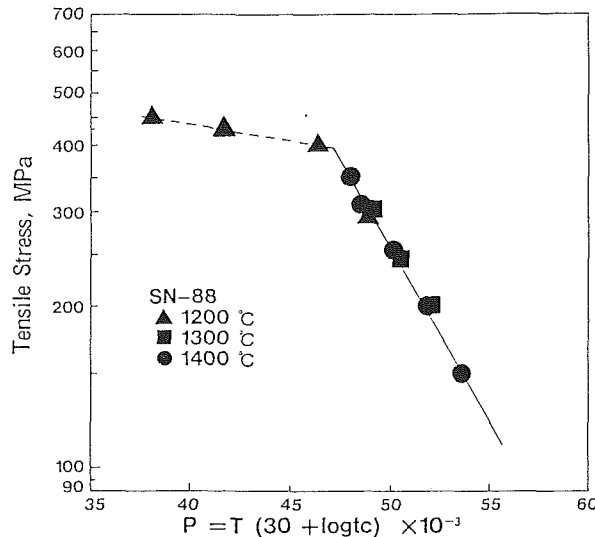


Fig. 10 Master Larson-Miller curve

that ruptured at higher stress were typically from pre-existing flaws such as machining damage, pores, and large grains. On the contrary, the fracture origins of most of the specimen that ruptured at a lower stress originate from surface flaws, and it is considered that these surface flaws were caused by creep deformation. During the creep testing at elevated temperature, the surface of the flaw was oxidized. For example, in case of the specimen that ruptured at 1400°C loaded at 150 MPa for 104 h and 1400°C loaded at 200 MPa for 9 h, the large oxidized region that might be caused by creep phenomena are observed. Typical fracture origins are shown in Fig. 9.

3-6 Creep Rupture Properties Described Using Larson-Miller Parameter. The fatigue life of ceramic components has been predicted using the power law crack propagation equation, which is expressed as follows [9]:

$$\frac{da}{dt} = AK_I^n \quad (2)$$

where A and n are constants, a is crack length, and K_I is the stress intensity factor.

As mentioned above, the results in Fig. 8 are divided into two stress regions. In the higher stress region, it is possible to apply the power law crack growth formulation to the static and dynamic fatigue data. In this region, the strength degradation was caused by slow crack growth from pre-existing flaws. In the lower stress region, however, it is not possible to apply the power law crack growth formulation. SN-88 showed creep deformation in this region. Therefore, it is necessary to use another life prediction procedure for this region.

The Larson-Miller parameter P , defined as follows, is widely used to predict life time of creep rupture in metallic materials [11]:

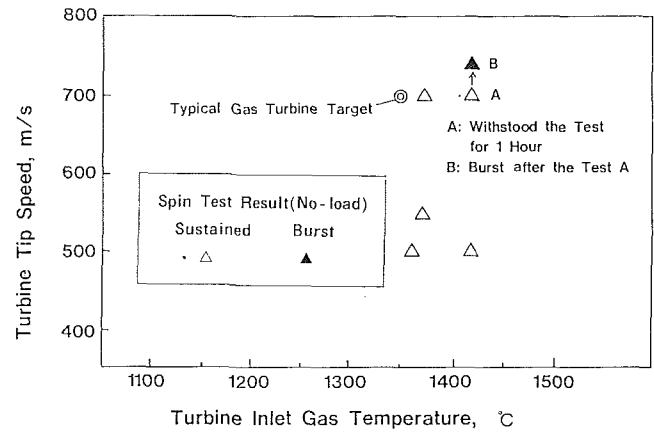


Fig. 11 Hot-gas spin test results for radial turbine wheel

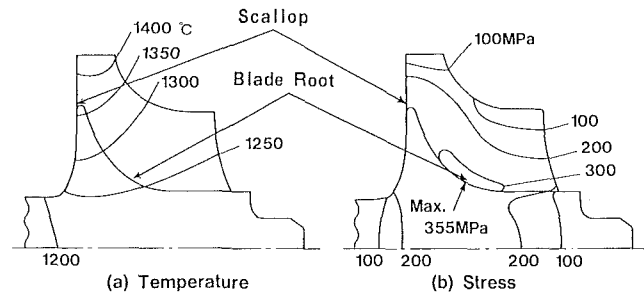


Fig. 12 Temperature and stress distribution of SN-88 turbine wheel at TIT 1400°C, turbine tip speed 700 m/s, and no load

$$P = T(C + \log t_r) \quad (3)$$

where T is absolute temperature, t_r is time to creep rupture, and C is a constant. A value for C of 20 in Eq. (3) is widely used for metallic materials.

Figure 10 shows the master Larson-Miller curve, where $C = 30$ for SN-88 is used. The result is represented by a line, and no dependence of temperature is shown. In the creep deformation regime, the Larson-Miller parameter is applicable to life prediction for hot components [7], [12].

3-7 Hot-Gas Spin Test. Figure 11 shows the results of the hot-gas spin tests of rotors where no aerodynamic loads were imposed (no-load condition). One wheel withstood the hot-gas spin test for one hour with a turbine inlet temperature (TIT) of 1410°C and turbine tip speed of 700 m/s. After this test, the turbine tip speed was increased to 742 m/s, and consequently the rotor burst to failure [12].

Figure 12 shows the temperature distribution under no-load conditions for the turbine inlet temperature of 1400°C and turbine tip speed of 700 m/s [10, 12]. The turbine's maximum stress of 355 MPa was found near the blade root of the wheel, and the temperature was 1250°C.

In the turbine wheel subjected to a one-hour endurance test under conditions, A , of hot-gas spin tests (TIT 1410°C, 700 m/s, and no load), the Larson-Miller parameter near the blade root of the turbine was estimated to be $P = 46$ and thus the point B_A in Fig. 13 was obtained. The point B_A is located below the allowable stress; thus, the wheel did not burst. However, after testing for one hour under conditions A , the rotor tip speed was gradually increased until failure was achieved at a speed of 742 m/s and TIT 1410°C. The stress and temperature under this condition B (Fig. 12) were estimated to be 400 MPa and 1250°C. The increasing rate of turbine tip speed was 50 m/s per 5 minutes, and the holding time could be assumed to be order of 0.01 h; the Larson-Miller parameter of the blade root area was $P = 43$, and point B_B was plotted. Point B_B is

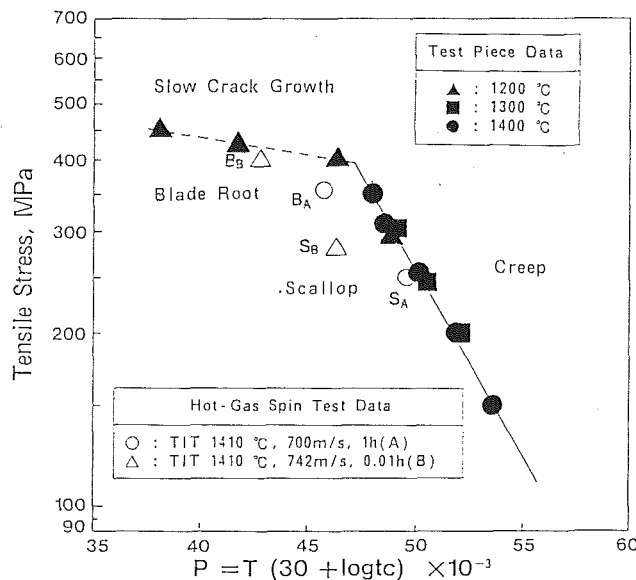


Fig. 13 Creep rupture properties of SN-88 described using Larson-Miller parameter

very close to the tolerance level estimated for the slow crack growth regime of the Larson-Miller master curve.

For condition *A* the temperature of the scallop section is very high, 1370°C, and the stress at this section is 250 MPa. When the Larson-Miller parameters are estimated in the same manner as for the blade root of the turbine, the resulting points S_A and S_B can be plotted in Fig. 13. Point S_A is also close to the tolerance level determined by creep.

From the above discussion, it can be assumed that the turbine wheel burst in the hot-gas spin test due to the slow crack growth at the blade root or the creep at the wheel scallop.

4 Conclusions

The following conclusions were reached in this study:

1 A heat-resistant, high-strength Si_3N_4 has been developed and a prototype fabrication process for a radial turbine wheel has been established.

2 The strength of specimens cut from the wheel was evaluated by Weibull statistical theory, and this was about 10 percent lower than comparable specimens cut from pressed billets.

3 The high-temperature tensile static fatigue test data could

be divided into two regions: a higher stress region governed by slow crack growth and a lower stress region governed by creep phenomena.

4 High-temperature tensile static fatigue test data could be described using a Larson-Miller parameter.

5 The fracture behavior of a radial turbine wheel in hot gas spin test was correlated to the master Larson-Miller curve.

Acknowledgments

The authors extend their gratitude to the following persons for their valuable help: Dr. Yoshito Kobayashi at the Ceramic Gas Turbine Group of Office of Truck and Bus Development and Engineering of Mitsubishi Motors Corporation, Mr. Eito Matsuo at Nagasaki Research and Development Center of Mitsubishi Heavy Industries, Ltd., and Mr. Toharu Inagaki at Nagoya Aerospace Systems Works of Mitsubishi Heavy Industries, Ltd.

References

- 1 Sato, H., Miyauchi, J., and Iwasaki, K., "Truck Turbine Engine Development at Mitsubishi," Paper No. 83-TOKYO-IGTC-88, 1983.
- 2 Miyauchi, J., and Kobayashi, Y., "Development of Silicon Nitride Turbine Rotors," SAE Paper No. 850313, 1985.
- 3 Kobayashi, Y., Matsuo, E., and Kato, K., "Hot-Gas Spin Testing of Ceramic Radial Turbine Rotor at TIT Around 1250°C," SAE Paper No. 880727, 1988.
- 4 Ozawa, T., Matsuhisa, T., Kobayashi, Y., Matsuo, E., and Inagaki, T., "Hot-Gas Spin Testing of Ceramic Turbine Rotor at TIT 1300°C," SAE Paper No. 890427, 1989.
- 5 Kobayashi, Y., Matsuo, E., Inagaki, T., and Ozawa, T., "Hot-Gas Spin Testing of Ceramic Radial Turbine Rotor at TIT 1400°C," SAE Paper No. 910401, 1991.
- 6 JIS R1606-1990, "Testing Method for Tensile Strength of High Performance Ceramics."
- 7 Masuda, M., and Matsui, M., "Fatigue in Ceramics (Part 4)—Static Fatigue Behavior of Sintered Silicon Nitride Under Tensile Stress," *J. Ceramic Soc. Japan*, Vol. 98, 1990, pp. 86–95.
- 8 Soma, T., Matsui, M., and Oda, I., "Tensile Strength of a Sintered Silicon Nitride," in: *Non-oxide Technical and Engineering Ceramics*, Stuart Hampshire, ed., Proceedings of the International Conference held at Limerick, Ireland, 10–12 July, 1985, pp. 361–374.
- 9 Evans, A. G., "Slow Crack Growth in Brittle Materials Under Dynamic Loading Conditions," *Int. J. Frac.*, Vol. 10, 1974, pp. 251–259.
- 10 Kobayashi, Y., Matsuo, E., and Watanabe, K., "Development and Hot-Gas Spin Testing of Silicon Nitride Radial Turbine Rotors," Paper No. 91-YOKOHAMA-IGTC, 1991.
- 11 Larson, F. R., and Miller, J., "A Time-Temperature Relationship for Rupture and Creep Stress," *Transactions of the ASME*, Vol. 74, 1952, pp. 765–775.
- 12 Watanabe, K., Ozawa, T., Kobayashi, Y., and Matsuo, E., "Development of Silicon Nitride Radial Turbine Rotors," *Proceedings of the 4th International Symposium on Ceramic Materials and Component for Engines*, Göteborg, Sweden, June 10–12, 1991, pp. 1009–1016.

Status of the Automotive Ceramic Gas Turbine Development Program

T. Itoh

Japan Automobile Research Institute, Inc.,
Tsukuba, Ibaraki, Japan

H. Kimura

Petroleum Energy Center,
Minato-ku, Tokyo, Japan

A seven-year program, designated "Research and Development of Automotive CGT," commenced in June 1990 with the object of demonstrating the potential advantages of ceramic gas turbine engines for automotive use. This program has been conducted by the Petroleum Energy Center (PEC) with the support of the Ministry of International Trade and Industry. The engine demonstration project in this program is being handled by a team from Japan Automobile Research Institute, Inc. (JARI). This paper describes the activities of the first year of the seven-year program, and includes the project goals and objectives, the program schedule, and the first-stage design of an experimental automotive ceramic gas turbine (CGT) engine and its components. The basic engine is a 100 kW, single-shaft gas turbine engine having a turbine inlet temperature of 1350°C and a rotor speed of 110,000 rpm. The primary engine components including the turbine hot flow path components have been designed using monolithic ceramics and are scheduled to be produced during the second year of the program.

Introduction

Early efforts for the development of a gas turbine engine as the prime mover for automobiles commenced in the latter part of the 1940s. Since then, the bulk of research and development for gas turbines has centered around metal gas turbines and has been performed by automobile manufacturing companies in America, Europe, and Japan. However, global energy awareness since the 1970s has led to an increased demand for higher thermal efficiencies and as a result, there has been continuing research into ceramic gas turbine engines that enable the turbine inlet temperatures to be increased, thus eliminating the necessity for cooling.

Japan is almost totally dependent upon imports for its petroleum needs and the stable supply and efficient use of energy resources are extremely important. Therefore, the advent is highly anticipated of an automotive engine that can run on a variety of fuels regardless of their octane value or cetane value, and which has a higher thermal efficiency and cleaner exhaust. Ceramic gas turbine engines are considered to have the greatest potential out of the candidates for such an engine. The program for "Research and Development of an Automotive Ceramic Gas Turbine Engine" was therefore started in June 1990, by the Petroleum Energy Center with the assistance of the Ministry of International Trade and Industry's Agency of Natural Resources and Energy, and with the active cooperation of the petroleum, automobile, ceramics, and other related industries.

The goal of this project is to develop and fabricate a prototype of a ceramic gas turbine engine, which can become the automotive engine of the future and provide an alternative to conventional reciprocating engines. This engine should not only meet the requirements of fuel diversification and envi-

ronmental control in the field of transportation in Japan, but should at the same time provide a higher thermal efficiency. Objectives to attain this goal include the practical verification of the following potential advantages of CGT engines:

- 1 ability to operate on a variety of fuels
- 2 greatly increased thermal efficiency
- 3 contribution to a cleaner environment

To attain these objectives, research and development is being carried out in the following four fields:

1 Research and Development of Combustion Technology for Diverse Fuels. The purpose of this is to ensure the stable supply and more efficient use of petroleum energy resources in the area of transportation through the development of technology for combustors of gas turbines that use fuels that currently have a low value-added component. These fuels include cracked light oil (light oil that has a low cetane value), light naphtha (gasoline that has a low octane value) and others. More specifically, this research involves clearly determining the characteristics of combustion for two-stage combustion, catalytic combustion and premixed, prevaporized combustion when such different fuels are used. This portion of the research and development activity will be mainly performed by the petroleum industry.

2 Research and Development of Technologies for Fabricating Components From High-Temperature Composite Materials. Current monolithic ceramic materials do not necessarily satisfy the conditions under which the components of gas turbines are used, and substantial improvements are required in their strength, fracture toughness, and reliability. The objective of this activity is to develop ceramic composite materials that can be expected to have improved characteristics in order to establish technologies for their processing, machining, and evaluation, which will lead to the production of components from such materials for use in gas turbines. More specifically, the technologies for the production of components should be

Contributed by the International Gas Turbine Institute and presented at the 37th International Gas Turbine and Aeroengine Congress and Exposition, Cologne, Germany, June 1-4, 1992. Manuscript received by the International Gas Turbine Institute January 13, 1992. Paper No. 92-GT-2. Associate Technical Editor: L. S. Langston.

developed for the materials of carbon-fiber reinforced composite ceramics, and for composite materials based on silicon nitride and silicon carbide. This portion of the research and development activity will be mainly performed by the petroleum industry, with the cooperation of ceramics manufacturers.

3 Research and Development of High-Temperature Lubricating Oils Technologies. The operating temperature of ceramic gas turbine engines for automotive applications will be very much higher than that of metallic engines and the operating speed will also be much faster. Currently, a sufficient amount of lubricating oil cannot be supplied since it is important to reduce mechanical loss as much as possible in order to improve the partial load fuel consumption. Conventional lubricating oils will not be able to meet these needs and it will be necessary to develop special gas turbine lubricating oils that have superior heat resistance, low friction characteristics, and oxidation stability. In particular, it is the objective of this activity to develop lubricating oils that have excellent thin-film oxide stability, thin-film coking prevention, high-temperature corrosion resistance, low friction characteristics, and high durability. This portion of the research and development activity will be performed by a cooperative team formed by the petroleum industry.

4 Research and Development of Automotive Ceramic Gas Turbine Engines. In order to have practical proof of the development objectives, a suitable engine type will be selected and the components for the selected engine will be designed and developed. Furthermore, the engine will be designed, fabricated, and then evaluated by dynamometer testing. In addition, the components fabricated using ceramics and other new heat-resistant materials will be evaluated under simulated load conditions to provide practical proof that they can be used as engine components. The results of these experiments will be used as the basis for investigating the potential of ceramic gas turbine engines for use in different types of automobiles in various fields of application. The Japan Automobile Research Institute Inc. (JARI) is to be in charge of this portion of the project.

This paper describes the area (4) of which the Japan Automobile Research Institute is in charge. This area is the design, fabrication, and evaluation of ceramic gas turbine engines, and will be described in detail in the following pages, centering around the basic plan of engine development and the preliminary engine design activities that were carried out during the first year of the program [1].

Engine Selection

Engines for automotive applications can be of various types, ranging from large engines for buses and trucks, to small engines for mini-cars. However, since it would be impossible in this program to prove the feasibility of ceramic gas turbine engines for all types of engines, a typical size will have to be selected first for experimentation during this project. The basic technical problems involved in realizing ceramic gas turbine engines of that size will have to be solved to develop the technology applicable to the development of different size engines. With this in mind, an investigation was performed into the engine size and type that should be developed in the course of the research and development activities of this project.

Why 100 kW? From the point of view of high efficiency for each engine component, gas turbine engines are basically suitable for large engines. However, since the application technology for ceramic engines is still immature, starting with an engine of as small a size as possible is preferable for reaching the level where the performance can be evaluated as a ceramic gas turbine. On the other hand, it is more difficult to attain

high efficiency in a small engine. Nevertheless, small cars comprise the largest proportion of vehicles in Japan, and an engine applicable to small cars would have the greatest impact. If the 100 kW class is chosen as the central value for small cars, then it would be easy to extend the technology to include engines for both large and small cars. This value was therefore chosen as the appropriate engine output to prove the practical performance of ceramic gas turbines in this project.

Why Single-Shaft? [2, 3]. Automotive gas turbines of the twin-shaft type have been developed because of their superior torque characteristics. However, the structure of the single-shaft type is simpler than that of the twin-shaft and also has the advantages of fewer components, light weight, and compactness. Single-shaft engines do not have suitable torque characteristics so they must be combined with a continuously variable transmission. Former projects considered the use of a twin-shaft type since a continuously variable transmission has not yet been developed for a gas turbine engine. Recent examples of practical continuously variable transmissions and the anticipated technical advances led to the belief that the adoption of a continuously variable transmission would not delay the project. Both the single-shaft and the twin-shaft engine types have their respective advantages and disadvantages to the extent that neither can be said to be clearly superior. Although research and development should of course be performed for both types, the resource limitations of this project preclude such parallel development. The need to solve the many problems involved in developing the ceramic engine technology and the need to prove the potential of ceramic gas turbines (with respect to fuel economy, exhaust gas emissions, and multifuel capability) within the limited time and resources available led to the selection of the single-shaft type with its fewer components, thus enabling the development efforts to be concentrated on the more important technical problems.

Objectives

The goal of this project is to demonstrate by dynamometer testing the significant potential advantages of an automotive ceramic gas turbine engine by March 1997. The following are the objectives of this demonstration:

- a thermal efficiency of over 40 percent.
- gaseous emission levels within the Japanese Emission standard for passenger cars.
- ability to use a variety of alternative fuels.

In addition to the demonstration of the above, it is hoped that the following issues will be clarified:

- the feasibility of ceramic components for use in automotive gas turbine engines.
- the marketability and technical assessment of CGT for individual automotive applications (such as buses, trucks, passenger car, and the like).

Development Schedule

Figure 1 shows the outline of the seven-year development schedule. The project is divided into four tasks: preliminary design of the engine, component development, engine system development, and marketability and technical assessment (research into technologies to apply ceramic gas turbines to various vehicles).

The task of preliminary engine design will involve an investigation into the engine configuration to be developed including the components thereof, and an investigation of the performance goals.

Under the task of component development, the work of developing the engine components will be carried out so as to achieve the component performances necessary to achieve the overall engine performance goals. In particular, since the high-

	FY 90	FY 91	FY 92	FY 93	FY 94	FY 95	FY 96
1. ENG. PRE. DESIGN	1ST REVIEW		2ND REVIEW				
2. COMP. DEV.	DESIGN/FABRICATION	DEVELOPMENT OF EACH ENGINE COMPONENT					
3. ENG. SYS. DEV.				94/10 DESIGN/FABRICATION	DEVELOPMENT OF CGT POWERTRAIN		
4. ASSESS. OF CGT				ASSESSMENT OF CGT FOR AUTOMOTIVE USE			
MILESTONE	COMPLETE PRELIMINARY DES.			ENG. DES. REVIEW ENG. DEV. START		OUTPUT GOAL	EMISSION EFF. GOAL

Fig. 1 Project schedule

Table 1 Engine and component design specifications

COMP	TYPE	SPECIFICATIONS	
ENGINE	1-SHAFT WITH CVT	OUTPUT POWER	100 kW
		THERMAL EFF.	40%
		PRESSURE RATIO	5.0
		TIT	1350°C
		AIR FLOW RATE	0.445 kg/sec
		AIR LEAKAGE	2.0% (n.i.c.d. from HE)
		PRESSURE LOSS	6.7% (n.i.c.d. in HE)
		MECHANICAL LOSS	9.1%
		SPEED	110,000 rpm
COMP.	CENTRIFUGAL	VIGV	RADIAL BLADES
		OUTLET	SCROLL
		ADIABATIC EFF.	81.0%
TURB.	RADIAL INFLOW	ROTOR INLET	SCROLL
		EXHAUST	DIFFUSER
		ADIABATIC EFF.	87.5%
COMB.	SINGLE CAN	COMBUSTION	PRE-MIXED, PRE-VAPORIZED, LEAN
		COMBUSTION EFF.	99.5%
		PRESSURE LOSS	3.0%
HEAT EXCH.	REGENERATIVE	NO. OF CORES	2
		MOUNT & DRIVE	OUTER SUPPORT, OUTER DRIVE
		EFFECTIVENESS	93%
		AIR LEAKAGE	5.0%
		PRESSURE LOSS	6.0% + 0.3%

temperature components are to be fabricated using ceramics, this development will be carried out incorporating applied ceramic technology. Furthermore, a sustained effort will be made throughout the project to improve the performance of the components.

The task of engine system development includes engine design and fabrication and the evaluation of the engine system performance. The first part of the project will use an engine as a test rig for the testing of all the assembled components. After individual component testing and evaluation, the engine will be assembled and tested again to provide results that will be fed back to modify the preliminary engine design.

The research into the application technology will use the results of the design, trial, fabrication and experimental evaluation of the 100 kW ceramic gas turbine to determine the suitability of the ceramic gas turbine for use as an automotive engine, and the feasibility of applying the technology to other sizes and applications.

The development period has been set at seven years, but the

engine development goals will not be achieved based on only the current performance levels of each of the components. For this reason, it is essential to carry out development work to improve the performance of each component prior to the commencement of the engine development. The seven-year period is broadly divided into two periods. The first period is for the three years from fiscal 1990 to 1992, and the second period spans the four years from fiscal 1993 to 1996. The first period is to be spent mainly on component development while the second period is spent on engine development. An interim review will be conducted in the fourth year, at the division between the two periods. At that time the development level of each component will be evaluated and the final engine design will commence. The following are the major "milestones" during the entire seven-year period:

- complete initial engine preliminary design review.
- interim review.
- complete final engine design review.
- start of engine development.
- engine output goal.
- engine fuel consumption goal.
- complete dynamometer testing of gaseous emissions.
- report of the overall results.

Description of the Initial Engine

Table 1 lists the expected performance of the initial engine and its components at their rated power, and shows their specifications. The following is a description of the major features of the initial engine.

Engine Cycle Parameters. According to the results of investigations performed in the feasibility studies prior to this project, the turbine inlet temperature was set at 1350°C in consideration of the thermal efficiency of the engine and the high-temperature characteristics of the ceramic materials. The compression ratio of the compressor was set at 5.0 by taking into consideration the effect of the compression ratio on the fuel consumption at partial load, and the rotor stress.

Engine Arrangement. Since the automotive gas turbine must achieve a certain performance in an engine compartment of limited space, the engine structure will have to be compact, lightweight, and sufficiently durable to withstand vibration and shock loads. However, for the preliminary engine design, it was decided to select a structure having sufficient size and material margins to give priority to achieving the performance of each engine component and to demonstrate the major functions. With this in view, the engine configuration was investigated with emphasis on the following points:

- (a) A structure to minimize air leakage between the ceramic components, as this greatly affects the engine performance.

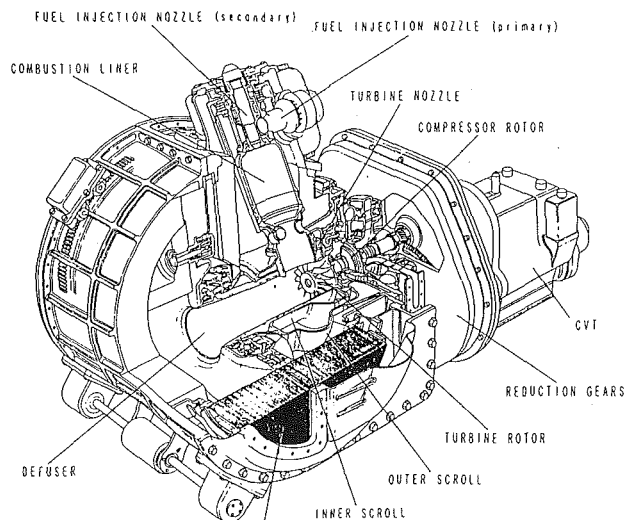


Fig. 2 Cutaway of powertrain

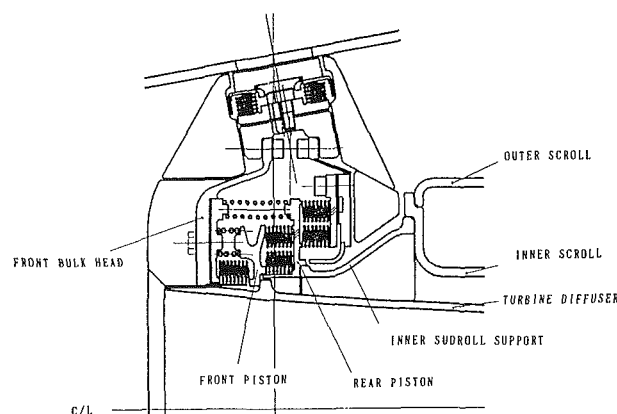


Fig. 3 Seal structure

(b) Support within the housing of static ceramic components that are brittle and weak with respect to deformation.

(c) Minimize the thermal deformation of the regenerator seal platform to decrease the air leakage.

(d) Maintain the concentric alignment between the high-speed rotating parts and the static parts.

Figure 2 shows a cutaway of the engine based on these considerations. The engine is of the single-shaft regenerative type and its main components are a single-stage centrifugal compressor, a single-stage ceramic radial inflow turbine, a ceramic lean premixed, prevaporized combustor, and ceramic regenerators. The transmission is a continuously variable transmission used with planetary gear sets.

Engine Housing. Functionally, the engine housing is an enclosure that optimizes the performance of each of the major components, including the ceramic components. In addition, it also forms the flow path of the high-temperature, high-pressure gas and thus functions as a pressurized container. Furthermore, it is also a heat-insulating container that minimizes the radiation of heat to the surroundings. In the earlier study, an investigation was performed for a two-piece construction having an outer steel housing and an inner ceramic housing. However, since the technology for the manufacture of the ceramic inner housing is still immature, and since the effect in terms of the thermal efficiency was not as great as expected, the adopted structure is a conventional structure having a metallic outer housing with thermal insulating material appropriately provided on the inside.

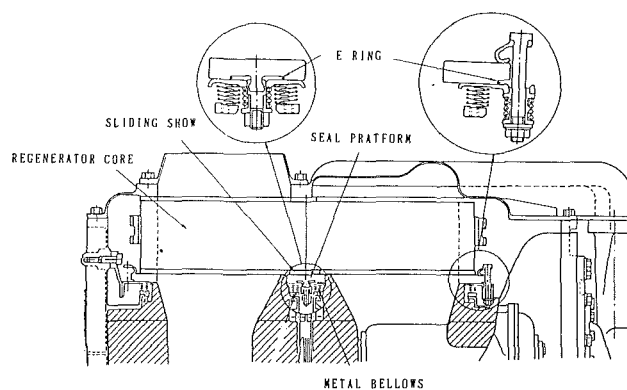


Fig. 4 Regenerator seal structure

The overall structure of the housing is such that the regenerator cores are located on either side of the aerodynamic components and the axis of rotation of these cores is inclined at an angle of 100 deg to the axis of the turbine rotor. This arrangement not only provides ample flow area to the turbine scroll within the limited engine width, but also facilitates installation and removal of the ceramic static component sub-assembly in the engine housing. The housing is made of a front and a rear part, with a double-walled bulkhead separating the high-pressure chamber from the low-pressure chamber. The bulkhead is insulated from the high-temperature gas, which contains a sealing mechanism to prevent the high-pressure regenerated air from leaking to the lower pressure turbine exit.

The housing will be heated by convection from the high-temperature air and gas, by conduction from adjacent high-temperature components, and by radiation. It will therefore be subjected to thermal stress and distortion and because distortions in the bulkhead and the regenerator seal platform induce leakage of the high-pressure air and greatly affect the engine performance. While minimizing such distortions, it is necessary to eliminate them from the structure of the sealing mechanism. The structures of the high-pressure seal mechanism and the regenerator seal platform are shown in Figs. 3 and 4, respectively. The material used for the high-pressure seal and the regenerator seal platform are ceramics that are not readily deformed due to heat, and the distortion of the housing is absorbed by a bellows structure. The seal portion inside the bulkhead and the crossarm section of the regenerator seal platform reach high temperatures and can be partially cooled if necessary by air discharged from the compressor.

Compressor. The compressor selected is a single-stage, backswept, centrifugal compressor with an upstream set of variable inlet guide vanes. The design is based on the requirement of a highly efficient stage that has a broad operating range. The initial compressor impeller has eight full blades and eight splitter blades. The radial diffuser design consists of a two-dimensional vane diffuser having 25 fixed blades and the radial flow variable inlet guide vane with a fixed leading edge and a movable trailing edge. The compressor rotation speed was selected to optimize the compressor and turbine efficiencies while at the same time maintaining acceptable levels of disk stresses.

The impeller backsweep angle was set at 40 deg so as to retain a broad operating range and a high efficiency. The inlet hub and shroud diameters were chosen to make the inlet relative Mach number as low as possible. Figure 5 shows the impeller vector diagrams. Figure 6 shows the impeller cross section. The main blade normal thickness distribution was selected to satisfy the blade stress and vibration criteria.

Turbine. The degree of reaction and the velocity triangles were optimized in the design of the rotor, taking into account

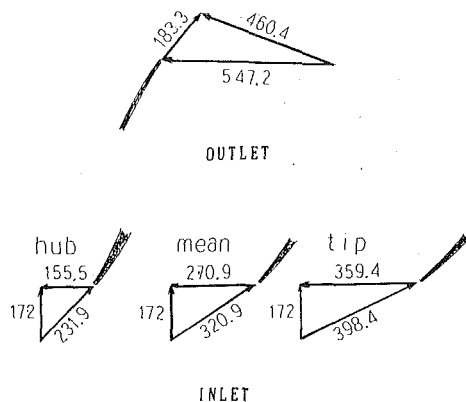


Fig. 5 Impeller vector diagrams

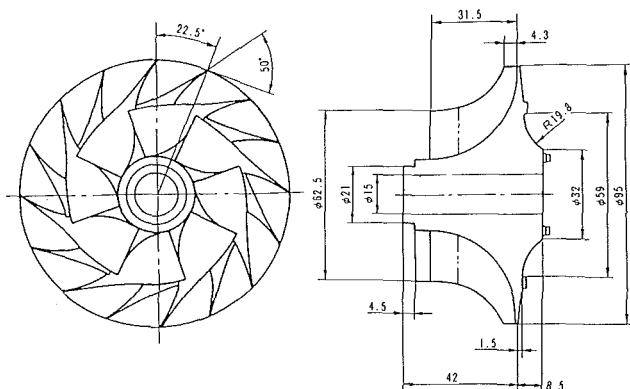


Fig. 6 Compressor impeller

the high efficiency at the partial load conditions frequently used in automotive engines, and the high tip speed within the allowable stress of the rotor. In order to obtain smooth variation of velocity and a uniform work distribution for the blade surfaces, three-dimensional blade-to-blade analysis and blade flow analysis were performed for the selection of the blade profile and the number of blades. Figure 7 shows the vector diagrams at the effective diameters of the inlet and outlet while Fig. 8 shows the final meridional view of the rotor and nozzle blades.

The nozzle flow path was determined on the basis of a basic blade profile that offers a low aerodynamic loss, considering the requirements resulting from the use of ceramic materials. A detailed investigation was therefore performed to optimize the blade shapes using 21 nozzle blades.

Combustor. In consideration of the symmetric structure of the engine and the ceramic components, an annular combustor would be superior, but a single-can type combustor, conventionally used in automotive gas turbine engines, was adopted, considering that exhaust emissions are a major technical problem in this project and there is no accumulation of data for the exhaust emissions from annular-type combustors. Although the diffusion combustion conventionally used in small gas turbines will not be sufficient to meet the stricter future emission standards (for NO_x levels in particular), an investigation was performed into a combination of the diffusion combustion system with the premixed, prevaporized lean combustion system (P-P-L) that has a high potential for future realization. More specifically, the premixed, prevaporized combustion system is used from idling to 30 percent of the rated load, and mixed combustion of the diffusion combustion system and the premixed, prevaporized combustion system achieved by directly injecting liquid fuel into the main combustion chamber is used from 30 percent to full rated load.

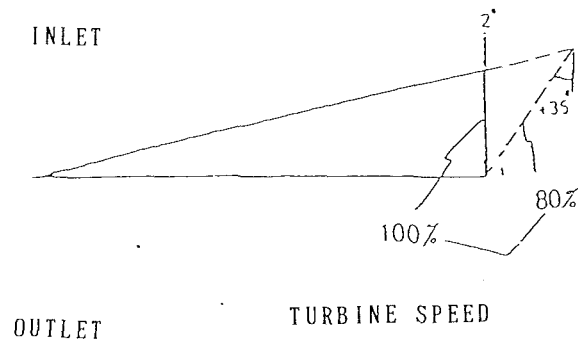


Fig. 7 Turbine vector diagrams

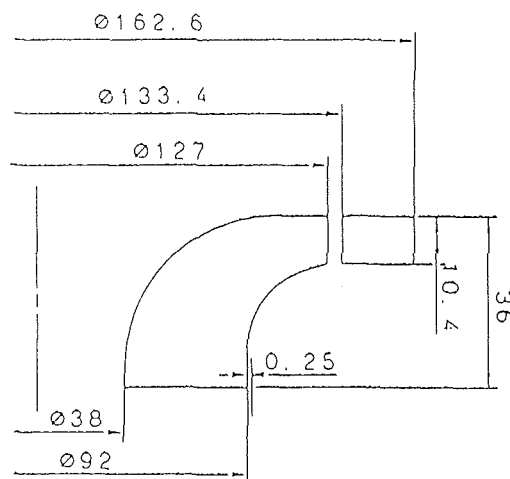


Fig. 8 Turbine stage meridional view

The overall structure was investigated in terms of a combination of factors such as the spatial relationship between the prevaporization region and the main combustion region, the air distribution control method between the prevaporization region and the lean combustion region, and the type of injection nozzle. Figure 9 shows a sectional view of the combustor.

Regenerator. The dimensions of the regenerator were determined in accordance with the design goal of a minimum effectiveness of 93 percent, and a maximum gas side pressure loss rate of 6 percent. The important factors for consideration in the design of the sealing structure are the wear resistance and the friction characteristics of the rubbing shoe of the seal, and the leakage characteristics of the static part (the diaphragm). Since the surface of the rubbing shoe should slide on a ceramic honeycomb material of high hardness and at a temperature of 1100°C , a solid lubricant is coated to the surface of the heat-resistant metallic substrate. On the other hand, a heat-resistant alloy was used for the diaphragm parts, since the pressure difference between the two sides of the diaphragm will be about 4 kg/cm^2 with the ambient temperature about 1100°C . A plate thickness of about 0.1 mm was selected in order to follow the

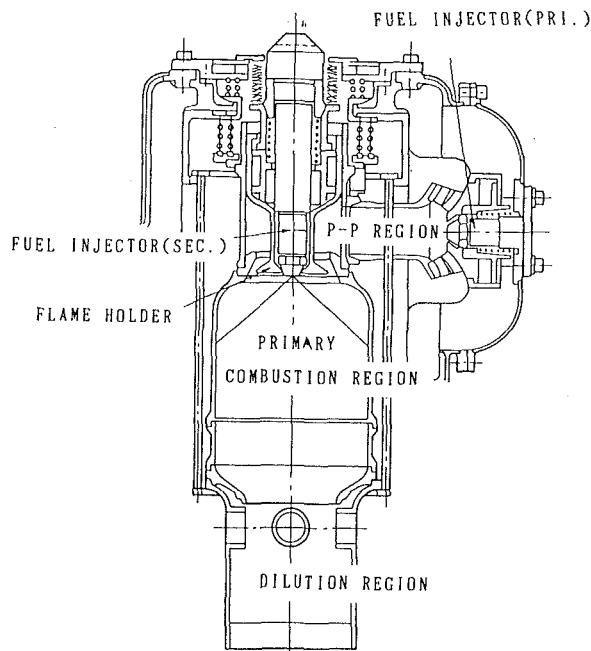


Fig. 9 Combustor sectional view

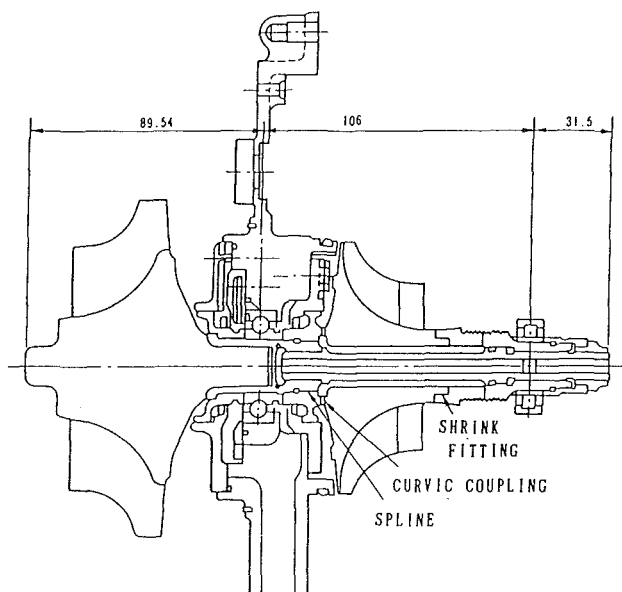


Fig. 10 Engine rotor system

distortion characteristics. The structure of the regenerator seal platform has already been described.

The regenerator core is driven through a ring gear and a pinion and is supported at three points on the external periphery of the core. The locations of these support points were determined so that the balance of forces between the three support points, i.e., the pinion gear roller, the fixed roller and the spring roller, is maintained, and the force balance is not disturbed when shock loads are applied to the engine, or when there is unexpected distortion in the sliding resistance between the regenerator seal and the core. Dry self-lubricating carbon bushings are used for the three support bearings because they will operate at temperatures of 200°C or more.

Rotor System. Figure 10 shows the rotating shaft assembly. The ceramic rotor is attached to the metallic shaft by either shrink fitting or brazing or a combination of both. The impeller

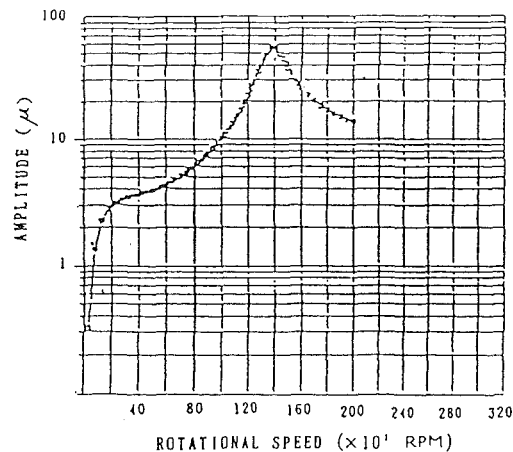


Fig. 11 Calculated rotor vibration

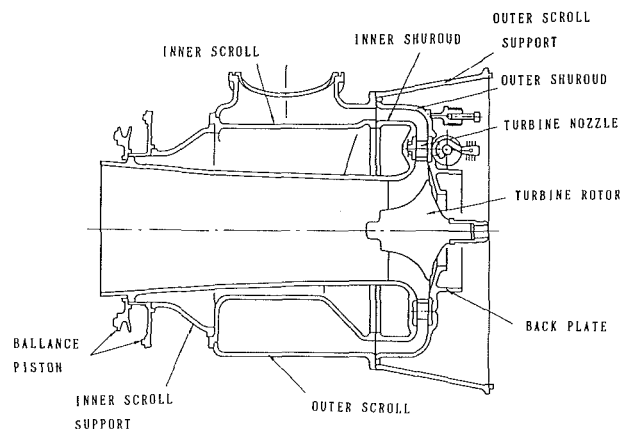


Fig. 12 Statics ceramic component subassembly

is coupled to the shaft with a curvic coupling at the back face of the impeller, and by the tie bolt at the center of the shaft. The shaft assembly is supported by a ball bearing between the impeller and the turbine rotor, and by a roller bearing in front of the impeller. The ball bearing should have a high DN value. As it is exposed to high temperatures, it should have effective lubrication and cooling using small amounts of lubricating oil that will be fed to it through the inner race from a feeder passage leading to the ball bearing in the tie shaft. An investigation is being performed also into the use of ceramic materials for the balls and the rollers of the two bearings. Vibration analysis of the shaft system was performed and the structure was designed so that the rigidity of the overall shaft assembly was retained. The primary and secondary vibration modes were damped by an oil film damper and it was confirmed that the third critical rotation speed of the bending mode was far from the operating speed. Figure 11 shows an example of the shaft system vibration analysis. Alignment of the turbine nozzle and the shroud to the rotating assembly involved inserting three rollers between the outer shroud and the engine housing as shown in Fig. 12 so as to allow for thermal expansion in the radial direction.

Transmission. Although the transmission is not a primary development topic of this project, it is essential to use a continuously variable transmission so as to improve the basic torque characteristics of the engine and thus enable the characteristics of the single-shaft gas turbine engine to be used for automotive applications. The development of a continuously variable transmission is currently being pursued for use with reciprocating engines. The types that offer the greatest poten-

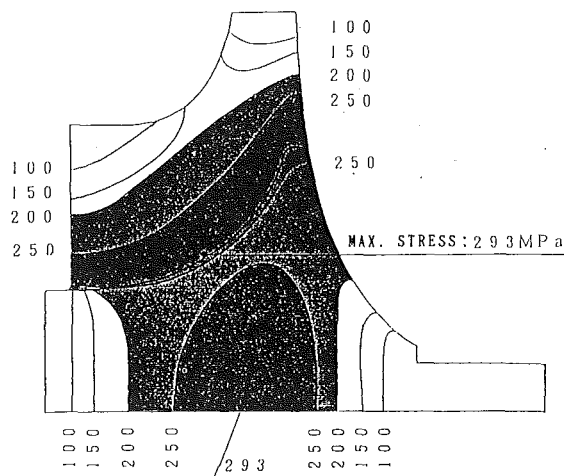


Fig. 13 Turbine rotor stress distribution

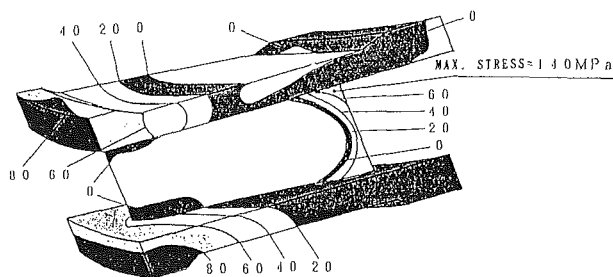


Fig. 14 Turbine nozzle stress distribution (cold start)

tial are the belt type and the traction type transmissions. In order to apply a continuously variable transmission to the gas turbine, we have selected an infinitely variable transmission (IVT) that can vary the speed from zero, and have entrusted a specialist manufacturer with the conceptual design for the performance, the size, and the structure.

Stress Analysis of Ceramic Components

Figure 12 shows an assembly drawing of the static ceramic components. The static ceramic components are surrounded by high-pressure air preheated in the regenerator. Experience has shown that face contact sealing is a simple and effective means of minimizing the leakage of air from the space between the ceramic components; therefore the static components were aligned on flat surfaces and stacked. The static component assembly is supported by an elastic support structure in which the entire stack of components is pressured from one side by spring force. A balance piston utilizing a differential air pressure is also provided to optimize the pressing force between the components. The structure of the diffuser at the turbine outlet is integrated with that of the turbine shroud to prevent air leakage between the two parts. The combustor is placed tangential to the turbine scroll and is independently supported to allow relative movement between the combustor and the scroll.

Reliability goals, material characteristics, boundary conditions, and the like were included in the investigation of the strength and reliability of the ceramic components. The thermal boundary conditions for each component were assumed by using the temperatures, pressures, and gas flow rates for each stage of the engine as obtained from engine cycle analysis. Temperature and stress distributions were calculated using FEM analysis under both rated operating and cold starting conditions, and the results were used as the basis to perform reliability analysis using Weibull theory. The time-dependent

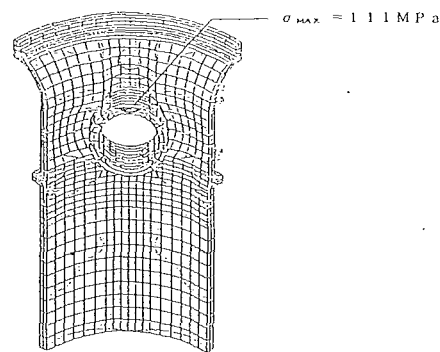


Fig. 15 Dilution liner maximum stress after cold start

failure probability of each component should be 10^{-5} or less after the vehicle has been run 100,000 km over a period of ten years. The following is an outline of the reliability analysis for each ceramic component.

Turbine Rotor. The ceramic turbine rotor is designed for fabrication from silicon nitride. The combined stress distribution of the mechanical stress and the thermal stress of the rotor at the rated operating conditions is shown in Fig. 13. The maximum stresses are 293 MPa at the root of the blades and at the center of the hub. The temperature at the root of the blades and at the center of the hub where the maximum centrifugal stress is generated will be in the range of 850°C to 900°C. According to the calculated temperature change at each location in the rotor after cold start, the critical stress for failure at the center of the hub will reach a maximum of 284 MPa about 40 seconds after starting. This value is less than the maximum stress under rated operating conditions.

Turbine Nozzle. The turbine nozzle is divided into six segments to facilitate fabrication. Stress analysis was performed for a segment including a single nozzle blade because the thermal stress upon cold start is very severe. The temperature and stress distribution of a silicon nitride nozzle reach a maximum value 10 seconds after start, as shown in Fig. 14. The maximum stress of 140 MPa is generated close to the side plate of the trailing edge and the temperature at that point is in the range of 500°C to 600°C. The failure probability after 10,000 starts was estimated at about 10^{-13} .

Combustor. Of all the combustor components, the primary combustor liner and the dilution liner are exposed to particularly high temperatures. Therefore a nonsteady thermal stress analysis was performed on these components. Figure 15 shows an example of the maximum non-steady-state thermal stress change with time and the location of its occurrence. The thermal stress increases rapidly after engine light off and reaches the maximum stress of 111 MPa after 30 seconds around the dilution hole in the liner. Under steady-state conditions, the maximum stress was found to be about half this value at 49 MPa. These results were then used to calculate the failure probability for these components based on the required engine life. The calculated value was extremely small, with all components satisfying the target values for the reliability.

Turbine Shroud With Turbine Diffuser. A reliability analysis under rated conditions and cold start conditions was carried out using combined stress analysis on the basis of the mechanical loading and temperature distribution. The material used for the analysis was silicon nitride. The maximum stress was found to be 127 MPa and the failure probability was very low at 10^{-17} . The combined stress reached a maximum of 414 MPa at about 19 seconds after cold start. Figure 16 shows the stress distribution at this time. The failure probability was

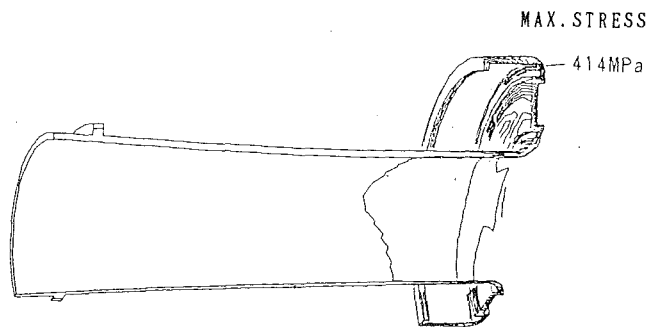


Fig. 16 Turbine shroud stress distribution (cold start)

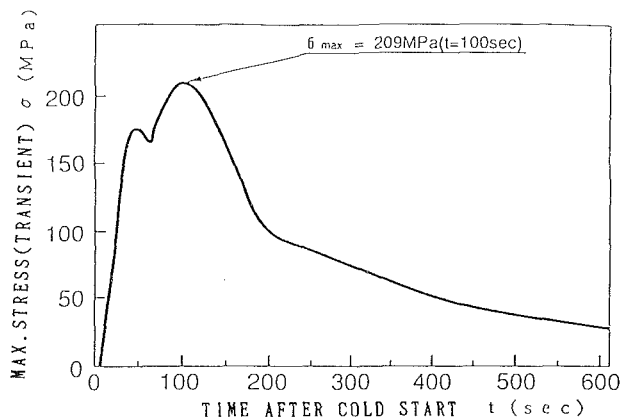


Fig. 17 Turbine scroll maximum stress after cold start

6.7×10^{-6} and this value must be reduced in the future in order to reduce the failure probability after the required life.

Turbine Scroll. The transient temperature distribution and the thermal stress after cold start were calculated using the material characteristics of silicon nitride. The maximum transient thermal stress in the outer scroll is shown in Fig. 17. The maximum stress of about 209 MPa occurs about 100 seconds after starting around the inlet where the dilution liner of the combustor is inserted. Under steady-state conditions, the maximum stress was found to be 200 MPa. At that time, the failure probability based on the required life of the engine was a quite satisfactory value of about 2.8×10^{-5} . Stress analysis for the inner scroll showed that the maximum stress of 106 MPa occurs at the flange periphery on the turbine outlet side about 80 seconds after cold start. This stress level is no cause for concern in terms of the material strength.

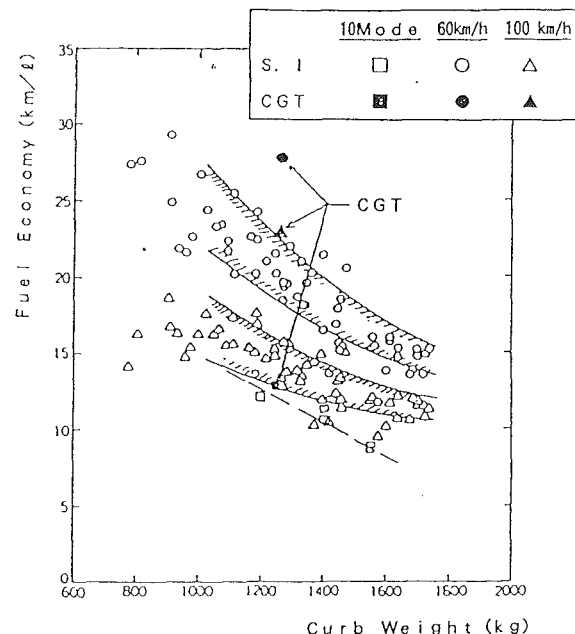


Fig. 18 Calculated fuel economy

Performance

Figure 18 shows the fuel economy in various operating modes, when compared to a spark ignition engine. The 10-mode fuel economy, for low load conditions, is clearly better than that of a piston engine, and the fuel economy under constant speed can be expected to be very good. According to preliminary calculations for acceleration, there are no problems attaining an acceptable acceleration time from 0 to 400 m that is conventionally used to measure the acceleration performance of vehicles. However, the delay inherent in gas turbine engines presents a performance problem immediately after acceleration. New ideas and further efforts are needed to achieve a balance between the acceleration performance and low fuel economy of gas turbine engines.

Summary

1 The program for "Research and Development of Automotive Ceramic Gas Turbine Engines" was commenced in 1990 as a seven-year program undertaken by the Petroleum Energy Center with the support of the Ministry of International Trade and Industry. The Japan Automobile Research Institute (JARI) is participating in this project and is conducting the design, fabrication, and experimental evaluation of the ceramic gas turbine engine.

2 Investigation of the basic plan of research and development, the major objectives (thermal efficiency, clean exhaust gas, and multifuel capability) the engine size (100 kW), the engine type (single-shaft gas turbine with CVT), and the development schedule for this project have been finalized.

3 The basic structure of the engine has been investigated and the first stage of design of the various components and elements has been completed.

4 The FEM analysis of the major ceramic components and the failure analysis have been carried out and the fabrication of the first set of molds have been completed.

5 The design of the individual testing equipment for the main elements of the engine has been completed.

6 The experimental evaluation of the various components will commence during fiscal 1991 using the individual test rigs for each of the components, including the ceramic ones.

Acknowledgments

The authors are grateful to the Agency of Natural Resources and Energy of MITI for making this research possible. We would like to thank Masumi Iwai, Itsuro Sakai, Masafumi Sasaki, and Katsutoshi Sugiyama of the JARI Team for technical support of the program efforts. We would also like to thank PEC for permitting publication of this paper.

References

- 1 Automotive Ceramic Gas Turbine Technology Development Report, Petroleum Energy Center, Mar. 1991 (PEC-90C01).
- 2 Report of 1988 New Seeds Exploration Study (Ceramic Gas Turbine), Petroleum Energy Center, Mar. 1989 (PEC-88T21).
- 3 Report of 1989 New Seeds Exploration Study (Ceramic Gas Turbine), Petroleum Energy Center, Mar. 1989 (PEC-89T11).

Current Status of 300 kW Industrial Ceramic Gas Turbine R&D in Japan

K. Honjo

R. Hashimoto¹

Agency of Industrial Science
and Technology, MITI,
Tokyo, Japan

H. Ogiyama

New Energy and Industrial Technology
Development Organization,
Tokyo, Japan

This paper gives an overview of the current status of Japan's national industrial ceramic gas turbine (CGT) project. The goals are 42 percent and higher thermal efficiency at the turbine inlet temperature (TIT) of 1350°C, and the emission from the exhaust gas should meet the regulatory values (for example, 70 ppm for NO_x). Also, ceramic material properties have the goals of 400 MPa for the minimum guaranteed strength at 1500°C, and 15 MPa√m for the fracture toughness. Currently, the basic metal gas turbine of TIT 900°C with all metallic components has already been fabricated and is running under some test conditions. The design of the basic ceramic gas turbine of TIT 1200°C has been completed and its manufacture is in progress. Research is addressing the production of large, complicated ceramic parts, and parts with less deformation and fewer defects can now be produced.

Introduction

Ceramic gas turbines (CGT) are expected to make a great economic and social impact with higher thermal efficiency in energy conservation technology.

R&D that focuses on ceramic engine components is being conducted by several gas turbine and automobile companies, especially for the development of turbocharger ceramic rotors, such as those that have been successfully commercialized during the past few years.

The Agency of Industrial Science and Technology of the Ministry of International Trade and Industry (MITI) began funding 300 kW CGT related R&D projects for cogeneration and mobile power generation use in the fall of 1988. The overall project's schedule covers nine years of R&D in the area of energy conservation technology. The organization and the schedule of this R&D project are shown in Fig. 1 and Table 1, respectively.

The project's objectives are to increase the thermal efficiency of small to medium capacity (1000 kW class) gas turbine engines and to decrease their emissions, as well as to promote their multifuel capability. Hence, R&D projects for heat-resistant ceramic materials and component technologies are under way. To integrate these technologies, three types of ceramic gas turbine engine will be built and tested. The goals of the project are shown in Table 2.

Regenerative Single-Shaft CGT for Cogeneration (CGT 301)

The CGT 301 is a recuperated single-shaft CGT for co-

¹Currently, Aeroengine Division, National Aerospace Laboratory, STA, Tokyo, Japan.

Contributed by the International Gas Turbine Institute and presented at the 37th International Gas Turbine and Aeroengine Congress and Exposition, Cologne, Germany, June 1-4, 1992. Manuscript received by the International Gas Turbine Institute January 13, 1992. Paper No. 92-GT-3. Associate Technical Editor: L. S. Langston.

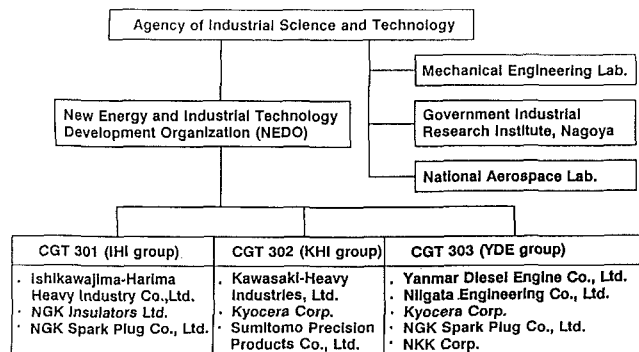


Fig. 1 Organization of 300 kW CGT R&D

generation use, which has characteristics for continuous full-load application.

A diagram of the engine is shown in Fig. 2. The ceramic parts are designed according to the axisymmetric structure design concept to reduce size, thermal stress, and deformations. One of the leading features of this constructive design is that it does not have a large scroll and the combustor is located on a shaft axis just before the turbine.

A rotor speed of 56,000 rpm has been selected by considering the reliability and durability of the ceramic materials under service conditions of TIT 1350°C, based on stress analyses and actual tests.

The compressor is a combination of axial flow and radial flow impellers. The turbine is a two-stage axial flow type with ceramic blades inserted into metal disks (hybrid-type turbine). The main engine specifications of the CGT 301 are shown in Table 3.

Axial Flow Turbine Blade. Concerning the three-dimensional curved blade, a fabrication process by injection molding

Table 1 R&D schedule of 300 kW CGT

FY	'88	'89	'90	'91	'92	'93	'94	'95	'96
Research items									
1. Heat-resistant ceramic component	Ceramic parts manufacturing technology								
2. Component technology	Fabrication and test element devices (compressor, combustion chamber, turbine, heat exchanger, bearing, instrumentation, etc.)								
3. Design, fabrication and test									
1) Basic design	Basic design								
2) Phase 1 design, fabrication and test		Fabrication and test of model GT (900°C)							
3) Phase 2 design, fabrication and test			Fabrication and test of model CGT (1200°C)						
4) Phase 3 design, fabrication and test							Fabrication and test of pilot model CGT (1350°C)		
4. Social adaptability research									
1) Study of environmental impact	Study of environmental impact								
2) Study of application systems	Study of load condition analysis, economic feasibility, operational control and management, etc.								
5. Performance Evaluation	Evaluation of ceramic and component technologies, and engine systems								

△ Interim Review

Table 2 Goals of 300 kW CGT R&D

ITEMS	GOALS			
Ceramic Gas Turbine	Thermal Efficiency	TIT	Axial Output	Exhaust Emissions
	≥ 42 %	1350°C	300 kW	Regulatory Values
Ceramic Components	Strength at High Temperature (1500°C)		Fracture Toughness (Room Temperature)	
	Minimum Strength	Wetbull Modulus (Reference)	≥ 15 MPa·√m	
	≥ 400 MPa	≥ 20		

Note: Thermal efficiency is defined by the ratio of the engine gross output to heat input measured by the lower heating value. Standard conditions are an atmospheric pressure (101325 Pa) and an ambient temperature (15°C)

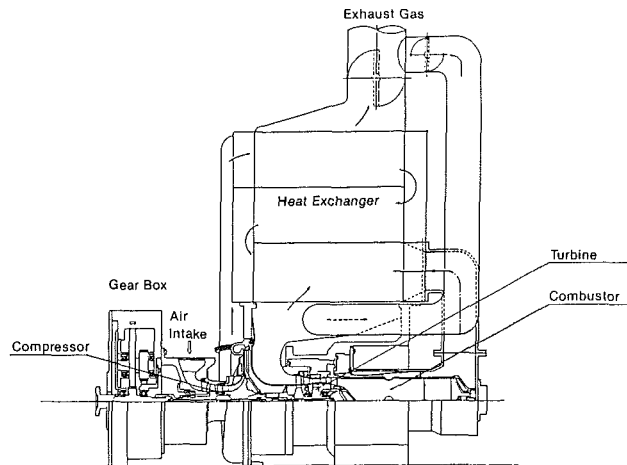


Fig. 2 Design of CGT 301

was studied and the appropriate mold construction was determined.

Turbine blade models were made by injection molding from SN-84 and were evaluated regarding the shape precision of blade. The sintered bodies were deformed by 0.48 mm toward the concave side at the tip end. This probably is caused by the lack of uniformity in density of the green body. Further research efforts will, therefore, be necessary for keeping a precise profile.

In order to measure material properties, a test specimen of $2 \times 1.5 \times 20$ mm was cut from the dovetail portion of a turbine blade model. The results are shown in Table 4. Our evaluation confirmed that it was comparable in four-point bending strength to rectangular sintered plates used as standards for comparison. The specimens cut from blades, however, showed a fairly large deviation in strength from one another. Cold-spin tests were conducted on 19 pieces of blade models to evaluate their reliability. All of these could withstand 120 per-

Table 3 Main engine specifications of CGT 301

Thermal Efficiency	≥ 42%
Turbine Inlet Temperature	1,350°C
Output Shaft Speed	3,000/3,600 rpm
Compressor	Axial + Centrifugal Type
Turbine	Two Stage Axial Type
Turbine Speed	56,000 rpm
Combustor	Single Can Type
Heat Exchanger	Recuperator Type

cent of the design speed. One of the blades on which a relatively large defect had been found at the high-stress area (the dovetail part on the pressure side of the blade) by nondestructive evaluation (NDE) was subjected to a burst speed test. It burst at 104,000 rpm, and a maximum stress of about 1020 MPa could be attained at that time, as shown in Fig. 3. If the four-point bending test bar and the model blades should be substantially

Table 4 Material properties (SN-84) of fabricated turbine blade

	Specimen Size (mm)	4-Point Bending Strength (MPa)		
		Room Temperature	1000°C	1200°C
Turbine Blade 1)	2 x 1.5 x 20	1430 ± 110	1280 ± 90	1140 ± 70
Standard Test Piece	2 x 1.5 x 20	1440 ± 130	1300 ± 100	1220 ± 160
(Injection Molding)	4 x 3 x 40	1230 ± 130	1190 ± 110	1070 ± 130

Note 1) Cutting portion of specimen from turbine blade

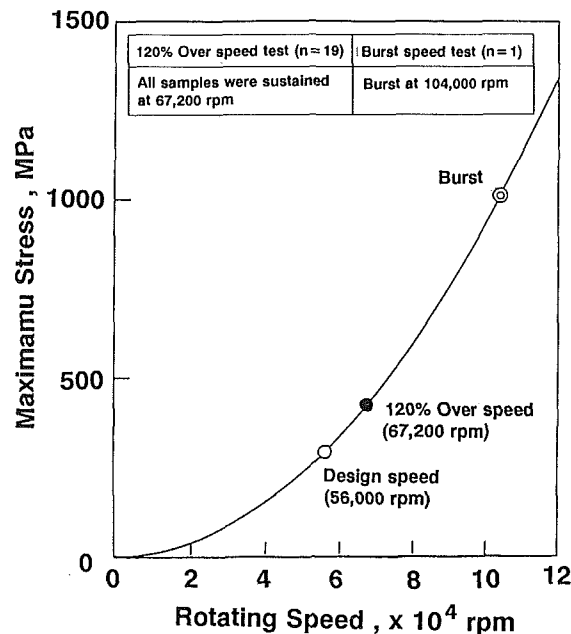
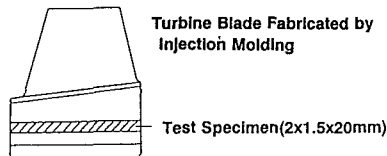
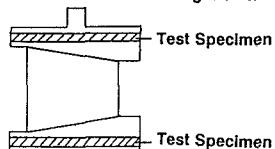


Fig. 3 Cold spin test result of ceramic turbine blade (CGT 301)

Table 5 Material properties (SN-88) of fabricated turbine nozzle

Specimen Size (mm)	4-Point Bending Strength (MPa)			
	Room Temperature		1400°C	
	4 x 1.5 x 20	4 x 3 x 40	4 x 1.5 x 20	4 x 3 x 40
Turbine Nozzle	810 ± 60	(750 ± 60)	780 ± 30	(720 ± 30)
Standard Test Piece	870 ± 20	790 ± 40	810 ± 30	760 ± 40

Note) Value of () are converted into the strength of the test bar of 4 x 3 x 40 mm



equal to each other in effective volume, the burst strength of the blade is in fairly good agreement with the average strength of the bending test bar.

Turbine Nozzle. Since the turbine nozzle temperature exceeds 1300°C, current silicon nitride (SN-84) cannot be applied to it. However, the newly developed material SN-88 is a high-strength material, whose four-point bending strength exceeds 700 MPa up to 1400°C and which has good oxidation resistance at high temperature. For this reason, we selected SN-88 for the turbine nozzle material. Turbine nozzle models were made

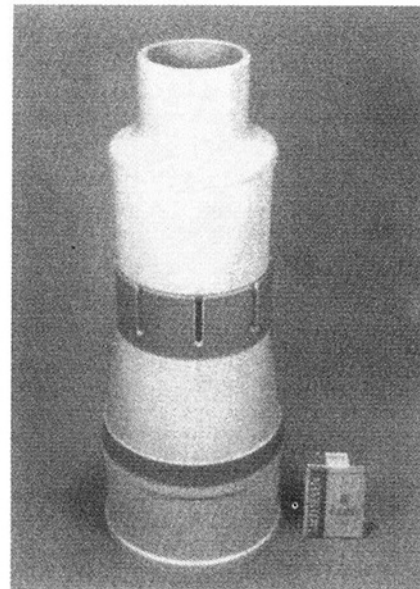


Fig. 4 Ceramic combustor liner (CGT 301)

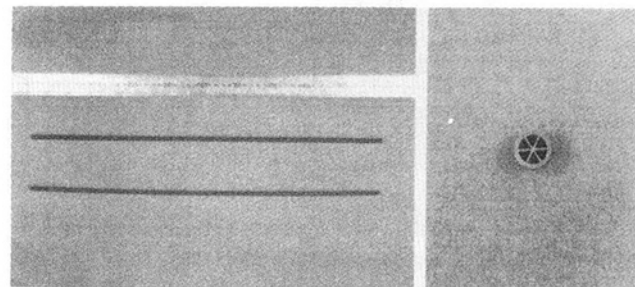


Fig. 5 Ceramic heat exchanger tube (CGT 301)

by injection molding, and four-point bending test bars of 4 x 1.5 x 20 mm were cut from each model in order to evaluate their strength. The results are shown in Table 5. Our evaluation confirmed that the test bars were comparable to standard test specimens in four-point bending strength at room temperature and also at 1400°C.

Combustor Liners. The fabrication process for a cylindrical component for the combustor was studied in terms of its basic design shape, and suitable shapes from the standpoint of manufacture were selected.

For the purpose of studying the fabrication process for combustor liners, a large cold isostatic press (CIP) apparatus having a vessel measuring 500 mm in diameter and 1200 mm in height and a maximum pressure of 490 MPa was purchased. We could ascertain the presence of a definite relationship between the pressing pressure and the density of the pressed body and of the sintered body, and the ability of the CIP apparatus to yield a sintered body with satisfactorily high density.

In order to obtain combustor liners having specified shapes after sintering, optimum primary and secondary pressing conditions were studied. Then, combustor liner models were made from SN-88. Figure 4 shows the fabricated combustor liners as assembled.

Heat Exchanger. In order to fabricate a 500 mm length of ceramic heat tube with a high level of straightness, drying and sintering methods were studied. As a result, 500 mm tubes with a deformation of only 0.6 ± 0.3 mm could be fabricated, and the straightness of the tubes was improved compared with

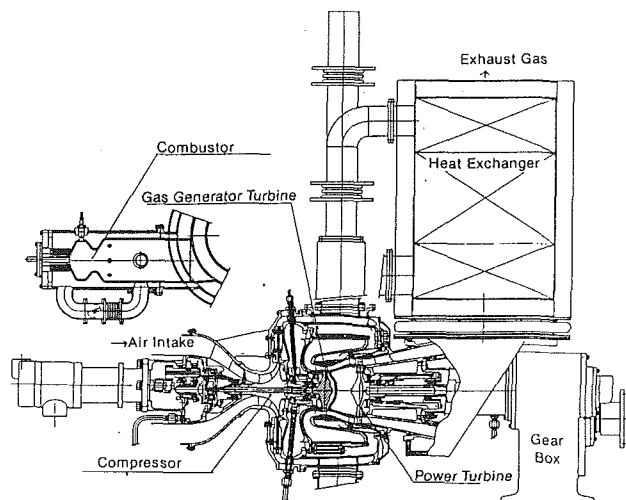


Fig. 6 Design of CGT 302

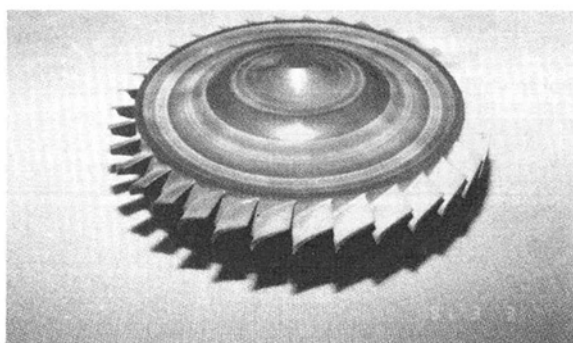


Fig. 7 Gas generator turbine rotor (CGT 302)

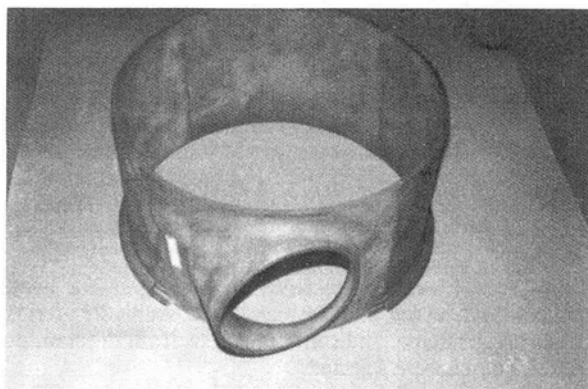


Fig. 8 Outer scroll before shipment (CGT 302)

that of last year. Figure 5 shows ceramic heat tubes of 500 mm in length.

The conditions for joining heat tubes and header plates for a heat exchanger were studied using an oxide glass bond. A highly airtight assembly of parts of silicon nitride bonded together by oxide glass was obtained during the last year from our study. The oxide glass bond was composed of SiO_2 , B_2O_3 , Na_2O , and Al_2O_3 . The surfaces of the parts to be joined were given oxidation treatment in advance. Attempts were made to bond parts in air, a vacuum, and a nitrogen atmosphere in order to clarify the influence of the bonding atmosphere. An evaluation for airtightness was carried out in the water, that is, supplying air into the heat tubes, and measuring the amount of air leaking out through the joints.

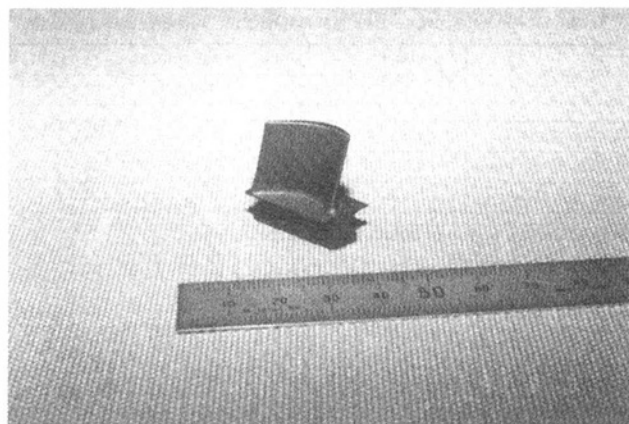


Fig. 9 Power turbine blade (CGT 302)

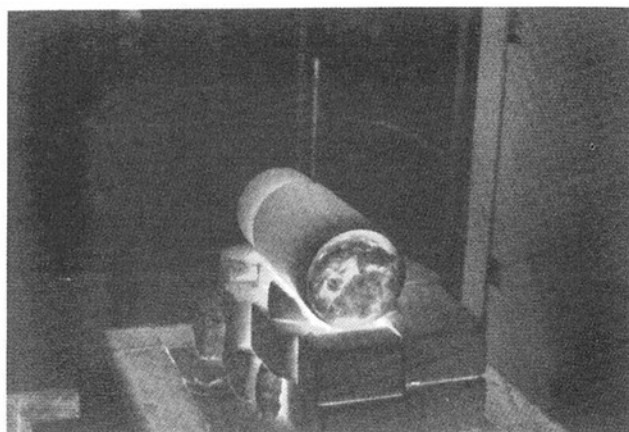


Fig. 10 Heat cycle test of ceramic combustor liner (CGT 302)

Table 6 Main engine specifications of CGT 302

Thermal Efficiency	$\geq 42\%$
Turbine Inlet Temperature	$1,350^\circ\text{C}$
Output Shaft Speed	3,000/3,600 rpm
Compressor	Single Stage Centrifugal Type
Gas Generator Turbine	Single Stage Axial Type
Gas Generator Turbine Speed	76,000 rpm
Power Turbine	Single Stage Axial Type
Power Turbine Speed	57,000 rpm
Combustor	Single Can Type
Heat Exchanger	Recuperator Type

Regenerative Two-Shaft CGT for Cogeneration (CGT 302)

The CGT 302 is a recuperated two-shaft CGT for cogeneration use suitable for partial load application in such facilities as hotels, hospitals, or office buildings, which experience daily or yearly changes in demand.

Figure 6 shows the basic design of the engine. The gas generator section is composed of a radial flow compressor and an all-ceramic axial flow turbine. The power turbine is an axial flow hybrid turbine. A turbine wheel without a center hole is used for the gas generator turbine rotor to obtain a high tip speed of 573 m/s. By adopting a high pressure ratio of 8, which optimizes thermal efficiency, it becomes possible to reduce the turbine outlet gas temperature so that a metallic recuperator can be used. The main engine specifications of the CGT 302 are shown in Table 6.

Gas Generator Turbine. The gas generator turbine rotor was an axial type rotor and had a rather thick body in the hub

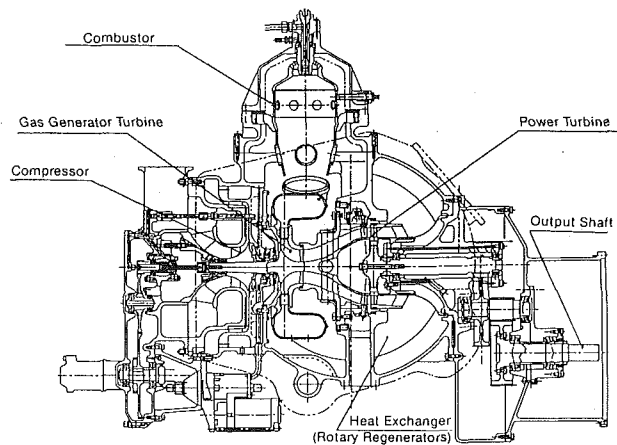


Fig. 11 Design of CGT 303

Table 7 Examples of the results of bend and tensile tests

Specimen	Damper Material	Fracture Strength (MPa)		Remarks
E-1	A	Bend Test	253	Fractured at the Ceramic Side
		Tensile Test	48	Fractured at the Ceramic Side
F-1	B	Bend Test	328	Fractured at the Ceramic Side
		Tensile Test	65	Fractured at the Ceramic Side

Table 8 Main engine specifications of CGT 303

Thermal Efficiency	≥ 42%
Turbine Inlet Temperature	1,350°C
Output Shaft Speed	3,000/3,600 rpm
Compressor	Single Stage Centrifugal Type
Gas Generator Turbine	Single Stage Radial Type
Gas Generator Turbine Speed	55,000 rpm
Power Turbine	Single Stage Axial Type
Power Turbine Speed	32,500/39,000 rpm
Combustor	Single Can Type
Heat Exchanger	Rotary Regenerator Type

section. This thickness seemed to be the prime cause of defects (mainly cracks) during production. Therefore, the geometry was modified to a thinner body after the design was reviewed by stress analysis. Also, minor modification was made in the blade root. After the design review, the maximum stress was analyzed to be 250 MPa, which is below the design standard.

The metal mold was modified to accommodate these changes, and forming, dewaxing, sintering and other processes were reviewed as well. Figure 7 shows the modified rotor design after sintering and machining.

Scroll. The outer scroll is first made of four smaller sections so that the effect of thermal shock can be alleviated. They are bound together in one piece by ceramic fibers, which are converted into fiber-reinforced ceramic.

The four sections were made separately by drain slip casting, sintering, and machining. Figure 8 shows a photo of these sections just before binding with ceramic fiber.

Power Turbine Blade. Stress concentration in the dovetail was most likely and stress analysis was carried out before ordering the casting mold. As a result of stress analysis, it was found that the maximum principal stress would reach a value over the design standard. Therefore, the design of the power turbine blade was reviewed, and the geometry was redesigned for reducing the stress level.

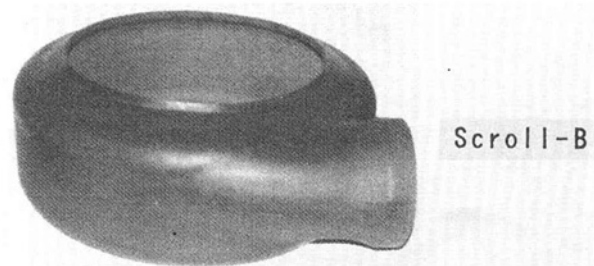


Fig. 12 Scroll B (CGT 303)

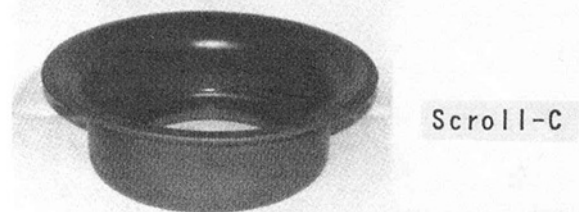
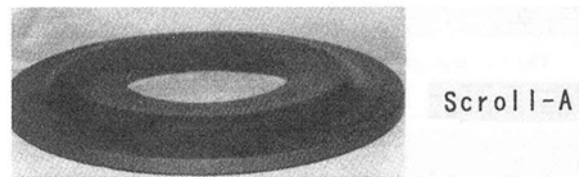


Fig. 13 Scroll A and C as-fired (CGT 303)

Figure 9 shows one of 42 blade tips that were produced after the redesigning of the first stage product.

Combustor Liner. Heat cycle tests of the Si_3N_4 combustor liner from 1350°C to room temperature were performed by using an electric furnace. This is the preliminary test to evaluate the appropriateness of the material strength and design shape under the condition of an extremely severe temperature distribution. The liner was investigated after the heat cycle tests using a penetration test. No crack was found. The general view of the combustor liner during the cooling stage is shown in Fig. 10.

Joining Technology (Gas Generator Turbine). Concerning the joining method of a ceramic gas generator turbine rotor and a metal shaft, it is necessary to insert a damper material between the metal and the ceramic because extremely large stress occurs when the metal is directly joined to the ceramic.

We could not accomplish the desired brazing strength in the tests using full-scale test specimens. Therefore, we performed a "Push Out Test" using the test specimens in order to improve the brazing method and select more effective damper materials (tungsten alloy), which can reduce the residual stress. We evaluated the following strengths:

- 1 Metal and damper-material strength.
- 2 Damper-material and ceramic strength.
- 3 Metal, damper-material, and ceramic strength.

After the evaluation by the "Push Out Test," we performed bending tests and tensile tests at room temperature using full-scale test specimens, which were prepared with the improved brazing method and selected damper materials.

Next, we performed the above tests using the full-scale test specimens whose thickness or configuration of damper materials were modified.

Examples of the results of bending tests and tensile tests are shown in Table 7.

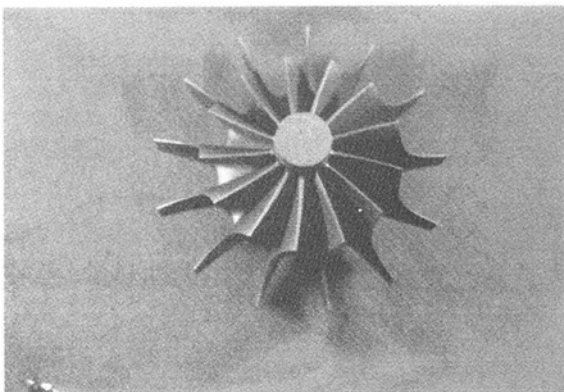


Fig. 14 Gas generator turbine rotor as-fired (CGT 303)

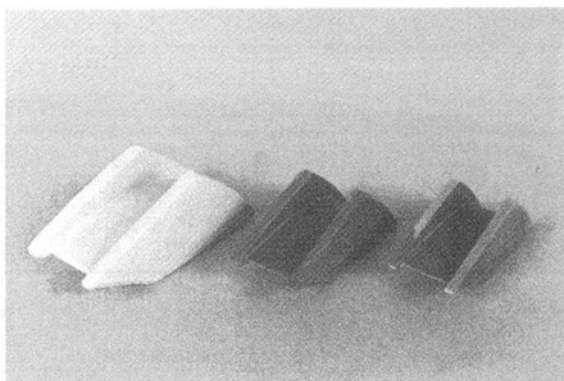


Fig. 15 Molded sintered and machined nozzle (CGT 303)

Surface Treatment Technology. According to the most recent research, the resistance to oxidation at high temperature of substrata (SN252) is considerably increased by chemical vapor deposition (CVD)- Si_3N_4 coating. However, the bending strength of coated substrata is reduced up to 50 percent of that of bare substrata.

On the basis of these data, the factors (heat treatment, coating condition of CVD, surface roughness, and so on) for the bending strength were evaluated. As a result, it was found that the bending strength of CVD-coated substrata amounted to 81–96 percent of that of bare substrata.

Regenerative Two-Shaft CGT for Mobile Power Generation (CGT 303)

The CGT 303 is a regenerative two-shaft CGT for mobile power generation use.

Figure 11 shows a diagram of the CGT 303. The gas generator turbine is a radial flow type and the power turbine is an axial flow hybrid type. To improve the thermal efficiency under partial load, the power turbine nozzle is designed based on variable geometry.

Two sets of 610 mm outside diameter rotary type heat exchangers are installed on both sides of the engine to obtain a high thermal efficiency. The design targets for the temperature efficiency of the heat exchanger and the air leakage rate are 92 and 4.5 percent, respectively. To optimize the thermal efficiency of the engine, the compressor pressure ratio is set at a low 4.5. The main engine specifications of the CGT 303 are shown in Table 8.

Scroll. As the scroll is quite a large size component with a maximum length of 540 mm, it is divided into three smaller

sections, i.e., Scroll A for the bottom section, Scroll B for the outer section with gas inlet, and Scroll C for the inner section.

Because of its size and complicated shape, it was difficult to calculate and make a precise estimate of shrinkage of Scroll B during sintering. As a result, deformation became the primary problem to be solved throughout the year for producing Scroll B.

Based on detailed measurements of green and sintered bodies, the coefficient of shrinkage was calculated for various parts of Scroll B, and casting molds were repeatedly reshaped for obtaining the optimum geometry.

Also, jigs were designed for alleviating the effect of contraction during sintering. As a result, deformation was corrected to an acceptable level and Fig. 12 shows the latest product.

The final geometry of Scroll B has yet to be finalized after reviewing the design from an assembly and machining point of view. In addition, further analysis has to be made on deformation for achieving the specified dimensions and optimum geometry of the mold, forming and sintering conditions, etc., which have yet to be found.

Figure 13 shows sintered Scroll A and Scroll C in an as-fired state. The design of these components also has to be reviewed for reducing the values of thermal stress, and the thickness may have to be reduced. The design of the casting mold, machining method, etc., also need to be studied further.

Gas Generator Turbine Rotor. The gas generator turbine (GGT) rotor is a radial type and has 13 blades with outer diameter of 162.2 mm. The design was reviewed in the previous year, and a casting mold was made based on the design review. A rotor was produced as a first-stage product for tests. Figure 14 shows a photo of the GGT rotor in an as-fired state.

Gas Generator Turbine Nozzle. Nozzle molding, dewaxing and sintering tests were performed and fundamental nozzle manufacturing conditions were established. However, as several cracks were observed in a part of the sintered body and slurry was present due to deformation of the mold, the nozzle mold was modified and the optimum injection conditions were re-investigated. The results show an improved inflow of slurry and no cracks were observed in the end plate. X-ray inspection also revealed no cracks in the dewaxed body. Sintering tests are currently in progress.

For machining of nozzles, jigs were manufactured and machining tests on the end plate revealed some problems in machining accuracy. Therefore, the fixing method of nozzle to jigs was modified and new jigs were designed and manufactured. Machining tests with the modified jigs confirmed that the required accuracy was satisfied. Figure 15 shows the molded nozzle and the sintered body before and after machining.

Ceramics to Metal Joining Technology. Regarding joining of the ceramic rotor and metal shaft, a method using shrink-fitting with braze-bonding is under development, and several types of shapes of joining section were studied in the previous year. Model pieces were made based on the findings from the previous year, and they were tested for their joining strength. The model pieces were tested for 500 heating cycles between room temperature and 700°C and the result was satisfactory.

Summary

The 300 kW industrial CGT national project for power generation was started in 1988.

As phase 1, a primary gas turbine composed of all metallic components with a 900°C turbine inlet temperature was completed in 1991. As phase 2, a basic 1200°C ceramic gas turbine is under development. However, there are many problems to be solved for applying ceramic materials to an advanced gas

turbine. Problems such as thermal stress at the ceramic-to-metal joining interface, forming/sintering of large-scale ceramic components, and precise machining must be solved for the success of this 300 kW CGT project. International information exchange on ceramics and CGT is essential for this purpose.

Acknowledgments

The authors wish to thank the three participating national

laboratories, the cooperating companies, and other concerned people for their assistance in publishing this paper.

References

- Nagamatsu, S., Mizuhara, K., Matsuda, Y., Iwanaga, A., and Ishiwata, S., 1991, "Current Status of Industrial and Automotive Ceramic Gas Turbine R&D in Japan," ASME Paper No. 91-GT-101.
- New Energy and Industrial Technology Development Organization (NEDO), 1991, "Ceramic Gas Turbine R&D," NEDO Annual Report 1990.
- Yamagishi, K., Yamada, Y., Echizenya, Y., and Ishiwata, S., 1989, "Current Status of Ceramic Gas Turbine R&D in Japan," ASME Paper No. 89-GT-114.

Ceramic Matrix Composite Applications in Advanced Liquid Fuel Rocket Engine Turbomachinery

J. W. Brockmeyer

Rocketdyne Division,
Rockwell International Corporation,
Canoga Park, CA 91303

Hot gas path components of current generation, liquid fuel rocket engine turbopumps (T/P) are exposed to severe thermal shock, extremely high heat fluxes, corrosive atmospheres, and erosive flows. These conditions, combined with high operating stresses, are severely degrading to conventional materials. Advanced turbomachinery (T/M) applications will impose harsher demands on the turbine materials. These demands include higher turbine inlet temperature for improved performance and efficiency, lower density for improved thrust-to-weight ratio, and longer life for reduced maintenance of re-usable engines. Conventional materials are not expected to meet these demands, and fiber-reinforced ceramic matrix composites (FRCMC) have been identified as candidate materials for these applications. This paper summarizes rocket engine T/M needs, reviews the properties and capabilities of FRCMC, identifies candidate FRCMC materials and assesses their potential benefits, and summarizes the status of FRCMC component development with respect to advanced liquid fuel rocket engine T/M applications.

Introduction

Use of high-temperature capability, low-density ceramics, and ceramic composites has been considered for a range of potential turbine engine applications. Utilization of these materials in rocket engine turbines presents a special set of challenges and requires development of materials tailored to meet these challenges. The following review summarizes the operating requirements posed by current and future generation liquid fuel rocket engines, evaluates the feasibility and assesses the potential of using FRCMC in rocket engine T/M, and summarizes the status of ongoing programs for development of FRCMC T/M components.

Rocket Engine T/M Versus Conventional T/M. Liquid fuel rocket engine T/M components face a unique operating environment (Table 1) and, consequently, are fabricated from specialized materials (Chandler, 1983). The materials currently in use for rocket engine applications have, in general, been developed by modifying materials originally developed for aircraft turbines (Fritzemeier and Brockmeyer, 1990). For hot gas path applications, superalloys have typically been used. Superalloys have demonstrated long-term durability in the aircraft environment, but, due to the severity of the rocket engine thermal/mechanical environment and the corrosive nature of rocket engine propellants, useful lifetimes of even the most

advanced superalloys are extremely limited in rocket engine applications.

SSME Materials and Requirements The Space Shuttle Main Engine (SSME) provides an example of current materials usage and limitations in advanced rocket engine T/M. The SSME is a highly advanced, liquid oxygen/liquid hydrogen (LOX/LH₂)

Table 1 Rocket engine T/M environment presents unique materials requirements

ITEM	ROCKET ENGINE TURBINES	AIRCRAFT GAS TURBINES
FUEL	HYDROGEN OR CH ₄	PETROLEUM DISTILLATE
OXIDIZER	OXYGEN	AIR
OPERATING SPEED (RPM)	36K - 110K	15K
BLADE TIP SPEED (M/SEC)	570	570
KW/BLADE	470	150-350
HEAT TRANSFER (kW/m ² ·°K)	310	3
THERMAL START/STOP TRANSIENTS (°C/SEC)	18,000/4,000	55/55
ENGINE STARTS	55-700	2,400
OPERATIONAL LIFE (HRS)	7.5-100	8,000

Contributed by the International Gas Turbine Institute and presented at the 37th International Gas Turbine and Aeroengine Congress and Exposition, Cologne, Germany, June 1-4, 1992. Manuscript received by the International Gas Turbine Institute February 28, 1992. Paper No. 92-GT-316. Associate Technical Editor: L. S. Langston.

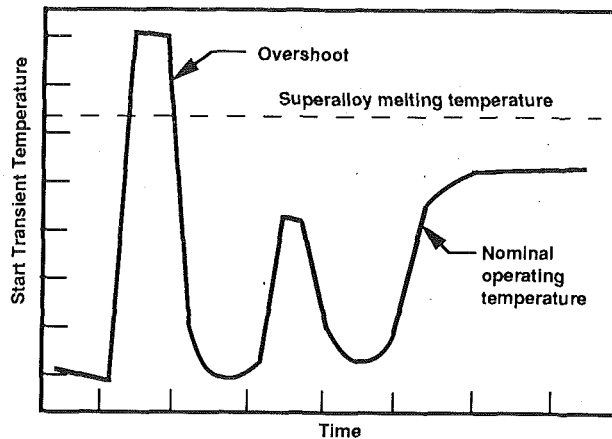


Fig. 1 SSME thermal transients reduce materials lifetimes

propelled, re-usable rocket engine. Three SSME are used to propel the space shuttle into orbit. Systems of the SSME (such as the high-pressure fuel turbopump, HPFTP) are confronted by temperatures ranging from the cryogenic temperatures (-253°C) of the liquid hydrogen fuel to the 3300°C temperatures reached within the main combustion chamber. Selected parts (such as the turbine blades) are exposed to thermal transients of approximately 1000°C occurring in as little as 0.1 second (as shown schematically in Fig. 1). The operating environment within the turbines consists of hydrogen-rich steam. Combined with the severe operating environment, the SSME requires re-usability and extended life versus conventional, "one-shot" rocket engines. This results in needs for materials with improved low cycle and high cycle fatigue properties and improved creep and stress rupture resistance.

To meet these extreme operating requirements, highly specialized materials were selected and have been used for SSME components. For example, the turbine blades are made of MAR-M246TM DS(Hf) alloy (a hafnium modified, directionally solidified superalloy produced by Martin-Marietta Corp.), which was the premier alloy for this application when selected in 1972. The turbine disk is made of WaspalloyTM (Waspalloy is a trademark of United Technologies Corp.) with a gold coating, which provides protection from hydrogen embrittlement. The extreme operating conditions of the SSME result in degradation of even these highly specialized materials during the nominal design life of 7.5 hours and 55 starts. Future generation rocket engines, with requirements for longer life, higher performance, and reduced weight, will demand development of advanced materials that exceed the capabilities of existing superalloys.

Next Generation Rocket Engine Material Needs. Extending

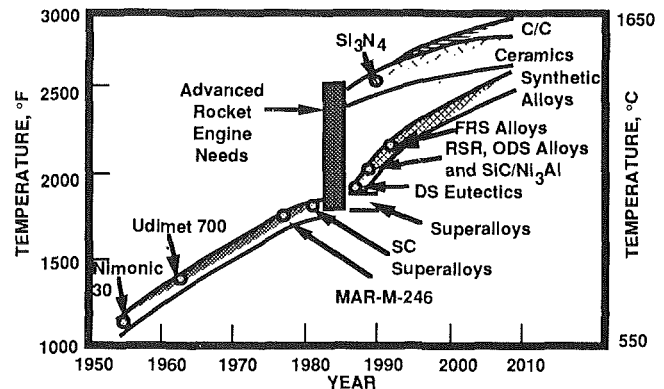


Fig. 2 Future generation rocket engines require development of new materials systems

the capabilities of superalloys presents only modest potential for extending the operating envelope of advanced rocket engines (Fig. 2) (Brockmeyer and Schnittgrund, 1990). Ceramics and FRCMC provide an alternative to "conventional" superalloys. Engineering ceramics typically combine low density and high specific strength with high operating temperature capability and resistance to corrosive and erosive environments. Unfortunately, monolithic ceramics are subject to brittle, catastrophic failure. FRCMC combine the desirable traits of monolithic ceramics with a "graceful" failure mode and, as a result, present considerable potential for future rocket engine use. Meeting the needs of future generation rocket engines with FRCMC will require continuing development of these emerging materials, and such development is being continued in current programs.

Rocket Engine Fundamentals

Understanding the needs for advanced materials and their potential benefits requires an understanding of the basic principles of rocket engines and specific engine cycles. These are reviewed briefly below.

Engine Types and Cycles. Rocket engines are classified as either solid fuel or liquid fuel types. Liquid fuel engines offer the advantages of higher efficiency (typically characterized as specific impulse, I_{sp} , which is a measure of thrust divided by the exhaust nozzle flow), throttle ability and restart capability. These advantages come at the expense of greater complexity, as indicated by the number of components that comprise a pump-fed liquid fuel rocket engine (Fig. 3). Liquid propellants are used for both earth-to-orbit and space-based engines. The liquid propellants can be fed to the combustion system either by pressure feed or by pump feed systems. For high-perform-

Nomenclature

C/C = carbon fiber-reinforced, carbon matrix composite(s)	I_{sp} = specific impulse	SiC/Si ₃ N ₄ = reinforced silicon carbide matrix composite(s)
CH ₄ = methane	LeRC = Lewis Research Center	silicon carbide fiber-reinforced silicon nitride matrix composite(s)
C/SiC = carbon fiber-reinforced, silicon carbide matrix composite(s)	LH ₂ = liquid hydrogen	SSME = Space Shuttle Main Engine(s)
CVI = chemical vapor infiltration	LOX = liquid oxygen	STBE = Space Transportation Booster Engine(s)
FRCMC = fiber-reinforced ceramic matrix composites	MMH = monomethylhydrazine	STME = Space Transportation Main Engine(s)
HPFTP = high-pressure fuel turbopump	NASA = National Aeronautics and Space Administration	T/M = turbomachinery
	NLS = National Launch System	T/P = turbopump(s)
	NTO = nitrogen tetroxide	2D = two-dimensional
	SiC = silicon carbide	
	SiC/SiC = silicon carbide fiber-	

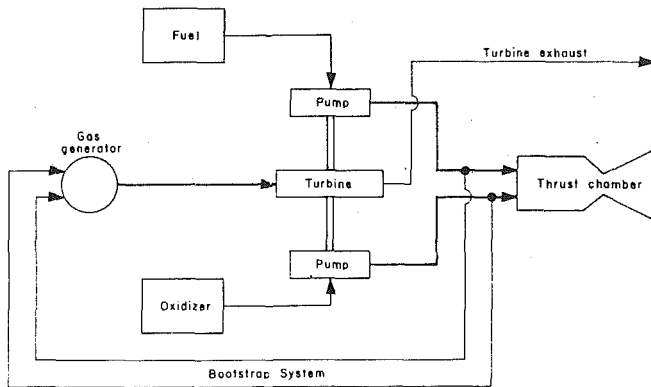


Fig. 3 Pump-fed liquid rocket engine components

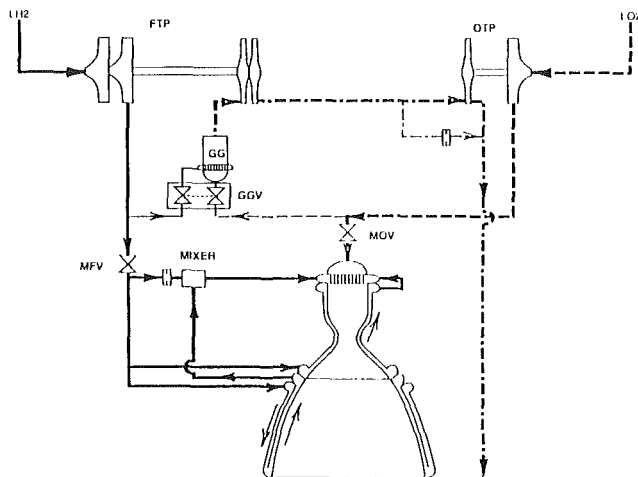


Fig. 4 Gas generator propulsion cycle

ance, long-duration operation without requiring thick-walled, heavy propellant tanks, pumps are preferred over pressurized tanks to feed the propellants. Centrifugal pumps driven by axial turbines (T/P) are often used for this. In spite of the relative complexity of these pumps, they have demonstrated acceptable reliability and provide high performance with minimum weight and a high level of design flexibility.

For pump-driven rocket engines, a number of engine cycles (including combined cycles) have been successfully used (Martinez, 1991). For reference, the gas generator cycle is shown in Fig. 4. Each of these cycles offers trades in performance, reliability, weight, and packaging (envelope size), and each would realize specific benefits from the use of advanced materials. Several representative cycles are discussed below with emphasis on the relationship between the turbine flow and the rocket engine flow.

Among the cycles used in rocket engines are staged combustion, gas generator, and expander cycles. In the staged combustion cycle (used for the SSME), the turbine flow is in series with the thrust chamber flow. The turbine flow is completely expanded in the exhaust nozzle, which, combined with other factors in the system, results in high performance. This cycle requires high pump discharge pressures and presents severe demands for T/M materials. As a result, the T/M materials are highly stressed (thermally and mechanically) and require high levels of maintenance.

In the gas generator cycle (Fig. 4), the turbine flow is in parallel with the rocket engine flow. Performance is generally lower than that achieved in the staged combustion cycle. Pump pressures are lower, and demands on the T/M materials are typically less severe than those of the staged combustion cycle.

Table 2 Use of FRCMC in rocket engine T/M results in increased I_{sp}

PERFORMANCE INCREASES AT VACUUM FOR TURBINE INLET TEMPERATURE INCREASE FROM 620-1400°C (1140-2540°F)		
ENGINE CONFIGURATION	LOX/CH ₄ STBE	LOX/H ₂ STME
Maximum Performance Engine I_{sp} Gain, sec	10.3	6.6
Baseline Engine I_{sp} Gain, sec	10.3	5.2
Minimum Weight Engine I_{sp} Gain, sec	6.5	3.7

SEA LEVEL PERFORMANCE INCREASES FOR TURBINE INLET TEMPERATURE INCREASE FROM 620-1400°C (1140-2540°F)		
ENGINE CONFIGURATION	LOX/CH ₄ STBE	LOX/H ₂ STME
Maximum Performance Engine I_{sp} Gain, sec	14.3	12.0
Baseline Engine I_{sp} Gain, sec	9.7	4.8
Minimum Weight Engine I_{sp} Gain, sec	6.7	3.3

The gas generator cycle is the most common cycle and dates back nearly 50 years; consequently, gas generator technology is relatively more mature than that of other cycles.

In the expander cycle, the turbine flow and thrust chamber flow are in series. The turbine propellant is heated by its use as the exhaust nozzle coolant. Turbine inlet temperature is generally lower than that of either the staged combustion or the gas generator cycle. Since the turbine flow is fully expanded in the exhaust nozzle, this cycle tends to be more efficient than the gas generator cycle.

Benefits of Advanced Materials. Potential benefits of using advanced materials, including FRCMC, in future generation rocket engines include reduced component weight, increased component lifetimes with reduced maintenance, and higher operating temperature with improved performance. For typical current generation engines, with hot section components fabricated from superalloys, one-for-one substitution of FRCMC would result in significant weight savings based on the density of FRCMC being about one-third that of the superalloys. However, consideration must be given to fabrication issues, to load bearing ability, to joining, etc., such that direction substitution is not likely (or even desirable), and determination of actual weight benefits must be made with respect to detailed component and, ultimately, system designs.

The database for advanced materials, such as FRCMC, is limited in scope. Life-related properties data (e.g., creep, fatigue, and stress rupture data), especially with respect to the rocket engine environment, are particularly limited in extent. Also, constitutive models for FRCMC life in the environment are not available. Thus, assessments of component life and predictions of savings through reduced maintenance cannot be made accurately. Such savings, which could be of tremendous magnitude, are feasible based on anticipated improvements in margin at the operating temperature, but further data are needed to quantify these benefits. The most readily quantified benefit, in the near term, is that related to increased operating temperature. This has been shown to be particularly beneficial for gas generator cycle engines (Table 2) and is discussed in detail in a following section (FRCMC Capabilities—Benefits Assessment).

FRCMC Capabilities

Rocket Engine TM Requirements. Materials intended for

Table 3 Typical materials usage in a small T/P

Component	MK44-F	MK44-O	MK48-F	MK48-O
Turbine manifold	Haynes 188	Haynes 188	Rene 41	Rene 41
Turbine nozzle	Haynes 188	Haynes 188	Haynes 188	Haynes 188
Turbine rotor	Astroloy	Astroloy	Astroloy	Waspaloy
Volute	Inco 718	321 CRES	Inco 718	Inco 718
Impellers	Inco 718	--	5-2.5 Titanium	Inco 718
Inducers	Titanium	K-Monel	--	K-Monel
Crossover	Inco 718	--	Inco 718	--
Housing	--	Hastalloy B	--	--

Table 4 Candidate FRCMC materials and screening criteria

FIBER/MATRIX SYSTEMS EVALUATED:	SCREENING CRITERIA USED:				
SiC/Lithium-alumino-silicate	Maximum operating temperature				
SiC/Magnesium-alumino-silicate					
SiC/Calcium-alumino-silicate	Thermal shock resistance				
SiC/Black glass					
C/Lithium-alumino-silicate	Environmental resistance				
C/Borosilicate					
C/Silica	Ultimate tensile strength				
C/Alumina					
SiC/Silicon nitride	Fracture toughness				
SiC/SiC					
C/SiC	Fabricability				
C/C					
	Maturity				
CANDIDATE SYSTEMS SELECTED					
Fiber/Matrix	Temp.	Ther. Shock	Enviro. Resist.	Mech. Props.	Maturity
SiC/Silicon nitride	1	1	1	4	3
SiC/SiC	1	1	1	2	2
C/SiC	1	1	2	1	1
C/C	1	1	2*	1-2	1
1 - Acceptable 2 - Marginal 3 - Not Acceptable 4 - Not Known					
* - Coating Necessary					

use as advanced rocket engine T/M components are required to meet a severe set of conditions, including:

1 Sustained operation in the corrosive combustion environment. For typical gas generator applications, hot gas path components are exposed to hydrogen-rich steam at the turbine inlet temperature. Storable propellant environments (such as nitrogen tetroxide (NTO) and monomethylhydrazine (MMH)) are also highly corrosive.

2 High operating temperatures ranging from 870°C for current applications to 1200°C (or above) for anticipated advanced applications.

3 High mean and alternating stresses. The rotating components, in particular, are exposed to high sustained stresses, including bore stresses and blade tip stresses, during operation, and the blades are exposed to high alternating stresses as they rotate past the nozzle vanes with the result that high cycle fatigue (to 10^9 cycles) is also a significant factor.

4 Possible erosion by the flowing gas stream.

5 Severe low cycle fatigue, especially thermal fatigue, resulting from the start/stop transients.

6 Combinations of the above conditions that could cause substantially greater degradation than that predicted based on the effects of discrete exposures to the individual operating conditions. For example, cyclic fatigue within the rocket engine environment would alternately open and close matrix micro-

Table 5 Key properties of preferred FRCMC systems

PROPERTY *	MATERIAL		
	C/SiC	SiC/SiC	C/C
Density [g/cm ³ (lb/in ³)]	2.1(0.08)	2.50 (0.09)	1.94 (0.07)
UTS [MPa (ksi)] at 20°C (70°F)	425 (62)	187 (28)	150 (22)
Strength/density [$\times 10^5$ cm(lin)] at 20°C (70°F)	20.2(8.2)	7.5 (3.1)	8.0 (3.14)
UTS [MPa (ksi)] at 1200°C (2200°F)	530 (77)	230 (33)	150 (22)
Str./den. [$\times 10^5$ cm (lin)] at 1200°C (2200°F)	25.3(10.3)	9.2 (3.7)	8.0 (3.14)
Maximum Operating Temperature [°C (°F)]	1650 (3000)	1430 (2600)	>2200 (>4000)
Young's Modulus [GPa (msi)]	76 (11)	211 (31)	83 (12)
Tensile Elongation [%]	0.93	0.22	N/A
Fracture Tough. [MPa \cdot m ^{0.5} (ksi \cdot in ^{0.5})]	40 (37)	24 (22)	N/A

* - 2D, in-plane

cracks present in FRCMC components, exposing the supporting fibers to the environment. This could degrade the fibers more rapidly that would be predicted based on the effects of static environmental exposures combined with fatigue effects predicted from inert environment tests.

Materials capable of enduring these conditions must also be fabricable into the complex geometries necessary for rocket engine components. Further consideration must additionally be given to joining and attachment to other components in the system and to compatibility with other component materials.

Candidate FRCMC Materials. Components of a rocket engine T/P (Table 3) face a broad range of requirements, which cannot be met by a single material. As discussed above, FRCMC, offer particular advantages for hot gas path components (such as the turbine stator and rotor), and the selection of candidate FRCMC materials was based primarily on their high temperature capability.

For high-temperature application, a number of FRCMC materials systems were identified and evaluated (Table 4). Initially, the fiber/matrix systems identified in Table 4 were screened using the criteria indicated. Based upon this initial screening, four systems were identified with near-term potential for T/P application, and these systems were studied in more detail. Of the four candidate systems, it was determined that the mechanical properties database was too limited for SiC/Si₃N₄; and, due to this relatively low level of maturity, this system was not considered further for near term use. Key properties of the remaining candidates are summarized in Table 5.

Due to its poor environmental stability and the associated need for protective coatings (which have not been effectively demonstrated for prolonged rocket engine use), C/C was also not considered to be a primary candidate. Consequently, the principal FRCMC materials considered for near-term rocket engine applications are C/SiC and SiC/SiC.

Properties and Capabilities of FRCMC. The two systems considered as primary candidates for near-term application are continuous fiber-reinforced, chemical vapor infiltrated (CVI), SiC matrix materials. Continuous fiber-reinforcement allows for directional "tailoring" of properties to meet specific load requirements. The CVI process provides high purity matrices and has been shown to produce high toughness structures, which offer "graceful" failure associated with fiber pull-out (Fig. 5).

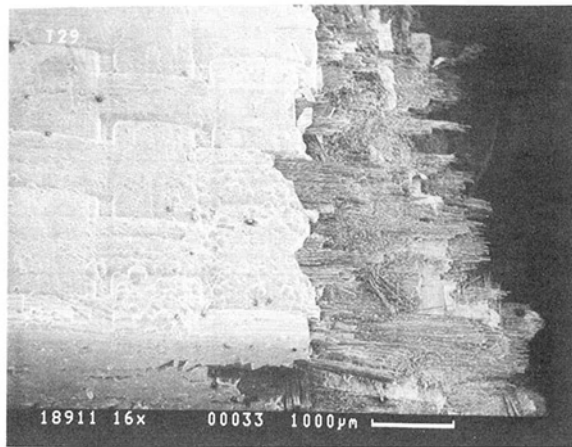


Fig. 5 Fiber pull-out in CVI FRCMC composite

Table 6 Properties of C/SiC FRCMC meet many advanced rocket engine needs

Physical Properties

PROPERTY	UNITS	NOMINAL VALUE
Fiber Content	Volume %	45
Density	lb/in ³ (g/cm ³)	0.075 (2.1)
Porosity	Volume %	10

Mechanical Properties

PROPERTY	UNITS	TEMPERATURE		
		73°F (23°C)	2192°F (1200°C)	
Tensile Strength	KSI (MPa)	61.6 (425)	77 (530)	
Elongation (Tensile)	%	.93	1.0	
Initial Young's Modulus (Tensile)	MSI (GPa)	11 (76)	17 (120)	
Compressive Strength				
In Plane	KSI (MPa)	75 (520)		
Flexural Strength	KSI (MPa)	65.9 (454)		
Flexural Elongation	%	.72		
Flexural Modulus	MSI (GPa)	9.9 (68.3)		
Cross Ply Tension	KSI (MPa)	1.72 (11.9)		
Shear Strength (Interlaminar)	KSI (MPa)	3.7		
Fracture Toughness	KSI √IN (MPa√m)	37 (40)		

Thermal Properties

PROPERTY	UNITS	TEMPERATURE		
		73°F (23°C)	1832°F (1000°C)	
Coefficient of Thermal Expansion				
In Plane	10 ⁻⁴ /°F (10 ⁻⁴ /°C)	1.7 (3)	1.7 (3)	
Thru the Thickness	10 ⁻⁴ /°F (10 ⁻⁴ /°C)	2.8 (5)	2.8 (5)	
Thermal Diffusivity				
In Plane	10 ⁻⁴ FT ² /S (10 ⁻⁴ m ² /S)	120 (11)	75 (7)	
Thru the Thickness	10 ⁻⁴ FT ² /S (10 ⁻⁴ m ² /S)	54 (5)	20 (2)	
Specific Heat	BTU/lbm °F (J/kg °C)	0.15 (620)	0.33 (1400)	
Total Emisivity	—	0.8	0.8	
Thermal Conductivity				
In Plane	BTU/HR FT • °F (Wm ⁻¹ • °C ⁻¹)	8.3 (14.3)	11.9 (20.6)	
Thru the Thickness	BTU/HR FT • °F (Wm ⁻¹ • °C ⁻¹)	3.8 (6.5)	3.4 (5.9)	

Use of SiC continuous fibers as reinforcement (SiC/SiC) provides an environmentally stable composite; however, current, multifilament, textile grade SiC fibers (e.g., NicalonTM fibers) (Nicalon is a trademark of Nippon Carbon) have two major limitations. Nicalon fibers lack the high strength of carbon fibers, with the result that SiC/SiC composites are limited to relatively low stress applications. Also, the Nicalon fibers contain impurities that cause rapid in situ degradation of the fibers at temperatures over 1200°C, even in inert environments. Improved SiC fibers are under development, but, in the near term, the carbon fiber reinforced composite (C/SiC) offers significant mechanical properties and operating temperature advantages, making it the preferred FRCMC system for high stress T/M applications (Table 6).

Fiber architecture has considerable influence over composite properties. In practice, a variety of architectures can be achieved by weaving or braiding of the carbon fiber reinforcement. Polar weaving offers potential benefits for rotating components. The weave architecture can be adjusted to achieve a

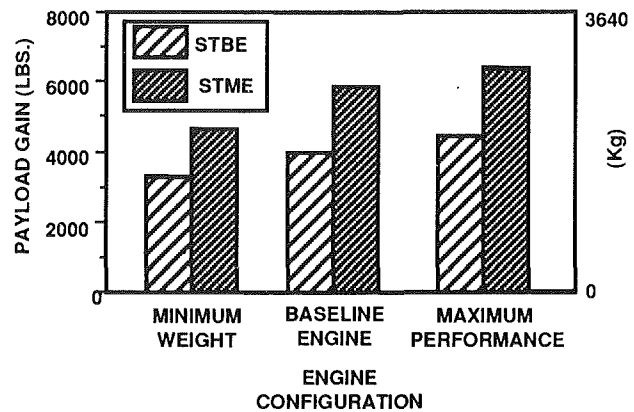


Fig. 6 Increased operating temperature capability of FRCMC results in greater payload

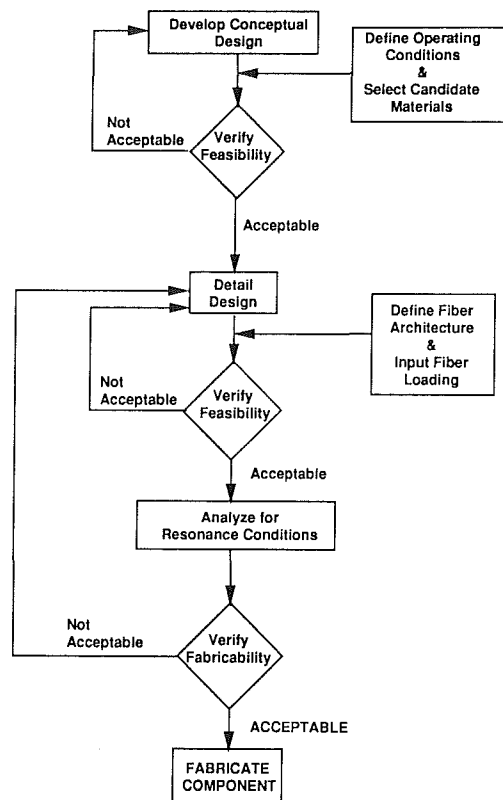


Fig. 7 FRCMC design and analysis methodology

desirable balance of properties for a specific application. Fiber loadings can be varied in selected directions to "tailor" the composite to the operating requirements. Consequently, the properties shown in Table 6 for an aligned, balanced lay-up represent only one possibility.

Benefits Assessment. Using C/SiC for the hot gas path components is anticipated to allow increases in turbine temperature from 870°C (typical for current rocket engines) to 1200°C or higher. The benefits of such an increase were evaluated with respect to gas generator cycle variants of the Space Transportation Main Engine (STME) and the Space Transportation Booster Engine (STBE), which have been considered for the National Launch System (NLS). The benefits assessment considered both LOX/LH₂ and LOX/CH₄ propellants. For both propellant combinations, substantial gains in efficiency (I_{sp}) with resultant gains in payload (Fig. 6) were found to result from the increased turbine inlet temperature.

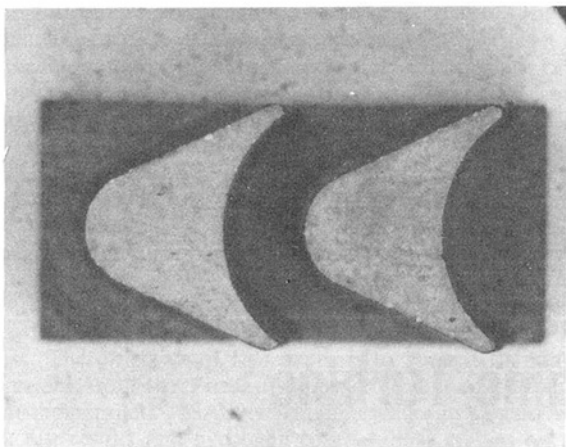


Fig. 8 Turbine blade pairs fabricated from 2D C/SiC

This benefit could be further enhanced by reconfiguration of the system to maximize the total benefit. However, with current launch costs on the order of several thousand U.S.\$/kg, the benefit shown would alone result in substantial savings.

Status of FRCMC Development for Rocket Engines

Design and Analysis Status. Design and analysis of FRCMC for structural applications is complicated by the nonlinear and anisotropic characteristics of the materials. Metallic structures have traditionally been treated as homogeneous and isotropic, although more recent work, especially with directionally solidified and single crystal alloys, has included anisotropic analyses.

Due to their emerging state of development, constitutive models are not available for FRCMC. A number of fiber architectures (e.g., rotated 2D and polar weave architectures) provide nominally isotropic in-plane properties, with the result that orthotropic analyses are acceptable for these architectures. In spite of the relative complexity of these nonlinear, anisotropic analyses, existing codes can be used for computerized analysis. Materials properties data needed to implement the codes effectively are often limited for FRCMC, but sufficient data are available for the preliminary analysis of the C/SiC system discussed herein. The design process for such a system follows the general approach shown in Fig. 7.

Component Development. Using the approach described above, rocket engine subelements and components have been designed and fabricated. Turbine blade pair subelements characteristic of blades that would be included in a bladed disk (bisk) were fabricated from 2D C/SiC (Fig. 8). These blade pairs incorporated critical fabrication features, such as leading and trailing edge radii and fillet radii, expected in a typical application.

Evaluation, including nondestructive inspection, of the blade pairs indicated that the blades were of high quality. No delaminations were found in the FRCMC structure. Geometry of the blade shapes corresponded to application requirements. Fibers were aligned within 3 deg of the principal stress orientations. Edge quality was very good with no significant machining problems evidenced. Thermal shock tests were run by NASA-Lewis Research Center under simulated rocket engine conditions on these blades (Herbell and Eckel, 1991). The blades were relatively unaffected by these tests with only minimal degradation observed after 50 thermal cycles to temperatures substantially above the intended use temperature of 1200°C.

Based on the successful results of the ongoing efforts de-

scribed, full-scale component fabrication and testing is being pursued. The eventual goal of this work is to fabricate and test both the stator and rotor of an advanced high-temperature T/P to demonstrate the capabilities of FRCMC. Initial ground tests are proposed using a water-cooled manifold from conventional materials; however, eventual flightweight studies will require high-temperature capability, uncooled manifolds, and housings.

Summary and Conclusions

Use of FRCMC in advanced T/M provides a range of potential benefits, including:

- 1 reduced weight
- 2 longer life and reduced maintenance
- 3 higher operating temperature and improved efficiency.

Thus far, the benefits associated with higher operating temperature have been quantitatively assessed and show that the potential benefits are significant.

Based on this potential, FRCMC systems have been identified with properties suited to near-term applications. Of the candidate materials systems, C/SiC has particularly attractive properties for use as hot gas path turbine components. Conceptual design studies have indicated the feasibility of applying C/SiC, and subelements were fabricated that verify selected fabrication features and key material properties. Inspection and subsequent tests of these subelements validated their capabilities.

Ongoing programs are continuing to develop FRCMC, specifically with the intent of fabricating full-scale FRCMC components for simulated rocket engine tests prior to actual T/P testing.

Initial T/P tests will be limited to ground tests using water cooled manifolds and housings. Flightweight T/P will also require high-temperature capability materials for these components. Other areas requiring development have been identified and are being pursued. These include:

- 1 improved FRCMC materials with long term resistance to the operating environment
- 2 improved modeling and analytical techniques for anisotropic, nonlinear materials, such as FRCMC
- 3 expanded databases and constitutive models for selected FRCMC systems.

Acknowledgments

The author gratefully acknowledges the support of several individuals and groups who continue to participate in the development of FRCMC for advanced rocket engine applications. Within Rocketdyne, he would like to thank Dr. Gary Schnittgrund and Jim Tellier, as well as the numerous others who have contributed with respect to their technical specialties, for their support and advice. He would also like to acknowledge the support and participation of the Société Européenne de Propulsion (SEP), E. I. DuPont de Nemours & Co., Inc. (Advanced Composites Div.), and Williams International. He would finally like to acknowledge the support of NASA LeRC (Dr. Thomas Herbell, program monitor) under whose aegis much of this work was completed.

References

- Brockmeyer, J. W., and Schnittgrund, G. D., 1990, "Fiber-Reinforced Ceramic Composites for Earth-to-Orbit Rocket Engine Turbines," Final Report for NASA-LeRC Contract No. NAS3-25468, Report No. CR-185264, July.
- Chandler, W. T., 1983, "Materials for Advanced Rocket Engine Turbopump Turbine Blades," Final Report for NASA-LeRC Contract No. NAS3-23536.
- Fritzemeier, L. G., and Brockmeyer, J. W., 1990 "Building a Better Blade," *Threshold—Engineering Journal of Power Technology*, Rockwell International Corp., Rocketdyne Div., Canoga Pk., CA, No. 6, pp. 30-41.
- Herbell, T. P., and Eckel, A. J., 1991, "Ceramics for Rocket Engine Components," *Aerospace Engineering*, Dec., pp. 21-23.
- Martinez, A., 1991, "Rocket Engine Propulsion Cycles," *Threshold—Engineering Journal of Power Technology*, Rockwell International Corp., Rocketdyne Div., Canoga Pk., CA, No. 7, pp. 14-26.

Ceramic Matrix Composites for Rocket Engine Turbine Applications

T. P. Herbell

A. J. Eckel

Lewis Research Center,
Cleveland, OH 44135

A program to establish the potential for introducing fiber-reinforced ceramic matrix composites (FRCMC) in future rocket engine turbopumps was instituted in 1988. A brief summary of the overall program (both contract and in-house research) is presented. Tests at NASA Lewis include thermal upshocks in a hydrogen/oxygen test rig capable of generating heating rates up to 2500°C/s. Post-thermal upshock exposure evaluation includes the measurement of residual strength and failure analysis. Test results for monolithic ceramics and several FRCMCs are presented. Hydrogen compatibility was assessed by isothermal exposure of monolithic ceramics in high-temperature gaseous hydrogen plus water vapor.

Introduction

Reusable rocket engines for space missions beyond the next decade must operate longer, withstand more duty cycles, and be more efficient than present and proposed future generation engines. The ability of the U.S. to put payloads into space has been restricted by the use of launch vehicles that still use 20 to 30-year-old technology (Paster and Hallinan, 1990). Today the most advanced reusable rocket engine is the Space Shuttle Main Engine (SSME). Metal turbopump blades, stator vanes, and other hot gas flow path components of this hydrogen/oxygen burning engine have limited durability and, as shown in Fig. 1, they are reaching their temperature limit. For improved efficiency, future Advanced Launch Systems (ALS) such as the Space Transportation Booster Engine (STBE) and Space Transportation Main Engine (STME) will require materials with greater temperature capability. One of the keys to developing improved rocket engine systems is the use of advanced materials and manufacturing techniques to enhance producibility, increase operating margins, and reduce cost (Strobl, 1991).

Materials with potential to outperform significantly the currently used superalloys include ceramics, synthetic alloys such as intermetallics, and carbon/carbon. Ceramic composites, specifically continuous fiber-reinforced ceramic matrix composites (FRCMC), are the leading candidate. Only FRCMC exhibit the desirable combination of high-temperature stability, structural stiffness, high strength-to-weight, and tolerance to aggressive environments.

Because FRCMCs possess high toughness, their in-service strength is essentially insensitive to processing and environmental (scratches and nicks) flaws. Failure occurs in a non-

catastrophic or graceful manner. These characteristics—in conjunction with their greater temperature capability—imply that FRCMC components offer potential for significant reliability improvement. This is particularly important for potential use in man-rated engine applications. Although the FRCMC property database is currently undergoing a considerable expansion, it is still quite limited. There is a paucity of information concerning the detailed design, fabrication, and testing of actual turbine hardware. The development of complex shaped FRCMC components, however, has been demonstrated (Herbell and Eckel, 1991).

In 1988 NASA Lewis initiated a two-phase 5-year contract to develop a technology plan to establish the feasibility of introducing FRCMC into future generation Earth-to-orbit rocket engine turbine components. Phase I of the effort (now complete) was conducted by Rocketdyne and General Electric

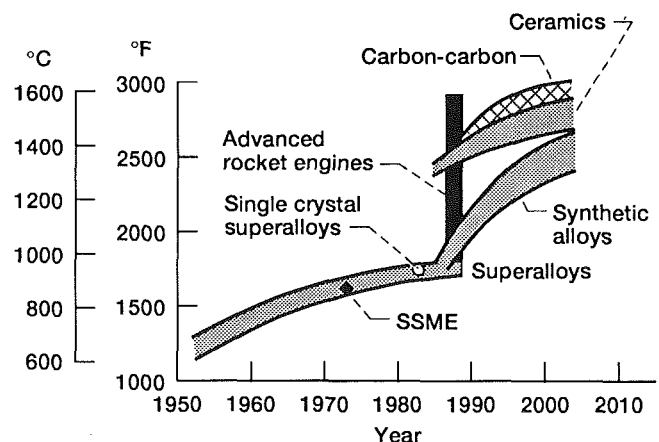


Fig. 1 Rocket engine turbine blade material needs and capabilities

Contributed by the International Gas Turbine Institute and presented at the 37th International Gas Turbine and Aeroengine Congress and Exposition, Cologne, Germany, June 1-4, 1992. Manuscript received by the International Gas Turbine Institute February 4, 1992. Paper No. 92-GT-394. Associate Technical Editor: L. S. Langston.

and identified the benefits and assessed the potential for the introduction of FRCMC in advanced earth-to-orbit rocket engine turbine components (Brockmeyer and Schnittgrund, 1990; Holloway et al., 1990). Phase II (being conducted by Rocketdyne) began in 1990 and includes tasks to design, fabricate, and test full-scale prototype stationary turbopump components. Plans to test an FRCMC rotor and stator in a flight size hydrogen turbopump in the 1995 time frame are currently being formulated.

Rocket engine turbopump components can experience heating rates in excess of 1000°C/s . This means that good thermal shock resistance is extremely important. If the engine uses $\text{H}_2\text{-O}_2$, hydrogen compatibility becomes a critical parameter for success. The objective of this paper is to present the major conclusions from the Phase I Contract studies and to summarize the parallel NASA Lewis high heating rate thermal upshock test results and hydrogen compatibility studies on the material system selected for use in the Phase II contract effort.

Summary of Phase I Contract Studies

Brockmeyer and Schnittgrund (1990) presented a detailed analysis of the material evaluation and selection criteria used in the Phase I contract at Rocketdyne as well as a summary of the benefits to be derived from the use of FRCMC. Although the material selection was different, the Phase I General Electric contract reached similar conclusions about the benefits of using FRCMC (Holloway et al., 1990). Three types of benefit can result from the introduction of FRCMC components into the hot section of a rocket engine turbopump: improved performance and increased payload capability, greater component life, and enhanced design flexibility.

Performance. Increased performance and payload capability are achievable due to the significant gains in specific impulse projected for engine design based on either minimum weight or maximum performance configurations as shown in Fig. 2. This increased performance can decrease the cost of putting payloads into space by increasing payload for a specific configuration, by allowing reconfiguration of the vehicle to decrease its weight, or by permitting an engine configuration that reduces the nozzle exit area and engine weight.

Component Life. Increased temperature capability of FRCMC leads to greater temperature margin and allows for greater temperature overshoot relative to superalloys, as shown in Fig. 3. Using the current design for the SSME high-pressure fuel turbopump, a direct substitution of FRCMC components would yield more than a 350°C increase in design temperature margin and a 20 to 35 percent reduction in turbine rotor mass. A reduction in rotor mass means a lower bearing load and possibly greater bearing life. Other benefits include the potential for increased bearing life due to improved balance.

Design Flexibility. Lower rotating mass leads to reduced residual imbalance requirements for the rotating components.

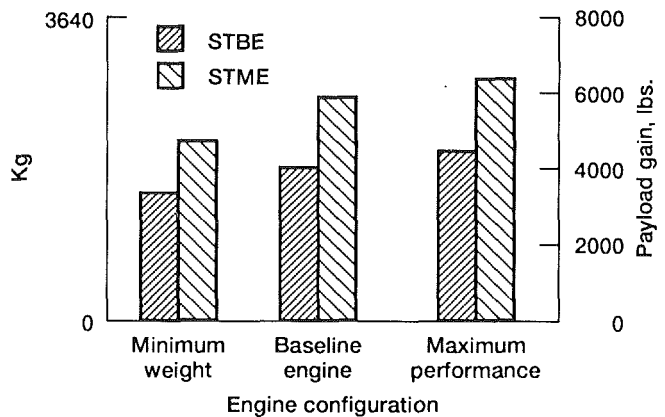


Fig. 2 Increased turbine inlet temperature results in higher payloads

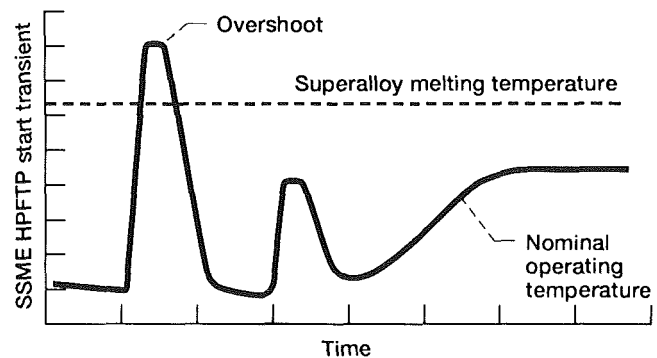


Fig. 3 Higher ceramic use temperature relative to superalloys permits greater overshoot with reduced component damage

Therefore, bearing shaft and disk requirements are relaxed and the airfoil envelope can be expanded to configurations closer to optimum.

Material Selection. Of the benefits derived from using FRCMCs, performance is the easiest to quantify directly. For a rocket engine turbine (like most heat engines) higher operating temperature means improved performance. The maximum desirable temperature, however, is often dictated by restrictions imposed by the engine system. With these restrictions in mind, an operating temperature of 1170°C was selected by Brockmeyer and Schnittgrund (1990). Both stationary (nozzle) and rotating (rotor) components were considered. A number of engine types, propellant systems, and materials were evaluated. The greatest gains were found to be for gas generator cycle engines. The propellant system selected was LOX/H_2 .

A large number of FRCMC materials were screened for potential consideration. Selection criteria included known or predicted properties, the ability to tolerate rocket engine ther-

Nomenclature

ALS = advanced launch system	FRCMC = fiber-reinforced ceramic matrix composites	STME = Space Transportation Main Engine
Al_2O_3 = aluminum oxide	H_2 = hydrogen	Si = silicon
C/C = carbon fiber reinforced carbon	LOX = liquid oxygen	$\alpha\text{-SiC}$ = alpha silicon carbide
C/SiC = carbon fiber reinforced SiC	MgO = magnesium oxide	SiC = silicon carbide
CH_4 = methane	O_2 = oxygen	SiC/SiC = SiC fiber reinforced SiC
CVD = chemical vapor deposition	ppm = parts per million by volume	SiC/Si ₃ N ₄ = SiC fiber reinforced Si ₃ N ₄
CVI = chemical vapor infiltration	SSME = Space Shuttle Main Engine	SiH = silicon hydride
	STBE = Space Transportation Booster Engine	SiH ₄ = silane
		Si ₃ N ₄ = silicon nitride

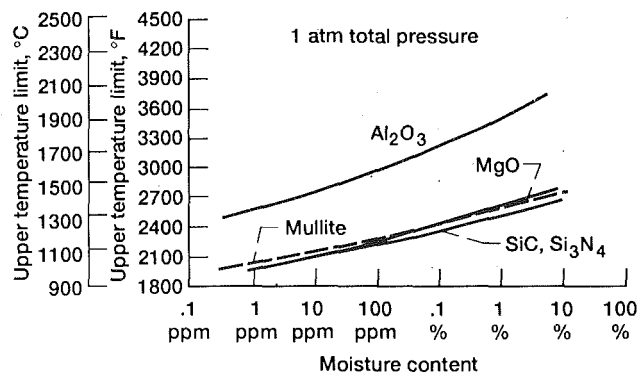


Fig. 4 Upper temperature limit for ceramic materials in $H_2 + H_2O$ atmospheres

mal transients, and durability in high-temperature hydrogen-rich steam. Based on these and other criteria, including projected rotor operating stresses, the final material selected was graphite fiber reinforced silicon carbide (C/SiC). This material has the requisite combination of mechanical properties, fabrication and test experience at the component level and an acceptable environmental resistance for an early component demonstration. Chemical vapor infiltration (CVI) emerged as the fabrication process of choice. Of the alternate materials, SiC/SiC has better environmental resistance, but lacks the load carrying capability at operating temperatures. Carbon/carbon (C/C) requires a coating system (as yet not successfully developed) for use in the engine environment and SiC/Si₃N₄ is not adequately developed for near-term consideration.

Hydrogen Compatibility of Selected Ceramics

Thermodynamic Analysis. The chemical stability of a large number of ceramic materials in hydrogen-containing environments has been analyzed from thermodynamic considerations for this and related NASA programs by Misra (1990). He utilized a computer program to make equilibrium calculations as a function of temperature (900 to 1400°C), total system pressure (1 to 30 atm), and moisture content (0 to 50 vol %).

The equilibrium thermodynamic stability of ceramic materials in $H_2 + H_2O$ atmospheres at high temperatures can be defined by selecting a limit of the partial pressure of reaction products present. For many applications the presence of 1×10^{-6} atm (1 ppm) of gaseous reaction product is a reasonable limit. For other applications a higher or lower level may be limiting. Figure 4 shows the projected stability of SiC, Si₃N₄, MgO, Al₂O₃, and mullite as a function of moisture content at 1 atm pressure based on 1 ppm of reaction product. Pure H_2 is a severe environment at high temperatures. The presence of water vapor improves the stability of many ceramics including those shown in the figure. SiC has been selected as the matrix material for the FRCMC to be utilized in the Phase II Rocket Engine Turbopump contract effort. It is for this reason we have chosen to describe the hydrogen compatibility of this ceramic material in some detail.

Thermodynamic calculations show that SiC will decompose in pure H_2 . This is consistent with results reported in the literature (Fischman et al., 1985; Hallum and Herbell, 1988; Kim, 1987). The primary equilibrium reaction product gases present for reaction of SiC with pure H_2 at 1 atm pressure are CH₄, SiH, and SiH₄. Although there are other possible gaseous species, calculations show these are predominant. The only stable solid phase is silicon. The partial pressures of the Si-H species are at least an order of magnitude less than that of CH₄ for these conditions; thus the primary reaction is the decomposition of SiC:

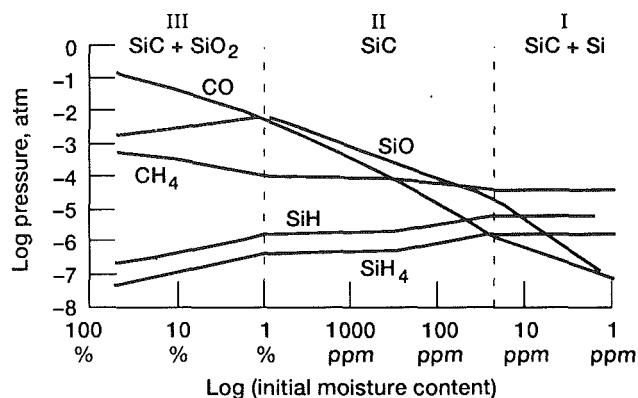
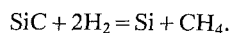


Fig. 5 Stability in SiC in $H_2 + H_2O$ at 1 atm and 1400°C

The partial pressure of CH₄—along with SiH and SiH₄—increases with increasing system pressure. Thus SiC would be expected to decompose at an increasing rate with increasing total system pressure in an environment of pure H_2 .

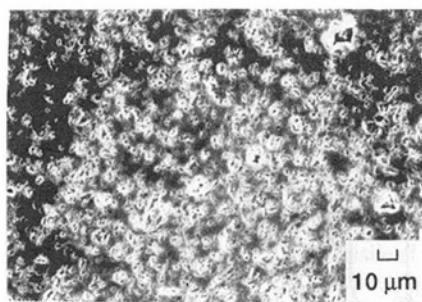
The stability of SiC in the presence of moisture is characterized by distinct regions of attack. Each region is defined by the thermodynamically stable solid phases. The calculated partial pressures of the major gaseous species and the stable condensed phases at 1400°C are seen in Fig. 5.

Regions I and II define the conditions for active attack of SiC. In Region I, the stable solids are silicon (Si) and SiC. This region is similar to that previously discussed for SiC in pure H_2 in that the predominant vapor species is CH₄, which forms as a result of the decomposition of SiC, as shown in the equation above. Region II is identified by the single stable solid phase of SiC. In this region SiC is degraded by the formation of the volatile suboxide SiO.

Region III is the region of passive oxidation; the stable solid species are SiC and SiO₂. Formation of SiO₂ is likely to provide protection against further oxidation. The effectiveness of the SiO₂ scale in inhibiting further oxidation would depend on the morphology and stability of the scale formed. Since this is the region in which H_2 -O₂ rocket engine turbopumps are expected to operate, from a thermodynamic view SiC is considered an excellent selection for a composite matrix material.

Morphology of Hydrogen Attack. To evaluate the validity of the thermodynamic predictions, scanning electron microscopy (SEM) was used to analyze the surface morphological characteristics of samples in the as-received condition and after exposure to two levels of wet hydrogen at 1300°C. Predicted behavior at 1300 and 1400°C are similar. The moisture levels were selected to be from the thermodynamically predicted Regions II and III of Fig. 5 since these are the regions of practical interest. The microstructures are shown in Fig. 6. Figure 6(a) shows the surface of the as-received sintered α -SiC, revealing grinding marks and surface damage. After exposure at an intermediate moisture level (Region II), active attack of the SiC grains is observed (Fig. 6(b)). At high moisture levels (Region III), a protective SiO₂ scale forms on the surface of the SiC (Fig. 6(c)).

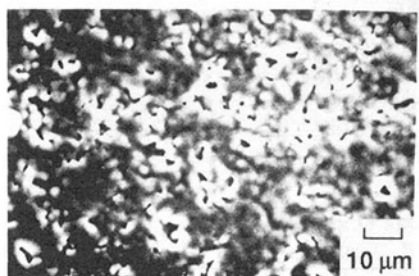
Residual Strength of Exposed Specimens. Test bars of monolithic sintered α -SiC exposed to wet H_2 (saturated with moisture at room temperature) for 100 h at temperatures to 1400°C were tested at room temperature to evaluate the effect of high-temperature exposure on residual room temperature strength. This exposure time is longer and the temperature greater than required for the turbopump component application. The moisture level falls within the previously described Region III where passive oxidation to form SiO₂ on the surface would be expected. As can be seen in Fig. 7, essentially no



(a) As received.



(b) Region II, active attack.



(c) Region III, protective SiO_2 formation.

Fig. 6 Surface morphology of $\alpha\text{-SiC}$ exposed to hydrogen at 1300°C

degradation of room temperature flexural strength was observed. Longer exposure times in dry hydrogen have, however, been observed to degrade the strength of this material (Hallum and Herbell, 1988).

Thermal Shock Testing

Materials and Test Procedure. In conjunction with the above H_2 compatibility evaluation, a number and variety of monolithic and composite ceramic materials were evaluated for thermal shock resistance. Thermal shock resistance is a critical parameter for any hot-section turbopump component due to the severe thermal transient experienced during the start-up cycle. Similar to the hydrogen compatibility tests, only those results pertaining to SiC matrix materials are discussed here.

The thermal shock tests were conducted by employing a stationary 1000 lb thrust hydrogen/oxygen rocket engine mounted in a horizontal position. The details of this specific engine, its characterization and operation are as described by Brindley and Nesbitt (1988). These authors have also shown that the thermal shock condition produced by this rocket engine test rig approximates that currently experienced in the SSME turbopumps.

A total of 22 bars of three types of monolithic SiC (sintered $\alpha\text{-SiC}$, hot-pressed SiC, and reaction-bonded SiC) were tested at various heat-up rates. The monolithic materials were all

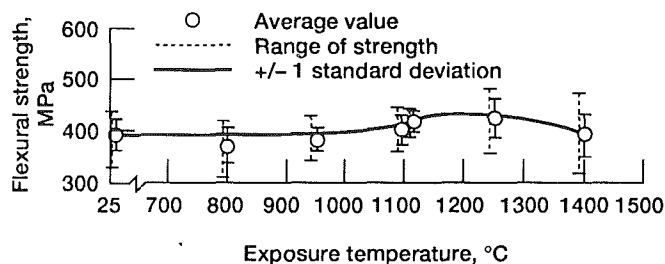


Fig. 7 Effect of elevated temperature H_2 exposure (100 h in Region III) on room temperature strength of sintered $\alpha\text{-SiC}$

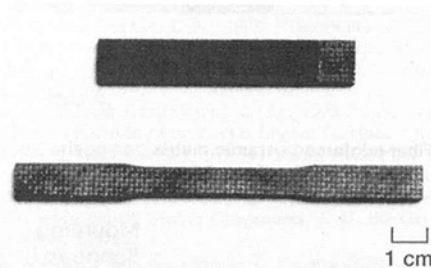


Fig. 8 FRCMC thermal shock test coupons

Table 1 Composite properties (room temperature)

	Nicalon/SiC	C/SiC
Fiber content, vol %	40	45
Porosity, percent	10	10
Density, g/cm^3	2.5	2.1
Tensile strength, MPa	200	350
Flexural strength, MPa	300	500
Tensile modulus, GPa	230	90
Fracture toughness, $\text{MPa}\sqrt{\text{m}}$	30	35

obtained commercially. Test specimens were machined in rectangular configuration of approximately 3 by 12.7 by 76 mm.

Most of the FRCMC coupon materials evaluated in this study were composites fabricated of plain woven Nicalon¹ fibers in a two-dimensional laminated CVI SiC matrix. Nicalon fiber reinforced CVI SiC was selected due to availability and the fact that it is expected to have thermal shock resistance similar to that of C/SiC. A limited number of C/SiC specimens were also tested. Two geometries were used for the ceramic composite coupons. One was identical to the monolithic geometry discussed above, and one had a reduced gage section (8.4 mm). The samples are seen in Fig. 8. Table 1 lists some of the physical and mechanical properties of the composites, as provided by the manufacturer.

An airfoil shape was also evaluated. The airfoil shaped composite was fabricated to simulate turbine blades for a rocket engine turbopump and is seen in Fig. 9. The airfoil shape was fabricated of woven graphite fibers reinforcing a CVI SiC matrix. The as-received blade pair was cut into two single blades, and each was tested separately. A CVD SiC top coat was applied after machining; thus there were no exposed fibers in the blade section of these components.

The rectangular coupon and tensile test specimens were positioned at the exit of the engine such that an edge of the bar was directly exposed to the rocket exhaust, as indicated in Fig. 10. The chamber pressure and corresponding gas pressure applied to the leading edge of the samples was approximately 100 psi. The coupons were held lightly on each end via a force

¹A Si-C-O fiber manufactured by Nippon Carbon Company, Tokyo, Japan.

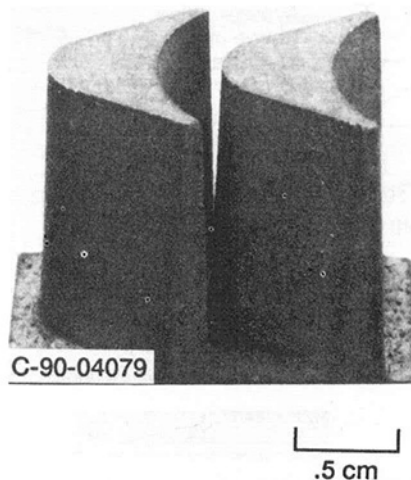


Fig. 9 Fiber-reinforced ceramic matrix composite turbine blade

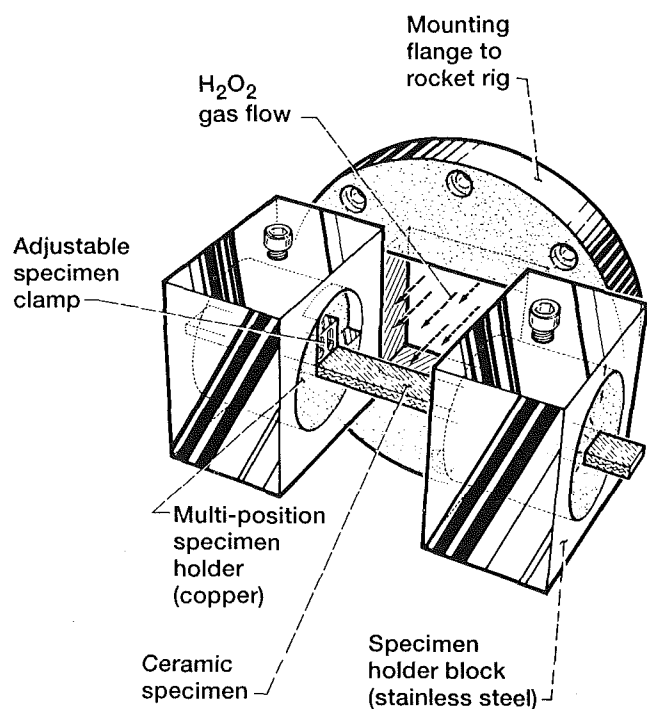


Fig. 10 Schematic of rocket engine setup used for thermal shock testing

applied normal to the flat side of the sample. This configuration resulted in the most severe thermal shock being applied to the center section of the sample, with the ends remaining "cold."

The thermal shock test is conducted by 1 s pulses of the engine. A typical temperature-time profile of the engine gas temperature and the approximate temperature on the hot side of a sample, during one cycle, are shown in Fig. 11. Altering the oxygen/hydrogen ratio allows control of the thermal shock temperature (ΔT in Fig. 11) from 1000 to 2500°C in the 1-s test. All of the tests are filmed at 400 frames per second to facilitate review of any significant events during the tests.

All of the FRCMC test bars were examined ultrasonically and by x-radiographic techniques prior and subsequent to thermal shock. Both the FRCMC rectangular coupons and the reduced gage section test bars were tensile tested after thermal shock tests.

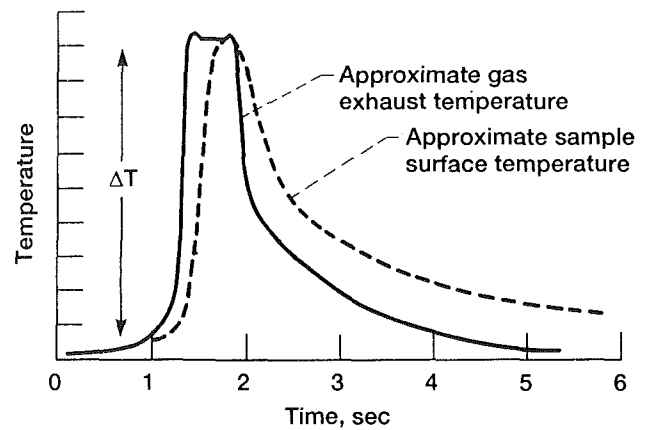


Fig. 11 Typical temperature-time profile for one second thermal shock test

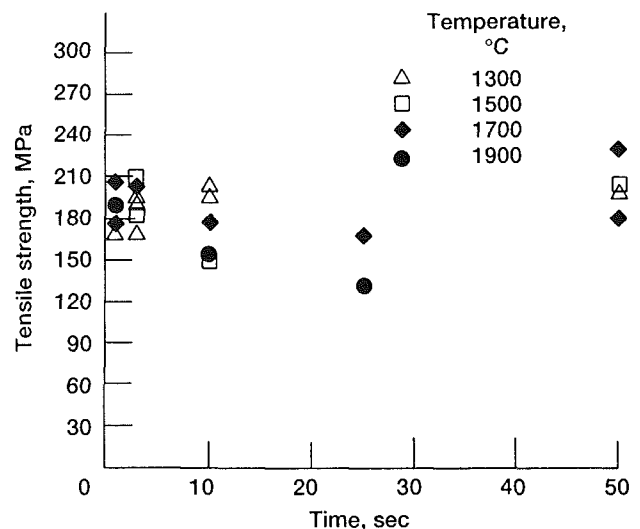


Fig. 12 Retained room temperature tensile strength of nicalon/SiC ceramic composites after thermal shock test

The airfoil shaped components were tested by mounting them in a cantilevered fashion in the exhaust. The specimens were held such that the airfoil shaped portion was directly in the exhaust. The component was positioned such that the gas impinging on the concave side of the turbine blade shape.

Results and Discussion

Monolithic Ceramics. The results for the monolithic ceramic coupons have been reported elsewhere (Eckel and Herbell, 1990). To summarize, the maximum ΔT without visible damage achieved for any of the monolithic materials was 1500°C (2730°F). Most of the samples failed during the cool-down portion of the thermal shock cycle. When a sample survived more than one cycle, it usually failed on ignition on a subsequent run. This would indicate that the critical crack was probably initiated during the cool-down portion of the previous cycle. The fact that the samples failed during the cool-down portion of the cycle would indicate that failure was caused by tensile forces generated at the sample surface. The average number of cycles to failure in the thermal shock condition of ΔT equal to 1400°C (2550°F) was 1.5 cycles for monolithic SiC. This result is consistent with predicted performance (Kingery, 1955).

Nicalon/Silicon Carbide Composites. The FRCMC sam-

ples were tested at thermal shocks, ΔT , ranging from 1300°C (2370°F) to 2300°C (4170°F) (Eckel, et al., 1991). In contrast to the monolithic materials, none of the composites failed catastrophically, even at the most severe test conditions! The retained ultimate tensile strength of the FRCMC samples as a function of severity and number of thermal shock cycles is seen in Fig. 12. There was no significant strength variation between the rectangular coupons and the reduced gage section tensile bars following identical thermal shock tests. The tensile strength data show little or no decrease in tensile strength for thermal shock ΔT up to 1700°C. There was also no degradation detected by x-radiographic or ultrasonic analysis. This thermal shock condition is greater than that of the current SSME turbopump. At ΔT equal to 1900°C the strength is seen to fall off with increasing number of thermal shock cycles. In these samples, degradation was clearly visible in the form of physical erosion of the leading edge of the samples. For example, the cross-sectional area of the sample subjected to 25 cycles at 1900°C was reduced by greater than 40 percent. In spite of this significant degradation, the sample still maintained 65 percent of its tensile strength. This qualitatively demonstrates both the thermal shock resistance and the notch insensitivity of this composite material.

Carbon/Silicon Carbide Composites. A program to thermal shock test a large number of C/SiC composite specimens is in progress. Preliminary data indicate no degradation after exposure to 50 thermal shock cycles at temperatures to 1650°C. This is a very significant result since the projected use temperature is only 1200°C where the thermal shock exposure had no effect on properties. These results also indicate that the material has a significant temperature margin. Degradation in the form of a 30 percent loss in strength did occur, however, after either 50 cycles at a temperature of 1900°C or three cycles at a temperature of 2400°C.

FRCMC Airfoil Components. The turbine airfoil shapes also performed well in the thermal shock tests. Both of the graphite fiber reinforced SiC blades were subjected to greater than 60 cycles of at least 1800°C each in separate tests. A small amount of chipping of the leading edge SiC matrix component was observed in each of the components after 20 to 30 cycles. These qualitative results for the turbine airfoil shapes are highly significant and demonstrate the viability of applying FRCMCs in the turbopump of advanced rocket engines.

Concluding Remarks

FRCMCs are an emerging class of materials. Their status

and fabricability into turbine components has been demonstrated. Thermal shock tests that approximate a rocket engine turbopump environment have produced encouraging results for Nicalon/SiC test bars and both test bars and prototype subcomponents made from C/SiC. Hydrogen exposure tests indicate that SiC is stable in hydrogen at the proposed turbopump use temperature. SiC is thus an acceptable matrix material for a FRCMC to be used in a hydrogen/oxygen rocket environment. Questions remain concerning the long-term stability of C/SiC in hydrogen, but the material appears to have the requisite properties for use in a full-scale rocket engine turbopump demonstration.

References

- Brindley, W. J., and Nesbitt, J. A., 1988, "Durability of Thermal Barrier Coatings in a High Heat Flux Environment," *Advanced Earth-to-Orbit Propulsion Technology 1988*, Vol. 1, R. J. Richmond and S. T. Wu, eds., NASA CP-3012-VOL-1, pp. 661-674.
- Brockmeyer, J. W., and Schnittgrund, G. D., 1990, "Fiber-Reinforced Ceramic Composites for Earth-to-Orbit Rocket Engine Turbines," RI/RD-90-163, Rocketdyne Division, Rockwell International Corp., NASA CR-185264.
- Eckel, A. J., and Herbell, T. P., 1990, "Thermal Shock of Fiber Reinforced Ceramic Matrix Composites," *Proceedings of 13th Annual Conference on Metal Matrix, Carbon, and Ceramic Matrix Composites*, J. D. Buckley, ed., NASA CP-3054, Part 1, pp. 153-162.
- Eckel, A. J., Gyekenyesi, J. Z., Herbell, T. P., and Generazio, E. R., 1991, "Thermal Shock of Fiber Reinforced Ceramic Matrix Composites," NASA TM-103777.
- Fischman, G. S., Brown, S. D., and Zangvil, A., 1985, "Hydrogenation of Silicon Carbide: Theory and Experiments," *Materials Science and Engineering*, Vol. 7, pp. 295-302.
- Hallum, G. W., and Herbell, T. P., 1988, "Effect of High-Temperature Hydrogen Exposure on Sintered α -SiC," *Advanced Ceramic Materials*, Vol. 3, No. 2, pp. 171-175.
- Herbell, T. P., and Eckel, A. J., 1991, "Ceramic Composites for Rocket Engine Turbines," SAE Paper 911108; also NASA TM-103743.
- Holloway, G. D., Eskridge, R., Singh, R., and Ward, S., 1990, "Fiber-Reinforced Ceramic Composites for Earth-to-Orbit Rocket Engine Turbines," NASA CR-185290.
- Jacobson, N. S., Eckel, A. J., Misra, A. K., and Humphrey, D. L., 1990, "Reactions of SiC With 5 Percent H_2 /Ar at 1300°C," *Journal of the American Ceramic Society*, Vol. 73, No. 8, pp. 2330-2332.
- Kim, H. E., 1987, "Gaseous Corrosion of SiC and Si_3N_4 in Hydrogen," Ph.D. Thesis, Ohio State University.
- Kingery, W. D., 1955, "Factors Affecting Thermal Stress Resistance of Ceramic Materials," *Journal of the American Ceramic Society*, Vol. 38, No. 1, pp. 3-15.
- Misra, A. K., 1990, "Thermodynamic Analysis of Chemical Stability of Ceramic Materials in Hydrogen Containing Atmospheres at High Temperatures," NASA CR-4271.
- Paster, R. D., and Hallinan, G. J., 1990, "SSME and Beyond: Future Earth-to-Orbit Propulsion in the U.S.A.," 41st Congress of the International Astronautical Federation, IAF Paper No. 90-237.
- Sirobl, W., 1991, "A Case for the Development of a New National Launch System Now," AIAA Paper No. 91-2384.

G. Stürmer

A. Schulz

S. Wittig

Lehrstuhl und Institut für Thermische
Strömungsmaschinen,
Universität Karlsruhe (T.H.),
D-7500 Karlsruhe,
Federal Republic of Germany

Lifetime Prediction for Ceramic Gas Turbine Components

At the Institute for Thermal Turbomachinery, University of Karlsruhe (ITS), theoretical and experimental investigations of ceramic gas turbine components are performed. For the reliability analysis by finite element calculations the computer code CERITS has been developed. This code is used to determine the fast fracture reliability of ceramic components subjected to polyaxial stress states with reference to volumetric flaws and was presented at the 1990 IGTI Gas Turbine Conference. CERITS-L now includes subcritical crack growth. With the new code CERITS-L, failure probabilities of ceramic components can be calculated under given load situations versus time. In comparing these time-dependent failure probabilities with a given permissible failure probability, the maximum operation time of a component can be determined. The considerable influence of the subcritical crack growth upon the lifetime of ceramic components is demonstrated at the flame tube segments of the ITS ceramic combustor.

Introduction

The advantages arising from the use of the ceramics in the hot flow path of gas turbines have been extensively discussed in the past. Also, a number of other applications of ceramics have been developed during the last few years. Common to all these applications is the necessity of a careful design with special emphasis on the typical characteristics of ceramics. Brittleness and high diversity in strength, resulting in completely different failure mechanisms compared to those of metals, require a new treatment in the theoretical analysis of the reliability of ceramic components. Fracture statistical methods have proved to be a powerful tool to describe the behavior of ceramics. Adequate computer codes based on finite element analysis have been developed at different places (see, e.g., Gyekenyesi, 1986; Lamon, 1988; Stürmer et al., 1991). Most of these codes are characterized by the assumption of fast fracture conditions for the failure. Thus the reliability of a component is judged without considering slow changes within the material caused by prolonged load. Only the instant load situation is taken into account. However, this approach does not reflect the true situation of ceramics. Due to the mechanism of subcritical crack growth, the failure probability may increase significantly for higher load durations. Subcritical crack growth leads to slow propagations of the cracks. After a certain time one of the cracks reaches its critical length. The component fails, although a high fast fracture reliability may have been predicted.

The behavior of ceramic materials regarding subcritical crack growth can be characterized by experimentally determined parameters like the numerical constants C and n and the critical mode I stress intensity factor K_{Ic} (see Eq. (3)). Given these

values, the well-known fracture statistical models of Weibull (1939) and Batdorf (Batdorf and Crose, 1974) can be used to calculate load and time-dependent failure probabilities. Modifications of these models have been published, e.g., by Wiederhorn and Fuller (1985), Aoki et al. (1985), and Hu et al. (1988). Peculiarities regarding polyaxial stress states are considered by Thiemeier (1989). A Weibull theory based computer code for life time predictions was developed by Hempel and Wiest (1986). This code was applied to turbine rotors made of silicon nitride.

The fracture statistics computer code CERITS for fast fracture reliability analysis of ceramic components developed at the ITS (Stürmer et al., 1991) has now been enhanced to consider subcritical crack growth. Thus, using the new version CERITS-L, load time-dependent failure probabilities can be calculated. In comparing these values with a maximum acceptable failure probability, the operation time for a component can be determined. As an example, the computer code CERITS-L is used to determine the lifetime of the ceramic components of the ITS small gas turbine combustion chamber (see Pfeiffer et al., 1991).

Theory

The fracture statistical model used in CERITS-L will be described in the following. It is an extension of the Batdorf theory for polyaxial stress states (Thiemeier, 1989). The current version is based on the assumption that failures are solely caused by volume flaws.

Starting with Batdorf's original model, the approach to describe subcritical growth is explained. Finally the equations to calculate the failure probability including subcritical crack growth are deduced.

Batdorf Model. Using the Batdorf model, the overall fail-

Contributed by the International Gas Turbine Institute and presented at the 36th International Gas Turbine and Aeroengine Congress and Exposition, Orlando, Florida, June 3-6, 1991. Manuscript received at the ASME Headquarters February 1991. Paper No. 91-GT-96. Associate Technical Editor: L. A. Rieckert.

Table 1 Different relations of equivalent stress

Symbol	Fracture criterion	Crack type	Equivalent stress
BAT-N	Normal stress criterion	Sphere	σ_n
BAT-SERR-GC	Strain energy release rate criterion	G.C.	$\sqrt{\sigma_n^2 + \tau^2}$
BAT-SERR-PSC	Strain energy release rate criterion	P.S.C.	$\sqrt{\sigma_n^2 + \frac{\tau^2}{(1-0.5\nu)^2}}$
BAT-RI-PSC	Richard criterion	P.S.C.	$\frac{1}{2} \left[\sigma_n + \sqrt{\sigma_n^2 + \frac{4\alpha_1^2 \tau^2}{(1-0.5\nu)^2}} \right]$

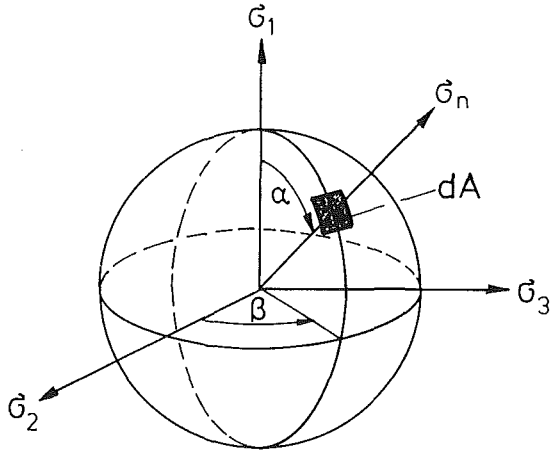


Fig. 1 Integration around the unit radius sphere

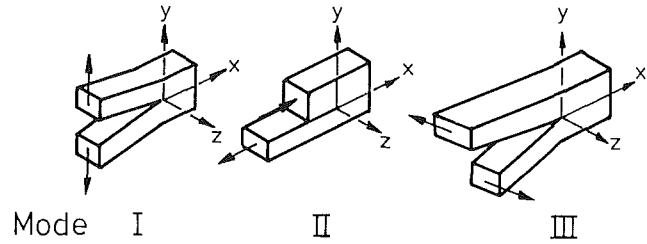


Fig. 2 Modes of crack surface displacement

$$P_f = 1 - \exp \left[- \frac{1}{4\pi} \frac{1}{V_o} \int_V \int_{\beta=0}^{2\pi} \int_{\alpha=0}^{\pi} \left(\frac{\sigma_{Ieq}}{\sigma_{Io}} \right)^m \sin \alpha \, d\alpha \, d\beta \, dV \right] \quad (2)$$

ure probability of a component can be calculated from (Batdorf and Crose, 1974)

$$P_f = 1 - \exp \left[- \int_V \int_0^\infty \frac{\Omega}{4\pi} \frac{dN}{d\sigma_{cr}} d\sigma_{cr} dV \right] \quad (1)$$

where $N(\sigma_{cr})$ represents the crack density function, σ_{cr} the critical stress, and Ω the solid angle in the principal stress space containing all crack orientations for which $\sigma_e \geq \sigma_{cr}$. With some tranformations of Eq. (1), the failure probability is finally given by (Stürmer et al., 1991)

where σ_{Ieq} is the equivalent stress and σ_{Io} is the Weibull scale parameter. Different relations of the equivalent stress, depending on fracture criterion and crack type, are implemented in CERITS-L (see Table 1). The Weibull scale parameter is calculated from three or four-point bending test results including the effects of test type and test bar geometry. The integrals of Eq. (2) are illustrated in Fig. 1.

Subcritical Crack Growth and Lifetime. To describe subcritical crack growth, a correlation between crack velocity and stress intensity factor is assumed:

Nomenclature

A = area
 a = crack size
 a_a = critical crack size at $t=0$
 a_f = critical crack size at $t=t_f$
 B = crack growth parameter (Eq. (9))
 b_c = Weibull scale parameter (experimental data)
 C = crack growth parameter (Eq. (3))
 E = Young's modulus of elasticity
 K_{Ic} = critical stress intensity factor (mode I)
 K_{Ieq} = equivalent stress intensity factor (mode I)

K_{IIc} = critical stress intensity factor (mode II)
 m = Weibull modulus
 N = crack density function
 n = crack growth parameter
 P_f = failure probability
 T = temperature
 t = time
 t_f = lifetime
 V = volume
 V_o = unit volume
 Y_I = shape factor (mode I)
 α = linear thermal expansion
 α = angle used in integration of unit radius sphere
 α_1 = parameter used in the

Richard criterion = K_{Ic}/K_{IIc}
 β = angle used in integration of unit radius sphere
 λ = thermal conductivity
 ν = Poisson ratio
 $\sigma_1, \sigma_2, \sigma_3$ = principal stresses
 σ_{Io} = Weibull scale parameter of the unit volume (polyaxial)
 σ_{Ic} = critical stress (mode I)
 σ_{Ieq} = equivalent stress (mode I)
 σ_{cr} = critical stress
 σ_e = effective stress
 σ_n = normal stress
 τ = shear stress
 Ω = solid angle for which $\sigma_e \geq \sigma_{cr}$

$$\frac{da}{dt} = C \cdot K_{Ieq}^n \quad (3)$$

where the stress intensity factor is defined as

$$K_{Ieq}(t) = \sigma_{Ieq}(t) \sqrt{a(t)} Y_I \quad (4)$$

Here, K_{Ieq} is the equivalent mode I stress intensity factor of polyaxial stress states (see Fig. 2). After substituting Eq. (4) into Eq. (3) and with separation of the variables we get

$$\sigma_{Ieq}(t)^n dt = \frac{1}{CY_I^n} \left(\frac{1}{\sqrt{a}} \right)^n da \quad (5)$$

Integration of Eq. (5) leads to

$$\int_{t=0}^{t_f} \sigma_{Ieq}(t)^n dt = \frac{1}{CY_I^n} \int_{a=a_0}^{a_f} a^{-n/2} da \quad (6)$$

Here, t_f is the lifetime, and the integration boundaries a_0 and a_f represent the critical crack length at the beginning of the loading and at failure, respectively. The relations for a_0 and a_f can be derived from the definition of the stress intensity factor (see Eq. (4)). We obtain

$$a_0 = \left(\frac{K_{Ic}}{\sigma_{Ic,a} Y_I} \right)^2 \quad \text{and} \quad a_f = \left(\frac{K_{Ic}}{\sigma_{Ieq,f} Y_I} \right)^2 \quad (7)$$

With these bounds the integration of Eq. (6) can be performed and Eq. (6) can be rewritten as

$$\int_{t=0}^{t_f} \sigma_{Ieq}(t)^n dt = \frac{2}{CY_I^2 (n-2) K_{Ic}^{n-2} \sigma_{Ic,a}^{n-2}} \left[1 - \left(\frac{\sigma_{Ieq,f}}{\sigma_{Ic,a}} \right)^{n-2} \right] \quad (8)$$

The constants of Eq. (8) are combined to a single coefficient

$$B = \frac{2}{CY_I^2 (n-2) K_{Ic}^{n-2} \sigma_{Ic,a}^{n-2}} \quad (9)$$

Assuming a constant load ($\sigma_{Ieq} = f(t)$) the term on the left-hand side of Eq. (8) can be integrated. Finally we get an expression for the lifetime t_f

$$t_f = B \sigma_{Ic,a}^{n-2} \sigma_{Ieq}^{-n} \left[1 - \left(\frac{\sigma_{Ieq}}{\sigma_{Ic,a}} \right)^{n-2} \right] \quad (10)$$

Failure Probability Including Subcritical Crack Growth. Combining the weakest link theory with subcritical crack growth, the following equation can be derived:

$$P_f(t) = 1 - \exp \left[-\frac{1}{4\pi} \frac{1}{V_o} \int_V \int_{\beta=0}^{2\pi} \int_{\alpha=0}^{\pi} \times \left(\frac{\sigma_{Ic,a}(t_f=t)}{\sigma_{Io}} \right)^m \sin \alpha d\alpha d\beta dV \right] \quad (11)$$

This equation corresponds to Batdorf's model (see Eq. (2)) and is appropriate to calculate time-dependent failure probabilities. Within Eq. (11) $\sigma_{Ic,a}$ has to be replaced by a term deduced from Eq. (10). There are two ways to introduce Eq. (10) into Eq. (11). In the first case the replacement of $\sigma_{Ic,a}$ by Eq. (10) leads to a relation for the failure probability, which holds for the entire load time of the part. However, the programming effort is relatively high. In the second case an approximation of Eq. (10) is used with fewer demands on the computational technique but with restrictions to higher lifetimes.

Exact Solution. Solving Eq. (10) for $\sigma_{Ic,a}$, the following equation is obtained:

$$\sigma_{Ic,a}(t_f=t) = \sigma_{Ieq}^{\frac{n}{n-2}} \left(\frac{t}{B} + \frac{1}{\sigma_{Ieq}^2} \right)^{\frac{1}{n-2}} \quad (12)$$

After Eq. (12) is placed in Eq. (11) the failure probability can be calculated from

$$P_f(t) = 1 - \exp \left\{ -\frac{1}{4\pi} \frac{1}{V_o} \int_V \int_{\beta=0}^{2\pi} \int_{\alpha=0}^{\pi} \times \left[\frac{\left(\frac{t}{B} \sigma_{Ieq}^{\frac{n}{n-2}} + \sigma_{Ieq}^{\frac{n}{n-2}} \right)^{\frac{1}{n-2}}}{\sigma_{Io}} \right]^m \sin \alpha d\alpha d\beta dV \right\} \quad (13)$$

The constant B in Eq. (13) contains the shape factor Y_I , which depends on the considered crack type. For Penny-Shaped-Cracks and Griffith-Cracks, respectively, the mode I shape factor is defined as follows:

$$Y_{I, PSC} = \frac{2}{\sqrt{\pi}} \quad Y_{I, GC} = \sqrt{\pi} \quad (14)$$

As already indicated Eq. (13) is valid for all time values including $t=0$, i.e., fast fracture. For this Eq. (13) becomes identical with Eq. (2), which is the relation for the failure probability of a component according to the Batdorf model without considering subcritical crack growth.

Approximation for Higher Lifetimes. After some transformations Eq. (10) can be rewritten as

$$t_f = B \sigma_{Ic,a}^{n-2} \sigma_{Ieq}^{-n} - B \sigma_{Ieq}^{-2} \quad (15)$$

Assuming that the second term in Eq. (15) can be neglected if $t_f \gg B \sigma_{Ieq}^{-2}$, we obtain

$$t_f = B \sigma_{Ic,a}^{n-2} \sigma_{Ieq}^{-n} \quad (16)$$

Consequently $\sigma_{Ic,a}$ is given by

$$\sigma_{Ic,a}(t_f=t) = \left(\frac{t}{B \sigma_{Ieq}^{-n}} \right)^{\frac{1}{n-2}} \quad (17)$$

Finally Eq. (17) is placed in Eq. (11) and this leads to the following approximation for the time-dependent failure probability:

$$P_f(t) = 1 - \exp \left\{ -\frac{1}{4\pi} \frac{1}{V_o} \int_V \int_{\beta=0}^{2\pi} \int_{\alpha=0}^{\pi} \times \left[\left(\frac{t}{B} \right)^{\frac{1}{n-2}} \left(\frac{\sigma_{Ieq}^{\frac{n}{n-2}}}{\sigma_{Io}} \right) \right]^m \sin \alpha d\alpha d\beta dV \right\} \quad (18)$$

It is obvious that Eq. (18) is not appropriate for $t=0$. For this case Eq. (18) has to be replaced by Eq. (2).

Program Description

With the computer code CERITS-L, time-dependent failure probabilities of ceramic components can be determined. For these calculations the stresses within the component are required. A preceding finite element analysis based on the well-known computer codes ADINA and ADINA-T (N. N., 1984) provides the stress distribution.

In addition to the stress distribution, the volumes of the finite elements are necessary for the lifetime prediction. To get these volumes, we use the pre- and postprocessing system PATRAN (N.N., 1988), since finite element volumes are not available in ADINA.

The different steps of the analysis using CERITS-L are depicted in Fig. 3. This figure also shows the data flow for CERITS-L. As already indicated, the principal stresses and the volumes of the finite elements are fed from ADINA and

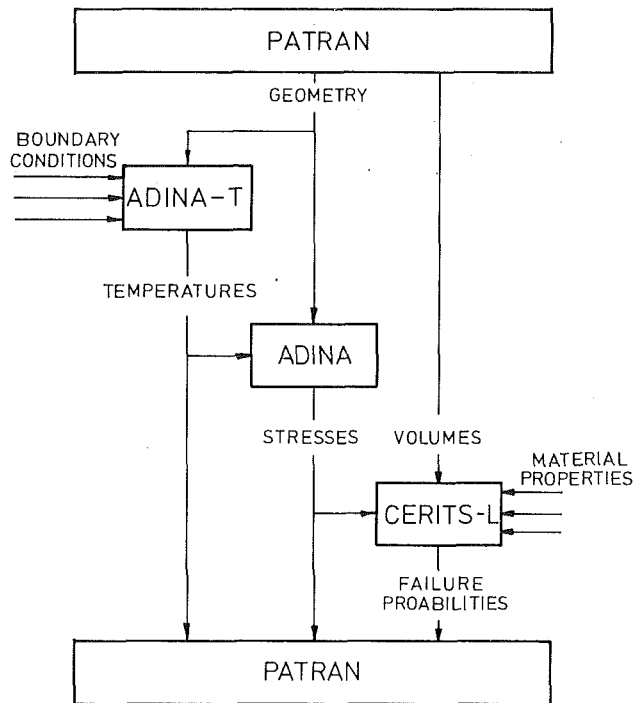


Fig. 3 Flow chart of the lifetime analysis

```

OUTPUT (CLASS 1)

NAME      : SEGMENT
MATERIAL  : SSIC

NUMBER OF ELEMENTS : 532

FRACTURE CRITERION (CRACK TYPE) : NORMAL STRESS-CRITERION

NUMBER OF INTEGRATIONS : 4256
INTEGRATIONS WITH REDUCED CONVERGENCE : 2

TYPE OF BENDING TEST : 4-POINT BENDING

INNER SPAN      : 20.00
OUTER SPAN      : 40.00
HIGHT OF TEST BAR : 4.00
WIDTH OF TEST BAR : 5.00

WEIBULL SCALE PARAMETER BC (EXPERIMENTAL DATA) : 384.00
WEIBULL MODULUS (EXPERIMENTAL DATA) : 8.60
WEIBULL SCALE PARAMETER SIGMA0 (CALCULATED) : 394.60
REFERENCE TEMPERATURE : 293.00

POISSON'S RATIO : 0.16
RICHARD-PARAMETER ALPHA1 :

CRACK GROWTH PARAMETER N : 35.00
CRACK GROWTH PARAMETER B : 6450.00
CRITICAL STRESS INTENSITY FACTOR KIC : 4.00
TIME OF LOADING TL : 100.00

OVERALL FAILURE PROBABILITY : 0.425510D-01
OVERALL PROBABILITY OF SURVIVAL : 0.957449D+00

END
  
```

Fig. 4 CERITS-L output

PATRAN, respectively. Moreover, a control file is read, which contains the statistical material properties and other input control data as shown in Table 2. The output file shows the component's failure probability and its probability of survival for the given duration of load (in hours). This file also contains a repetition of the complete input control data and information on the convergence of the numerical integration (see Fig. 4).

Example

The analysis of a ceramic flame tube segment with CERITS-

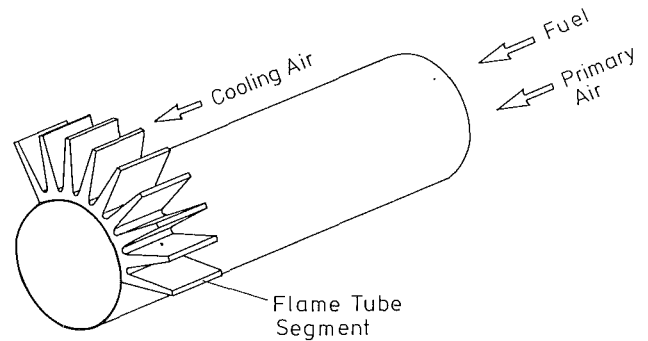


Fig. 5 Flame tube

Table 2 Required input control data

Variable	Entry	Format
NAME	Heading information	A20
WSTOFF	Material	A20
EMAX	Number of finite elements	I10
BK	Fracture criterion	I10
OUTPUT	Output control parameter	I10
ZAHL	Output control parameter	I10
TEST	Type of bending test	I10
M	Weibull modulus	F10.2
BC	Weibull scale parameter (experimental data)	F10.2
LI	Inner span	F10.2
LA	Outer span	F10.2
H	Height of test bar	F10.2
W	Width of test bar	F10.2
ALPHA1	Richard-parameter	F10.2
NUE	Poisson's ratio	F10.2
TEMP0	Reference temperature	F10.2
N	Crack growth parameter	F10.2
B	Crack growth parameter	F10.2
KIC	Critical stress intensity factor	F10.2
TL	Time of loading	F10.2

Table 3 Material properties of SiC

$T[K]$	$\lambda[\frac{W}{mK}]$	$E[GPa]$	$\nu[-]$	$\alpha[10^{-6}K^{-1}]$
293	-	433.0	0.16	3.05
473	60.2	429.8		3.05
673	51.0	426.2		3.03
873	44.5	422.6		3.02
1073	40.5	419.0		3.02
1273	38.2	415.4		3.04
1473	36.0	411.8		3.11
1673	34.8	408.0		3.25
1773	34.2	406.4		3.35

L will be described in the following. The flame tube is part of the small gas turbine combustion chamber of the Institute for Thermal Turbomachinery. The shape and the arrangement of the segments within the combustor is shown in Fig. 5. Three segments form a complete ring and the whole flame tube consists of a number of such rings. The air path is also indicated in Fig. 5. For a more detailed description of the flame tube

Table 4 Weibull and crack growth parameters of SiC

T [K]	m [—]	b_c [MPa]	K_{Ic} [MPa \sqrt{m}]	n [—]	$\log C$ [for da/dt in m/s and K_{Ic} in MPa \sqrt{m}]
293	8.6	384.0	4.0	73	-43.5
1073			4.0	48	-36.0
1473			4.0	35	-25.0

Table 5 Typical results of the finite element analysis

T_{min} [K]	T_{max} [K]	σ_{1max} [MPa]	σ_{3min} [MPa]
1206	1596	168	-116

see Pfeiffer et al. (1991), where a report on the design and operation of the complete combustor is given.

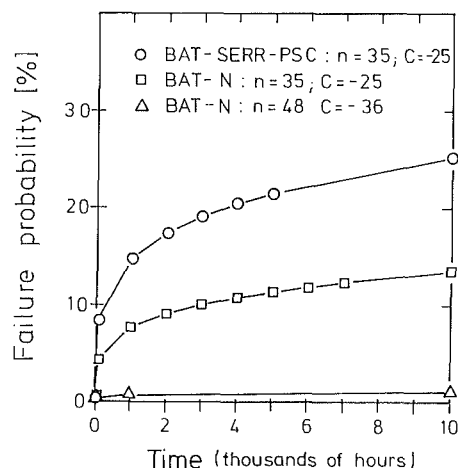
Boundary Conditions and Material Properties. The predominant load of the current design is caused by thermal stresses. Mechanical forces are negligible, due to the flexible support of the components. A careful thermal analysis by a finite element technique is therefore imperative. For this purpose adequate thermal boundary conditions had to be established. The free-stream temperature of the hot gases at the inner side of the flame tube was assumed to be 1700°C. The cooling air at the outer side of the elements had a temperature of 800°C. The corresponding heat transfer coefficients at the inner and outer side were 245 W/(m²K) and 565 W/(m²K), respectively. The radiative heat transfer inside the flame tube was considered to have a radiation exchange coefficient of 0.6. The geometric boundary conditions, i.e., the support of the elements, have been selected for unrestrained expansion in all directions.

Sintered silicon carbide (SSiC) was selected as material for the investigated segment. The material properties including thermal dependencies are given in Table 3. Additional fracture statistical parameters, needed for the failure probability calculations, are shown in Table 4. While the critical stress intensity factor and the parameters of subcritical crack growth are related to the considered temperature range of about 1200 K to 1600 K (see Table 5), the Weibull parameters are only provided for room temperature. Here no data for higher temperatures are available. The critical stress intensity factor K_{Ic} is nearly constant over the whole temperature range. The crack growth parameters n and C , however, show a reasonable temperature dependency. The data are taken from investigations by Himsolt et al. (1989) and Kleer et al. (1984).

Finite Element Analysis. According to the special operating conditions of the flame tube segment, the first step of the life time analysis was the calculation of the temperature distribution. This was done by the finite element code ADINA-T using the previously discussed thermal conditions and material parameters. All thermal conditions were taken to be constant. A nearly linear temperature distribution between the hot inner wall and the tips of the cooling ribs was found. Due to the underlying boundary conditions, no temperature gradients were observed in the axial direction. To give an illustration, just the highest and lowest temperatures within the segment are listed in Table 5.

Table 6 Failure probability in percent (fast fracture)

BAT-N	BAT-SERR-PSC
0.1162	0.2318



BAT-SERR-PSC: Strain Energy Release Rate Criterion - Penny Shaped Cracks
BAT-N: Normal Stress Criterion

Fig. 6 Time-dependent failure probabilities

Based on the results of the temperature field calculations, the stresses within the flame tube segment were determined. This was done by the finite element code ADINA. As indicated before, only thermal stresses are taken into account. As characteristic results the maximum values of the first and third principle stresses are given in Table 5. As expected, the highest tensile stresses were found at the roots of the cooling ribs. Higher compressive stresses occurred at the inner wall of the segment and at the tips of the cooling ribs. However, compressive stresses are generally neglected by computations with CERITS-L due to the fact that the fracture statistical model is based on weakest link theory, which is dominated by the tensile stress criterion.

Lifetime Prediction. In the third part of the analysis, the time-dependent failure probabilities are calculated by CETRIS-L under the assumption of constant stresses during the operation. For these calculations several failure criteria are available (see Table 1). Here as an example some results for the normal stress criterion and for the strain energy release rate criterion with Penny-Shaped-Cracks are shown. In addition to the fracture criterion, the calculation is determined by the Weibull parameters and the parameters of subcritical crack growth (see Table 4). The calculation of subcritical crack growth was performed for two temperatures representing the hottest and coldest areas of the component (see Table 5). Furthermore, the great influence of the temperature dependency of the crack growth parameters on the failure probability can be demonstrated by these two calculations. In Fig. 6 the failure probabilities versus operational time of up to 10,000 hours are shown.

The influence of the fracture criterion on the calculated fast fracture reliability has been discussed for quite some time (see, e.g., Batdorf and Heinisch, 1978; Gyekenyesi, 1986). For the given flame tube segment, the failure probabilities for various fracture criteria were calculated by Stürmer et al. (1991). The

results obtained for the two fracture criteria mentioned above are shown in Table 6. The investigations described in this paper show how failure probabilities diverge with increasing time when using the same Weibull and crack growth parameters but different fracture criteria (see Fig. 6). This indicates that the selection of the correct fracture criterion becomes even more important than for calculations based on fast fracture.

Figure 6 also demonstrates the influence of the crack growth parameters on the failure probability. For the same fracture criterion but different crack growth parameters due to different temperatures, very different relations are found. This shows an additional problem of lifetime predictions. Reliable results can only be achieved if the crack growth parameters of the material are known for the considered temperatures. To improve the accuracy of the calculations for components with relatively high temperature gradients (as with the flame tube segment) temperature-dependent crack growth parameters should be used.

Finally, Fig. 6 indicates that in the case of strong subcritical crack growth, the flame tube segment exhibits a high failure probability even for very few hours of operation. If a probability of survival of, e.g., 99 percent is required, operating times as needed for gas turbine components can only be achieved if the subcritical crack growth is very low.

Conclusions

The computer code CERITS-L for the lifetime prediction of ceramic components with respect to volumetric flaws is presented. The algorithm is an extension of the well-known Batdorf model to account for subcritical crack growth and includes different fracture criteria. CERITS-L is connected to the finite element code ADINA and to the pre- and postprocessing system PATRAN.

The lifetime prediction is demonstrated using the flame tube segments of the ceramic small gas turbine combustor of the Institute of Thermal Turbomachinery. Referring to previous calculations under fast fracture conditions, the differences between various fracture criteria are increased considerably if subcritical crack growth is included. Therefore, the selection of the correct fracture criterion is very important. Furthermore, it becomes obvious that reliable predictions are only possible if the crack growth parameters and their temperature dependencies are precisely known for the material under consideration. In the future, further effort has to be undertaken to select the right fracture criterion for a given situation as well as to determine the correct crack growth parameters and their temperature dependencies.

For the investigated ceramic flame tube segment a high increase in failure probability is observed even for relatively few hours of operation. Lifetimes as required for small gas turbine combustors can only be achieved if the selected material exhibits a very low subcritical crack growth.

References

- Aoki, S., Ohta, I., Sakata, M., and Ohnabe, H., 1985, "Finite-Element Analysis of Probability of Delayed Failure in Brittle Structures," *Engineering Fracture Mechanics*, Vol. 22, pp. 465-473.
- Batdorf, S. B., and Crose, J. G., 1974, "A Statistical Theory for the Fracture of Brittle Structures Subjected to Nonuniform Poly-axial Stress," *ASME Journal of Applied Mechanics*, Vol. 41, pp. 459-464.
- Batdorf, S. B., and Heinisch, H. R., Jr., 1978, "Weakest Link Theory Reformulated for Arbitrary Fracture Criterion," *Journal of the American Ceramic Society*, Vol. 61, pp. 355-358.
- Gyekenyesi, J. P., 1986, SCARE: A Postprocessor Program to MSC/NASTRAN for Reliability Analysis of Structural Ceramic Components," *ASME JOURNAL OF ENGINEERING FOR GAS TURBINES AND POWER*, Vol. 108, pp. 540-546.
- Hempel, H., and Wiest, H., 1986, "Structural Analysis and Life Prediction for Ceramic Gas Turbine Components for the Mercedes-Benz Research Car 2000," *ASME Paper No. 86-GT-199*.
- Himsolt, G., Fett, T., Keller, K., and Munz, D., 1989, "Fracture Toughness Measurements on Silicon Carbide," *Mat.-wiss u. Werkstofftech.*, Vol. 20, pp. 148-153.
- Hu, X.-Z., Mai, Y.-W., and Cotterell, B., 1988, "A Statistical Theory of Time-Dependent Fracture for Brittle Materials," *Philosophical Magazine A*, Vol. 58, pp. 299-324.
- Kleer, G., Richter, H., Prümmer, R., and Pfeiffer-Vollmar, H.-W., 1984, "Festigkeitsverhalten keramischer Werkstoffe unter langzeitiger Belastung," *Keramische Komponenten für Fahrzeug-Gasturbinen III*, W. Bunk et al., eds., Springer-Verlag, Berlin, pp. 487-512.
- Lamon, J., 1988, "Ceramics Reliability: Statistical Analysis of Multiaxial Failure Using the Weibull Approach and the Multi-axial Elemental Strength Model," *ASME Paper No. 88-GT-147*.
- N. N., 1984, ADINA Theory and Modeling Guide," Report AE 84-4, ADINA Engineering Inc., Watertown, MA.
- N. N., 1988, "PATRAN Plus User Manual," P/N 2191020, PDA Engineering, Costa Mesa, CA.
- Pfeiffer, A., Schulz, A., and Wittig, S., 1991, "Principles of the ITS Ceramic Research Combustor Design: Segmented Flame Tube and Staged Combustion," submitted for publication.
- Richard, H., 1985, "Bruchvorhersagen bei überlagerter Normal und Schubbeanspruchung von Rissen," VDI-Forschungsheft 631/85, VDI-Verlag, Düsseldorf, Federal Republic of Germany.
- Stürmer, G., Fundus, M., Schulz, A., and Witting, S., 1991, "Design of Ceramic Gas Turbine Components," *ASME JOURNAL OF ENGINEERING FOR GAS TURBINES AND POWER*, Vol. 113, pp. 621-627.
- Thiemeier, T., 1989, "Lebensdauervorhersage für keramische Bauteile unter mehrachsiger Beanspruchung," Dissertation, Universität Karlsruhe, Federal Republic of Germany.
- Weibull, W., 1939, "A Statistical Theory of the Strength of Materials," *Ingeniörsvetenskapsakademiens Handlingar*, No. 151.
- Wiederhorn, S. M., and Fuller, E. R., Jr., 1985, "Structural Reliability of Ceramic Materials," *Materials Science and Engineering*, Vol. 71, pp. 169-186.

K. G. Nickel

Eberhard-Karls-Universität Tübingen,
Institut für Mineralogie,
Petrologie, und Geochemie,
D-7400 Tübingen,
Federal Republic of Germany

Z. Fu

P. Quirnbach

Max-Planck-Institut für Metallforschung,
Institut für Werkstoffwissenschaft,
Pulvermetallurgisches Laboratorium,
D-7000 Stuttgart 80,
Federal Republic of Germany

High-Temperature Oxidation and Corrosion of Engineering Ceramics

The problems of high-temperature oxidation and corrosion of Si_3N_4 and SiC are discussed. Other ceramics usually do not meet the requirements of structural applications at high temperatures. If the application has to meet very defined limits of size change, it is necessary to specify the exact material composition, as well as the atmosphere composition and physical environment to be able to specify the limits. This is in any case true for extremely reducing conditions or very high temperatures. Under oxidizing conditions, the region between ≈ 850 and 1100°C should be avoided when salty, sulfurous, and wet fuel conditions are expected. High temperature limits for long-time applications of Si_3N_4 in oxidizing environments are between 1200 and 1400°C , corresponding to eutectic temperatures of the glass phase. The ultimate limit for long-time use of SiC is likely to be between 1700 and 1800°C , where bubble formation and spallation may become inevitable.

Introduction

Defining *engineering ceramics for high-temperature applications* as those used to build structures to endure mechanical or thermomechanical stress at temperatures $\geq 1000^\circ\text{C}$, we are mainly left with Si_3N_4 - and SiC -based ceramics. Oxides, silicides, and other types often have good corrosion resistance at high temperatures but are not strong enough to be used for structural applications.

The term "oxidation of Si-based non-oxide ceramics" is historically established. From a chemical point of view the processes involved describe reactions with oxygen toward equilibrium phases without a formal positive valency change of silicon (Nickel, 1990). Thus, regardless of the reacting species, all processes described here are corrosion reactions.

The two forms of corrosion (active, passive) and the conditions for the boundary will therefore be discussed using examples from Si_3N_4 - and SiC -based ceramics.

Both Si_3N_4 and SiC are ceramic materials that have high oxidation resistance (Schlichting, 1979a, 1979b; Nickel and Quirnbach, 1991) in atmospheres dominated by oxygen. The temperature limits are dependent on the application requirements (length of treatment, erosional forces, etc.). In general SiC can be used to higher temperatures compared to Si_3N_4 .

The excellent oxidation resistance comes from the formation of a protective layer based on SiO_2 . It may consist of SiO_2 in glassy and/or crystalline form and is modified by the additives used for the sintering process and impurities deposited during application.

In particular, in Si_3N_4 ceramics, significant amounts of additives are used. During oxidation the interaction of SiO_2 and these additives results in the formation of secondary phases

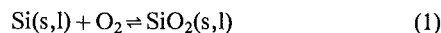
like silicates or the existence of a complex glass. Examples for this interaction with additives and salts ("hot corrosion") will be given.

However, if the atmosphere is strongly reducing, this layer is no longer formed and the material is free to react with its environment. In this case Si-based ceramics may react very rapidly with metals such as Fe and Ni to form silicides and liquids at temperatures even below 1000°C (Schröder, 1986). They may also react with gas species in an active oxidation mode, i.e., they are decomposed to gaseous species.

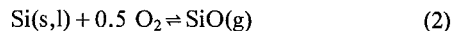
For high-temperature applications it is thus crucial to be aware of the limits of the protective SiO_2 -film production on these ceramics ("passive oxidation"). The transition to the active mode is usually described in terms of a critical $P(\text{O}_2)$ at a given temperature. The theoretical derivation of this transition has been described by Wagner (1958) and is briefly outlined below.

On the Active-Passive Boundary

Wagner (1958) discussed the problem for the case of metallic silicon. The thermodynamic stability of SiO_2 based on the reaction



extends to very low oxygen partial pressures. At $P(\text{O}_2)$ conditions much higher than those predicted via reaction (1) Si begins to oxidize actively, i.e., it is consumed according to



The solution of this problem is thought to be a transport problem (Fig. 1). A boundary layer exists in the atmosphere next to the material, because oxygen is used up very rapidly at the interface by reaction (2), producing a partial pressure $P(\text{SiO(g)})^*$ at the gas/material interface. The product gas (SiO(g)) has to diffuse outward while O_2 is diffusing toward

Contributed by the International Gas Turbine Institute and presented at the 37th International Gas Turbine and Aeroengine Congress and Exposition, Cologne, Germany, June 1-4, 1992. Manuscript received by the International Gas Turbine Institute February 24, 1992. Paper No. 92-GT-434. Associate Technical Editor: L. S. Langston.

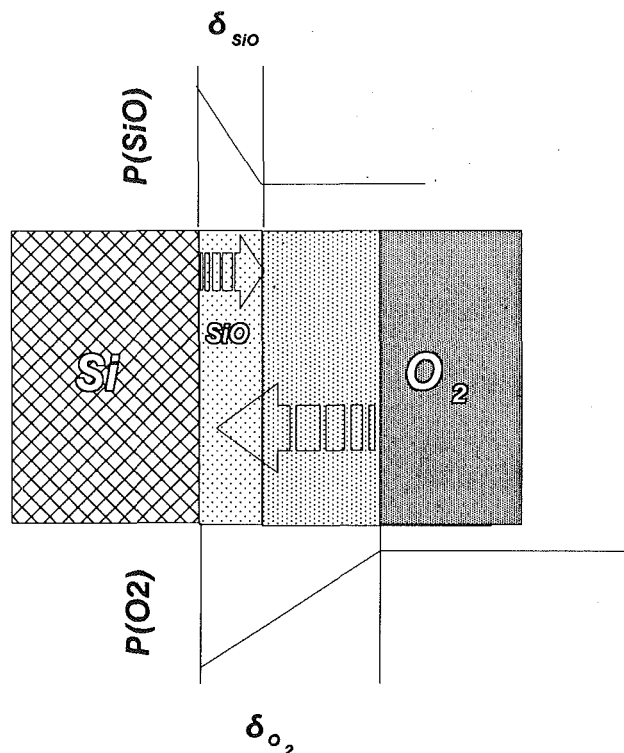
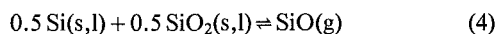


Fig. 1 Outline of the Wagner (1958) model for the active/passive oxidation boundary: A boundary layer at the material/atmosphere interface with gradients of $P(O_2)$ and $P(SiO(g))$ is established through O_2 -consumption and diffusion. The critical pressures are determined by the compatibility of substrate and oxide layer (reaction (4)).

the material surface. Accordingly a gradient of $P(O_2)$ and $P(SiO(g))$ is established. Its build-up depends on the individual effective thickness of the boundary layer for each species ($\delta(O_2)$, $\delta(SiO(g))$) and the diffusion coefficients (D_{O_2} , D_{SiO}). The $P(SiO(g))^*$ may hence be related to the $P(O_2)$ in the bulk gas by

$$P(SiO(g))^* = 2 P(O_2) \frac{\delta_{SiO} D_{O_2}}{\delta_{O_2} D_{SiO}} \quad (3)$$

The critical pressure of $SiO(g)$ is given by the reaction



At equilibrium, the $P(SiO(g))$ for this reaction defines the compatibility between substrate and the oxide layer (one may view this also as the condensation of $(SiO(g))$). This $P(SiO(g))$ determines via Eq. (3) the critical oxygen partial pressure $P(O_2)_{max}$. Using the relation

$$\frac{\delta_{SiO}}{\delta_{O_2}} = \left(\frac{D_{SiO}}{D_{O_2}} \right)^{0.5} \quad (5)$$

Wagner (1958) derived the estimate of $P(O_2)_{max}$ for Si:

$$P(O_2)_{max} = 0.5 (D_{SiO}/D_{O_2})^{0.5} P(SiO(g))_{eq} \quad (6)$$

Nomenclature

a = area, m^2	k_{lin} = linear rate constant, $m s^{-1}$	T = temperature, K
CVD = abbreviation for "produced by chemical vapor deposition"	k_{log} = logarithmic rate constant	u = stoichiometric factor
D_x = diffusion coefficient, $m^2 s^{-1}$, of species x	k_p = parabolic rate constant, $m^2 s^{-1}$ or $kg^2 m^{-4} s^{-1}$	$P(i)$ = partial pressure, Pa, of species i
G = Gibbs free energy, $J mol^{-1}$	M = molecular weight, $kg mol^{-1}$	x = thickness of a layer, m
H = enthalpy, $J mol^{-1}$	R = gas constant = $8.3143 J mol^{-1} K^{-1}$	δ_x = effective thickness of boundary layer for gas species x
	REE = rare earth elements	ρ = density, $kg m^{-3}$
	S = entropy, $J mol^{-1} K^{-1}$	

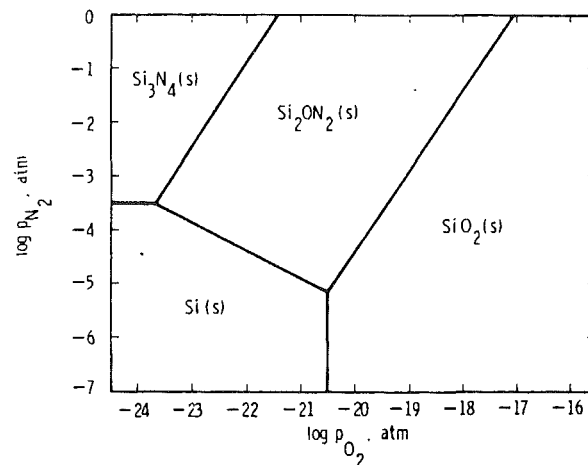


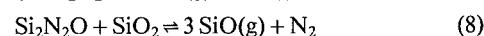
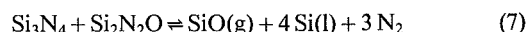
Fig. 2 Thermochemical analysis of the Si-N-O system at 1600 K after Singhal (1976)

where $P(SiO(g))_{eq}$ is the $P(SiO(g))$ calculated for reaction (4). For ceramics appropriate reactions for active and passive oxidation can be formulated.

This compatibility between substrate and oxide layer may be called the "primary" active/passive transition, because here the oxide *cannot* form. There are situations where the pressure of the product gas exceeds the ambient pressure without exceeding $P(O_2)_{max}$. In this case an oxide *must* form but is removed by spallation and bubble formation. Continuously repeating this process would lead to a bare surface and overall weight losses. Thus macroscopically it would be recognized as an active oxidation. The critical condition for exceeding the ambient pressure could therefore be called a "secondary" active/passive boundary.

Thermodynamics show that Si_3N_4 and SiO_2 cannot coexist stably at any temperature (Singhal, 1976, Fig. 2). If a gradient of $P(O_2)$ exists during the oxidation of Si_3N_4 , then it must range from values corresponding to the equilibrium between Si_3N_4 and Si_2N_2O at the interface up to the $P(O_2)$ of the bulk gas. If the $P(O_2)$ of the bulk gas is in the stability field of SiO_2 the formation of a Duplex-layer consisting of an "inner" Si_2N_2O -layer at the material interface and an "outer" SiO_2 -layer at the gas-layer interface is predicted by Fig. 2. This has been confirmed experimentally.

Accordingly the compatibility reaction defining the critical reaction may either be between material and inner layer or between inner and outer layer. For Si_3N_4 we find



Using estimates of diffusion coefficients similar to the Wagner treatment, the critical conditions were calculated by Nickel and Quirnbach (1991) (Fig. 3).

For SiC the conditions are more complicated, because condensed SiO is a possible phase to create an "inner" layer

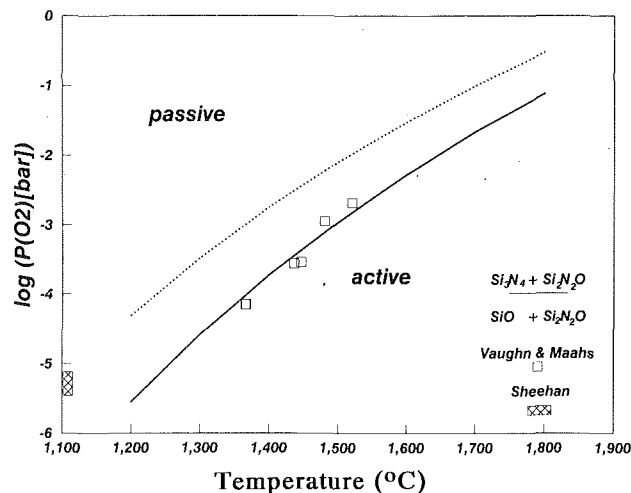
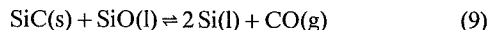


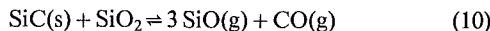
Fig. 3 Active-to-passive oxidation transition of Si_3N_4 in the Si-N-O system: experimental data of Sheehan (1982), Vaughn and Maahs (1990) and calculated values using reactions (7) (solid line) and (8) (stippled line) (Nickel and Quirnbach, 1991)

between SiC and SiO_2 . However, this phase would be difficult to observe as it is unstable at low temperatures and its coexistence limits with SiC depend on carbon activity.

Based on the data of Chase et al. (1985), Kubaschewski and Alcock (1979), and Nagamori et al. (1986), Nickel (1991) derived new estimates of thermodynamic parameters for condensed SiO and argued that at low carbon activities and high temperatures the critical $P(\text{O}_2)$ for the active/passive boundary for SiC is dependent on the reaction



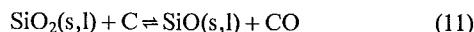
while at high carbon activities or low temperatures the reaction



is critical. The comparison between the theoretical calculations and experimental data is shown in Fig. 4.

The production of SiC involves the existence of free carbon. SiC used in an application would thus start with a carbon activity of 1. If free carbon cannot be removed fast enough to lower the carbon activity, the CO pressure will eventually exceed 1 bar. Here, at the "secondary" active/passive transition, large bubbles are inevitably formed and spallation must occur. This boundary is as low as 1520°C for high carbon activities, but will rise to approximately 2050°C for carbon activities appropriate for the coexistence of Si(l), SiC(s), and SiO(l).

If the oxide layer on SiC can indeed be described as consisting of an inner layer of SiO(l) and an outer layer of SiO_2 we will approach this secondary transition at temperatures of 1700 – 1800°C because the reaction



produces CO pressures greater than 1 bar.

Experimental evidence for the existence of this "secondary" boundary has been presented by Schneider et al. (1990) (Fig. 5). This secondary transition may well be the ultimate boundary for the use of SiC at high temperatures in oxidizing environments at least for long time exposures.

In inert gases or in a vacuum SiC is always in the active range, because a dissociation pressure according to



is calculatable or measurable.

The active-passive transition in other gases is for many pure gas species relatively low. For Cl_2 weight losses of SiC were observed at temperatures below 1000°C (Park et al., 1990) due to the formation of gaseous chlorides:

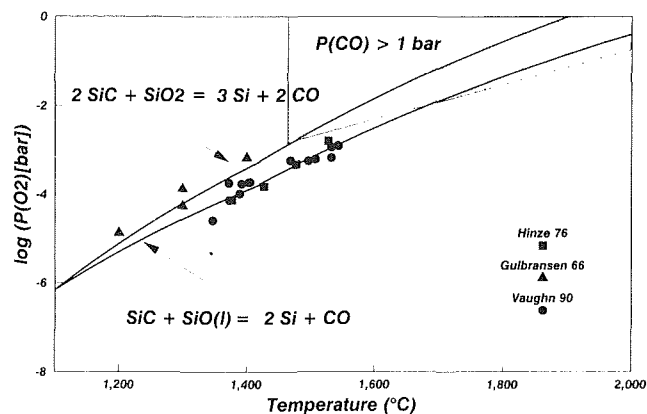


Fig. 4 Active-to-passive boundary for SiC in the Si-C-O system: experimental data of Gulbranson et al. (1966), Hinze and Graham (1976) and Vaughn and Maahs (1990), compared to the prediction by Nickel (1991). The shaded area corresponds to the secondary boundary.

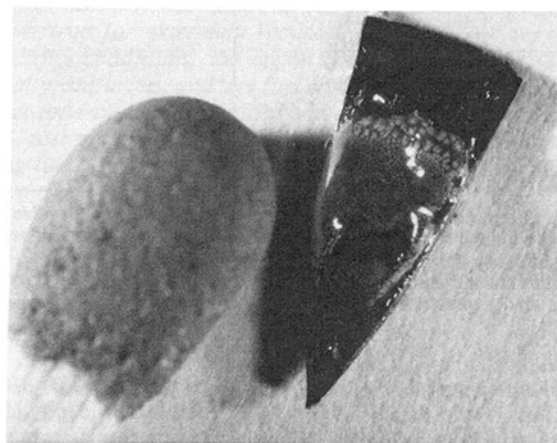
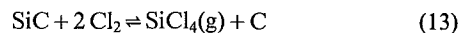
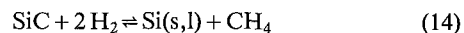


Fig. 5 Large bubble produced on SiC after punctual exposure to $\approx 1760^\circ\text{C}$ in air for a few seconds; matchhead for scale



The effect of an oxygen addition to Cl is dependent on the O_2 content of the gas, the C content of the SiC, and the temperature. 2 percent O_2 in Cl_2 may show a faster active corrosion at 1000°C (Marra et al., 1989), but passive oxidation at 1300°C .

Hydrogen puts SiC likewise into the active regime because even at low temperatures the equilibria favor the production of gaseous species, e.g.,



However, these reactions are kinetically hampered at low temperatures and thus significant weight losses are observed only at temperatures $\geq 1500^\circ\text{C}$.

Oxygen addition to hydrogen corresponds to an H_2O attack with active corrosion at 1000 – 1300°C at concentrations as low as 25 ppm H_2O (Hallum and Herbell, 1988). The active-passive boundary is at low H_2O pressures (4×10^{-7} MPa at 1000°C and $\approx 10^{-5}$ – 3×10^{-6} MPa at 1200°C , Antill and Warburton, 1971).

The active-passive boundary for many gases is not known and difficult to access by experiment. Nonetheless for most gas turbine environments the low critical pressures for O_2 and/or H_2O imply a passive oxidation up to high temperatures for both Si_3N_4 and SiC.

Passive Oxidation and the Limits of Applicability

The formation of an oxide layer on Si-based non-oxide ce-

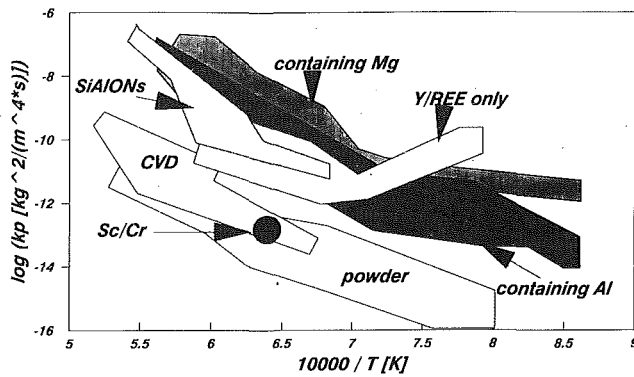


Fig. 6 Parabolic rate constants for the oxidation of Si_3N_4 with different additive systems in comparison to data from powder, CVD- Si_3N_4 and SiAlONs (Nickel and Quirnbach, 1991)

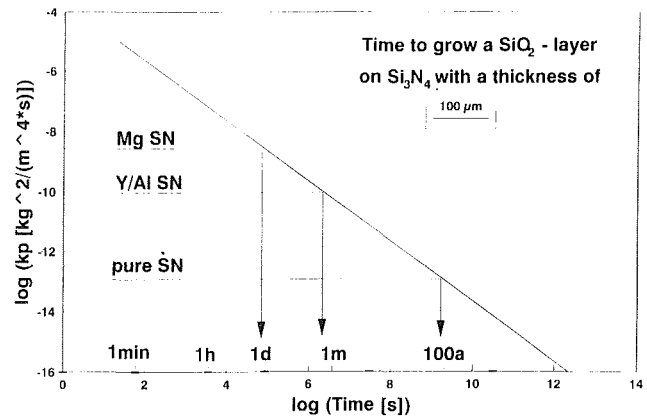


Fig. 8 Chart exemplifying the different times needed to produce a layer of SiO_2 on Si_3N_4 with material having different parabolic rate constants

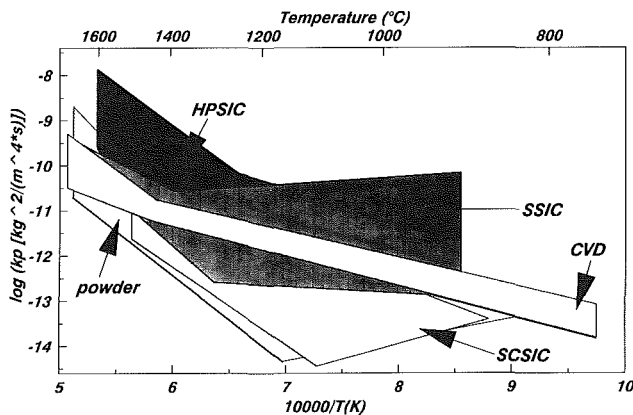


Fig. 7 Parabolic rate constants for SiC for different types (HP: hot pressed, SSiC: pressureless sintered) compared to powder, CVD, and single crystal (SCSiC) data (Nickel and Quirnbach, 1991)

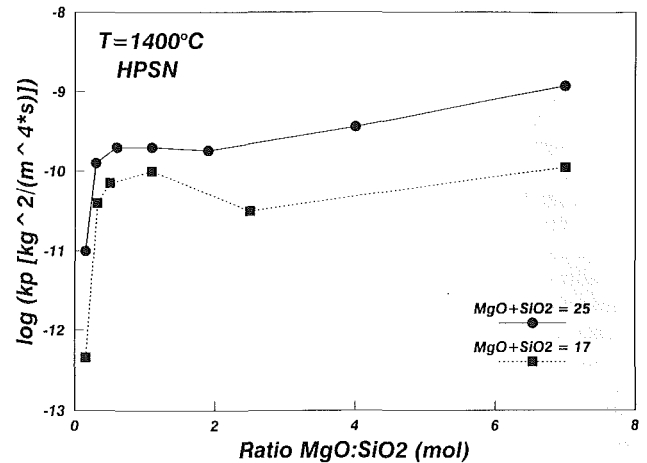


Fig. 9 Parabolic rate constants of Mg-containing Si_3N_4 at various $\text{MgO}:\text{SiO}_2$ ratios and amounts of 1400°C after Clark and Lange (1980)

ramics follows linear, parabolic, logarithmic, or mixed growth laws. The formulae for the basic laws are:

$$x = k \cdot t \quad (15)$$

$$x^2 = 2k_p \cdot t \quad (16)$$

$$x = c + k_{\log} \cdot \log(t) \quad (17)$$

The applicability of each law is dependent on the characteristics of the layer. If it is porous diffusion in the gas phase is rate controlling. Then, for a constant gas stream over a component, Eq. (15) is true. A homogeneous layer with constant properties and composition over time will follow the parabolic law (Eq. (16)), while a constant change of properties of the layer with time (e.g., partial crystallization) will result in a logarithmic law (Eq. (17)). Given a critical condition, e.g., a critical size change of a component, life times can be calculated from Eqs. (15)–(17).

In real application cases no simple law is followed exactly and changes in growth laws and discontinuities are observed. However, often a model forcing the data to yield parabolic rate constants may be used to compare materials. This has been done for SiC and Si_3N_4 (Figs. 6 and 7) with different additive systems and processing routes.

From Figs. 6 and 7 it is evident that the oxidation resistance of SiC can be as high as the pure material itself, but Si_3N_4 rarely preserves the inherent oxidation resistance. This is understandable in light of the fact that the sintering of Si_3N_4 is done with much higher amounts of sintering additives and thus the influence of these additives on the properties of the formed layer cannot be neglected.

It is also evident from Figs. 6 and 7 that the rate constants

of a family of SiC or Si_3N_4 (defined as materials with the same type of additive or processing route) typically have differences of two to four magnitudes of order at a given temperature. Figure 6 demonstrates that these differences in parabolic rate constants have a significant effect for the material behavior: If the application in mind can tolerate a change of size of the component of $100 \mu\text{m}$, the lifetime of the component may change from a day to almost infinite by a change of rate constants from $\approx 10^{-9}$ to $10^{-13} [\text{kg}^2/(\text{m}^4 \cdot \text{s})]$! The values of Fig. 8 are taken from Fig. 7 for 1300°C using data from a “poor” MgO-doped, a “good” $\text{Y}_2\text{O}_3 + \text{Al}_2\text{O}_3$ -doped Si_3N_4 (Mg SN and Y/Al SN, respectively) compared with data for pure (powder) Si_3N_4 .

The differences between the families are explained by either the changes in reaction mechanisms or the changes in properties of the oxide layer. For example, Mg may diffuse rapidly through the intergranular glass phase. Its diffusion as a cation may become rate controlling for a MgO-doped Si_3N_4 (Clarke, 1983), while the slow diffusion of Y in a Y_2O_3 -doped Si_3N_4 renders the molecular oxygen transport through SiO_2 as the rate controlling factor (Ernstberger, 1985).

Within the family the knowledge of the phase relations is required to explain the differences. Figure 9 shows a general trend, exemplified for data for MgO-containing Si_3N_4 of Clarke and Lange (1980): An increase in amount of sintering additives leads to an increase in rate constants (hence a poorer oxidation resistance). A change in relative proportions of the components of the sintering additive can further influence the oxidation

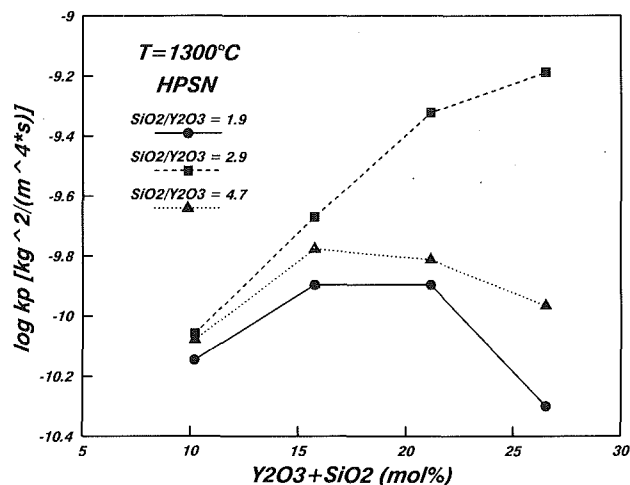
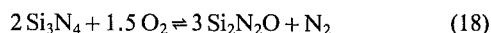


Fig. 10 Parabolic rate constants for Y-containing Si_3N_4 with different $\text{Y}_2\text{O}_3:\text{SiO}_2$ ratios and amounts (Babini and Vincenzini, 1983)

resistance: Very low $\text{MgO}:\text{SiO}_2$ ratios in Fig. 9 drastically enhance the oxidation resistance because the system approaches the pure $\text{Si}_3\text{N}_4\text{-O}_2$ system. A change in $\text{MgO}:\text{SiO}_2$ ratio at higher MgO levels additionally modifies the oxidation resistance because the properties of the glass phase (D_{O_2} , D_{Mg} , D_{N_2}) are changed.

The detailed influence of chemistry, and hence phase relation change can be much more complicated, as shown by the data of Babini and Vincenzini (1983) (Fig. 10) on $\text{Y-Si}_3\text{N}_4$. Here simple rules like "increases in ratio $x:y$ leads to increase of oxidation resistance" or "more additives necessarily mean poorer oxidation resistance" fail. This is due to the fact that here different phases *within* the ceramic body are stable (N-apatite, N-wollastonite, or N-melilite) at different chemistries and each phase has a different oxidation behavior on top of a modification of the layer, which may crystallize Y-silicates. Detailed knowledge of the phase relations is necessary to understand the behavior. This means on the other hand that this knowledge may be used to tailor ceramics toward an improved oxidation behavior!

Raising the temperatures above critical temperatures causes a strongly accelerated oxidation and the formation of reaction product gas bubbles, e.g., of N_2 according to



Bubble formation is favored by differences in D_{O_2} and $D_{\text{Product gas}}$ in the glass. The effect is enhanced by the crystallization of N-free phases like silicates and SiO_2 in the scale, trapping N_2 . As a result we have a structured scale with layers and the tendency to separate the interface material-oxide (Nickel et al., 1989) (Fig. 11).

Naturally the scale in Fig. 11 would be easily eroded in turbine applications and could not act as a protective layer. The critical conditions are usually related to the eutectic melting points of the sintering additive system; for $\text{Y-Al-Si}_3\text{N}_4$ this is approximately 1350°C .

Thus, apart from the conditions that have to be specified by the requirements of the application, e.g., the allowable size change, there are temperature limits by this bubble formation process. These may be controlled by the sintering additive system.

The fact that much less sintering additives are used for SiC makes this ceramic superior in its limits, because the melting point of pure SiO_2 is at very high temperatures. A good material can be used in oxidizing conditions at least to 1600°C .

The modifications of the surface layer may also come from external sources, i.e., substances deposited on it during application or other reactive gas species. Many questions here

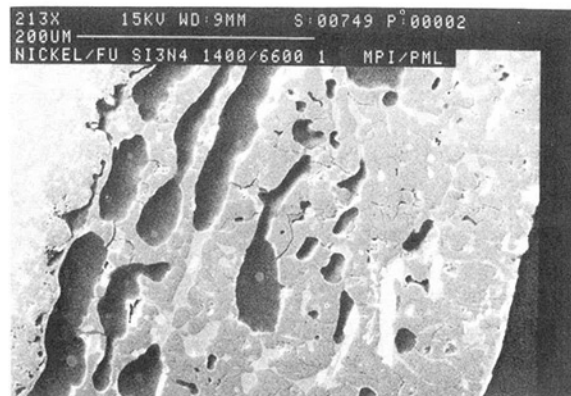


Fig. 11 Large bubbles of N_2 are trapped at the interface between Si_3N_4 (light material in the upper left side) and its oxide scale after 110 h exposure to O_2 at 1400°C

remain unanswered, in general a decrease in oxidation resistance with impurity content is expected.

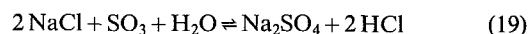
It is known from metals that in particular molten salts can cause severe corrosion. This is known as hot corrosion.

Hot Corrosion

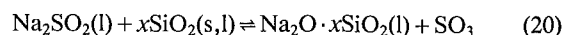
Hot corrosion studies of structural ceramics are as yet few and not well quantified. At higher temperatures ($>1100^\circ\text{C}$, above the dew point of Na_2SO_4) there is evidence that both Si_3N_4 and SiC are highly resistant to corrosion by oxidizing fuels containing Na, V, and S (Singhal, 1974).

The critical conditions for hot corrosion are, like those for metals, between the melting point of the salt (for Na_2SO_4 884°C) and its dew point (up to $\approx 1050^\circ\text{C}$ for usual jet fuel and low salt loadings at several atmospheres pressure).

The Na_2SO_4 in real applications is not a primary impurity but caused by the burning of salt- and sulfur-bearing wet fuel:



Tests with melt immersion, thin sheet application and burner rigs with Na_2CO_3 and Na_2SO_4 at $900\text{--}1000^\circ\text{C}$ (Jacobson and Fox, 1988; Fox and Jacobson, 1988; Fox and Smialek, 1990) show that the SiO_2 layer is attacked by processes like



The SiO_2 is produced simultaneously via oxygen transport through the scale. True comparable data for the speed of corrosion are scarce. It seems however, that the ceramics are corroded slower than Si or superalloys and that Si_3N_4 is superior to SiC . The last fact is attributed to either a $\text{Si}_2\text{N}_2\text{O}$ layer at the Si_3N_4 interface or N_2 diffusion as rate controlling factor.

However, it should be noted that the hot corrosion of ceramics leads to pitting. The high strength of ceramics is obtained by very small critical flaws. Pits act as relatively large critical flaws and thus substantial reductions in strength are observed and expected (Smialek and Jacobson, 1986).

As mentioned above the problem can be overcome by raising the temperature above the dew point, and ceramics may still be strong enough at high temperatures.

The temperature cannot be raised indefinitely without running into other corrosion problems: The gaseous species become more reactive and active corrosion occurs above the limits discussed above.

Active Oxidation and the Limits of Application

If the material oxidized actively, i.e., it is decomposed into gaseous species, the rate-controlling step is the exchange of reactive gas species and reaction product. For constant conditions linear kinetics according to Eq. (15) are expected.

The prediction of the rate of weight loss involves a theoretical model for each specific application. In particular, the velocity of gas flow over the component and the character of the gas flow (laminar, turbulent) have to be known. If enough data of the system are available, the corrosion speed can be estimated via diffusion coefficients and gas rheology parameters (Kim and Ready, 1989).

Simple models for still and slow-flowing atmospheres have been presented by Nickel (1989). In these models it is argued that a slow to moderate gas flow may be treated as a repeated exchange of an atmosphere of constant volume, which goes into equilibrium. For equilibrium conditions at constant volume of the gas chamber, thermodynamics dictate that the corrosion depth x is governed by

$$x = (M \cdot P_i \cdot V_{gc}) / (a \cdot u \cdot \rho \cdot R \cdot T) \quad (21)$$

where M and ρ are the molecular weight and density of the material, a is the area of material exposed to the volume of the gas chamber V_{gc} filled with the corrosive environment, P_i is the partial pressure of the species, which is the main contributor to weight loss and u is the stoichiometric factor relating this species to material loss. A thermodynamic analysis to identify this main reaction and the partial pressure of the species is required to calculate the value x .

Treating a gas flow as repeated exchanges of this atmospheres leads to a calculation of a corrosion rate \dot{x} [depth/time]

$$\dot{x} = (M \cdot P_i \cdot \dot{V}) / (a \cdot u \cdot \rho \cdot R \cdot T) \quad (22)$$

where \dot{V} is the gas flow [volume/time].

A natural boundary condition for a maximum corrosion speed is given by a Hertz-Langmuir-type behavior, where kinetic hindrances are neglected. Here the assumption that every gaseous particle produced at the surface is immediately removed with a speed only governed by gas kinetics leads to:

$$J_{\max} = P_i / (2 \cdot \pi \cdot M \cdot R \cdot T)^{0.5} \quad (23)$$

with J_{\max} being the maximum obtainable mass flux for extreme cases.

Using Eqs. (22) and (23) parameter studies of a given application situation show the influence of the physical parameter \dot{V} (Nickel et al., 1992) (Fig. 12). The theoretical corrosion rates were calculated for a situation depicted in the inlet of Fig. 10: An SiC tube of 320 mm length and 200 mm diameter is exposed to flowing hydrogen.

The peculiar shape of the loss curves in Fig. 10 below 1500°C reflect the increase of stability of CH_4 with decreasing temperature. At these low temperatures the model cannot be applied because of the slow kinetics of CH_4 formation from SiC.

Such charts may be read in different ways: If a certain corrosion rate is allowed for by the application, the level of maximum temperatures of use can be read. Due to the simplifications inherent in these models, they are to be viewed as a guide to estimate magnitudes of order, not to estimate corrosion rates exactly. Confirmation by realistic experimental testing will always be required.

Summary

Even when restricting oneself to two types of ceramics, Si_3N_4 and SiC, it has to be noted that there is no single behavior for a type. The ceramic has to be specified in terms of composition including sintering additives just as exactly as any alloy is treated by engineers.

Furthermore the application has to be specified in terms of physical (gas flow, etc.) and chemical parameters (e.g., composition of atmosphere) to be able to predict the test and the behavior of the material.

As a rule of thumb, most gas turbine environments are oxidizing for the Si-based non-oxide ceramics. Within such conditions SiC can be used to high temperatures, while Si_3N_4

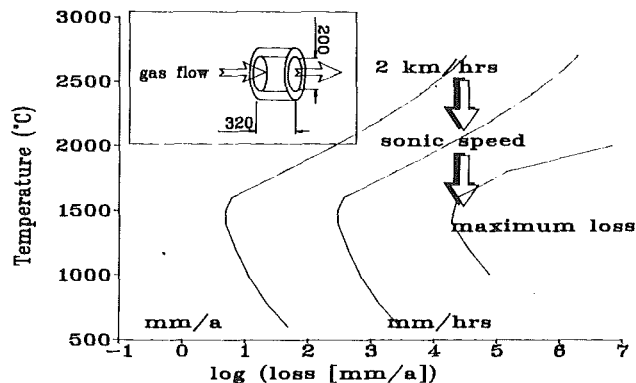


Fig. 12 Calculated corrosion rates for a model case, where SiC is exposed to hydrogen at different flow conditions (Nickel, 1992, using Eqs. (22) and (23))

may show a higher resistance to hot corrosion. Hot corrosion can be avoided using temperatures greater than 1100°C.

High temperature limits for the use of Si_3N_4 are the eutectic temperatures for the glass phase, usually on the order of 1200–1500°C.

A likely high temperature boundary for SiC is ≈ 1700 – 1800°C , where a secondary active-to-passive transition by bubble formation and spallation occurs.

Acknowledgments

Support by an BMFT-funded project (03 M 2012), "Development of Thermally and Mechanically Highly Stressed Advanced Ceramics," is gratefully acknowledged.

References

- Antill, J. E., and Warburton, J. B., 1971, "Active to Passive Transition in the Oxidation of SiC," *Corrosion Science*, Vol. 11, pp. 337–342.
- Babini, G. N., and Vincenzini, P., 1983, "Oxidation Kinetics of Hot-Pressed Silicon Nitride," in: F. L. Riley, ed., *Progress in Nitrogen Ceramics*, Martinus Nijhoff Pub., Boston, pp. 427–438.
- Chase, M. W., Davies, C. A., Downey, J. R., Frurip, D. J., McDonald, R. A., and Syverud, A. N., 1985, *JANAF Thermochemical Tables*, 3rd ed., *J. Phys. Chem. Ref. Data*, Vol. 14.
- Clarke, D. R., 1983, "Thermodynamic Mechanism for Cation Diffusion Through an Intergranular Phase: Application to Environmental Reactions with Nitrogen Ceramics," in: F. L. Riley, ed., *Progress in Nitrogen Ceramics*, Martinus Nijhoff Pub., Boston, pp. 439–446.
- Clarke, D. R., and Lange, F. F., 1980, "Oxidation of Si_3N_4 - SiO_2 - MgO ," *J. Am. Ceram. Soc.*, Vol. 63, pp. 586–593.
- Gulbranson, E. A., Andrew, K. F., and Brossart, F. A., 1966, "The Oxidation of Silicon Carbide at 1150° to 1400°C and at $9 \cdot 10^{-3}$ to $5 \cdot 10^{-1}$ Torr Oxygen Pressure," *J. Electrochem. Soc.*, Vol. 113, pp. 1311–1314.
- Ernstberger, U., 1985, "Oxidations- und Kriechverhalten von dichten Siliziumnitridwerkstoffen verschiedener Zusammensetzungen," Dissertation, University of Karlsruhe.
- Fox, D. S., and Jacobson, N. S., 1988, "Molten-Salt Corrosion of Silicon Nitride: I, Sodium Carbonate," *J. Am. Ceram. Soc.*, Vol. 71, pp. 128–138.
- Fox, D. S., and Smialek, J. L., 1990, "Burner Rig Hot Corrosion of Silicon Carbide and Silicon Nitride," *J. Am. Ceram. Soc.*, Vol. 73, pp. 303–311.
- Hallum, G. W., and Herbell, T. P., 1988, "Effect of High-Temperature Hydrogen Exposure on Sintered α -SiC," *Advanced Ceramic Materials*, Vol. 3, pp. 171–175.
- Hinze, J. W., and Graham, H. C., 1976, "The Active Oxidation of Si and SiC in the Viscous Gas-Flow Regime," *J. Electrochem. Soc.*, Vol. 123, pp. 1066–1073.
- Jacobson, N. S., and Fox, D. S., 1988, "Molten-Salt Corrosion of Silicon Nitride: II, Sodium Sulfate," *J. Am. Ceram. Soc.*, Vol. 71, pp. 139–148.
- Kim, H. E., and Ready, D. W., 1989, "Active Oxidation of SiC in Low Dew-Point Hydrogen Above 1400°C," *Silicon Carbide Transactions*, Vol. 2, Ohio State University, pp. 301–312.
- Kubaschewski, O., and Alcock, C. B., 1979, *Metallurgical Thermochemistry*, 5th ed., Pergamon Press, New York, pp. 221–226.
- Marra, J. E., Kreidler, E. R., Jacobson, N. S., and Fox, D. S., 1989, "The Behaviour of SiC and Si_3N_4 Ceramics in Mixed-Oxidation-Chlorination Environments," *Ceramic Transactions*, Vol. 2, pp. 275–287.
- Nagamori, M., Malinsky, I., and Claveau, A., 1986, "Thermodynamics of the Si-C-O System for the Production of Silicon Carbide and Metallic Silicon," *Metall. Trans.*, Vol. B 17, pp. 503–514.
- Nickel, K. G., Danzer, R., Schneider, G. A., and Petzow, G., 1989, "Oxi-

- ation and Corrosion of Advanced Ceramics," *Powdermetallurgy International*, Vol. 21, pp. 29-34.
- Nickel, K. G., 1990, "Entwicklung Rechnergestützter Material-prüfungsmethoden," *Ingenieur-Werkstoffe*, Vol. 2/90, pp. 37-39.
- Nickel, K. G., and Quirnbach, P., 1991, "Gaskorrosion nichtoxidischer keramischer Werkstoffe," in: J. Kriegesmann, ed., *Handbuch Technische Keramische Werkstoffe*, Deutsche Keramische Gesellschaft, 6. Erg. Lfg., Kapitel 5.4.1.1, pp. 1-76.
- Nickel, K. G., 1992, "The Role of Condensed Silicon Monoxide in the Active-to-Passive Oxidation Transition of Silicon Carbide," *J. Europ. Ceram. Soc.*, Vol. 9, in press.
- Nickel, K. G., Lukas, H. L., and Petzow, G., 1992, "High-Temperature Corrosion of SiC in Hydrogen-Oxygen Environments," submitted to: K. Hack, ed., *Computer Assisted Thermochemistry*, Springer-Verlag, Berlin.
- Nickel, K. G., and Petzow, G., 1992, "Phase Diagrams—Key to Advanced Ceramics Development," *Proc. ISS. Conference Sintering '91*, Vancouver, July 23-27, 1991, submitted.
- Park, D. S., McNallan, M. J., Park, C., and Liang, W. W., 1990, "Active Corrosion of Sintered Silicon Carbide in Oxygen-Chlorine Gases at Elevated Temperatures," *J. Am. Ceram. Soc.*, Vol. 73, pp. 1323-1329.
- Schiroky, G. H. O., 1987, "Oxidation Behaviour of Chemically Vapor-Deposited Silicon Carbide," *Advanced Ceramic Materials*, Vol. 2, pp. 137-141.
- Schlichting, J., 1979a, "Siliciumcarbid als oxidationsbeständiger Hochtemperaturwerkstoff. Oxidations- und Heißkorrosionsverhalten, I," *Ber. Dt. Keram. Ges.*, Vol. 56, pp. 196-200.
- Schlichting, J., 1979b, "Siliciumcarbid als oxidationsbeständiger Hochtemperaturwerkstoff. Oxidations- und Heißkorrosionsverhalten, II," *Ber. Dt. Keram. Ges.*, Vol. 56, pp. 256-261.
- Schneider, G. A., Nickel, K. G., Danzer, R., and Petzow, G., 1990, "Thermal Shock and Corrosion of SiC—a Combustion Chamber Model Case Study," in: R. Freer, ed., *Physics and Chemistry of Carbides, Nitrides, and Borides*, Kluwer Academic Pub., Dordrecht, NL, pp. 387-401.
- Schröder, F., ed., 1986, *Gmelin Handbook of Inorganic Chemistry, Silicon B2*, Springer-Verlag, Berlin, pp. 367-369.
- Sheehan, J. E., 1982, "Passive and Active Oxidation of Hot-Pressed Silicon Nitride Materials With Two Magnesia Contents," *J. Am. Ceram. Soc.*, Vol. 65, pp. 111-113.
- Singhal, S. C., 1974, "Corrosion Resistant Structural Ceramic Materials for Gas Turbines," *Proc. 1974 Gas Turbine Materials and Marine Environment Conference*, Batelle Metals and Ceramics Inf. Centre, MCIC 75-27, pp. 311-334.
- Singhal, S. C., 1976, "Thermodynamic Analysis of High-Temperature Stability of Silicon Nitride and Silicon Carbide," *Ceramurgia Int.*, Vol. 2, pp. 123-130.
- Smialek, J. L., and Jacobson, N. S., 1986, "Mechanism of Strength Degradation for Hot Corrosion of α -SiC," *J. Am. Ceram. Soc.*, Vol. 69, pp. 741-752.
- Vaughn, W. L., and Maahs, H. G., 1990, "Active-to-Passive Transition in the Oxidation of Silicon Carbide and Silicon Nitride in Air," *J. Am. Ceram. Soc.*, Vol. 73, pp. 1540-1543.
- Wagner, C., 1958, "Passivity During the Oxidation of Silicon at Elevated Temperatures," *J. Appl. Physics*, Vol. 29, pp. 1295-1297.

Impact Design Methods for Ceramic Components in Gas Turbine Engines

J. Song

J. Cuccio

H. Kington

Garrett Auxiliary Power Division,
Allied-Signal Aerospace Company,
Phoenix, AZ 85010

Garrett Auxiliary Power Division of Allied-Signal Aerospace Company is developing methods to design ceramic turbine components with improved impact resistance. In an ongoing research effort under the DOE/NASA-funded Advanced Turbine Technology Applications Project (ATTAP), two different modes of impact damage have been identified and characterized: local damage and structural damage. Local impact damage to Si_3N_4 impacted by spherical projectiles usually takes the form of ring and/or radial cracks in the vicinity of the impact point. Baseline data from Si_3N_4 test bars impacted by 1.588-mm (0.0625-in.) diameter NC-132 projectiles indicates the critical velocity at which the probability of detecting surface cracks is 50 percent equalled 130 m/s (426 ft/sec). A microphysics-based model that assumes damage to be in the form of microcracks has been developed to predict local impact damage. Local stress and strain determine microcrack nucleation and propagation, which in turn alter local stress and strain through modulus degradation. Material damage is quantified by a "damage parameter" related to the volume fraction of microcracks. The entire computation has been incorporated into the EPIC computer code. Model capability is being demonstrated by simulating instrumented plate impact and particle impact tests. Structural impact damage usually occurs in the form of fast fracture caused by bending stresses that exceed the material strength. The EPIC code has been successfully used to predict radial and axial blade failures from impacts by various size particles. This method is also being used in conjunction with Taguchi experimental methods to investigate the effects of design parameters on turbine blade impact resistance. It has been shown that significant improvement in impact resistance can be achieved by using the configuration recommended by Taguchi methods.

Introduction

Impact damage has been identified as a primary failure mode for ceramic turbine rotors and stators in a number of ceramic engine programs. One example is shown in Fig. 1, in which a ceramic turbine rotor was destroyed by impact damage after completing 85 hours of engine testing [1].

Efforts at Garrett to develop advanced ceramic technology for gas turbine engines date from 1976, in the Ceramic Turbine Engine Demonstration Program funded by DARPA [2, 3]. This program has been followed by numerous independent research and development (IR&D) projects and other major programs at Garrett including the Advanced Gas Turbine (AGT) Technology Program funded by DOE and administered by NASA [4].

These programs showed that ceramic components can operate in the severe environment of a gas turbine engine, but failed to demonstrate the degree of component reliability adequate for industry to commit to production. The main chal-

lenge is to improve significantly the reliability and durability of ceramic components through continuous efforts in material property improvement and design methodology development. These are precisely the objectives of the current DOE/NASA-funded Advanced Turbine Technology Applications Project (ATTAP) for ceramic turbine engine development ongoing at Garrett Auxiliary Power Division (Garrett). We believe that proper design of ceramic components to survive impact conditions plays a critical part in the successful application of ceramic technology to gas turbine engines.

Sources of impact particles in a gas turbine engine include ingestion of foreign objects ("FOD"), fragments of upstream components, carbon deposits from the combustor, and fragments from engine instrumentation. These particles are carried into the turbine at relatively low tangential velocity, but the turbine blades impact these particles with a relative velocity close to the blade tip speed, > 400 m/s (> 1300 ft/sec).

A multiphased program has been initiated at Garrett to develop methods for designing ceramic turbine wheels with improved impact resistance. This program includes characterizing ceramic impact damage and developing analytical tools to predict impact damage produced by engine impact conditions.

Contributed by the International Gas Turbine Institute and presented at the 36th International Gas Turbine and Aeroengine Congress and Exposition, Orlando, Florida, June 3-6, 1991. Manuscript received at ASME Headquarters February 20, 1991. Paper No. 91-GT-115. Associate Technical Editor: L. A. Riekert.

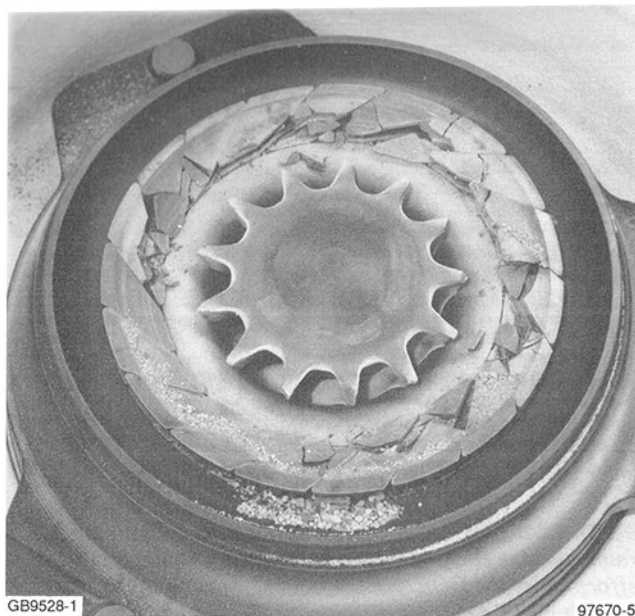


Fig. 1 AGT101 ceramic turbine rotor and stator sustained impact damage after 85 hours of operation

Extensive particle impact tests on silicon nitride (Si_3N_4) cubes, test bars, and turbine blades revealed two distinct impact damage modes for ceramics. One is local damage, in the form of ring and/or radial cracks in the vicinity of the impact center, and the other is structural damage, associated with bending stress introduced by impact (Fig. 2). Experimental and analytical progress has been made in studies of both types of impact damage.

Specimen Impact Tests for Local Damage

A large number of specimen impact tests have been conducted to characterize local impact damage and to identify the most significant variables affecting the local impact damage resistance of Si_3N_4 .

The impact targets were $3.175 \times 6.35 \times 50.8$ mm ($0.25 \times 0.50 \times 2.0$ in.) bars with crowned edges. The target material for the baseline case was SN-84 type Si_3N_4 and the projectiles were 1.588 mm (0.0625 in.) diameter NC-132 Si_3N_4 spheres.

For the baseline case, 28 specimens were tested with one projectile shot at the center of each specimen. Following impact, each specimen was examined visually with a stereo-microscope at 30 to 100 \times magnification to determine if surface damage occurred at the specific impact velocity. A maximum-likelihood approach was used to fit the data points to a Weibull

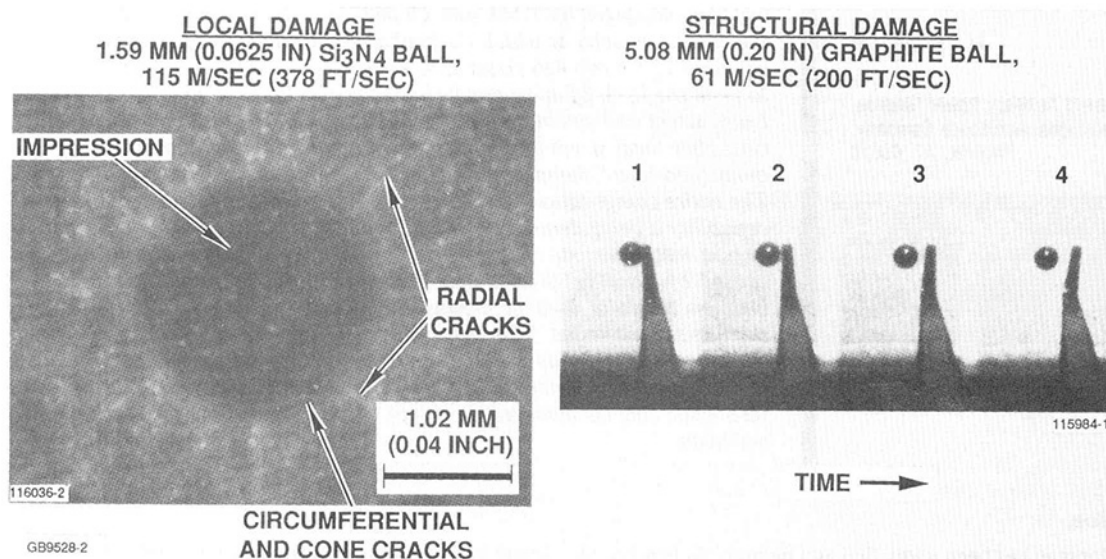


Fig. 2 Ceramics exhibit two modes of impact damage

Nomenclature

AGT = Advanced Gas Turbine
ATTAP = Advanced Turbine Technology Applications Project
DARPA = U.S. Defense Advanced Research Projects Agency
 $^{\circ}\text{C}$ = degrees Celsius
DOE = U.S. Dept. of Energy
 E = Specific internal energy [Eq. (1)]
EPIC = Elastic and Plastic Impact Computation
 $^{\circ}\text{F}$ = degrees Fahrenheit
FOD = Foreign Object Damage

ft = foot
in. = inch
IR&D = Independent Research and Development
ksi = thousands of pounds per square inch
 L_8 = eight-element orthogonal array (Taguchi matrix)
 L_{12} = twelve-element orthogonal array (Taguchi matrix)
m = meter
mm = millimeter
MPa = Megapascal
NASA = U.S. National Aeronautics and Space Administration

P = hydrostatic pressure [Eq. (1)]
PMMA = polymethylmethacrylate
s = second
 Si_3N_4 = silicon nitride
UDRI = University of Dayton Research Institute
 ϵ = equivalent plastic strain [Eq. (3)]
 σ = elastic strength [Eq. (3)]
 μ = volumetric strain [Eq. (1) and (2)]
 Γ = Gruneisian coefficient [Eq. (1)]

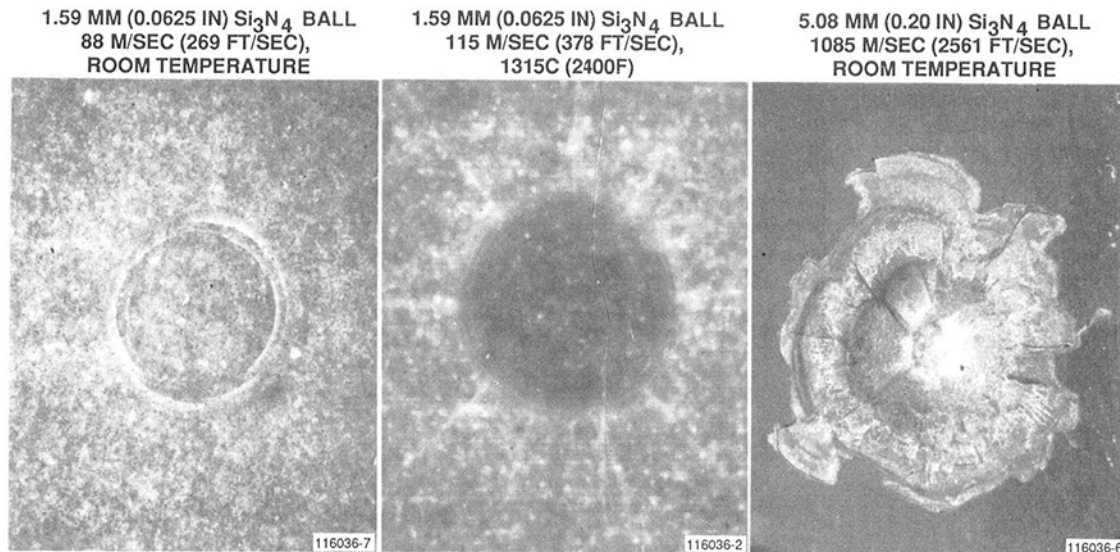


Fig. 3 Impacted specimen micrographs show impact damage is affected by impact velocity and temperature

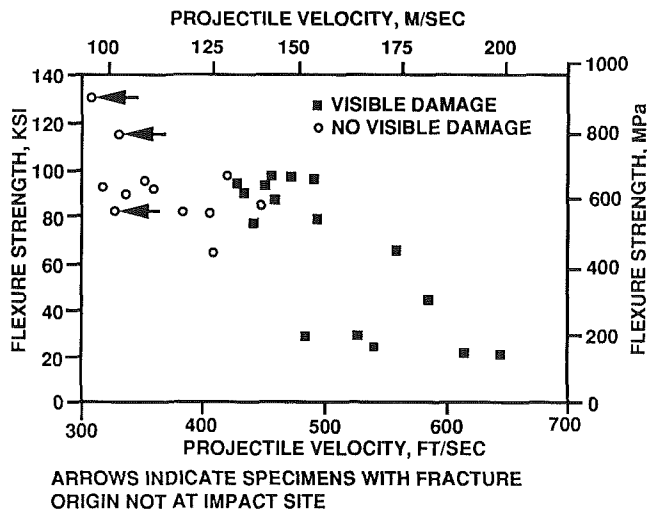


Fig. 4 Residual flexure strength of Si_3N_4 specimens impacted by NC-132 spheres

distribution. For the baseline case, the critical velocity was determined to be 130 m/s (426 ft/sec). This implies that if a specimen is impacted by a projectile of the same material at 130 m/s (426 ft/sec), there is a 50 percent probability that surface cracks will be detected.

Spherical projectiles impacting at velocities slightly above the critical value cause ring cracks centered around the impact point. These circular cracks are usually segmented, rather than complete circles. The cracks are located immediately outside of the contact area and are oriented perpendicular to the target surface. With higher impact velocities, the depth of the ring cracks increases, and the orientation of the ring cracks changes to an acute angle with respect to the surface. Thus, the ring cracks turn into cone cracks. With higher impact velocities, radial cracks emanating from the impact center appear; at even higher impact velocities, lateral cracks develop. These cracks usually extend from the subsurface to the surface, causing chipping around the impact center (Fig. 3). At high temperature, radial cracks appear at lower impact velocities than ring cracks, as described later.

The 28 baseline specimens were flexure tested in four-point bending after impact. Fractures initiated from the impact sites for all but three specimens. When the residual strength was plotted against the corresponding impact velocities (Fig. 4), there appeared to be a significant reduction of flexure strength

at an impact velocity of about 146 m/s (479 ft/sec), slightly higher than the critical velocity for detection of surface damage. Since the ring cracks are usually segmented circles, the orientation of these cracks with respect to the tensile stress in the flexure specimens is expected to affect the strength significantly. This observation explains, in part, the large scatter existing in the residual strength data.

The effects of a number of variables on ceramic impact damage resistance were also investigated. These impact variables and their corresponding critical impact velocities for detectable surface damage are shown in Fig. 5.

It is worth pointing out that the thin specimens [0.762 mm (0.03 in.) thickness] failed by fast fracture at an impact velocity of 46.6 m/s (153 ft/sec); these specimens fractured into multiple pieces. Fractography revealed that failure originated from the opposite side of the impact site, at the location of maximum bending stress. This observation suggests that the thin specimens failed in a structural impact damage mode rather than the local impact damage mode observed in the other specimens.

Results from high-temperature impact tests showed lower damage resistance [critical velocity of 90 m/s (295 ft/sec) versus 130 m/s (426 ft/sec)]. There was also a change in the damage topography. At room temperature, the typical impact damage with impact velocities just above the critical velocity is circumferential cracks, with radial cracks appearing at higher impact velocities. At 1315°C (2400°F), radial cracks appeared first for the low-velocity range, >90 m/s (>295 ft/sec). Circumferential cracks did not appear until the impact velocity was higher than 114 m/s (374 ft/sec). This change is believed to be caused by the change of stress field in the vicinity of the impact center. Substantially more permanent deformation at the impact center at elevated temperatures probably changes the direction of the maximum principal stresses from radial to circumferential.

Local Impact Damage Model Development

A mechanistic model has been developed to predict critical impact velocities causing local impact damage under different impact conditions.

The basic assumptions made in the local impact damage model are:

- 1 Ceramics behave inelastically by developing microcracking when local impact stresses exceed threshold values.
- 2 Microcracks nucleate when the maximum principal stress exceeds the tensile strength, or when the compressive hydrostatic stress exceeds the Hugoniot strength of the material.

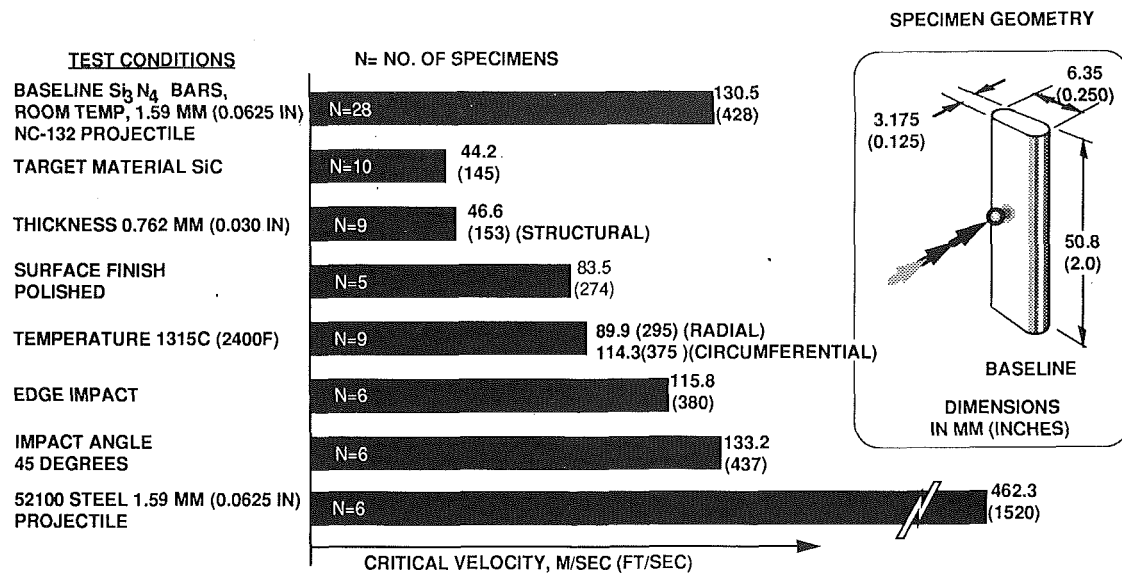


Fig. 5 Effects of test variables on critical impact velocities were demonstrated

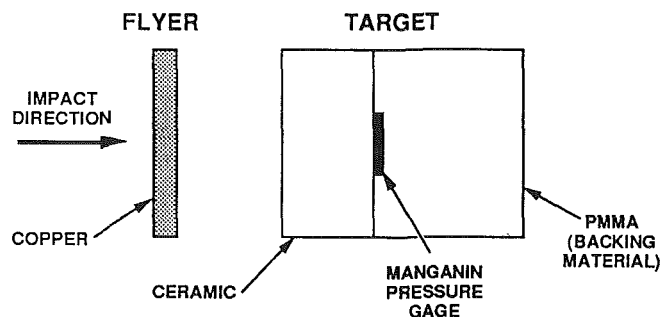


Fig. 6 Numerical simulation of plate impact was conducted for model verification

3 Growth of microdamage is governed by Griffith flaw criterion.

4 Damage of the material is measured by the volume fraction of cracks and pores introduced by impact.

5 Impact damage degrades the elastic modulus of the material, thus altering the stress wave propagation.

Microphysics model based on these assumptions has been developed by Dr. A. M. Rajendran and his co-workers at the University of Dayton Research Institute (UDRI), in Dayton, OH, for the ATTAP program. Impact damage occurring at the microstructural level under a propagating stress wave will change the load-carrying capability of the material. Because both stress and damage evolve concurrently during an impact event, the material behavior model and the damage model are incorporated into each time integration step computed, using the Elastic-Plastic Impact Computation (EPIC-3) stress wave code [5]. This model has shown promising success for simple cases of impact problems. Two of the examples being studied are presented below.

EPIC-3 Simulations of Local Impact Damage

A simulation of a plate impact event was conducted using the test setup illustrated in Fig. 6. Stress predicted from the analysis at the interface of the Si_3N_4 plate and the PMMA backing material is plotted as a function of time. When the stress recorded by the pressure gage during the plate impact test was plotted on the same graph, the agreement was excellent (Fig. 7). In a low-velocity impact at 50 m/s (164 ft/sec), the compressive stress was not high enough to cause damage. That is why there is no stress relaxation associated with degradation of modulus during the compressive period of loading. This is

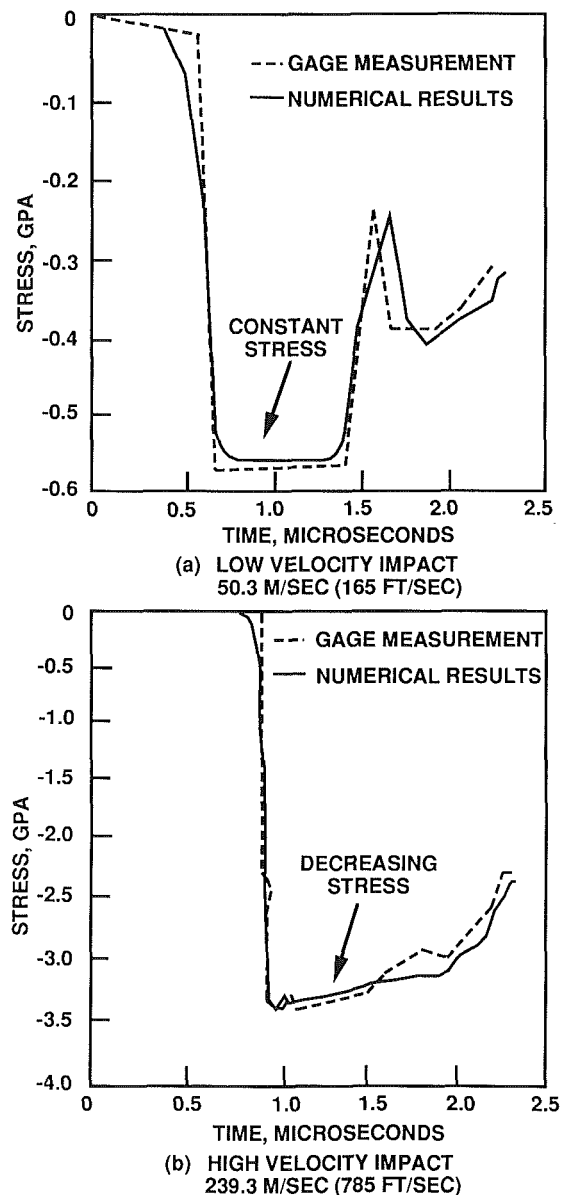


Fig. 7 Numerical results agreed well with experimental results

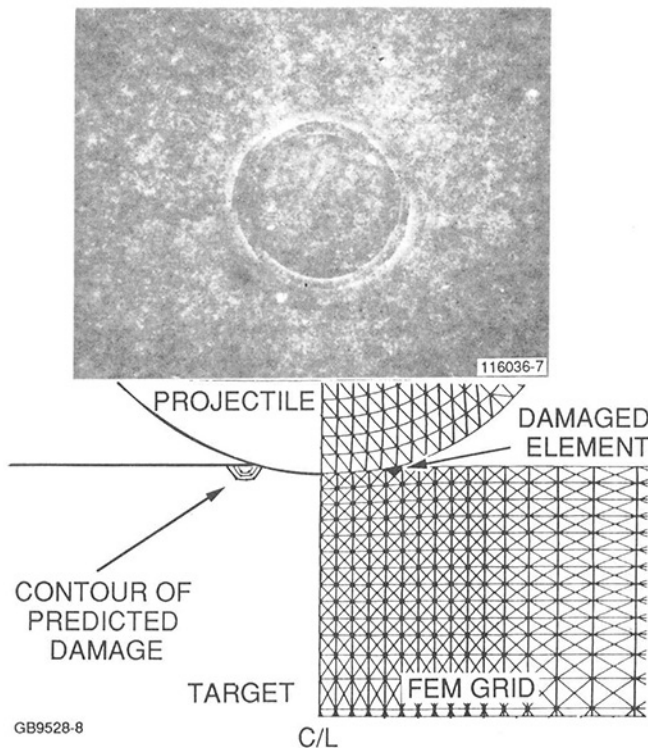


Fig. 8 Finite element model of particle impact was used for local damage prediction

indicated by the approximately constant compressive stress during the first wave [Fig. 7(a)]. For a higher-velocity impact at 239 m/s (784 ft/sec), the magnitude of the compressive stress wave was great enough to cause material damage. The accumulating material damage caused a decrease in the material load-carrying capability. This was demonstrated by the decrease of the stress wave magnitude described by the slanted line during the first compressive wave in Fig. 7(b).

Figure 8 shows a finite element model of a sphere impacting a flat plate. This model was used to simulate the baseline local impact damage test reported in Fig. 5. When the critical impact velocity determined from the experiment was used in the analysis, the most severe damage predicted by the model was concentrated in the element corresponding to the location of circumferential cracks in the specimens. This example demonstrated that the model can successfully predict the critical impact velocity required to cause local impact damage. The agreement between the test results and the analytical results on the location of the cracks reassured the validity of this model.

The next step in local impact damage model development is to convert the two-dimensional (2-D) version into three dimensions (3-D). The 3-D model will then be used to predict the critical impact velocity and the pattern of local cracks for ceramic components with more complicated geometry. These analyses will be verified by ceramic stator impact tests.

Turbine Blade Impact Tests for Structural Damage Modeling

In a parallel effort, particle impact tests were conducted on a number of turbine blades of differing geometry and materials. The tests were intended to simulate combustor carbon particle impact, the most likely particles occurring in gas turbine engines. Graphite spheres ranging from 1.27-mm (0.05-in.) to 5.08-mm (0.2-in.) diameter were used. The radial rotors impacted all had the same geometry, and were constructed of three different Si_3N_4 materials, SN-250, SN-252, and SN-84.

The test results of the radial turbine wheel impacts showed

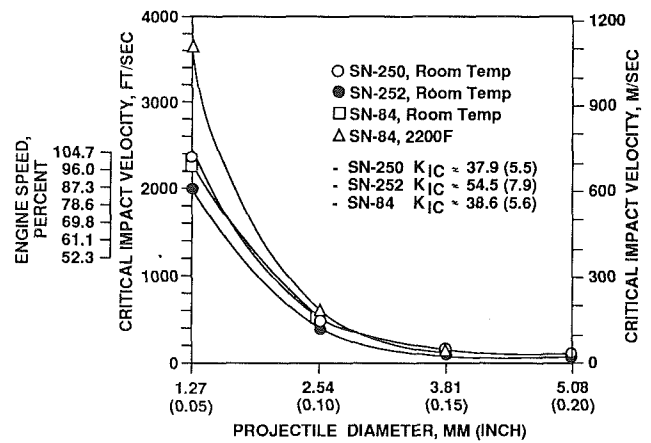


Fig. 9 Critical impact velocities causing structural failure of radial blades under different impact conditions

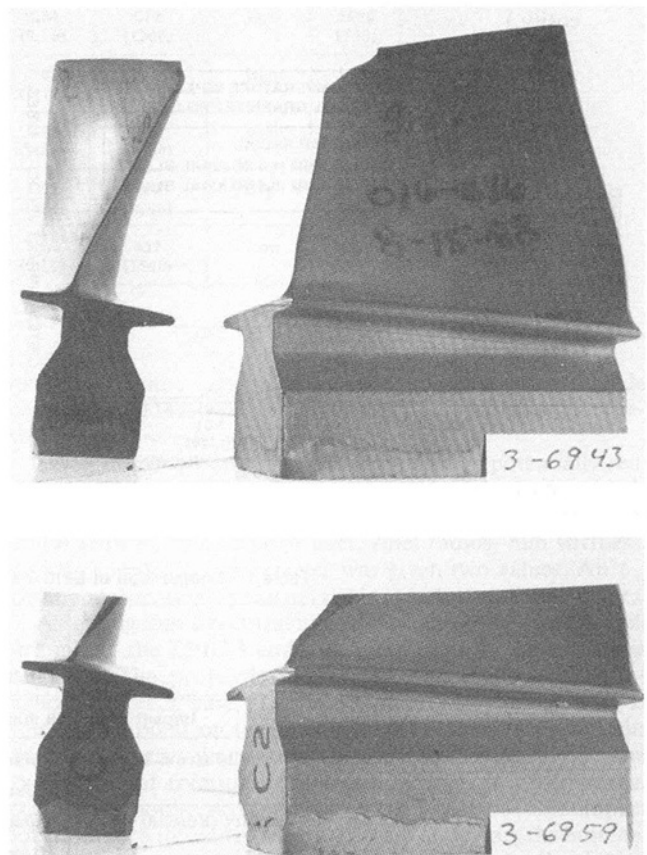


Fig. 10 Full length and shortened axial blades were impact tested

that all failures were associated with bending stress, and fractures originated approximately 2.5 to 5.0 mm (0.1 to 0.2 in.) from the blade tip (Fig. 2). The critical velocities for different projectile sizes and rotor materials are presented in Fig. 9. It is worth noting that fracture toughness does not appear to have a strong effect on impact resistance to structural damage.

Graphite sphere impact tests were also conducted on axial blades made of an early development version of NT154 silicon nitride. In order to examine how blade length affects impact resistance, some of the axial blades were shortened from 38.1 mm (1.5 in.) original length to 12.7 mm (0.5 in.) (Fig. 10). Both blades failed due to bending upon impact. A comparison of the critical impact velocities is given in Fig. 11.

Structural Impact Failure Prediction for Turbine Blades

Having established that ceramic blades are susceptible to structural impact damage at relatively low impact velocity, it became necessary to develop an effective analytical tool to design ceramic turbine rotors that can survive impact conditions in gas turbine engines. The EPIC-3 computer code was adopted for that purpose. EPIC-3 is a finite element impact code using Lagrangian representation. The behavior of the interface between target and projectile is modeled by the so-called slideline logic, which includes conservation of mass, momentum, and energy between the nodes of the target and the nodes of the projectile which come into contact. The code uses an explicit time integration scheme to solve the governing equations. The time integration loop [6] includes the following steps:

- 1 Determine the strains and the strain rates in the elements at each new time step from motion of the nodes with discretized mass.
- 2 Determine the stresses in the elements using constitutive equations. (The stresses consist of elastic stress, plastic deviator stresses, hydrostatic pressure, and artificial viscosity.)

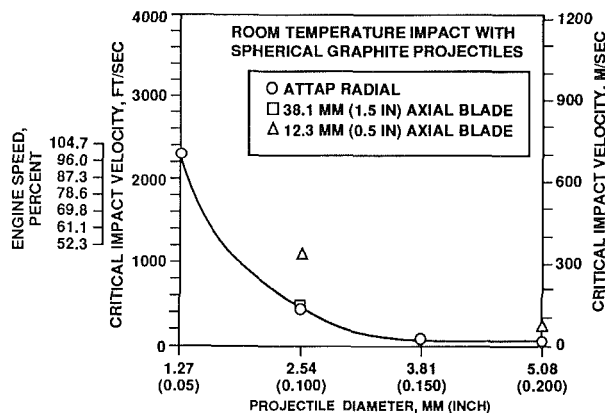


Fig. 11 Comparison of critical velocities for three impacted blade geometries

- 3 Determine the equivalent concentrated forces acting on the nodes.
- 4 Determine the integration time increment.
- 5 Apply the equations of motion to the nodes for the integration time increment.

The Mie-Gruneisen equation of state [7] is used to determine the hydrostatic pressure:

$$P = (K_1\mu + K_2\mu^2 + K_3\mu^3 + (1 - \Gamma\mu/2) + \Gamma p_o)E \quad (1)$$

where

$$\mu = p/p_o - 1 = v_o/v - 1 \quad (2)$$

The specific internal energy, E , can be obtained from the work done on the element by the various stresses. K_1 , K_2 , and K_3 are material constants and Γ is the Gruneisen coefficient. The elastic strength of the material is considered to be a function of strain hardening, strain rate, and temperature. The Johnson-Cook model [8] is used in the following equation to calculate the elastic strength:

$$\sigma = (C_1 + C_2\epsilon^n) (1 + C_3 \ln \dot{\epsilon}^*) (1 - T^{*m}) \quad (3)$$

where ϵ is the equivalent plastic strain, $\dot{\epsilon}^* = \dot{\epsilon}/\dot{\epsilon}_o$ is the dimensionless strain rate of $\dot{\epsilon} = 1.0 \text{ s}^{-1}$, and T^* is the homologous temperature. C_1 , C_2 , C_3 , n , and m are material constants.

EPIC-3 was used to calculate impact stresses for three different ceramic blades: an AGT101 radial turbine blade, a full-length axial turbine blade, and a shortened axial turbine blade.

Fracture was assumed to occur when the maximum principal stress on a blade surface reached the flexure strength of that material. Critical impact velocities associated with different blades and different projectile sizes determined in these impact tests were used as initial impact velocities in the EPIC-3 analyses and the principal stresses obtained were compared with the flexure strength of various blade materials. The results are tabulated in Table 1.

The maximum principal stress in the radial blades was 400 MPa (58 ksi) for the 5.08 mm (0.20 in.) graphite sphere impacting at 36 m/s (118 ft/sec) and 386 MPa (56 ksi) for the 2.54 mm (0.10 in.) sphere impacting at 148 m/s (485 ft/sec). For both cases, the stresses were in close agreement with the flexure strength of this material, 379 MPa (55 ksi). For the

Table 1 Comparison of EPIC-3 analyses and blade impact test results

	Units	Blade Type		
		Radial	Full Length Axial	Shortened Axial
Impact with 5.08 mm (0.20 Inch) Graphite Ball				
Critical Velocity (from Test)	m/sec (ft/sec)	36.6 (120)	35.7 (117)	68.6 (225)
Impact Velocity (EPIC-3)	m/sec (ft/sec)	36.6 (120)	36.6 (120)	68.6 (225)
Flexure Strength	MPa (ksi)	379 (55)	324 (47)	324 (47)
Maximum Tensile Stress	MPa (ksi)	400 (58)	393 (57)	896 (130)
Impact with 2.54 mm (0.10 Inch) Graphite Ball				
Critical Velocity (from Test)	m/sec (ft/sec)	140.2 (460)	148.4 (487)	339.8 (1115)
Impact Velocity (EPIC-3)	m/sec (ft/sec)	148.4 (487)	148.4 (487)	339.8 (1115)
Flexure Strength	MPa (ksi)	379 (55)	324 (47)	324 (47)
Maximum Tensile Stress	MPa (ksi)	386 (56)	372 (54)	930 (135)

Table 2 Orthogonal array of 12 blades and impact stress analysis results

Blade No.	Thickness, mm (inch)	Taper Ratio	Height*	Beta Angle, Deg	Fillet Radius, mm (inch)	V _{impact} , m/sec (ft/sec)	Hub Stiffness	σ_1 (max), MPa (ksi)
1	1.524 (0.06)	1.0	S	31.35	1.02 (0.04)	457 (1500)	High	4468 (648)
2	1.524 (0.06)	1.0	S	31.35	1.02 (0.04)	579 (1900)	Low	5364 (778)
3	1.524 (0.06)	1.0	T	51.35	2.54 (0.10)	457 (1500)	High	2047 (297)
4	1.524 (0.06)	2.0	S	51.35	2.54 (0.10)	457 (1500)	Low	2240 (325)
5	1.524 (0.06)	2.0	T	31.35	2.54 (0.10)	579 (1900)	High	3978 (577)
6	1.524 (0.06)	2.0	T	51.35	1.02 (0.04)	579 (1900)	Low	4102 (595)
7	2.540 (0.10)	1.0	T	51.35	1.02 (0.04)	457 (1500)	Low	1399 (203)
8	2.540 (0.10)	1.0	T	31.35	2.54 (0.10)	579 (1900)	Low	2020 (293)
9	2.540 (0.10)	1.0	S	51.35	2.54 (0.10)	579 (1900)	High	1503 (218)
10	2.540 (0.10)	2.0	T	31.35	1.02 (0.04)	457 (1500)	High	2585 (375)
11	2.540 (0.10)	2.0	S	51.35	1.02 (0.04)	579 (1900)	High	2213 (321)
12	2.540 (0.10)	2.0	S	31.35	2.54 (0.10)	457 (1500)	Low	2571 (373)

*S = Shortened; T = Tall (Full Length)

full-length axial blades, the maximum principal stress was 393 MPa (57 ksi) for the 5.08 mm (0.20 in.) sphere impacting at 36 m/s (118 ft/sec) and 372 MPa (54 ksi) for the 2.54 mm (0.10 in.) sphere impacting at 148 m/s (485 ft/sec). In both cases, the stresses were close to the material flexure strength of 324 MPa (47 ksi).

The fact that the principal stresses for impacts of two different ball sizes at different velocities are consistent and also remain in agreement with the flexure strength for two different blades indicates that the assumption of the structural impact failure criterion is valid. This conclusion is also supported by another observation, that the predicted maximum principal stress location corresponds to the location of fractures in both radial and axial blades.

The maximum principal stress obtained from EPIC-3 analyses for the shortened axial blade was much higher than the flexure strength. This discrepancy is attributed to the fact that the maximum principal stress was found at locations very close to the blade root. In the finite element model, all the nodes at the bottom surface of the blade are rigidly constrained, because EPIC-3 does not allow elastic boundary conditions. The rigid boundary condition did not represent the real situation in the test setup, in which the blades were held at the base, approximately 12 mm (0.47 in.) below the platform.

This study has demonstrated that the EPIC-3 code can be successfully used to predict structural impact failure. This method, aided by a series of new pre- and postprocessing capabilities developed for our applications, is now being used in our design process to define impact-resistant ceramic turbine blade configurations.

Application of Impact Design Methods

Impact design methods are being used with Taguchi statistical experiment design methods in the design of an impact-

resistant ceramic turbine wheel to arrive at a turbine blade configuration that will have significantly improved impact resistance.

Seven design parameters were identified as potentially sensitive to blade impact resistance. These parameters are: blade thickness at the hub, blade taper-ratio from hub to tip, blade width at inlet, beta angle at inlet, fillet radius, hub stiffness, and tip speed. Each parameter was given two values. An L_{12} orthogonal array was created (Table 2) with 12 different blades.

Assuming that structural impact damage is the primary failure mode, the EPIC-3 code was then used for impact stress analyses. The projectiles were 2.54 mm (0.1 in.) graphite spheres. In each case, the impact point was chosen to be at the contact point on the suction side blade surface when the ball is in contact simultaneously with the shroud surface and the surface of rotation of the leading edge. In other words, the impact point corresponded to the worst possible impact location, with the ball at the farthest distance from the hubline. The worst-case particle impact scenario assumed for the turbine wheel was a particle entering with negligible tangential velocity, hit by a rotating blade at full speed.

The calculated maximum principal stress for each blade is listed in Table 2. It is worth noting the difference between the highest stress, 5364 MPa (778 ksi) for Blade 2, and the lowest, 1399 MPa (203 ksi) for Blade 7. The results from the Taguchi study are summarized in Table 3. The strongest factors were blade thickness, beta angle, fillet radius, and tip speed. Taper-ratio, hub stiffness, and blade height had little effect. The optimal configuration was a blade with 2.54 mm (0.10 in.) hub thickness, taper-ratio equal to one, 15 percent taller than the current design, 51.35 deg beta angle, 2.54 mm (0.10 in.) fillet radius, and the current hub design.

The predicted maximum principal stress for the recommended blade, based on the Taguchi methods, was 624 MPa (90.5 ksi). The maximum principal stress in the confirmation

Table 3 Summary of Taguchi impact study results

	(A)	(B)	(C)	(D)	(E)	(F)	(G)
	Thickness	Taper Ratio	Height	Beta Angle	Fillet Radius	Impact Velocity	Hub Stiffness
Level 1	3700 (536.7)	2800 (406.2)	3060 (443.8)	3498 (507.3)	3356 (486.7)	2551 (370.0)	2950 (427.8)
Level 2	2049 (297.2)	2949 (427.7)	2689 (390.0)	2251 (326.5)	2394 (347.2)	3197 (463.7)	2799 (406.0)
Influence	1651 (239.5)	-148 (-21.5)	371 (53.8)	1247 (180.8)	962 (139.5)	-645 (-93.5)	150 (21.8)
Stress values for each combination in MPa (ksi).							

test was 1448 MPa (210 ksi). This discrepancy between prediction and confirmation may indicate a strong interaction among variables, or that the influence of these variables on the stress level is nonlinear. Since an L_{12} orthogonal array is not capable of evaluating interactions, a further study using an L_8 orthogonal array will be conducted. The goal of this study is to identify an impact-resistant blade configuration with maximum principal stress reduced to 50 percent of the value for the current design. Impact tests will be conducted on single-blade subelements constructed according to this configuration to confirm the prediction.

It should be noted at this point that the impact analyses performed in the Taguchi study were elastic analyses, meaning that both projectile and target were given infinite strength. Since graphite balls do fracture and even pulverize at the impact velocities used in this study, according to experimental observation the impact stresses obtained must be higher than the real impact stresses. The difference may be attributed to two factors:

- First, a portion of the energy in the system is consumed in generating a large amount of new surface during pulverization of the projectile.
- Second, the impact load imparted by the pulverized, small particles is expected to be much less than a single particle of the same mass as simulated in the analyses.

This simplification is necessary at this stage of the analyses, due to a lack of material model characterizing pulverization process. A graphite particle impact study is under way, to generate the required information to account for the effects of carbon ball pulverization.

Summary

Significant progress has been made by Garrett in the ATTAP program to develop design methods for ceramic gas turbine components with improved impact resistance. Our progress to date includes:

- Two distinct impact damage modes, local and structural, have been identified for structural ceramics.
- Local impact damage has been characterized based on the surface damage topography.
- A series of variables have been investigated for their effects on ceramic impact resistance to local damage.
- An analytical model is being developed for predicting local impact damage.
- The EPIC-3 code has been successfully adapted to predict structural impact failure for ceramic turbine blades.

- Ceramic structural impact resistance is controlled primarily by material surface strength.

Considerably more progress is needed before impact problems with ceramic components in gas turbine engines can be routinely addressed. However, continuing development in impact design methods will allow ceramic engine components to be designed with improved impact resistance and provide direction for developing and selecting more impact-resistant ceramics.

Acknowledgments

The work in ceramic impact design methods development presented in this paper was conducted under subcontract to the Advanced Turbine Technology Applications Project (ATTAP) currently under way at Garrett Auxiliary Power Division, funded by the U.S. Dept. of Energy (DOE) and administered by the National Aeronautics and Space Administration (NASA), under Contract No. DEN3-335. The authors would like to acknowledge the analytical and experimental work performed by Dr. A. M. Rajendran, R. S. Bertke, and their co-workers at the University of Dayton Research Institute, Dayton, OH. The efforts of our colleagues at Garrett, especially those of H. T. Fang, are also appreciated.

References

- 1 Richerson, D. W., and Johansen, K. M., "Ceramic Gas Turbine Engine Demonstration Program," Final Report, Contract N00024-76-C-5352, May 1982.
- 2 Richerson, D. W., and Wimmer, J. M., "Ceramic Component Development for Limited Life Propulsion Engines," Paper No. AIAA-82-1050, 1982.
- 3 Engineering Staff of Garrett Auxiliary Power Division, Allied-Signal Aerospace Company, "Advanced Gas Turbine (AGT) Technology Development Project," Final Report, DOE/NASA/0167-12, Contract DEN3-167, Mar. 1988.
- 4 Boyd, G. L., and Kreiner, D. M., "AGT101/ATTAP Ceramic Technology Development," *Proceedings of the Twenty-Fifth Automotive Technology Development Contractors Coordination Meeting*, Dearborn, MI, Oct. 1987, p. 101.
- 5 Johnson, G. R., and Stryk, R. A., "User Instructions for the EPIC-3 Code," AFATL-TR-87-10, Air Force Armament Laboratory, May 1987.
- 6 Johnson, G. R., "Analysis of Elastic-Plastic Impact Involving Severe Distortion," *ASME Journal of Applied Mechanics*, Vol. 43, 1976, pp. 439-444.
- 7 Walsh, J. M., et al., "Shock-Wave Compression of Twenty-Seven Metals, Equations of State of Metals," *Physics Review*, Vol. 108, No. 2, Oct. 1957, pp. 196-216.
- 8 Johnson, G. R., and Cook, W. H., "Fracture Characteristics of Three Metals Subjected to Various Strains, Strain Rates, Temperatures and Pressures," *Engineering Fracture Mechanics*, Vol. 21, No. 1, 1985, pp. 31-48.

A. Chulya

NASA Resident Research Associate;
Department of Civil Engineering,
Cleveland State University,
Cleveland, OH 44115

J. P. Gyekenyesi

Structural Integrity Branch.

R. T. Bhatt

Propulsion Directorate,
U.S. Army Aviation Systems Command.

NASA Lewis Research Center,
Cleveland, OH 44135

Mechanical Behavior of Fiber-Reinforced SiC/RBSN Ceramic Matrix Composites: Theory and Experiment

The mechanical behavior of continuous fiber-reinforced SiC/RBSN composites with various fiber contents is evaluated. Both catastrophic and noncatastrophic failures are observed in tensile specimens. Damage and failure mechanisms are identified via in-situ monitoring using NDE techniques throughout the loading history. Effects of fiber/matrix interface debonding (splitting) parallel to the fibers are discussed. Statistical failure behavior of fibers is also observed, especially when the interface is weak. Micromechanical models incorporating residual stresses to calculate the critical matrix cracking strength, ultimate strength, and work of pull-out are reviewed and used to predict composite response. For selected test problems, experimental measurements are compared to analytic predictions.

I Introduction

There is need for strong, tough, and sufficiently stable continuous fiber-reinforced ceramic matrix composites (CMC) that can survive in oxidizing environments at temperatures approaching 1600°C. Monofilament silicon carbide fiber in a reaction-bonded silicon nitride matrix (SiC/RBSN) is a promising candidate CMC material for the harsh conditions that often arise in advanced aerospace applications. It is also necessary to have micromechanical models that account for the observed failure behavior and allow tailoring of composites for optimal properties.

Currently, we have an adequate understanding of the mechanical behavior of unidirectional fiber-reinforced CMCs that incorporate small-diameter Nicalon¹ fibers into glass or glass-ceramic matrices, particularly when they are loaded in the fiber direction (Prewo and Brennan, 1980, 1982; Brennan and Prewo, 1982; Prewo, 1986). We can also demonstrate the influence of fiber/matrix interfaces and a variety of fiber coatings on the behavior of these composite systems (Kerans et al., 1989). Micromechanical models that include the fiber/matrix interface effects correlate well with experimental results (Aveston et al., 1971; Budiansky et al., 1986; Marshall et al., 1985; McCartney, 1987). However, understanding of failure mechanisms and the development and validation of analytical deformation and fracture models are not mature for SiC/RBSN. We especially lack sufficient knowledge of the initiation and propagation of matrix cracks and fiber breakage. This lack of understanding also hinders composite development, which primarily depends on obtaining optimal interface properties and maintaining high fiber strength at elevated temperatures.

¹Nicalon, Nippon Carbon, Tokyo, Japan.

Contributed by the International Gas Turbine Institute and presented at the 36th International Gas Turbine and Aeroengine Congress and Exposition, Orlando, Florida, June 3-6, 1991. Manuscript received at ASME Headquarters March 4, 1991. Paper No. 91-GT-209. Associate Technical Editor: L. A. Riekert.

The overall mechanical behavior is very complex and involves a large number of independent variables at the micro-structural level. Fiber/matrix interfaces that are too weak may cause fiber/matrix interface debonding (splitting). Fiber/matrix interfaces that are too strong may prevent the multiple matrix cracking phenomenon and induce catastrophic failure. Fiber strength also plays a critical role. If the fibers are sufficiently strong and uniform with optimized interfaces, cracks will propagate first only through the matrix and the fibers will likely fail later between the crack surfaces. The composite will fail as predicted by existing micromechanical theories. If the fibers are weak and nonuniform, they will tend to fail throughout the bridging zone and also away from the growing macrocrack. In this latter case the fibers will break in a random, statistical manner and fibers will break in a random, statistical manner continue to bridge the cracks during pull-out.

The objectives of this work were: (1) to investigate and understand the mechanical behavior of SiC/RBSN composites throughout their loading history, (2) to study the effects of fiber/matrix interface debonding, (3) to identify the occurrence and nature of damage and failure mechanisms, and (4) to validate micromechanical models so that they can be further developed and optimized.

Both experimental and theoretical studies were made. Test coupons of 1-, 3-, 5-, and 8-ply unidirectional SiC/RBSN composites were loaded to failure under tension. Characterization of damage and failure mechanisms was performed through in-situ monitoring using an acoustic emission (AE) technique. X-radiographic technique was also used to monitor all tests at different load levels and to confirm the AE results. Interfacial shear strength was obtained from the matrix crack spacing method. Micromechanical models for predicting the critical matrix cracking strength were examined. A parametric study

Table 1 Room temperature mechanical property data for unidirectional SiC/RBSN composites

Specimen identification	Number of plies	Interface characteristic	Fiber ratio, percent	Primary modulus		Proportional limit		Ultimate strength, MPa
				Experiment, GPa	ROM, ^a GPa	Stress, MPa	Strain, percent	
S1A	1	Weak	8	149	132	104	0.070	104
S1B	1	Strong	8	157	132	166	.106	166
M3A	3	Weak	16	178	155	178	.100	178
M5A	5	Weak	19	171	163	186	.108	222
M5B	5	Weak	19	197	163	226	.115	228
M5C	5	Weak	19	171	163	179	.105	227
M8A	8	Weak	24	175	167	195	.124	576

^aRule of mixtures.

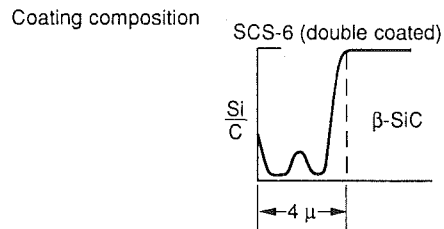
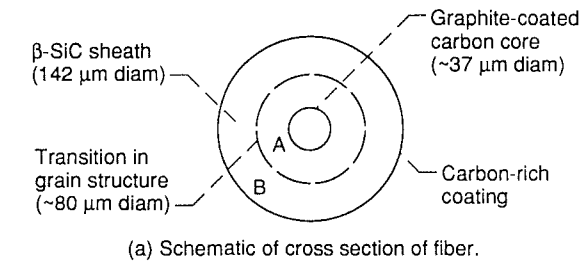


Fig. 1 Details of CVD SiC fiber

was performed to determine the effect of selected constituents. The ultimate strength and work of pull-out based on weakest link statistics were evaluated and compared with experimental strength data. The main contribution presented herein is a comprehensive study, which predicts and measures the critical points in the primary composite tensile stress-strain curve of a unidirectional lamina.

II Experimental Procedures

Materials. SiC/RBSN composite tensile specimens were fabricated using SCS-6 SiC fiber monofilaments from Textron Specialty Materials² and high-purity silicon powder. The fibers were produced by chemical vapor deposition from methyltrichlorosilane onto a heated carbon substrate. The outer surface of the 142-μm-dia SiC fiber contained two layers of carbon-rich surface coatings, which served several objectives. Firstly, it healed surface irregularities on the SiC substrate providing abrasion resistance and improved fiber strength. Secondly, it provided a weak interface for assuring crack deflection and noncatastrophic failure. A schematic diagram of the cross section of SiC fiber is shown in Fig. 1(a). Each layer is a mixture of amorphous carbon and SiC. The elemental composition of the fiber surface coating is shown in Fig. 1(b). Typical cross sections and an enlarged view of the fiber/matrix interface are shown in Fig. 2. The manufacturer designates this fiber as double-coated SCS-6 SiC fiber. High-purity silicon powder obtained from Union Carbide was used for the silicon nitride matrix. The as-received powder contained large ag-

²Textron Specialty Materials, Lowell, MA.

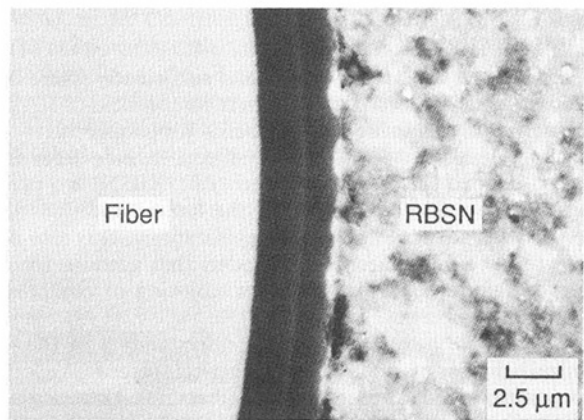
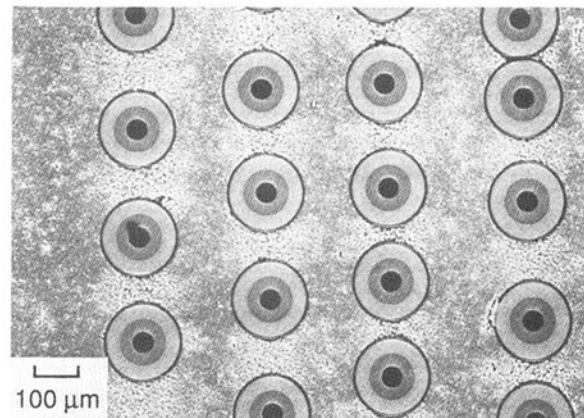
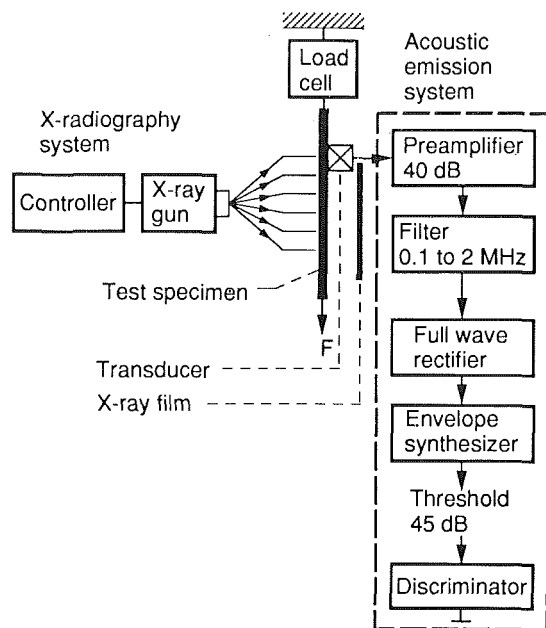


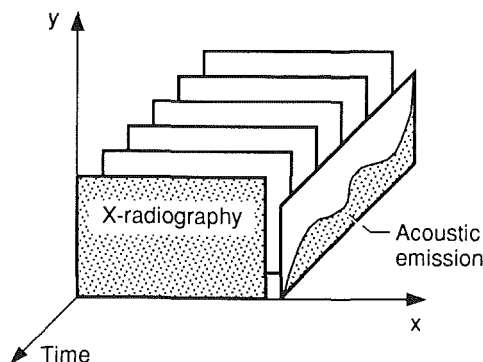
Fig. 2 Typical cross-section and the interface region of SiC/RBSN composites

glomerates and required attrition milling to reduce its particle size and to improve its reactivity to nitrogen during a later nitridation step. The average particle size of the attrition milled powder was 0.3 μm. A detailed description of the composite fabrication is reported elsewhere (Bhatt, 1987).

Test panels of unidirectional laminates containing various numbers of plies with different fiber volume ratios were fabricated. The length and width of the as-nitrided composite panels were 150 mm by 50 mm, respectively. The composite matrix contained approximately 30 percent porosity and displayed local density variations around the fibers. The dimensions of the test specimens taken from the panels were 12.74 mm wide by 125 mm long. The single ply specimens were 1.05 mm thick; the 3-ply, 1.64 mm thick; the 5-ply, 2.4 mm thick;



(a) Acoustic emission and x-radiography setups on the loadframe.



(b) Acoustic emission showing real time dependence.

Fig. 3 Tensile specimen with acoustic emission and x-radiography

and the 8-ply, 2.2 mm thick. The specimens are described in Table 1.

The average room temperature tensile strength of 20 individual as-received SiC fibers with a representative gage length was 3.9 GPa while that of the fibers heated at 1200°C in N₂ for 40 h was 2.86 GPa (Bhatt and Phillips, 1988). The elastic modulus of the fibers was 390 GPa (DiCarlo and Williams, 1980) while that of the RBSN matrix estimated to be 110 ± 10 GPa (Bhatt and Phillips, 1988). Matrix density and average matrix pore size were 2.3 g/cc and 0.025 μm, respectively (Bhatt and Kiser, 1990). The measured matrix fracture toughness was 2.0 MPam^{1/2} (Haggerty, 1989), or in terms of the critical matrix energy release rate, the value was 36 J/m². The coefficients of thermal expansion (CTE) up to 1450°C were 4.2E-6 and 3.8E-6°/C for the fiber and matrix, respectively (Bhatt, 1989).

Testing Procedure. Tensile tests were conducted with an Instron³ 8562 loadframe with a 50-kN load cell at a crosshead speed of 0.025 mm/min. A clip-on extensometer was used in combination with two strain gages. The latter were glued on the top and bottom parts of the specimen on opposite sides. The piezoelectric transducer for AE was mounted on the upper half of the specimen with Dow Corning high-vacuum grease as the coupling agent. This transducer had a resonant frequency

³Instron Co., Canton, MA.

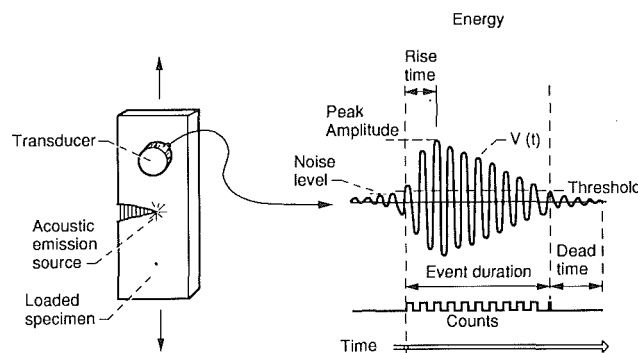


Fig. 4 Definition of an acoustic emission event or hit

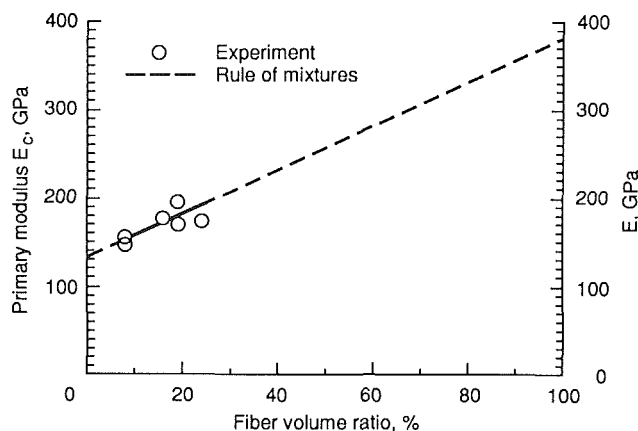


Fig. 5 Primary modulus of SiC/RBSN composite from experiment and the rule of mixtures

of 250 kHz. The bandpass of the preamplifiers and the AE system was 200 to 400 kHz. The AE and x-ray apparatus are shown in Fig. 3. The definition of an acoustic event is given in Fig. 4 along with some commonly used terminology. All the specimens were scanned before and after testing by using a 60-kV microfocus x-radiographic system to detect any major flaws or any evidence of major failure events. Another film x-radiographic instrument with 160 kV was mounted on the Instron load frame for in-situ monitoring. The kilovoltage and duration used for each x-ray film were different for each specimen, depending on the respective thicknesses. The analog signals for load and strain from the loadframe were also fed to the AE system. Stresses were calculated from the imposed loads, while the axial strains in the gage section were measured by an extensometer. The strain gages were only used to check bending effects during testing. This was due to the fact that the strain gages were sensitive only to cracking in a small area around the gages, and were unlikely to detect first matrix crack formation within the entire gage length. Failed and failing specimens were also examined visually and photomicrographically.

III Failure Characteristics

Effect of Fiber Content. SiC/RBSN composites with four different fiber volume ratios were tested. Results are shown in Table 1. The effect of fiber content on mechanical properties and failure behavior is evident from the listed data. The composite primary modulus, E_c , obtained from initial linear portions of the stress-strain curves, increased with increasing fiber volume ratio, f (Fig. 5). These data points were best-fitted with a straight line, which then was extrapolated to all f values, using the rule of mixtures, $E_c = fE_f + (1-f)E_m$, where the fiber elastic modulus, E_f , and the average matrix elastic modulus, E_m , were estimated to be 381 and 133 GPa, respectively. This fiber modulus was about 2 percent less than the expected

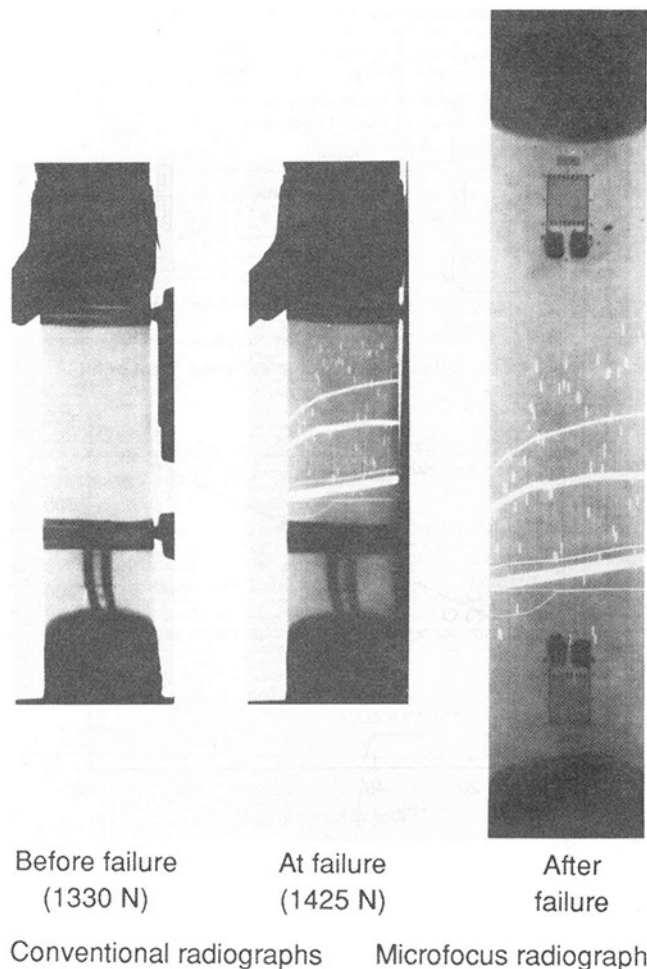


Fig. 6 X-radiographic results for specimen S1A

value of 390 GPa (DiCarlo and Williams, 1980) while the matrix modulus was 21 percent more than the expected value of 110 GPa (Bhatt, 1988). The difference in the matrix modulus is rather high, but it could be due to the matrix densities being higher in the low-fiber fraction (1- and 3-ply) specimens than in the high-fiber fraction (5- and 8-ply) specimens. In addition, in-situ properties do not necessarily agree with individual constituent measurements. The composite primary moduli based on the rule of mixtures were in reasonable agreement with the experimental primary moduli as shown in Table 1.

The effect of fiber content on failure modes was also apparent. Catastrophic failure occurred in the 1- and 3-ply specimens where the fiber volume ratio was 8 and 16 percent, respectively, for both strong and weak interfaces. In the 5- and 8-ply specimens that had weak interfaces and fiber volume ratios of 19 and 24 percent, respectively, failure was always noncatastrophic. With increasing fiber content, the proportional limit and the ultimate strengths were enhanced significantly. In contrast, the proportional limit strains were essentially unaffected by changes in fiber content. This observation is due to the change in the proportional limit stress being offset by the change in composite stiffness to keep the proportional limit strain unchanged.

Catastrophic Failure Mechanisms. Specimens S1A, S1B, and M3A were tested under tension and failed catastrophically. For S1A, x-radiographs taken at increasing loads up to 1330 N showed no evidence of any failure. Radiographs taken after ultimate failure (Fig. 6) showed transverse matrix cracking, fiber fracture, and minimal fiber pull-out. Fiber fractures occurred throughout the gage length, sometimes twice in the same fiber, due to the statistical behavior of fiber strength. Fiber/

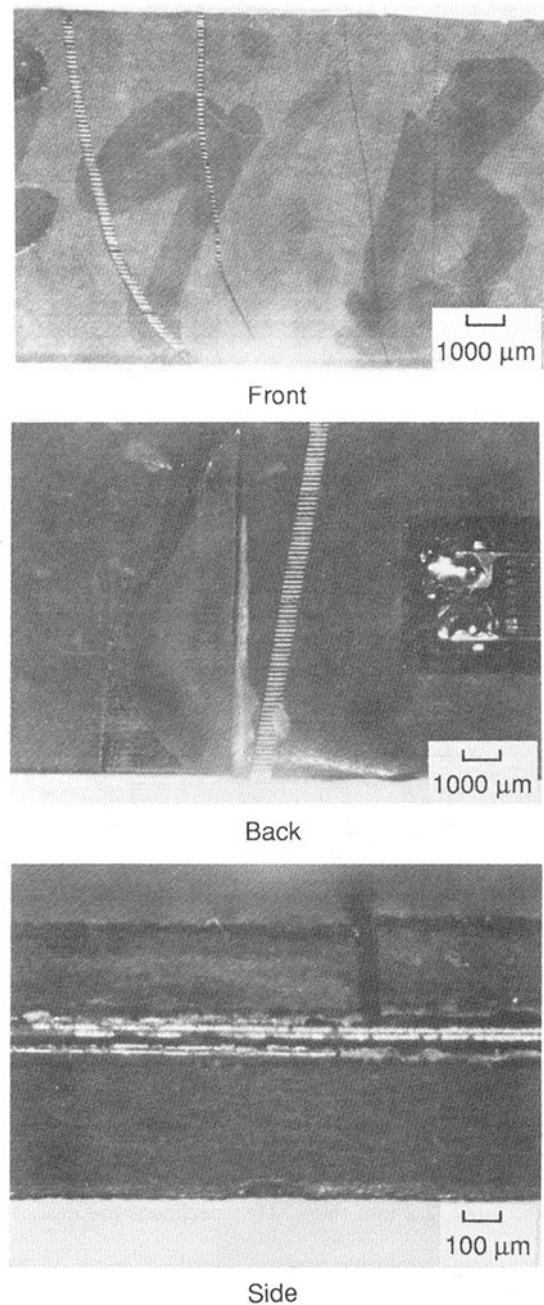


Fig. 7 Optical photomicrographs of matrix cracking and debonding for specimen S1A

matrix interface debonding (splitting) and transverse matrix cracking can be observed in the optical photomicrographs (Fig. 7). It should be noted that these transverse matrix cracks were not through-the-thickness cracks. It is also evident from the listed loads in Fig. 6 that the fiber pull-out mechanism occurred only at the very end of the rupture process. As expected, when the fiber content is small, even though the interface is weak, fiber pull-out action cannot guarantee graceful failure.

The linear stress-strain curve for these specimens and x-ray results taken alone gave no indication of any failure events before the proportional limit or, in this case, the ultimate strength. By contrast, AE results clearly indicated the occurrence of fiber breakage, transverse matrix cracking and fiber/matrix interface debonding throughout the loading history as shown in Fig. 8. These major failure mechanisms were identified via three AE parameters: event duration, peak amplitude, and energy. The energy parameter was used to separate microscopic events from macroscopic events. A transverse matrix

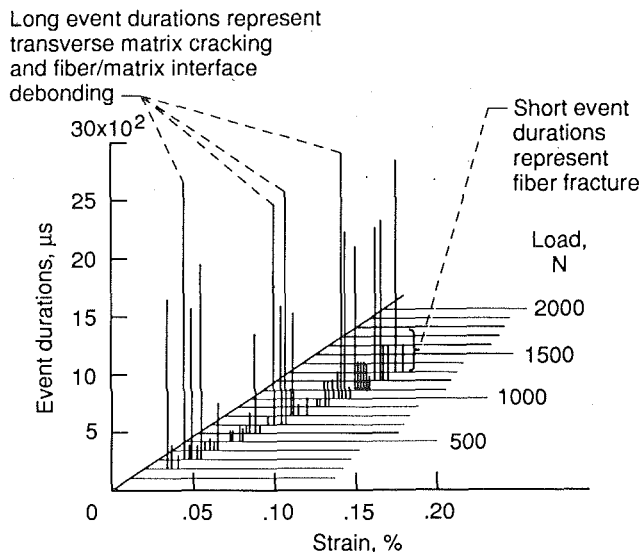


Fig. 8 Three-dimensional plot of event durations, load, and strain for specimen S1A

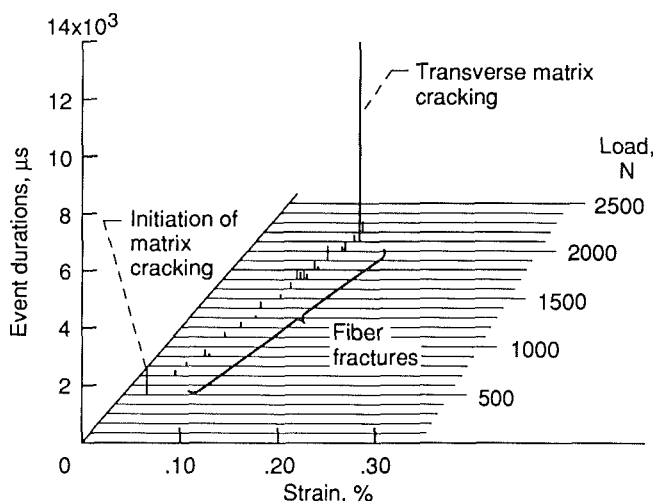


Fig. 9 Three-dimensional plot of event durations, load, and strain for specimen S1B

crack was defined as an event with long duration ($>400 \mu s$) and medium peak amplitude (51 to 70 dB), while a fiber fracture event was characterized as short duration ($<400 \mu s$) and high peak amplitude (>70 dB). For an interfacial debonding event, high peak amplitude (>70 dB) and long event duration ($>400 \mu s$) were detected (Chulya et al., 1990).

For specimen S1B, which had a strong fiber/matrix interface, the failure mode was also catastrophic but with only one single transverse through-the-thickness matrix crack. X-radiography showed no sign of fiber breakage scattered throughout the gage length. Photomicrography showed no evidence of fiber/matrix interface debonding. Transverse matrix cracking and fiber fracture were the only major failure mechanisms observed. These results were confirmed by the AE analysis. As shown in Fig. 9 by means of a three-dimensional AE plot, a small single matrix crack occurred first, followed by a series of fiber breaks near the crack location until the load reached 2100 N. At this load the small matrix crack propagated all the way through the specimen and catastrophic fiber fractures followed.

The 3-ply SiC/RBSN specimen (M3A) with weak interfaces and 16 percent fiber content also failed catastrophically in tension. Optical photomicrography showed multiple transverse matrix cracks (not through-the-thickness but initiating from

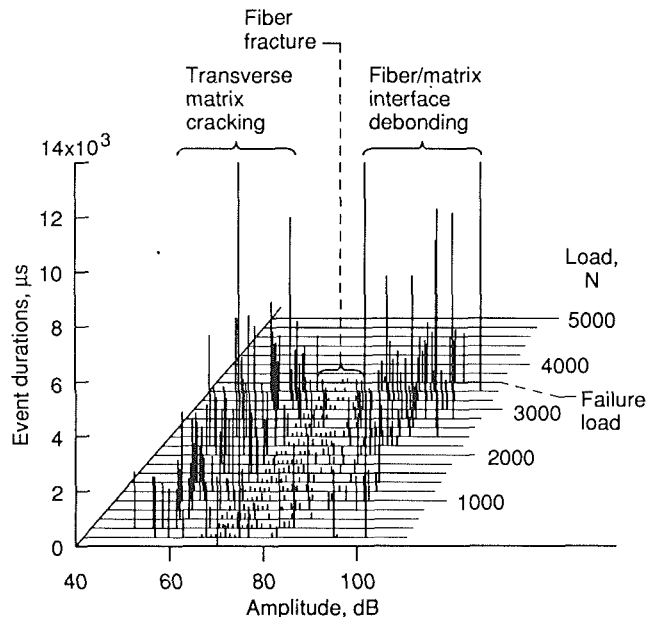


Fig. 10 Three-dimensional plot of event durations, amplitude, and load for specimen M3A

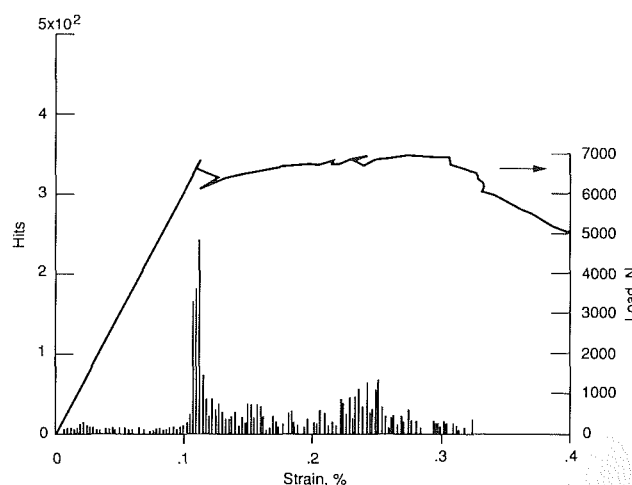


Fig. 11 Load-strain curve with AE hit parameter for specimen M5B

both sides of the specimen) and multiple fiber/matrix interface debonding. X-radiographic results again shown fiber fracture scattered throughout the gage length. The plot of AE event duration and amplitude versus the applied load shown in Fig. 10 shows that transverse matrix cracking and fiber fracture occurred early in the loading stage and continued throughout the loading history, while fiber/matrix interface debonding occurred only after approximately two-thirds of the failure load. The stress-strain curve is linear and does not have the ability or resolution to reflect these failure events. Apparently, the 16-percent fiber content improved the ultimate strength, but still could not prevent catastrophic failure.

Noncatastrophic Failure Mechanisms. The load-strain curve and AE results for a 5-ply specimen are shown in Fig. 11. With higher fiber content and weak interfaces, all five-ply composites failed noncatastrophically. X-ray results again did not detect any failure events in the linear region of the load-strain curve. However, AE analysis showed that some matrix cracking, fiber breaking, and fiber/matrix interface debonding occurred throughout the linear region (Figs. 11 and 12). These phenomena were observed in all 5-ply specimens. Since the fibers started to fail early, it appears that the fiber strength

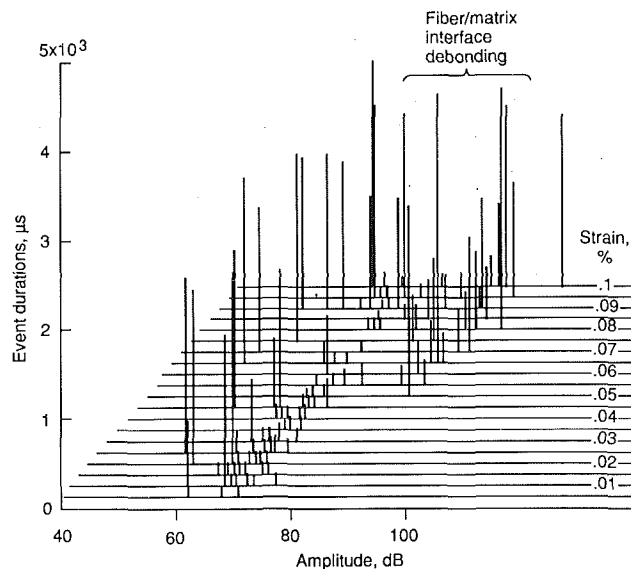


Fig. 12 AE parameter plot in the linear strain regime for specimen M5B

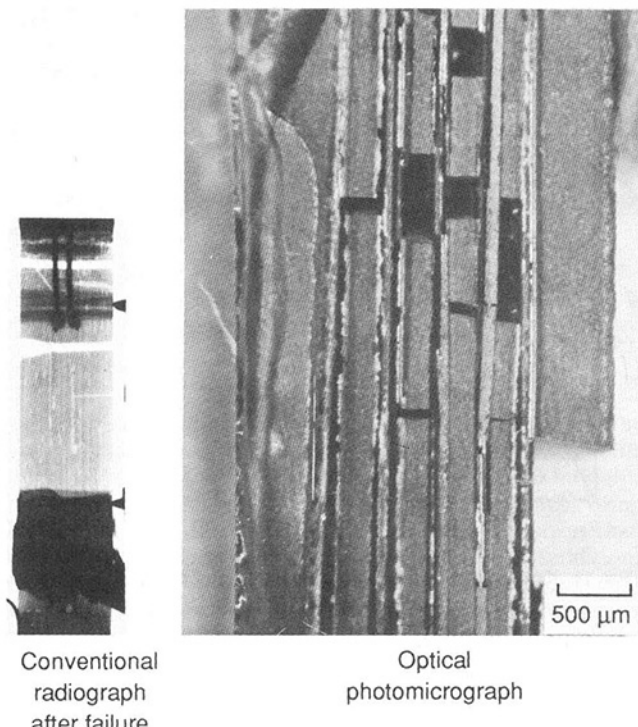


Fig. 13 X-ray film and optical photomicrograph at failure for specimen M5C

was not adequate, probably because of damage during fabrication. It was also noted from testing specimen S1B that strong interfaces tended to minimize random fiber fracture. These results suggest that, for a high critical matrix cracking stress, fiber strength must be adequate to carry the entire proportional limit load and the interfacial shear strength should be increased.

At the proportional limit, fiber failure occurred extensively but not at any particular surface crack. Instead fiber failure was widely scattered throughout the gage length. Due to this extensive fiber breakage, ultimate strength was very close to the proportional limit for specimen M5B (Fig. 11). Photomicrographic examination of the failed specimens (Fig. 13) showed no sign of steady-state matrix damage, i.e., through-the-thickness transverse cracks. After exceeding the propor-

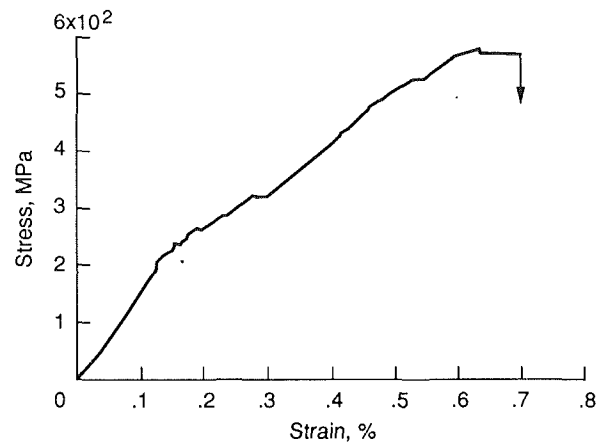


Fig. 14 Stress-strain curve for specimen M8A

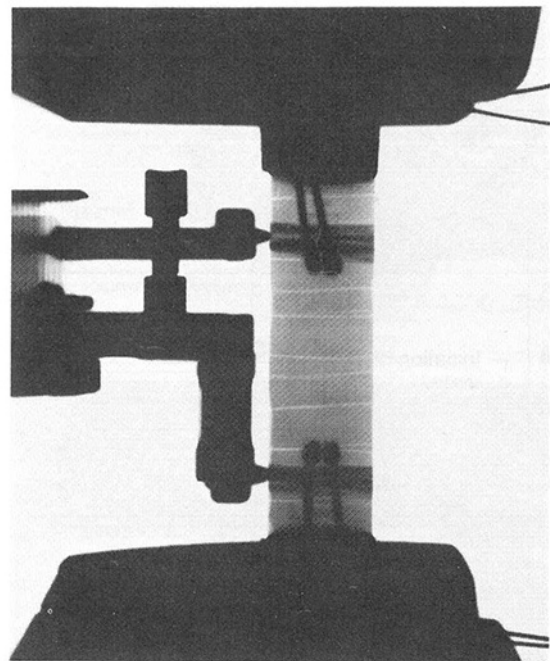


Fig. 15 X-ray film for specimen M8A showing transverse matrix crack spacing

tional limit, acoustic emission results indicated that matrix cracking and fiber/matrix debonding continued extensively. Beyond the ultimate load, some fiber pull-out took place. Radiography (Fig. 13) also showed evidence of similar failure events in the nonlinear region.

The room temperature tensile stress-strain curve for an 8-ply specimen with 24-percent fiber content is shown in Fig. 14. The proportional limit stress and strain were measured as 195 MPa and 0.124 percent, respectively. After reaching the proportional limit, additional matrix cracks were formed at regular intervals along the gage length upon further loading. This was evident from radiographs taken during the test (Fig. 15 and Baaklini and Bhatt, 1991). This transition region corresponds to stress levels between 200 and 270 MPa in Fig. 14. Beyond this region, due to extensive matrix cracking, the deformation of the composite is almost entirely controlled by the fibers. With continued loading beyond the composite ultimate strength, the stress-strain curve showed a drastic drop, resulting in a very short descending tail, which indicated the absence of extensive fiber pull-out. Extensive fiber/matrix interface splitting was observed as shown in Fig. 16. This, consequently, diminished the pull-out phenomenon. The macroscopic cracks observed by radiography (Fig. 15) and

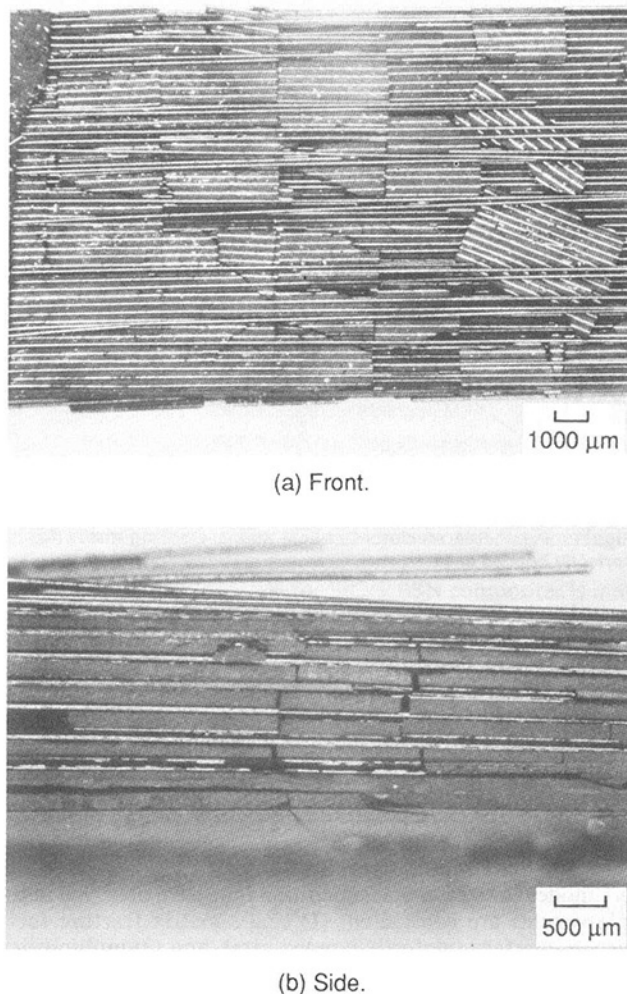


Fig. 16 Optical photomicrographs of specimen M8A

optical photomicrography (Fig. 16) were now the previously reported through-the-thickness transverse cracks with expected matrix crack spacing. This spacing was used to determine the interfacial shear strength. It is also clear that by increasing the fiber content from 19 to 24 percent, the ultimate strength improved drastically, as shown in Table 1. Such significant improvement is due both to higher fiber content and to different fiber degradation occurring during fabrication of the 5-ply and the 8-ply specimens. Results from testing these specimens clearly show that with adequate fiber content and optimized interfaces, ideal composite behavior is obtained, that is, periodic matrix cracks, high ultimate strength, and graceful failure will be observed.

IV Interface Characteristics

Fiber/Matrix Interface Debonding. Failure mechanisms that were observed in the 1-, 3-, 5-, and 8-ply tensile specimens confirm that the strength of the fiber/matrix interface, τ , is very critical to composite behavior. For weak interfaces, the debonding (splitting) mechanism can be described as follows: During tensile loading, the matrix starts to crack and the crack propagates normal to the fiber direction. Once the crack front hits the fiber layer, rather than extending across the interface and around the fibers in the thickness or width directions, the weak interface allows the crack to propagate parallel to the fiber between the fiber and the matrix. This phenomenon occurs only when the fracture energy of the interface is lower than that of the matrix. The location of interface splitting or debonding was mostly between the two carbon-rich coating

layers, and not between the matrix and fiber outer coating, which usually had a strong chemical bond (Eldridge and Honey, 1990). Hence, the monofilament fibers contained an engineered interface, which, when protected from processing damage, resulted in low values of τ . The resulting interface debonding, especially for low fiber content laminates, not only prevented the occurrence of through-the-thickness matrix cracks, but also reduced the work of fiber pull-out (to be discussed in Section V). This interface debonding also leads to load redistribution from the cracked areas into the undamaged portion of the specimen, causing the fibers to support more load there, which then induces progressive fiber failure below expected levels. For specimen S1B, which had strong interfacial shear strength, interface debonding was never detected and the proportional limit strength was much higher than for specimen S1A. Assuming fiber integrity, we conclude that the fracture energy of the matrix, G_m , should be lower than that of the interface, G_i , and G_j should be lower than that of the fiber, G_f . This will assure debonding within the desired interface and prevent the crack from kinking into the fiber to cause premature fiber breakage. Therefore, the condition, $G_m < G_i < G_f$, must be satisfied for an optimized composite. The critical ratio of G_j and G_f was also studied analytically by He and Hutchinson (1989). However, G_i is very difficult to determine experimentally because of interface variation from processing conditions as well as the porous nature of the matrix.

Interfacial Frictional Properties. When interface splitting does not occur, the interfacial frictional stress has the potential to improve the overall strength and toughness of the composite. In order to develop and evaluate micromechanical models that precisely correlate composite behavior with interface frictional properties, interfacial shear strength must be accurately measured. Considerable work meeting this need has been reported (Eldridge and Honey, 1990; Marshall, 1984; Marshall and Oliver, 1987). For the SiC/RBSN composite with optimized interfaces, the work reported by Eldridge and Honey (1990) used the push-out test to determine the interfacial shear strength at room temperature. The measured value of 8.1 ± 0.5 MPa includes the radial residual stress effect, which will be discussed below. Of course, τ can vary significantly within a composite and the push-out technique will give only average values that are subject to processing conditions, matrix porosity, and effects of neighboring fibers. Another approach to measuring τ is the periodic matrix crack spacing method (Aveston et al., 1971). For valid periodic matrix crack spacing measurements, multiple matrix cracks must occur and they must be through-the-thickness and across-the-width. This is defined as a steady-state condition. In reality, these cracks are seldom evenly spaced. Therefore, an average value of the crack spacing had to be used. This value, x , measured in specimen M8A by x-ray film radiography (Fig. 15), was 3.85 mm. In-situ film radiography proved to be a most effective way to measure the crack spacing, since the cracks will close after unloading due to the axial residual compression stress in the matrix. This spacing is a function of the interfacial shear strength, τ , and from equilibrium considerations we have (Aveston et al., 1971)

$$\tau = \beta R(1 - f)E_m \sigma_{cr} / (2fE_c x) \quad (1)$$

where β is a constant equal to 1.337 (Kimber and Keer, 1987), σ_{cr} is the critical matrix cracking stress, and R is the fiber radius. Assuming that σ_{cr} is the proportional limit or microcrack yield stress, the calculated τ based on the material constituents of specimen M8A was 5 MPa. Microstructurally, the interfacial shear strength of this composite is governed by the integrity of the carbon-rich fiber surface coating. For fabrication and heat treatment conditions where the carbon-rich coating remains intact, the composite will display a weak interfacial behavior. Based on our observations, the values of 5

and 8.1 MPa may be too low to yield high critical matrix cracking strength and optimized toughness. Interfacial shear strength is often controlled through heat treatment or with a new coating that has the requisite mechanical properties both at room and high temperatures.

V Micromechanical Models

The above experiments showed that SiC/RBSN composites must have sufficient interfacial shear strength for load transfer to occur and to prevent interface splitting or debonding. The interface must be weak enough to allow slipping and substantial pull-out lengths of fibers for toughness. Fiber-reinforced ceramic matrix composites must also have high fiber content, 19 percent or more in this case, with high fiber strength and stiffness for enhancements in composite primary modulus, proportional limit strength, ultimate strength, and work of pull-out. Once a transverse matrix crack passes through the matrix, the fibers must provide bridging forces across the crack to prevent catastrophic failure. Micromechanical models presented below can predict the failure behavior of the above-described composite throughout its loading history. These models can also be used to obtain the optimum composite properties best suited to the desired applications.

The micromechanical models presented herein are focused on four important design issues: (1) residual stress, (2) critical matrix cracking strength, (3) ultimate strength, and (4) work of pull-out. Single and multiple matrix cracks are considered for both strong and weak interface conditions. The Weibull distribution is linked to the composite ultimate strength and work of pull-out due to the statistically distributed strength properties of fibers observed in the experiments. Comparisons with experimental results are made and the discrepancies are explained.

Residual Stresses. The processing temperature of 1200°C used for the SiC/RBSN composites in this study clearly caused strain mismatches between the fiber and matrix when the composite was cooled to room temperature. This effect should not be neglected. If the coefficients of thermal expansion (CTE) were appreciably different, extensive initial cracking would be observed (Moschler, 1988). The residual stresses arise both in the radial direction, i.e., normal to the fiber, and axial direction, i.e., parallel to the fiber. The radial interface pressure, q , has a significant effect on the interfacial shear strength, which in turn controls the overall failure behavior of the composite. The axial matrix residual stress, σ'_m , will enhance the critical matrix cracking strength if it is in compression. Based on an analysis using the shear lag model, and given isotropic properties for both the fibers and matrix, the following expressions were used to obtain q and σ'_m from the thermal strain mismatch ϵ_T (Budiansky et al., 1986):

$$q = (E_m/2\phi_1)[(1-f)/(1-\nu_m)]\epsilon_T \quad (2)$$

$$\sigma'_m = (E_m\phi_2/\phi_1)[E_f/E_c][f/(1-\nu_m)]\epsilon_T \quad (3)$$

where

$$\epsilon_T = (\alpha_f - \alpha_m)\Delta T \quad (4)$$

and if we assume that the Poisson ratio $\nu = \nu_f = \nu_m$,

$$\phi_1 = 1 - 0.5[(1-2\nu)/(1-\nu)](1-E_c/E_f) \quad (5)$$

$$\phi_2 = 0.5(1+E_c/E_f) \quad (6)$$

The subscripts f and m refer to the fiber and matrix, respectively, and ΔT is the temperature change during cooling. The quantity ϵ_T is negative when CTE of the fiber is greater than that of the matrix.

When q is compressive and the Coulomb friction law, $\tau_R = \mu q$ applies, τ_R increases the interfacial shear strength. For the SiC/RBSN composite, the fiber has a slightly higher coefficient of thermal expansion than the matrix (Bhatt, 1989). Conse-

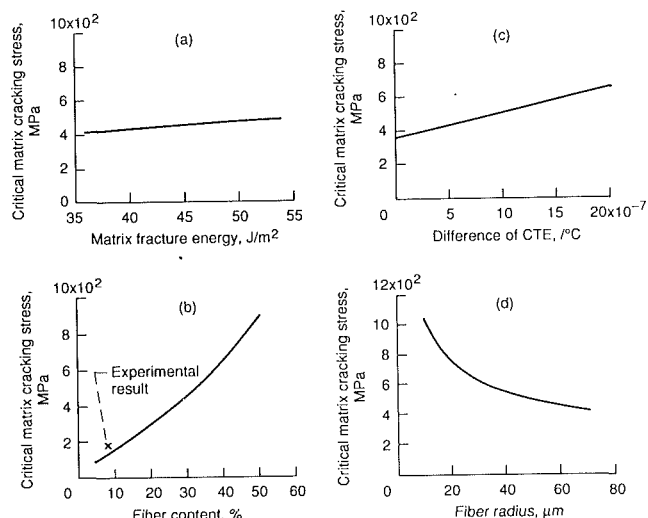


Fig. 17 Parametric studies of critical matrix cracking stress for the perfectly bonded case

quently, the interfacial pressure, q , is tensile, which weakens the bond between the fiber and the matrix or that between the carbon layers. To account for this weakening, the Coulomb friction law is used and τ_R now acts to reduce the frictional shear strength. It is also evident that initial axial compressive stresses exist before any mechanical loading is applied and these stresses are a source of extra strength for the matrix. The residual stresses are included in all calculations herein of the critical matrix cracking stress and the ultimate strength.

Steady-State Matrix Cracking Stress. Two distinctive failure modes for steady-state condition that were observed in the experiments are considered: (1) single matrix fracture for a strong interface (perfectly bonded case), and (2) multiple matrix fracture for a weak interface (slipping fibers case). For single matrix fracture to occur, the SiC/RBSN composite was fabricated at a temperature of 1350°C, instead of 1200°C, in $N_2 + 4$ percent H_2 for 72 hr. These processing conditions degrade the usual double carbon-rich coating of the fiber and destroy the weak interface between them. A model that predicts the steady-state matrix cracking stress for single matrix fracture was first proposed by Aveston and Kelly (1973) and later refined by Budiansky et al. (1986) using fracture mechanics theory, giving the following relations:

$$\sigma_{ss}^s = B \left[\frac{6E_c^3 f^2 E_f}{(1-f)^2 (1+\nu_m)} \right]^{1/4} \left[\frac{G_m}{E_m R} \right]^{1/2} \quad (7)$$

where

$$B = \left[\frac{2(1-f)^3}{-6 \ln(f) - 3(1-f)(3-f)} \right]^{1/4} \quad (8)$$

Since the radial residual stress has no effect for the perfectly bonded case, the critical matrix cracking strength becomes

$$\sigma_{cr} = \sigma_{ss}^s - \sigma'_m E_c / E_m \quad (9)$$

The effects on σ_{cr} of G_m , f , R , and the difference in α_f and α_m are presented in Fig. 17. For a selected fiber content of 28 percent and Poisson ratio of 0.22, the critical matrix cracking stress varies little with G_m . If the difference in CTE increased for $\alpha_f > \alpha_m$, the critical matrix cracking stress would rise significantly. In Fig. 17(d), it is clear that σ_{cr} is maximum for small fiber diameters. As anticipated, the model predicts that increasing the fiber content would also enhance σ_{cr} . Since it was impossible to measure accurately the critical matrix cracking stress experimentally, the ultimate strength of specimen S1B was used to compare the prediction of the model at 8 percent fiber content. The measured experimental value was

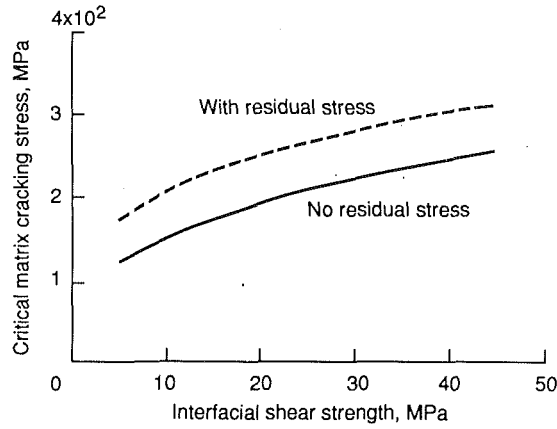


Fig. 18 Variation of critical matrix cracking stress with interfacial shear strength for multiple matrix cracking (slipping fibers) case

slightly higher than the expected strength from theory (Fig. 17(b)). Note that σ_{ss}^s in Eq. (7) is independent of the interfacial shear strength.

The desired failure mode for SiC/RBSN composites is multiple matrix fracture, which exploits the high-fiber properties and provides graceful failure for the laminate. Micromechanical models to predict the matrix cracking stress for weak interface conditions have been proposed by a number of researchers using different methodologies. An early model, originally proposed by Aveston et al. (1971), is based on the energy-balance approach, and is derived herein using fracture mechanics theory and the assumption of intact bridging fibers (Marshall and Cox, 1988). Based on the J-integral method, the relation for steady-state matrix cracking is

$$J_c/2 = \sigma_a u_a - \int_0^{u_a} p(u) du \quad (10)$$

where $2u_a$ is the critical crack opening corresponding to the applied stress, σ_a . If there is no ligament failure accompanying crack propagation, then the fracture criterion for matrix cracking is

$$J_c = (1-f)G_m \quad (11)$$

The crack closing pressure, $p(u)$, arising from the bridging fibers can be calculated from (McCartney, 1987)

$$p(u) = \left[\frac{4\tau f^2 E_f E_m^2}{R(1-f)^2 E_m^2} \right]^{1/2} u^{1/2} \quad (12)$$

By substituting Eqs. (11) and (12) into Eq. (10) and setting $\sigma_a = p(u_a)$, the steady-state matrix cracking stress for multiple matrix fracture becomes

$$\sigma_{ss}^M = \left[\frac{6\tau G_m f^2 E_f E_c^2}{R(1-f)^2 E_m^2} \right]^{1/3} \quad (13)$$

Therefore, the expression for predicting the critical matrix cracking strength with residual stress effects is

$$\sigma_{cr} = \sigma_{ss}^M (\tau + \tau_R) - \sigma_m' E_c / E_m \quad (14)$$

where σ_{ss}^M is a function of an effective interfacial shear strength, that is $\tau_e = \tau + \tau_R$.

Parametric calculations using Eq. (14) were made for the SiC/RBSN composite with 28-percent fiber content, interfacial frictional strength, τ , of 10 MPa, and μ equal to 0.1. The results are plotted in Fig. 18 showing the effects of residual stresses and interfacial shear strength. With the strain mismatch producing an initial matrix compressive stress, the composite critical matrix cracking strength is obviously improved. Clearly, the residual stresses cannot be neglected even though they may decrease significantly as the operating temperature increases. Equation (13) is valid only up to a certain value of τ that assures multiple transverse matrix cracking, and the

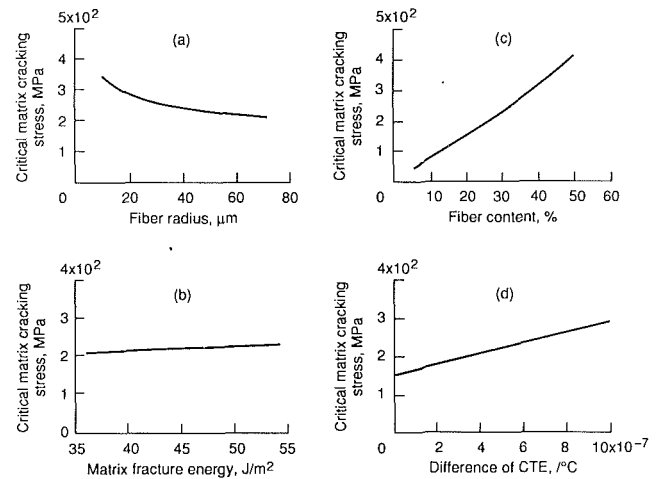


Fig. 19 Parametric studies of critical matrix cracking stress for multiple matrix cracking (slipping fibers) case

maximum τ used herein for this failure mode was 45 MPa. This value is based on the maximum value of τ that can be successfully measured from the push-out test in our laboratory. In Fig. 19(a), the critical matrix cracking strength is plotted as a function of fiber radius using Eqs. (2), (3), (13) and (14). As mentioned before, small radius fibers will enhance the microcrack yield strength of unidirectional CMC's. However, improving matrix fracture toughness will not have a significant effect on the matrix cracking strength (Fig. 19(b)). Figure 19(c) shows an almost linear relation between σ_{cr} and the fiber content. Figure 19(d) shows that higher strain mismatch improves the critical matrix cracking strength, at least when loaded in the fiber direction. The tradeoff is that as the strain mismatch increases, the radial residual stress would cause higher tension in the interface. This would weaken the interfacial shears strength, decrease σ_{ss}^M , and induce interface debonding.

Ultimate Strength. The ultimate strength, which is reached after multiple matrix cracking, was calculated from the strength of initially strong fibers that were degraded during composite fabrication. This was evident when in-situ fibers broke sequentially at unexpectedly low loads rather than simultaneously at higher loads before reaching the ultimate point. This was observed experimentally and has been previously discussed herein. X-radiographic results precisely showed the locations of fiber fracture and the statistical nature of fiber failure in weak interface composites. Therefore, the micromechanical model used to predict the ultimate strength of composites must be based on a statistical distribution. Using weakest link statistics, a recent model (Evans, 1989) is applied, which in terms of the fiber Weibull Modulus, m , is

$$\sigma_u = f S_u \exp \left\{ - \frac{\left[1 - \left(1 - \frac{\tau X}{R S_u} \right)^{m+1} \right]}{(m+1) \left[1 - \left(1 - \frac{\tau X}{R S_u} \right)^m \right]} \right\} \quad (15)$$

with

$$\left(\frac{R S_u}{\tau X} \right)^{m+1} = \left(\frac{A_o}{2\pi R L} \right) \left(\frac{R S_o}{\tau X} \right)^m \left[1 - \left(1 - \frac{\tau X}{R S_u} \right)^m \right]^{-1} \quad (16)$$

$$S_o = \frac{\bar{s}}{\Gamma \left(1 + \frac{1}{m} \right)} (2\pi R H)^{1/m} \quad (17)$$

where L is the gage length of the composite test specimen, A_o is an area normalizing factor, S_o is the scale parameter, \bar{s} is the average fiber strength, H is the fiber gage length, Γ is the

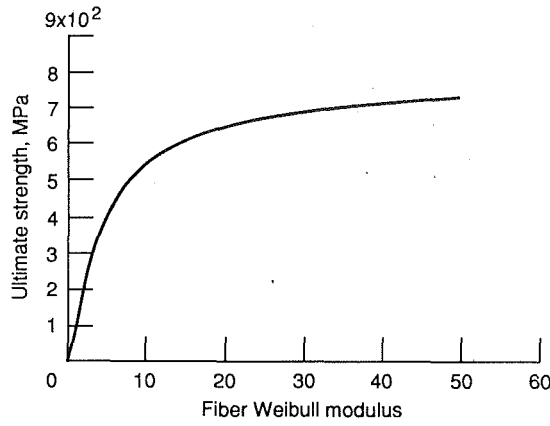


Fig. 20 Variation of ultimate strength with fiber Weibull modulus: $A_o = 1 \text{ m}^2$; $S_o = 2.86 \text{ GPa}$; $L = 0.1016 \text{ m}$; $f = 0.28$; $\tau = 10 \text{ MPa}$

gamma function, S_u is determined from Eq. (16), and x is the matrix crack spacing obtained from Eq. (1) as

$$x = 1.337R(1-f)E_m\sigma_{ss}^s/(2fE_c\tau) \quad (18)$$

Using the SiC/RBSN composite properties, and average fiber strength of 2.86 GPa, and selected values of A_o , h , and L as 1 m^2 , 0.025, and 0.1016 m, respectively, the ultimate strength as a function of Weibull modulus was calculated and the results are shown in Fig. 20. Clearly, the ultimate strength varies rapidly when $m < 20$, that is, when the variation in fiber strength is high. The experimental value of the Weibull parameter, m , for the SCS-6 SiC fiber was evaluated from uniaxial fiber tension tests performed on finite length specimens of 25 mm and was estimated to be 8.2 (Bhatt and Phillips, 1988). However, the Weibull modulus of in-situ fibers could be considerably different from those measured independently, since the fiber flaws are expected to change during composite processing. Equation (15) also shows that τ has a very small effect on composite ultimate strength. An approximate check of the composite ultimate strength is often made from using the rule of mixtures, but in case of brittle fibers, the value of in-situ fiber strength to use in the prediction can only be an estimate.

Work of Pull-out. Pull-out usually occurs in composites after complete matrix failure with the bridging fibers also containing many random breaks away from the transverse matrix cracks. When interfacial shear strength is low, pull-out lengths are long and the work of pull-out is maximized, providing the composite load carrying capability beyond the ultimate strength. As observed through x-ray results, fibers exhibit variable pull-out lengths after complete failure and the lengths are governed by the Weibull strength distribution parameters. Hence, the work of pull-out must also be expressed in terms of the fiber Weibull modulus and scale parameter.

The work of pull-out had not been given much attention in the past even though Kelly (1970) had demonstrated its significance. Recently, Thouless and Evans (1988) and Sutcu (1989) have investigated the pull-out contribution to the toughness of ceramic matrix composites. In this paper, we will examine a model proposed by Sutcu. For fiber failure caused by a single matrix crack, the peak fiber stress is assumed to occur in the plane of the matrix crack and then drop to zero over a sampling length, L . The slope is governed by the interfacial shear stress and the fiber radius resulting in an expression for $\sigma(z)$ given by (Fig. 21)

$$\sigma(z) = 2\tau(L-z)/R \quad (19)$$

Based on the Weibull probability density function and the assumption of Eq. (19), it is possible to derive the average pull-out length L_p^s for a single matrix crack (Sutcu, 1989)

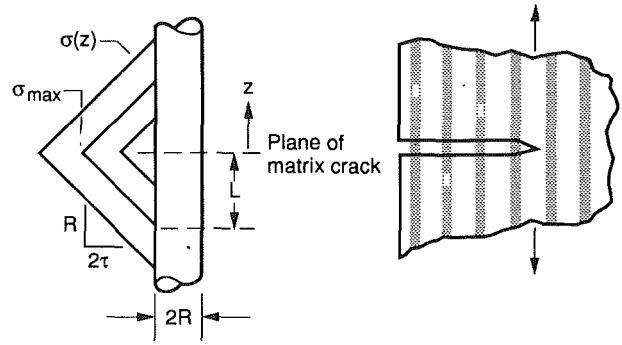


Fig. 21 Fiber stress distribution near a single matrix crack

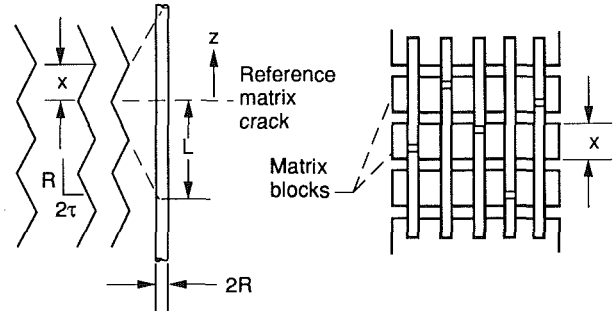


Fig. 22 Fiber stress distribution in a multiple matrix crack composite

$$L_p^s = \frac{\alpha}{2} R^{\frac{m-1}{m+1}} \left(\frac{S_o}{\tau} \right)^{\frac{m}{m+1}} \quad (20)$$

where

$$\alpha = 1.1m/(m+1)^2 \quad (2 < m < 60) \quad (21)$$

and s_o is obtained from Eq. (17). The energy release per fiber from pull-out can be obtained by integrating the force caused by τ over the slipping distance z . The resulting expression for the work of pull-out per unit area of the composite for a single crack is

$$W_p^s = \frac{\beta}{4} f R^{\frac{m-3}{m+1}} \frac{S_o^{\frac{2m}{m+1}}}{\tau^{\frac{m-1}{m+1}}} \quad (22)$$

where

$$\beta(m) = \frac{2.14(m-1)}{m^2(m+2)} [1 - \exp(-0.387m)] \quad (23)$$

For fiber failure with multiple matrix cracking, the stress in the fibers is assumed to be of a saw-tooth form as shown in Fig. 22 with the peak stress, σ_{\max} , given by

$$\sigma_{\max} = 2\tau L/R \quad (24)$$

However, for simplicity a uniform stress profile was used by Sutcu (1989) to derive the following results. The average pull-out length for multiple matrix cracking, L_p^M , is given by

$$L_p^M = \frac{\alpha'}{2} R^{\frac{m-1}{m+1}} \left(\frac{S_o}{\tau} \right)^{\frac{m}{m+1}} \quad (25)$$

where

$$\frac{\alpha'}{\alpha} = \frac{(m+1)^{\frac{m}{m+1}}}{2} \quad (26)$$

Finally, the work of pull-out for multiple matrix cracking is similar to the case of single matrix cracking and is defined by

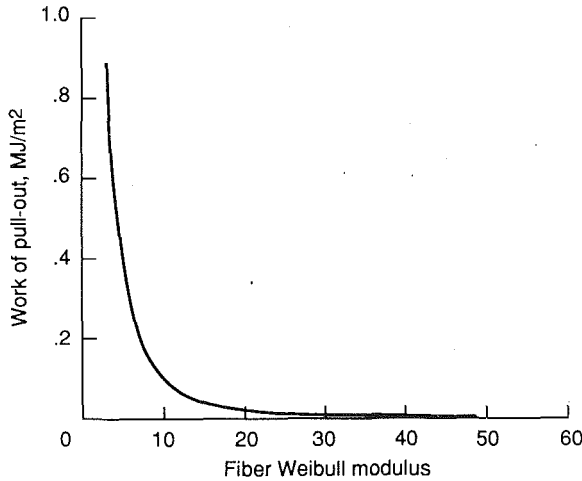


Fig. 23 Variation of work of pull-out with fiber Weibull modulus for single matrix cracking

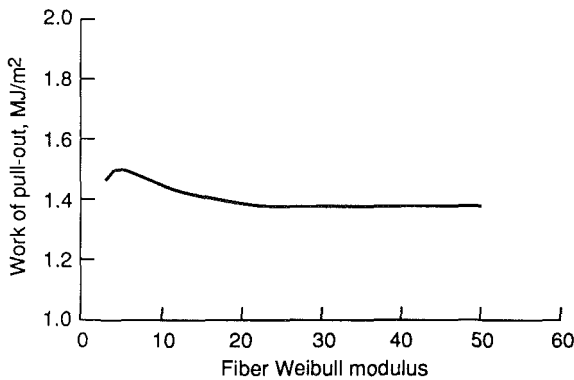


Fig. 24 Variation of work of pull-out with fiber Weibull modulus for multiple matrix cracking (slipping fibers) case

$$W_p^M = W_p^s \left(\frac{m+2}{6} \right) (m+1)^{\frac{m-1}{m+1}} \quad (27)$$

Note that the assumption of a uniform, rather than periodic, stress distribution leads to a larger pull-out length and subsequent work of pull-out. Hence these results must be regarded as upper bounds.

The work of pull-out for both single and multiple matrix cracking increases with average fiber strength and fiber radius, but decreases with increasing value of τ . Similar trends can be observed in the average fiber pull-out lengths. The work of pull-out for single matrix cracking is plotted in Fig. 23 as a function of the Weibull modulus. It shows that the fibers should have a low Weibull modulus to enhance fiber pull-out beyond the ultimate strength. Furthermore, the work of pull-out approaches zero when the variation of fiber strength decreases, which is what was observed experimentally in composites with brittle failure modes. Figure 24 shows that the work of pull-out for multiple matrix cracking initially increases and then decreases gradually with increasing m ; it asymptotically approaches a particular value, which can be explained as follows. The stresses in the fibers are highest in the matrix cracking planes. Therefore, for deterministic fiber strength, the fibers will fail at different matrix crack surfaces, not necessarily at the same crack. In this case the broken fibers can still bridge the cracks and eventually produce the work of pull-out.

Numerical Example. An example is given below for comparison of predicted and measured stress-strain curves for specimen M8A. It should be noted that the micromechanical models herein assume that no fiber breakage and matrix cracking occur

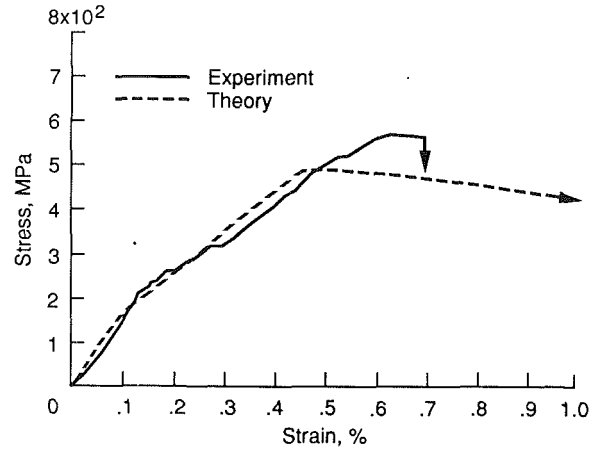


Fig. 25 Stress-strain curves for specimen M8A

before reaching the critical matrix cracking strength, while actual test specimens showed some fiber fracture and matrix cracking before the proportional limit strength was reached. The nominal values of parameters used in the prediction are:

$$\begin{aligned} m &= 8.2 \\ E_m &= 110 \text{ GPa} \\ E_f &= 390 \text{ GPa} \\ \nu_m &= 0.22 \\ K_m &= 2 \text{ MPa m}^{1/2} \\ G_m &= 36 \text{ J/m}^2 \\ R &= 71 \text{ } \mu\text{m} \\ f &= 0.24 \\ \alpha_f &= 4.2\text{E-}6/^{\circ}\text{C} \\ \alpha_m &= 3.8\text{E-}6/^{\circ}\text{C} \\ \Delta T &= -1175^{\circ}\text{C} \\ A_o &= 1 \text{ m}^2 \\ \bar{S} &= 2860 \text{ MPa} \\ L &= 0.04 \text{ m} \end{aligned}$$

The interfacial shear strength used was 5 MPa, based on the matrix crack spacing method. This value includes the effect of the radial residual stress. Hence, the critical matrix cracking strength was calculated from Eqs. (3), (13), and (14). The ultimate strength and work of pull-out were determined from Eqs. (15) and (27), respectively. Results are plotted in Fig. 25 together with the experimental stress-strain curve. For the critical matrix cracking strength, the value of 155 MPa is calculated and compared with the measured value of 195 MPa which is taken as the proportional limit stress. Ignoring early damage, the prediction is conservative and it also requires precise knowledge of the in-situ material constituent properties, especially τ . However, caution should be exercised when one defines the critical matrix cracking strength from macroscopic experiments, since some irreversible damage occurs earlier, which is not evident from the linear portion of the stress-strain curves. The predicted ultimate strength is 492 MPa, which is 15 percent lower than the experimental estimate (Table 1). For the work of pull-out, the experimental result shows a very small value of 42 kJ/m², which is significantly less than the predicted result of 2158 kJ/m². The source of this discrepancy is mainly due to interfacial debonding (splitting) that occurred extensively in the 8-ply sample and, consequently, the modeled pull-out phenomenon was never realized in the test. Furthermore, as previously noted, the predicted value is an upper bound solution.

VI Concluding Remarks

Failure mechanisms in unidirectional fiber-reinforced SiC/RBSN ceramic matrix composites under tension have been investigated. It is possible to detect damage accumulation and

various failure processes while loading the specimens via in-situ acoustic emission monitoring and x-radiography. Tests of samples with various fiber fraction show that the transition from catastrophic to noncatastrophic failure occurs at approximately 16 to 19 percent fiber content. Based only on stress-strain curves and x-ray results, there was no indication of any failure event before catastrophic failure when low fiber content specimens were tested. However, acoustic emission results indicate that some fiber breakage, transverse matrix cracking, and some fiber/matrix interface debonding had occurred long before catastrophic fracture. Similar phenomena took place in the noncatastrophically failed samples during the linear portion of their stress-strain curves. The macroscopic effect of this early (microscopic) damage on overall composite design philosophy and behavior requires additional studies and investigation. The interfacial shear strengths of the selected SiC/RBSN composites measured by the push-out test and the matrix crack spacing method were low. For this case, extensive interface debonding or splitting occurs and causes a reduction in the work of pull-out. This debonding or axial splitting is very undesirable. To obtain composites with high strength and toughness, the interfacial shear strength should be high enough to prevent interface debonding but low enough to allow steady-state cracking and substantial fiber pull-out lengths for graceful failure. Micromechanical models incorporating residual stresses to predict the critical matrix cracking strength, ultimate strength, and work of pull-out were used and the predictions were compared to measured values. The fiber Weibull modulus is an important parameter for both the ultimate strength and the work of pull-out. When variation in fiber strength is low, the ultimate strength is high. Conversely, when the variation is high, the work of pull-out is also high. By comparing predictions from these models with experiments, we can conclude that they are valid only if steady-state conditions occur and fiber breakage is minimized, at least for loads below the critical matrix cracking condition. For these reasons, only two specimens were used to validate these models since the other specimens did not show the required steady-state response. Accurate knowledge of in-situ material constituent properties is also equally important. Based on parametric studies and experimental observations, the optimum SiC/RBSN composite should meet the following requirements: fiber content as high as permitted by processing considerations (above 30 percent), fiber radius for optimum critical matrix cracking strength (below 35 μm), slightly higher fiber CTE than that of the matrix, an optimum fiber Weibull modulus for ultimate strength and work of pull-out (between 8 and 20), and the optimum ratio of interfacial shear strength divided by the fiber radius for high multiple matrix cracking strength and adequate pull-out toughness depending on design considerations and applications.

References

- Aveston, J., Cooper, G. A., and Kelly, A., 1971, "Single and Multiple Fracture, in the Properties of Fiber Composites," Conference Proceedings, National Physical Laboratory, Guildford, IPC Science and Technology Press Ltd., Surrey, United Kingdom, pp. 15–26.
- Aveston, J., and Kelly, A., 1973, "Theory of Multiple Fracture of Fibrous Composites," *Journal of Materials Science*, Vol. 8, pp. 352–362.
- Baaklini, G. Y., and Bhatt, R. T., 1991, "X-Ray Monitoring of Damage Accumulation in SiC/RBSN Tensile Specimens," to appear in *Ceramic Engineering and Science Proceedings*, 15th Annual Conference on Composites and Advanced Ceramic Materials, Cocoa Beach, FL, Jan. 13–16.
- Bhatt, R. T., 1987, "Method of Preparing Fiber-Reinforced Ceramic Materials," U.S. Patent No. 4689188.
- Bhatt, R. T., and Phillips, R. E., 1988, "Laminate Behavior for SiC Fiber-Reinforced Reaction-Bonded Silicon Nitride Matrix Composites," NASA TM-101350.
- Bhatt, R. T., 1989, unpublished report.
- Bhatt, R. T., and Kiser, J. D., 1990, "Matrix Density Effects on the Mechanical Properties of SiC/RBSN Composites," NASA TM-103098.
- Brennan, J. J., and Prewo, K. M., 1982, "Silicon Carbide Fiber-Reinforced Glass-Ceramic Matrix Composites Exhibiting High Strength and Toughness," *Journal of Materials Science*, Vol. 17(8), pp. 2371–2383.
- Budiansky, B., Hutchinson, J. W., and Evans, A. G., 1986, "Matrix Fracture in Fiber-Reinforced Ceramics," *Journal of the Mechanics and Physics of Solids*, Vol. 34, pp. 167–189.
- Chulya, A., Baaklini, G. Y., and Bhatt, R. T., 1990, "Characterization of Damage and Fracture Mechanisms in Continuous Fiber-Reinforced SiC/RBSN Ceramic Matrix Composites by Acoustic Emission," NASA CP-10051, *The 3rd Annual HITEMP Review Proceedings*, pp. 55–1–55–15.
- DiCarlo, J. A., and Williams, W., 1980, "Dynamic Modulus and Damping of Boron, Silicon Carbide, and Alumina Fibers," NASA TM-81422.
- Eldridge, J. I., and Honey, F. S., 1990, "Characterization of Interfacial Failure in SiC Reinforced Si_3N_4 Matrix Composite Material by Both Fiber Push-out Testing and Auger Electron Spectroscopy," *Journal of Vacuum Science and Technology*, Series A, Vol. 8, May–June, pp. 2101–2106.
- Evans, A. G., 1989, "The Mechanical Performance of Fiber-Reinforced Ceramic Matrix Composites," *Materials Science and Engineering*, Vol. A107, pp. 227–239.
- Haggerty, J. S., 1989, "Ceramic–Ceramic Composites With Reaction Bonded Matrices," *Materials Science and Engineering*, Vol. A107, pp. 117–125.
- He, M., and Hutchinson, J. W., 1989, "Crack Deflection at an Interface Between Dissimilar Elastic Materials," *International Journal of Solids and Structures*, Vol. 25(9), pp. 1053–1067.
- Kelly, A., 1970, "Interface Effects and the Work of Fracture of a Fibrous Composite," *Proceedings Royal Society of London*, Series A, Vol. 319, pp. 95–116.
- Kerans, R. J., Hay, R. S., Pagano, N. J., and Parthasarathy, T. A., 1989, "The Role of the Fiber-Matrix Interface in Ceramic Composites," *The American Ceramic Society Bulletin*, Vol. 68(2), pp. 429–442.
- Kimber, A. C., and Keer, J. G., 1987, "On the Theoretical Average Crack Spacing in Brittle Matrix Composites Containing Aligned Fibers," *Journal of Materials Science Letters*, Vol. 1, pp. 353–354.
- Marshall, D. B., 1984, "An Indentation Method for Measuring Matrix-Fiber Frictional Stresses in Ceramic Composites," *Journal of American Ceramic Society*, Vol. 67, Dec. pp. C-259–C-260.
- Marshall, D. B., Cox, B. N., and Evans, A. G., 1985, "The Mechanics of Matrix Cracking in Brittle-Matrix Fiber Composites," *Acta Metallurgica*, Vol. 33(11), pp. 2013–2021.
- Marshall, D. B., and Oliver, W. C., 1987, "Measurement of Interfacial Mechanical Properties in Fiber-Reinforced Ceramic Composites," *Journal of American Ceramic Society*, Vol. 70(8), pp. 542–548.
- Marshall, D. B., and Cox, B. N., 1988, "A J-integral Method for Calculating Steady-State Matrix Cracking Stresses in Composites," *Mechanics of Materials*, Vol. 7, pp. 127–133.
- McCartney, L. N., 1987, "Mechanics of Matrix Cracking in Brittle-Matrix Fiber-Reinforced Composites," *Proceedings Royal Society of London*, Series A, Vol. 409, pp. 329–350.
- Moschler, J. W., 1988, "Investigation of Failure Modes in Fiber Reinforced Ceramic Matrix Composites," MS Thesis, Air Force Institute of Technology, Wright-Patterson AFB, OH, Dec.
- Prewo, K. M., and Brennan, J. J., 1980, "High-Strength Silicon Carbide Fiber-Reinforced Glass-Matrix Composites," *Journal of Materials Science*, Vol. 15, (2), pp. 463–468.
- Prewo, K. M., and Brennan, J. J., 1982, "Silicon Carbide Yarn Reinforced Glass Matrix Composites," *Journal of Materials Science*, Vol. 17, (4), pp. 1202–1206.
- Prewo, K. M., 1986, "Tension and Flexural Strength of Silicon Carbide Fiber-Reinforced Glass-Ceramics," *Journal of Materials Science*, Vol. 21, pp. 3590–3600.
- Sutcu, M., 1989, "Weibull Statistics Applied to Fiber Fracture in Ceramic Composites and Work of Fracture," *Acta Metallurgica*, Vol. 37(2), pp. 651–661.
- Thouless, M. D., and Evans, A. G., 1988, "Effects of Pull-out on the Mechanical Properties of Ceramic-Matrix Composites," *Acta Metallurgica*, Vol. 36(3), pp. 517–522.

S. F. Duffy¹

J. L. Palko¹

Cleveland State University,
Department of Civil Engineering,
Cleveland, OH 44115

J. P. Gyekenyesi

NASA Lewis Research Center,
Structural Integrity Branch,
Cleveland, OH 44135

Structural Reliability Analysis of Laminated CMC Components

For laminated ceramic matrix composite (CMC) materials to realize their full potential in aerospace applications design, methods and protocols are a necessity. This paper focuses on the time-independent failure response of these materials and presents a reliability analysis associated with the initiation of matrix cracking. It highlights a public domain computer algorithm that has been coupled with the laminate analysis of a finite element code and which serves as a design aid to analyze structural components made from laminated CMC materials. Issues relevant to the effect of the size of the component are discussed, and a parameter estimation procedure is presented. The estimation procedure allows three parameters to be calculated from a failure population that has an underlying Weibull distribution.

Introduction

Structural components produced from laminated ceramic matrix composite (CMC) materials are being considered for a broad range of aerospace applications that include propulsion subsystems in the national aerospace plane, the space shuttle main engine, and advanced gas turbine engines. Specifically, composite ceramics may be used as segmented engine liners, small missile engine turbine rotors, and exhaust nozzles. These materials will improve fuel efficiency by increasing engine temperatures and pressures, which will, in turn, generate more power and thrust. Furthermore, these materials have significant potential for raising the thrust-to-weight ratio of gas turbine engines by tailoring directions of high specific reliability. The emerging composite systems, particularly those with a silicon nitride or silicon carbide matrix, can compete with metals in many demanding applications. The capabilities of laminated CMC prototypes have already been demonstrated at temperatures approaching 1400°C, well beyond the operational limits of most metallic materials.

Adding a second ceramic phase with an optimized interface to a brittle matrix improves fracture toughness, decreases the sensitivity of the brittle ceramic matrix to microscopic flaws, and could also improve strength. The presence of fibers in the vicinity of the crack tip modifies fracture behavior by increasing the required crack driving force by several mechanisms. These mechanisms include crack pinning, fiber bridging, fiber debonding, and fiber pull-out. This increase in fracture toughness allows for "graceful" rather than catastrophic failure. A unidirectional ply loaded in the fiber direction retains substantial strength capacity beyond the initiation of matrix cracking despite the fact that neither of the constituents would exhibit such behavior if tested alone. First matrix cracking consistently occurs at strains greater than in the monolithic matrix material. As additional load is applied, the matrix tends to break in a series of cracks bridged by the ceramic fibers,

until the ultimate strength of the composite is reached. The region of a typical stress-strain curve between the first matrix cracking and the ultimate tensile strength illustrates an intrinsic damage tolerance not present in monolithic ceramics.

Laminated CMC material systems have several mechanical characteristics that must be considered in the design of structural components. In regard to an individual ply, the most deleterious of these characteristics are low strain tolerance, low fracture toughness, and a large variation in failure strength in the material orientation transverse to the fiber direction. Thus analyses of components fabricated from ceramic materials require a departure from the usual deterministic philosophy of designing metallic structural components (i.e., the factor-of-safety approach). Although the so-called size effect has been reported to be non-existent in the fiber direction (see DiCarlo, 1989), the bulk strength of unidirectional-reinforced ply will decrease transverse to the fiber direction as the component volume increases. Since failure in the transverse direction will be dominated by the scatter in strength, statistical design approaches must be employed. These approaches must, on the one hand, allow for elevated strength, reduced variability in strength, and a diminished effect of bulk specimen size in the fiber direction, and, on the other hand, increased scatter in strength and effects of bulk size in the transverse direction. Simply stated, a reliability analysis must rationally account for material symmetry imposed by the reinforcement. Computational structural mechanics philosophies must emerge that address the issues of scatter in strength, size effect, and material anisotropy. There is a need for test-bed software programs that incorporate stochastic design protocols, that are user friendly, that are computationally efficient, and that have flexible architectures that can readily incorporate changes in design philosophy. The C/CARES (Composite Ceramics Analysis and Reliability Evaluation of Structures) program, which will be highlighted in this article, was developed to fulfill this need. C/CARES is a public domain computer algorithm, coupled to a general purpose finite element program, which predicts the fast fracture reliability of a laminated structural component under multiaxial loading conditions.

¹NASA Resident Research Associate at Lewis Research Center.

Contributed by the International Gas Turbine Institute and presented at the 36th International Gas Turbine and Aeroengine Congress and Exposition, Orlando, Florida, June 3-6, 1991. Manuscript received at ASME Headquarters March 4, 1991. Paper No. 91-GT-210. Associate Technical Editor: L. A. Riekert.

Stochastic Design Issues

For a number of composite material systems, several authors (see for example Batdorf and Ghaffarian, 1984; Wu, 1989) have reported a diminished size effect in the fiber direction; and DiCarlo (1989) has reported this effect for ceramic composites, in particular. This phenomenon is an important feature that must be addressed by any reliability model. How it is addressed depends on whether the material is modeled as a series system, a parallel system, or a combination. Current analytical practice uses finite element methods to determine the state of stress throughout the component. It is assumed that failure depends on the stress state in a component, such that deformations are not controlling design. Since failure may initiate in any of the discrete volumes (elements), it is useful to consider a component from a systems viewpoint. A component comprised of discrete volumes is a series system if it fails when one of the discrete volumes fail. This approach gives rise to weakest-link theories. In a parallel system, failure of a single element does not necessarily cause the component to fail, since the remaining elements may be able to sustain the load through redistribution. The parallel system approach leads to what has been referred to in the literature as "bundle" theories.

The basic principles underlying these bundle theories were originally discussed by Daniels (1945) and Coleman (1958). Their work was extended to polymer matrix composites by Rosen (1964) and Zweben (1968). Here, a relatively soft matrix serves to transfer stress between fibers and contributes little to the composite tensile strength. Hence, when a fiber breaks, the load is transferred only to neighboring fibers. Their analysis is rather complex and limited to establishing bounds on the stress at which the first fiber breaks and the stress at which all the fibers are broken. Harlow and Phoenix (1978) proposed a rather abstract approach that established a closed-form solution for all the intermediate stress levels in a two-dimensional problem, and Batdorf (1982) used an approximate solution to establish the solutions for the three-dimensional problem. Batdorf's model includes the two-dimensional model as a special case. In both of the latter two models, the authors proposed that the effective Weibull modulus increases with increasing component volume. This implies a diminished size effect. However, these current bundle theories are predicated on the fact that fibers are inherently much stronger and stiffer than the matrix. In laminated CMC materials this is not always the case. The strength and stiffness of both the fiber and matrix are usually closer in magnitude. For this reason bundle theories will not be considered in this paper.

We advocate the use of a weakest-link reliability theory for designing components manufactured from laminated CMC materials that do not exhibit strong size effects in specific directions. Assuming that a laminated structure behaves in a weakest-link manner allows a conservative estimate of structural reliability to be calculated. Thomas and Wetherhold (1990) point out that this assumption is equivalent to predicting the probability of the first matrix crack occurring in an individual ply. For most applications the design failure stress for a laminated material is assumed to coincide with this first ply matrix cracking because matrix cracking usually allows the fibers to oxidize at high temperatures, embrittling the composite.

Next, we address the righteousness of applying weakest-link theory to a material that in some sense does not exhibit size effects. In general, the mean strength of a sample population representing uniaxial tension test specimens can be obtained by integrating the probability of survival P_s with respect to the applied tensile stress; that is,

$$\bar{\sigma} = \int_0^{\infty} P_s d\sigma \quad (1)$$

Here $\bar{\sigma}$ is the mean tensile strength, σ is the applied tensile

stress, and P_s is the probability of survival. The form of P_s depends on the probability density function that best represents the failure data, which in turn depends on whether the structural component acts as a parallel or series system. Adopting a three-parameter Weibull cumulative distribution function, and assuming a weakest-link system (a conservative assumption) gives the following form to Eq. (1):

$$\bar{\sigma} = \int_{\gamma}^{\infty} \exp \left[- \left(\frac{\sigma - \gamma}{\beta} \right)^{\alpha} V \right] d\sigma \quad (2)$$

Here V is the volume of the tensile test specimen, β is the scale parameter, α is the Weibull shape parameter, and γ is the threshold stress. This integral has the following closed-form solution (see DeSalvo, 1970):

$$\bar{\sigma} = \gamma + \left[\frac{\beta}{(V)^{1/\alpha}} \right] \Gamma \left(1 + \frac{1}{\alpha} \right) \quad (3)$$

which depends on volume, the Weibull parameters, and the gamma function Γ . When an argument originally outlined by Jayatilaka (1979) is followed, two uniaxial tensile specimen populations with distinctly different specimen volumes will yield different mean strengths. Associating $\bar{\sigma}_1$ with V_1 gives

$$\bar{\sigma}_1 = \gamma + \left[\frac{\beta}{(V_1)^{1/\alpha}} \right] \Gamma \left(1 + \frac{1}{\alpha} \right) \quad (4)$$

Similarly associating $\bar{\sigma}_2$ with V_2 gives

$$\bar{\sigma}_2 = \gamma + \left[\frac{\beta}{(V_2)^{1/\alpha}} \right] \Gamma \left(1 + \frac{1}{\alpha} \right) \quad (5)$$

If the effective mean is defined as

$$(\bar{\sigma})_{\text{eff}} = \bar{\sigma} - \gamma \quad (6)$$

then the ratio of the effective mean strengths depends only on the specimen volume and the Weibull modulus; that is,

$$\frac{(\bar{\sigma}_1)_{\text{eff}}}{(\bar{\sigma}_2)_{\text{eff}}} = \frac{\bar{\sigma}_1 - \gamma}{\bar{\sigma}_2 - \gamma} = \left(\frac{V_2}{V_1} \right)^{1/\alpha} \quad (7)$$

As the Weibull modulus of a particular material increases, the ratio of the effective mean strengths approaches unity. In this situation the material exhibits no size effect (even though the distribution of failure strength may be represented by a Weibull probability density function). From a practical standpoint, doubling the specimen size of a material whose Weibull modulus is ≈ 15 would yield less than a 5 percent difference in the effective mean failure strengths of the two populations. We expect an elevated Weibull modulus to be associated with the strength of CMC materials in the fiber direction. Reports of an apparent lack of size effect associated with the strength in the fiber direction (see DiCarlo, 1989) could easily be an artifact of an increasing shape parameter (or small sample size). However, at this time there is an insufficient quantity of CMC failure data from which to estimate the Weibull parameters. In general, the weakest-link theory allows for diminishing size effects as the Weibull modulus increases.

Reliability Model

The ongoing metamorphosis of ceramic material systems and the lack of standardized design data have in the past tended to minimize the emphasis on modeling. Many structural components fabricated from ceramic materials were designed by "trial and error," since emphasis was placed on demonstrating feasibility rather than on fully understanding the processes controlling behavior. (This is understandable during periods of rapid improvements in material properties for any system.) In predicting failure behavior, there is a philosophical division that separates analytical schools of thought into microstructural methods (usually based on principles of fracture mechanics) and phenomenological methods. Blass and Ruggles

(1990) point out that analysts from the first school would design the material assuming that the constituents are distinct structural components and would consider the composite ply (or lamina) a structure in its own right. Analysts from the latter school of thought would design with the material (i.e., they would analyze structural components fabricated from the material). Rigorous fracture mechanics criteria have been proposed (e.g., Budiansky et al., 1986; Marshall et al., 1985) that adopt the microstructural viewpoint, but since they are all deterministic criteria, they will not be considered here. Fracture mechanics has been combined with a probabilistic Weibull analysis of failure location to determine the stress-strain behavior and subsequent work of fracture for unidirectional composites (e.g., Thouless and Evans, 1988; Sutcu, 1989). However, the focus here is first matrix cracking, and we note that mature reliability-based design methods using fracture mechanics concepts will not surface until a coherent mixed-mode fracture criterion has been proposed.

The aforementioned second school of thought represents the ply (or lamina) as a homogenized material with strength properties that are determined from a number of well-planned phenomenological experiments. The authors currently embrace this philosophy, and there are practical reasons for initially adopting this viewpoint. We fully recognize that the failure characteristics of these composites are controlled by a number of local phenomena, including matrix cracking, debonding and slipping between matrix and fibers, and fiber breakage, all of which interact strongly. Understanding the underlying analytical concepts associated with the microstructural viewpoint allows one to gain insight and intuition prior to constructing multiaxial failure theories that in some respect reflect the local behavior. Tensile failure in the fiber direction is dependent on these local mechanisms, and the future intent is to extend reliability methods to the constituent level in a rational and practical manner. However, a top-down approach, that is first proposing design models at the ply level, will establish viable and working design protocols. Initially adopting the bottom-up approach allows for the possibility of becoming mired in detail (experimental and analytical) when multiaxial reliability analyses are conducted at the constituent level.

There is a great deal of intrinsic variability in the strength of each brittle constituent of a ceramic matrix composite, but depending on the composite system, the transverse matrix cracking strength may either be deterministic or probabilistic. Statistical models are a necessity for those composite systems that exhibit any scatter in the initiation of first matrix cracking. We treat it in a probabilistic fashion, requiring that deterministic strength be a limiting case that is readily obtainable from the proposed reliability model. Predicting the reduction in reliability due to loads in the fiber direction addresses an upper bound for ply reliability in a structural design problem. Conversely, a tensile load applied transverse to the fiber direction results in failure behavior similar to a monolithic ceramic, which corresponds to the lower bound of ply reliability. Thus multiaxial design methods must be capable of predicting these two bounds as well as account for the reduction in reliability due to an in-plane shear stress, and compressive stresses in the fiber direction and transverse to the fiber direction.

A number of macroscopic theories exist that treat unidirectional composites as homogenized, anisotropic materials. These methods use phenomenological strength data directly without hypothesizing specific crack shapes or distributions. Theories of this genre generally are termed noninteractive if individual stress components are compared to their strengths separately. In essence, failure mechanisms are assumed not to interact, and this results in component reliability computations that are quite tractable. Work by Thomas and Wetherhold (1990), Duffy and Arnold (1990), Duffy and Manderscheid (1990), and Duffy et al. (1990) is representative of multiaxial noninteractive reliability models for anisotropic materials. In ad-

dition Wu (1989), and Hu and Goetschel (1989) have proposed simpler unidirectional reliability models for laminated composites that can be classified as noninteractive. Alternatively, one can assume that for multiaxial states of stress, failure mechanisms interact and depend on specific stochastic combinations of material strengths. Usually a failure criterion is adapted from existing polymer matrix design technologies. The probability that the criterion has been violated for a given stress state is computed using Monte Carlo methods (de Roo and Paluch, 1985) or first-order-second-moment (FOSM) methods (Yang, 1989; Miki et al., 1989). The interactive approach often results in computationally intensive reliability predictions.

In this paper a noninteractive phenomenological approach has been chosen such that a unidirectional ply is considered a two-dimensional structure, assumed to have five basic strengths (or failure modes). They include a tensile and compressive strength in the fiber direction, a tensile and compressive strength in the direction transverse to the fiber direction, and an in-plane shear strength. In addition each ply is discretized into individual sub-ply volumes. For reasons discussed in the previous section we assume that failure of a ply is governed by its weakest link (or sub-ply volume). Under this assumption, events leading to failure of a given link do not affect other links (see, for example, Batdorf and Heinisch, 1978; Wetherhold, 1983; Cassenti, 1984); thus the reliability of the i th ply is given by the following expression:

$$R_i = \exp \left(- \int_V \psi_i dV \right) \quad (8)$$

where V is the component volume. Here, $\psi_i(x_j)$ is the failure function per unit volume at position x_j within the ply, given by

$$\psi_i = \left[\frac{\langle \sigma_1 - \gamma_1 \rangle}{\beta_1} \right]^{\alpha_1} + \left[\frac{|\tau_{12} - \gamma_2|}{\beta_2} \right]^{\alpha_2} + \left[\frac{\langle \sigma_2 - \gamma_3 \rangle}{\beta_3} \right]^{\alpha_3} + \left[\frac{\langle (-1)(\sigma_1 + \gamma_4) \rangle}{\beta_4} \right]^{\alpha_4} + \left[\frac{\langle (-1)(\sigma_2 + \gamma_5) \rangle}{\beta_5} \right]^{\alpha_5} \quad (9)$$

The α 's associated with each term in Eq. (9) correspond to the Weibull shape parameters, the β 's correspond to Weibull scale parameters, and the γ 's correspond to the Weibull threshold stresses. In addition, σ_1 and σ_2 represent the in-plane normal stresses that are aligned with and transverse to the fiber direction, respectively. Also, τ_{12} is the in-plane shear stress. The normal stresses appear twice, and this allows for different failure modes to emerge in tension and compression. Note that the brackets indicate a unit step function; i.e.,

$$\langle x \rangle = x \cdot u[x] = \begin{cases} x & x > 0 \\ 0 & x \leq 0 \end{cases} \quad (10)$$

Inserting Eq. (9) into the volume integration given by Eq. (8) yields the reliability of the i th ply, and the probability of first ply failure for the laminate is given by the expression

$$P_{fpf} = 1 - \prod_{i=1}^n R_i \quad (11)$$

where n is the number of plies.

This reliability model can be readily integrated with laminate analysis options available in several commercial finite element codes. A preliminary version of a public domain computer algorithm (C/CARES) that is coupled with MSC/NASTRAN has been developed at NASA Lewis Research Center to perform this analysis. A simple benchmark application illustrates the approach. A thin-wall tube is subjected to an internal pressure and an axial compressive load. The component is fabricated from a three-ply laminate, with a $90^\circ/\theta/90^\circ$ layup. Here angle θ is measured relative to the longitudinal axis of

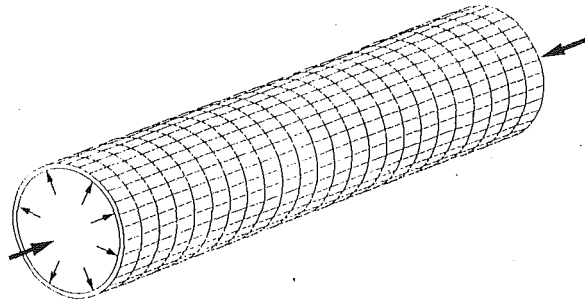


Fig. 1 Finite element mesh of thin-wall tube with three-ply (90°/0°/90°) layup; internal pressure, 4.25 MPa; axial compressive stress, 87.5 MPa

Table 1 Composite Weibull parameters for thin-wall tube [Weibull threshold stress, $\gamma_i = 0$]

Index ^a	Type and direction of stress	Weibull parameters	
		Shape, α_i	Scale, β_i
1	Normal tensile stress in fiber direction	25	450
2	In-plane shear stress	22	420
3	Normal tensile stress transverse to fiber direction	10	350
4	Normal compressive stress in fiber direction	35	4500
5	Normal compressive stress transverse to fiber direction	30	3500

^aIndices correspond to subscripts in Eq. (9).

the tube (see Fig. 1). An arbitrary internal pressure of 4.25 MPa and an axial compressive stress of 87.5 MPa were applied to the tube. The Weibull parameters were also arbitrarily chosen (see Table 1). Note that the threshold stresses are taken as zero for simplicity. In design, setting the threshold stresses equal to zero would represent a conservative assumption. The overall component reliability is depicted as a function of the midply orientation angle (θ) in Fig. 2. The ply orientation has a decided effect on component reliability, as expected. Similar studies could demonstrate the effects of component geometry, ply thickness, load, and/or Weibull parameters on component reliability. Hence, the C/CARES code allows the design engineer a wide latitude to optimize a component relative to a number of design parameters.

Parameter Estimation

We anticipate that laminated CMC materials will exhibit threshold behavior, at least in the fiber direction. Hence, a three-parameter Weibull distribution is used in the stochastic failure analysis of the components. The threshold stress parameter is included to allow for zero probability of failure when the load is below a predetermined level. The three-parameter distribution has been somewhat ignored due to difficulties encountered in extracting the parameters from experimental data. Several authors (including Weibull, 1939; Weil and Daniel, 1964; Schneider and Palazotto, 1979) have proposed estimation methods for the three-parameter distribution. For various reasons, these techniques have not been widely accepted. However, Cooper (1988) recently proposed a nonlinear regression method to estimate parameters. Regression analysis postulates a relationship between two variables. In an experiment, typically one variable can be controlled (the independent variable) while the response variable (or dependent variable) is uncontrolled. In simple failure experiments the material dictates the strength at failure, indicating that the failure stress is the response variable. The ranked probability of failure Φ_i can be controlled by the experimentalist since it is functionally dependent on the sample size N . If the observed failure stresses ($\sigma_1, \sigma_2, \sigma_3, \dots, \sigma_N$) are placed in ascending order, then

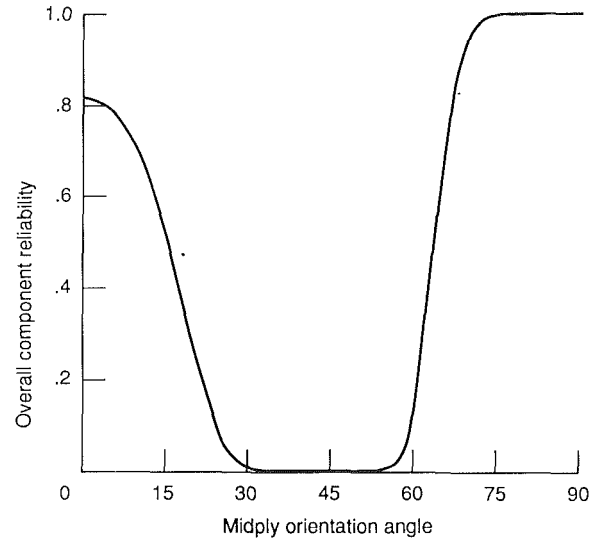


Fig. 2 Component reliability versus midply orientation angle for thin wall tube

$$\Phi_i(\sigma_i) = \frac{i - 0.3}{N + 0.4} \quad (12)$$

Clearly one can influence the ranked probability for a given stress level by increasing or decreasing the sample size. Cooper's procedure adopts this philosophy, and the specimen failure stress is treated as the dependent variable. The associated ranked probability of failure then becomes the independent variable. The basic three-parameter Weibull expression for probability of failure can be expressed as

$$\tilde{\sigma}_i = \tilde{\gamma} + \tilde{\beta} \left[\ln \left(\frac{1}{1 - \Phi_i} \right) \right]^{1/\tilde{\alpha}} \quad (13)$$

where $\tilde{\sigma}_i$ is an estimate of the dependent variable, and $\tilde{\gamma}$, $\tilde{\beta}$, and $\tilde{\alpha}$ are estimates of the threshold parameter, the characteristic strength, and the shape parameter, respectively. Defining

$$\delta_i = \tilde{\sigma}_i - \sigma_i \quad (14)$$

as the i th residual, where as before σ_i is the i th failure stress, then

$$\sum_{i=1}^N (\delta_i)^2 = \sum_{i=1}^N (\tilde{\gamma} + \tilde{\beta} W_i^{1/\tilde{\alpha}} - \sigma_i)^2 \quad (15)$$

where we adopt Cooper's notation and take

$$W_i = \ln \left(\frac{1}{1 - \Phi_i} \right) \quad (16)$$

Setting the partial derivatives of the sum of the squares of the residuals with respect to $\tilde{\gamma}$, $\tilde{\beta}$, and $\tilde{\alpha}$ equal to zero yields the following three expressions:

$$\tilde{\beta} = \frac{N \left[\sum_{i=1}^N \sigma_i (W_i)^{1/\tilde{\alpha}} \right] - \left[\sum_{i=1}^N \sigma_i \right] \left[\sum_{i=1}^N (W_i)^{1/\tilde{\alpha}} \right]}{N \sum_{i=1}^N (W_i)^{2/\tilde{\alpha}} - \left[\sum_{i=1}^N (W_i)^{1/\tilde{\alpha}} \right] \left[\sum_{i=1}^N (W_i)^{1/\tilde{\alpha}} \right]} \quad (17)$$

$$\tilde{\gamma} = \frac{\left[\sum_{i=1}^N (W_i)^{2/\tilde{\alpha}} \right] \left[\sum_{i=1}^N \sigma_i \right] - \left[\sum_{i=1}^N \sigma_i (W_i)^{1/\tilde{\alpha}} \right] \left[\sum_{i=1}^N (W_i)^{1/\tilde{\alpha}} \right]}{N \sum_{i=1}^N (W_i)^{2/\tilde{\alpha}} - \left[\sum_{i=1}^N (W_i)^{1/\tilde{\alpha}} \right] \left[\sum_{i=1}^N (W_i)^{1/\tilde{\alpha}} \right]} \quad (18)$$

Table 2 Monolithic alumina failure data^a

Specimen number	Stress, MPa	Specimen number	Stress, MPa	Specimen number	Stress, MPa	Specimen number	Stress, MPa
1	307	10	337	19	357	28	385
2	308	11	343	20	364	29	388
3	322	12	345	21	371	30	395
4	328	13	347	22	373	31	402
5	328	14	350	23	374	32	411
6	329	15	352	24	375	33	413
7	331	16	353	25	376	34	415
8	332	17	355	26	376	35	456
9	335	18	356	27	381		

^aFor specimen shown in Fig. 3.

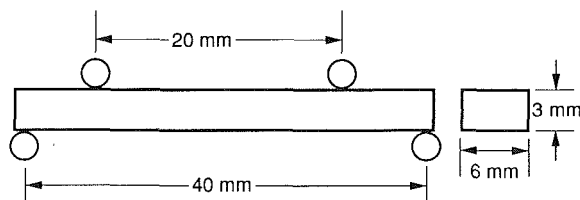


Fig. 3 Monolithic alumina specimen geometry

Number of parameters	Shape, α	Weibull parameters Scale, β	Threshold stress, γ
3	1.15	803.41	298.48
2	13.2	376.0	
○	Data (35 points)		

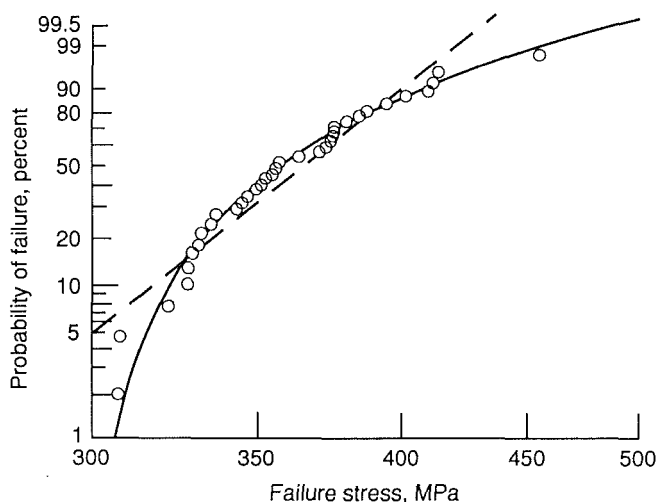


Fig. 4 Two-parameter and three-parameter distributions determined from the alumina failure

and

$$\sum_{i=1}^N \sigma_i (W_i)^{1/\tilde{\alpha}} \ln(W_i) = \tilde{\gamma} \sum_{i=1}^N (W_i)^{1/\tilde{\alpha}} \ln(W_i) + \tilde{\beta} \sum_{i=1}^N (W_i)^{2/\tilde{\alpha}} \ln(W_i) \quad (19)$$

in terms of the parameter estimates. The solution of this system of equations is iterative. One assumes an initial value for $\tilde{\alpha}$ (a small value, usually equal to 1), computes $\tilde{\beta}$ from Eq. (17) and $\tilde{\gamma}$ from Eq. (18). These values of the parameter estimates are then inserted into Eq. (19), and this expression is checked to

see if it satisfies some predetermined tolerance. If Eq. (19) is not satisfied, $\tilde{\alpha}$ is increased and a new iteration is conducted. This procedure continues until a set of parameter estimates are determined that satisfy Eqs. (17)–(19).

Currently we do not have enough CMC failure data to estimate Weibull parameters for a given material orientation. So to illustrate the technique, parameter estimates were determined for two-parameter and three-parameter distributions from a failure population representing a monolithic ceramic (alumina) reported by Quinn (1989). The failure data and specimen geometry are shown in Table 2 and Fig. 3. Figure 4 is a plot of probability of failure versus failure stress for the data. The straight line represents the two-parameter fit to the data, using Quinn's (1989) values for the shape and scale parameters. The nonlinear curve represents the three-parameter fit to the data. Note that the three-parameter distribution is more efficient in predicting the failure data in the high reliability region.

Summary and Future Directions

In this paper we discuss stochastic issues related to size effects in the fiber direction of a unidirectional CMC material. In addition, we present a reliability model along with a simple application that highlighted the C/CARES computer algorithm. (This public domain algorithm is capable of predicting component reliability from the state of stress and temperature distribution within the component.) The authors anticipate that CMC materials will exhibit threshold behavior; hence a nonlinear regression analysis was outlined to determine three parameters for a Weibull distribution from failure data.

Ceramic material systems will play a significant role in future elevated-temperature applications. To this end, there are a number of issues that must be addressed by the structural mechanics research community. We begin by pointing out that total failure of an individual ply effectively reduces the overall laminate stiffness. This causes local redistribution of the load to adjacent layers. In addition, delamination between plies relaxes the constraining effects among layers, allowing in-plane strains to vary in a stepwise fashion within a laminate. These effects require the development of rational load redistribution schemes. It is also apparent that before ceramics are used as structural components in harsh service environments, thoughtful consideration should be given to reliability degradation due to time-dependent phenomena. Thus, issues germane to component life, such as cyclic fatigue and creep behavior, must be addressed analytically. Computational strategies are needed to extend current methods of analysis from subcritical crack growth and creep rupture to laminated CMC materials that are subject to multiaxial states of stress.

An important aspect that has not been addressed in detail is the effect of a rising *R*-curve behavior, where fracture toughness is a function of crack size. Clearly fiber-toughened ma-

trices have process zones around the crack tip. Within this zone, energy dissipates locally, which develops a damage tolerance by increasing the resistance to crack growth with crack extension. Failure of materials exhibiting *R*-curve behavior would depend on the rate at which resistance increases with crack growth. During crack extension this behavior would modify the strength distribution. Modeling efforts by Kendall et al. (1986) and others have accounted for this behavior in monolithic ceramics, and it is reasonable to extend their work to ceramic composite material systems. Furthermore, if ceramic materials mimic ductile failure locally, cyclic fatigue may become a design issue. Under cyclic loads, the process zone advances as the crack tip extends; therefore, brittle fracture mechanics may need to be modified to account for pseudo-ductile fracture. Hence, application of modified metallic fatigue analyses may be a distinct possibility.

In addition, recent progress in processing ceramic material systems has not been matched by mechanical testing efforts. There is a definite need for experiments that support the development of reliability models. Initially this effort should include experiments that test the fundamental concepts (e.g., quantifying the size effect in the fiber direction) within the framework of current stochastic models. For example, probing experiments could be conducted along various biaxial load paths to establish level surfaces of reliability in a particular two-dimensional stress space (similar to probing yield surfaces in metals). One could then verify such concepts as the maximum stress response, which is often assumed in the noninteractive reliability models proposed for these materials. After establishing a theoretical framework, characterization tests should then be conducted to provide the functional dependence of model parameters with respect to temperature and environment. Finally data from structural tests that are multiaxial (and possibly nonisothermal) would be used to challenge the predictive capabilities of models through comparison to benchmark response data. These tests involve nonhomogeneous fields of stress, deformation, and temperature, and would include two-bar tests as well as plate and shell structures. Results from structural testing provide feedback for subsequent modification, but ad hoc models result in the absence of structured interaction between the experimentalist and the theoretician. The validity of these models is then forever open to question. Furthermore, we cannot overemphasize that this kind of testing supports methods for designing components, not the materials. Currently this effort is hampered by the quality and scarcity of data (note the lack of failure data necessary to estimate composite Weibull parameters). Finally, ceramic properties pertinent to structural design (which include stochastic parameters) vary with test methods. The mechanics research community is beginning to realize this, and a consensus is beginning to form regarding standards. However, we wish to underscore the fundamental need for experimental programs that are relevant to structural mechanics issues.

In closing, we recognize that when failure is less sensitive to imperfections in the material, stochastic methods may not be as essential. Yet, trends in design protocols are moving in the direction of probabilistic analyses (even for metals) and away from the simplistic safety-factor approach. In this sense, brittle ceramics will serve as prototypical materials in the study and development of reliability models that will act as the basis of future design codes.

References

- Batdorf, S. B., and Heinisch, H. L., Jr., 1978, "Weakest Link Theory Reformulation for Arbitrary Fracture Criterion," *Journal of the American Ceramic Society*, Vol. 61, pp. 355–358.
- Batdorf, S. B., 1982, "Tensile Strength of Unidirectionally Reinforced Composites—I," *Journal of Reinforced Plastics and Composites*, Vol. 1, No. 2, pp. 153–164.
- Batdorf, S. B., and Ghaffarian, R., 1984, "Size Effect and Strength Variability of Unidirectional Composites," *International Journal of Fracture*, Vol. 26, pp. 113–123.
- Blass, J. J., and Ruggles, M. B., 1990, "Design Methodology Needs for Fiber-Reinforced Ceramic Heat Exchangers," ORNL/TM-11012, Oak Ridge National Lab., TN.
- Budiansky, B., Hutchinson, J. W., and Evans, A. G., 1986, "Matrix Fracture in Fiber-Reinforced Ceramics," *Journal of the Mechanics and Physics of Solids*, Vol. 34, No. 2, pp. 167–189.
- Cassenti, B. N., 1984, "Probabilistic Static Failure of Composite Material," *AIAA Journal*, Vol. 22, No. 1, pp. 103–110.
- Coleman, B. D., 1958, "On the Strength of Classical Fibers and Fiber Bundles," *Journal of the Mechanics and Physics of Solids*, Vol. 7, No. 1, pp. 66–70.
- Cooper, N. R., 1988, "Probabilistic Failure Prediction of Rocket Motor Components," PhD Thesis, Royal Military College of Science (Avail. Univ. Microfilms Inc.).
- Daniels, H. E., 1945, "The Statistical Theory of the Strength of Bundles of Threads," *Proceedings of the Royal Society of London, Series A*, Vol. 183, No. 995, pp. 405–435.
- de Roo, P., and Paluch, B., 1985, "Application of a Multiaxial Probabilistic Failure Criterion to a Unidirectional Composite," *Developments in the Science and Technology of Composite Materials*, A. R. Bunsell, P. Lamicq, and A. Massiah, eds., Association Européenne des Matériaux Composites, Bordeaux, pp. 328–334.
- DeSalvo, G. J., 1970, "Theory and Structural Design Applications of Weibull Statistics," WNL-TME-2688, Westinghouse Astronuclear Laboratory.
- DiCarlo, J. A., 1989, "CMC's for the Long Run," *Advanced Materials and Processes*, Vol. 135, No. 6, pp. 41–44.
- Duffy, S. F., and Arnold, S. M., 1990, "Noninteractive Macroscopic Reliability Model for Whisker Reinforced Ceramic Composites," *Journal of Composite Materials*, Vol. 24, No. 3, pp. 293–308.
- Duffy, S. F., and Mandersheid, J. M., 1990, "Noninteractive Macroscopic Reliability Model for Ceramic Matrix Composites With Orthotropic Material Symmetry," *ASME JOURNAL OF ENGINEERING FOR GAS TURBINES AND POWER*, Vol. 112, No. 4, pp. 507–511.
- Duffy, S. F., Wetherhold, R. C., and Jain, L. K., 1990, "Extension of a Noninteractive Reliability Model for Ceramic Matrix Composites," NASA CR-185267.
- Harlow, D. G., and Phoenix, S. L., 1978, "The Chain-of-Bundles Probability Model for the Strength of Fibrous Materials—I. Analysis and Conjectures," *Journal of Composite Materials*, Vol. 12, No. 2, pp. 195–214.
- Hu, T. G., and Goetschel, D. B., 1989, "The Application of the Weibull Strength Theory to Advanced Composite Materials," *Tomorrow's Materials: Today*, Vol. 1, Proceedings of the 34th International SAMPE Symposium and Exhibition, G. A. Zakrzewski et al., eds., SAMPE, Covina, CA, pp. 585–599.
- Jayatilaka, A. S., 1979, *Fracture of Engineering Brittle Materials*, Applied Science Publishers, London, United Kingdom, pp. 249–257.
- Kendall, K., Alford, N. M., Tan, S. R., and Birchall, J. D., 1986, "Influence of Toughness on Weibull Modulus of Ceramic Bending Strength," *Journal of Materials Research*, Vol. 1, No. 1, pp. 120–123.
- Marshall, D. B., Cox, B. N., and Evans, A. G., 1985, "The Mechanics of Matrix Cracking in Brittle Matrix Fiber Composites," *Acta Metallurgica*, Vol. 33, No. 11, pp. 2013–2021.
- Miki, M., Murotsu, Y., Tanaka, T., and Shao, S., 1989, "Reliability of the Strength of Unidirectional Fibrous Composites," *30th Structures, Structural Dynamics and Materials Conference*, Part 2, AIAA, Washington, DC, pp. 1032–1040.
- Quinn, G. D., 1989, "Flexure Strength of Advanced Ceramics—A Round Robin Exercise," MTL TR-89-62 (Avail. NTIS, AD-A212101).
- Rosen, B. W., 1964, "Tensile Failure of Fibrous Composites," *AIAA Journal*, Vol. 2, No. 11, pp. 1985–1991.
- Schneider, D., and Palazotto, A. N., 1979, "A Technique for Evaluating a Unique Set of Three Weibull Parameters Considering Composite Materials," *Fibre Science and Technology*, Vol. 12, No. 4, pp. 269–281.
- Sutcu, M., 1989, "Weibull Statistics Applied to Fiber Failure in Ceramic Composites and Work of Fracture," *Acta Metallurgica*, Vol. 37, No. 2, pp. 651–661.
- Thomas, D. J., and Wetherhold, R. C., 1990, "Reliability Analysis of Continuous Fiber Composite Laminates," NASA CR-185265.
- Thouless, M. D., and Evans, A. G., 1988, "Effects of Pull-Out on the Mechanical Properties of Ceramic-Matrix Composites," *Acta Metallurgica*, Vol. 36, No. 3, pp. 517–522.
- Weibull, W. A., 1939, "Statistical Theory of the Strength of Materials," *Ingenjors Vetenskaps Akademiens Handlingar*, No. 151.
- Weil, N. A., and Daniel, I. M., 1964, "Analysis of Fracture Probabilities in Nonuniformly Stressed Brittle Materials," *Journal of the American Ceramic Society*, Vol. 47, No. 6, pp. 268–274.
- Wetherhold, R. C., 1983, "Statistics of Fracture of Composite Material Under Multiaxial Loading," PhD Dissertation, University of Delaware.
- Wu, H. F., 1989, "Statistical Analysis of Tensile Strength of ARALL Laminates," *Journal of Composite Materials*, Vol. 23, No. 10, pp. 1065–1080.
- Yang, L., 1989, "Reliability of Composite Laminates," *Mechanics of Structures and Machines*, Vol. 16, No. 4, pp. 523–536.
- Zweiben, C., 1968, "Tensile Failure of Fiber Composites," *AIAA Journal*, Vol. 6, No. 12, pp. 2325–2331.

S. F. Duffy

NASA Resident Research Associate.

L. M. Powers

NASA Resident Research Associate.

Cleveland State University,
Cleveland, OH 44115

A. Starlinger

National Research Council
NASA Research Associate,
NASA Lewis Research Center,
Cleveland, OH 44135

Reliability Analysis of Structural Ceramic Components Using a Three-Parameter Weibull Distribution

This paper describes nonlinear regression estimators for the three-parameter Weibull distribution. Issues relating to the bias and invariance associated with these estimators are examined numerically using Monte Carlo simulation methods. The estimators were used to extract parameters from sintered silicon nitride failure data. A reliability analysis was performed on a turbopump blade utilizing the three-parameter Weibull distribution and the estimates from the sintered silicon nitride data.

Introduction

To date, most reliability analyses performed on structural components fabricated from ceramic materials have utilized the two-parameter form of the Weibull distribution. The use of a two-parameter Weibull distribution to characterize the random nature of material strength implies a nonzero probability of failure for the full range of applied stress. This represents a conservative design assumption when analyzing structural components. A three-parameter form of the Weibull distribution is available. The additional parameter is a threshold stress that allows for zero probability of failure when applied stress is at or below the threshold value. By employing the concept of a threshold stress, design engineers can effectively tailor the design of a component to optimize structural reliability.

Difficulties in estimating parameters as well as a lack of strength data with corresponding fractographic analysis has limited the use of this distribution. Several authors (including Weibull, 1939; Weil and Daniel, 1964; Schneider and Palazotto, 1979) have proposed estimation methods for the three-parameter distribution. For various reasons these techniques have not been widely utilized. The nonlinear regression method proposed by Margetson and Cooper (1984) is adopted here to establish estimators for the three-parameter Weibull formulation. Estimators are applied using failure data obtained from the open literature. Specifically, Weibull parameters are estimated from failure data reported by Chao and Shetty (1991). The data were generated from test specimens fabricated from a monolithic silicon nitride. Strength tests were conducted on this material using three-point bend, four-point bend, and pressurized-disk specimen geometries. Here the Weibull pa-

rameters are estimated from the four-point bend test data, and failure data from the three-point bend tests and pressurized-disk tests are subsequently used to challenge structural reliability predictions made for these latter two geometries. To conduct structural reliability analyses, the three-parameter Weibull distribution was embedded in a reliability model known as the principle of independent action (PIA). We point out that the three-parameter form of the Weibull distribution can be extended to Batdorf's (1974, 1978) model and reliability models proposed for ceramic matrix composites (see Duffy et al., 1993; or Thomas and Wetherhold, 1991). All reliability computations presented here were made utilizing the integrated design program CARES (Ceramic Analysis and Reliability Evaluation of Structures) (Nemeth et al., 1990).

In general, the objective of parameter estimation is the derivation of functions (or estimators) that are dependent on the failure data and that yield, in some sense, optimum estimates of the underlying population parameters. Various performance criteria can be applied to ensure that optimized estimates are obtained consistently. Two important performance criteria are estimate invariance and estimate bias. An estimator is invariant if the bias associated with the estimated value is independent of the true parameters that characterize the underlying population. Bias is a measure of deviation of the estimated parameter from the true population parameter. Here the functional value of an estimator is a point estimate (in contrast to an interval estimate) of the true population parameter. The values of the point estimates computed from a number of samples obtained from a population will vary from sample to sample. A sample is defined as a collection (i.e., more than one) of observations taken from a specified population, and a population represents the totality of all possible observations about which statistical inferences could be made. In this paper, the observations are the failure strengths of test specimens fabricated from ceramic materials. The issues of bias and invariance and their relationship to the functions proposed by

Contributed by the International Gas Turbine Institute and presented at the 37th International Gas Turbine and Aeroengine Congress and Exposition, Cologne, Germany, June 1-4, 1992. Manuscript received by the International Gas Turbine Institute, February 24, 1992. Paper No. 92-GT-296. Associate Technical Editor: L. S. Langston.

Margetson and Cooper (1984) are explored numerically. In the numerical studies, distributions of the point estimates are obtained by taking numerous samples from the population and computing point estimates as a function of sample size. If the mean of a distribution of such estimates is equal to the value of the true parameter for a given sample size, the associated estimator is said to be unbiased. If an estimator yields biased results, the value of the individual estimates can be corrected if the estimators are invariant (see Thoman et al., 1969, for the procedure associated with two-parameter maximum-likelihood estimators). The Monte Carlo simulations that are presented later demonstrate that the functions are neither invariant nor unbiased.

Estimating Weibull Distribution Parameters

Weibull (1939, 1951) proposed the first probabilistic model that accounted for scatter in failure strength and the size effect encountered in structural components fabricated from brittle materials. His approach is based on the weakest link theory (WLT) attributed to Midgley and Pierce (1926). This earlier research (sponsored by the textile industry) focused on modeling yarn strength. Unlike Midgely and Pierce, who assumed a Gaussian distribution for yarn strength, Weibull proposed a unique probability density function for failure strength that now bears his name. Weibull's three-parameter probability density function has the following form:

$$f(x) = \left(\frac{\alpha}{\eta}\right) \left(\frac{x-\lambda}{\eta}\right)^{(\alpha-1)} \exp\left(-\left(\frac{x-\lambda}{\eta}\right)^\alpha\right) \quad (1)$$

for a continuous random variable x , when $0 \leq \lambda < x$, and

$$f(x) = 0 \quad (2)$$

for $x \leq \lambda$. The cumulative distribution function is given by the expression

$$F(x) = 1 - \exp\left(-\left(\frac{x-\lambda}{\eta}\right)^\alpha\right) \quad (3)$$

for $x > \lambda$, and

$$F(x) = 0 \quad (4)$$

for $x \leq \lambda$. Here $\alpha(>0)$ is the Weibull modulus (or the shape parameter), $\eta(>0)$ is the scale parameter, and $\lambda(>0)$ is the threshold parameter. When applied to analyses of structural components, the random variable x usually represents a component of the Cauchy stress tensor or an invariant of this tensor. For a uniaxial stress field in a homogeneous isotropic material, application of Weibull's theory yields the following expression for the probability of failure

$$\Phi = 1 - \exp(-B) \quad \sigma > \gamma \quad (5)$$

where

$$B = \int_V \left(\frac{\sigma - \gamma}{\beta}\right)^\alpha dV \quad (6)$$

and

$$\Phi = 0 \quad \sigma \leq \gamma \quad (7)$$

Note that α , β , and γ are material parameters and will not depend on the geometry of the test specimen. In this context β has the dimension of (stress) \cdot (volume) $^{1/\alpha}$, γ has the dimension of stress, and α is dimensionless.

Certain monolithic ceramics have exhibited threshold behavior (e.g., Quinn, 1989; Chao and Shetty, 1991). It is anticipated that ceramic matrix composites will similarly exhibit

this behavior (Duffy et al., 1993). Threshold behavior is demonstrated if the failure data display a nonlinear behavior when the ranked probability of failure (Φ_i) is represented as a function of the corresponding failure values. Careful fractography must yield clear evidence that only one type of defect is causing failure. Thus, the fractographic analysis must demonstrate that the nonlinear behavior of the failure data is not the result of competing failure mechanisms. When experimental data indicate the existence of a threshold stress, a three-parameter Weibull distribution should be employed in the stochastic failure analysis of structural components. However, the three-parameter form of the Weibull distribution has been somewhat ignored as a result of difficulties encountered in extracting estimates of the parameters from experimental data. Margetson and Cooper (1984) proposed a relatively simple nonlinear regression method to estimate the three distribution parameters. Regression analysis postulates a relationship between two variables. In an experiment, typically one variable can be controlled (the independent variable) while the response variable (or dependent variable) is uncontrolled. In simple failure experiments the material dictates the strength at failure, indicating that the failure stress is the response variable. The ranked probability of failure (Φ_i) can be controlled by the experimentalist since it is functionally dependent on the sample size (N). After numbering the observed failure stresses ($\sigma_1, \sigma_2, \sigma_3, \dots, \sigma_N$) in ascending order, and specifying

$$\Phi_i(\sigma_i) = (i - 0.5)/N \quad (8)$$

then clearly the ranked probability of failure for a given stress level can be influenced by increasing or decreasing the sample size. The procedure proposed by Margetson and Cooper (1984) adopts this philosophy. They assume that the specimen failure stress is the dependent variable, and the associated ranked probability of failure becomes the independent variable.

Using Eq. (5), an expression can be obtained relating the ranked probability of failure (Φ_i) to an estimate of the failure strength ($\hat{\sigma}_i$). Assuming uniaxial stress conditions in a test specimen with a unit volume, Eq. (5) yields

$$\hat{\sigma}_i = \hat{\gamma} + \hat{\beta}[\ln(1/1 - \Phi_i)]^{1/\hat{\alpha}} \quad (9)$$

where $\hat{\sigma}_i$ is an estimate of the ranked failure stress. In addition, $\hat{\alpha}$, $\hat{\beta}$, and $\hat{\gamma}$ are estimates of the shape parameter (α), the scale parameter (β), and the threshold parameter (γ), respectively. Defining the residual as

$$\delta_i = \hat{\sigma}_i - \sigma_i \quad (10)$$

where σ_i is the i th ranked failure stress obtained from actual test data, then the sum of the squared residuals is expressed as

$$\sum_{i=1}^N (\delta_i)^2 = \sum_{i=1}^N (\hat{\gamma} + \hat{\beta} W_i^{1/\hat{\alpha}} - \sigma_i)^2 \quad (11)$$

Here the notation of Margetson and Cooper (1984) is adopted where

$$W_i = \ln(1/1 - \Phi_i) \quad (12)$$

Note that the forms of $\hat{\sigma}_i$ and W_i change with specimen geometry (see the discussion in a later section relating to the four-point bend specimen geometry). It should be apparent that the objective of this method is to obtain parameter estimates that minimize the sum of the squared residuals. Setting the partial derivatives of the sum of the squares of the residuals with respect to $\hat{\alpha}$, $\hat{\beta}$, and $\hat{\gamma}$ equal to zero yields the following three expressions:

$$\hat{\beta} = \frac{N \left(\sum_{i=1}^N \sigma_i (W_i)^{1/\hat{\alpha}} \right) - \left(\sum_{i=1}^N \sigma_i \right) \left(\sum_{i=1}^N (W_i)^{1/\hat{\alpha}} \right)}{N \sum_{i=1}^N (W_i)^{2/\hat{\alpha}} - \left(\sum_{i=1}^N (W_i)^{1/\hat{\alpha}} \right) \left(\sum_{i=1}^N (W_i)^{1/\hat{\alpha}} \right)} \quad (13)$$

$$\hat{\gamma} = \frac{\left(\sum_{i=1}^N (W_i)^{2/\hat{\alpha}} \right) \left(\sum_{i=1}^N \sigma_i \right) - \left(\sum_{i=1}^N \sigma_i (W_i)^{1/\hat{\alpha}} \right) \left(\sum_{i=1}^N (W_i)^{1/\hat{\alpha}} \right)}{N \sum_{i=1}^N (W_i)^{2/\hat{\alpha}} - \left(\sum_{i=1}^N (W_i)^{1/\hat{\alpha}} \right) \left(\sum_{i=1}^N (W_i)^{1/\hat{\alpha}} \right)} \quad (14)$$

and

$$\left| \sum_{i=1}^N \sigma_i (W_i)^{1/\hat{\alpha}} \ln(W_i) - \hat{\gamma} \sum_{i=1}^N (W_i)^{1/\hat{\alpha}} \ln(W_i) - \hat{\beta} \sum_{i=1}^N (W_i)^{2/\hat{\alpha}} \ln(W_i) \right| \leq \kappa_{\text{conv}} \quad (15)$$

in terms of the parameter estimates. The solution of this system of equations is iterative. The third expression is used to check convergence of the iterative solution. The initial solution vector for this system is determined after assuming $\hat{\alpha} = 1$. Then $\hat{\beta}$ is computed from Eq. (13) and $\hat{\gamma}$ is calculated from Eq. (14). The values of these parameter estimates are then inserted into Eq. (15) to determine if the convergence criterion is satisfied to within some predetermined tolerance (κ_{conv}). If this expression is not satisfied, $\hat{\alpha}$ is updated and a new iteration is conducted. This procedure continues until a set of parameter estimates are determined that satisfy Eq. (15).

Bias and Invariance

Issues relating to estimate bias and invariance are examined numerically using Monte Carlo simulation methods. In this study uniform random numbers are generated in groups of N (which characterizes the sample size), and this is repeated 10,000 times for each value N . Each group of uniform random numbers is generated on the interval 0 to 1 using the Cray random number function RANGET. The uniform random number is converted to a strength observation by employing the inverse of the three-parameter Weibull distribution for failure strength given in Eq. (9). Defining $(S_i)_N$ as the i th random number on the interval 0 to 1 in a sample of size N , then the i th failure strength is

$$(\sigma_i)_N = \gamma + \beta \left[\ln \left(\frac{1}{1 - (S_i)_N} \right) \right]^{1/\alpha} \quad (16)$$

where α , β , and γ are the true distribution parameters of an infinite population characterized by a three-parameter Weibull distribution. Again, uniaxial stress conditions are imposed on a specimen of unit volume. However, this method can be extended to other specimen geometries as well.

Once a sample of N random numbers is generated and converted to failure strength observations, the estimators described by Eqs. (13)–(15) are used to obtain the point estimates $\hat{\alpha}$, $\hat{\beta}$, and $\hat{\gamma}$. Percentile distributions of the point estimates, as well as a mean value of the point estimates, can be constructed by repeating this sampling procedure for each value of N . Here the Monte Carlo simulations are carried out 10,000 times for each N . The arithmetic mean of each estimated parameter is a measure of the bias associated with the estimator in determining that parameter, and is usually characterized as a function of the sample size (N). This is depicted graphically in Fig. 1. In this figure the vertical axes represent a ratio of the point estimate value to the parameter true value used to generate the failure observations. The true population parameters are arbitrarily chosen, with $\alpha = 1.75$, $\beta = 1000$, and $\lambda = 300$. The horizontal axes represent the sample size N . Note that for all three estimators the mean value of the ratio approaches 1 for large values of N . Thus, each estimator exhibits the attractive property of decreasing bias with increasing sample size. However, the arithmetic mean associated with each

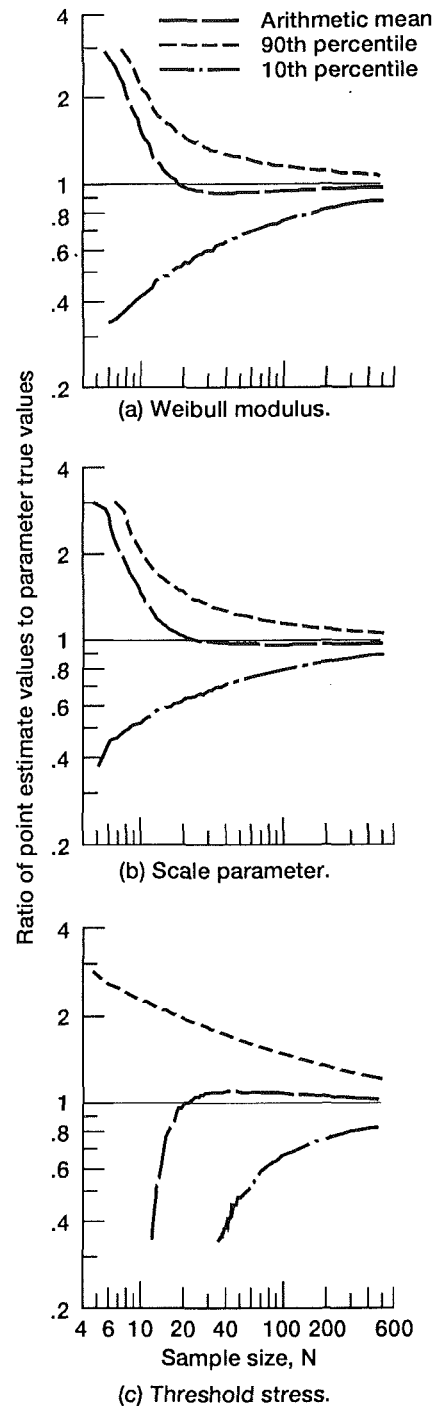


Fig. 1 Arithmetic mean values and percentile distributions of the ratio of the point estimate to the true population parameter for each estimator ($\alpha = 1.75$, $\beta = 1000$, $\gamma = 300$)

parameter is not invariant with respect to the underlying population parameter. This is evident in Fig. 2, which depicts the arithmetic mean values of the parameter estimates from the previous example along with arithmetic mean values from a second example. For the second sample, the true population parameter α has been increased such that $\alpha = 2.75$, and the other values of the true parameters are unchanged. Clearly the arithmetic means associated with the Weibull modulus (α), the scale parameter (β), and threshold stress (γ) change for sample sizes of less than 100. If the mean values remained invariant, then the three curves in each graph in Fig. 2 would coincide regardless of the values assumed for the true population pa-

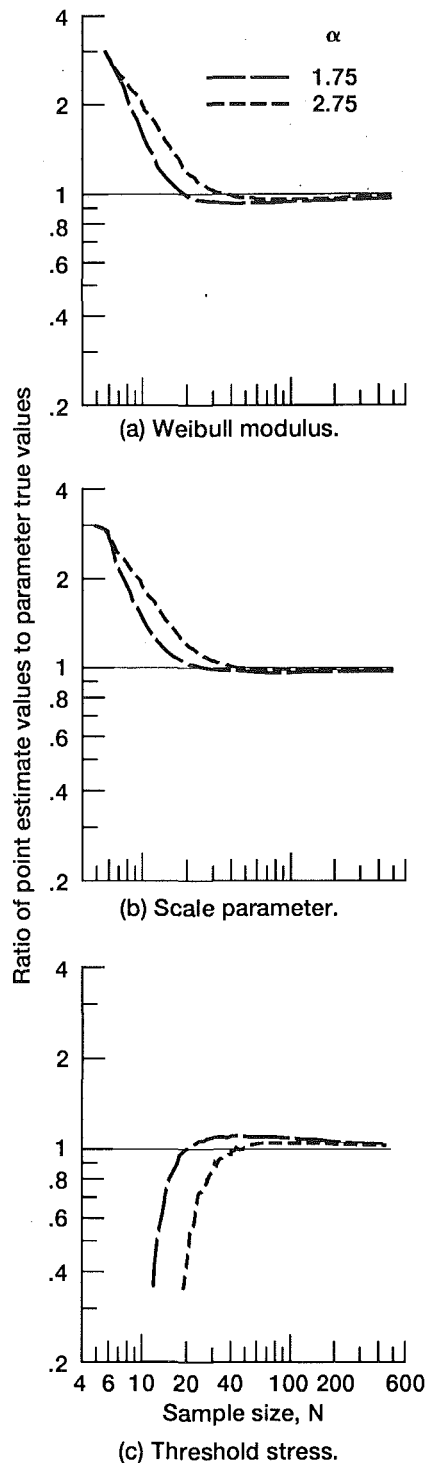


Fig. 2 Arithmetic mean values of the ratio of the point estimate to the true population parameter for each estimator ($\beta = 1000$, $\gamma = 300$)

rameters. This lack of invariance precludes unbiasing the point estimates obtained using this method. If the estimators were invariant, the bias could be removed in a systematic fashion using the method outlined by Thoman et al. (1969) for the maximum-likelihood estimate of the Weibull modulus. The authors indicate that the ratio associated with the two-parameter maximum-likelihood estimator for the scale parameter is also not invariant with respect to the underlying population parameters. However, Thoman et al. (1969) were able to construct a function that contained the ratio associated with the scale parameter and the estimate of the Weibull modulus, but

was not dependent on the true population parameters. This function enabled Thoman et al. (1969) to establish unbiasing factors and confidence bounds for the maximum-likelihood estimate of the two-parameter scale parameter. Similar functions for the nonlinear regression estimators discussed in this paper have not been developed. Thus, removing the bias associated with these estimators is not possible, and the design engineer should recognize that the amount of bias may be significant for small sample sizes.

Along with the mean value, the 10th and 90th percentile distributions are depicted for each estimator in Fig. 1. These percentile distributions are related to confidence bounds for a point estimate. The percentile distributions are obtained by ranking in order (from lowest to highest value) the ratios of point estimates to the true value of the distribution parameter. In this case the 10th percentile distribution represents the ratio associated with the 1000th ranked value. Hence, 999 ratios had lesser values. Similarly, the 90th percentile distribution represents the ratio associated with the 9000th ranked value. If the number of samples was increased from 10,000 to infinity, then these ranked values would yield the exact confidence bounds for the estimators. Note that for these estimators the confidence bounds narrow with increasing sample size (N). This is indicated by the decreasing separation in the percentile distributions. However, the percentile distributions are not invariant with respect to the true population parameters. Again, increasing α from 1.75 to 2.75 affected the percentile distributions (Fig. 3). This precludes the computation of confidence bounds on parameter estimates since the value of the true population parameter (the quantity being estimated) would have to be known a priori.

Application—Parameter Estimation and Reliability Analysis

In this section, parameters from the sintered silicon nitride (grade SNW-1000, GTE Wesgo Division) data presented by Chao and Shetty (1991) are estimated. The four-point bend, the three-point bend, and the pressurized-disk data are listed in Table 1. Focusing on the four-point bend specimen, the support span for this test fixture was 40.373 mm and the inner load span was 19.622 mm. The cross sections of the test specimens were 4.0138 mm in width and 3.1106 mm in height.¹ All failures occurred within the 19.6-mm gage section. Thus, each specimen is assumed to be subjected to pure bending. Under this assumption, Eq. (6) becomes (see Weibull and Daniel, 1964)

$$B = \left(\frac{V}{2(\alpha + 1)} \right) \left(\frac{\sigma - \gamma}{\sigma} \right) \left(\frac{\sigma - \gamma}{\beta} \right)^\alpha \quad (17)$$

where

$$V = bhl = 243.0 \text{ mm}^3 \quad (18)$$

and $\sigma (=Mc/I)$ is the outer fiber stress, assuming that the material behaves in a linear elastic fashion. Chao and Shetty examined the fracture surfaces of failed specimens using optical and scanning electron microscopy. These studies indicate that failures were initiated at subsurface pores (i.e., a volume defect). This type of fracture site consistently occurred in all three specimen geometries.

Once again, Eq. (5) can be used to express the functional relationship between the ranked probability of failure (Φ_i) and the estimate of the failure strength ($\hat{\sigma}_i$). Using the definition of B given in Eq. (17), then the following relationship exists between Φ_i and $\hat{\sigma}_i$:

$$\hat{\sigma}_i = \hat{\gamma}^* + \hat{\beta}^* [\hat{\sigma}_i \ln(1/1 - \Phi_i)]^{1/\hat{\alpha}^*} \quad (19)$$

¹All specimen dimensions and failure stresses in Table 1 (including the three-point and the pressurized-disk geometries) were obtained from a personal communication with Chao and Shetty.

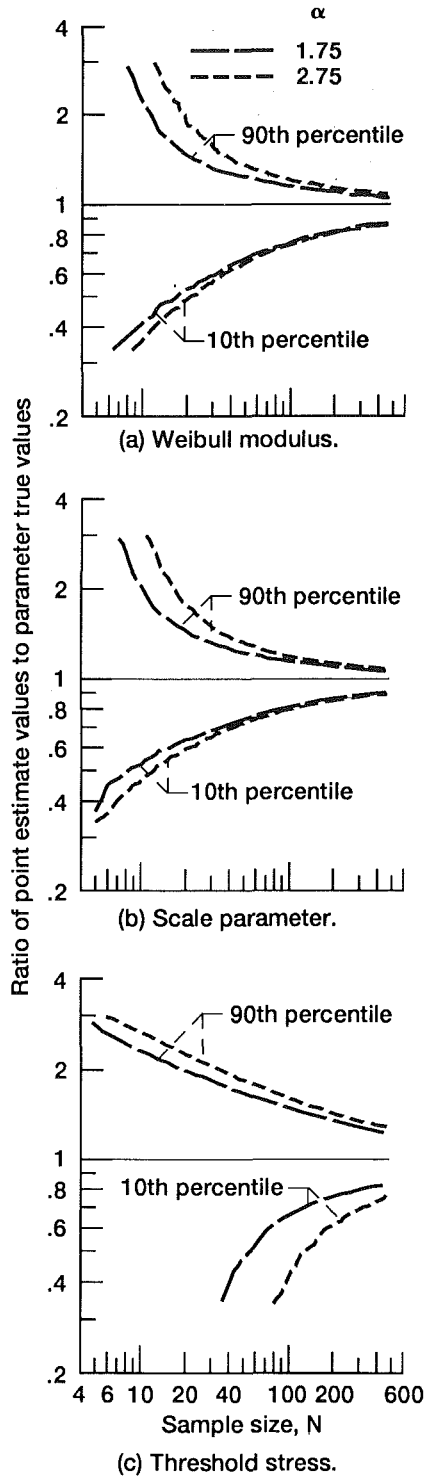


Fig. 3 Percentile distributions of the ratio of the point estimate to the true population parameter for each estimator ($\beta = 1000$, $\gamma = 300$)

for pure bending conditions. Here

$$\hat{\alpha}^* = \hat{\alpha} + 1 \quad (20)$$

$$\hat{\beta}^* = \left[\left(\frac{2(\hat{\alpha} + 1)}{V} \right) (\hat{\beta})^{\hat{\alpha}} \right]^{1/(\hat{\alpha} + 1)} \quad (21)$$

and

$$\hat{\gamma}^* = \hat{\gamma} \quad (22)$$

are introduced. At this point the residual defined by Eq. (10) cannot be formulated since Eq. (19) cannot be solved explicitly

Table 1 Estimated parameters for silicon nitride

Specimen number	Strength, MPa		
	Three-point bend	Four-point bend	Pressurized disk
1	715.6	613.9	549.7
2	729.6	623.4	575.5
3	741.0	639.3	587.4
4	758.6	642.1	622.0
5	771.4	653.8	636.7
6	773.1	662.4	639.3
7	824.2	669.5	642.6
8	830.4	672.8	646.3
9	832.8	681.3	659.3
10	863.2	682.0	659.6
11	868.2	699.0	660.4
12	870.9	714.5	661.4
13	878.3	717.4	667.8
14	881.1	725.5	668.9
15	899.4	741.6	670.8
16	900.6	744.9	684.8
17	905.0	751.0	686.2
18	913.8	761.7	691.3
19	916.8	763.9	693.8
20	928.0	774.2	698.1
21	931.0	791.6	706.9
22	934.6	795.2	718.1
23	935.1	829.8	718.8
24	941.1	838.4	726.4
25	941.6	856.4	732.3
26	949.1	868.3	738.1
27	951.6	882.9	748.2
28	953.8	-----	771.5
29	956.5	-----	780.7
30	979.9	-----	786.3
31	-----	-----	796.2
32	-----	-----	811.6

for the estimated ranked failure stress ($\hat{\sigma}_i$). However, several alternatives can be pursued to effect a solution. Margetson and Cooper (1984) indicate that the actual ranked failure stress (σ_i) should be substituted for $\hat{\sigma}_i$ on the right-hand side of Eq. (19). Defining

$$W_i = \sigma_i \ln(1/1 - \Phi_i) \quad (23)$$

then Eqs. (13)–(15) can be solved for $\hat{\alpha}^*$, $\hat{\beta}^*$, and $\hat{\gamma}^*$. Estimated values of the material parameters α , β , and γ would then be computed from Eq. (20)–(22). However, once the substitution of

$$\hat{\sigma}_i = \sigma_i \quad (24)$$

is made, Eq. (11) no longer defines the sum of the squared residuals. Exactly what is being minimized is difficult to define (an approximate residual, perhaps). However, this approximate method yields fairly good results (Duffy et al., 1993). This becomes evident in the following discussion in which results of the approximate method are compared to a more rigorous solution.

Note that Eqs. (13)–(15) and Eq. (19) represent $N + 3$ equations in terms of $N + 3$ unknowns ($\hat{\alpha}^*$, $\hat{\beta}^*$, $\hat{\gamma}^*$, and $\hat{\sigma}_i$). The alternative solution involves finding an initial estimate of the Weibull parameters using the approach where the estimated failure strengths are substituted with the actual strength data. After computing an initial estimate of the parameters, Eq. (19) is solved numerically (N times) for $\hat{\sigma}_i$. With Eq. (12) redefined as

$$W_i = \hat{\sigma}_i \ln(1/1 - \Phi_i) \quad (25)$$

then Eqs. (13) and (14) are solved for undated values of $\hat{\beta}^*$ and $\hat{\gamma}^*$ (using the previous value of $\hat{\alpha}^*$). The convergence criterion given by Eq. (15) is checked. If the criterion is not satisfied, $\hat{\alpha}^*$ is updated, and Eq. (19) is again solved numerically for $\hat{\sigma}_i$. This iterative process is repeated until the convergence criterion is satisfied.

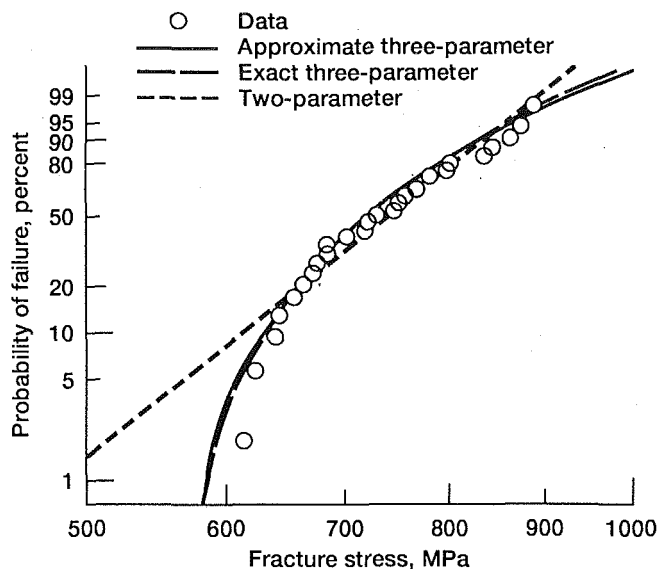


Fig. 4 Comparison of the probability of failure for the four-point specimen using the two- and three-parameter Weibull distribution

Both procedures are used to estimate parameters from the four-point bend test data listed in Table 1. The approximate method produces estimates of $\hat{\alpha} = 1.55$, $\hat{\beta} = 988.6$, and $\hat{\gamma} = 559.67$. The procedure that includes the solution for $\hat{\sigma}_i$ yields parameter estimates of $\hat{\alpha} = 1.68$, $\hat{\beta} = 861.6$, and $\hat{\gamma} = 558.1$. In addition, maximum-likelihood estimators are used to obtain point estimates for a two-parameter Weibull distribution. This technique gives estimated parameter values of $\hat{\alpha} = 10.2$ and $\hat{\beta} = 978.1$ (with $\hat{\gamma} \equiv 0$). The values obtained from the two-parameter maximum-likelihood estimators differ from the values reported by Chao and Shetty (1991). They used an averaging technique proposed by Batdorf and Sines (1980) that combines data from several test specimens. The pooled data are used to compute estimates from the three and four-point bend data. The estimated scale parameters from both configurations are averaged and, if the method of Batdorf and Sines (1980) is strictly adhered to, then the residuals from two data points are minimized. The authors feel that for this method to yield meaningful results, more than two specimen geometries are needed. The results of the maximum-likelihood estimators and both nonlinear regression methods are presented in Fig. 4, where the probability of failure is plotted as a function of the failure stress; that is, Eq. (5) is graphed using the different parameter estimates. The failure data are included using Eq. (8) to establish the vertical position of each data point. The straight line represents the two-parameter fit to the data. The nonlinear curves represent the three-parameter fit to the data. It is evident that the estimated three-parameter distributions are more efficient in predicting the failure data in the high-reliability region. Also note that there is very little difference between the two procedures used to establish the three-parameter estimates.

With the estimated Weibull parameters obtained using the procedure that includes the solution for $\hat{\sigma}_i$, reliability predictions are made for the three-point bend and the pressurized-disk geometries used in the experimental study by Chao and Shetty (1991). Both specimen geometries are depicted in Fig. 5. The geometries are modeled using MSC/NASTRAN to determine the structural response of the specimens to mechanical loads. The three-point bend geometry is modeled with 136 eight-node elements (MSC/NASTRAN CQUAD8). The mesh for this specimen is shown in Fig. 6. The stress distribution obtained from the finite element analysis is subsequently used as input for the integrated design program CARES (Nemeth

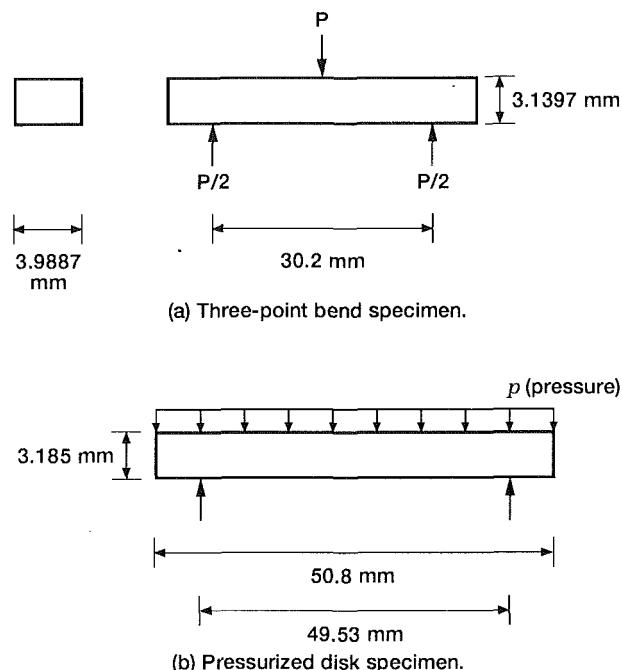


Fig. 5 Geometry of the three-point bend specimen and the pressurized disk specimen

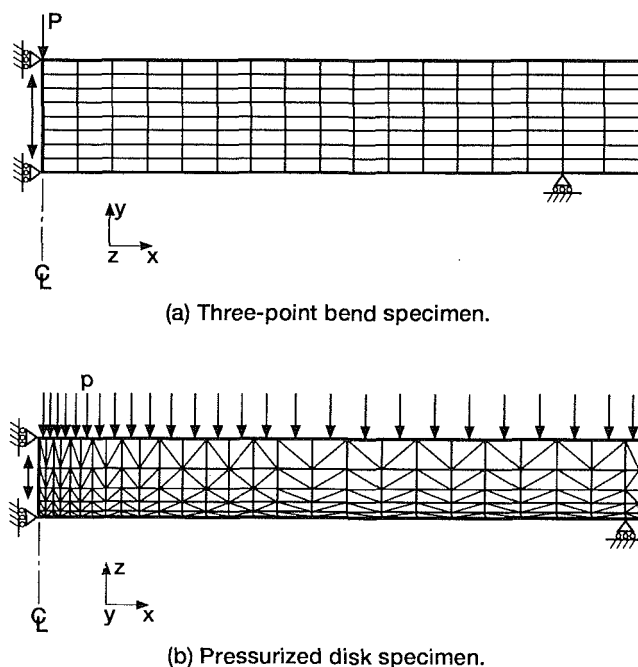


Fig. 6 Finite element discretization

et al., 1990). A volume flaw analysis is performed where the volume of a shell element is determined by calculating the midplane area and multiplying this value by the thickness of the element. The probability of failure curve is obtained by scaling (i.e., linearly increasing and decreasing) a single stress distribution a number of times. For each stress distribution a reliability analysis is performed with the CARES algorithm. An appropriate number of reliability computations are made to produce the nonlinear curve in Fig. 7. The linear (two-parameter) curve is established by determining the probability of failure at a single point on the curve and drawing a straight line through this point using the estimated Weibull modulus,

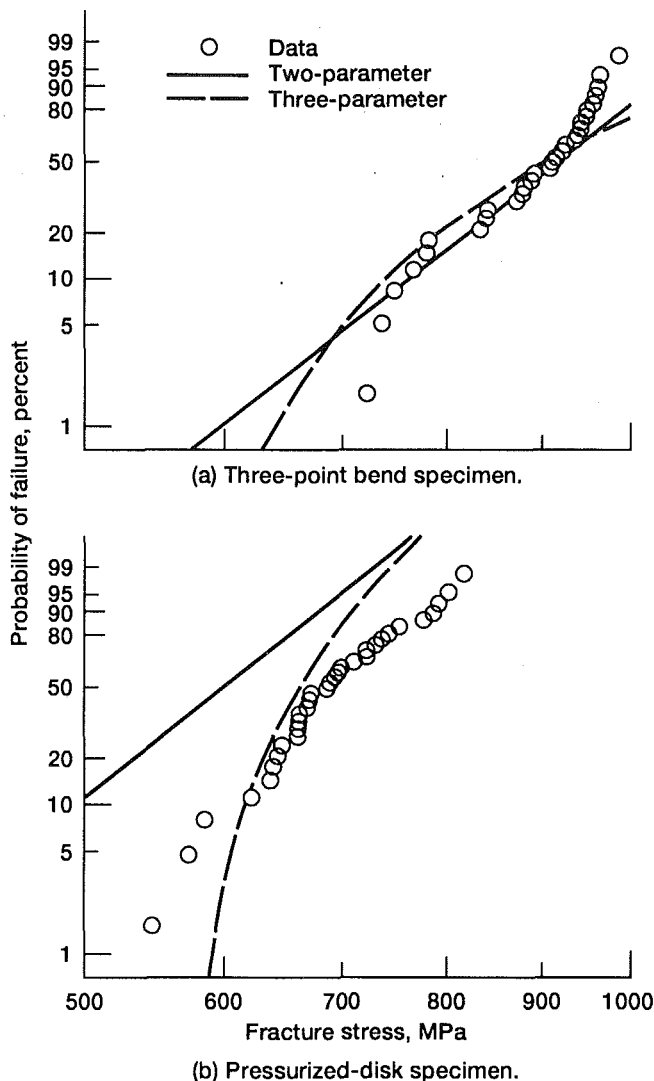


Fig. 7 CARES probability of failure results and failure data

which coincides with the slope of the linear curve. The data clearly indicate nonlinear behavior; however, both the two- and the three-parameter formulations yield conservative estimates in the high-reliability regions, but nonconservative estimates in the high probability of failure region. Both follow the trend of the data in the 5 to 60 percent probability of failure range of the graph.

The pressurized-disk geometry is modeled with 260 six-node elements (MSC/NASTRAN CTRIA6). The axisymmetric mesh for this specimen is also shown in Fig. 6. The probability of failure curves are depicted in Fig. 7. All probability of failure curves are generated by computing component reliability from numerous stress distributions that are obtained, once again, by linearly increasing and decreasing a single stress distribution. Here the three-parameter formulation clearly yields a better fit to the data. The two-parameter formulation is distinctly conservative at all stress levels which can lead to over-designed structural components. To demonstrate this, the parameter estimates obtained from the four-point bend data are used to compute the probability of failure of an aerospace component. Specifically, the component analyzed is a space shuttle main engine (SSME) high-pressure turbopump blade. The finite element mesh used to analyze this turbopump blade is depicted in Fig. 8. Moss and Smith (1987) used this mesh to analyze the dynamic characteristics of the blade. The mesh consists of 1025 brick elements (MSC/NASTRAN CHEXA).

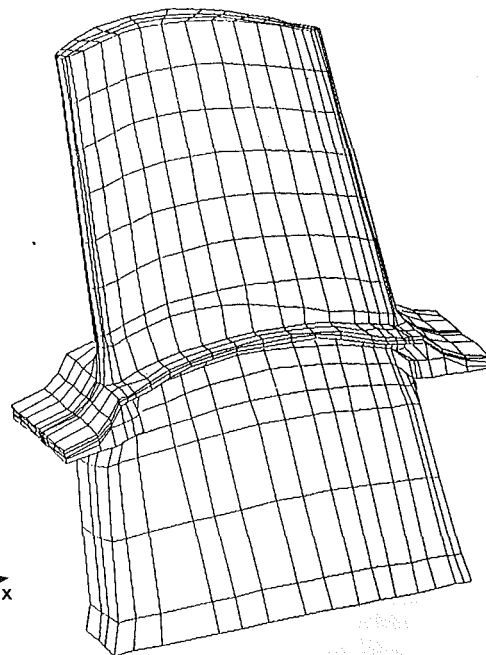


Fig. 8 Finite element discretization of turbopump blade

The shank of the blade is fully constrained. For the purpose of demonstration, it is assumed that the blade is fabricated from the monolithic silicon nitride material discussed in Chao and Shetty (1991). In the analysis Young's modulus is taken as 285.0 GPa and the Poisson ratio is 0.23. The specific load case studied represents a rotational speed of 40,000 rpm at room temperature. At this rotational speed the two-parameter formulation (using the PIA model) results in a component failure probability (P_f) of 75.2 percent. The three-parameter formulation results in a failure probability (P_f) of 0.04 percent. Utilization of the monolithic material would be summarily rejected based on the limited data available and the results of the two-parameter estimates. However, the results from the three-parameter formulation could prompt further consideration. The notable difference in the probability of failure does not indicate conclusively that the underlying population is characterized by a three-parameter Weibull distribution. Additional test data may clearly demonstrate whether the underlying population is characterized by a two- or three-parameter Weibull distribution. In addition, possible design studies could result in a further reduction in the component failure probability. Whether or not further redesign would bring the component failure probability within the stringent limits established for various shuttle components is not the issue here. The authors do not advocate using monolithic silicon nitride in the fabrication of SSME turbopump blades. Rather, this aerospace example emphasizes that the common use of the two-parameter formulation can lead to extremely conservative design decisions.

Conclusions

Enough experimental data exists to suggest threshold behavior (indicated by a nonlinear behavior similar to that displayed in Fig. 4) in certain monolithics. However, whether nonlinear behavior can be attributed to the existence of a threshold stress or competing failure mechanisms is open to question because of the lack of careful fractographic analysis for most data sets (except for the Chao and Shetty data discussed previously and obtained through personal communication). This paper has reviewed a number of aspects related

to the simple nonlinear regression technique proposed by Margetson and Cooper (1984). From limited numerical studies it is concluded that the estimators are well-behaved in the sense that bias is minimized, and confidence bounds tighten as the sample size is increased. However, the estimators are not invariant with respect to the underlying parameters that characterize a population. This precludes establishing exact confidence bounds and unbiasing factors.

The estimators perform reasonably well in comparison to the two-parameter maximum-likelihood estimators when both are applied to the silicon nitride data of Chao and Shetty (1991). Using an improved estimator based on the method proposed by Margetson and Cooper (1984), the three-parameter Weibull distribution easily captures the nonlinear trend of the failure data. All reliability computations are made using the simplified PIA model but better correlation to the failure data might be obtained if other more rigorous reliability models were employed. The authors are currently pursuing this analytical approach.

Although the three-parameter formulation obviously provides a better fit to the pressurized-disk data, this may not be readily evident with the three and four-point bend data. Goodness-of-fit statistics such as the Kolmogoroff-Smirnoff statistic and the Anderson-Darling statistic should be used to establish which form of the Weibull distribution would best fit the experimental data. These approaches are currently being studied by the authors.

Finally an aerospace component is analyzed, and the results may indicate the conservativeness of the two-parameter formulation. The authors advocate the use of the three-parameter formulation of the Weibull distribution when experimental data exhibits threshold behavior. Even though the estimates proposed by Margetson and Cooper (1984) are not invariant, additional testing can be conducted to minimize the bias associated with the parameter estimates. As the reliability analysis of the SSME turbopump blade indicates, the costs from additional tests may be well worth the dramatic decrease in a component probability of failure.

References

- Batdorf, S. B., and Crose, J. G., 1974, "A Statistical Theory for the Fracture of Brittle Structures Subjected to Nonuniform Polyaxial Stresses," *ASME Journal of Applied Mechanics*, Vol. 41, pp. 459-464.
- Batdorf, S. B., and Heinisch, H. L., 1978, "Weakest Link Theory Reformulation for Arbitrary Fracture Criterion," *Journal of the American Ceramic Society*, Vol. 61, No. 7-8, pp. 355-358.
- Batdorf, S. B., and Sines, G., 1980, "Combining Data for Improved Weibull Parameter Estimation," *Journal of the American Ceramic Society*, Vol. 63, No. 3-4, pp. 214-218.
- Chao, L.-Y., and Shetty, D. K., 1991, "Reliability Analysis of Structural Ceramics Subjected to Biaxial Flexure," *Journal of the American Ceramic Society*, Vol. 74, No. 2, pp. 333-344.
- Duffy, S. F., Palko, J. L., and Gyekenyesi, J. P., 1993, "Structural Reliability Analysis of Laminated CMC Components," *ASME JOURNAL OF ENGINEERING FOR GAS TURBINES AND POWER*, Vol. 115, this issue, pp. 103-108.
- Margetson, J., and Cooper, N. R., 1984, "Brittle Material Design Using Three Parameter Weibull Distributions," *Probabilistic Methods in the Mechanics of Solids and Structures*, S. Eggwertz and N. C. Lind, eds., Springer-Verlag, Berlin, pp. 253-262.
- Midgley, E., and Pierce, F. T., 1926, "The Weakest Link Theorems on Strength of Long and of Composite Specimens," *Journal of the Textile Institute*, Vol. 17, No. 2, pp. T355-T368.
- Moss, L. A., and Smith, T. E., 1987, "Dynamic Characteristics of Single Crystal SSME Blades," *Structural Integrity and Durability of Reusable Space Propulsion Systems*, NASA CP-2471, pp. 211-214.
- Nemeth, N. N., Manderscheid, J. M., and Gyekenyesi, J. P., 1990, "Ceramics Analysis and Reliability Evaluation of Structures (CARES), Users and Programmers Manual," NASA TP-2916.
- Quinn, G. D., 1989, "Flexure Strength of Advanced Ceramics—A Round Robin Exercise," MTL TR-89-62 (available NTIS, AD-A212101).
- Schneider, D., and Palazotto, A. N., 1979, "A Technique for Evaluating a Unique Set of Three Weibull Parameters Considering Composite Materials," *Fibre Science and Technology*, Vol. 12, No. 4, pp. 296-281.
- Thoman, D. R., Bain, L. J., and Antle, C. E., 1969, "Inferences on the Parameters of the Weibull Distribution," *Technometrics*, Vol. 11, No. 3, pp. 445-460.
- Thomas, D. J., and Wetherhold, R. C., 1991, "Reliability Analysis of Continuous Fiber Composite Laminates," *Composites Structures*, Vol. 18, No. 4, pp. 277-293.
- Weibull, W. A., 1939, "A Statistical Theory of the Strength of Materials," *Ingeniors Ventenskaps Akademien Handlingar*, Vol. 151, pp. 5-45.
- Weibull, W. A., 1951, "A Statistical Distribution Function of Wide Applicability," *ASME Journal of Applied Mechanics*, Vol. 18, pp. 293-297.
- Weil, N. A., and Daniel, I. M., 1964, "Analysis of Fracture Probabilities in Nonuniformly Stressed Brittle Materials," *Journal of the American Ceramic Society*, Vol. 47, No. 6, pp. 268-274.

Reliability Analysis of Ceramic Matrix Composite Laminates

D. J. Thomas¹
Research Assistant.

R. C. Wetherhold
Associate Professor.

Department of Mechanical and
Aerospace Engineering,
State University of New York,
Buffalo, NY 14260

At a macroscopic level, a composite lamina may be considered as a homogeneous orthotropic solid whose directional strengths are random variables. Incorporation of these random variable strengths into failure models, either interactive or non-interactive, allows for the evaluation of the lamina reliability under a given stress state. Using a noninteractive criterion for demonstration purposes, laminate reliabilities are calculated assuming previously established load sharing rules for the redistribution of load as the failure of laminae occurs. The matrix cracking predicted by ACK theory is modeled to allow a loss of stiffness in the fiber direction. The subsequent failure in the fiber direction is controlled by a modified bundle theory. Results using this modified bundle model are compared with previous models, which did not permit separate consideration of matrix cracking, as well as to results obtained from experimental data.

1 Introduction

Composite materials often find their use in advanced engineering applications; this is particularly true for brittle matrix/brittle fiber composites. These specialized uses have created a need for improved failure analysis capabilities. The high variabilities in material strengths demonstrated by composites have therefore focused attention on the application of probabilistic approaches to laminate failure modeling. In order to formulate such models, we must first consider the mechanics involved in the potential fracture modes.

There are five typical failure modes for composite laminates under in-plane loadings: *matrix normal stress*—transverse to and/or parallel to the fiber orientation, *matrix shear*, *delamination*, and *fiber failure*. Of these potential failure modes, only delaminations (either free edge or localized at internal crack sites) are caused by interlaminar stresses (Pipes and Pagano, 1970; Pagano and Pipes, 1971). Through careful design of the stacking sequence, these stresses may be greatly reduced or even eliminated. The remaining four failure modes mentioned are all the result of in-plane stresses; therefore, by assuming that proper consideration has been given to the layup design, we can formulate our failure criteria as a function of these in-plane stresses only. These four in-plane failure modes may all be involved in the failure of a laminate. The unique properties of ceramic matrix composites (CMC's) with brittle matrices provide the additional possibility of matrix cracking perpendicular to the fibers.

Preliminary efforts have been made in the area of stiffness degradation and load redistribution (Petit and Waddoups, 1969; Reifsnider and Highsmith, 1981; Thomas and Wetherhold, 1991a, 1991b). The ground work for the analyses performed in this paper have been discussed in detail (Thomas

and Wetherhold, 1991a, 1991b). In this paper we will investigate a proposed improvement to the ply failure model through the consideration of a *modified bundle* analysis.

2 Laminate Failure Model

In analyzing the reliability of a laminate, the unit of failure to be considered must first be defined. Two possible units are proposed here:

1 *Ply failure* considerations assume that the units of failure are the individual plies that make up the laminate; thus in an n -ply laminate there are n failure units.

2 *Modal failure* considerations allow for the recognition of multiple modes of failure within each ply. Therefore, for an n -ply laminate having m modes per ply, there are $m \cdot n$ failure units.

Expressions for ply reliabilities may be formulated using either a noninteractive approach such as the Principle of Independent Action (PIA) or an interactive approach as in the Maximum Distortional Energy (MDE) criterion. Both of these are discussed below.

PIA: The expression for layer reliability using PIA is given as

$$R_{\text{layer}} = \exp \left\{ - \sum_{i=1,2,6} \left[\left(\frac{\langle \sigma_i \rangle}{\beta_i^T} \right)^{\alpha_i^T} + \left(\frac{\langle -\sigma_i \rangle}{\beta_i^C} \right)^{\alpha_i^C} \right] \right\} \quad (1)$$

where α_i^T , β_i^T and α_i^C , β_i^C are the Weibull scale and shape parameters for tension and compression, respectively; and we define the following notation:

$$\langle x \rangle \equiv x \cdot u[x] = \begin{cases} 0, & x \leq 0 \\ x, & x > 0 \end{cases} \quad (2)$$

MDE: The layer reliability using MDE may be written

$$R_{\text{layer}} = \Pr(f < 1) \quad (3)$$

where

¹Current address: Aerospace Design and Fabrication, Brook Park, OH 44142; NASA-LeRC Research Associate.

Contributed by the International Gas Turbine Institute and presented at the 36th International Gas Turbine and Aeroengine Congress and Exposition, Orlando, Florida, June 3-6, 1991. Manuscript received at ASME Headquarters March 4, 1991. Paper No. 91-GT-211. Associate Technical Editor: L. A. Riekert.

$$f = \left(\frac{\sigma_1}{X_1}\right)^2 + \left(\frac{\sigma_2}{X_2}\right)^2 - \frac{\sigma_1\sigma_2}{X_1^2} + \left(\frac{\sigma_6}{X_6}\right)^2 \quad (4)$$

and the values of the strengths, X_i , are random variables. A Monte Carlo analysis may be used to evaluate Eq. (3).

Modal reliability considerations single out the active stress and its corresponding strength for evaluation. By partitioning Eq. (1) accordingly, three potential modes may be identified and evaluated. Interactive reliability criteria cannot distinguish the failure mode, and are applied to the ply as a whole.

3 Load Redistribution Considerations

We obtain a reliability estimate for a laminate by modeling the physics of the fracture process. At the microscopic level, an exact model of the failure process is impossible due to the very large number of possible fracture sequences and interactions. However, at the macroscopic level, a tractable phenomenological model that emulates the actual failure sequence is possible by making certain physically plausible assumptions.

3.1 Problem Definition. Before proposing a failure algorithm, the process to be modeled should be more precisely defined. We choose to simulate a load controlled test. As the load is applied, the layers within the laminate experience various failure mechanisms. These failures result in stiffness degradations and internal load redistributions. Thus, the problem at hand is:

- Defining what constitutes a failure and when it occurs.
- Detailing the method of load redistribution from the failed element.
- Modeling the corresponding stiffness degradations induced by the failures.

Ideally, a failure tree would be used to model the failure process. However, the number of branches and their attendant failure rules quickly becomes very large, and the addition of new plies within the laminate or any reorganization of the stacking sequences requires the entire tree to be rebuilt. A more suitable method is through computer simulation. By inverting the distribution function for the lamina strengths, realizations (i.e., hypothetical sample values) of those strengths may be determined. In this way a sample population of laminates may be created within the computer's memory. The strengths of these laminates may then be calculated by the failure rules we select. In a simplification for clarity, we shall neglect the effect of bending-extensional coupling; that is, symmetry of ply strengths is assumed.

3.2 Failure Criteria. The first option here is the choice of the unit of failure to be considered, either *ply* or *modal*. Ply failure is normally used in conjunction with an interactive criterion. The advantage of such a definition is that it satisfies an instinctive feeling that all stress components should contribute collectively toward the failure of the ply. However, its disadvantage is that it obscures the mode by which failure occurred. In other words, all that is known is that the layer has failed, and nothing is known about the manner of failure. It is this reason that makes the modal failure criterion attractive. Modal failure assumes that the stresses act independently of one another, with each stress being active within its own failure function. This approach allows the ply to fail in stages.

For a ply failure case, Eq. (4) may be used to analyze each layer for failure. For the modal case, failure functions for the individual stresses are presented below. The laminate reliability calculation in this paper will be performed using a Monte Carlo analysis. For each simulation performed, realizations of the random variables contained in the failure functions will be used, thus allowing for the evaluation of this failure function.

Longitudinal Stress, σ_1 . In describing ply failure under a longitudinal load, we may simply test a unidirectional 0 deg

ply for strength $(X_1)_{ult}$, or we may attempt a more physically detailed model. Two modes of failure typically occur due to the longitudinal stress: matrix cracking transverse to the fibers, and fiber breaking. Matrix cracking is particularly common in brittle matrix composites such as CMC's. Of the two modes, matrix cracks should appear first, and occur at periodic spacings dependent on shear stress transfer at the fiber/matrix interface. This is a noncatastrophic failure, which results in the ply's being arranged into segments held together by bridging fibers. A failure function for axial matrix cracking is given:

$$f_{1m} = \frac{\langle \sigma_1 \rangle}{X_{1m}^T} + \frac{\langle -\sigma_1 \rangle}{X_{1m}^C} \quad (5)$$

where X_{1m}^T and X_{1m}^C are random variables for the tensile and compressive matrix cracking strengths, and f_{1m} is also a random variable with $f_{1m} \geq 1$ denoting failure.

After matrix cracking has occurred, the longitudinal strength of the ply is governed by the intact fibers that bridge the matrix crack sites. Daniels (1945) has characterized the strength of a bundle of fibers under a tensile axial load as having a normal distribution with

$$S_u = n s_f [1 - b(s_f)] \quad (6)$$

$$\hat{\sigma} = s_f \sqrt{nb(s_f)[1 - b(s_f)]} \quad (7)$$

where S_u and $\hat{\sigma}$ are the average ultimate load and standard deviation of load, respectively, for the bundle; with n being the number of fibers, $b(s)$ the cumulative distribution function for the failure of a single fiber under load s , and s_f the fiber load that maximizes the expression $s[1 - b(s)]$. For the problem at hand, a modified bundle theory has been proposed in the literature (Walls, 1986; Evans and Marshall, 1989) in which the bridging fibers are analogous to Daniels' fiber bundle, with the added complexity of the fibers being embedded in a periodically cracked matrix, thus producing an axial variation in the fiber stress.

In general, an applied load s to a fiber results in a state of stress that is a function of both the load and the position, $\sigma = \sigma(s, x, r, \theta)$ using cylindrical coordinates. The probability of failure for the fiber may be described by a Weibull distribution:

$$b(s) = 1 - \exp \left[- \int_V \left(\frac{\sigma(s, x, r, \theta)}{\beta_v} \right)^\alpha dv \right] \quad (8)$$

where α is called the Weibull shape parameter and is dimensionless, and β_v is the Weibull scale parameter and has dimensions of $[\text{stress}] \cdot [\text{volume}]^{1/\alpha}$. Assuming the stress to be constant over the cross-sectional area of the fiber, A , the above equation may be expressed in terms of a new Weibull scale parameter, β_l , based on length. Equation (8) can be reduced to a single integral over the fiber length, L .

$$b(s) = 1 - \exp \left[- \int_L \left(\frac{\sigma(s, x)}{\beta_l} \right)^\alpha dx \right] \quad (9)$$

The relationship between β_l and β_v is given by

$$\beta_l = \beta_v A^{-1/\alpha} \quad (10)$$

Neither β_l nor β_v can be measured directly from experiment. However, tensile failure data obtained for fiber specimens all having the same experimental volume, V_O , and where each specimen was under a state of uniform stress may be fit to a Weibull distribution of the form

$$b(\sigma) = 1 - \exp \left[- \left(\frac{\sigma}{\beta} \right)^\alpha \right] \quad (11)$$

The Weibull scale parameter in Eq. (11) is based on the experimental volume, and may be inferred directly from the experimental data. From this value of β we can then obtain the parameters β_l and β_v from the expressions below:

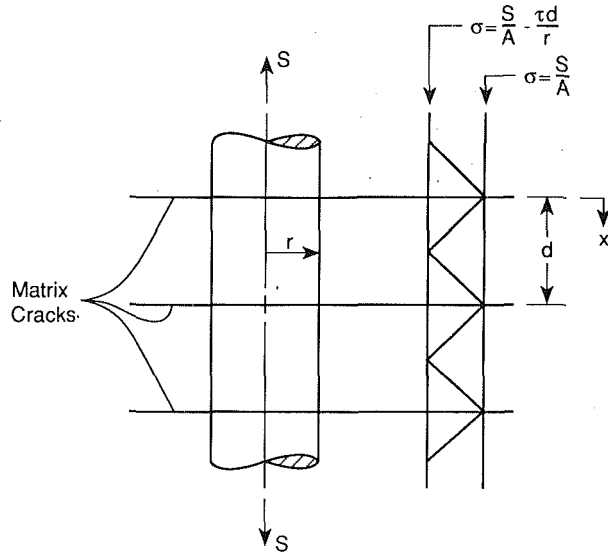


Fig. 1 Axial stress distribution within fiber

$$\beta_v = \beta V_O^{1/\alpha} \quad (12)$$

$$\beta_l = \beta \left(\frac{V_O}{A} \right)^{1/\alpha} \quad (13)$$

These parameters are now in the proper form for use in either Eqs. (8) or (9).

For the case of a fiber that bridges a matrix crack, with the shear stress (τ) at the fiber/matrix interface assumed to be constant, the axial stress variation along the fiber will be linear. The maximum values will occur at the matrix crack faces and minimum values midway between the cracks (see Fig. 1). Evaluating the stress through a force balance,

$$\sigma(s, x) = \frac{s}{A} - \frac{2\tau}{r} x; \quad 0 \leq x \leq \frac{d}{2} \quad (14)$$

Here s is more specifically defined to be the fiber load at the matrix crack face, x is the longitudinal position measured from the crack face and d is the crack spacing, which must have a value between x' and $2x'$ (Aveston et al., 1971),

$$x' = \left(\frac{V_m}{V_f} \right) \frac{\sigma_{mu} r}{2\tau} \quad (15)$$

with (V_f , V_m) being the (fiber, matrix) volume fraction and σ_{mu} the critical matrix cracking stress. Using the above expression (Eq. (14)) for the fiber stress in Eq. (9), leads to the following form of the cumulative distribution function for a single fiber:

$$b(s) = 1 - \exp \left\{ \frac{\beta_l L r}{\tau d (\alpha + 1)} \left[\left(\frac{s}{A \beta_l} - \frac{\tau d}{r \beta_l} \right)^{\alpha+1} - \left(\frac{s}{A \beta_l} \right)^{\alpha+1} \right] \right\} \quad (16)$$

Performing the necessary maximization results in an implicit expression for s_f , Eq. (17), which may be solved numerically.

$$s_f = A \beta_l \left\{ \frac{\beta_l L r}{\tau d} \left[1 - \left(1 - \frac{\tau A d}{s_f r} \right)^{\alpha} \right] \right\}^{-1/(\alpha+1)} \quad (17)$$

This may in turn be used in Eqs. (6) and (7) to characterize X_{lf} the post-matrix-cracking ply strength; and a failure determination may be made with a function similar to Eq. (5), i.e.,

$$f_{lf} = \frac{\langle \sigma_1 \rangle}{X_{lf}^T} + \frac{\langle -\sigma_1 \rangle}{X_{lf}^C} \quad (18)$$

Assuming a regular crack spacing, calculations performed for

values of both x' and $2x'$ resulted in approximately a 4 percent difference in the predicted value of X_{lf} . A crack spacing of x' returned the more conservative value and is therefore used in the example calculations for this paper.

It should be noted that if we assume that the shear stress τ is negligible, then the derivation would revert to the simple bundle strength of the fibers. In this case, the value of the maximizing load for use in Eqs. (6) and (7) would be given by

$$s_f = A \beta_l (\alpha L)^{-1/\alpha} \quad (19)$$

Transverse Stress (σ_2) and Shear Stress (σ_6). Unlike the longitudinal stress, which caused failure in stages, σ_2 and σ_6 have only one stage of failure. Their respective failure functions are of a form similar to Eq. (5) and are given below:

$$f_2 = \frac{\langle \sigma_2 \rangle}{X_2^T} + \frac{\langle -\sigma_2 \rangle}{X_2^C} \quad (20)$$

$$f_6 = \frac{\langle \sigma_6 \rangle}{X_6^T} + \frac{\langle -\sigma_6 \rangle}{X_6^C} \quad (21)$$

For the present work, we will assume that the random variables of strength X_2^T , X_6^C possess identical distributions; and as before we will take them to be described by a Weibull distribution (except for X_{lf} , which Daniels has derived for a normal distribution in Eqs. (6) and (7)).

3.3 Load Redistribution. After an individual unit (either ply or mode) has failed, the load it had previously carried must be redistributed and its stiffness reduced for future loading considerations. For a ply failure analysis, we are forced to degrade the entire stiffness matrix uniformly. In the case of modal failures, we have the ability to reduce selectively the individual stiffness elements corresponding to the particular mode of failure. Upon the occurrence of matrix cracking transverse of the fibers, we will reduce the Q_{11} and Q_{12} elemental stiffnesses by the ratio of the realizations of that layers' matrix strength to fiber strength.

$$(Q_{1j})_{\text{reduced}} = Q_{1j} \left(1 - \frac{X_{lm}}{X_{lf}} \right); \quad j = 1, 2 \quad (22)$$

For all other failure modes, we will conservatively reduce the appropriate stiffnesses to zero.

The load that had been carried by the failed unit must then be redistributed. Several physically plausible redistribution schemes are briefly described below. For greater detail see Thomas and Wetherhold (1991b).

Global Redistribution. The load is redistributed among all remaining unfailed units in accordance with the laminate constitutive law, which accounts for the relative stiffnesses of the plies (including the failed units in which the appropriate stiffnesses have been reduced) and with the deformation assumptions requiring plane sections to remain planar and perpendicular to the midsurface.

Local Redistribution. The load is evenly distributed between the two adjacent plies. If either of these plies have failed or contain modes that have failed, that portion of the load is globally redistributed.

Tapered Redistribution. The load is distributed among the four neighboring plies. The two immediately adjacent plies receive one third of the load each, and the two outside plies each accept one sixth of the loading. Any load that cannot be distributed locally is distributed globally.

In addition to the abovementioned schemes, orientation sensitive methods of local load redistribution may also be implemented. In these cases, preference in load redistribution is given to neighboring plies having the closest relative orientation to the ply containing the failure.

Table 1 Weibull strength parameters for SiC/RBSN (Bhatt and Phillips, 1990)

Modal strength, X_i	α	β (MPa)
X_{1m}	6.5	244.
$(X_1)_{ult}$	5.2	741.
X_2	10.9	28.
X_6 (estimate)	7.5	56.

Table 2 Elastic material properties for SiC/RBSN (Bhatt and Phillips, 1990)

E_1	193. GPa
E_2	69. GPa
G_{12}	31. GPa
ν_{12}	0.21

Table 3 Modified bundle strength predictions for X_{1f}

α_f	Mean Strength (MPa)	Standard Deviation (MPa)
7.0	632.	31.1
8.2	658.	29.8
9.0	673.	29.0
experimental	682.	150.

4 Example

As an example, we conduct a reliability analysis using a modal failure criterion and local load redistribution scheme for a $[O_2/9O_2]_s$ silicon carbide fiber-reinforced/reaction-bonded silicon nitride matrix composite (SiC/RBSN). Experimental determination of the material properties was carried out by Bhatt and Phillips (1990) and have been reprinted here in Tables 1 and 2. Their test specimens measured 12.7 mm wide, had a layer thickness of 0.25 mm, and a gage length of 25 mm. The fiber volume fraction was 0.3, and the fiber radius was 71 μ m. The Weibull strength parameters of Table 1 were calculated mathematically from the published values of their respective means and standard deviations and are based on the experimental volume. Since the Weibull scale parameters are volume dependent, the same lamina volume is assumed for subsequent calculations. If the volume of the calculated specimen were different from the original test specimen, the Weibull scale parameters would be corrected for this volume change.

Additionally, Bhatt and Phillips (1990) reported a value of 18 MPa for the value of the interfacial shear stress. They also performed 20 separate tensile tests on individual nitrogen-treated SiC fibers at a gage length of 25 mm and reported an average tensile strength for the fibers of 2860 MPa with a standard deviation of 440 MPa and a Weibull modulus of 8.2. From these values a Weibull scale parameter, β , based on the experimental volume can be calculated to be 3043 MPa. Using Eq. (13), we can then obtain the proper form of the Weibull scale parameter, β_i , for use in the modified bundle theory.

The analysis was performed for a $[O_2/9O_2]_s$ laminate using the strength parameters for X_{1m} , X_2 , X_6 given in Table 1 and the values of the mean and standard deviation for X_{1f} predicted by modified bundle theory. The resulting reliability curve is plotted in Fig. 2. The results fell within previously proposed

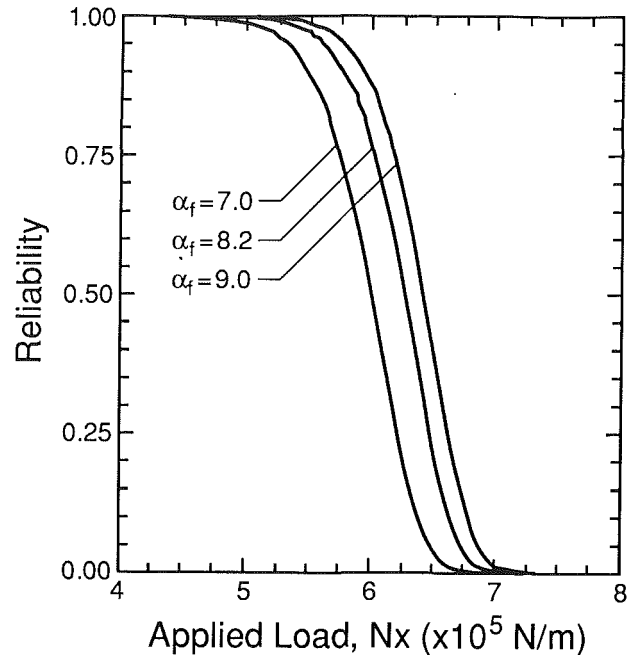


Fig. 2 Effect of α_f on reliability curves for $[O_2/9O_2]_s$ laminate

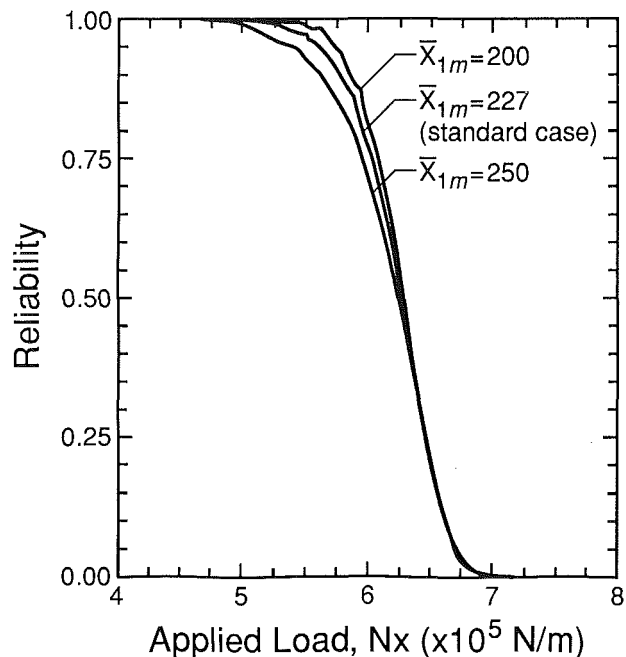


Fig. 3 Effect of mean matrix strength in the fiber direction, \bar{X}_{1m} , on reliability curves for $[O_2/9O_2]_s$ laminate

formal reliability bounds (Thomas and Wetherhold, 1991a, 1991b), but these bounds proved to be too far apart and are therefore omitted from further discussion. Also given in Fig. 2 are the reliability curves that result after performing slight perturbations in the values of the fiber Weibull modulus. The mean lamina strength and associated standard deviation in the fiber direction predicted by modified bundle theory for each value of α_f as well as the corresponding experimental results are given in Table 3. The effects of perturbations in the mean matrix cracking stress on the laminate reliability analysis are shown in the reliability curves of Fig. 3.

In Fig. 4, the reliability curve is compared against the results of the earlier failure model (Thomas and Wetherhold, 1991b), which used the values for $(X_1)_{ult}$, X_2 , X_6 from Table 1 and did not account for periodic matrix cracking. A comparison is also

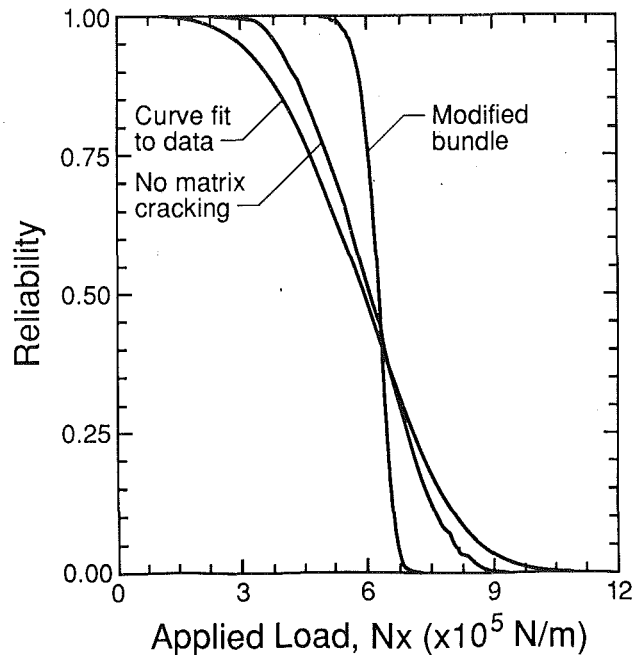


Fig. 4 Comparison of failure models

made against a Weibull reliability curve corresponding to the experimental results of a mean ultimate strength for the laminate of 294 MPa and a standard deviation of 87 MPa reported by Bhatt and Phillips (1990).

5 Discussion

The inclusion of periodic matrix cracking along with its corresponding stiffness reductions and load redistributions as a potential failure mode within our laminate failure model is appealing from a physical standpoint. Instead of using a single strength for the longitudinal direction, we should be able to obtain a more physically correct model by considering matrix cracking along with the subsequent failure of the bridging fibers. We incorporated this cracking phenomenon, modeled the degraded fiber direction strength using a modified bundle theory, and demonstrated the sensitivity of this model with respect to various model parameters.

The results of the bundle theory are shown to be very sensitive to changes in the Weibull modulus of the fiber (α_f). These changes are small enough to be within the realm of our ability to accurately measure α_f . Changes in the matrix cracking stress caused only moderate changes in the reliability curves (Fig. 3), while alterations in the fiber/matrix interface shear stress (not shown) did not cause any appreciable changes in the results.

The mean value predicted by modified bundle theory for the strength in the fiber direction of the lamina appears reasonable, though slightly low. The tight distribution predicted for the strength in the fiber direction of the lamina, as evidenced by the relatively small values of the standard deviations in Table 3, results in a very steep slope for the reliability curve. In accordance with the bundle theory, the relative variability of the bundle is less than the variability of the individual fibers. This does not agree with the experimental results; see Fig. 4. A possible explanation for the small values predicted for the coefficient of variation could be that all the fibers, due to an initial waviness, are not equally strained. Another possibility is that within bundle theory, once a fiber fails, it is assumed that it is no longer capable of sustaining any load. This is not true for our case, since even a periodically cracked matrix provides fiber reloading. Also shown in Fig. 4 are predictions made using the earlier failure model neglecting periodic matrix cracking. They agree very well with the experimental results, at least for this $[O_2^*/9O_2^*]_s$ configuration. This lends credence to the basic approach employed, and any future success achieved in incorporating more physically based failure models within it should serve to make it more robust.

Acknowledgments

This research was supported by NASA-Lewis Research Center under Contract No. NAG3862.

References

- Aveston, J., Cooper, G. A., and Kelly, A., 1971, "The Properties of Composite Materials," *IPC Sci. Tech.*, pp. 15-26.
- Bhatt, R. T., and Phillips, R. E., 1990, "Laminate Behavior for SiC Fiber-Reinforced Reaction-Bonded Silicon Nitride Matrix Composites," *J. Comp. Tech. Res. (ASTM)*, Vol. 12, pp. 13-23; also NASA TM 101350, 1988.
- Daniels, H. E., 1945, "The Statistical Theory of the Strength of Bundles of Threads. I," *Proc. Royal Soc. London*, Vol. 183A, pp. 405-435.
- Evans, A. G., and Marshall, D. B., 1989, "The Mechanical Behavior of Ceramic Matrix Composites," *Acta Metall.*, Vol. 37, pp. 2567-2583.
- Pagano, N. J., and Pipes, R. B., 1971, "The Influence of Stacking Sequences on Laminate Strength," *J. Comp. Matl.*, Vol. 5, pp. 50-57.
- Petit, P. H., and Waddoups, M. E., 1969, "A Method for Predicting the Nonlinear Behavior of Laminated Composites," *J. Comp. Matl.*, Vol. 3, pp. 2-19.
- Pipes, R. B., and Pagano, N. J., 1970, "Interlaminar Stresses in Composite Laminates Under Uniform Axial Extension," *J. Comp. Matl.*, Vol. 4, pp. 538-548.
- Reifsnider, K. L., and Highsmith, A., 1981, "The Relationship of Stiffness Changes in Composite Laminates to Fracture Related Damage Mechanisms," *Frac. of Comp. Matl.*, Proc. of 2nd USA-USSR Symposium, Bethlehem, PA, G. C. Sih and V. P. Tamuzs, eds., pp. 279-290.
- Thomas, D. J., and Wetherhold, R. C., 1991a, "Reliability Analysis of Continuous Fiber Composite Laminates," *Compos Structures*, Vol. 17, pp. 277-293.
- Thomas, D. J., and Wetherhold, R. C., 1991b, "Reliability Analysis of Composite Laminates With Load Sharing," *J. Comp. Matl.*, Vol. 25, pp. 1459-1475.
- Walls, D. J., 1986, M.S. Thesis, Univ. of California, Berkeley.

Micromechanical Analysis of the Failure Process in Ceramic Matrix Composites

A. A. Rubinstein

Department of Mechanical Engineering,
Tulane University,
New Orleans, LA 70118

An analysis of the effectiveness of fiber reinforcement in brittle matrix composites is presented. The analytical method allows consideration of discrete fiber distribution and examination of the development of crack growth parameters on the microscale. The problem associated with bridging zone development is addressed here; therefore, the bridging zone is considered to be smaller than the main pre-existing crack, and the small-scale approach is used. The mechanics of the reinforcement is accurately accounted for in the process zone of a growing crack. Closed-form solutions characterizing the initial failure process are presented for linear and nonlinear force-fiber pullout displacement relationships. The implicit exact solution for the extended bridging zone is presented as well.

Introduction

Reinforced ceramics have very promising potential in structural applications. Generally, ceramics exhibit high performance at elevated temperature, but suffer from a brittle failure pattern under tensile stress. A significant technological effort is devoted to development of ceramic-based compositions, such that the high-temperature performance qualities will be preserved, and the undesirable brittleness will be reduced. In relation to this, several models have been introduced in the literature, providing analysis of the effectiveness of the reinforcement. A detailed literature survey and a complete description of the mechanical processes taking place and the main efforts in modeling these processes are given by Aveston et al. (1971), and Rose (1987). The common feature in the development of the models (Budiansky et al., 1986; Budiansky and Amazigo, 1988, 1989; Nemat-Nasser and Hori, 1987) in these references is a substitution of the action of discrete fibers by a distribution of forces, which, supposedly, produces a similar toughening effect. Usually, the analysis of the model is based on a formulation and numerical solution of a singular integral equation, which reflects the force-displacement relation in the process zone. The analytical approach presented in this study departs from this well-established fracture mechanics scheme.

The analysis outlined below is based on consideration of a two-dimensional model, which captures the main features of the fiber reinforcement process. The subject of the analysis is microprocesses occurring within the process zone formed ahead of a growing crack, and, therefore, the small-scale framework is used. The two-dimensional formulation is chosen to represent a plane perpendicular to the crack front, which passes through the array of reinforcing fibers. The load is assumed

to be aligned with the fibers, and the analysis is concentrated on a crack growing in transverse direction to the fibers. The crack growth resistance mechanism in this material is based on the formation of the bridging zone, the process zone in this case, where the cracked matrix is held together by the remaining intact fibers behind the crack front (crack through the matrix). Thus, the high-intensity stress field typical for the vicinity of the crack tip is distributed among these bridging fibers and the leading crack tip arrested by the matrix. The energy release rate associated with the crack growth under the described conditions consists of two parts: the energy absorption rate due to the friction on the fiber matrix interface associated with the crack advance, and the energy release rate due to the crack advance within the matrix.

The fracture resistance R of the composite may be represented as an applied load required to maintain the crack growth as a function of the crack advancement from the instant prior to formation of the bridging zone. Thus, assuming that for the crack advancement the leading stress intensity factor acting on the matrix K_L has to be maintained at the critical value for the matrix K_{IC} , the material resistance can be represented as

$$R = K_{IC} \frac{K_{\infty}}{K_L} \quad (1)$$

Here the ratio K_{∞}/K_L characterizes the fiber reinforcement effect, that is, a relative reduction of the local, leading, stress intensity factor as compared with the stress intensity factor on the macroscale. This ratio will be referred to here as a dimensionless fracture resistance of the composite, and is one of the primary subjects of this investigation.

The model described here is based on the following *assumptions*: The elastic properties of the fibers are assumed to be very similar to the properties of the matrix with no significant difference in values of elastic constants. The difference between the strain magnitude in the fiber and in the matrix is insignificant at a finite distance from the crack surface, $|y| > 0$.

Contributed by the International Gas Turbine Institute and presented at the 36th International Gas Turbine and Aeroengine Congress and Exposition, Orlando, Florida, June 3-6, 1991. Manuscript received at ASME Headquarters February 19, 1991. Paper No. 91-GT-95. Associate Technical Editor: L. A. Rieker.

The local debonding (meaning here fiber separation from the matrix) at the fiber-matrix interface does not influence to a significant degree the resulting stress field at locations remote from the interface, and, therefore, for purposes of this analysis, no debonding is allowed. *The bridging zone is represented as an array of microcracks between the fibers with misfits on the ligaments (fibers) equal to the amount of the fiber pull-out*, Fig. 1. Two different relationships between the amount of the fiber pullout and the force acting on the fiber will be discussed below. The profile of the matrix separation along the fibers has to retain axial symmetry, and, thus, the misfit at each ligament corresponding to a fiber has to have a constant value along that ligament. The magnitude of the misfit on each ligament is different and is controlled by the fiber pullout-force relationship.

The length of the bridging zone may be controlled by several factors: the toughness of reinforcing fibers, the total load capacity of these fibers, or the geometric restrictions on the amount of the fiber pullout. The first fiber in the bridging zone (counting from the main crack in the direction toward the leading crack tip) experiences the maximal loading. In terms of the present model, the fiber matrix debonding is not included in the consideration and, therefore, the parameters characterizing the stress state in the vicinity of the fibers within the bridging zone are local stress intensity factors and a net force on the fiber.

Analysis

This analysis is aimed at evaluating the principal fracture mechanics parameters associated with the processes taking place during the bridging zone development ahead of the macrocrack. The crack size is assumed to be significantly larger than the bridging zone size, and, therefore, the small-scale approach may be used. In the framework of this analysis, the applied load is represented through the remote stress intensity factor, K_∞ , which controls the outer stress field of the process zone. The geometry and notations of the considered configurations are given in Fig. 1. The methodology of the following analysis was developed by Rubinstein (1985, 1987) and Rubinstein and Xu (1992). The basic relationships of the linear plane theory of elasticity in terms of the complex potentials are employed here (Muskhelishvili, 1963):

$$p\sigma_{11} + \sigma_{22} = 4\text{Re}\phi'(z)$$

$$\sigma_{22} - \sigma_{11} + 2i\sigma_{12} = 2(\bar{z}\phi''(z) + \psi'(z))$$

$$2\mu(u_1 + iu_2) = \kappa\phi(z) - z\bar{\phi}'(z) - \bar{\psi}(z). \quad (2)$$

Here μ is a shear modulus, ν is the Poisson ratio, and $\kappa = 3 - 4\nu$ for plane strain, or $\kappa = (3 - \nu)/(1 + \nu)$ for plane stress. Limiting our attention to Mode I loading and the direction of applied tension parallel to the direction of fibers, the symmetry condition on $y=0$ can be stated as

$$\sigma_{12}(z=x) = 0 = \text{Im}(\bar{z}\phi''(z) + \psi'(z)). \quad (3)$$

Functions ϕ and ψ are analytic in the plane with cuts along $y=0$, and, therefore, they may be considered as analytic in the upper half plane. Using condition (3) and applying the principle of analytical continuation, one obtains the relationship between the analytic potentials, which is true up to a real constant,

$$\psi'(z) = -z\phi''(z). \quad (4)$$

The constant may be dropped since both sides of Eq. (4) have to vanish as $z \rightarrow \infty$. With relation (4), the expressions for the normal stress and displacement components along $z=x$ become

$$\sigma_{22} = 2\text{Re}\phi'(x), \quad u_2 = \frac{\kappa+1}{2\mu} \text{Im}\phi(x). \quad (5)$$

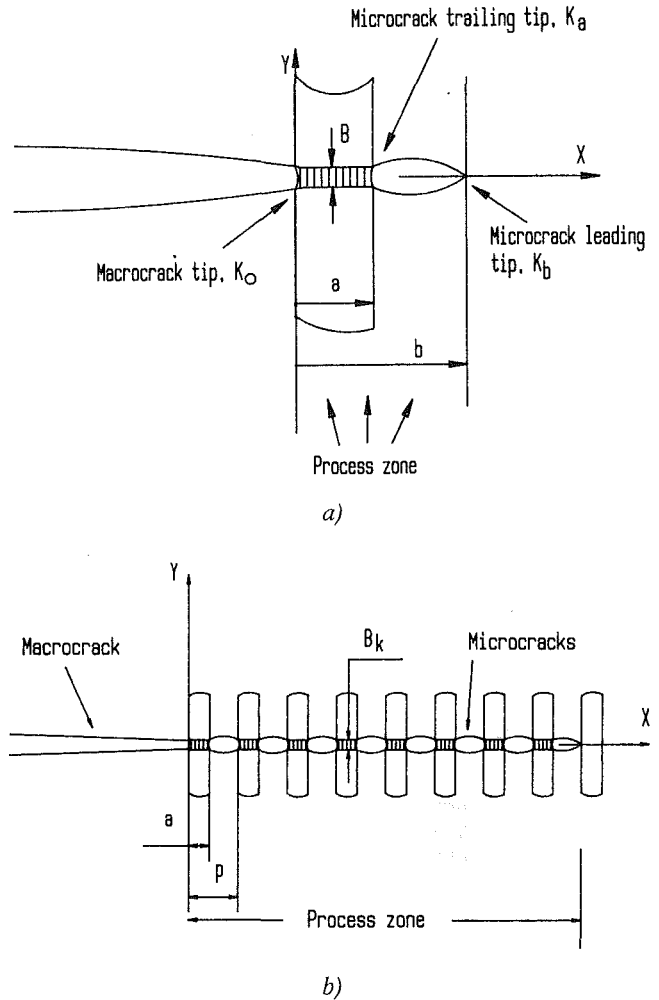


Fig. 1 Geometry of the bridging zone and notations used in the analysis

Thus, only one analytic function ϕ has to be determined, and the boundary conditions can be written in terms of this function. The condition at infinity states that the function ϕ' has to match the applied stress field, which should be given in terms of a remote stress intensity factor K_∞ (we consider Mode I loading only),

$$\phi'(z) \rightarrow \frac{K_\infty}{2\sqrt{2\pi z}} \text{ as } z \rightarrow \infty. \quad (6)$$

The boundary value problem for the unique determination of the physically suitable function ϕ' will be completed with the addition of statements of the traction-free surface on the main crack and microcracks, and statements specifying constant displacements, B_k , on the ligaments corresponding to the bridging fibers. As was mentioned above, the last condition follows from the local axial symmetry in the vicinity of each fiber. Thus, the boundary condition along the bridging zone of arbitrary length is

$$\text{Re}\phi'(x) = 0 \text{ on } x < 0 \text{ and } a + pk < x < p(k+1)$$

$$\text{Im}\phi'(x) = 0 \text{ on } pk < x < a + pk \text{ and } pN < x,$$

$$k = 0, 1, 2, \dots, N-1. \quad (7)$$

The physically suitable analytical function that satisfies all conditions stated above is chosen by Rubinstein and Xu (1992) as

$$\phi'(z) = \frac{K_\infty}{2\sqrt{2\pi z}} \frac{\prod_{k=0}^{N-1} (z - d_k)}{\prod_{k=0}^{N-1} (z - a - pk)^{1/2} (z - p(k+1))^{1/2}} \quad (8)$$

The branch of the square root function is chosen with the condition that for $z = x > pN$ the result of the square root is real and positive. N real constants d_k have to be determined from the conditions on the fibers. Assuming that the constants d_k are found, the stress intensity factors are determined by taking the appropriate limits; for the leading microcrack tips the results are

$$K_{pj} = K_\infty \frac{\prod_{k=0}^{N-1} (pj - d_k)}{\sqrt{p^N j(p-a)} \prod_{k=0, k \neq j+1}^{N-1} (j-k+1)^{1/2} (p(j-k)-a)^{1/2}} \quad (9)$$

$j = 1, 2, \dots, N.$

The case $j = N$ determines the stress intensity factor at the leading end of the bridging zone, the value acting on the uncracked matrix. This value determines the resistance of the material to the bridging zone extension. A complete set of expressions for all crack tips is given by Rubinstein and Xu (1992).

The bridging zone initiation may be analyzed by taking $N = 1$. The final expressions for the stress intensity factors acting at the main crack K_o , at the leading tip of the microcrack crack K_b , and at the trailing tip of the microcrack K_a are

$$K_o = K_\infty \frac{d}{\sqrt{ab}}, \quad K_a = K_\infty \frac{d-a}{\sqrt{a(b-a)}}, \quad K_b = K_\infty \frac{b-d}{\sqrt{b(b-a)}} \quad (10)$$

Thus, the missing step in this solution is determination of the constants d_k . The physical interpretation of these constants is simple, and it follows from the stress potential (8) and relations (5). These constants correspond to locations of maximal crack opening of each microcrack. As mentioned above, the necessary set of equations for determination of these constants should be given by the friction or fiber pullout-force relationship on the fibers. The pullout displacement B_k on a fiber k consists of the cumulative displacements on fibers ahead of fiber k plus a misfit at the microcrack immediately in front of it ΔB_k . The force F_k acting on a fiber k is determined from the given stress distribution (8) with (5). The friction law relating the fiber pullout to the acting force is not completely understood. The general form of this relationship may be written as

$$\lambda H(F_k - f) = B_k^\alpha, \quad k = 0, 1, 2, \dots, N-1. \quad (11)$$

Here f is a threshold force, and α is a parameter determining the power of this relationship and λ is a constant. Most commonly these parameters are assumed as $f = 0$ and $\alpha = 1$ (linear relationship), to simplify the analysis. Two cases will be discussed below: linear relationship and parabolic relationship, $f = 0$, $\alpha = 1/2$.

The energy absorbed by the fiber pullout process due to the bridging zone extension, G_f , can be evaluated by employing the Rice J -integral. Thus, in the case of one fiber link

$$K_o^2 - K_a^2 + K_b^2 = K_\infty^2 = G_f + K_b^2 \quad (12)$$

or

$$G_f = K_b^2 - K_a^2 = K_\infty^2 \frac{2bd - d^2 - ba}{b(b-a)}. \quad (13)$$

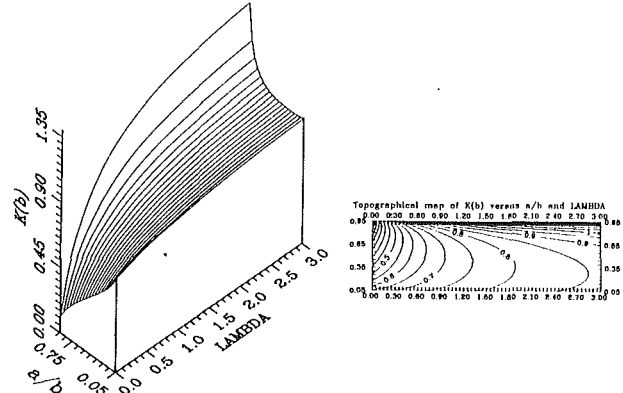


Fig. 2 Local stress intensity factor for a single fiber link

The energy absorbed by the fiber pull-out process will produce a positive contribution if

$$b > d > b - \sqrt{b(b-a)}. \quad (14)$$

Negative contribution is physically possible because of the restriction on fiber bending, which is implicitly assumed in the formulation. The analysis of the linear friction case clearly demonstrates that this case occurs when the microcrack emerging after the first fiber is too short. This simple analysis of the energy relationships cannot be used for the general case inasmuch as d is not an independent parameter; it depends on a friction law and the a/b ratio.

Linear Force-Pullout Displacement Relationship

The linear case solution was obtained by Rubinstein and Xu (1992) in closed form for the case $N = 1$ and numerically for an increasing bridging zone up to $N = 18$. The nondimensional friction coefficient is introduced as

$$\Lambda = 2 \frac{\lambda \mu}{\kappa + 1}. \quad (15)$$

The constant d , for the case $N = 1$, is

$$\frac{d}{b} = \frac{E\left(1 - \frac{a}{b}\right) + \Lambda \left[K\left(\frac{a}{b}\right) - E\left(\frac{a}{b}\right) \right]}{K\left(1 - \frac{a}{b}\right) + \Lambda \cdot K\left(\frac{a}{b}\right)}. \quad (16)$$

$E(m)$ and $K(m)$ are complete elliptic integrals, as given by Abramowitz and Stegun (1972). The expression for the force per unit thickness acting on the fiber cell becomes

$$F = K_\infty \sqrt{\frac{b}{2\pi}} \frac{\pi}{K\left(1 - \frac{a}{b}\right) + \Lambda \cdot K\left(\frac{a}{b}\right)}. \quad (17)$$

The case $N = 1$ characterizes the bridging zone initiation process. In Fig. 2, the data characterizing the variation of the leading stress intensity factor versus the fiber spacing and parameter Λ are presented. During the development of the microcrack the fiber not only restrains the separation of the matrix but also restrains the shape of the matrix at the fiber-matrix interface; namely, it restrains the rotation of this ligament. Inequality (14) is not satisfied, and this results in high values of the stress intensity factor K_b for the short microcrack when the parameter Λ is large. The three-dimensional surface corresponding to these data demonstrates that the relatively small microcrack, with respect to a fiber thickness, is unlikely to exist for intermediate, nonzero, values of Λ . The small microcrack will represent an unstable situation. The fiber spac-

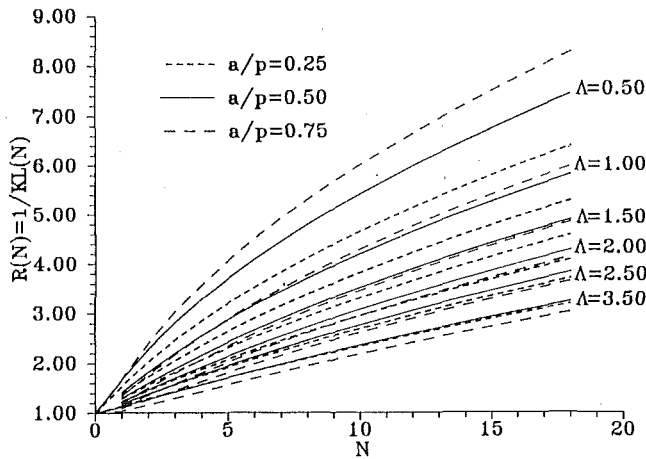


Fig. 3 Resistance curves for bridging zone extension

ing in the matrix becomes an important factor for optimal reinforcement. This spacing has to accommodate this unstable microcrack growth before it reaches the next fiber; otherwise, this unstable matrix failure will extend through the array of fibers.

The topographical map in combination with the three-dimensional diagram of the values of K_b in Fig. 2 show that there exists an optimal combination of the fiber-spacing ratio and the fiber pullout parameter Λ when values of the leading stress intensity factor are minimal, and thus the material resistance is maximal. Equation (12) suggests that the optimum reinforcement will take place when $K_a = 0$. A special case $K_o = K_b = 0.7071K_\infty$ takes place at $a/b = 0.5$, $\Lambda = 1.0$, $K_a = 0$.

The analysis of the extended bridging zone was limited by the applicability of the small-scale model. The leading microcrack in a very long bridging zone is no longer controlled by the applied stress intensity factor. The influence of the higher order terms in the Williams expansion becomes significant; namely, the zero-order term (constant) becomes a dominant factor. All microcracks in the array formed by the bridging zone are assumed to be of the same length, including the leading microcrack, for the reason discussed above. The maximal number of microcracks involved in the generated numerical data was $N = 18$.

The physical limitation on the length of the bridging zone is the maximal load capacity of the fiber. The natural expectation is that with elongation of the bridging zone, the load on the fiber separating the bridging zone from the main crack (first fiber) will increase. The first fiber is experiencing the maximal load in the array, but this load, in most cases, is reached after development of a few microcracks. A similar effect is observed in the behavior of the stress intensity acting on the fibers. The maximal stress intensity acting on the fibers is applied on the first fiber, as well. The maximal value is reached after development of a few microcracks, as in the case of the force on the fiber. Thus, long bridging zones may develop, and a primary limitation on this length is the leading stress intensity factor, which acts on the uncracked matrix, and the length of the fiber available for pull-out.

The data for dimensionless fracture resistance, measured as a value inverse to the stress intensity factor acting on the uncracked matrix normalized by the value of the applied stress intensity factor, are given in Fig. 3. These data represent the fracture resistance development with the bridging zone growing from zero length to the length equivalent to the array of eighteen microcracks. The fiber spacing ratios considered here are $a/p = 0.25; 0.50; 0.75$. The variation of the parameter Λ was analyzed from $\Lambda = 0.0$ to $\Lambda = 3.5$. The case $\Lambda = 0.0$ is not shown in Fig. 3; the resistance in this case becomes so high as compared to other cases that it is unsuitable to have it on the same

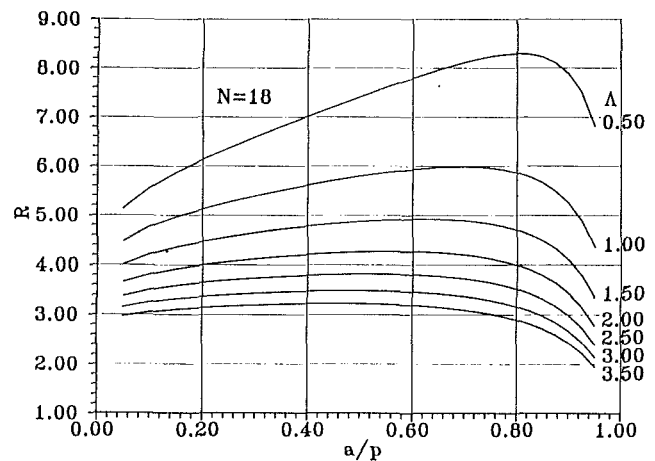


Fig. 4 Dependence of the fracture resistance on fiber-spacing ratio and fiber pullout parameter. The length of the bridging zone is constant for these data.

plot. The resistance curves show a significant spread of resistance values over the given values of Λ . The high values of Λ allow significant matrix separation in the bridging zone, and that contributes to the load redistribution, which causes higher values of the leading stress intensity factor; i.e., lower fracture resistance. These resistance curves differ from the curves obtained by Budiansky and Amazigo (1989), where the spread of the resistance factor over all the possible values of the parameter characterizing the fiber pull-out is not as high as in the cases obtained here. The difference may be attributed to the difference of these parameters and to the different normalization of the length of the bridging zone.

The data in Fig. 3 demonstrate that the fiber spacing ratio is an important contributor to the fracture resistance mechanism. Detailed data characterizing the influence of the fiber spacing on the resistance factor are given in Fig. 4. These data were obtained for fiber spacing ratios from $a/p = 0.05$ to 0.95 ; the length of the bridging zone is constant for these data, $N = 18$; and values of the parameter Λ correspond to the previous data. These data support the conclusion from the exact solution describing the bridging zone initiation that *there is an optimal combination of the fiber spacing ratio and the fiber pullout parameter at which the maximal fracture resistance may be achieved*.

Nonlinear Force-Pullout Displacement Relationship

The nonlinear case brings several interesting aspects into the process, which may require redesigning the experimental procedure for composite evaluations. Therefore, to obtain a better understanding of the nonlinear phenomenon, only the one fiber link case is analyzed here.

The method of solution of the problem can be easily applied to any rational power of the force-pullout displacement. After setting $\alpha = 0.5$ and $f = 0$ in Eq. (11), taking the square of both sides, and substituting the following expressions for the force and displacement, which are obtained by integration of the stress function (8),

$$F = 2 \frac{K_\infty \sqrt{b}}{\sqrt{2\pi}} \left[-K \left(\frac{a}{b} \right) + E \left(\frac{a}{b} \right) + \frac{d}{b} K \left(\frac{a}{b} \right) \right], \quad (18)$$

$$B = \frac{\kappa + 1}{\mu} \frac{K_\infty}{2\sqrt{2\pi}} 2\sqrt{b} \left[E \left(1 - \frac{a}{b} \right) - \frac{d}{b} K \left(1 - \frac{a}{b} \right) \right], \quad (19)$$

the quadratic equation for the ratio d/b is obtained. An important aspect of the obtained result has to be pointed out. In addition to the dimensionless friction Λ given by Eq. (15), which includes the interface property λ and material constants μ and ν , the nonlinear case includes the loading parameter

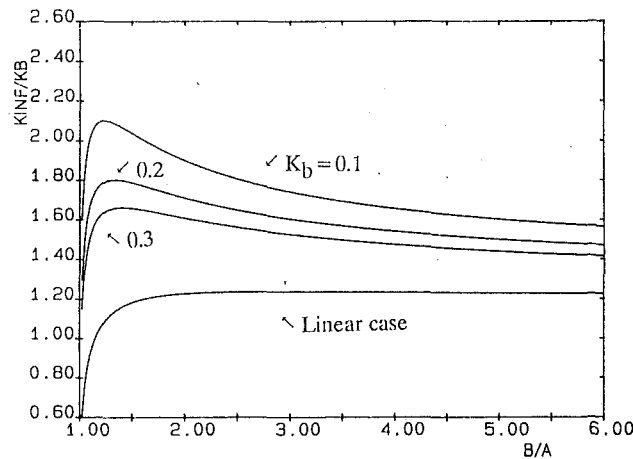


Fig. 5 Fracture resistance curves for a single fiber link for the nonlinear and linear cases

$$K^* = \frac{K_\infty (\kappa + 1)}{\mu} \sqrt{\frac{a}{2\pi}} \quad (20)$$

Thus, contrary to the linear case, the composite resistance curve pattern depends on the matrix toughness in addition to the fiber spacing aspect ratio and fiber-matrix interface friction. The dimensionless resistance parameter based on the ratio K_∞/K_L cannot be used for the nonlinear case. It is clear from the derivation, that this is a general property for any nonlinear case. On the other hand, one can use the experimental resistance curve obtained for this simple geometry as data for the inverse problem, and, thus, the friction law can be accurately determined.

The final equation for d/b is

$$A_1(d/b)^2 + A_2(d/b) + A_3 = 0 \quad (21)$$

with

$$A_1 = K^2(a/b), \quad A_2 = 2K(a/b) + K(1 - a/b)/\Lambda^2 K^*(a/b)^{1/2}$$

$$A_3 = -E(1 - a/b)/\Lambda^2 K^*(a/b)^{1/2} + [E(a/b) - K(a/b)]^2.$$

Equation (21) has two real roots, one of which corresponds to the position of the maximal microcrack opening. Loading curves for $\Lambda=2$ and dimensionless matrix toughness $K_b(\kappa+1)(a/2\pi)^{1/2}/\mu=0.1, 0.2, 0.3$ and for the linear case are given in Fig. 5; the curves are distributed in the same order of toughness decrease. The interesting feature of this nonlinear case is that the composite formed with the matrix with lower toughness has a higher resulting toughness enhancement. The nonlinearity of the force-displacement relation (11) is a significant factor in terms of the composite toughening. The fiber spacing is more critical for the optimal toughness than in the linear case. The region of matrix weakening due to the fiber inflexibility is observed here as well as in the linear case; however, the region and intensity of this effect are different. The

region and intensity of unstable matrix cracking are increased significantly as compared with the linear case. The general pattern of the curves given in Fig. 5 was observed for other values of Λ ; the location of the maximal K_∞/K_b value moves to lower values of b with lower values of Λ , the intensity of this maximum increases at the same time, and for higher values of b , the effect of differences in matrix toughness disappears.

Conclusions

The micromechanical toughening model for the fiber reinforcement of brittle matrix was presented. The analysis of the model is based on discrete fiber distribution and addresses such important aspects as fiber spacing ratio and fiber flexibility.

Two types of fiber pull-out displacement-force laws were considered. Exact closed-form solutions are given for the bridging zone initiation in the cases of the linear and square root force-displacement relationships.

In the case of the nonlinear force-displacement relationship, the experiments conducted on a laboratory composite cannot be directly transferred to other types of composites. The patterns of the resistance curves depend strongly on the friction parameter and the matrix toughness. To be reliable, these experiments must be carefully designed.

Acknowledgments

This work was supported by NASA Lewis Research Center under Grant No. NAG3-967.

References

- Abramowitz, M., and Stegun, A., 1972, *Handbook of Mathematical Functions*, Dover, New York.
- Aveston, J., Cooper, G. A., and Kelly, A., 1971, *Conference on the Properties of Fiber Composites*, National Physical Laboratory, Guildford, Surrey: ICP Science and Technology Press, pp. 15-26.
- Budiansky, B., Hutchinson, J. W., and Evans, A. G., 1986, "Matrix Fracture in Fiber-Reinforced Ceramics," *J. Mech. Phys. Solids*, Vol. 34, pp. 167-189.
- Budiansky, B., and Amazigo, J. C., 1988, "Small-Scale Bridging and the Fracture Toughness of Particulate-Reinforced Ceramics," *J. Mech. Phys. Solids*, Vol. 36, pp. 167-187.
- Budiansky, B., and Amazigo, J. C., 1989, "Toughening by Aligned, Frictionally Constrained Fibers," *J. Mech. Phys. Solids*, Vol. 37, pp. 93-109.
- Muskhelishvili, N. I., 1963, *Some Basic Problems of the Theory of Elasticity*, Noordhoff, Groningen, The Netherlands.
- Nemat-Nasser, S., and Hori, M., 1987, "Toughening by Partial or Full Bridging of Cracks in Ceramics and Fiber Reinforced Composites," *Mechanics of Materials*, Vol. 6, pp. 245-269.
- Rose, L. R. F., 1987, "Crack Reinforcement by Distributed Springs," *J. Mech. Phys. Solids*, Vol. 35, pp. 383-405.
- Rubinstein, A. A., 1985, "Macrocrack Interaction With Semi-infinite Microcrack Array," *International Journal of Fracture*, Vol. 27, pp. 113-119.
- Rubinstein, A. A., 1987, "Semi-infinite Array of Cracks in a Uniform Stress Field," *Engineering Fracture Mechanics*, Vol. 26, pp. 15-21.
- Rubinstein, A. A., and Xu, K., 1992, "Micromechanical Model of Crack Growth in Fiber Reinforced Ceramics," *Journal of the Mechanics and Physics of Solids*, Vol. 40, No. 1, pp. 105-125; NASA Contractor report 4321.

Stability Analysis of Bridged Cracks in Brittle Matrix Composites

R. Ballarini

Associate Professor.

S. Muju

Graduate Student.

Department of Civil Engineering,
Case Western Reserve University,
Cleveland, OH 44106

The bridging of matrix cracks by fibers is an important toughening mechanism in fiber-reinforced brittle matrix composites. This paper presents the results of a non-linear finite element analysis of the Mode I propagation of a bridged matrix crack in a finite size specimen. The composite is modeled as an orthotropic continuum and the bridging due to the fibers is modeled as a distribution of tractions that resist crack opening. A critical stress intensity factor criterion is employed for matrix crack propagation, while a critical crack opening condition is used for fiber failure. The structural response of the specimen (load-deflection curves) as well as the stress intensity factor of the propagating crack is calculated for various constituent properties and specimen configurations for both tensile and bending loading. By controlling the length of the bridged crack, results are obtained that highlight the transition from stable to unstable behavior of the propagating crack.

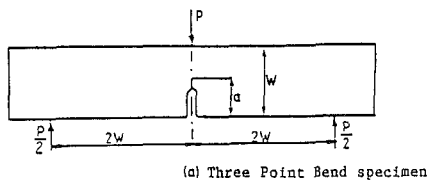
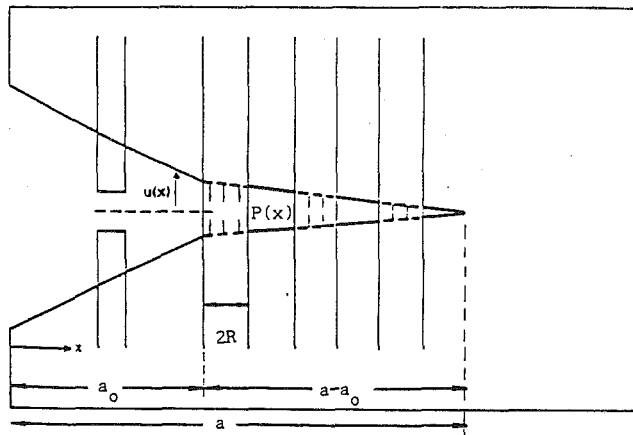
Introduction

Crack bridging is an important toughening mechanism in many engineering materials, including fiber and whisker-reinforced ceramic and metal matrix composites, plain and fiber-reinforced concrete, matrices reinforced with ductile secondary phases, and glassy polymers. This fact has led to a significant amount of research aimed at gaining a better understanding of the mechanics of bridged cracks. Various models have been proposed by researchers in different fields in which the bridging is modeled as a distribution of discrete forces or continuous stresses which resist crack opening. While they differ in the conditions specified to calculate the lengths of the bridging zone and the propagation criterion, all of the proposed models are essentially of the Dugdale-Barenblatt type [1, 2].

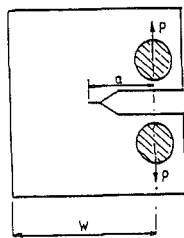
A typical model for a bridged crack is shown in Fig. 1(a). The "effective" crack length is the sum of a traction-free length and of a "process zone," within which a traction is prescribed that models the bridging arising from the active mechanisms. In this figure the process zone consists of fibers. However, the mechanisms may include aggregate interlock, microcracking, crazing, plastic yielding, fiber bridging, etc. In metals the Dugdale model has been used to simulate yielding ahead of a crack tip. In this model the closing stress is equal to the yield stress of the material, and the length of the process zone is calculated by requiring the stress intensity factor due to the closing stress to cancel the one resulting from the applied loading. Propagation is assumed to occur when the crack opening displacement at the tip of the traction-free crack reaches a specified critical value. The reason the stress intensity factor is taken as zero is that the energy release rate associated with the stress

intensity factor is negligible compared to the energy dissipated in the yielding process. A zero net stress intensity factor has also been assumed in several models for plain and fiber-reinforced mortar and concrete [3, 4], since the energy dissipated in the stretching of steel fibers is much greater than the fracture energy of the matrix. In these strain-softening materials the closing stress is taken as a monotonically decreasing function of crack opening displacement [3-6]. In composites composed of brittle fibers and matrix, the assumption that the fracture toughness of the matrix is negligible is not valid. Marshall and Cox [7, 8] have developed a model for ceramic matrix composites in which the crack is assumed to propagate when the net stress intensity factor reaches the critical stress intensity factor of the matrix. Using a micromechanical model they determined [7] that the stress that resists crack opening is proportional to the square root of the crack opening displacement. Using this relation, they obtained extensive numerical results, which provide a much better understanding of possible failure mechanisms in tension loaded ceramic matrix composites. In particular, they showed that the fiber strength is a parameter that governs whether a matrix crack will be fully bridged or partially bridged as it propagates through the specimen. Strong fibers lead to fully bridged cracks, which can grow in the matrix through the specimen while the fibers remain intact. As shown schematically in Fig. 2, this "noncatastrophic," or "ductile" mode of failure leads to large strains, since further loading beyond the first matrix crack leads to multiple matrix cracking and an ultimate strength, which is governed by the bundle strength. Relatively weak fibers, on the other hand, lead to matrix cracks, which are bridged in a relatively small region behind the crack tip as they propagate. Moreover, as a partially bridged crack propagates, the fibers behind the crack tip break sequentially, eventually breaking the specimen in two. In this paper a model similar to the one

Contributed by the International Gas Turbine Institute and presented at the 36th International Gas Turbine and Aeroengine Congress and Exposition, Orlando, Florida, June 3-6, 1991. Manuscript received at ASME Headquarters February 19, 1991. Paper No. 91-GT-94. Associate Technical Editor: L. A. Rieker.



(d) Three Point Bend specimen



(b) compact Tension Specimen

Fig. 1 Crack configuration and typical fracture specimens

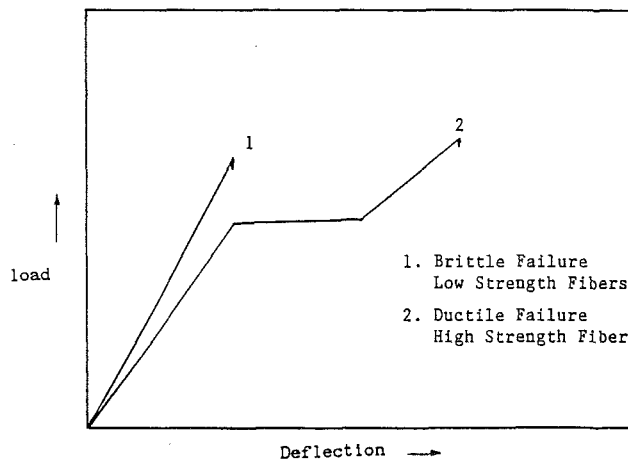


Fig. 2 Possible failure modes of brittle matrix composites

developed by Marshall and Cox is used to study the effects of loading and specimen size on the behavior of bridged cracks in continuously reinforced brittle matrix composites. Of particular interest in this study is the transition from ductile to brittle behavior of such cracks, and how this transition is affected by constituent properties, specimen size, and type of loading. This transition will be highlighted by controlling the length of the bridged crack, as was done by Carpinteri [9] in his study of crack growth in concrete. In the course of this investigation the authors became aware that Cox and Marshall [10, 11], using an integral equation approach, performed an

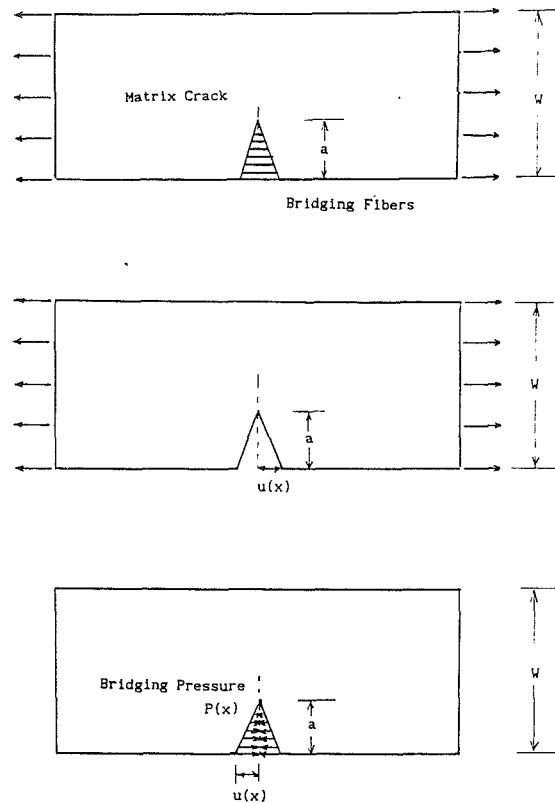


Fig. 3 Superposition scheme

analysis similar to the one presented in this paper. The advantage of the numerical model presented in this paper is its ability to treat complicated geometries, anisotropic materials, nonhomogeneous structures, and cracks that propagate in directions that do not coincide with principal axes.

Finite Element Model

The present work is directed toward developing a numerical analysis tool that can be used to analyze anisotropic fracture specimens of finite size. Typical examples include, as shown in Fig. 1(b), the edge-notched beam and the compact tension specimens. Moreover, the crack surfaces are bridged as shown in Fig. 1(a). The fibers within a distance $a - a_0$ from the crack tip remain intact and bridge the crack, while the remaining fibers over distance a_0 from the crack mouth are broken and do not contribute to crack tip shielding. Failure of the composite may be initiated either by fiber failure or matrix crack growth.

The influence of fiber shielding is to restrain the crack opening, and, consequently, reduce the stress field in the vicinity of the matrix crack tip. The bridged crack can be viewed as the superposition of a traction-free crack subjected to a remote loading, and a crack whose surfaces are loaded with the forces arising from the fibers (Fig. 3). For closely spaced fibers and relatively long cracks, the discrete forces are assumed to be equivalent to a continuous distribution of closing stress $p(x)$. This superposition can be performed using different techniques. For cracks in infinite bodies and for relatively simple finite geometries, a singular integral equation approach can be used. With this approach the problem is reduced to an integral equation, which represents the traction boundary condition along the crack surfaces. The integral equation is then solved for the unknown dislocation density along the crack line, which can be used to calculate relevant physical quantities such as stress intensity factor and crack opening displacement. Because the closing stress is a nonlinear function of the crack

opening displacement, or dislocation density, the integral equation is nonlinear and an iterative solution is needed. This approach has been used in studies of plain and fiber reinforced concrete [6]. An integral equation approach in which the crack opening displacements are treated as unknowns has been used for ceramic matrix composites [7, 8, 10, 11].

In the present work, the finite element method is implemented for this superposition. The physics is assumed as follows. The matrix crack will propagate when the stress intensity factor in the matrix reaches a critical value K_{IC}^m , which is related to the composite stress intensity, K_{IC}^c , by the relation $K_{IC}^c = K_{IC}^m E_c / E_m$ [7]. This relation is based on strain compatibility between fibers and matrix, and hence is not rigorously valid for very short cracks, nor for fibers slipping ahead of the crack tip. The closing stress relation is given by [7]

$$p(x) = 2V_f[\tau E_f(1 + \eta)/R]^{1/2}(u(x))^{1/2} \quad (1)$$

where

$V_f(V_m)$ = volume fraction of fibers (matrix)

τ = interfacial shear strength

$E_f(E_m)$ = elastic modulus of fiber (matrix)

R = fiber radius

$\eta = E_f V_f / E_m V_m$

$u(x)$ = crack opening displacement

Equation (1), which represents a closing stress that increases monotonically with crack opening displacement, was derived with the assumption of a single valued fiber strength. A closing stress function that initially increases and subsequently decreases was derived, assuming the fiber strengths satisfy weakest link theory, by Thouless and Evans [12]. Their analysis led to the following equation for the stress displacement relation for the bridging fibers:

$$(\sigma/\Sigma) = (u/u_n)^{1/2} \exp[-(u/u_n)^{(m+1)/2}] + \frac{1}{(1+\eta)(m+1)} \{1 - \exp[-(u/u_n)^{(m+1)/2}]\} \times \left\{ \gamma[(m+2)/(m+1), (u/u_n)^{(m+2)/2}] - \frac{\Sigma(m+1)}{2E_f} \left[\frac{u}{u_n} \right] \right\} \quad (2)$$

where

$$\Sigma = \langle s \rangle / T \left[\frac{m+2}{m+1} \right] \\ u_n = \frac{\Sigma^2 R (1 - V_f) E_m}{4\tau E_f E}$$

m = Weibull modulus of fiber strength distribution

$\langle s \rangle$ = Average strength of the fiber bundle

$$\gamma[(m+2)/(m+1), \alpha] = c \int_0^\alpha \beta^{1/(m+1)} e^{-\beta} d\beta$$

$$\Gamma(\delta) = \int_0^\infty \beta^{\delta+1} \exp(-\beta) d\beta$$

$$\alpha = (u/u_n)^{(m+1)/2}$$

For the case of single-valued strength fibers, $m = \infty$, $\langle s \rangle = \sigma_{fu}$, where σ_{fu} is the ultimate fiber strength, and Eq. (2) reduces to Eq. (1), which is used in the present analysis. A recent analysis of tension loaded notched beams by Cox and Marshall [11] was performed for several values of m . Equation (1) can be conveniently represented as

$$p(x) = \begin{cases} A\sqrt{u(x)} & x \geq a_o \\ 0 & x \leq a_o \end{cases} \quad (3a)$$

where

$$A = 2V_f[E_f\tau(1 + \eta)/R]^{1/2} \quad (3b)$$

The quantity u_n corresponds to the critical opening, which

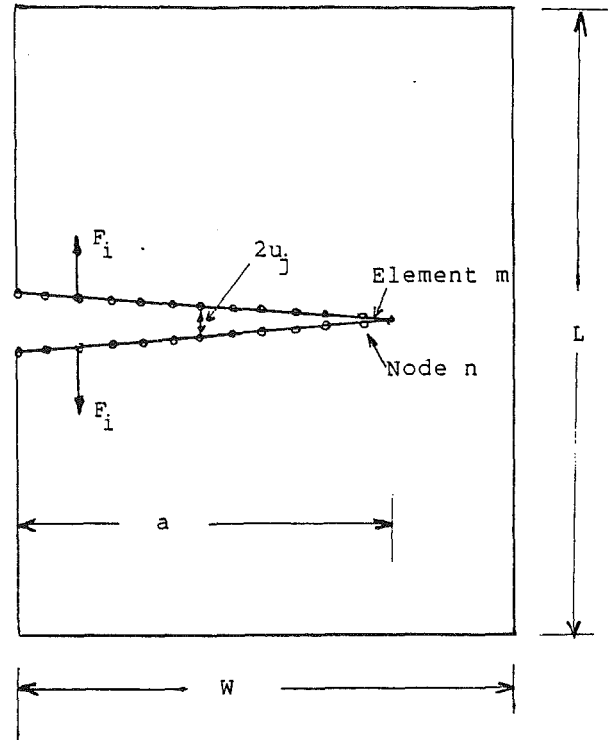


Fig. 4 Finite element nodes representing the crack line

produces a stress in the fiber equal to σ_{fu} . In this work fiber failure is assumed to occur when the crack opening equals u_n . It should be noted that the assumption of single-valued strength implies that fiber failure first occurs at the far edge of the bridging zone, since the crack opening displacements decrease monotonically towards the crack tip (this has been confirmed in [8] and in the present work). A statistical fiber strength distribution may lead to fibers nearest to the crack mouth remaining intact while others closer to the crack tip breaking.

With reference to Fig. 4, n nodes are distributed along the fracture line. The crack opening displacements can be represented as

$$u_i = K_{ij}F_j + \sigma C_i \quad i, j = 1, \dots, n \quad (4)$$

where

u_i = crack opening at node i

F_j = load (due to the fibers) at node j

C_i = influence coefficients representing crack opening at node i due to unit applied far field stress

K_{ij} = influence coefficients representing crack opening at node i due to unit load F_j

σ = applied stress

The load point deflection can be represented as

$$\Delta = D_j F_j + \sigma \Delta_o \quad j = 1, \dots, n \quad (5)$$

where

D_j = influence coefficients for load-point displacement due to F_j

Δ_o = load-point displacement due to unit applied stress.

Equations (4) and (5) can be modified for any far-field loading by appropriately modifying the remote loading σ . For the single-edge notch specimen considered in this paper, the deflection Δ is measured, for tensile loading, at point A of the typical finite element model shown in Fig. 5, while for the three-point bend loading, it is measured at the point B. The specimen has length $L = 20$ cm and width $W = 5$ cm. The geometry is modeled with quadratic elements. To calculate the

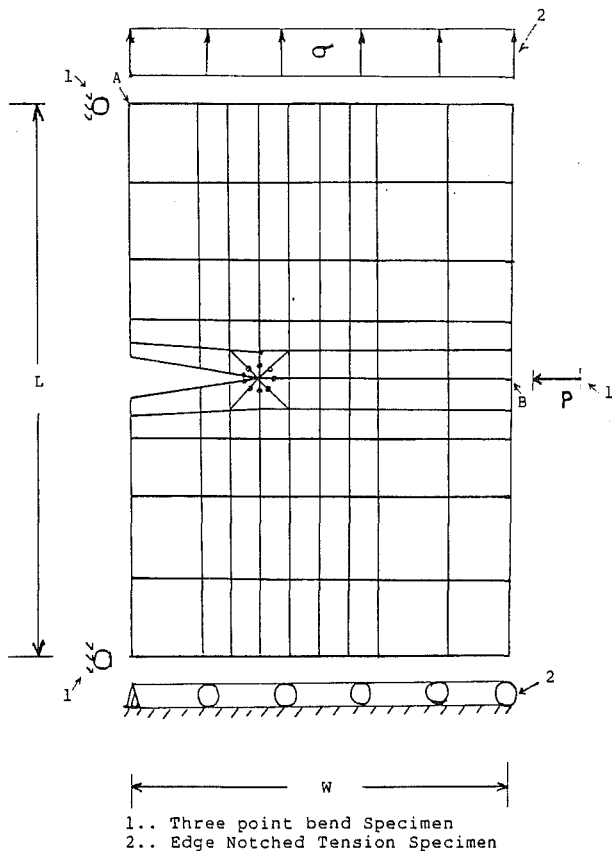


Fig. 5 Schematic of finite element model for constant tension and three-point bending

stress intensity factors accurately, the elements emanating from the crack tip were converted to singularity elements by shifting their midside nodes to the quarter point. The stress intensity factor calibration, which provides the Mode I and Mode II stress intensity factors as functions of the displacements of certain nodes of the singularity elements behind the crack tip, is given in [13]. The K_{ij} and C_i were calculated for the orthotropic material by modifying the element stiffness matrix of an isotropic finite element program. Although the comparisons are not presented here, the stress intensity factors calculated for $p(x)=0$ agreed within a few percent with those presented by Bowie [14] for the tested values $0.1 \leq a/w \leq 0.7$.

The system was loaded in $n+1$ different loading conditions, corresponding to unit loads at each node and a unit far field stress. For each loading case the displacements of each node were calculated including the load-point displacement. This procedure provided the nxn terms of K_{ij} , and the n terms of C_i . Note that the global stiffness matrix needs to be inverted only once for a given crack length. Once the coefficients are calculated, the problem is reduced to a system of n non-linear algebraic equations as follows. Recalling that $p(x) = A\sqrt{u(x)}$, the expression for nodal forces becomes

$$F_j = A \frac{a}{2q} \sqrt{u_j} = \bar{A} (u_j)^{1/2} \quad (6)$$

where a is the crack length and q is the number of quadratic displacement elements along the crack line. The resulting system of equations for crack opening becomes

$$u_i = \bar{A} [K_{ij}] u_j^{1/2} + \sigma \{C_i\} \quad i, j = 1, \dots, n \quad (7)$$

The nonlinear system of equations was solved using the IMSL routine 'DNEQNF,' which is based on the Levenberg-Marquadt and Powell algorithms [15].

It should be noted that Eq. (6) assumes that each node acts as an independent (leaf) spring. Although the work-equivalent

Table 1 Constitutive material properties

Constituent	Young's modulus, GPa	Poisson ratio	K_{IC} MPa \sqrt{m}
SiC fibers	390	0.3	5.0
Si ₃ N ₄ matrix	206	0.3	4.6

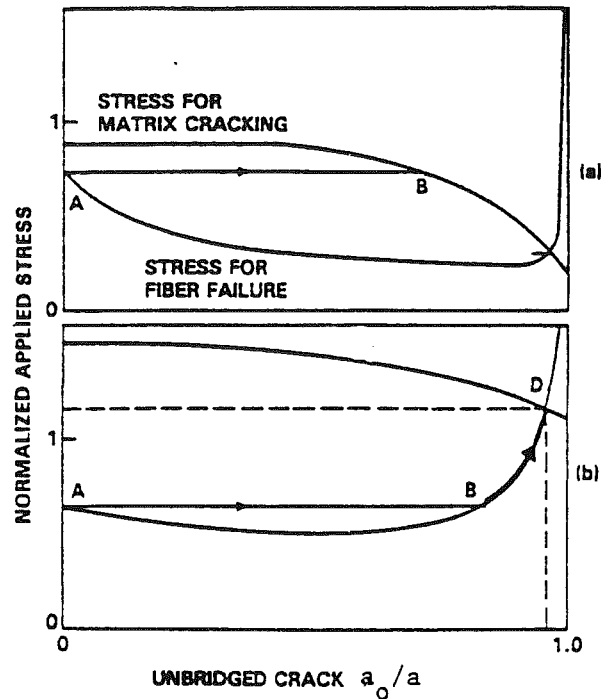


Fig. 6 Possible failure modes for brittle matrix composites [8]

nodal forces for the distributed closing stress for a quadratic element should be used in the calculations, numerical experimentation showed differences of approximately 4 percent in stress intensity factors between "exact" nodal forces and the "leaf" springs. Subsequent results were calculated using independent springs.

Results

The material properties used for the constituents are shown in Table 1. They correspond to the properties of a SiC reinforced Si₃N₄ matrix composite. The volume fraction of the 100 μ m-dia ($2R$ in Fig. 1a) fibers is $V_f = 0.4$. The shear strength of the fiber-matrix interface is taken as $\tau = 10$ MPa. Consistent with these values, the orthotropic bulk properties are [16, 17]: $E_{11} = 253.9$ GPa, $E_{22} = 279.6$ GPa, $\nu_{12} = 0.3$, and $G_{12} = 97.66$ GPa.

Composite failure is initiated when the applied stress exceeds the smaller of the matrix cracking stress σ_m (the stress that makes the stress intensity factor in the matrix equal to the fracture toughness of the matrix) and fiber failure stress σ_f . Subsequent failure events (at constant applied stress) involve combinations of stable and unstable fiber failure and/or matrix cracking. The sequence of these events depends on initial crack configuration a and a_o , specimen configuration, type of loading, and fiber strength σ_{fu} . As shown in Fig. 6, taken from [8], for initially fully bridged cracks two different sequences of failure events are possible for the case when the fiber failure stress is less than the matrix cracking stress. The first corresponds to the case in which the matrix cracking stress is slightly greater than the first fiber failure stress. Fiber failure initiates at point A and is unstable until point B. At this point the matrix cracks. Beyond point B the fibers fail as the matrix crack propagates. The second possibility corresponds to a ma-

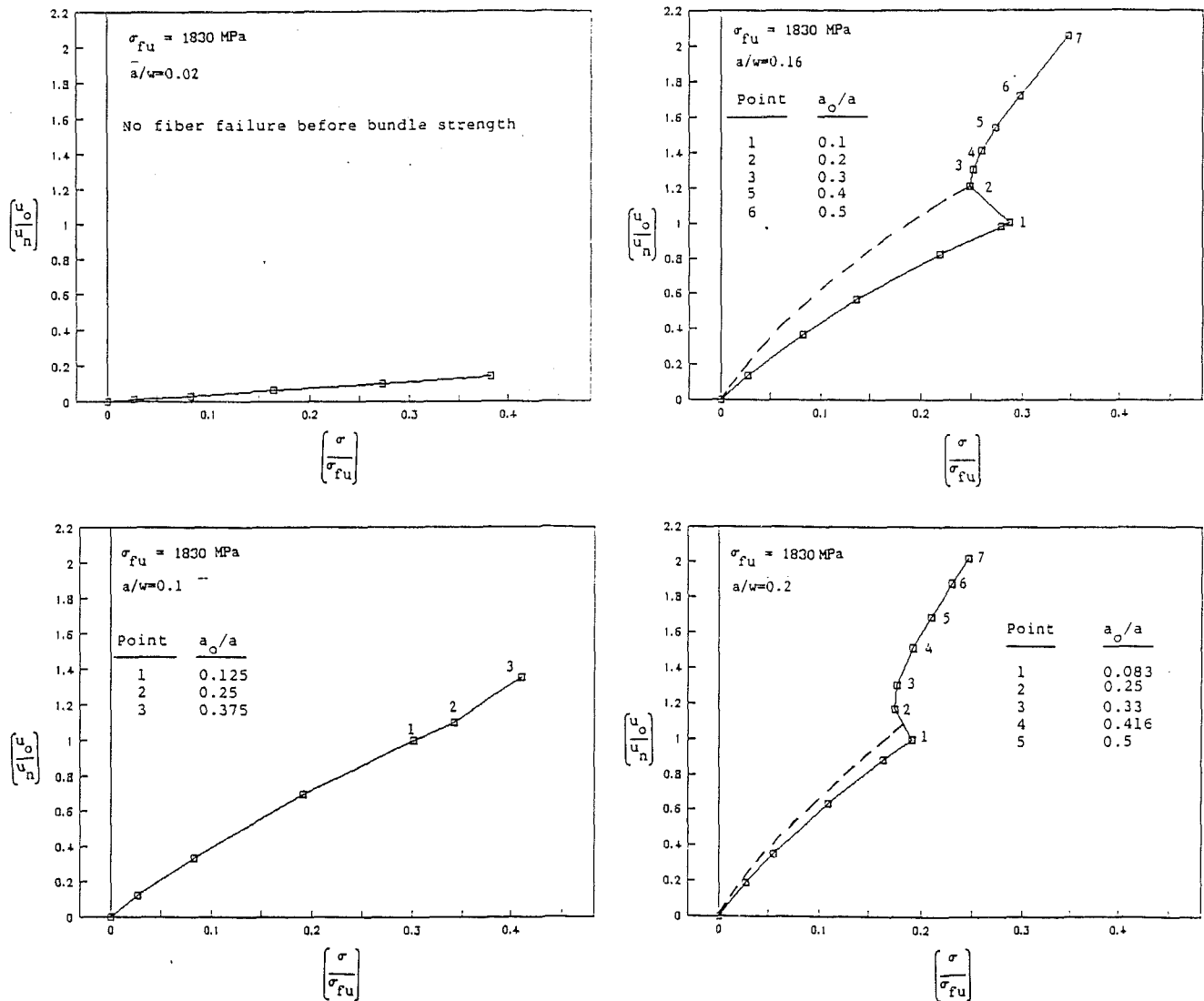


Fig. 7 Normalized CMOD as functions of normalized applied stress, tensile loading

trix cracking stress much greater than the fiber failure stress. In this case fiber failure is initiated at point *A* and is unstable until point *B*. At point *B* the system stabilizes. That is, an increasing stress is required to break additional fibers. This continues until point *D*, at which point the matrix cracks in an unstable manner. The third possible scenario corresponds to high fiber strengths in which the matrix cracks without any fiber failure, and hence the matrix cracks through the specimen leaving fibers intact. All of these possible events have been captured in the present analysis by varying σ_{fu} and crack length.

Two types of simulation were performed in this work for each type of loading (tension and bending). In the first, the total crack length was held constant while the load was monitored in such a way as to capture the stability characteristics of fiber failure. In these simulations the stress intensity factor at the tip of the matrix crack was not specified. The second type corresponds to a matrix crack propagating at a constant specified value of stress intensity factor. All of the cracks considered are initially fully bridged.

Fixed Crack Length Simulations—Constant Stress Loading

Effects of a/w . Numerical calculations were performed first for tension loading at fixed crack lengths in the range

$0.02 \leq a/w \leq 0.8$. However, only the results for $0.02 \leq a/w \leq 0.2$ are presented, since it was observed that for the tension loading and the considered specimen width the stable to unstable transition occurs in this range.

In the first type of simulation the far-field stress is increased for a fixed length, initially fully bridged crack until the crack opening at a point reaches the critical value u_n . When this critical crack opening is reached at a node, the node is released, and the applied stress is either increased or decreased, depending on the stability of fiber failure. If the stress level has to be increased to break additional fibers, the event is termed stable. If the stress level that produces fiber failure at a node is held constant, and additional fibers fail, the event is termed unstable. It may be possible, however, for unstable events to stabilize. For the unstable events, the load has to be controlled in order to capture the sequence of fiber failure (trace the unstable path).

Figures 7(a–d) are plots of normalized crack mouth opening displacement (CMOD) u_o as functions of normalized stress for $\sigma_{fu} = 1830$ Mpa. For very short crack lengths ($a/w = 0.02$) no fiber failure occurs for normalized stress levels less than 0.4, which corresponds to the bundle strength $V_{f\sigma_{fu}}$. This implies that most likely matrix cracking will occur before any fiber failure. For $a/w = 0.1$ the failure of the first fiber is stable, since increasing stress is required for additional fiber failure.

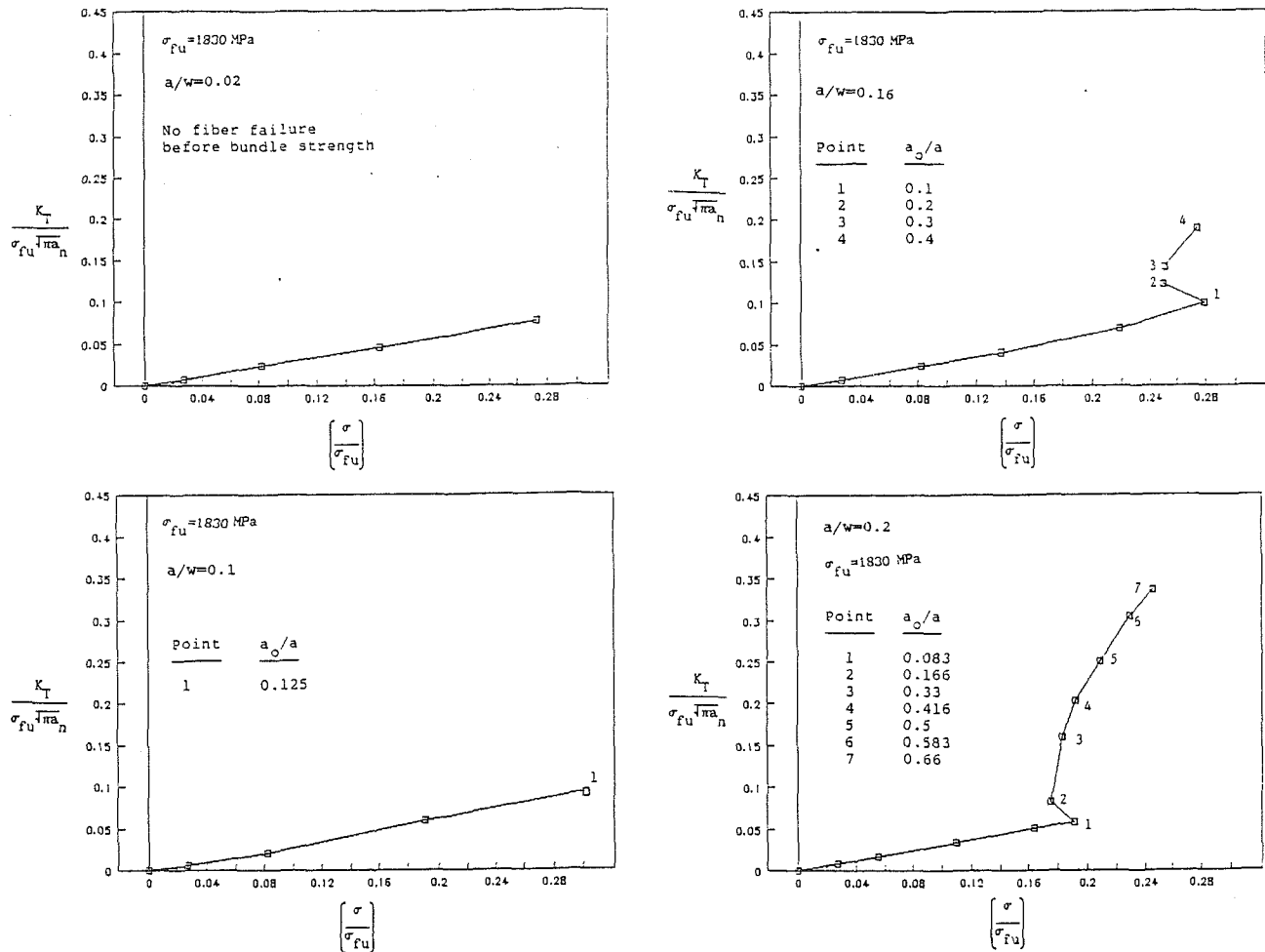


Fig. 8 Normalized stress intensity factor as functions of applied stress, tensile loading

For cracks longer than $a/w = 0.16$, initial fiber failure (until $a_o/a = 0.1$) is unstable. Fiber failure stabilizes, for this configuration, at $a_o/a \approx 0.4$. Consider point 1 in Fig. 7(c). If the stress were held constant, additional fibers would fail until $a_o/a \approx 0.4$. The stress would then have to be increased to break additional fibers. Moreover, if the stress is not decreased at point 1, subsequent fiber failure produces a discontinuity in the CMOD.

Consider next the stress intensity factors. The net stress intensity factor K_T is related to the far-field (K_A) and fiber bridging (K_F) stress intensity factors by $K_T = K_A - K_F$, so that the shielding due to the fibers is $K_F = K_A - K_T$.

Figures 8(a-d) and 9(a-d) are plots of normalized K_T and K_F , respectively, as functions of applied stress. The length a_n is defined by

$$a_n = [\pi \Sigma R (1 - V_f) E_m] / [16 \tau V_f E_f (1 - \nu^2)] \quad (8)$$

As discussed in [11], a_n , which is associated with a fully bridged crack in an infinitely extended material and is referred to as the bridging length scale, has special significance. For $a < a_n$, the crack is considered short in the sense that its bridging zone is still developing. For these short fully bridged cracks the forces in the fibers are relatively small, since the crack opening displacements are small. Hence the fibers do not shield the crack tip significantly, and the stress required to propagate the matrix crack is inversely proportional to the square root of the crack length, as for a monolithic matrix. For $a > a_n$ the crack is termed long, because the bridging zone has fully developed and a steady state is reached for matrix cracking (the

stress required to propagate the matrix crack is independent of crack length). For the considered composite $a_n = 0.256$ mm, 1.56 mm, and 2.56 mm for fiber strengths (which will be discussed subsequently) $\sigma = 300$ MPa, 1830 MPa, and 3000 MPa, respectively.

The stability of the fiber failure can also be seen in these figures. For example, compare K_F for $a/w = 0.02$ and $a/w = 0.16$. For 0.02 the shielding monotonically increases, while for 0.16 there is a sharp reduction after the first nodal failure (which corresponds to the discontinuous increase in K_T in Fig. 8c). Also note that for 0.16, even if the stress is reduced at the point of first fiber failure, the net stress intensity factor still increases. If the normalized matrix toughness were high enough (above point 4 in Figs. 8c and 8d), unstable nodal failure would occur before matrix cracking until $a_o/a \approx 0.4$, at which point the fiber failure stabilizes. If, on the other hand, the matrix toughness is below point 1, the matrix would crack before fiber failure.

From these graphs the qualitative response of initially partially bridged cracks can also be seen. Take, for example, Fig. 7(c). If a partially bridged crack of total length $a/w = 0.16$ ($a_o/a = 0.2$) has propagated in the matrix from an initial (unbridged) notch of length a/w ($a_o/a = 1.0$), no instability would be observed, since the CMOD versus applied stress curve would be as shown in dashed lines. For a crack length $a/w = 0.2$ with the same unbridged length ($a_o/a = 0.16$), the curve would be also as shown in dashed lines, and instability would still be observed. This suggests that for initially partially bridged cracks the transition from stable to unstable fiber failure occurs at longer crack lengths.

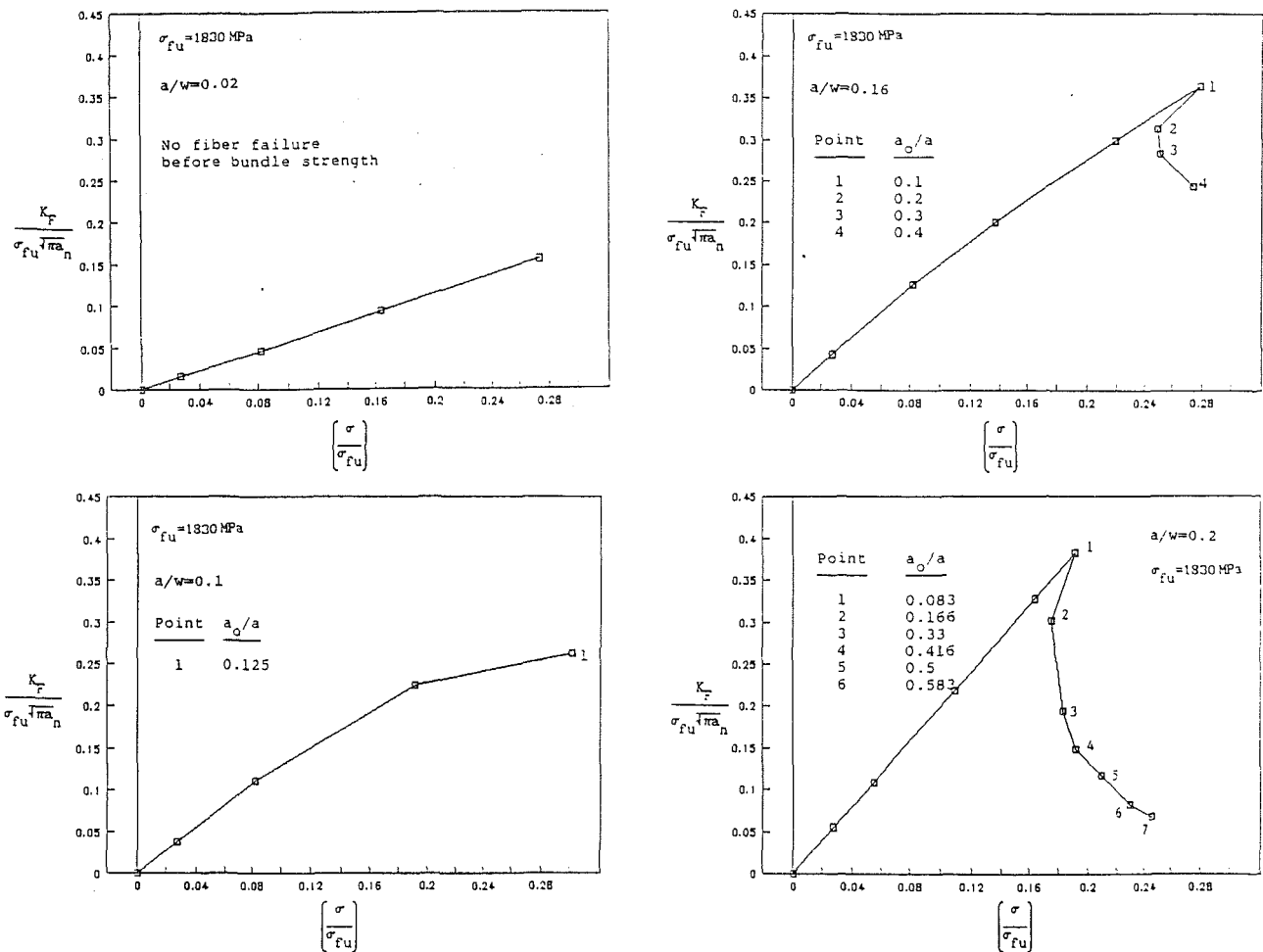


Fig. 9 Normalized shielding stress intensity factor as functions of applied stress, tensile loading

Effects of σ_{fu} . To investigate the effects of fiber strength on the stability of fiber failure, the following values of fiber strength were used: $\sigma_{fu} = 300, 1830$, and 3000 MPa.

The effects of fiber strength on the stability of fiber failure can be observed by comparing Figs. 7(d) and 10(a). For $\sigma_{fu} = 1830$ MPa, initial fiber failure is unstable, but stabilizes at $a_o/a \approx 0.42$. For $\sigma_{fu} = 3000$ MPa, on the other hand, unstable fiber failure does not stabilize.

This effect can also be observed by comparing Figs. 8(d) and 10(b). The net stress intensity factor for the lower fiber strength increases monotonically as the unstable fiber failure is traced. However, an increasing stress is needed to increase the net stress intensity factor after fiber failure stabilizes. For the higher fiber strength, on the other hand, as the unstable path is traced, the stress intensity factor increases drastically at stress levels less than the level that caused first fiber failure. These differences are also observed in Figs. 9(d) and 10(c), which show that the reduction in shielding beyond first fiber failure for the higher fiber strength is much more drastic than for the lower strength.

Matrix Crack Propagation Simulations—Constant Stress Loading

In these simulations, an initially fully bridged crack of length $a/w = 0.02$ is loaded until the stress intensity factor at its crack tip is equal to the fracture toughness of the matrix, taken as $4.6 \text{ MPa}\cdot\text{m}^{1/2}$. As the load is increased, if the crack opening displacement at any node reaches u , the node is released. When

the stress intensity factor reaches the critical value, the matrix crack is extended.

Load Deflection Curves. Figure 11(a) is a plot of applied stress versus load point displacement for $\sigma_{fu} = 300$ MPa. Figure 11(b) is an enlarged view of the snap back region in Fig. 11(a). The stress is increased until point 1, at which time approximately 63 percent of the fibers behind the crack tip have failed, and the matrix cracks. The matrix crack extends to $a/w = 0.1$. At this point the stress is reduced to point 2, at which time the fibers at the trailing edge of the bridging zone start breaking. The stress is then increased until point 7, at which time all the nodes are released (it may be possible that a few fibers remain intact, but since the first node behind the crack tip is a finite distance from the crack tip, this is not captured), $a_o/a = 1.0$, and the matrix crack extends to $a/w = 0.2$, with $a_o/a = 1.0$. This process of complete fiber rupture/matrix crack extension continues (points 10, 12, 14) until point 16 at which point $a/w = 0.6$. Figure 11(a) was obtained by monitoring the fiber failure events. If the total crack length were controlled the stress-deflection curve would be as shown in Fig. 12. Note, however, that information is gained by monitoring the fiber failure events. For example, if the stress is kept constant at point 1 of Fig. 11(a) (or point A of Fig. 12), the extension of the matrix crack through the specimen is accompanied by simultaneous fiber failure. Thus the failure is catastrophic.

For $\sigma_{fu} = 1830$ MPa, Figs. 13 and 14 show that the failure is not catastrophic, since as the matrix crack propagates through the specimen most of the fibers behind the crack remain intact ($a_o/w \approx 0.25$). Although the simulations were not continued

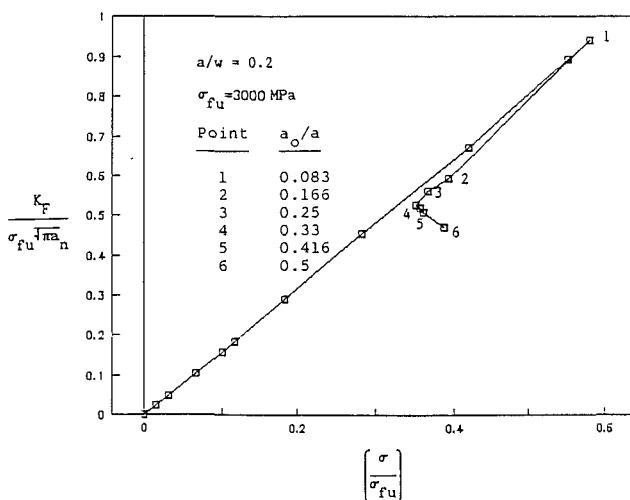
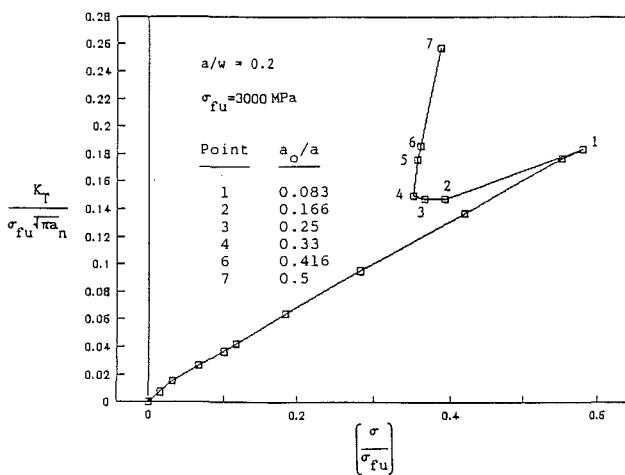
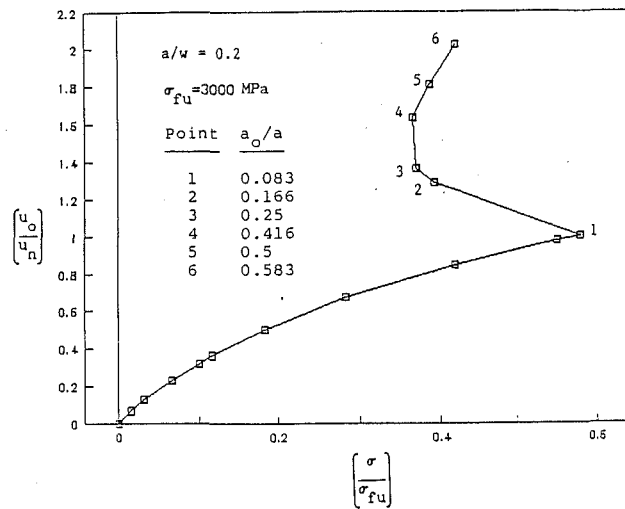


Fig. 10 Normalized (a) CMODs, (b) stress intensity factors, and (c) shielding stress normalized applied stress, tensile loading

beyond point 16 in Fig. 13, an increase in stress is needed to break the remaining fibers.

For the highest fiber strength considered, Fig. 15 shows that the matrix crack propagates through the specimen while all the fibers behind the crack tip remain intact. This will lead to

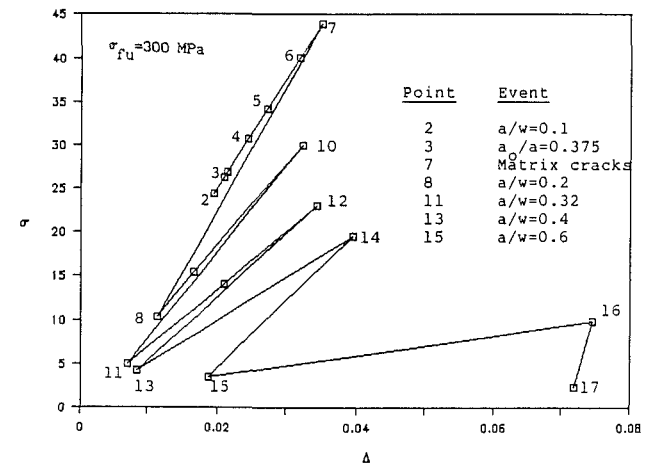
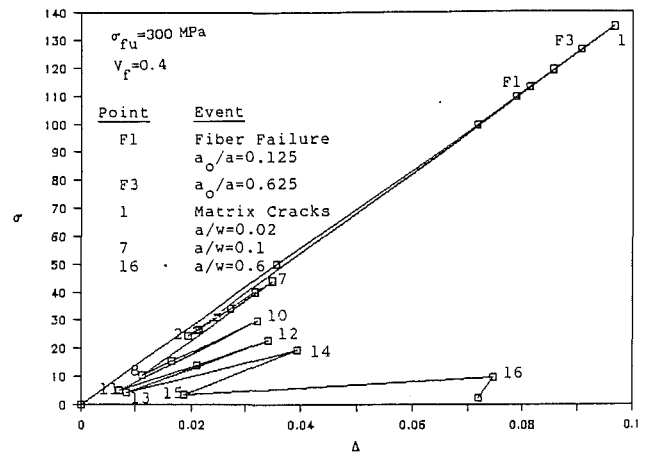


Fig. 11 Stress-deflection curves, tensile loading

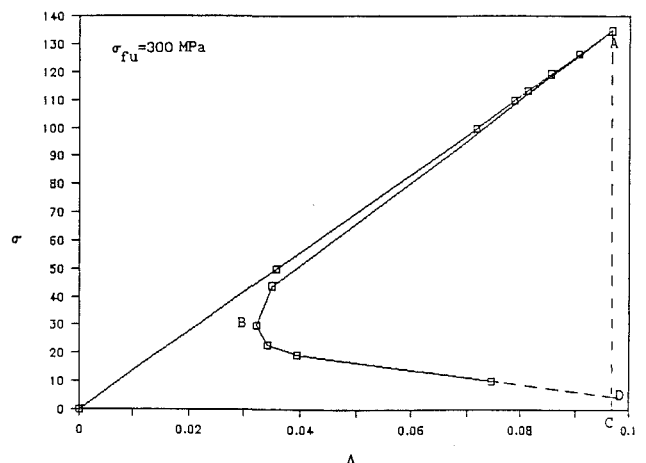


Fig. 12 Stress-deflection curve, tensile loading

multiple matrix cracking and an ultimate strength governed by the bundle strength.

The stress-deflection curves clearly demonstrate the brittle to ductile transition of the considered initially fully bridged cracks. It should also be noted that the critical stress for crack extension and the strain to failure are higher for the noncatastrophic failure modes than for the catastrophic failure modes.

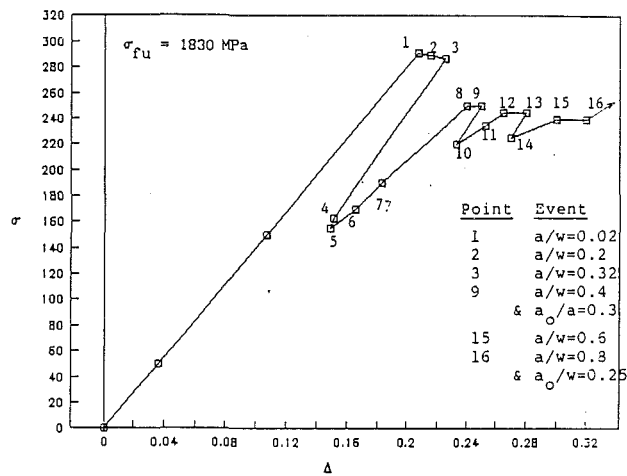


Fig. 13 Stress-deflection curve, tensile loading

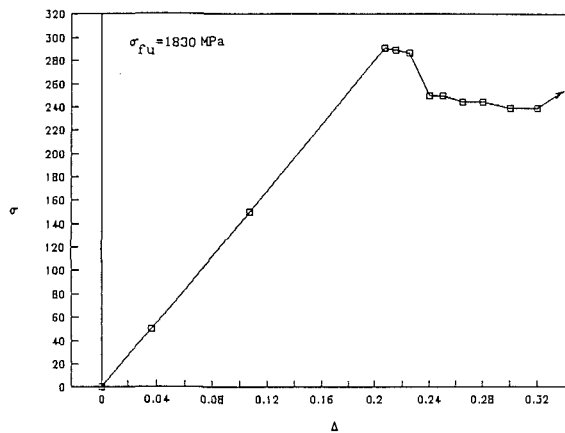
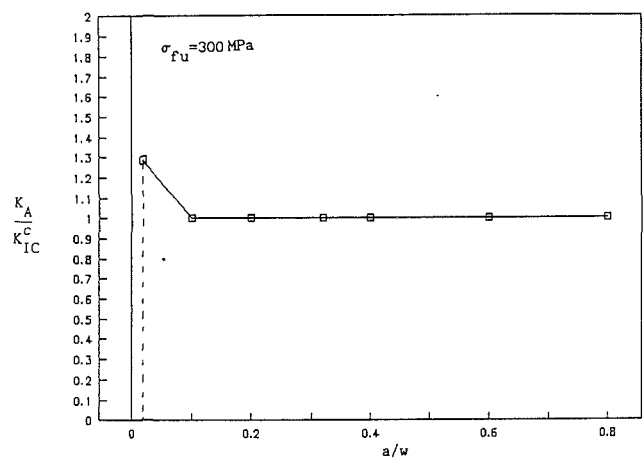


Fig. 14 Stress-deflection curve, tensile loading

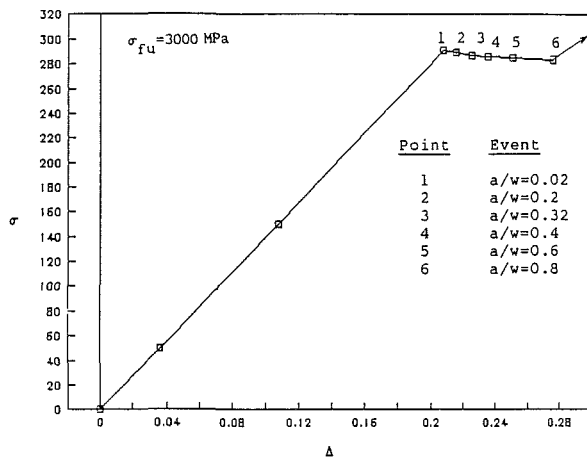
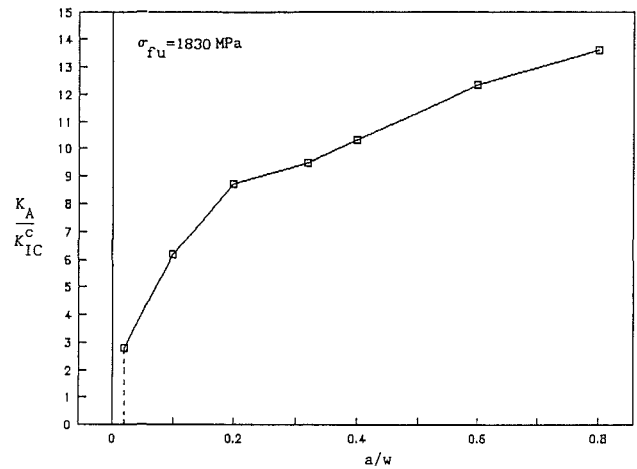


Fig. 15 Stress-deflection curve, tensile loading

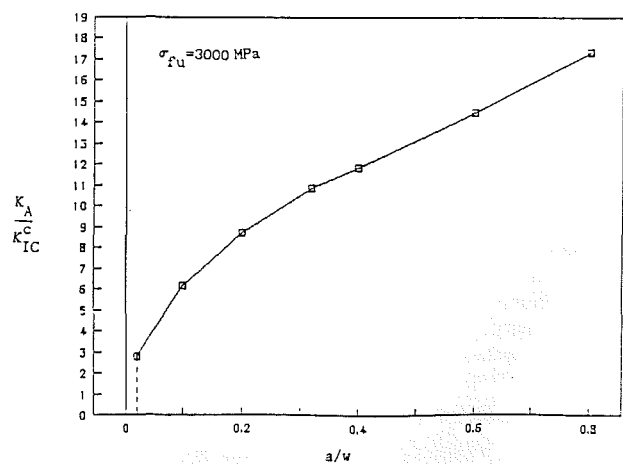


Fig. 16 Normalized resistance curves, tensile loading

Resistance Curves. Figures 16(a-b) are plots of the normalized applied stress intensity factor, which leads to matrix crack growth as functions of matrix crack length for the different fiber strengths. For $\sigma_{fu} = 300$ MPa, the applied stress intensity factor is greater than the fracture toughness of the matrix for $a/w \leq 0.1$, since the crack is partially bridged. Beyond $a/w = 0.1$ the normalized applied stress intensity factor

is equal to 1.0, since for each crack length all the fibers break before the matrix crack extends.

For $\sigma_{fu} = 1830$ MPa, Fig. 16(b) shows that the applied stress intensity factor increases monotonically as the matrix crack extends through the specimen. For this value of fiber strength

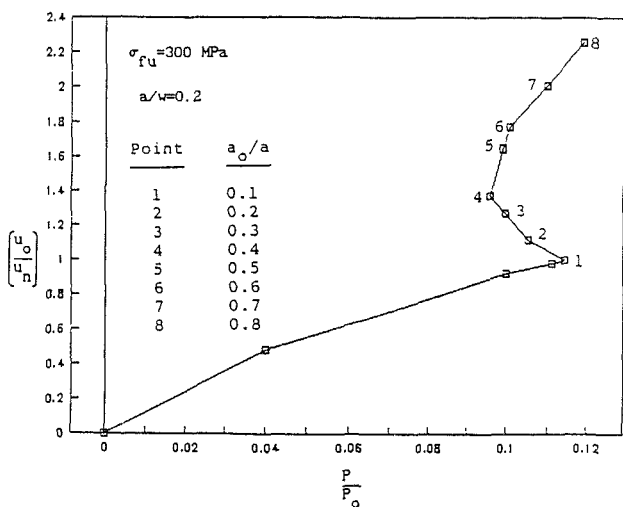
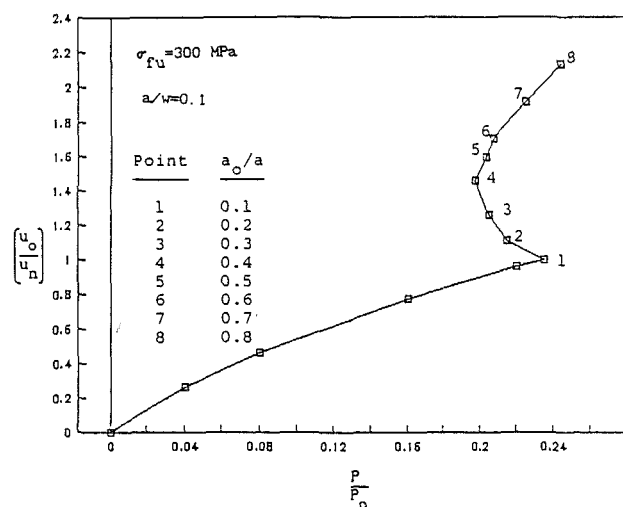
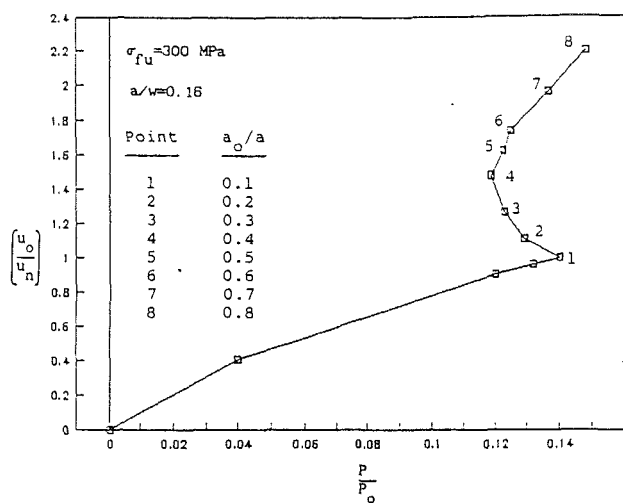
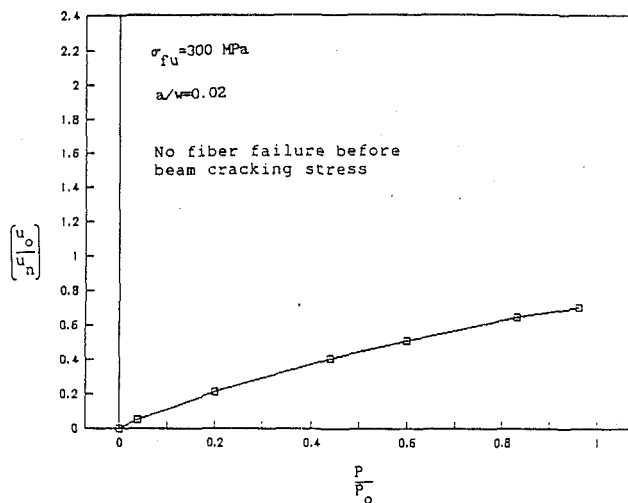


Fig. 17 Normalized CMOD as functions of three-point bending load

a steady-state value is not reached, but this figure suggests that if the simulation were carried out for slightly lower strength, steady state would be reached. Recall that for this fiber strength matrix crack growth is accompanied by fiber failure. If a smaller fiber strength was used in the calculations the fiber bridging would be limited to a relatively small region behind the crack tip, and as the matrix crack propagates, for every fiber the crack crosses, a fiber behind the crack tip would fail. For $\sigma_{fu} = 3000 \text{ MPa}$, the normalized applied stress intensity factor also increases monotonically. Although the simulations were not continued beyond $a/w = 0.8$, Fig. 16(c) suggests that the stress intensity factor would increase drastically as the matrix crack approaches the free edge.

Three-Point Bend Loading

The results presented in the preceding section demonstrate the effects initial crack length and fiber strength have on the stability of fiber failure. Similar results are presented next for the three-point bending case. These will demonstrate that the distribution of stresses that result from the applied loads also strongly influence the failure mechanisms.

Figures 17–20, which are similar to the figures presented for the constant tension loading, clearly show the effects of external loading on the stability of the bridged cracks. Figures 17–19 are for fixed a/w , while Fig. 20 is for a propagating

matrix crack. The load P is nondimensionalized with respect to the load P_o , which represents the load that would produce a stress equal to σ_{fu} at the outer fibers in an unnotched monolithic beam made out of fiber material. Recall that for the constant tension specimen, the crack lengths $a/w = 0.02$ and 0.10 were stable, while cracks of length $a/w = 0.16$ and 0.2 exhibited instabilities in fiber failure. Moreover, the severity of the instabilities increased with increasing fiber strength. Figure 17(b) shows an instability in $a/w = 0.1$ at the lowest fiber strength. Furthermore, when the fiber failure stabilizes at point 8, 80 percent of the fibers behind the crack tip are broken. Figure 20 is the stress-displacement curve of a matrix crack propagating from an initially fully bridged length $a/w = 0.1$. The load increases to point 1, at which point the unbridged length is $a_o/a = 0.8$ and the matrix crack propagates. If the stress is held constant there is a discontinuity in the curve and the matrix crack ends up at $a/w = 0.6$ at a relatively low stress.

The results clearly show that the bending specimen inherently more unstable than the constant tension specimen.

Conclusions and Recommendations

The examples considered in this paper clearly demonstrate that:

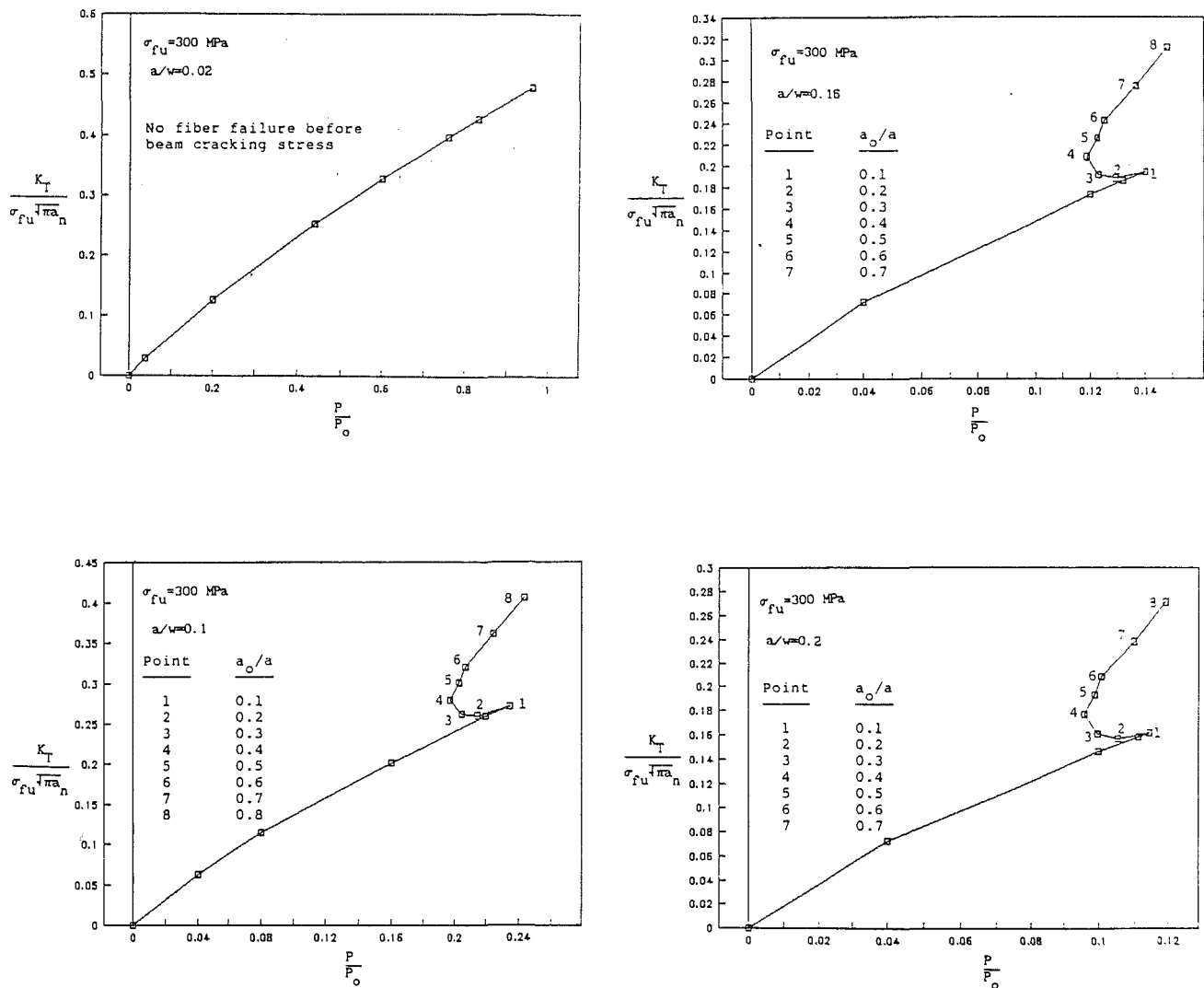


Fig. 18 Normalized stress intensity factor as functions of three-point bending load

1 Specimen configuration, distribution of applied loads, and constituent properties (fiber strength, etc.) *strongly* influence the amount of crack tip shielding the fibers provide in a bridged crack.

2 If two specimens having different configurations (or if they have the same configuration but are loaded differently) have the same *applied* stress intensity factor, their failure characteristics may differ significantly. One may fail catastrophically, while the other may fail noncatastrophically.

3 The critical stress for crack extension and the strain to failure for noncatastrophic failure are higher than for catastrophic failure.

4 As pointed out in [11], conclusions 1, 2, and 3 may lead to nonconservative predictions of material properties if current testing standards are applied to materials that exhibit crack bridging, since these procedures were developed for materials that do not exhibit crack bridging.

5 The bridging force-crack opening displacement (C.O.D.) relation $p(x) = p(\text{C.O.D.})$ should be included in analyses of experimental specimens or components. This relation should be treated as an engineering property of the material.

Acknowledgments

This work was funded by NASA Lewis Research Center

under Grant NAG3-856 and by the Defense Advanced Research Projects Agency through the University Initiative Program of C.W.R.U. under ONR Contract N-0013-86-K-0773. The first author thanks Dr. B. N. Cox for many helpful discussions and for providing us with unpublished manuscripts [10, 11].

References

- 1 Barenblatt, G. I., "The Mathematical Theory of Equilibrium Cracks in Brittle Fracture," *Advances in Appl. Mech.*, Vol. 7, 1962, pp. 55-129.
- 2 Dugdale, D. S., "Yielding of Steel Sheets Containing Slits," *J. Mech. Phys. Sol.*, Vol. 8, 1960, pp. 100-108.
- 3 Visalvanich, K., and Naaman, A. E., "Fracture Model for Fiber Reinforced Concrete," *ACI Journal*, Mar.-Apr. 1983, pp. 128-138.
- 4 Hillerborg, A., Modeer, M., and Petersson, P. E., "Analysis of Crack Formation and Crack Growth in Concrete by Means of Fracture Mechanics and Finite Elements," *Cement and Concrete Research*, Vol. 6, 1976, pp. 773-782.
- 5 Catalano, D. M., and Ingraffea, A. R., "Concrete Fracture: A Linear Elastic Fracture Mechanics Approach," Report No. 82-1, Department of Structural Engineering, Cornell University, 1982.
- 6 Ballarini, R., Shah, S. P., and Keer, L. M., "Crack Growth in Cement Based Composites: Influence of Fiber Strength," *Engineering Fracture Mechanics*, Vol. 20, 1984, pp. 433-445.
- 7 Marshall, D. B., Cox, B. N., and Evans, A. G., "The Mechanics of Matrix Cracking in Brittle-Matrix Fiber Composites," *Acta Metallurgica*, Vol. 33, 1985, pp. 2013-2021.
- 8 Marshall, D. B., and Cox, B. N., "Tensile Fracture of Brittle Matrix Composites," *Acta Metallurgica*, Vol. 35, 1987, pp. 2607-2619.

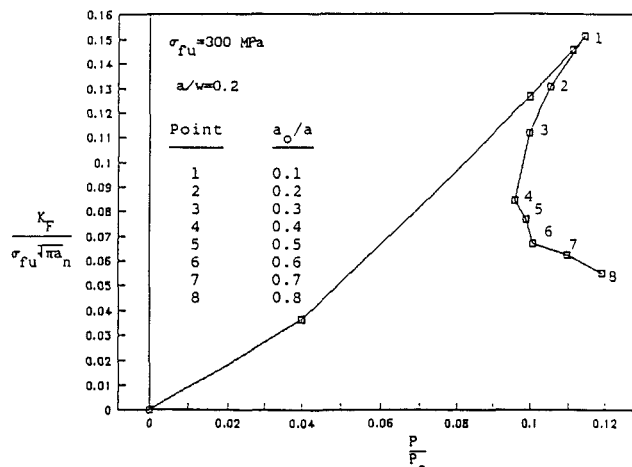
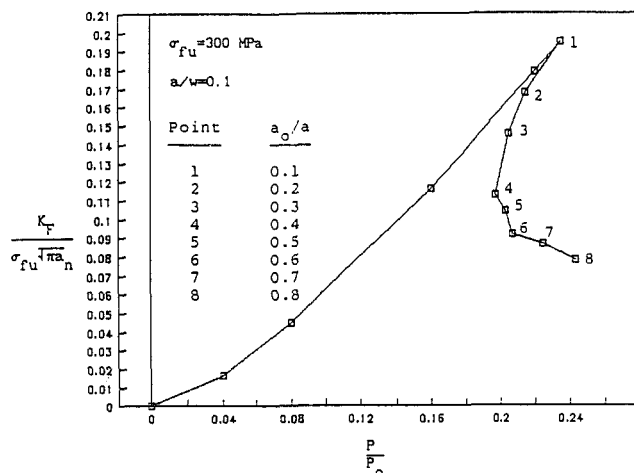
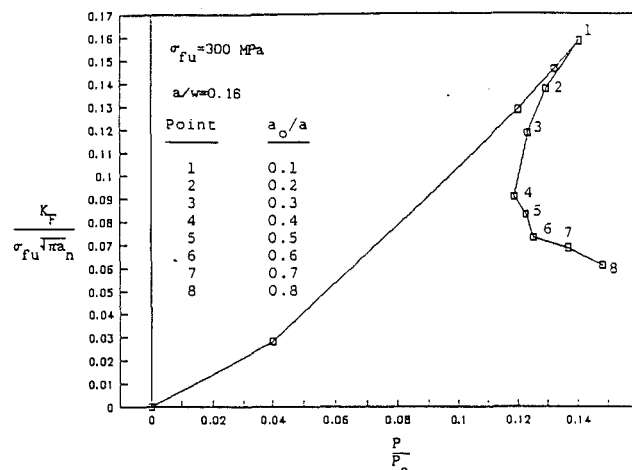
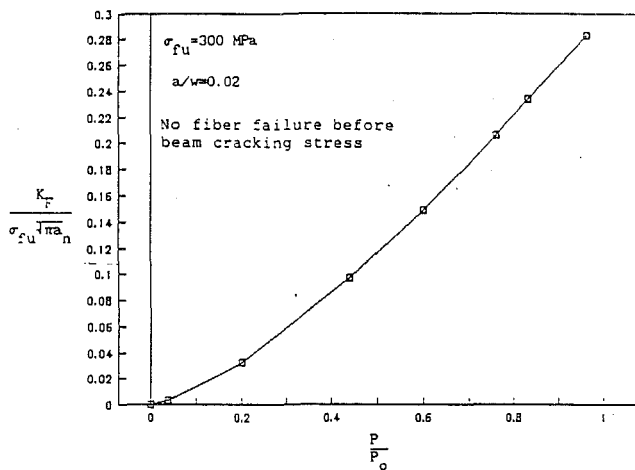


Fig. 19 Normalized shielding stress intensity factor as functions of three-point bending load

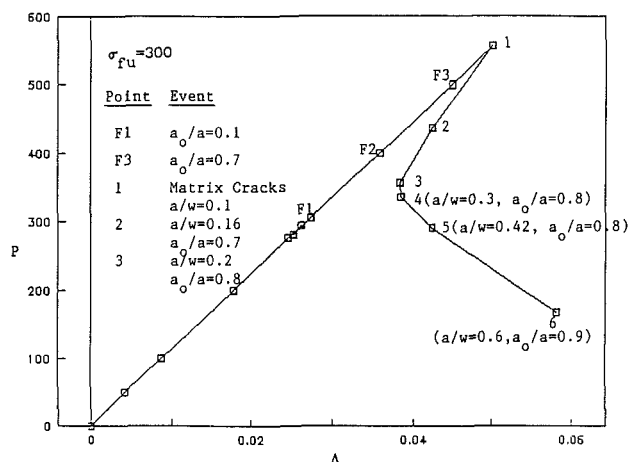


Fig. 20 Load-deflection curve for three-point bend specimen

9 Carpinteri, A., "Cusp Catastrophe Interpretation of Fracture Instability," *J. Mech. Phys. Sol.*, Vol. 37, 1989, pp. 567-582.

10 Cox, B. N., and Marshall, D. B., "Stable and Unstable Solutions for Bridged Cracks in Various Specimens," *Acta Metallurgica*, Vol. 39, 1991, pp. 579-589.

11 Cox, B. N., "Extrinsic Factors in the Mechanics of Bridged Cracks," submitted for publication.

12 Thouless, M. D., and Evans, A. G., "Effects of Pull-out on the Mechanical Properties of Ceramic-Matrix Composites," *Acta Metallurgica*, Vol. 36, 1988, pp. 517-522.

13 Muju, S., "Stability Analysis of Bridged Cracks in Ceramic Matrix Composites," M.S. Thesis, Case Western Reserve University, Jan. 1991.

14 Bowie, O. L., and Freese, C. E., "Central Crack in Plane Orthotropic Sheet," *International Journal of Fracture Mechanics*, Vol. 8, 1972, pp. 49-57.

15 More, J. J., Garbow, B. S., and Hillstrom, K. E., "User Guide for Minpack-1," Argonne National Lab ANL-80-74.

16 Ballarini, R., and Ahmed, S., "Local-Global Analysis of Crack Growth in Continuously Reinforced Ceramic Matrix Composites," *ASME JOURNAL OF ENGINEERING FOR GAS TURBINES AND POWER*, in press.

17 Kanninen, M. F., "Applications of Fracture Mechanics to Fiber Composite Materials and Adhesive Joints: A Review," *Proceedings of the 3rd International Conference on Numerical Methods in Fracture Mechanics*, Swansea, United Kingdom, 1984, pp. 641-680.

M. van Roode

J. R. Price

Solar Turbines Incorporated,
San Diego, CA 92186

C. Stala

Salomon Brothers,
New York, NY

Ceramic Oxide Coatings for the Corrosion Protection of Silicon Carbide

Silicon carbide is currently used as a structural material for heat exchanger tubes and related applications because of its excellent thermal properties and oxidation resistance. Silicon carbide suffers corrosion degradation, however, in the aggressive furnace environments of industrial processes for aluminum remelting, advanced glass melting, and waste incineration. Adherent ceramic oxide coatings developed at Solar Turbines Incorporated, with the support of the Gas Research Institute, have been shown to afford corrosion protection to silicon carbide in a simulated aluminum remelt furnace environment as well as in laboratory-type corrosion testing. The coatings are also protective to silicon carbide-based ceramic matrix composites.

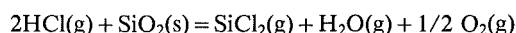
Introduction

Silicon carbide (SiC) ceramics have a unique combination of light weight, strength, thermal conductivity, and thermal shock and oxidation resistance at temperatures in excess of 1000°C. The combination of properties of SiC compares favorably with those of metals and oxide ceramics, and SiC is therefore a candidate material for a number of high-temperature applications, such as heat transfer surfaces of heat exchangers and structural materials for hot section components of advanced gas turbines.

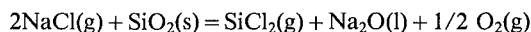
Unfortunately, the favorable high-temperature properties of SiC are compromised by the degradation in certain corrosive furnace atmospheres containing alkalis (Na, K), halides (Cl, F), and sulfur (S). The corrosive degradation limits the service life of SiC components exposed to these environments. A review of the corrosive degradation of silicon-based ceramics (SiC and Si₃N₄) has been given by Jacobson et al. (1988). The corrosion is attributed to the presence of liquid deposits of alkali metal salts and oxide slags in contact with the silicon-based surface. The survey by Jacobson et al. focuses on sodium sulfate (Na₂SO₄) induced corrosion. The key reactant is Na₂O, which reacts with the normally protective silica (SiO₂) scale to form liquid Na₂O·x(SiO₂), which is nonprotective, and the underlying silicon-based material is exposed to extensive attack. Na₂SO₄-induced corrosion can be expected to be important in heat engines with SiC or Si₃N₄ hot section components operating on liquid fuels containing S while Na is ingested with the intake air, e.g., from a marine environment or industrial process using Na-based raw materials. This type of corrosion is not unlike the hot corrosion of turbine alloys observed under Na₂SO₄ generating conditions, since both processes involve the fluxing of protective oxide scales.

Related corrosive degradation processes have been observed in industrial processes using alkali halide fluxes for the secondary refining of metals. An example is the aluminum remelt industry, which uses mixtures of alkali halides sometimes with the addition of the highly corrosive cryolite (Na₃AlF₆) to remove surface oxides. Van Roode et al. (1988) describe surface recession rates of 2.5–10 mm/yr measured for SiC heat exchanger tubes exposed to aluminum remelt operations using corrosive alkali halide containing fluxes. Similar high recession rates have been described by Goldfarb (1988) for tubular SiC heat exchanger materials exposed to sodium silicate vapors of an advanced glass melting environment.

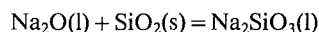
McNallan et al. (1989) have calculated free energies of reaction [$\Delta G^\circ(1400\text{ K})$] for potential reactions at the SiC surface in the corrosive aluminum remelt environment. Thermodynamic data for similar reactions were also reported earlier by Federer et al. (1985). The thermodynamic calculations show that it is unlikely that the protective SiO₂ surface layer will react to any great extent with only hydrogen or alkali halides. On the other hand reactions between SiO₂ and Na₂O or K₂O have negative $\Delta G^\circ(1400\text{ K})$ values, indicating that these reactions are a principal source of accelerated corrosion in these environments.



$$\Delta G^\circ(1400\text{ K}) = +117\text{ kcal}$$



$$\Delta G^\circ(1400\text{ K}) = +183\text{ kcal}$$



$$\Delta G^\circ(1400\text{ K}) = -52\text{ kcal}$$

McNallan et al. (1989) have also pointed to the important role of water vapor in the corrosion process. While reactions in the absence of water vapor generally have positive $\Delta G^\circ(1400\text{ K})$ values the same reaction written with H₂O as a reactant

Contributed by the International Gas Turbine Institute and presented at the 36th International Gas Turbine and Aeroengine Congress and Exposition, Orlando, Florida, June 3–6, 1991. Manuscript received at ASME Headquarters February 6, 1991. Paper No. 91-GT-38. Associate Technical Editor: L. A. Riekert.

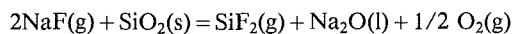
Table 1 Properties of ceramic oxides (van Roode and Price, 1987)

Coating	Coeff. of Thermal Expansion (cm/cm/°C x 10 ⁻⁶)	CTE Range (°C)	Modulus (GPa)*	Melting Point (°C)
Zircon	5.6	25-1204	76-103	1680
Mullite	5.6	25-1500	145	1850
Chromia	5.4-7.5	27-1200		
Spinel	5.0	25-1200	234-289	2266
Zirconia (unstab.)	4.4	25-1000	241	2700
Zirconia (part.-stab.)	8.0-10.6		205	
Alumina	7.9-11.9	21-1760	358	2015
SiC	4.3	24-871	654	2700
	5.4	538-2204	482	

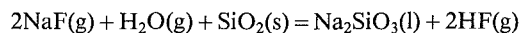
* Converted from psi in the reference

** Data from Ceramic Source '89 for partial stabilized zirconia

and HCl or HF as a reaction product have negative ΔG° (1400 K) values.



$$\Delta G^\circ(1400 \text{ K}) = +130 \text{ kcal}$$



$$\Delta G^\circ(1400 \text{ K}) = -29.5 \text{ kcal}$$

The thermodynamic calculations also show that reactions involving fluoride species have more negative free energy of reaction values than reactions involving chloride species consistent with the industrial experience that fluorides are more corrosive than chlorides. Once the protective SiO_2 surface layer has been removed, reactions between the underlying SiC and alkali halides have been shown to be thermodynamically favored (McNallan et al., 1989).

The corrosive degradation of SiC can be reduced by modifying the surface of the substrate by applying a coating of a material that has better corrosion resistance than SiC itself. Suitable materials for surface modification are ceramic oxides, such as alumina, mullite, or zirconia. These materials by themselves are no replacement for SiC because of their inferior thermal conductivity and thermal shock resistance. But combining the superior corrosion resistance of these materials with the attractive combination of other properties provided by SiC could result in a structural material that could meet the demanding requirements of advanced heat engines and heat recovery devices in a broad range of high-temperature applications in severely corrosive environments.

A protective coating for SiC has several functions. In the first place it creates a barrier between the substrate and condensing corrosive species in the environment. The coating is partially sacrificial; its degradation postpones attack on the substrate. Secondly, the coating may contain certain refractory oxides that when combined with the condensing and reacting species at the substrate surface increase their softening point. The increased viscosity of these deposits lessens hot corrosion and, hence, improves substrate service life.

Work at Solar Turbines Incorporated started in March of 1986 to develop a coatings technology aimed at improving the corrosion resistance of silicon-based heat transfer surfaces of recuperators. The work carried out under a program sponsored by the Chicago-based Gas Research Institute focused on heat exchanger applications for the secondary aluminum melter industry, but the technology is believed to be applicable to heat recovery for a wider range of corrosive industrial processes including advanced glass melting and waste incineration. Subsequent work has demonstrated that the concept of a protective coatings technology is equally applicable to other silicon-based ceramic systems such as Si_3N_4 and SiC-based ceramic matrix composites. This paper summarizes the major aspects of the

coating development and evaluation. Details of the experimental work have been presented elsewhere and can be found in referenced publications, conference proceedings, and GRI reports.

Coating Development on Monolithic SiC

The basic philosophy of the coating development program is to apply adherent coatings of a material that is inherently more corrosion resistant than the SiC substrate using an inexpensive commercially available process. Ceramic oxide materials were chosen as the coating precursors because of their known superior corrosion resistance over SiC. For example, Goldfarb (1988) reported that dense alumina ceramics have two to four times greater corrosion resistance than SiC in a corrosive glass melting environment. Federer and Jones (1985) reported that while SiC corroded at a projected rate of 0.5 mm/yr in an aluminum remelt furnace, alumina was essentially unaffected.

The following factors were found to be important for the selection of coating precursor materials:

- Good chemical stability up to $\approx 1300^\circ\text{C}$.
- A coefficient of thermal expansion that closely matches that of SiC.
- A low modulus of elasticity.
- The availability of the precursor as a commercial plasma spray powder.

Table 1 lists selected properties of ceramic oxides evaluated under the program.

Although mullite as a coating material has obvious advantages from an adherence point of view, this coating's corrosion resistance is less than that of other SiO_2 -free oxides (mullite has the composition $3\text{Al}_2\text{O}_3 \cdot 2\text{SiO}_2$). Federer (1989) reported that the corrosion resistance of mixed ceramic oxides improved with a reduced SiO_2 content. Alumina- and zirconia-based coatings can be expected to provide better corrosion resistance than mullite but, unfortunately, these materials have expansivities and elastic moduli that result in thermal stresses leading to cracking and debonding during thermal cycling. A strategy well known from thermal barrier coating development for gas turbine applications was therefore used to incorporate these corrosion-resistant materials in multilayer coating systems.

The coatings were deposited using conventional air plasma spraying, which is a rapid inexpensive surface modification process. Surface roughening is essential for the deposition of an adherent plasma spray coating. An impediment to plasma spraying SiC substrates is that this material has a greater hardness than most of the commercially available grit blast media, with the exception of SiC. But SiC is not an effective blasting medium since its hardness can be expected to match that of the substrate. In our work at Solar we have found a proprietary

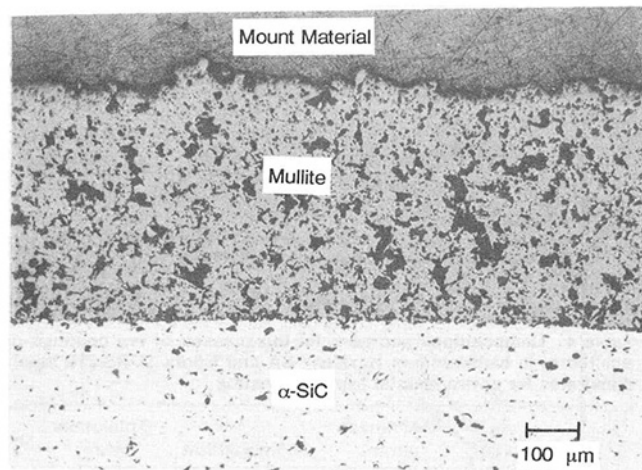


Fig. 1 Mullite coated Hexaloy® SA after isothermal and cyclic heat treatment (van Roode and Price, 1987)

Table 2 Advanced coating systems on Hexaloy® SA (van Roode et al., 1990)

Duplex Coating (A)		Graded Multi-layer Coating (B)	
Component	CTE(cm/cm/°C×10 ⁻⁶)	Component	CTE(cm/cm/°C×10 ⁻⁶)
Mullite	5.6	Mullite	5.6
Alumina	~8.8	75Mullite/25Alumina	6.4
		50Mullite/50Alumina	7.2
		25Mullite/75Alumina	8.0
		Alumina	8.8

surface treatment that is not based on grit blasting useful in preparing the surface for plasma spray deposition.

Early coating deposition trials using α -sintered (Carborundum's Hexaloy® SA) substrates showed that only mullite gave coatings that remained adherent and crack-free following isothermal (1093°C/120 h) and cyclic (1010–371°C/60 one hour cycles). Mullite has an expansivity close to that of SiC and its elastic modulus is relatively low, thus confirming the coatings selection criteria. The mullite coating was subsequently applied to a number of other SiC substrates including Coors' reaction bonded SCRB-210, Norton's reaction bonded NC-430, and Norton's recrystallized and sintered CS-101K. Figure 1 shows an early coating applied at a thickness of ≈ 0.50 mm to Hexaloy® SA. Mullite coatings as thick as 1.25 mm have since been deposited under this program. All other coatings were inferior to mullite. The zircon coating appeared visually adherent, although cracks could be seen microscopically. The alumina coating remained adherent upon thermal cycling but tensile cracks could be observed. The chromia, spinel, and zirconia coatings had tensile cracks and easily flaked off the substrate following thermal cycling.

The approach followed was to bridge the coefficient of thermal expansion difference between the low-expansion SiC substrate and the high-expansion oxide with a material with an intermediate expansivity. The multilayer coating system has graded expansivities. Two coating systems based on mullite and alumina are shown in Table 2. A simple duplex coating (A) showed no observable cracking upon cursory visual examination following isothermal and cyclic heat treatment, but tensile cracking was observed upon further microscopic examination. A multilayer coating with a more gradual change in thermal expansion from mullite to alumina (B) showed no cracking upon visual and microscopic examination following the isothermal and cyclic heat treatment.

Graded coating systems incorporating yttria and yttria-stabilized zirconia were also deposited. These systems also were shown to remain adherent and crack-free following the standard isothermal and cyclic heat treatments.

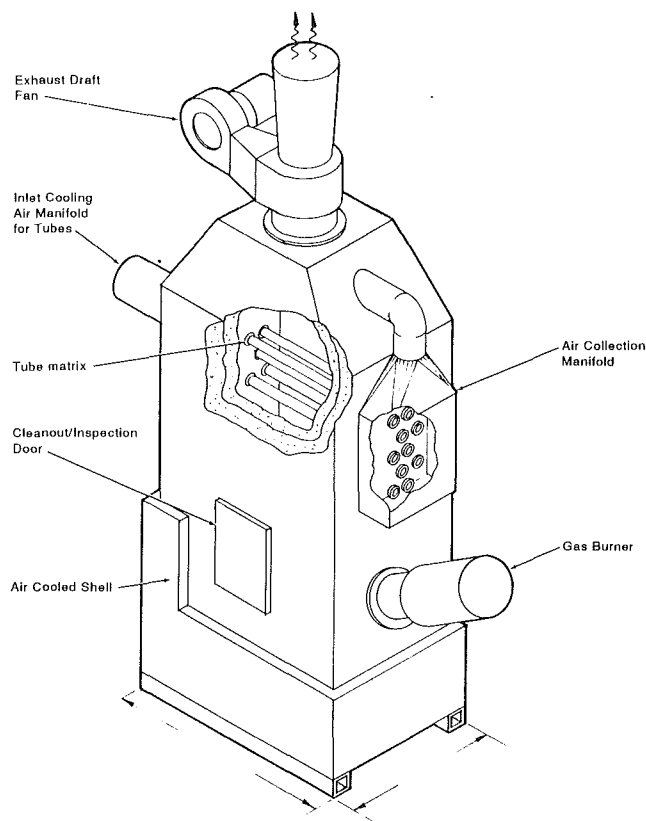


Fig. 2 Aluminum remelt simulator schematic (van Roode and Price, 1987)

Several other strategies were followed to improve the corrosion resistance of the coatings. One approach involved the application of a seal coat to the surface of the plasma spray coating to prevent the ingress of corrosive species into the porous plasma spray coat. A number of different seal coat systems were evaluated, including a slurry sprayed and fired Solaramic® vitreous phase ceramic (VPC) seal coat, and slurry sprayed seal coats containing hafnia (HfO_2) or erbia (Er_2O_3). Other approaches involved the densification of mullite coatings by plasma spraying with finer powders, spraying at higher deposition power, pre-stressing of the coating to reduce residual stresses, and the application of graded density coatings.

Coating Evaluation in Aluminum Remelt Simulator

The ceramic oxide coatings applied to monolithic SiC substrates have been subjected to several corrosion tests. Since the prime focus of the development work was corrosion protection of SiC heat exchanger tubes for recuperators used in the secondary aluminum melting industry, coatings were evaluated in a corrosive environment typical for that application. Figure 2 shows the schematic of a test rig that was designed and constructed under the program to simulate the corrosive flue atmosphere typical of a secondary aluminum melter. Figure 3 shows the actual simulator in operation. The test rig allows simultaneous testing of ten heat exchanger tubes placed in horizontal positions across the furnace stack.

Since information in the literature on contaminant levels in aluminum remelters is scant, species concentrations in the furnace stack were calculated by M. McNallan of the University of Illinois at Chicago using the SOLGASMIX-PV computer program of Besmann (1977). Table 3 lists SOLGASMIX concentrations together with actual contaminant levels measured in the aluminum remelt simulator and a few rare data points from industrial exposures. Evidently, the SOLGASMIX and

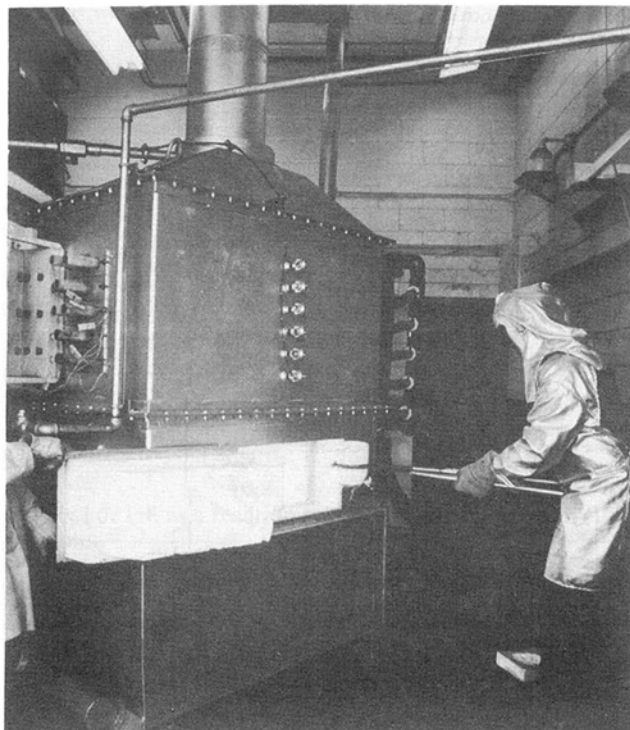


Fig. 3 Aluminum remelt simulator in operation (Price and van Roode, 1989)

remelt simulator furnace stack concentrations of chlorine are close to those of an industrial remelter. The fluorine concentration of the test rig also closely approximates that of an actual industrial environment, but the SOLGASMIX concentration of this element is a few orders of magnitude too low, presumably because of assumptions about this element in the model. The concentrations of Na and K from the SOLGASMIX computations are close to those in the simulator furnace stack. Details of the aluminum remelt simulator and the exposure tests can be found in GRI program reports (van Roode and Price, 1987; Price and van Roode, 1989).

First 2000-h Exposure Test. The ten coatings schematically represented in Table 4 were applied as 0.75-cm-wide bands to five Carborundum Hexaloy® SA and to five Coors SCRB-210 open-ended tubes. In the first test, coated tubes were exposed for 2000 h at temperatures of 760, 871, 982, 1093, and 1204°C. The tube temperatures were maintained by blowing air at various flow rates through the inside of the tube. The inside wall temperatures monitored with thermocouples were maintained to within 25°C of the mean. Tubes were rotated 180 deg along the furnace stack axis to average temperature differentials along the tube axis. Care was taken to keep the leading edge of the tubes at the same position relative to the burner. The furnace was shut down every 500 h and the tubes were inspected for corrosion damage following cooldown. After the 2000-h exposure the tubes were subjected to ten deep thermal cycles from room temperature to the maximum target temperature of the isothermal testing. Surface recessions were determined at the conclusion of the test. Selected coatings were examined metallographically for corrosion damage.

The first 2000-h exposure test showed substantial differentiation between the coatings in protecting the SiC substrate. In general, it was observed that the coatings that were applied to SCRB-210 survived better than those applied to Hexaloy® SA. We believe that the surface preparation technique preceding plasma spraying is more effective on substrates containing free silicon. Presumably, the presence of free Si in

Table 3 Concentrations of corrosive species (in g·L⁻¹) (van Roode et al., 1990)

Species	Aluminum Remelter ¹	SOLGASMIX ² (760°C)	Test Rig ³
Na	--	4.23 x 10 ⁻⁵	5.18 x 10 ⁻⁵
K	--	8.63 x 10 ⁻⁵	3.93 x 10 ⁻⁵
Cl	(1.1-1.8) x 10 ⁻⁴	1.76 x 10 ⁻⁴	1.23 x 10 ⁻⁴
F	(3.5-5.3) x 10 ⁻⁶	8.14 x 10 ⁻⁶	6.38 x 10 ⁻⁶

¹ Russell et al. (1983)

² Bath temperature 760°C, Maximum furnace stack temperature: 1316°C

³ Average of maximum concentrations during stack sampling

Table 4 Compositions and nominal thicknesses of ten coatings deposited onto carborundum Hexaloy® SA and Coors SCRB-210 tubular substrates for environmental exposure testing

Composition	Thickness (mm)	Composition	Thickness (mm)
M/VPC	0.50	MZ	0.50
M1	0.50	MZ/A	0.62
M2	0.75	MZ/AYZ	1.05
M/A	0.75	M/Y	0.75
M/A/YZ	1.05	M/YZ	0.88

* M: mullite A: alumina Y: yttria YZ: yttria-stab. zirconia
Z: zircon
M/A graded mullite/alumina coating, etc.
MZ: 50% mullite/50% zircon blend
VPC vitreous phase ceramic seal coat

SCRB-210, and its absence in Hexaloy® SA, is the main reason that the coatings had improved adherence on SCRB-210. Secondly, it was noted that none of the coatings survived at the highest exposure temperature of 1204°C. The limit of effectiveness of these coatings appears to be at around 1093°C.

The coatings that showed superior survival in the corrosion test and optimal protection of the SiC substrates were single-layer mullite or multilayer compositions with mullite and alumina or yttria. On the other hand, multilayer compositions containing yttria-stabilized zirconia all failed early on in the test. Presumably, the lower thermal expansion coefficients of alumina and yttria compared to yttria-stabilized zirconia result in less thermal expansion mismatch between the coating constituents and between the coating and the substrate, and hence in better coating survival.

Figures 4 and 5 compare leading edge surface recessions of the coatings applied to Coors SCRB-210 and Hexaloy® SA. It can be seen that uncoated SiC suffered significant surface recession, in excess of 40 mils (1 mm) at 760°C (1400°F). The coatings that remained adherent during exposure testing such as single-layer mullite and graded mullite/alumina and graded mullite/yttria show a substantial reduction in surface recession compared to uncoated SiC. The mullite-zircon mixed coating, which failed early on in the test, shows some reduction in surface recession compared to uncoated SiC, but the improvement is not very substantial. An interesting trend is the reduction in corrosive degradation of the uncoated SiC with increasing temperature. Presumably, this can be attributed to the reduction in condensation of the corrosive species with increasing temperature. It is worthwhile in this respect to examine the surface deposits on the tubes following completion of the corrosion test in Table 5. As the tube surface temperature during the exposure test is increased, the content of Na₂O in the surface deposits decreases, suggesting a decrease in the condensation of this oxide, which is believed to be a major factor in the corrosive degradation of SiC.

The data from the first 2000-h exposure test suggest that the coatings will be particularly useful at the lower range of temperatures encountered in the aluminum remelt process, i.e., in

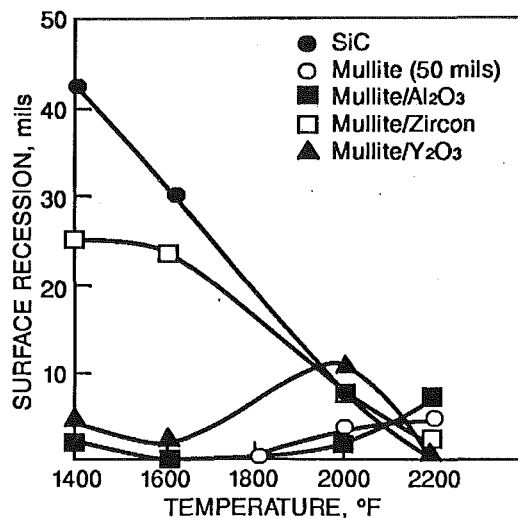


Fig. 4 Leading edge surface recession versus exposure temperature for Coors SCRB-210 following 2000 h of exposure plus 10 thermal cycles (Price and van Roode, 1989)

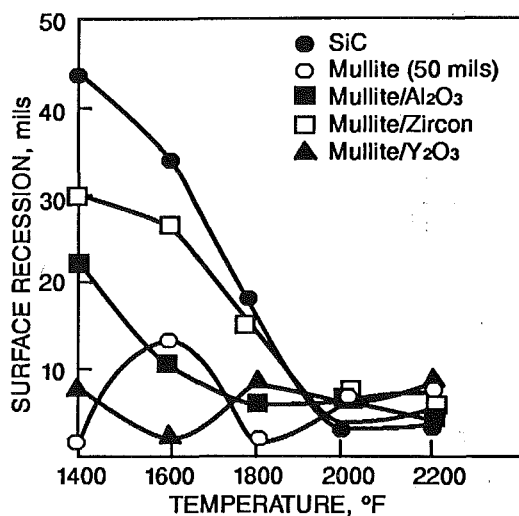


Fig. 5 Leading edge surface recession versus exposure temperature for Hexaloy® SA following 2000 h of exposure plus 10 thermal cycles (Price and van Roode, 1989)

Table 5 Mole percent of oxides in surface deposit (van Roode et al., 1990)

Oxide	760°C*	871°C*	982°C*	1093°C*	1204°C*
Al ₂ O ₃	2.55	2.19	2.78	5.36	1.78
SiO ₂	73.25	78.07	77.46	78.00	84.98
Na ₂ O	20.23	15.89	17.54	12.69	10.24
K ₂ O	3.97	3.85	3.24	3.97	3.00

* Tube temperature during rig test

the 750–1000°C range where the corrosion of SiC can be expected to be most damaging.

Metallographic analysis gives an insight into the mechanism of corrosion protection and coating degradation. It can be expected that the coating acts as a sacrificial substrate since the SiO₂ constituent in mullite is similar to the SiO₂ surface layer of the SiC. Corrosion degradation can be expected to proceed through external degradation of the coating surface and internal degradation along pores. Figure 6 shows a mullite coating with a VPC seal coat in the as-coated condition. Figure

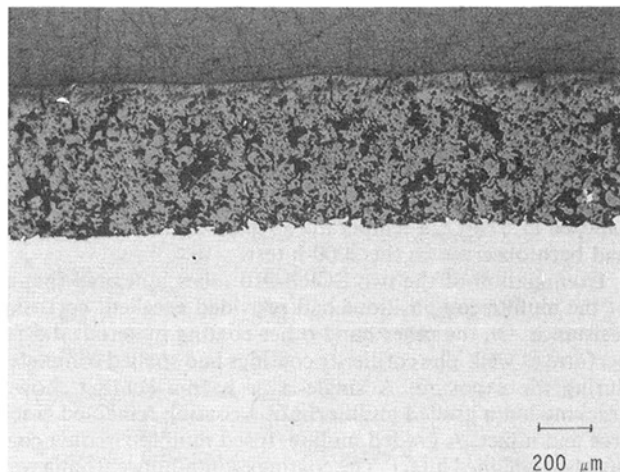


Fig. 6 Optical micrograph of as-coated mullite + VPC seal coat (M/VPC in Table 4) on SCRB-210 substrate (Price and van Roode, 1989)

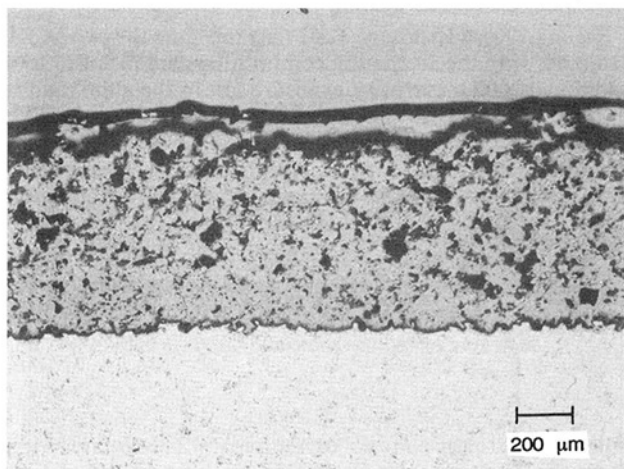


Fig. 7 Optical micrograph of M/VPC coating of Fig. 6 after 2000 h of corrosion testing at 871°C plus thermal cycles (Price and van Roode, 1989)

7 shows the same coating after exposure testing. The surface deposit is evidence of corrosion at the exterior of the coating. Figure 8 shows SEM micrographs and EDX spectra of the corroded coating. The external coating layer shows the presence of Al, Si, Ba, and Ca from the sealant glass. The presence of Al and Si can also be attributed to the mullite constituent of the coating. The presence of Na and K is evidence of corrosion. The high electron density interface between the corrosion layer and the coating contains predominantly residual sealing glass as well as some coating corrosion products. The interior of the coating shows predominantly Al and Si, but a trace of Na indicates coating penetration by corrosive species from the flue gases. Figures 7 and 8 also show good adhesion of the coating to the substrate following corrosion testing.

1000-h Exposure Test. Following the completion of the first 2000-h exposure test, a second test was performed in the aluminum remelt simulator. The objective of this second test was to optimize the best coatings of the first test by appropriate process modification. A total of 24 coating compositions was investigated in this second test. About half of these involved some modification of single-layer mullite. Mullite coating modification involved particle size, spray deposition power, prestressing of the coating and the application of a number of

seal coats, including a Solaramic® vitreous phase ceramic (VPC), and HfO_2 and Er_2O_3 slurry coatings, as mentioned previously. Other plasma spray coating systems investigated were based on hafnia (HfO_2), chromia (Cr_2O_3), cordierite ($5\text{MgO} \cdot 2\text{Al}_2\text{O}_3 \cdot 2\text{SiO}_2$), and a fused mullite-zirconia compound. Figures 9 and 10 show two SCRB-210 tubes coated with 5.00 cm bands of the 24 coating compositions prior to and after the 1000-h exposure test. Both of these tubes were exposed at 871°C , a temperature where significant corrosion had been observed in the 2000-h test.

Examination of the two SCRB-210 tubes indicated that all of the mullite compositions had provided excellent corrosion resistance. On the other hand other coating materials did not perform as well. The cordierite coatings had spalled completely during the exposure. A single-layer hafnia coating showed cracking but a graded mullite/hafnia coating remained crack-free and intact. A graded mullite/fused mullite-zirconia coating also remained intact. The coatings containing chromia were heavily degraded following exposure. None of the seal coats appeared to improve the corrosion resistance of mullite significantly. Densification of mullite seems to eliminate the need for seal coatings. Details of the 1000-h exposure test can be found in a GRI annual report (Price and van Roode, 1991).

Second 2000-h Exposure Test. At this time the two SCRB-210 tubes with the 24 coating compositions are included in an additional 2000-h corrosive exposure test in the aluminum remelt simulator. As in the 1000-h test these two tubes will be exposed at a temperature of 871°C . This test also includes three Hexaloy® SA and three SCRB-210 tubes, which are coated with seven coatings based on single-layer mullite from coarse

and fine powders, and multilayer graded mullite/alumina, mullite/hafnia, and mullite/fused mullite-zirconia compositions. This second 2000-h test is in progress.

Coating Evaluation at ORNL

The ten coatings listed in Table 4 on Hexaloy® SA were evaluated separately in high-temperature thermal cycling and corrosion testing at Oak Ridge National Laboratory. Details of the ORNL evaluation have been reported by Federer et al. (1989). The ORNL test protocol involved a single thermal cycle between room temperature and 1300°C at a heating rate of about 200°C/h , followed by 60 thermal cycles between 300

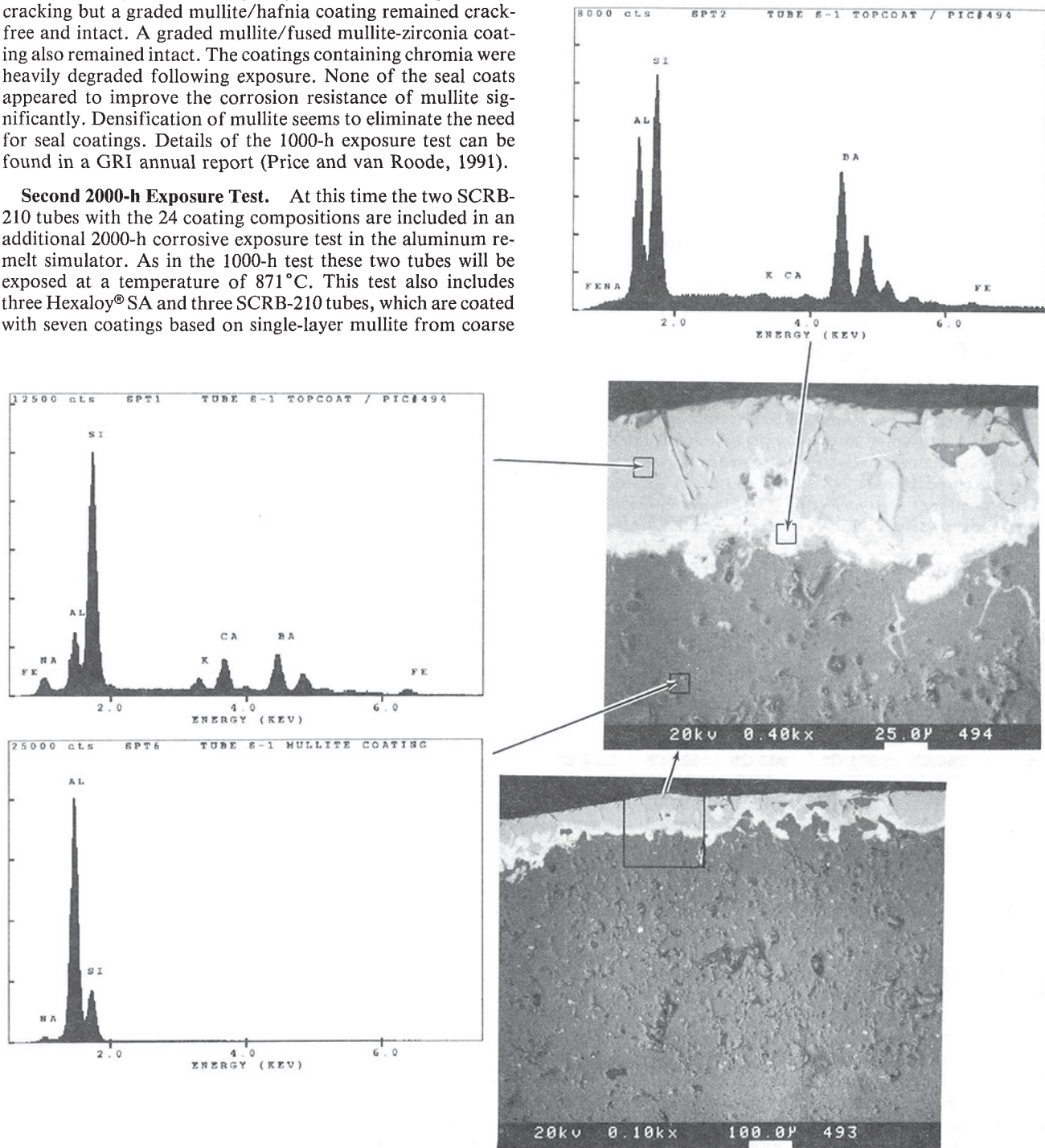


Fig. 8 SEM micrograph and EDX spectra of M/VPC coating of Fig. 7 (Price and van Roode, 1989)

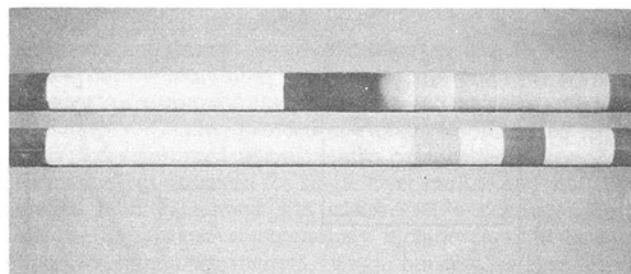


Fig. 9 SCRB-210 tubes with 24 coatings prior to 1000 h corrosive exposure test (Price and van Roode, 1991)

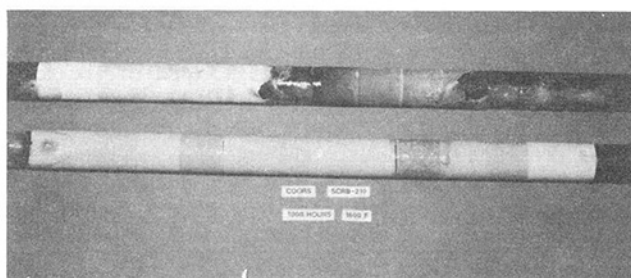


Fig. 10 SCRB-210 tubes with 24 coatings after 1000 h corrosive exposure test (Price and van Roode, 1991)

and 1300°C at a heating rate of 500°C/h. The coatings that survived the thermal cycle test were then subjected to a corrosion test in a tube furnace at 1200°C in an atmosphere consisting of N₂-21.3 wt.% O₂-4.2 wt.% H₂O-0.04 wt.% Na₂CO₃ for various times. Coatings contain yttria-stab. zirconia were found to crack severely or crack and spall off the substrate. These coatings were not included in the corrosion testing. It is noteworthy that these coatings also performed poorly in the first 2000-h corrosive exposure test in the aluminum remelt simulator described previously.

Table 6 summarizes the results of the corrosion testing at ORNL. All of the coatings except M/A showed obvious signs of degradation such as cracking and debonding (M/VPC, M2, MZ, MZ/A, M/Y). A transparent reaction product was observed that wetted the coating adjacent to the cracks (MZ, MZ/A). However, all the coatings subjected to the corrosion test had been protective to the substrate for the duration of the testing since the surface recession was negligible within experimental error. Uncoated SiC on the other hand had suffered severe wall recession, extrapolated to 21.3 mm/yr.

Metallographic examination showed that most of the corrosive reaction appeared to have occurred within the coatings. Corrosion-tested coatings that debonded from the SiC had a layer of transparent reaction product on the substrate surface, and some of this material has infiltrated or formed in the coatings. X-ray diffraction showed the reaction products to be one or more sodium aluminum silicates while sodium silicates had also formed. Coating surface degradation as was observed in testing with the aluminum remelt simulator at Solar was not observed. It is likely that the different degradation modes reflect differences in the corrosive attack in testing at ORNL and Solar. The heavy degradation at the coating/substrate interface observed at ORNL suggests that corrosive species could have infiltrated the pores of the coating in the gas phase and preferentially attack the substrate surface below the coating. The degradation at the surface of the coatings indicates that condensed species were predominantly responsible for the corrosive attack in the aluminum remelt simulator.

Coating Development for Ceramic Matrix Composites

Recently Solar-funded development work was initiated to

Table 6 Change in diameter of coated and uncoated Hexaloy® SA substrates caused by corrosion at 1200°C (Federer et al., 1989)*

Composition	Exposure Time (hr)	Change in Diameter (mm)
M/VPC	300	+0.10
M2	500	-0.07
M/A	500	-0.04
MZ	150	+0.05
MZ/A	300	0
M/Y	500	0
Uncoated SiC	350	-1.70

* Coating designations from Table 4

Table 7 Coating designations, nominal thicknesses, and surface recessions after 200 h corrosion test at ORNL (Price et al., 1990)*

Specimen	Thickness (mm)	Surface Recession (mm)	
		1000°C	1190°C
CM-2	0.51	0.02	0.30
FM-S	0.51	0.02	0.05
FM	0.51	0.00	0.18
CM-A	0.38 + 0.10	0.05	0.27
Uncoated		0.53	0.43

* CM: coarse mullite -106/+45 microns

FM: fine mullite - 45/+10 microns

A: alumina -75/+45 microns S: hafnia seal coat

apply ceramic oxide coatings to ceramic matrix composites (CMC). The impetus for this work came from Solar's work with high-pressure heat exchangers (HiPHES), which are being designed to use ceramic matrix composites in header components. Solar is working on this project under the auspices of the Department of Energy, Office of Industrial Technology. A candidate material for the header components is continuous fiber reinforced (Nicalon) chemical vapor infiltrated SiC. This CMC is manufactured by Amercom of Chatsworth, California. The Nicalon-SiC contains about 35 vol.% of Nicalon fiber and 50 vol.% of SiC. The remaining 15 vol.% is porosity. Since SiC is a major constituent of this CMC, corrosive attack similar to that observed for monolithic SiC can be expected in aggressive environments. The substantial porosity of the CMC increases the effective surface area of the corrosive attack.

Coatings similar to those applied to monolithic SiC were plasma spray deposited onto small rectangular test coupons, 2.65 cm × 0.85 cm × 0.20 cm in size. The Solar proprietary surface treatment was modified to roughen the surface of the CMC prior to coating application. The coatings applied are listed in Table 7.

The coated coupons were subjected to a Na₂CO₃ corrosive furnace environment at ORNL for 200 h at temperatures of 1000 and 1190°C, respectively. The corrosive atmosphere had the following composition: N₂: 73.5 percent, O₂: 22.6 percent, Ar: 1.3 percent, H₂O: 2.6 percent, Na₂CO₃: 0.02 percent. The data in Table 7 show that within experimental error after exposure testing at 1000°C the coated specimens showed no measurable recession compared to 0.53 mm recession for the uncoated CMC. More degradation was observed after exposure

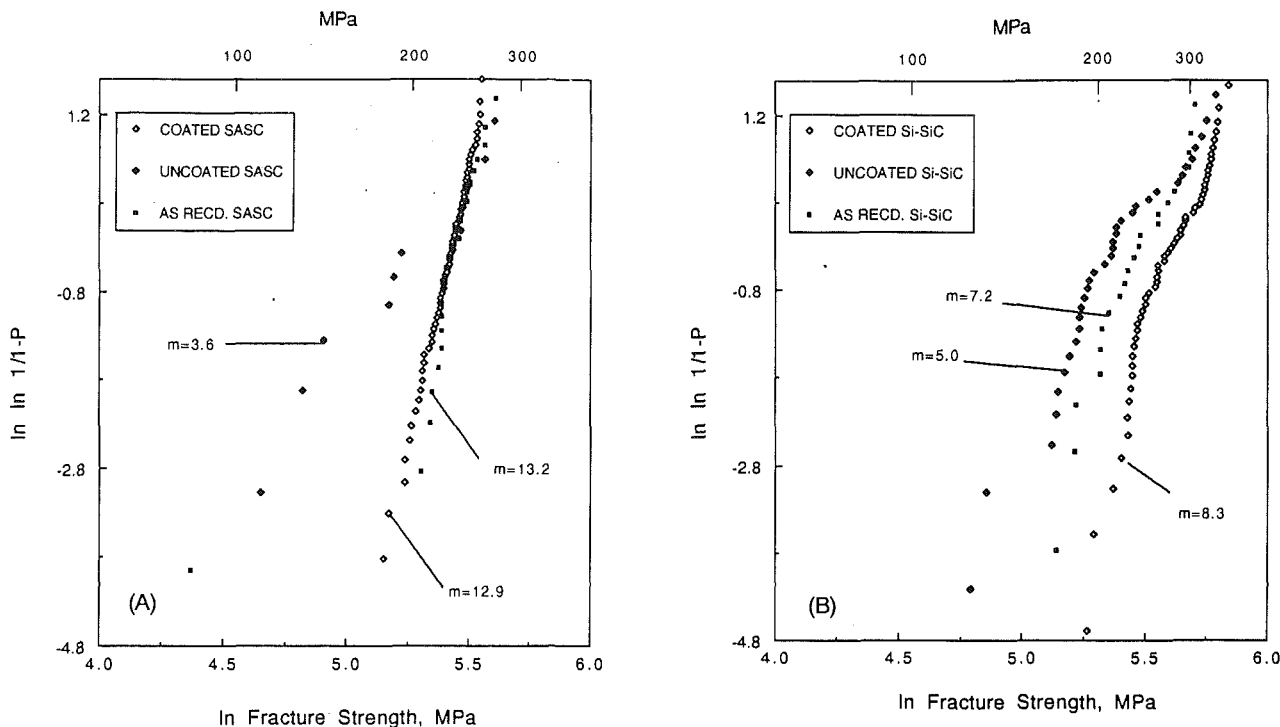


Fig. 11 Weibull distribution of fracture strength for plasma spray coated, uncoated but surface treated, and as-received SASC (Hexaloy® SA) (A) and SSC (SCR B-210) (B) (Price and van Roode, 1989)

at 1190°C, but surface recession rates of the coated specimens (0.05–0.30 mm) were still lower than those of the uncoated CMC (0.43). Superior protection was afforded by the fine mullite coatings (FM and FM-S) compared to the coatings sprayed with the coarse mullite powder (CM-2 and CM-A). Details of the coating study on the CMCs have been reported by Price et al. (1990).

Mechanical Properties of Coated SiC

Parallel with the coatings development and evaluation on monolithic SiC, a study was undertaken at the Center for Advanced Materials (CAM) at the Pennsylvania State University with the support of the Gas Research Institute under a separate contract to study the effect of the coatings on the mechanical properties of the substrate materials. This aspect was felt to be important since it was reported by Goldfarb (1988) that tubular silicon carbide lost considerable strength due to surface pitting. The CAM study, which used c-ring flexure testing to measure mechanical strength, has been described in a paper by Butt et al. (1990).

Figure 11 shows Weibull distributions for coated and uncoated Hexaloy® SA and SCR B-210. The curves include grouped data of all ten coating systems investigated in the first 2000-h corrosion test (Table 4). The curves show that the surface preparation lowers the strength of the SiC, presumably by increasing the number of surface flaws, but that the subsequent application of the coating restores (Hexaloy® SA) or even increases (SCR B-210) the strength of the substrate. The more beneficial effect of the coatings on SCR B-210 is attributed to the better bond between this coating and the reaction bonded substrate compared to the coating to substrate bond for the sintered Hexaloy® SA. The good mechanical bond between the coating and the substrate provides some load transfer from failure initiating defects in the substrate into the coatings. The coatings with their lamellar type grain structure are able to withstand relatively high strains.

More recently mechanical testing has been conducted on

coated SiC specimens subjected to the 2000-h corrosive exposure test. Preliminary data show that the protection afforded by the coatings translates into better retention of the strength of the as-coated SiC (Darroudi, 1990).

Future Developments

Efforts to develop further the coatings for monolithic SiC for heat exchanger applications are continuing at Solar with the support of the Gas Research Institute. Of immediate interest is the application of the coatings to low-cost SiC substrates. The anticipated improvement in service life could make these materials attractive replacements for the currently expensive tubular SiC ceramics with better mechanical properties. The presence of additives in these low-cost ceramics, less desirable from the perspective of high strength, may actually improve the coating adherence since it could facilitate the surface preparation. The development work has reached the stage at which the commercial potential of the technology is being assessed. At this time field sites are being identified to test the coatings in an industrial environment. Other tubular ceramics applications, such as immersion heaters and radiant burners, are also being investigated. The successful application of the coating to continuous fiber-reinforced SiC-based ceramic composites further broadens the range of potential applications of the novel technology. The application of protective ceramic oxide coatings for Si₃N₄ is also under investigation at Solar. Future uses include silicon-based gas turbine components for operation under corrosive conditions encountered in coal-fired or liquid fuel-fired operations.

Summary

Adherent ceramic oxide coatings have been applied using conventional air plasma spraying to monolithic SiC and SiC-based composite ceramic substrates and evaluated in thermal shock and corrosion testing. Corrosion testing in an aluminum remelt simulator has shown that these coatings reduce the

surface recession of tubular monolithic SiC heat exchanger substrates and thereby improve their service life. The corrosion data from the aluminum remelt simulator correlate with laboratory corrosion studies performed at Oak Ridge National Laboratory. Coating protection extends to SiC-based continuous fiber reinforced ceramic matrix composites. Superior performance was observed for single-layer mullite and multilayer graded mullite/alumina and mullite/yttria coatings. Applications for the novel technology include ceramic heat exchangers, immersion melters, radiant burners, and gas turbine hot section components.

Acknowledgments

The work on monolithic silicon carbide was performed under Gas Research Institute contract No. 5086-232-1233. The authors wish to thank GRI staff, Dr. R. Ruiz and M. E. Schreiner (formerly with GRI) for many helpful suggestions during this program. Thanks is also expressed to technical personnel at the Center for Advanced Materials of the Pennsylvania State University, Drs. D. P. Butt, J. J. Mecholsky, and T. Darroudi, and to J. I. Federer of Oak Ridge National Laboratory for aspects of the work reported here.

References

- Besmann, T. M., 1977, "SOLGASMIX-PV, A Computer Program to Calculate Equilibrium Relationships in Complex Chemical Systems," ORNL-TM/5775.
- Butt, D. P., Mecholsky, J. J., van Roode, M., and Price, J. R., 1990, "Effects of Plasma-Sprayed Ceramic Coatings on the Strength Distribution of Silicon Carbide," *J. Am. Ceram. Soc.*, Vol. 73, pp. 2690-2696.
- "Ceramic Source '89," Vol. 4, 1989, The American Ceramic Society, Inc., Westerville, OH, p. T8.
- Darroudi, T., 1990, Pennsylvania State University, private communication.
- Federer, J. I., Robbins, J. M., Jones, P. J., and Hamby, C., Jr., 1985, "Corrosion of SiC Ceramics in Synthetic Combustion Atmospheres Containing Halides," ORNL/TM-6258.
- Federer, J. I., and Jones, P. J., 1985, "Oxidation/Corrosion of Metallic and Ceramic Materials in an Aluminum Remelt Furnace," ORNL/TM-9741.
- Federer, J. I., 1989, "High-Temperature Corrosion of Heat Exchanger Materials," presented at the International Symposium on Corrosion and Corrosive Degradation of Ceramics, Anaheim, CA.
- Federer, J. I., van Roode, M., and Price, J. R., 1989, "Evaluation of Ceramic Coatings on Silicon Carbide," *Surface and Coatings Technology*, Vol. 39/40, pp. 71-78.
- Goldfarb, V., 1988, "Material Testing for an Advanced Glass Melter Heat Exchanger," GRI Contract No. 5086-232-1274, Final Report.
- Jacobson, N. S., Smialek, J. L., and Fox, D. S., 1988, "Molten Salt Corrosion of SiC and Si₃N₄," NASA TM-101346.
- McNallan, M., van Roode, M., and Price, J. R., 1989, "The Mechanisms of High-Temperature Corrosion of SiC in Flue Gases From Aluminum Remelting Furnaces," presented at the International Symposium on Corrosion and Corrosive Degradation of Ceramics, Anaheim, CA.
- Price, J. R., and van Roode, M., 1989, "Corrosion Resistant Coatings for Ceramic Heat Exchanger Tubes Operating in Highly Corrosive Environments," GRI Contract No. 5086-232-1233, Annual Report GRI-90-0107.
- Price, J. R., and van Roode, M., 1991, "Corrosion Resistant Coatings for Ceramic Heat Exchanger Tubes Operating in Highly Corrosive Environments," GRI Contract No. 5086-232-1233, Annual Report, in press.
- Price, J. R., van Roode, M., Parthasarathy, V. M., Federer, J. I., and Beyermann, W. E., 1990, "Corrosion Resistant Coatings for Silicon Carbide Matrix Composites," presented at the International Conference on Metallurgical Coatings, Apr., San Diego, CA; publication in press.
- Russell, A. D., Smeltzer, C. E., and Ward, M. E., 1983, "Waste Heat Recuperation for Aluminum Furnace," GRI Contract No. 5081-342-0493, Final Report.
- van Roode, M., and Price, J. R., 1987, "The Development of Protective Coatings for Ceramic Tubular Components," GRI Contract No. 5086-232-1233, Topical Report GRI-88-0005.
- van Roode, M., Price, J. R., Gildersleeve, R. E., and Smeltzer, C. E., 1988, "Ceramic Coatings for Corrosion Environments," *Ceram. Eng. Sci. Proc.*, Vol. 9, pp. 1245-1259.
- van Roode, M., Price, J. R., and Stala, C., 1990, "Corrosion Resistant Coatings for Ceramic Heat Exchanger Tubes Operating in Highly Corrosive Environments," presented at the 7th CIMTEC—World Ceramics Congress and Satellite Symposia, Faenza, Italy.

Precision Drilling of Ceramic-Coated Components With Abrasive-Waterjets

M. Hashish

QUEST Integrated, Inc.
(formerly Flow Research, Inc.),
Kent, WA 98032

J. Whalen

G. E. Aircraft Engines,
Cincinnati, OH 45215

This paper addresses an experimental investigation on the feasibility of using abrasive-waterjets (AWJs) for the precision drilling of small-diameter holes in advanced aircraft engine components. These components are sprayed with ceramic thermal barrier coating (TBC), and the required holes are typically 0.025 in. in diameter with a drilling angle of 25 deg. The parameters of the AWJ were varied to study their effects on both quantitative and qualitative hole drilling parameters. The unique techniques of assisting the abrasive feed process, ramping the waterjet pressure during drilling, and varying the jet dwell time after piercing were effectively implemented to control hole quality and size. The results of the experiments indicate the accuracy and repeatability of the AWJ technique in meeting the air flow and hole size requirements. Production parts were drilled for prototype engine testing.

Introduction

The drilling of small-diameter holes in composite (Boldt and Chanani, 1987) and layered (or coated) materials presents significant challenges to existing techniques. The use of ceramic coatings for thermal protection in hot sections of new jet engines is an example of an application in which holes need to be drilled for cooling. Drilling such materials with solid drill bits is often not possible, due to the great difference in the nature of the composite components and their response to the drill bit action. Although lasers can drill composites quickly, the use of lasers on many composites results in undesired surface characteristics, and additional processing is generally required, which significantly increases the cost of machining. Added to the difficulty of drilling advanced composites is the fact that holes at shallow angles are often required. In the specific application herein, fluid film cooling on ceramic-coated engine parts requires that holes be drilled at angles of about 25 deg or less. Finally, lasers and drill bits are limited to holes of relatively small length-to-diameter ratios, especially for hole diameters around 0.025 in., even for homogeneous metallic parts.

In this paper, the use of abrasive-waterjets (AWJs) to drill holes in thermal barrier coating (TBC) materials is investigated. Background information is presented first, followed by the program objectives and a discussion of the experimental investigation. The results of drilling components for engine testing are then presented, and conclusions and recommendations are presented at the end of this paper.

Background

Waterjet Cutting. High-speed waterjets have been used as cutting tools in a wide variety of industries since the early 1970s. In this technique, water is pumped at pressures up to 60 ksi and expelled through a sapphire orifice to form a fine cutting stream. Typical stream diameters and velocities are 0.003 to 0.020 in. and 1000 to 3000 ft/sec, respectively. Most nonmetals can be cut efficiently at high speeds with no dust, no distortion, and minimal waste.

To enhance the performance of the waterjet, abrasive particles can be added to the high-velocity liquid stream in a nozzle system as shown in Fig. 1 to form an abrasive-waterjet (Hashish, 1982). The flow of the high-velocity waterjet stream into the concentrically aligned mixing tube creates a vacuum, which is used to transport abrasives from a hopper to the nozzle. A typical abrasive material is garnet, with abrasive flow rates up to 3 lb/min. Medium to fine abrasives (mesh 60 to mesh 200) are most commonly used for cutting metal, glass, and resin composites. Abrasives are accelerated and focused in the mixing tube, which has a length-to-diameter ratio ranging from 50 to 100. Typical tube diameters are 0.03 to 0.09 in. with lengths up to 6 in.

The momentum transfer between the water and the abrasives creates a focused high-velocity stream of particles that exits the nozzle and performs the cutting. Almost all known materials can be cut with the AWJ (Hashish, 1984).

Hole Drilling With Abrasive-Waterjets. In the past, the use of AWJs for hole drilling has been limited to making starting holes for internal shape cutting. Hole quality is not a concern in this case as long as fracture or hole imperfections do not affect the required shapes to be cut. Recent studies on hole drilling with AWJs (Hashish, 1988a) reported the capability of drilling 1.5-in.-long holes of 0.03-in. diameter in glass.

Contributed by the International Gas Turbine Institute and presented at the 36th International Gas Turbine and Aeroengine Congress and Exposition, Orlando, Florida, June 3-6, 1991. Manuscript received at ASME Headquarters March 4, 1991. Paper No. 91-GT-232. Associate Technical Editor: L. A. Riekert.

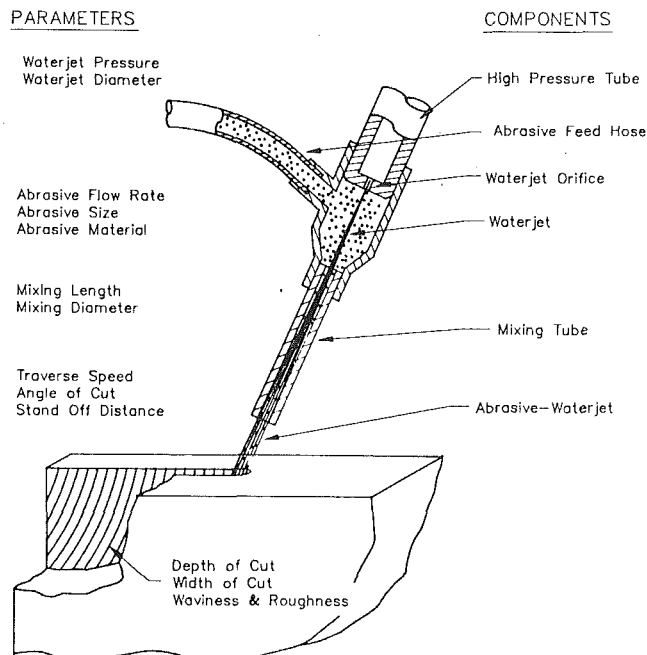


Fig. 1 Abrasive-waterjet nozzle concept and parameters

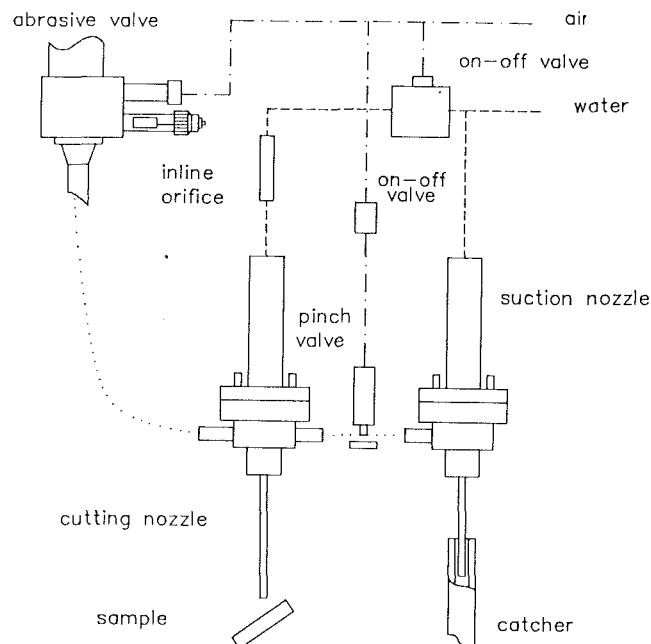


Fig. 2 Schematic of vacuum-assisted AWJ

It has also been shown (Hashish, 1988b) that holes up to 12 in. long can be drilled in glass but with relatively large diameters (over 0.25 in.).

With commercially available AWJ nozzles, holes are limited in diameter to 0.030 in. The general practice for piercing holes in a fragile material is to lower the pressure at the nozzle so that the impact of the waterjet does not cause fracture. At low pressures, however, abrasive feed is not consistent, especially if the abrasives are to be transported over a relatively long distance or when the abrasives are fine. Abrasive clogging or interruption will result in cracks and fractures in the target material. To overcome the above problems, the following concepts have been under investigation:

- An AWJ nozzle with a dual-feed port was used to entrain abrasives from one port and water from the other. The water suction was used temporarily to weaken the waterjet while piercing without having to lower the pump pressure. The suction water flow rate was gradually reduced to increase the strength of the jet gradually. Water suction resulted in significantly enlarged holes, but cracking was eliminated. The concept of ramping the waterjet pressure was suggested by these experiments.

- The waterjet was modulated on the upstream side by inserting a pin in the high-pressure tube above the orifice. The location of the pin controls the jet strength and its impact characteristics. Pin location and position control were found to be difficult to achieve.

- Vacuum assist was used on glass drilling to entrain the abrasives through the AWJ nozzle before and while piercing at low pressures. Figure 2 illustrates this system.

When AWJ technology was first identified as a potential candidate process for drilling cooling holes in TBC, it was explored using conventional AWJs. These exploratory tests failed; the holes produced were chipped and spalled from the substrate component. The initial tests did reveal, however, the necessity for parameter optimization as well as the potential of the high-pressure water profiling approach as an alternative technique. These findings initiated the study discussed in this paper.

Laser Drilling. Lasers can drill TBC cooling holes in a few seconds and are much faster than AWJs. However, the laser

process introduces heat to the component. This heat causes the TBC component to expand thermally. Since the TBC and the metal substrate have different thermal expansion coefficients, the differing expansion causes delamination of the TBC from the substrate. Although it is unknown whether this delamination is detrimental to the component, it is viewed as unfavorable.

Objectives

The main goal of this research was to develop the AWJ process for the drilling of small-diameter holes in TBC components. Ultimately, the AWJ technique, combined with robotic positioning, is to be used to generate film cooling holes in TBC components in production parts. Specifically, the technical objectives of this research were as follows:

- Determine the optimal AWJ parameters.
- Drill test coupons to demonstrate the process.
- Drill engine test hardware components.

Experimental Investigation

To achieve the above objectives, an experimental investigation was undertaken. In the following sections, we describe the experiments and results.

Experimental Plan. The experimental investigation involved the varying of parameters to determine their optimum values for the drilling of small-diameter holes in TBC components. Figure 3 shows the geometry of the hole to be addressed in this optimization effort and also for the coupon drilling demonstration. The investigation was conducted in two phases, preliminary tests and experimental tests.

Preliminary Tests. Some preliminary tests were conducted using a conventional AWJ (without vacuum assist) to identify the general characteristics of AWJ-drilled holes in TBC. Figure 4 shows representative hole shapes obtained with the following parameters:

Waterjet diameter: 0.009 in.

Pressure: 10, 20, and 30 ksi

Abrasive material: garnet

Abrasive particle size: mesh 100

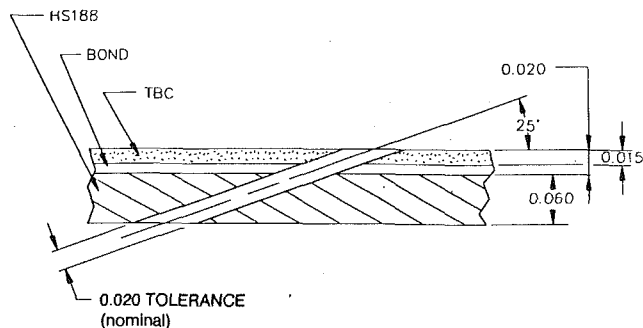


Fig. 3 Geometry of drilling requirement (units are inches)

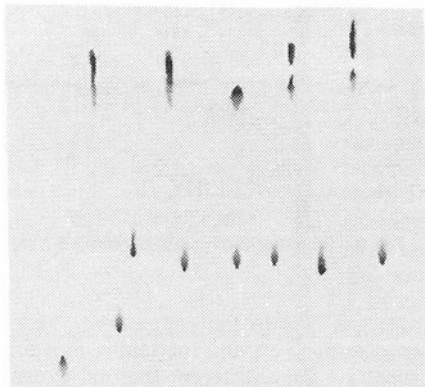


Fig. 4 Sample with AWJ-drilled holes

Abrasive flow rate: 0.2 lb/min
 Mixing tube length: 3 in.
 Mixing tube diameter: 0.018 to 0.023 in.
 Angle of drilling: 25 deg
 Standoff distance: 0.01 in.
 Side of drilling: metal and ceramic side
 Masking: aluminum plate

The observations and conclusions of the preliminary tests are:

- The lag of abrasive delivery to the jet is a significant source of initial fracture and chipping. When the abrasive line length was reduced, chipping was reduced.
 - High pressures up to 30 ksi produced inconsistent surface cracking and fracture results.
 - It was observed that changes in the noise level while drilling is indicative of fracturing. However, no distinction can easily be made while drilling through the layers of the material if no fracturing occurs.
 - Most cracks are circumferential and appear to emanate from the interface between the ceramic and metal.
 - Lateral jet flow between the mask and the surface of the workpiece was observed. Good bonding or hard clamping was required to continue these tests but was found unfeasible.
 - Drilling from the metal side produced chipping as the jet breaks through. Chipping was consistent at 30 ksi.
- It may be instructive at this point to characterize the different hole shapes and hole integrity problems that have been observed or may occur in TBC drilling. Integrity features are classified here based on whether they affect the surface or subsurface. These surface integrity features are illustrated in Fig. 5 and are described below.
- Surface chipping: A chip is removed from the surface.
 - Surface cracks: A crack is evident on the surface. This may actually emanate from subsurface pressurization or from wave loading under high shock loads.

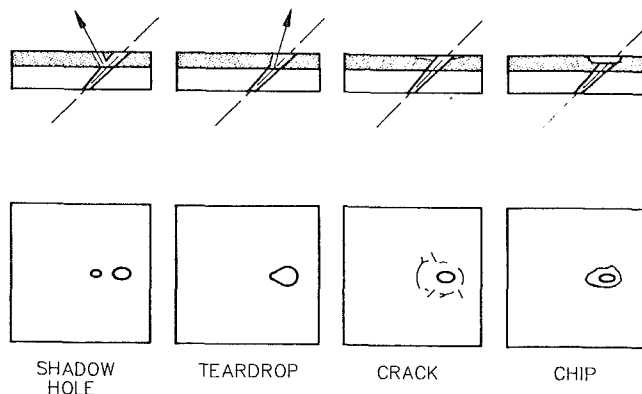


Fig. 5 Problems of drilling with AWJ

- Teardrops: In this case, the hole is not elliptical in shape but looks like a teardrop. This is actually a jet rebound effect.
 - Shadow holes: Shadow holes are exaggerated cases of teardrops but two distinct holes appear on the surface. The rebound of the jet off the metal interface produces another "shadow" hole. This effect becomes more obvious for shallower angles.
 - No damage: No surface damage is observed, but hole shape may not be ideal.
- Subsurface integrity problems are:
- Gouging: A cavity is formed due to rebounding.
 - Delamination: This may occur at the ceramic-bond-metal interfaces.
 - Pitting: This may occur in the wall of a hole as a result of a relatively large and hard abrasive impact.

Hole shapes produced by waterjets and AWJs depend on the jet structure and the duration of drilling. The jet structure is a function of the hydraulic, mixing, and abrasive parameters. The duration of drilling includes the piercing time and the dwell time. To control the hole shape, both the jet structure and duration of drilling need to be determined. It should be recognized, however, that a hole shape is not simply an impression of the effective portion of the jet, as the return flow plays a role in altering the shape. Figure 6 shows possible hole geometries that may be produced by jets.

Experimental Test Process Parameters. The independent parameters, dependent parameters, and constant variables used in the experimental tests are listed below.

Independent Parameters:

- Waterjet diameter: 0.006 to 0.015 in.
- Pressure: 5 to 30 ksi
- Abrasive material: garnet, olivine, tungsten carbide, aluminum oxide
- Abrasive particle size: mesh 80 to mesh 400
- Abrasive flow rate: up to 1 lb/min
- Mixing tube length: 2 in. (minimum)
- Mixing tube diameter: 0.018 to 0.023 in.
- Dwell time after piercing: up to 30 s

Dependent Parameters:

- Drilling (piercing) time

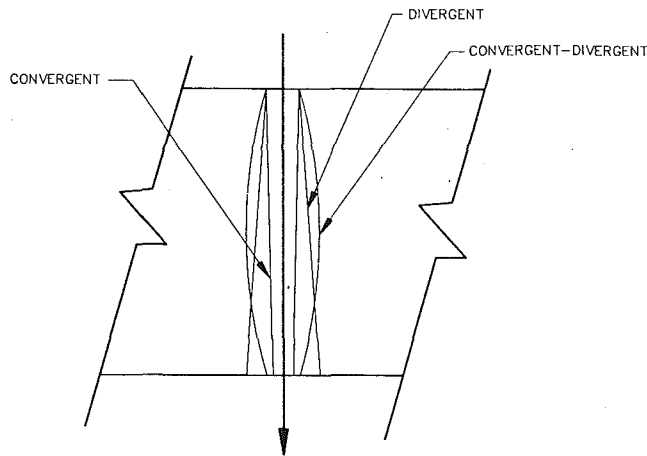


Fig. 6 General shape of AWJ-drilled holes

- Quality of hole surface (surface finish, delamination, etc.)
- Hole diameter
- Hole shape (taper, edge rounding, roundness, etc.)

Constant Variables:

- Angle of drilling at 25 deg
- Standoff distance less than 0.01 in.

Experimental Setup. The experimental setup consisted of the following components:

- High-pressure pump: An intensifier pump was used to supply the high-pressure water to the nozzle. Pressures up to 55 ksi can be generated at flow rates up to 3 gpm. Details of the intensifier pump operation can be found elsewhere (Crossland and Logan, 1972).
- Nozzle: Figure 7 shows the AWJ nozzle used for drilling. This nozzle is similar to the one shown schematically in Fig. 1 but with a vacuum assist port.
- Manipulator: An Adept-1 robot was used to position the nozzle over the workpiece. The robot was used in its five-axis configuration for the drilling of the production parts. Coupon drilling at 25 deg was accomplished by using an inclined fixture under a vertical jet.
- Catcher: A tank-type catcher was used to catch the exhaust jet.
- Breakthrough sensor: A microphone was used to sense jet breakthrough. The microphone signal was used to initiate after-piercing operations.

Experimental Tests. In these tests, a vacuum-assisted abrasive feed system was used to eliminate abrasive starving at the waterjet. The tests addressed drilling from the ceramic side only without a mask.

Low-Pressure Drilling. Vacuum assist was provided to the drilling nozzle by an auxiliary nozzle as shown in Fig. 2. The auxiliary nozzle served as a vacuum pump for the laboratory tests. The drilling pressure in this series of tests (68 holes) was limited to a constant (unramped) 12.5 ksi.

The effect of abrasive material was studied as part of the low-pressure drilling tests. Four types of abrasives were used, including garnet, olivine, tungsten carbide (WC), and aluminum oxide. Drilling times with WC abrasives were comparable to those obtained with garnet and olivine. This indicates that the significantly dense WC abrasives were not accelerated to sufficiently high speeds or that their shape and size are not optimal. No further tests with WC abrasives were conducted due to their high cost and limited performance. The relatively inexpensive olivine abrasives, on the other hand, resulted in relatively faster drilling times, i.e., 75 seconds versus 92 seconds for garnet. Hole size was also improved with olivine. Different

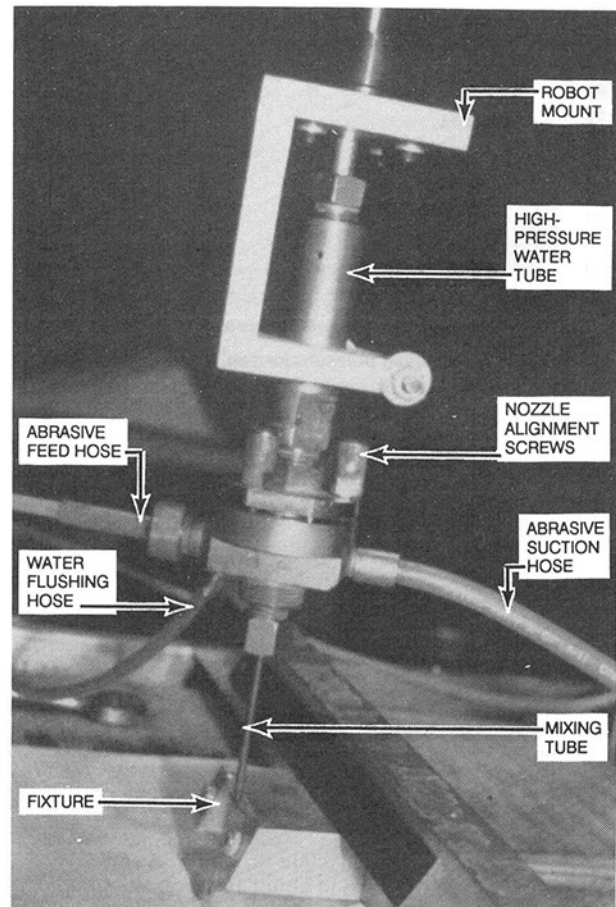


Fig. 7 AWJ drilling nozzle

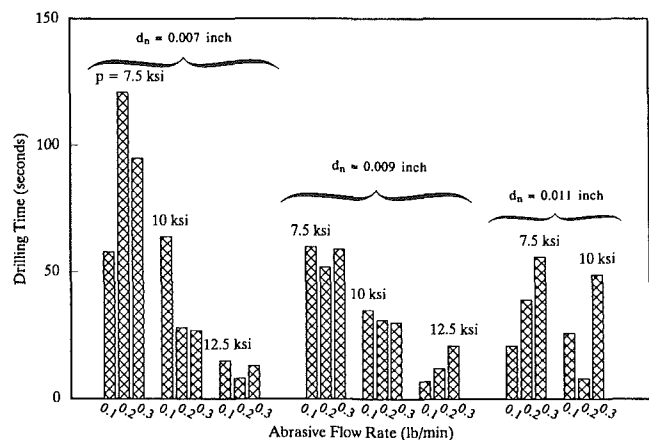


Fig. 8 Effect of pressure (P), waterjet diameter (d_n), and abrasive flow rate on drilling time

olivine sizes were tested, and it was found that coarser olivine (mesh 80) drilled faster than finer olivine (mesh 150). Tests with aluminum oxide abrasives did not result in any improvements. Olivine was used to study the effect of pressure, abrasive flow rate, and waterjet orifice size on drilling time. However, chipping and cracking were observed in holes drilled at pressure levels of 12.5 ksi and at the lower constant pressures of 7.5 and 10 ksi.

Figure 8 shows the effects of pressure, waterjet diameter, and abrasive flow rate on the drilling time. Observe that no trend could be determined on the effect of abrasive flow rate. These tests did indicate that the 0.009-in. waterjet is optimal

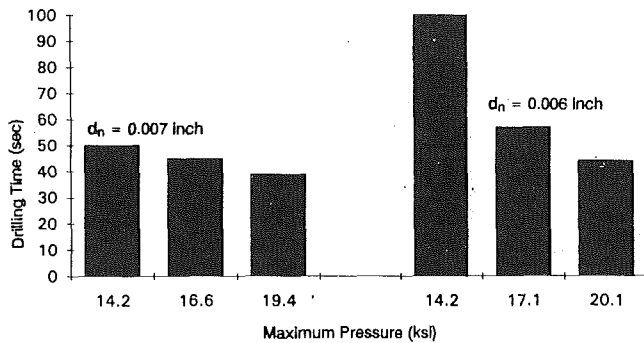


Fig. 9 Effect of ramping pressure for two waterjet diameters (d_n)

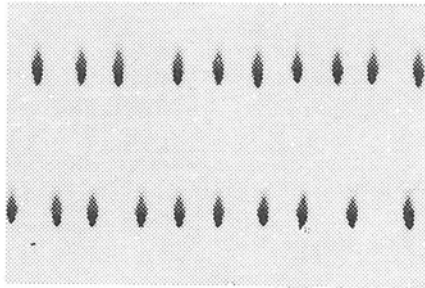


Fig. 10 Holes drilled at 25 deg. using 0.005-in. waterjet

for drilling time. Hole quality and shape were not consistent in these tests.

Continued tests with the 0.009-in. waterjet indicated that drilling can be accomplished in about 10 seconds, but chipping or cracking consistently occurs at the constant 12.5-ksi pressure.

The low-pressure tests did not yield satisfactory trends for optimization. Therefore, the drilling process was modified as described below.

Drilling With Pressure Ramping. The drilling of brittle materials with high-velocity abrasive-waterjets is a critical process. It was observed that the consistency and steadiness of the flow of abrasives are essential for fracture prevention and hole size control. For example, when the abrasive flow rate is interrupted while drilling, cracking occurs. Abrasives that are not properly sieved have variations in particle size distribution.

Using a constant low pressure for drilling was shown to have the following disadvantages:

- Low-pressure waterjets are inconsistent for drilling.
- Low-pressure drilling is slow.
- Low pressure is not suitable for metallic substrate, as it results in jet rebound with associated cracking and gouging. The rebound randomly distorts the hole geometry.

To overcome the above problems, pressure ramping was investigated. This concept uses an unsteady jet pressure for drilling. Unsteady ramping pressures up to 25 ksi were evaluated. One way to accomplish this is by using an orifice upstream of an accumulator, which in turn feeds the drilling nozzle (Hashish and Craigen, 1990), or by using a computer to control the pressure profile.

The vacuum assist is especially important at the early stages of pressure ramping, because the drilling waterjet will be incapable of transporting abrasives from the hopper. Figure 2 shows a schematic of a vacuum-assisted nozzle. The vacuum is provided by the suction effect of another AWJ nozzle. The suction AWJ nozzle can be replaced with a suitable vacuum pump. As the pressure increases, the drilling jet will entrain more and more abrasives. To deactivate the drilling jet quickly,

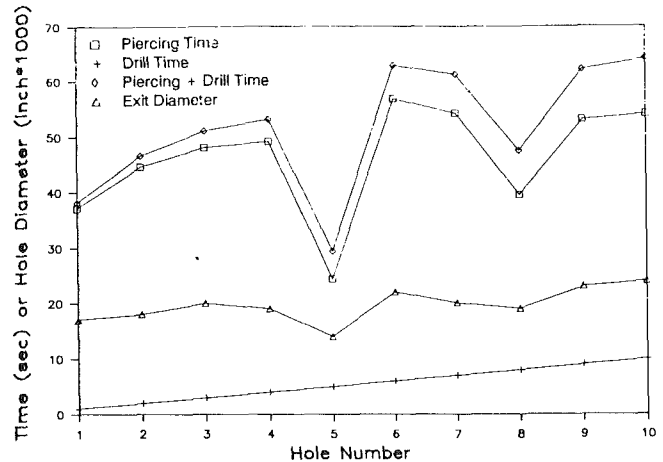
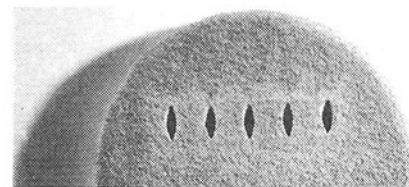
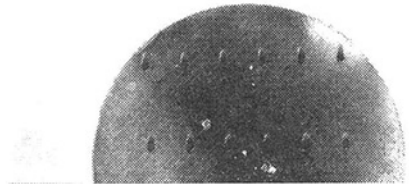


Fig. 11 Correlation of drilling time with hole size



a. Front (TBC)



b. Back (metal)

Fig. 12 AWJ-drilled coupon

a dump nozzle was added to the circuit. The dump nozzle is also used to control the starting pressure when the dump nozzle on/off valve is opened before the drilling nozzle on/off valve. To increase the waterjet pressure suddenly, an on/off valve was added to the circuit so that the high-pressure water can be allowed to bypass the accumulator.

Tests were conducted to determine the effect of maximum pressure (and flow rate) on the hole drilling time and hole quality. With a 0.007-in. waterjet, ramping to 14.2 ksi produced no cracks but ramping to 19.4 ksi did produce cracks. When the abrasive flow rate was increased from 0.125 to 0.2 lb/min, no cracks were formed at 19.4 ksi. Figure 9 shows that drilling time is reduced by increasing the final ramping pressure. With a 0.006-in. waterjet, a maximum ramping pressure of 20.1 ksi was used to drill holes with no chipping or cracking. Drilling time for ten holes ranged from 36 to 46 seconds, indicating the inconsistency of drilling time at this condition.

A 0.005-in. waterjet was used to drill holes with a maximum pressure of 29.2 ksi. Four holes were drilled in 41, 42, 40, and 41 seconds without any chipping or cracking. Figure 10 shows 20 holes drilled without chipping or cracking.

To explore the effect of drilling parameters further, a 0.004-in. waterjet was used with a 0.015-in.-dia. mixing tube. None of the holes drilled were cracked, even with pressure ramps up to 31 ksi. However, the drilling time was 90 seconds and the holes measured 0.024 in. on the ceramic side and 0.021 in. on the metal side.

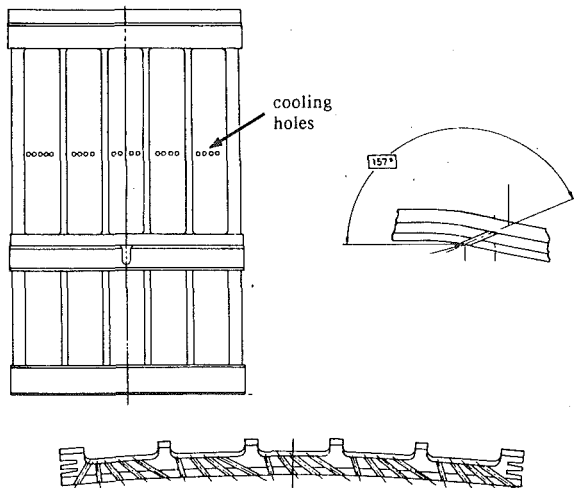


Fig. 13 Shroud geometry

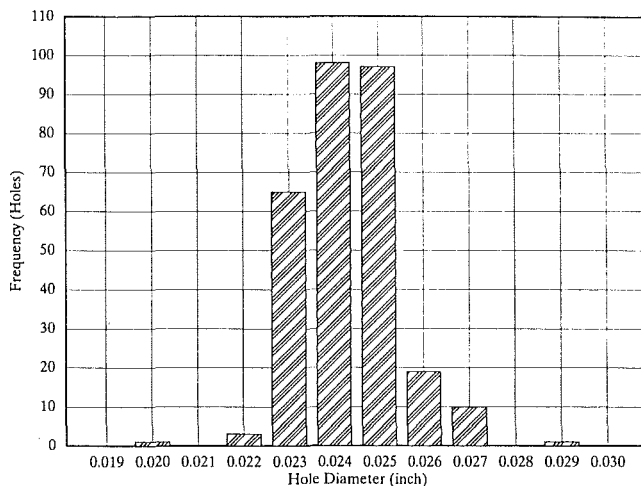


Fig. 14 Frequency distribution of hole sizes

The above tests were conducted with off-the-shelf olivine abrasive, which after analysis was found to be inconsistent in size. When replaced with screened garnet abrasives, consistent drilling times were observed. Also, garnet was found consistently to reduce the drilling time from 50 seconds with olivine to about 42 seconds.

Coupon Drilling

The following parameters were selected for coupon drilling:

- Maximum pressure: 22 ksi
- Waterjet diameter: 0.005 in.
- Mixing tube diameter: 0.018 in.
- Abrasive flow rate: 0.09 lb/min.
- Particle size: mesh 120
- Abrasive material: garnet

A number of test holes were drilled in test coupons to determine the dwell time required to control the hole size. This timing was automatically controlled by stopping the jet a few seconds after breakthrough. At breakthrough, there is a sudden increase in jet noise, which is used to trigger the timing watch via a microphone. It was determined that the dwell time needed to be adjusted to account for variations in piercing time. The drilling data for the coupons are shown in Fig. 11, while Fig. 12 shows the front and back sides of a coupon with AWJ-drilled holes.

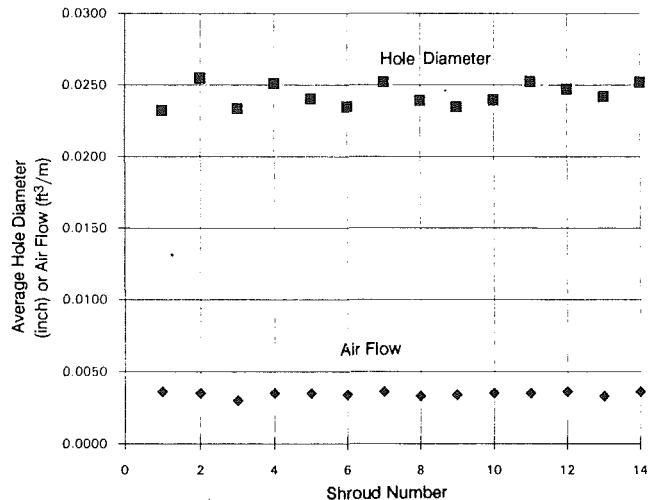


Fig. 15 Average shroud hole diameter and corresponding air flow rate for selected shrouds

Engine Test Hardware Drilling

Over 200 shrouds (see Fig. 13) were drilled using the above conditions. Some shrouds have 21 cooling holes, while others have only 7. Hole location accuracy is highly dependent on the positioning system. The true position requirement of 0.025 in. was met using the five-axis Adept robot system. Figure 14 shows the frequency distribution of hole diameters for a selected number of shrouds, each containing 21 holes. The air flow rate and average diameter for each shroud are given in Fig. 15.

As a final test to differentiate between the laser and AWJ drilling processes, a "Rainbow" engine test was performed. Shrouds drilled by both processes were assembled in a test engine and the engine was run in a test cell. When disassembled, the shrouds were evaluated and no distinct differences were noted. But to assure that the highest quality component would be used, the AWJ process was selected to drill the remainder of the engine shrouds. This decision was based on the following factors:

- Abrasive-waterjets produce crack-free holes more consistently and repeatedly than lasers.
- The overall drilling and hole finishing time and cost are higher for lasers than for AWJs.

Conclusions

The following conclusions are made as a result of our experimental investigation into drilling small-diameter holes in TBC using abrasive-waterjets.

- High-quality holes can be obtained with AWJ drilling. The ceramic TBC does not fracture or chip when drilling from the TBC side.
- Pressure profiling is a significant advance for hole drilling in composite materials.
- Hole size control can be accomplished. However, the current control process requires continuous adjustment. A closed-loop system with an automatic in-process hole size sensor needs to be developed.
- Holes with diameters in the range of 0.016 to 0.025 in. can be drilled. However, holes greater than 0.020 in. can be drilled more consistently.
- Holes at less than 25 deg require further investigation.
- The hole drilling time consists of the piercing time plus the dwell time, which controls the hole size.

Acknowledgments

The work described in this paper was funded by the U.S. Air Force under Contract No. F33657-83-C0281, for which the authors are grateful.

References

- Boldt, J. A., and Chanani, J. P., 1987, "Solid Tool Machining and Drilling," *Engineered Materials Handbook, Vol. 1, Composites*, J. R. Reinhart, ed., ASM International, pp. 667-672.
- Crossland, B., and Logan, J. G., 1972, "Development of Equipment for Jet Cutting," *First Intl. Symp. on Jet Cutting Technology*, BHRA, Coventry, United Kingdom, pp. C1-C12.
- Hashish, M., 1982, "Steel Cutting With Abrasive-Waterjets," *Proc. 6th Intl. Symp. on Jet Cutting Technology*, BHRA, United Kingdom, Apr., pp. 465-487.
- Hashish, M., 1984, "Cutting With Abrasive-Waterjets," *Mech. Eng.*, Mar., pp. 60-66.
- Hashish, M., 1988a, "Turning, Milling and Drilling With Abrasive-Waterjets," *Proc. 9th Intl. Symp. on Jet Cutting Technology*, BHRA, Sendi, Japan, Oct., pp. 113-131.
- Hashish, M., 1988b, "Visualization of the Abrasive-Waterjet Cutting Process," *J. Experimental Mech.*, June, pp. 159-169.
- Hashish, M., and Craigen, S., 1990, "Method and Apparatus for Drilling Small-Diameter Holes in Fragile Material With a High-Velocity Liquid Jet," U.S. Patent No. 4,955,164, Sept.

D. W. Seaver

A. M. Beltran

General Electric Company,
Schenectady, NY 12345

Nickel-Base Alloy GTD-222, a New Gas Turbine Nozzle Alloy

This paper summarizes the key properties of GTD-222 (Wood and Haydon, 1989), a new cast nickel-base nozzle alloy developed by GE for use in land-based gas turbines. GTD-222 is being introduced as a replacement for FSX-414 in second and third-stage nozzles of certain machines. Presented in this paper are comparisons of the tensile, creep-rupture, and fatigue properties of GTD-222 versus FSX-414. In addition, the results of a long-term thermal stability study, high-temperature oxidation, and hot corrosion evaluation as well as weldability results will be discussed.

Introduction

This paper outlines the studies conducted to assess the mechanical properties, environmental behavior, and weldability of GTD-222, a new investment cast nickel-base gas turbine nozzle alloy. GTD-222 is being introduced as a replacement for cobalt-base alloy FSX-414 in selected second and third-stage nozzles.

Experience with latter stage FSX-414 nozzles indicated that creep deflection due to higher firing temperatures required more frequent maintenance attention than desired.

A program was initiated to identify an alternate material to FSX-414 with improved creep resistance and reasonable weldability and oxidation/hot-corrosion resistance. An improvement of 200°F in creep resistance over FSX-414 was the total goal established for the new material. This challenge dictated that a cast nickel-base alloy be used.

GTD-222 is a gamma prime strengthened nickel-base superalloy that is vacuum heat-treated in two steps: 2100°F for four hours followed by 1475°F for eight hours. Table 1 compares the composition of GTD-222 with FSX-414 and with three nickel-base alloys: IN-738 is a cast gamma prime strengthened gas turbine bucket alloy; Nimonic 263 is a wrought gamma prime strengthened alloy used in gas turbine combustion system hardware; Waspaloy is a candidate filler metal.

Tensile Properties

Figures 1 and 2 compare tensile strength and ductility, respectively, of four of the alloys in Table 1. At gas turbine operating temperatures, the ranking in terms of descending order of strength is: IN-738, GTD-222, Nimonic 263, and FSX-414. In terms of ductility, Nimonic 263, a wrought alloy, is most ductile, followed by FSX-414, with GTD-222, and IN-738 having nearly the same ductility.

Thermal Aging Studies

Thermal aging studies were conducted to assess the effect

of long-term exposure on GTD-222 stability. Isothermal exposures were conducted at 1400°F and 1600°F for up to 8000 hours. The aging effect was assessed by means of Charpy impact data using unnotched Charpy bars.

Fully machined Charpy bars, along with Charpy specimen blanks, were aged in air atmosphere furnaces and removed for testing after the following time intervals: 100, 500, 1000, 2000, 4000, and 8000 hours. Charpy specimens were machined from the specimen blanks and tested at room temperature along with the aged fully machined specimens. Comparisons of impact data derived from the two specimen configurations permitted surface and volumetric effects to be evaluated.

Figures 3 and 4 show the results from the 1400°F and 1600°F aging tests, respectively. Figure 3 shows that aging at 1400°F reduces room temperature Charpy energy with increasing time of exposure, with the maximum reduction appearing after 1000 hours. Aged fully machined specimens, as well as specimens machined from aged blanks, were found to have similar values of Charpy energy even after 8000 hours of exposure. Thus, no environmentally induced embrittlement was observed.

Figure 4 displays the results of the room temperature unnotched Charpy tests on GTD-222 aged at 1600°F. Charpy energy initially increases with exposure time, peaking after 4000 hours and then decreasing, reaching a minimum at 8000 hours. GTD-222 at 1600°F is slowly being overaged, thus accounting for the increase in Charpy energy with exposure time. Environmentally induced embrittlement effects apparently begin to dominate after 4000 hours. Oxidation appears to account for both the reduction in Charpy energy after 4000 hours and the lower Charpy energy for the aged fully machined specimens relative to specimens machined from aged specimen blanks.

Creep Test Program

The goal of the creep program was to develop 0.2 to 0.5 percent creep properties of GTD-222. All tests were conducted on bare specimens. Over 60 tests representing material from three heat lots of GTD-222 were evaluated in the program over the temperature range from 1400°F to 1700°F, with a limited number of tests approaching 10,000 hours.

Creep tests were conducted under constant load conditions using a lever arm creep stand. Specimen temperature was main-

Contributed by the International Gas Turbine Institute and presented at the 36th International Gas Turbine and Aeroengine Congress and Exposition, Orlando, Florida, June 3-6, 1991. Manuscript received at ASME Headquarters February 12, 1991. Paper No. 91-GT-73. Associate Technical Editor: L. A. Riekert.

Table 1 Gas turbine alloy compositions

ELEMENT (%)	GTD-222	FSX-414	NIMONIC 263	Waspaloy	IN-738
Nickel	Balance	10.50	Balance	Balance	Balance
Chromium	22.50	29.50	20.00	19.5	16.00
Molybdenum	-----	-----	5.80	4.2	1.75
Cobalt	19.00	Balance	20.00	13.5	8.50
Iron	0.35	2.0 max	0.70 max	2 max	0.5 max
Carbon	0.10	0.25	0.06	0.06	0.175
Aluminum	1.20	-----	0.45	1.4	3.50
Titanium	2.30	-----	2.15	3.1	3.50
Tungsten	2.00	7.00	-----	-----	2.60
Niobium	0.80	-----	-----	-----	0.85
Tantalum	1.00	-----	-----	-----	1.75
Zirconium	0.023	-----	-----	0.04 max	0.10
Boron	0.008	0.010	-----	0.006	0.010

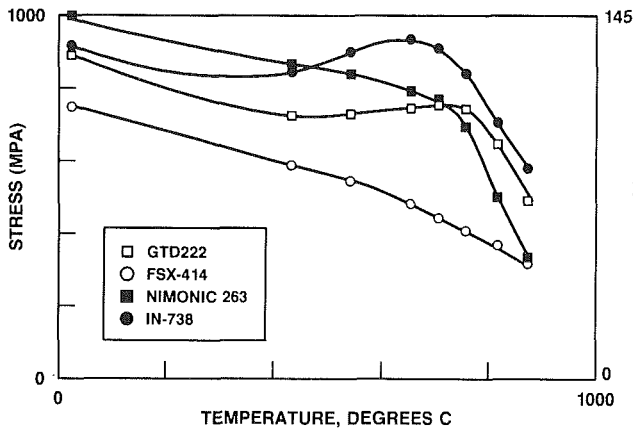


Fig. 1 A tensile strength comparison of candidate alloys

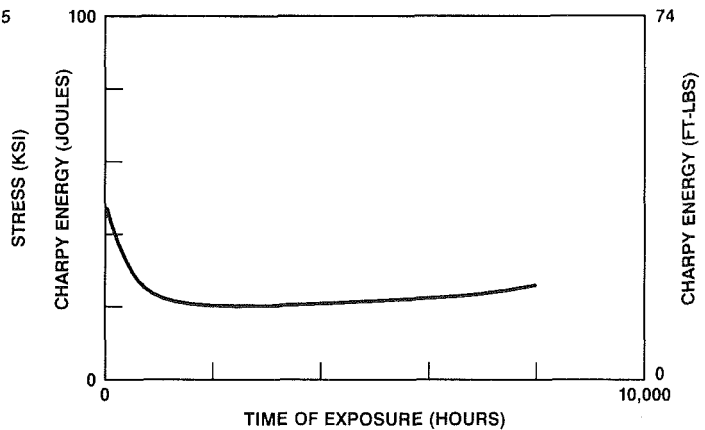


Fig. 3 Effect of thermal aging at 1400°F

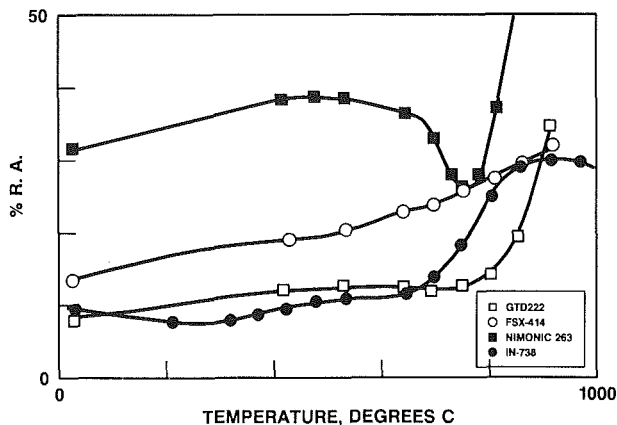


Fig. 2 A ductility comparison of candidate alloys

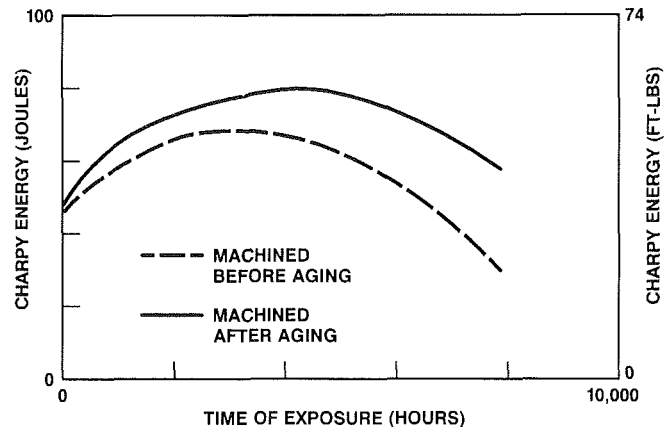


Fig. 4 Effect of thermal aging at 1600°F

tained within $\pm 3^\circ\text{F}$ over the gage length of the specimen. Specimens were radiant heated using electric resistance furnaces.

Test specimens were threaded end bars with an overall length of 8 in. The gage section was 5.4 in. in length with a cross-sectional area of 0.1 in.² Specimens were machined from cast slabs of GTD-222 that had been solution heat treated and aged prior to machining.

An initial creep program was conducted to assess the effect of two heat treatments: (a) a four-step procedure requiring 50 hours of furnace time, and (b) a simpler two-step heat treatment totalling 12 hours. That program revealed that both heat treatments produced the same creep response in GTD-222. Therefore, the simpler two-step heat treatment was selected, consisting of a 2100°F/4 h solution cycle followed by

an aging heat treatment at 1475°F for 8 hours, the same heat treatment as used for Nimonic 263.

Figure 5 shows the temperature improvement of GTD-222 over FSX-414 at both 0.2 and 0.5 percent creep strain. Figure 5 reveals that GTD-222 meets or exceeds the temperature improvement goal under machine operating conditions.

Low Cycle and Thermal Mechanical Fatigue Test Programs

An extensive low cycle fatigue test program was also conducted on GTD-222. The goal of the LCF program was to characterize the strain control fatigue properties of GTD-222 over the operating range of the nozzle applications.

All tests were conducted under total strain control conditions

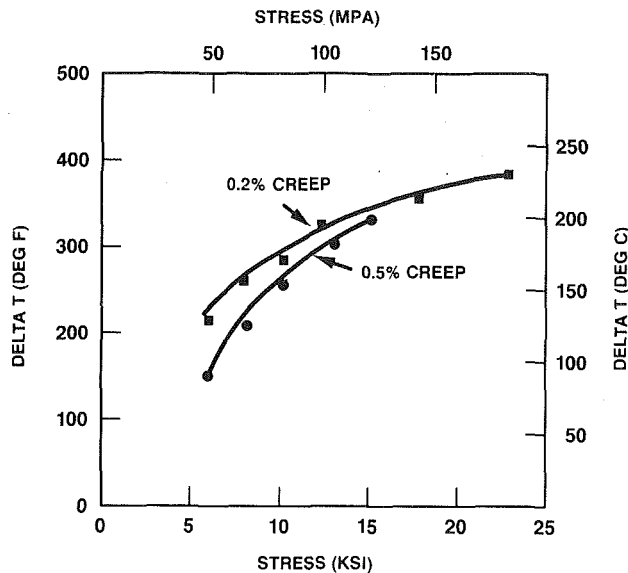


Fig. 5 Temperature improvement of GTD-222 over FSX-414 at both 0.2 and 0.5 percent creep strain

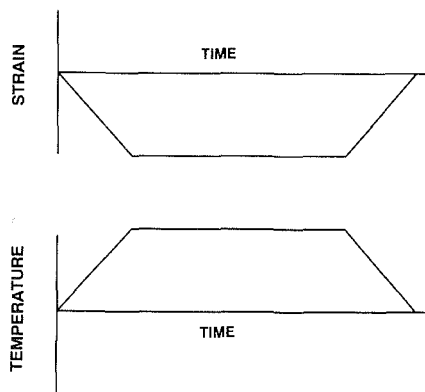


Fig. 6 TMF wave-shape schematic

using a closed-loop, servo-controlled, hydraulically actuated fatigue machine. Threaded end, uniform 0.25 in. gage diameter LCF induction-heated specimens were used for the entire test program. These specimens were also machined from cast slabs, and finished by low stress grinding.

Isothermal LCF tests were conducted in air at 1200°F, 1400°F, 1500°F, and 1600°F. Two basic strain versus time waveshapes were used in the program. The first was a fully reversed sawtooth wave with a frequency of 20 cycles per minute (CPM). The 20 CPM wave is commonly used to assess time-independent LCF material properties. The other basic waveshape used was the compression hold period. This waveshape is used to assess the effects of time-dependent inelastic strain on the LCF resistance of a material.

Thermal-mechanical fatigue (TMF) testing more closely models the time-temperature-strain history experienced by actual hardware than isothermal LCF tests. In the TMF test both strain and temperature are varied throughout the cycle, whereas in the LCF test only strain is varied and the temperature is held constant. A simple linear out-of-phase (LOP) cycle with a two minute hold in compression at the maximum temperature was used in this program. The term linear out of phase refers to the temperature ramping in a linear fashion to the maximum value while the strain ramps in a linear fashion to its minimum value (Fig. 6). The TMF program used the same specimen as used in the isothermal program.

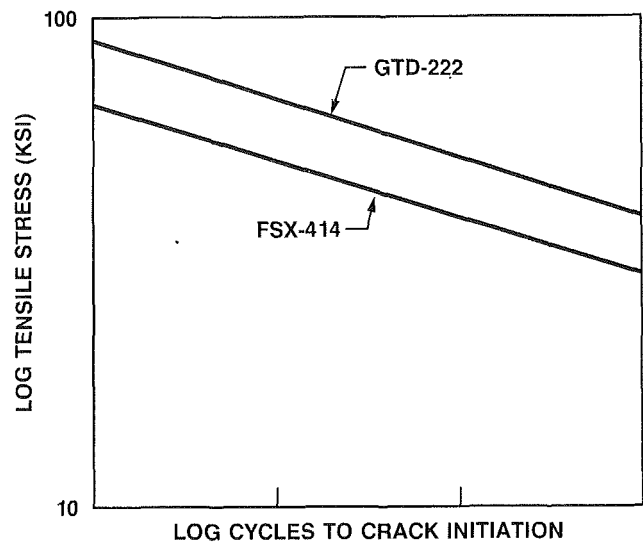


Fig. 7 A comparison of the LCF properties of GTD-222 and FSX-414 at 1400°F

LCF and TMF Test Results

Total strain range, one of the controlling variables in the LCF test, is made up of plastic and elastic components. Stress-strain response from LCF tests on cast nickel-base alloys typically involves very low levels of plastic strain. Thus, the main component of total strain is the elastic strain range component. Under those conditions, correlating LCF data with maximum stress is most appropriate.

Figure 7 compares the LCF properties of GTD-222 and FSX-414 at a temperature of 1400°F. This comparison is based on a maximum stress versus crack initiation life correlation. Crack initiation life is defined as the cyclic number or point in time when the first perceptible change in either plastic strain or load occurs after load stabilization. Figure 7 reveals that GTD-222 can sustain a higher peak tensile stress than FSX-414.

Results from the limited number of TMF tests performed confirm the superiority of GTD-222 over FSX-414 observed in the LCF program.

Oxidation and Hot-Corrosion Behavior

The environmental behavior of gas turbine alloys and coatings is evaluated using small combustion burner rigs located in Schenectady. Hot corrosion tests are run using doped diesel oil containing 1 percent sulfur and 125 ppm sodium in the fuel, which is burned at an air:fuel ratio of 50:1. The combustion products flow at approximately 70 feet per second over stationary specimens, which are air quenched to room temperature every 50 hours. Oxidation tests are conducted in undoped natural gas combustion products. Metallographic measurements are made to determine average surface metal loss and maximum subsurface penetration, including internal oxidation or sulfidation.

The literature classically distinguishes between two types of hot-corrosion attack on superalloys, categorized as Type I and Type II. Type I corrosion generally proceeds via reaction of sodium from the air environment with sulfur from the burned fuel to produce Na_2SO_4 . Deposition on a superalloy in the temperature range 1500–1700°F causes fluxing of the protective oxide, sulfur penetration, and subsurface internal sulfidation attack of the alloy.

Type II corrosion occurs below the nominal solidus temperature for Na_2SO_4 and requires a significant partial pressure of SO_2 . Deposition of the solid salt is followed by reaction with the surface oxide and selective leaching of cobalt, for

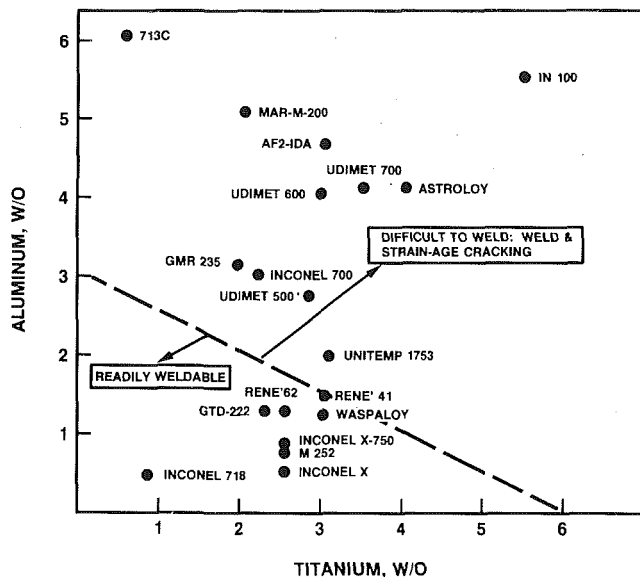


Fig. 8 Alloy weldability map

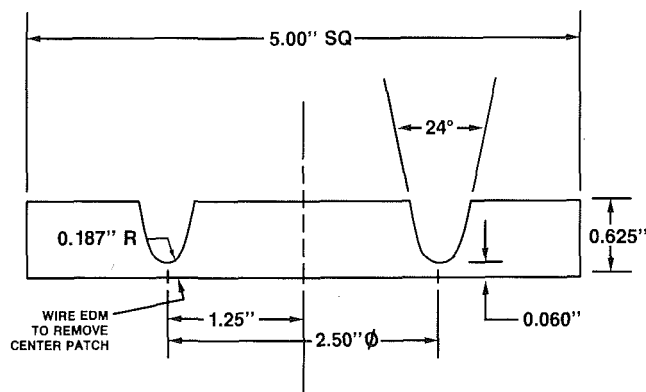


Fig. 9 Weld patch test specimen

example, to form a low melting point eutectic salt mix, which causes heavy localized pitting of the superalloy without internal sulfide formation in the temperature range 1100 to 1400°F.

Burner rig hot-corrosion testing demonstrated that GTD-222 is substantially more resistant to Type II corrosion at 1350°F than FSX-414. However, with increasing temperature and a shift to Type I hot corrosion, GTD-222 showed somewhat less corrosion resistance than FSX-414, especially at 1700°F.

Similarly, the natural gas oxidation resistance of GTD-222 was somewhat lower than that of FSX-414 above about 1600°F. The rate of internal oxidation attack was also somewhat higher than that of FSX-414. The application of a simple pack aluminate or Pt-Al coating to GTD-222 resulted in substantial improvement in oxidation resistance, as expected.

Weldability

Since gamma prime strengthened Ni-base alloys exhibit sensitivity to strain age cracking, the chemical composition of GTD-222 was balanced to provide good weldability in thick sections while retaining high creep and fatigue strength with good castability. The alloy definition of weldability as provided by Prager and Shira (1968) (Fig. 8) indicates that GTD-222 is safely within the weldable alloy range.

Differential thermal analysis (DTA) was performed to generate the gamma prime solvus and solidus/liquidus temperatures of cast GTD-222 and candidate filler alloy weld wire of Nimonic 263 and Waspaloy. These measurements were made

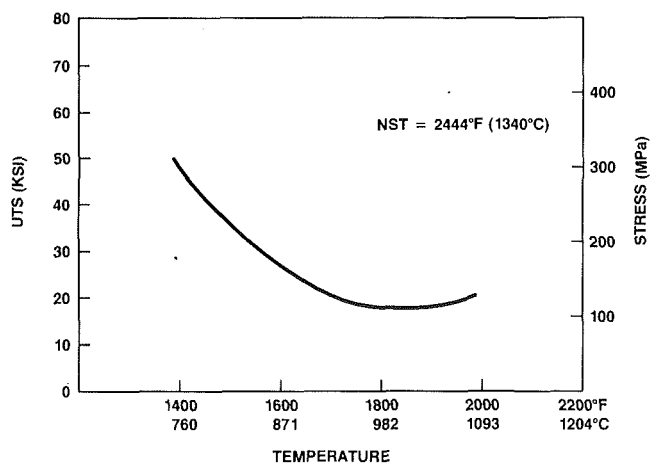


Fig. 10 Ultimate tensile strength measured on-cooling from NST

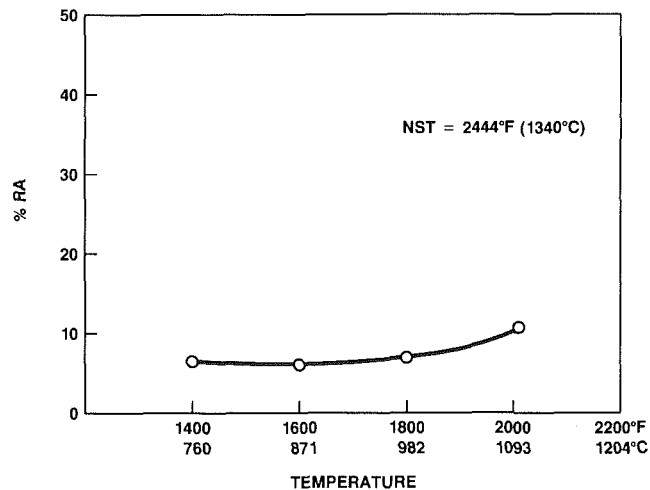


Fig. 11 Ductility measured on-cooling from NST

Table 2 DTA phase transition temperatures

ALLOY	FORM	GAMMA PRIME SOLVUS, F	SOLIDUS, F	LIQUIDUS, F
GTD-222	Cast	1868	2431	2518
Nimonic 263	Wire	<1650	2446	2534
Waspaloy	Wire	1926	2403	2507

Table 3 Crossweld tensile results

FILLER ALLOY	TEST TEMP, F	UTS ksi	0.2%YS ksi	0.02%YS ksi	%EL	%RA
GTD-222	70	113.8	94.8	86.2	5.3	11.6
	1200	100.2	74.1	62.1	9.5	17.4
	1400	113.2	80.2	70.1	6.3	10.8
Nimonic 263	70	108.2	86.2	76.1	6.5	9.4
	1200	99.2	67.1	59.1	11.9	12.4
	1400	107.6	68.1	59.1	11.8	13.8
Waspaloy (aged 1400F)	70	107.2	101.8	91.2	3.6	4.8
	1200	94.2	86.2	78.1	4.8	9.4
	1400	99.8	84.5	76.1	5.7	10.2

using a Dupont 9900 system with alumina liners and a platinum reference with helium gas. The actual measurements were taken from the second cycle "on-heating"; a ramp rate of 38°F (20°C) per minute was used throughout.

Gleeble tests (Yeniscavich, 1987) were also performed on cast GTD-222 slab material to characterize the "nil strength temperature" (NST) and "on-cooling" strength and ductility response at 2000, 1800, 1600, and 1400°F, using a cooling rate of 200°F (111°C) per minute from the NST. This test is used to determine the rate at which the alloy increases strength and

decreases ductility to simulate the thermal gradient within the heat-affected zone (HAZ). Specimens were tested in the 2100°F/4 hour solution treated condition.

To assess crossweld mechanical properties using different strength filler alloys, 0.5-in.-thick V-block butt-weld slabs of cast GTD-222 were prepared with GTAW weld deposits of Nimonic 263, Waspaloy, and GTD-222 filler wire; the base metal was in the 2100°F solutioned condition. The following general GTAW welding parameters were employed:

Current	80–120 amps
Current polarity	d-c straight
Voltage	16–18 volts
Electrodes	1/16–3/32 in. dia 2 percent thoriated
Shielding gas	Ar-He 80/20
Gas flow	15–20 CFH
Interpass temperature	350°C maximum

In each case, dye penetrant inspection of the root pass and the final weldments was done to ensure absence of defects. Each plate was then radiographically inspected prior to final postweld solution treatment at 2100°F for 4 hours and aging at 1475°F for 8 hours in vacuum. Test specimens were EDM-trepanned and final machined to standard 0.25 in. diameter gage section bars with the weldment in the center of the gage. Some additional specimens were aged for 3000 hours at 1400°F in air prior to tensile testing for comparison to unaged material.

To simulate highly restrained component GTAW weldments, circular patch test specimens were machined using U-grooved cast plates as illustrated in Fig. 9. Fluorescent penetrant inspection, radiographic inspection, and postweld heat treatments were conducted, and evaluations were performed before and after the simulated 1400°F/3000 hour service age.

Welding Results

A summary of the transition temperatures determined by DTA for GTD-222, Nimonic 263, and Waspaloy is shown in Table 2. For these three alloys, the solidus and liquidus temperatures are inversely proportional to the gamma prime volume percent, which increases in the order Nimonic 263, GTD-222, and Waspaloy. The gamma prime solvus temperature increases with increasing Al + Ti; this was not determined for Nimonic 263 since DTA data collection began at about 1652°F (900°C), which is above the gamma prime solvus of the alloy (about 1600°F).

The Gleeble test results for cast GTD-222 are summarized in Figs. 10 (UTS) and 11 (%RA). The NST was determined to be 2444°F, which substantially exceeds that of IN-738, for instance (2320°F). As expected, a comparison of tensile strength on-cooling from their respective NST's shows GTD-222 to be of lower strength and higher ductility, thus enhancing its weldability.

The results of GTAW-deposit crossweld tensile tests at room temperature, 1200, and 1400°F are listed in Table 3. Visual and metallographic inspection of the fractured specimens showed that all specimens broke in the parent casting alloy, thus indicating that the weldments of all three filler alloys are stronger in tension than parent metal cast GTD-222.

The results of short-time rupture tests conducted on crossweld specimens between 1450 and 1750°F are plotted in Fig. 12. All of these specimens fractured in the weldments, with the exception of the 1550 and 1625°F Waspaloy specimens, which broke in the HAZ. The results therefore reflect actual weldment strength levels, and rank in increasing order as follows: Nimonic 263, GTD-222, and Waspaloy.

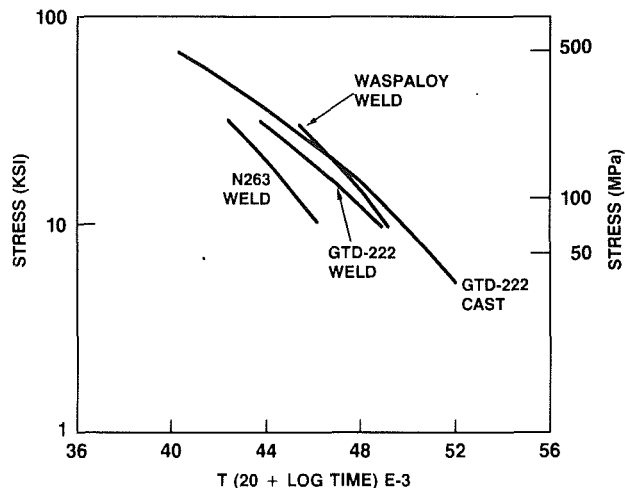


Fig. 12 Crossweld stress rupture results

Evaluation of the U-groove patch test plates showed that Nimonic 263 and GTD-222 filler alloy welds were sound before and after postweld heat treatment and the simulated service aging treatment at the 1400°F for 3000 hours. The Waspaloy filler welds were somewhat prone to minor HAZ fissuring, but sound welds were produced, which subsequently showed no post-age cracking.

Summary of GTD-222 Properties

Results of this study indicate that GTD-222 represents a very substantial improvement over FSX-414 in creep resistance. The initial goal of a 200°F improvement in the creep strength has been achieved. Thus, nozzle downstream creep deflection, which was the primary focus of this program, should be minimized or eliminated by use of this alloy.

The LCF properties of GTD-222 are typical of cast nickel base alloys, and demonstrate superiority over FSX-414 in the critical high cyclic life regime.

GTD-222 offers excellent hot-corrosion resistance at the temperatures anticipated for second and third-stage nozzle applications. However, above about 1600°F the use of simple aluminide coatings is recommended for long-term environmental protection.

GTD-222 has proven to be castable and weldable in large nozzle segments. DTA results demonstrated that gamma solvus increases and solidus/liquidus temperatures decrease with increasing volume percent gamma prime content in the alloy, which increases in the order Nimonic 263, GTD-222, and Waspaloy. The tensile strength of all three GTAW filler alloys exceeds that of cast GTD-222. However, short-time crossweld rupture tests also produced weldment strength levels in increasing order of volume percent gamma prime: Nimonic 263, GTD-222, and Waspaloy. Initial sets of second-stage nozzles have now successfully acquired in excess of 12,000 hours of service exposure.

References

- Prager, M., and Shira, C. S., 1968, *Welding Research Council Bulletin*, Vol. 128.
- Wood, J. H., and Haydon, J. S., 1989, United States Patent No. 4,810,467, Mar. 7.
- Yeniscavich, W., 1987, in: *Superalloys II*, C. T. Sims, N. S. Stoloff, and W. C. Hagel, eds., Wiley, New York, pp. 495–516.

Effect of Cold Work and Aging Upon the Properties of a Ni-Mo-Cr Fastener Alloy

M. F. Rothman

S. K. Srivastava

Haynes International, Inc.,
Kokomo, IN 46901

HAYNES® alloy 242 is a promising new Ni-Mo-Cr alloy for high-strength, high-temperature aerospace fastener applications. Age-hardenable by virtue of a long-range-order strengthening mechanism, 242™ alloy is capable of developing very high strength, particularly in the cold-worked condition. A key difference from other fastener materials is its attendant good ductility. The relationship between the amount of cold work, aging temperature and time, and the properties of this alloy has not been previously explored in detail. In the present work, the nature of the interaction between cold work and aging will be examined, and the properties of the material relevant to aerospace fastener applications will be described.

Introduction

The basic characteristics of 242 alloy have been previously described by Rothman and Srivastava (1989) and Srivastava and Lai (1989). It is a nickel-molybdenum-chromium alloy, the composition of which is given in Table 1. The alloy exhibits a long-range-order strengthening response when aged for relatively short times at temperatures between about 1100 to 1300°F (595 to 705°C). This strengthening response is associated with the formation of small ordered domains of Ni₂(Mo, Cr) phase, with crystal structure similar to Pt₂Mo (Tawancy, 1980). A key feature of this age-hardening mechanism is that the relatively high strength obtained is accompanied by retention of good ductility in the aged condition.

As already described by previous investigators, 242 alloy is a candidate material for various wrought gas turbine components such as seal rings, casings and containment structures. Features that support the alloy's use include high strength up to 1300°F (705°C), low thermal expansion characteristics, good oxidation resistance, good retained ductility and toughness, and good fatigue resistance (Srivastava and Rothman, 1990). These same characteristics support consideration of the alloy for aerospace fastener applications. Many of the alloys currently used for aerospace fasteners are precipitation-hardened superalloys, such as alloys A-286 and 718, which are most often employed in the cold-worked and direct-aged condition. The effect of prior cold work upon the nature of the long-range-order strengthening mechanism in 242 alloy has not previously been examined in detail, and is therefore the focus of the present study.

Previous work by Tawancy and Asphahani (1985) on other Ni-Mo-Cr alloys has indicated that the formation of Ni₂(Mo, Cr) ordered phase can be influenced by cold working prior to

aging at about 1100°F (595°C). The effect is largely manifested by a significant increase in the speed of the ordering reaction, with strengthening being observed in some cases in less than 100 hours as compared to thousands of hours required without prior cold work. It was, therefore, expected that the standard commercial aging treatment for 242 alloy of 1200°F (650°C) for 24 hours might not be optimum for cold-worked material. While this heat treatment was employed in our initial characterization of 242 alloy, the rest of our study was directed at examining various aging temperatures and times in combination with prior cold reduction.

Initial Characterization

In order to establish an initial appreciation for the effect of cold work upon the strength and ductility of 242 alloy, commercially produced 0.125-in. (32-mm) thick sheet¹ was obtained and subjected to 0, 20, and 40 percent cold rolling reduction prior to aging for 24 hours at 1200°F (650°C). Standard duplicate room temperature tensile tests were performed in the transverse direction for each set of cold-worked and aged conditions, and also for material cold-worked only. Results are given in Table 2, together with average hardness determinations.

The response of material that did not receive any prior cold work to the standard aging treatment was an approximate doubling of the yield strength and a corresponding increase in hardness from about R_c23 to R_c38 . Tensile ductility fell from about 46 percent to a still relatively high value of about 32 percent. With the imposition of both 20 and 40 percent prior cold work, the aging treatment produced yield strengths about an additional 33 and 68 percent higher than that for no prior cold work. Hardness increased from about R_c38 to R_c46 and R_c50 , respectively. Tensile ductility was reduced, but still ex-

¹Contributed in the International Gas Turbine Institute and presented at the 36th International Gas Turbine and Aeroengine Congress and Exposition, Orlando, Florida, June 3-6, 1991. Manuscript received at ASME Headquarters January 25, 1991. Paper No. 91-GT-14. Associate Technical Editor: L. A. Riekert.

¹Mill-annealed condition, 1950°F (1065°C) bright anneal.

Table 1 Nominal composition of alloys

Material	Composition, Weight %											
	Ni	Fe	Cr	Mo	Cb	Ti	Al	Si	Mn	C	B	Co
HAYNES® alloy 242	Ba1	2*	8	25	-	-	.5*	.8*	.8*	.03*	.006*	2.5*
MP35N® alloy	35	1	20	10	-	.8	-	-	-	.005	-	Ba1
Alloy 718	Ba1	19	18	3	5	1	.6	.35*	.35*	.05	.004	1*
Alloy X-750	Ba1	7	15.5	-	1	2.5	.8	.35*	.35*	.08*	-	1*
Alloy A-286	26	Ba1	15	1.25	-	2.15	.2	.4	1.4	.05	.003	

*Maximum

®HAYNES and 242 are trademarks of Haynes International, Inc.

MP35N is a registered trademark of SPS Technologies, Inc.

Table 2 Room temperature tensile and hardness properties for 242 alloy sheet product as influenced by cold work*

Condition	Ultimate Tensile Strength		0.2% Yield Strength		Elongation %	Hardness Rockwell C
	Ksi	MPa	Ksi	MPa		
M.A. + 0% C.W.	137.6	950	65.3	450	46.7	23.3
M.A. + 20% C.W.	169.6	1170	138.5	955	19.6	39.0
M.A. + 40% C.W.	217.6	1500	181.3	1250	7.5	44.2
M.A. + 0% C.W. + Age	192.0	1325	130.4	900	32.1	38.0
M.A. + 20% C.W. + Age	209.5	1445	173.0	1195	20.8	46.4
M.A. + 40% C.W. + Age	244.7	1685	219.7	1515	10.9	50.1

*Average of 2 or more tests per condition

M.A. = Mill Anneal, C.W. = Cold Work, Age = 1200°F (650°C)/24 Hr./AC

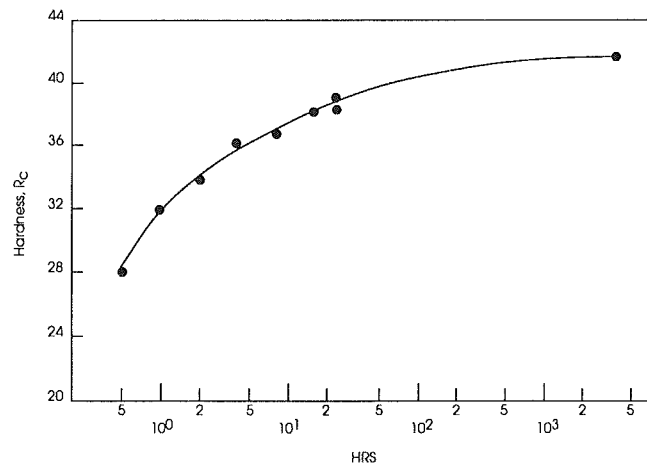


Fig. 1 Effect of aging time at 1200°F (650°C) on the hardness of mill-annealed 242 alloy

ceeded 10 percent even with the imposition of 40 percent prior cold work.

It is observed that the apparent hardening response is significantly less for cold-worked material than that for annealed material. While aging annealed material increases the yield strength about 65 Ksi (450 MPa) and hardness about 15 R_c points, aging cold-worked material increases yield strength only about 34 to 38 Ksi (235 to 260 MPa) and hardness about 6 to 7 R_c points. Judging from the tensile elongation data, however, there appears to be some recovery of the cold work taking place during the aging treatment. Rather than a decrease in elongation, as experienced when aging annealed material, a slight increase in ductility is observed for the cold-worked and aged samples. This may indicate that the contribution of the cold work to both strength and hardness actually decreases during aging, partially offsetting the strengthening effect of the long-range-ordering reaction.

Isolating the relative contributions of the ordering reaction and the partial recovery of the cold-worked structure during aging is exceedingly difficult. There is also the question of whether or not there is any synergistic effect between the cold work and the ordering reaction. Long-term aging effects at 1200°F (650°C) upon the hardness of annealed material are illustrated in Fig. 1. After 4000 hours of aging, the hardness appears to level off at about R_c42 , compared to about R_c38 after 24 hours. If the influence of the cold work upon the ordering reaction is only acceleration of kinetics, then the maximum contribution to the 40 percent cold-worked and aged material of the ordering reaction is a hardness of R_c42 . This

leaves the increase from R_c42 to R_c50 as the contribution of the cold work itself, or 8 R_c points, compared to the increase of about 21 R_c points as cold-worked before aging. This would mean that there is a very significant recovery effect during aging. If the cold work has some type of synergistic effect upon the ordering reaction that increases its hardening contribution, then the recovery effect is even greater. Considering that the aging temperature is relatively low, experience with nickel-base alloys in general would mitigate against a complete loss of the contribution of the cold work itself due to recovery. An examination of the 40 percent cold-worked and aged material by electron microscopy reveals ample evidence of residual dislocation substructure together with the ordered domains, confirming that at least some contribution of the cold work to both strength and hardness is maintained after aging. A typical electron micrograph is shown in Fig. 2.

Whatever the relative contributions of the cold work and the ordering reaction may be, the properties obtained in this initial characterization are quite good compared to alloy 718 and alloy A-286. Similar cold rolling and direct-aging studies were performed for alloy 718 for comparison. Average results for 0.120-in. (3-mm) sheet cold-reduced 40 percent and aged at 1325°F (720°C)/8 h/furnace cooled to 1150°F (620°C)/8 h/AC are shown in Fig. 3, compared with the earlier results for 242 alloy and results reported by Raring et al. (1963) for alloy A-286. The ultimate tensile strength and yield strength for 242 alloy are roughly comparable to those for alloy 718,

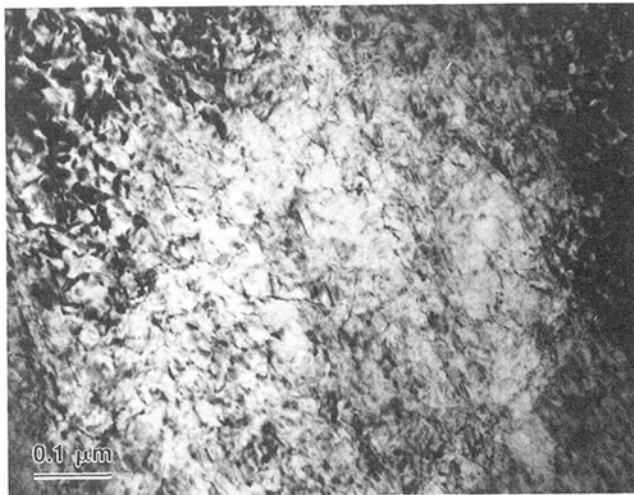


Fig. 2 Transmission electron micrograph of 40 percent cold-reduced and 1200°F (650°C)/24 hour aged 242 alloy sheet

and significantly higher than those for alloy A-286. The key result, however, is that 242 alloy exhibits higher ductility, with elongation roughly double that for alloy 718 and almost 1.5 times that for alloy A-286. This ductility advantage may be of great importance in terms of fatigue resistance, crack growth rate, and critical flaw size considerations.

In view of the favorable property comparison at room temperature, it was decided to evaluate the elevated temperature tensile properties of 40 percent cold-reduced and direct-aged 242 alloy and alloy 718 sheet materials. Results are given in Table 3. From these results, it appears that alloy 718 is somewhat stronger than 242 alloy up to 1300°F (705°C); however, 242 alloy has a significant ductility advantage up to 1200°F (650°C).

Effect of Aging Temperature and Time

As mentioned previously, it was not known whether the standard 1200°F (650°C)/24 h/AC aging treatment normally utilized for mill-annealed 242 alloy was optimum for 242 alloy in the cold-worked condition. In order to explore variations in aging temperature and time, hardness was selected as the most direct measure of aging response. For purposes of comparison, parallel studies were performed for both 40 percent cold-reduced sheet and mill-annealed sheet of comparable thickness. The mill-annealed sheet was prepared using a 1950°F (1065°C)/30 min/WQ treatment.

Aging treatments consisting of exposures at 1100°F (595°C), 1200°F (650°C), and 1300°F (705°C) for from 3 minutes to 1440 minutes (24 hours) were performed upon coupons taken from each lot of material. Exposures under 30 minutes were only performed for the cold-reduced material, since no effects were expected for the annealed samples. Results for each of the three aging temperatures are presented in Figs. 4–6 for the 40 percent cold worked material, and in Fig. 7 for the annealed material. Hardness values shown are averages of at least five measurements per coupon.

An inspection of Figs. 4–6 reveals that aging 40 percent cold-reduced material at all three temperatures resulted in a very rapid initial increase in hardness from the 45.3 R_c level as cold-rolled. The response in the first three minutes of aging was greatest for aging at 1100°F (595°C), lowest for aging at 1300°F (705°C), and in between for aging at 1200°F (650°C). In all three cases, little or no further increase in hardness occurred for about 15 to 120 minutes following this initial increase. Continued aging at all three temperatures resulted in another rapid increase in hardness, gradually leveling off at a maximum

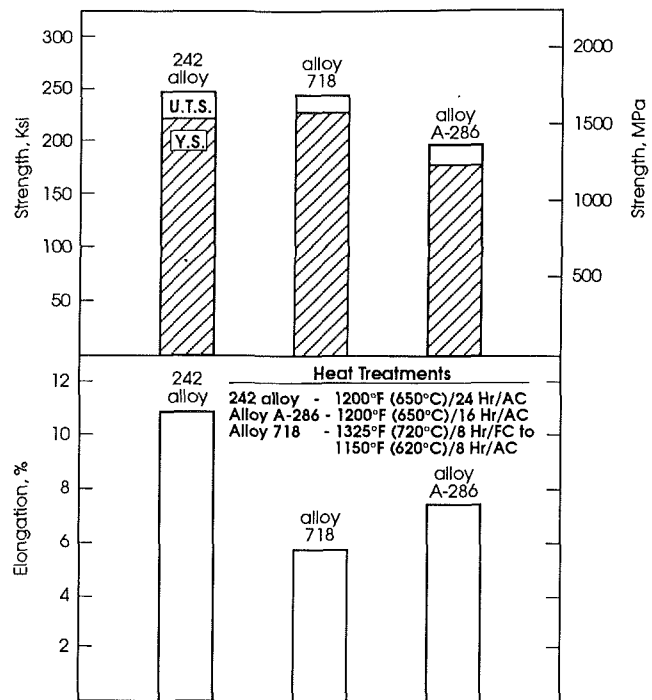


Fig. 3 Room temperature tensile properties of 40 percent cold-reduced and direct-aged sheet; alloy A-286 results from Raring et al. (1963)

Table 3 Elevated temperature tensile properties for 40 percent cold-reduced and direct-aged sheet of 242 alloy and alloy 718⁽¹⁾⁽²⁾

Test Temperature °F °C	Material	Ultimate Tensile Strength		0.2% Yield Strength		Elongation %
		Ksi	MPa	Ksi	MPa	
70 20	242 Alloy	245	1690	220	1515	10.9
	Alloy 718	243	1675	229	1580	5.6
1000 540	242 Alloy	208	1435	180	1240	13.7
	Alloy 718*	214	1475	200	1380	4.1
1100 595	242 Alloy	203	1400	175	1205	11.0
	Alloy 718	208	1435	194	1340	4.1
1200 650	242 Alloy	195	1345	160	1105	8.0
	Alloy 718	203	1400	183	1260	4.4
1300 705	242 Alloy	184	1270	134	925	11.5
	Alloy 718	190	1310	161	1110	14.1

* Single test result

(1) Two or more tests per condition

(2) 242 alloy aged 1200°F (650°C)/24 Hr/AC

alloy 718 aged 1325°F (720°C)/8 Hr/FC to 1150°F (620°C)/8 Hr/AC

value after about 120 to 600 minutes, depending upon temperature.

The variation in the magnitude of the initial increase in hardness for cold-worked material with aging temperature is consistent with the variation in hardening kinetics for the annealed material aged at these same temperatures. The hardness response curves shown in Fig. 7 indicated that, for annealed material, hardening occurs most rapidly with aging at 1100°F (595°C) and most slowly with aging at 1300°F (705°C). Thus, with the kinetics of the ordering reaction accelerated by the imposed cold work, the increase in hardness observed in the first few minutes of aging cold-worked material should be greatest for the 1100°F (595°C) exposure and least for the 1300°F (705°C) exposure, as is the case.

The halt or plateau in the hardness response curves (shown

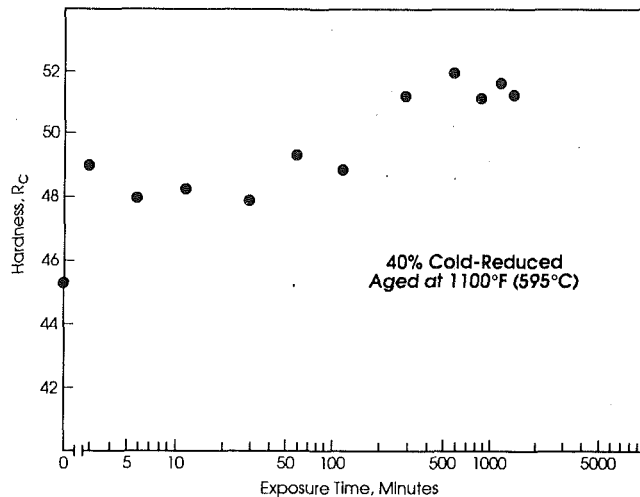


Fig. 4 Room temperature hardness of 242 alloy sheet cold-reduced 40 percent and aged at 1100°F (595°C)

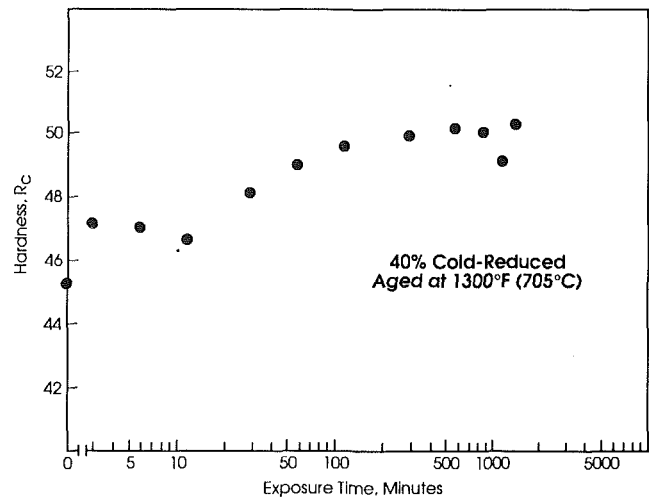


Fig. 6 Room temperature hardness of 242 alloy sheet cold-reduced 40 percent and aged at 1300°F (705°C)

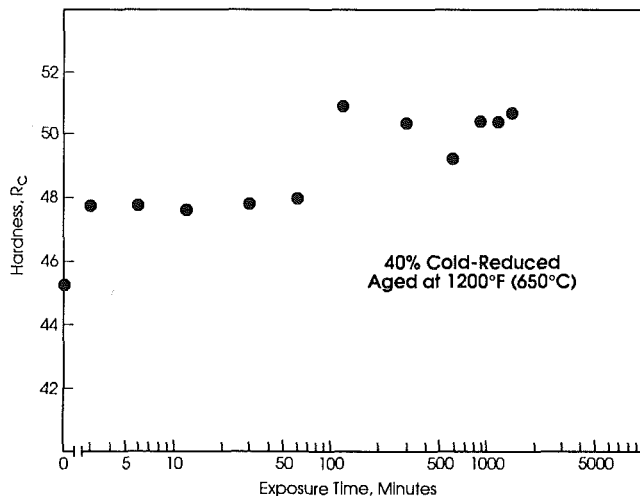


Fig. 5 Room temperature hardness of 242 alloy sheet cold-reduced 40 percent and aged at 1200°F (650°C)

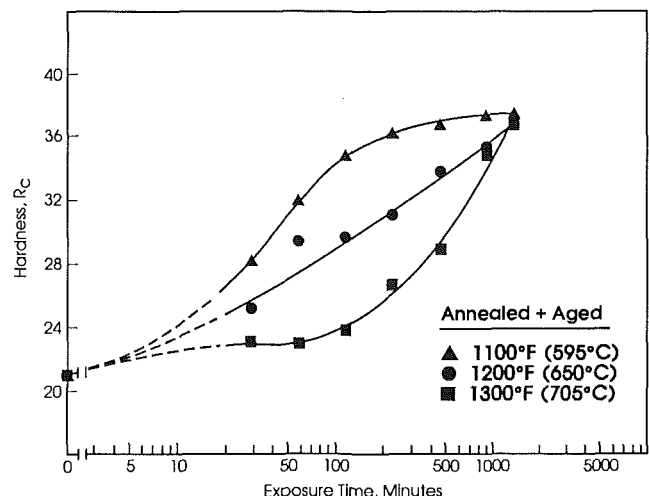


Fig. 7 Room temperature hardness of 242 alloy sheet, annealed 1950°F (1065°C)/30 min/wq plus aged at various temperatures

in Figs. 4-6) that follows the initial increase in hardness likely corresponds to the interval during which hardening as a function of the ordering reaction is being offset by softening due to recovery of the cold work. It might be expected that, unlike the kinetics of the ordering reaction, the rate of recovery would increase with increasing aging temperature. This is again consistent with the results observed. For cold-worked material aged at 1300°F (705°C), the ordering reaction proceeds at the slowest rate, while recovery proceeds at the fastest rate. Thus, the initial hardness increase is the lowest for the three aging temperatures, but the halt or plateau in the hardness response curve is shortest at about 15 minutes. For 1100°F (595°C) aging of cold-worked material, ordering proceeds at the fastest rate and recovery at the slowest rate. Thus, the initial hardness increase is highest and the plateau longest at about 120 minutes. Aging at 1200°F (650°C) produces intermediate results.

Once the process of recovery at the three aging temperatures begins to reach some degree of completeness, the continued hardening by virtue of the ordering reaction would no longer be offset by softening due to recovery, and a further increase in hardness level would be expected. This is the observed behavior, as shown in Figs. 4-6.

From the hardness results obtained in this portion of the study, it appears that full strengthening may occur in 40 percent

cold-reduced 242 alloy after as little as 2 hours of aging at 1200°F (650°C), and that slightly increased strength may accrue from aging for from 5 to 24 hours at 1100°F (595°C). This latter approach remains to be confirmed by future work, but tensile testing of material given the shorter age at 1200°F (650°C) has been performed. Results are presented in Table 4, compared with the 24 hour aging results repeated from Table 3. Clearly, strengths obtained with the two hour aging treatment are at least equivalent to those obtained after aging for 24 hours. Tensile ductility, however, may be slightly lower overall, perhaps reflecting slightly less effective stress relief over the shorter aging period.

Other Considerations Relevant to Fastener Applications

In addition to strength and ductility, there are a number of additional properties relevant to the use of materials for fasteners. Our studies continue, but two important performance criteria for 242 alloy have been evaluated: (1) resistance to hydrogen embrittlement, and (2) resistance to chloride stress corrosion cracking. Results for standard notched room temperature tensile tests performed in pressurized hydrogen and air reveal that 242 alloy is superior to alloy 718, alloy X-750, and MP35N alloy in resisting hydrogen embrittlement. Notched

Table 4 Elevated temperature tensile properties for 40 percent cold-reduced 242 alloy sheet direct-aged for 2 hours versus 24 hours⁽¹⁾

Test Temperature °F °C	Aging Time at 1200°F (650°C)	Ultimate Tensile Strength		0.2% Yield Strength		Elongation %
		Ksi	MPa	Ksi	MPa	
70 20	2 Hours	244	1680	222	1530	9.4
	24 Hours	245	1690	220	1515	10.9
1000 540	2 Hours*	202	1395	184	1270	10.1
	24 Hours	208	1435	180	1240	13.7
1100 595	2 Hours*	197	1360	177	1220	9.9
	24 Hours	203	1400	175	1205	11.0
1200 650	2 Hours	196	1350	164	1130	8.3
	24 Hours	195	1345	160	1105	8.0
1300 705	2 Hours*	184	1270	134	925	8.6
	24 Hours	184	1270	134	925	11.5

* Single test result

(1) Duplicate tests

Table 5 Notched tensile strength ratios for pressurized hydrogen versus air for various alloys*

Material	Hydrogen Pressure			Ratio of Notched Tensile Strength Hydrogen/Air
	Psi	MPa	Kt	
242 alloy	5,000	34	8.0	.74
Alloy 718	5,000	34	8.0	.53
MP35N alloy	10,000	69	6.3	.50
Alloy 718	10,000	69	8.0	.46
Alloy X-750	7,000	48	6.3	.26

* Tests performed in MIL-P27201B grade hydrogen, with a crosshead speed of 0.005 in/min (0.13mm/min). All materials were annealed plus fully aged. Results for all alloys except 242 alloy from Franklin (1987), and Harris and Van Wanderham (1973).

tensile strength ratios for these alloys were reported by Franklin (1987) and Harris and Van Wanderham (1973), and are compared to 242 alloy in Table 5.

As for resistance to chloride stress cracking, tests have been run using standard U-bend specimens immersed in 310°F (154°C) boiling 45 percent MgCl₂. Results of triplicate tests reveal no cracking in 242 alloy material tested in the 1200°F (650°C)/24 hour/AC aged condition after 1008 hours of exposure. Similar tests run in duplicate for standard aged alloy 718 resulted in specimens cracking within 24 hours of exposure. Tests were performed using a modified ASTM G-36 procedure.

Summary and Future Work

The influences of cold work, aging temperature, and aging time upon the properties of a candidate aerospace fastener

material, HAYNES alloy 242, have been explored. It was found that 242 alloy, subjected to cold work and direct aging, is capable of exhibiting strength that is competitive with cold-worked and aged alloy 718, and superior to that for cold-worked and aged alloy A-286. One key advantage of 242 alloy over these materials is higher tensile ductility: double that for alloy 718, and 1.5 times that for alloy A-286.

Studies aimed at optimizing the aging temperature and time for cold-worked 242 alloy revealed that the hardening response of cold-worked material is a somewhat discontinuous reaction. This is believed to reflect a competition between the long-range-order strengthening reaction and simultaneous recovery of the cold-worked structure. Limited tensile test results indicated that the full 24 hour aging treatment normally employed for annealed material is not required to achieve full strength in cold-worked material. Comparable strengths were exhibited for both 2 hour and 24 hour ages at 1200°F (650°C). In addition, hardness data indicate that 1100°F (595°C) aging may produce higher strength in cold-worked 242 alloy than the standard aging temperature of 1200°F (650°C).

Collateral studies on key environmental behaviors have been performed. Results of both hydrogen embrittlement resistance testing and testing for resistance to stress corrosion cracking in boiling 45 percent MgCl₂ indicate superior performance relative to alloy 718 and some other fastener materials.

Our work continues in this area. Future efforts will concentrate upon more detailed structural evaluation of the 242 alloy cold-worked material subjected to the various aging treatments, and more definitive tensile property evaluation. Characterization of cold-reduced bar product, more relevant to actual fastener manufacture, is in progress for cold reductions up to 60 percent.

Acknowledgments

The authors would like to thank Professor Vijay Vasudevan of the University of Cincinnati for providing the electron micrograph used in this paper.

References

- Franklin, D. B., 1987, "Corrosion of Space Boosters and Space Satellites," *Metals Handbook*, 9th ed., Vol. 13, The American Society of Metals, Metals Park, OH, pp. 1101-1104.
- Harris, J. A., Jr., and Van Wanderham, M. C., 1973, "Properties of Materials in High Pressure Hydrogen at Cryogenic, Room and Elevated Temperatures," NASA CR-124394, Marshall Space Flight Center, AL, p. VIII-2.
- Raring, R. H., Freeman, J. W., Schultz, J. W., and Voorhees, H. R., 1963, "Progress Report of the NASA Special Committee on Materials Research for Supersonic Transports," NASA Technical Note D-1798, Washington, DC, pp. 131-137.
- Rothman, M. F., and Srivastava, S. K., 1989, "A New Long-Range-Order-Strengthened Superalloy," *World Aerospace Profile 1989*, Sterling Publications, Ltd., London, United Kingdom, pp. 121-124.
- Srivastava, S. K., and Lai, G. Y., 1989, "A New Low-Thermal Expansion, High-Strength Alloy for Gas Turbines," ASME Paper No. 89-GT-329.
- Srivastava, S. K., and Rothman, M. F., 1990, "An Advanced Ni-Mo-Cr Alloy for Gas Turbines," *High Temperature Materials for Power Engineering 1990*, proceedings of conference held in Liege, Belgium, Sept. 24-27, 1990, in press.
- Tawancy, H. M., 1980, "Order Strengthening in a Nickel-Base Superalloy (HASTELLOY alloy S)," *Metallurgical Transactions A*, Vol. 11A, The American Society for Metals and The Metallurgical Society of AIME, New York, pp. 1764-1765.
- Tawancy, H. M., and Asphahani, A. I., 1985, "Ordering Behavior and Corrosion Properties of Ni-Mo and Ni-Mo-Cr Alloys," *Materials Research Society Symposium on High-Temperature Ordered Intermetallic Alloys, Proceedings*, Materials Research Society, Pittsburgh, PA, pp. 485-494.

Extending the Fatigue Life of Aircraft Engine Components by Hole Cold Expansion Technology

A. C. Rufin

Fatigue Technology Inc.,
Seattle, WA 98188

The split-sleeve cold expansion process has been used successfully for over 20 years to extend the fatigue life of holes in aircraft structures. Cold expansion technology can also be applied to enhance engine low-cycle fatigue (LCF) performance in both production and repair applications. Specific test data are presented showing that fatigue life extension can be attained by cold expansion of holes in a wide range of situations (including nonround hole geometries and low edge margins), and in components subjected to high operating temperatures. A cold expanded bushing system is compared to standard shrink-fit bushing installations. Finally, two case studies are used to illustrate the application of cold expansion to full-scale engine components.

1 Introduction

The high centrifugal forces imposed on rotating engine components during normal operation result in high stress in areas such as fastener holes, cooling holes, drain holes, and blade attachments. In these areas, the controlling failure mechanism is usually low-cycle fatigue (LCF).

The creation of permanent compressive stresses near holes has long been recognized as a means to extend LCF life in fatigue-critical components. The compressive stresses can retard crack initiation and growth. Methods commonly used to induce compressive residual stresses include shotpeening, roller burnishing, coining, and extrude honing. However, these techniques produce only relatively shallow residual compression zones, which are sensitive to manufacturing variables and, often, operator proficiency. Consequently, these surface treatment methods have only a limited ability to prolong fatigue life effectively.

Unlike most of the aforementioned processes, hole cold expansion: (1) generates a large, controllable residual compression zone with high compressive stresses, (2) is not significantly affected by final surface finish, and (3) produces only a minimal amount of surface upset (typically less than 0.002 inches [0.05 mm] in titanium and nickel-base alloys; slightly higher in aluminum).

In the split-sleeve process conceived by The Boeing Company and developed as an integrated system by Fatigue Technology Inc. (FTI), expansion of the hole is accomplished by pulling a tapered mandrel, prefitted with a lubricant split sleeve, through the hole (see Fig. 1). The mandrel and sleeve are designed to generate a prescribed optimum amount of plastic deformation next to the hole, which in turn creates a state of

biaxial residual compressive stress in that area. In a typical application of this process, the peak compressive stress near the edge of the hole is almost equal to the compressive yield strength of the material. The compressive stresses are balanced by residual tensile stresses away from the hole with a magnitude of 10 to 25 percent of the tensile yield strength of the material (Fig. 2). Cold expanded hole fatigue lives generally range from 2 to 10 times the fatigue life of similar noncold expanded holes, as shown in the example of Fig. 3.

The disposable split sleeve reduces mandrel pull force, ensures controlled radial expansion, and allows one-sided processing. Cold expansion creates a slight permanent enlargement of the hole. The hole can then be either reamed to a specific final diameter or left in the as-expanded condition. Additional documentation on the process and its advantages in airframe applications can be found in an extensive body of literature dating back to the inception of the process in the late sixties (for example, see Phillips, 1974).

A significant variation of the process (known as FTI Force

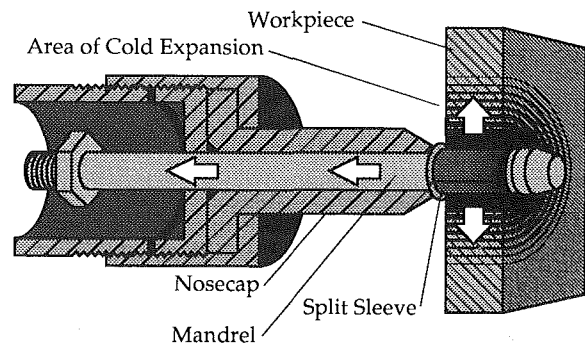


Fig. 1 The split-sleeve cold expansion process

Contributed by the International Gas Turbine Institute and presented at the 37th International Gas Turbine and Aeroengine Congress and Exposition, Cologne, Germany, June 1-4, 1992. Manuscript received by the International Gas Turbine Institute February 4, 1992. Paper No. 92-GT-77. Associate Technical Editor: L. S. Langston.

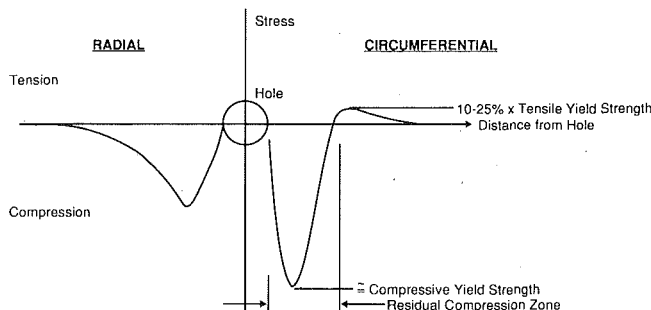


Fig. 2 Typical residual stress distributions at a cold expanded hole

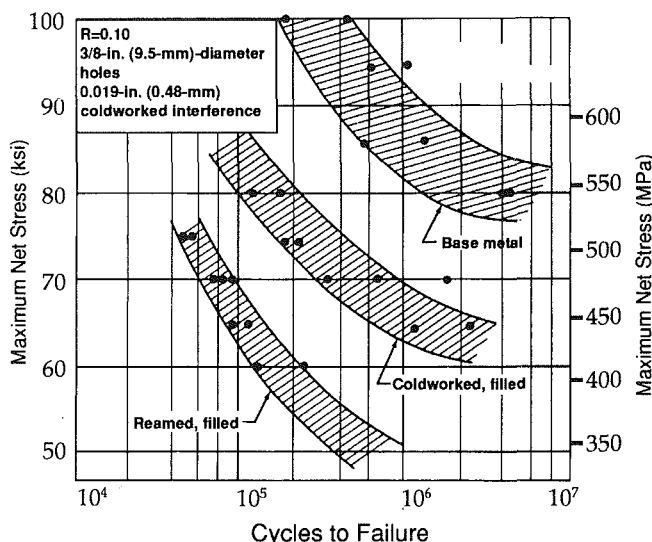


Fig. 3 Filled hole and base metal zero-load transfer constant amplitude fatigue scatter bands for Ti 6Al-4V, annealed (from Phillips, 1974)

Mate®) involves permanent installation of bushings or thick-walled inserts at high interference levels, typically as a hole repair procedure (Champoux and Landy, 1986). This is accomplished by replacing the split sleeve in the standard cold expansion process with the prelubricated bushing, as shown in Fig. 4. The initially clearance-fit bushing is locked in place by the mandrel-induced expansion and the resulting residual stresses. The bushing is usually reamed afterward to its final desired size, although it may also be expanded to size. The process can be performed with just one-sided access to the hole. An important benefit of this technique is that the material around the hole is simultaneously cold expanded as the bushing is installed, due to the high applied expansion level.

In the following sections, cold expansion (including the ForceMate system) is reviewed in the context of generic engine applications. Key related issues such as residual stresses, edge margins, high-temperature effects, and noncircular hole geometries are addressed in detail. Finally, two component case studies are used to illustrate the application of this technology for LCF life extension.

2 Cold Expansion Process Performance Assessment

Residual Stresses and LCF. Residual stresses are difficult to measure accurately (particularly in nonferrous alloys), in spite of recent advancements in X-ray diffraction and displacement and strain measurement techniques (Link and Sanford, 1990; Prevey, 1991). On the other hand, some analytical methods can be used effectively to model cold expansion in simple cases, and thus allow at least a fundamental under-

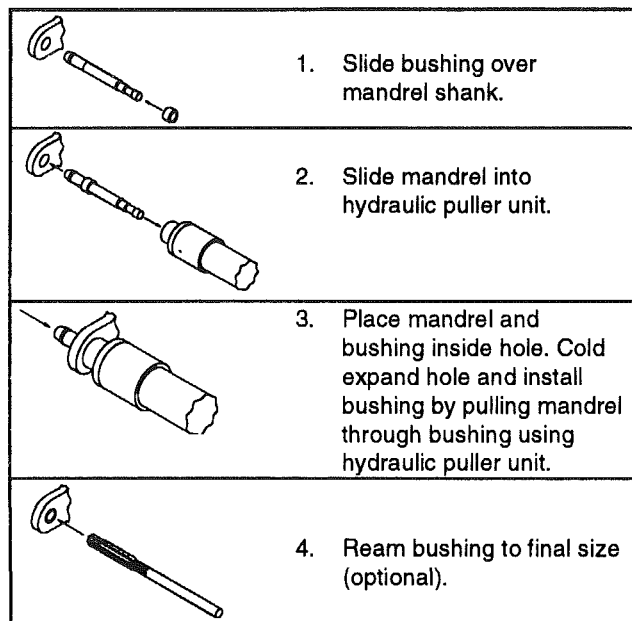


Fig. 4 Bushing cold expansion installation process (ForceMate)

standing of how the process contributes to fatigue life enhancement. An approach used successfully by the author involves representing the cold expanded hole by a two-dimensional axisymmetric finite element model with axial and radial loads applied sequentially, to simulate mandrel travel through the hole.

Figure 5 shows typical results obtained using this technique. In this example, the circumferential stresses were determined for a 0.461-in. (11.7-mm) diameter hole in a 2.25-in. (57.2-mm) wide, 0.145-in. (3.68-mm) thick Ti-6Al-2Sn-4Zr-6Mo (Ti-6246) plate, at an applied expansion of 3.9 percent. The ALGOR finite element analysis was performed using an elastic-plastic material model (Von Mises yield, linear isotropic hardening). ALGOR is a commercially available finite element analysis package with nonlinear analysis capabilities. Notice in Fig. 5 the stress variation from the mandrel entry side to the opposite plate surface.

The large compressive stress peaks near the hole in effect truncate the high stresses created by remotely applied loads. Figure 6 shows the results of Fig. 5 superimposed on elastic stresses resulting from a 100-ksi (690-MPa) remote gross tensile stress acting on the plate. The figure also shows the stress distribution for the same size noncoldworked (NCx) hole, from a two-dimensional plane stress nonlinear finite element model. The stress reduction near the hole lowers stress intensity factors and the effective stress ratio (R), which in turn act to retard crack initiation and growth. In a study performed by Pratt & Whitney for the U.S. Air Force (Fowler et al., 1981), LCF life for Ti-6246 specimens with cold expanded holes similar to the example just discussed showed a 77 percent improvement over NCx holes.

The high tensile stresses shown at the edge of the cold expanded hole in Fig. 6 are virtually inconsequential from a damage tolerance standpoint, because most common-size defects would bridge that region, and the stresses drop sharply beyond it. Notice also that linear superposition in this instance predicts combined stresses well in excess of the tensile yield strength of Ti-6246 (159 ksi [1095 MPa]). While, overall, this does not invalidate the previous discussion (this anomaly is restricted to a very small area), it does illustrate the limitations of this method when high applied loads are present.

Finally, by examining Fig. 3, it is evident that fatigue life improvement from cold expansion is smaller (though still significant) at high stress. This is a consequence of the diminishing

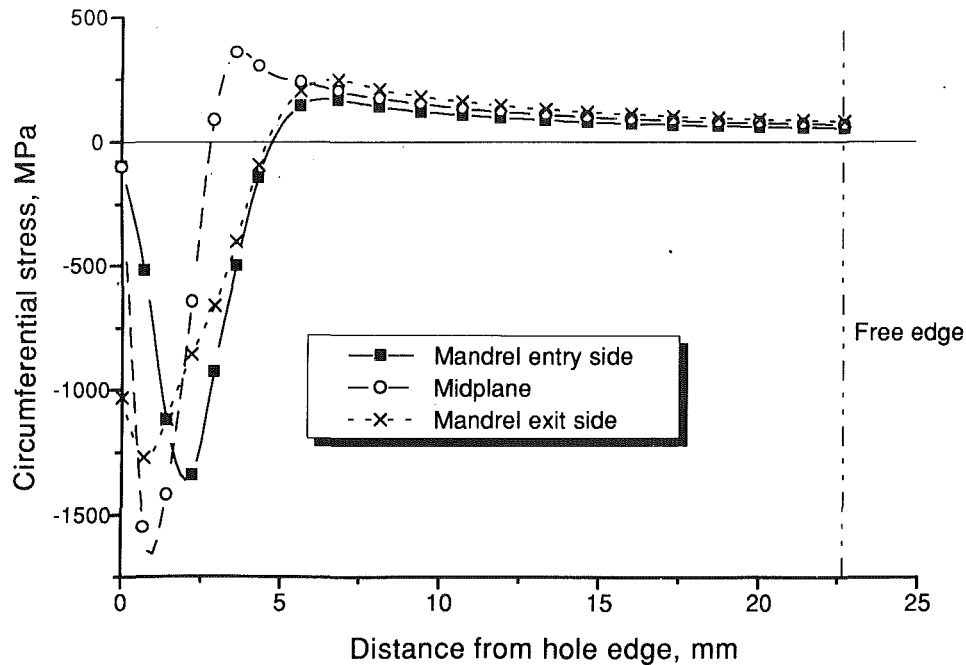


Fig. 5 Cold expansion residual stresses in Ti-6246

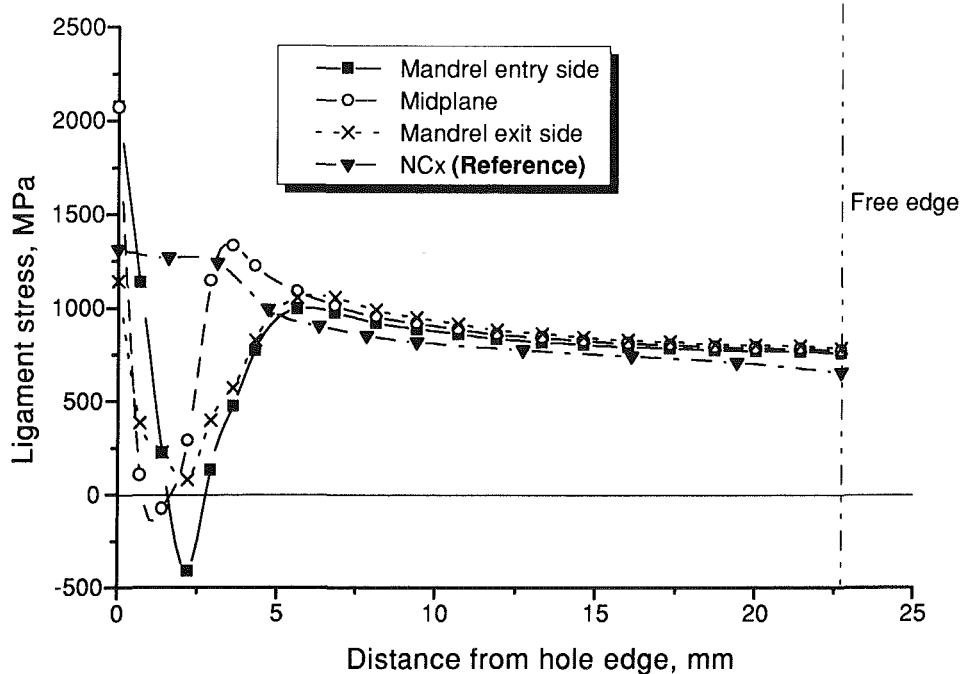


Fig. 6 Combined applied and residual stresses in Ti-6246

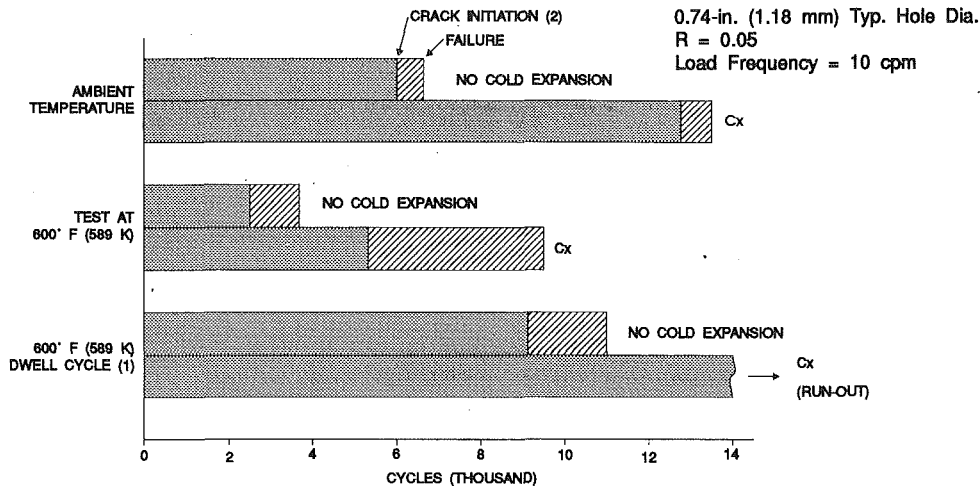
contribution of residual stresses to the effective stress ratio, as well as possible crack retardation in the NCx holes caused by large-scale yielding under high applied loads.

Cold Expansion in High-Temperature Components. Many of the engine components that might benefit from cold expanded holes are required to operate at high temperatures for extended periods. Stress relaxation, if present, could lead to sharply reduced residual stresses and hence, a decrease in LCF life improvement.

Tests on Ti-6Al-4V specimens in the solution treated and aged (STA) condition after a prolonged heat soak (1500 hours at 550°F [560 K]) have shown that even under those extreme conditions, the process results in considerable life improvement (Easterbrook, 1988). The specimens for these tests contained

3/8-in. (9.53-mm) nominal diameter open holes, some of which had been cold expanded. Half the specimens were tested at ambient temperature under constant-amplitude fatigue conditions, with a maximum net stress of 50 ksi (345 MPa) and $R=0.05$. The other half were tested at 550°F (560 K) under the same load parameters. Minimum cold expansion life improvement for the specimens tested at ambient temperature was about 400-to-1 (17,467,984 [run-out] versus 43,784 log average cycles to failure). For the high-temperature specimens, the minimum improvement was roughly 5-to-1 (260,717 versus 52,629 log average cycles to failure). A follow-on program is under way at FTI to investigate further temperature effects in cold expanded holes in titanium and nickel-base alloys.

Under the previously mentioned Pratt & Whitney study (Fowler et al., 1981), cold expanded and as-fabricated Ti-6246



Notes: (1) 120-second steps, cyclic (126 s period)
(2) Crack initiation to 0.031-in. (0.79 mm) crack

Fig. 7 High-temperature LCF test data for Ti-6246 (from Fowler et al., 1981)

specimens were tested at ambient temperature, 600°F (589 K), and under a combined LCF/temperature dwell cycle. In all instances, significant life improvement was obtained, as summarized in Fig. 7. The reason for the unexpected large increase in the number of cycles to failure for the combined LCF/dwell cycle has not been established.

Cold Expansion of Low-Edge Margin Holes. Bolt holes or lugs with short edge distances (i.e., where the hole diameter D and the edge distance e are of similar magnitude) are often found in engine components such as blade pin attachments. The general shape of the residual circumferential stress distribution around a cold expanded hole in Fig. 2 is typical of holes with relatively large edge distances. At edge margins (e/D) below 3.0, the balancing tensile stresses at the edge of the part can be significant. At first glance, this might imply that below a certain edge margin and under high applied loads, cold expansion could be deleterious, because of potential crack propagation from the free edge (especially if stress corrosion is a factor).

Extensive testing, however, discounts this hypothesis. For example, recent tests involving 7075-T6 aluminum specimens showed improved or comparable fatigue lives after cold expansion down to edge margins of 0.75. The specimens featured (0.780-in. (19.8-mm) open holes, and were subjected to maximum gross stresses of up to 20 ksi (138 MPa) at $R = 0.05$. At the lowest e/D value and maximum gross stresses above 15 ksi (103 MPa), fatigue life extension was almost negligible. At those stress levels, there is significant yielding of the ligament. In spite of that, all fatigue cracks (regardless of edge margin and cold expansion level) started at the hole, instead of the specimen edge. These results could be attributed to the stress concentration at the hole far exceeding any cold expansion-induced edge effects. Similar results have been reported elsewhere (Petrak and Stewart, 1976).

Results from two additional independent studies show that under load transfer conditions, e.g., in lugs, life improvement from cold expansion can be considerable at low edge margins, as discussed by Schijve et al (1978) and Impellizzeri and Rich (1976). Airframe spectrum fatigue loads were used in both studies; the latter dealt with fatigue crack growth only. Life improvements of 5-to-1 and 12-to-1 were obtained for 2024-T3 and 7075-T6 aluminum lugs at an edge margin of 0.83 by Schijve et al. Cold expanded Ti-6Al-4V (mill-annealed con-

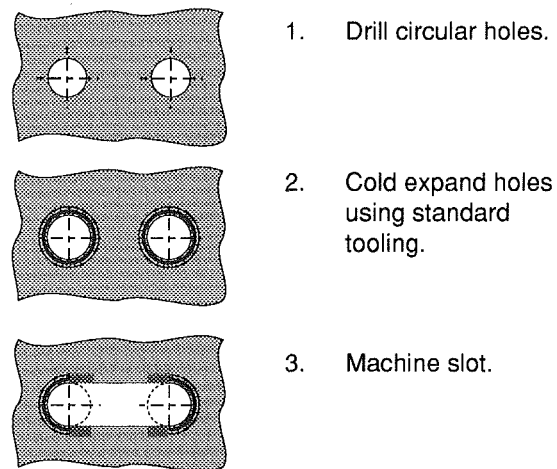


Fig. 8 Processing of noncircular holes—example (slot)

dition) lugs with an edge margin of 1.2 outperformed their non-cold expansion counterparts by better than 6-to-1 in Impellizzeri and Rich's investigation.

Noncircular Holes. In certain details such as compressor spool drain holes, use of an elongated (or "racetrack") hole geometry may be more efficient than a larger-diameter circular hole. In the case of a drain hole, for instance, the stress concentration may be reduced without changing hole surface area. Use of cold expansion can further extend the fatigue life of the noncircular detail. In the absence of final heat treatment or stress relief requirements, the best approach in production to process such a geometry is to delineate the desired contour with two or more circular holes and machine the final shape after cold expanding the holes, as shown in Fig. 8. A recent fatigue test program addressing slot and rectangular cutout geometries (Weiss, 1988) has shown this method to have considerable merit (Fig. 9).

When using this approach, care must be exercised to ensure that as little material as possible is removed in the area(s) where fatigue cracks are most likely to originate. In addition to potentially introducing critical flaws, excessive machining could wipe out the residual compression zone and thus severely curtail fatigue life improvement.

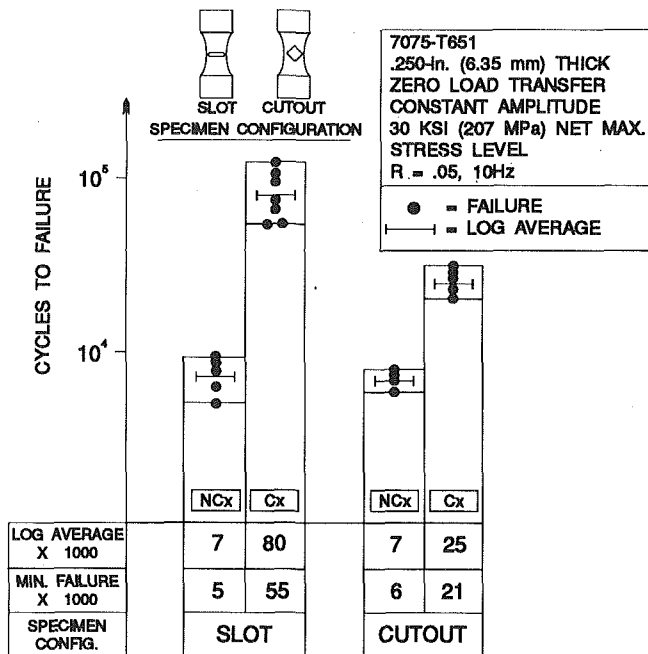


Fig. 9 Test results—fatigue life enhancement of noncircular structural details

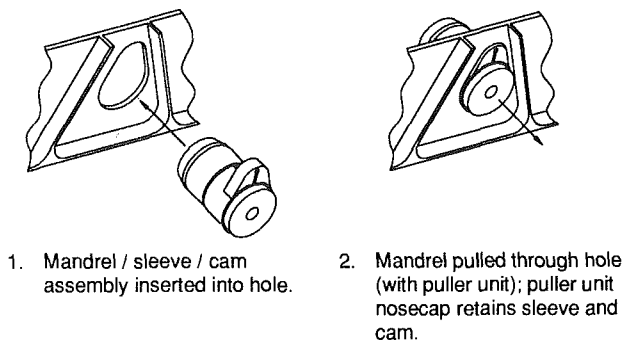


Fig. 10 Cold expansion of existing noncircular holes

An alternate technique particularly apt for rework of existing holes, involves an FTI-patented adapter and method, as illustrated in Fig. 10. This approach has been successfully demonstrated in cold expansion of F-16 aircraft bulkhead pear-shaped holes, but it is more limited than the previous method in terms of hole size and geometry (it is best suited for large oval holes).

High-Interference Bushing Placement by Cold Expansion. Bushings or cylindrical inserts are found in pinned joints where lubrication, fretting, and/or wear properties are of concern. Another important use is in rework applications, where it may be desirable to “return” a repaired hole to its original diameter (an example is discussed in detail later in this paper).

In the standard shrink-fit bushing installation process, the slightly oversize bushing is first immersed in a cryogenic fluid (usually liquid nitrogen) to temporarily reduce its outer diameter and enable it to fit inside the hole. As the bushing warms back up to ambient temperature, it locks in place with a moderate amount of diametrical interference (up to about 0.003 in. [0.076 mm]). This process has many drawbacks, including: (1) possible scoring and galling of the hole surface and bushing, (2) corrosion potential due to removal of outer surface coating on the bushing and water condensation (the water is entrapped after the bushing expands), and (3) the

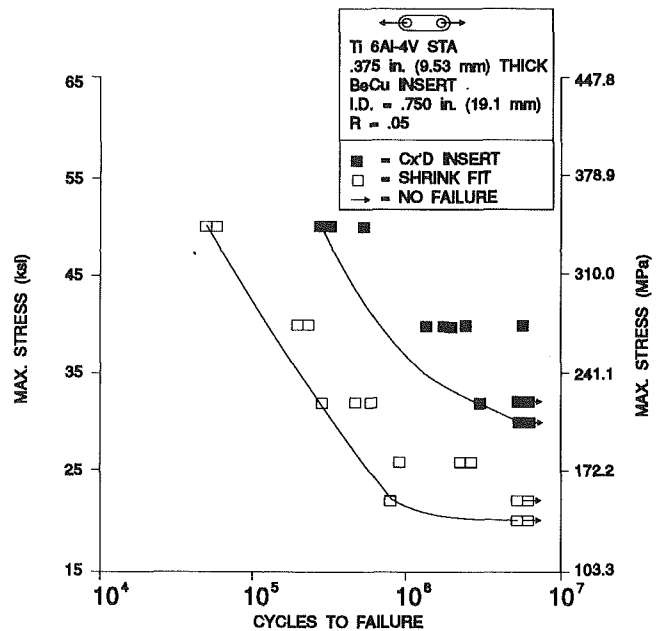


Fig. 11 Fatigue test data; shrink-fit versus cold expanded bushings in titanium lugs

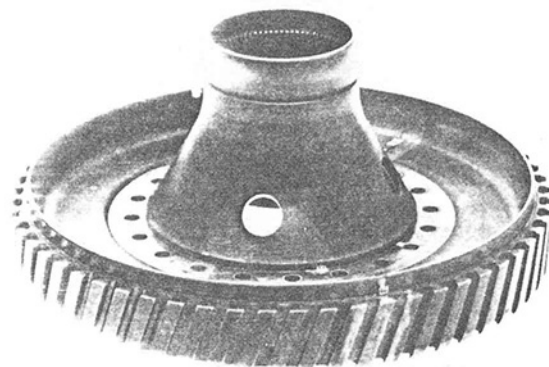


Fig. 12 F100 2nd-stage fan disk (from Fowler et al., 1981)

process must be performed in a very short time (this may be a problem in deep holes or in restricted access areas). These limitations place bounds on the amount of permanent interference at the hole, which in turn adversely affect fatigue life improvement and bushing retention.

The FTI bushing cold expansion installation process (Force-Mate) described earlier is not subject to these constraints (Boltstad and Easterbrook, 1988). Damage to the bushing outer surface and the hole is avoided by virtue of the initial clearance fit of the bushing. Corrosion protection is facilitated by selecting a galvanically compatible bushing or using a barrier coating on the bushing outer diameter. But the most significant advantage of this system over shrink-fit installations is the high interference levels (typically above 0.006 in. [0.150 mm]) obtainable, which result in significant fatigue life extension and high bushing retention forces. As with any other bushing installation method, in-service inspection of a hole processed in this manner is more difficult than with a clean hole, because starting cracks may be buried under the bushing and may consequently go undetected until they meet the plate surface(s). This, as well as the projected fatigue life improvement, must be factored in the design of the component.

In fatigue tests performed on Ti-6Al-4V STA lugs with beryllium-cooper bushings (Boltstad and Easterbrook, 1988),

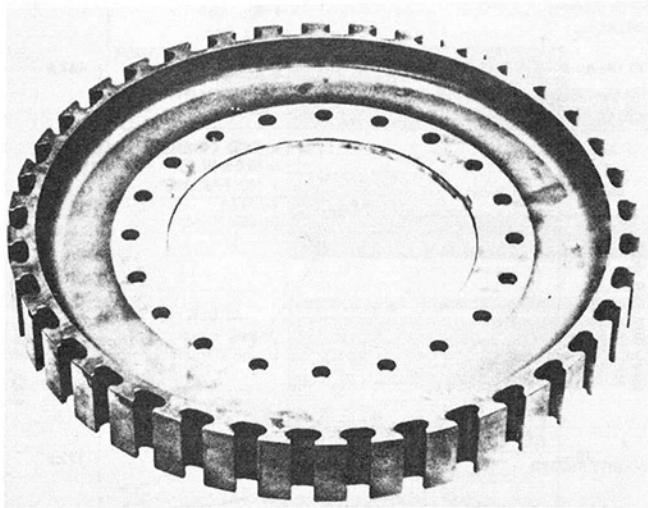


Fig. 13 Ferris wheel test article (from Fowler et al., 1981)

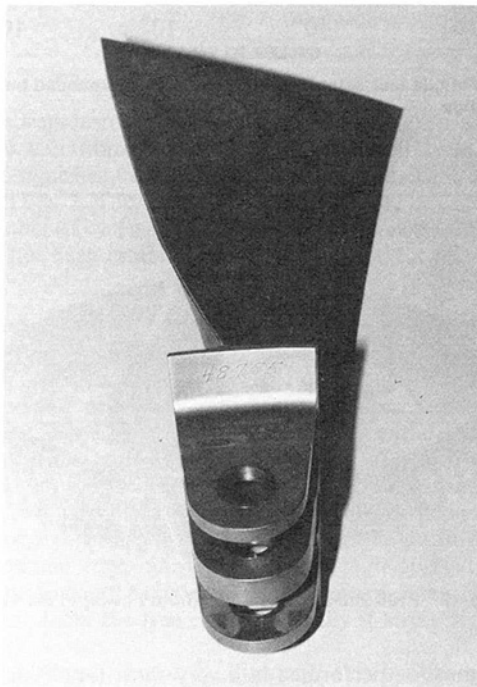


Fig. 14 TF-34 fan blade with cold expanded bushings

specimens with cold expanded bushings consistently outlasted shrink-fit bushed specimens (Fig. 11). Similar results have been reported on 7075-T651 aluminum lugs with a variety of bushing materials (Champoux and Landy, 1986).

3 Cold Expansion Processes in Engine Components

Pratt & Whitney F100 Second-Stage Fan Disk. In their laboratory study, Fowler et al. (1981) investigated the split-sleeve as a means for potentially extending the LCF life of the F100 engine's second-stage fan disk (Fig. 12). A set of 20 radially equidistant bolt holes had been found to be the LCF life-limiting elements in the component. The study involved coupon-level tests (some of which were discussed earlier in this paper) as well as tests on a full-size replica of the fan disk (Fig. 13), in a "ferris wheel" configuration. The full-size test article evaluation demonstrated a 44 percent increase in LCF life due to cold expansion of the bolt holes. The referenced study did not include an actual engine test of the modified fan disk.

The ferris wheel setup was designed to impart radial loads

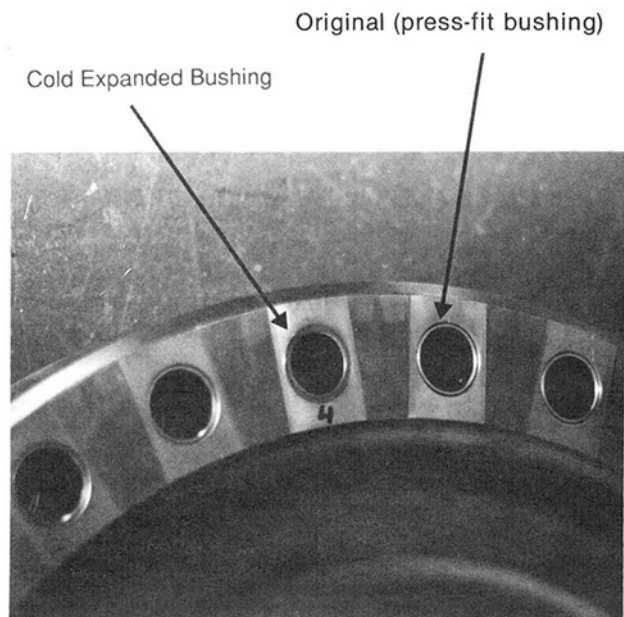


Fig. 15 TF-34 fan disk

cyclically on a rotor that simulated spin loads without overstressing the rim area. Loads were introduced by several hydraulically actuated pull bars connected to rim slots on the test part. A triangular wave pattern at a frequency of 2 cycles per minute (cpm) and R of 0.05 were used. The maximum loads were calculated to match in-service bolt hole strains. Two disks were tested, one with no holes cold expanded (baseline) and the other one with all 20 holes cold expanded. Crack initiation was tracked using acetate film replicas and by eddy-current nondestructive inspection (NDI). The baseline test article failed after 3830 cycles, with no signs of cracking at more than 2500 cycles (a result indicative of a very small critical flaw size and high crack propagation rate). On the other hand, its cold expanded bolt hole counterpart showed initial cracking at 3500 cycles, and failed at 5528 cycles.

GE TF-34-400 Fan Disk. Fan blades and disks have been identified by the U.S. Navy as engine life-limiting components in the TF-34-400 engine. The titanium blades are rated to 4300 hours (17,200 cycles), with their three-pronged lug attachment being the primary fatigue damage site. Other users of the TF-34 engine currently refurbish the blades by enlarging the lug hole diameter from 0.750 in. nominal to 0.770 in. (19.1 mm to 19.6 mm) and replacing the original Inconel 718 with a pin enlarged by flame spraying.

Under an ongoing contract from AeroStructures, Inc., FTI is investigating a potentially longer-lasting blade repair process using cold expanded bushings. This method keeps the original pin diameter and simultaneously cold expands the lugs. By allowing re-use of the pins, it also avoids some of the manufacturing and dimensional tolerance problems sometimes associated with flame spraying. To date, beryllium copper and titanium bushings have been successfully installed in the blades. One of the repaired blades is shown in Fig. 14.

The blade attachment holes on the titanium fan disk are also a concern from a durability standpoint. Present repairs call for hole enlargement and the installation of a press-fit Inconel 718 bushing. Tests presently performed on alternate Ti-6Al-4V cold expanded bushings (Fig. 15) show 20 percent higher required bushing push-out forces and at least 65 percent higher interference with the latter method. Although no comparative mechanical tests have been performed on the repaired disks, the push-out force and interference figures would indicate that significant LCF gains are likely with the cold expansion bushing installation process.

4 Conclusions

Several cold expansion processes currently in use in production and repair of aircraft structures also have a demonstrated potential for use in engine components designed to meet stringent LCF requirements. These processes include (but are not limited to) basic split-sleeve hole cold expansion and its related bushing placement process. With relatively few limitations, possible use of these systems spans high-temperature components, low edge margin conditions, and nonround holes and structural details. Bushing installation by cold expansion significantly outperforms the shrink-fit and press-fit processes in fatigue-critical applications as a result of the high amount of coldworking imparted to the component at the hole.

Acknowledgments

Work on the TF-34-400 fan blade repair was performed under AeroStructures, Inc., contract No. 90104, "TF-34 Fan Blade Repair." The contract is funded by the U.S. Navy.

References

- Bolstad, R. T., and Easterbrook, E. T., 1988, "Fatigue Life Enhancement of Titanium Lugs Due to the ForceMate Bushing Installation Process," FTI report No. 7288-1.
- Champoux, R. L., and Landy, M. A., 1986, "Fatigue Life Enhancement and High Interference Bushing Installation Using the ForceMate Bushing Installation Technique," Report No. STP 927, pp., 39-52.
- Easterbrook, E. T., 1987, "F-16 Peace Marble II Bulkhead Cx Evaluation," FTI report No. 7104-2.
- Easterbrook, E. T., 1988, "Effect of Elevated Temperature on Cold Expanded Titanium Holes," FTI report No. 7180-2.
- Fowler, R. L., Jr., et al., 1981, "Fan Disk Life Extension," Air Force Materials Laboratory Report No. AFWAL-TR-81-4017.
- Impellizzeri, L. F., and Rich, D. L., 1976, "Spectrum Fatigue Crack Growth in Lugs," ASTM STP 595, pp. 320-336.
- Link, R. E., and Sanford, R. J., 1990, "Residual Strains Surrounding Split-Sleeve Cold Expanded Holes in 7075-T651 Aluminum," *AIAA Journal of Aircraft*, Vol. 27, No. 7, pp. 599-604.
- Petrak, G. J., and Stewart, R. P., 1976, "Retardation of Cracks Emanating From Fastener Holes," *Engineering Fracture Mechanics*, Vol. 6, pp. 275-282.
- Phillips, J. L., 1974, "Sleeve Coldworking Fastener Holes," Vol. I, Air Force Materials Laboratory Report No. AFML-TR-74-10.
- Prevey, P. S., 1991, "Problems With Nondestructive Surface X-Ray Diffraction Residual Stress Measurement," *Proc. ASM 3rd Intl. Conf. on Practical Applications of Residual Stress Technology*, C. Ruud, ed., ASM International, pp. 47-54.
- Schijve, J., et al., 1978, "Flight Simulation Fatigue Tests on Lugs With Holes Expanded According to the Split Sleeve Cold Work Method," Netherlands National Aerospace Laboratory (NLR) report No. NLR TR 7813U.
- Weiss, M. R., 1988 "Fatigue Life Enhancement of Non-circular Structural Details," FTI report No. 6119-1A.

Multikilowatt Lasers in Manufacturing

C. M. Banas

United Technologies Industrial Lasers,
East Hartford, CT 06108

The fundamentals of laser beam interactions with materials are discussed briefly and unique laser processing capabilities are noted. Introduction of this processing capability to manufacturing is reviewed. Typical high-volume production application requirements are identified and representative performance and production experience are described. Specific multikilowatt laser welding, piercing, and hardfacing applications in aerospace production are described. The evolution of production processes is discussed against the background of required processing capability. Also discussed are the unique laser processing capabilities that resulted in selection of the laser for production. Production experience is reviewed and cost saving factors are noted.

Introduction

Three decades have elapsed since the first successful operation of a laser. During that period, a myriad of systems and applications have been developed, and the word "laser" has become synonymous with high technology. Despite this extensive development, however, only two lasers (carbon dioxide and YAG) currently demonstrate sufficient average power and efficiency for significant application to manufacturing.

Both YAG and carbon dioxide laser systems are used in a wide range of drilling, cutting, and small-scale welding applications at power levels up to 2 kW. Thousands of laser cutting systems are in cost-effective production use throughout the world.

Beyond 2 kW, only the carbon dioxide laser is currently available in an industrialized form. Principal applications for higher power systems are in high-speed welding; however, some cost-effective applications in cutting and surface treating exist. Although production installations at 5 kW and above number less than 200, it is anticipated that significant growth will occur in this area within the next few years. The focus of this paper is on this high-power (≥ 5 kW) segment of industrial laser applications.

Background

Fundamental Characteristics. The multikilowatt industrial carbon dioxide laser possesses a virtually unlimited power intensity capability, which makes it a highly versatile thermal processing tool [1-4]. The significance of intensity in materials processing is illustrated in the composite spectrum shown in Fig. 1 [5]. It is noted that the product of the ordinate and abscissa of this plot represents process specific energy. It is further noted that power densities of the order of 10^6 W/cm²

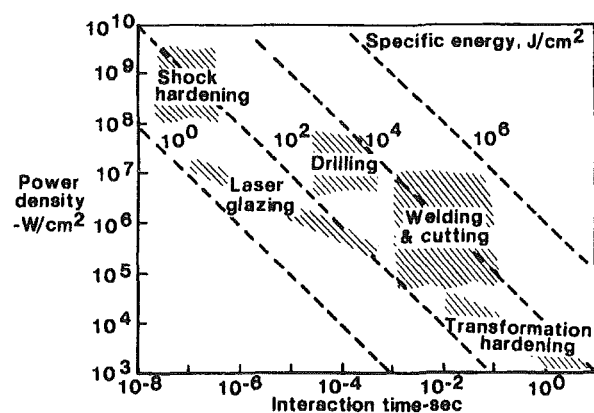


Fig. 1 Laser processing spectrum

and above can only be conveniently attained with lasers and electron beams.

Further physical insight into the role of power intensity in materials processing may be obtained by relating beam power intensity to the temperature of an equivalent thermal source (thermal source brightness temperature required to yield the same power intensity) by means of the Stefan-Boltzmann blackbody radiation equation

$$I = \sigma T^4 \quad (1)$$

in which I is the intensity of radiation, σ is the Stefan-Boltzmann radiation constant, and T is the absolute temperature.

From Eq. (1), we find that an intensity of a million watts per square centimeter (associated with the onset of keyhole welding, discussed below) corresponds to a thermal source temperature of 21,600 K!

Intensities generally suited for surface treating applications (Fig. 1) are substantially lower than those for welding and cutting. Such lower power concentrations represent relatively low equivalent temperatures and are readily attainable with more conventional sources such as plasma arc, oxyacetylene

Contributed by the International Gas and Turbine Institute and presented at the 36th International Gas Turbine and Aeroengine Congress and Exposition, Orlando, Florida, June 3-6, 1991. Manuscript received at ASME Headquarters March 4, 1991. Paper No. 91-GT-233. Associate Technical Editor: L. A. Riekert.

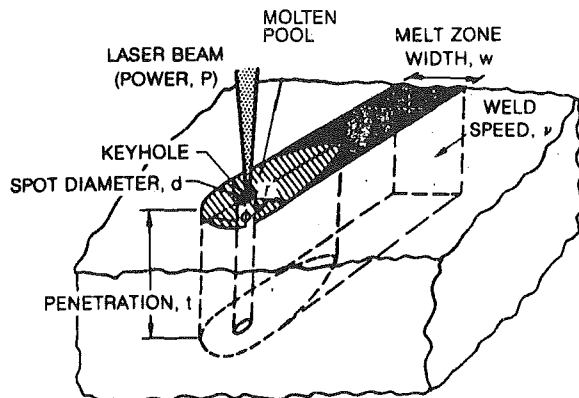


Fig. 2 Keyhole welding characteristics

torch, and/or induction heating devices. For this reason, despite initial laser community optimism, it is much more difficult to justify laser applications in this area. This is not to say that the laser cannot perform many surface treating tasks effectively; it simply calls attention to the fact that many of these tasks can be accomplished with less sophisticated, and less expensive, equipment.

Technically and economically viable laser surface processing can occur under special circumstances such as: (1) Treatment must be restricted to a precisely defined and highly localized area, e.g., the wear surface of a gear tooth, (2) thermal energy input must be minimized in order to reduce part distortion, (3) controlled depth alloying or melting is desired, (4) controlled depth densification of, or purification of, a previously deposited coating is required, etc.

Keyhole Welding. It has been noted above that "keyhole" welding occurs at incident beam power intensities of the order of a million watts per square centimeter and above. The nature of this process is illustrated in Fig. 2. The laser beam is focused into a small spot on the surface of a material such that the local rate of energy delivery exceeds the thermal diffusion capability of the metal; essentially instantaneous vaporization occurs. With adequate incident power, the vapor column extends through the thickness of the material. The vapor pressure offsets the hydrodynamic forces of the liquid metal surrounding it. With appropriate relative motion between the incident beam and the workpiece, the vapor column (keyhole) is dynamically stable. Melting takes place at the leading edge of the interaction zone with resultant liquid metal flow to the rear. Solidification occurs in a characteristic chevron pattern signifying solidification isotherms at the rear of the molten material.

In this welding mode, energy is deposited not only at the material surface, but also throughout the material depth. Energy deposition can be represented by an unsteady cylindrical heat source model and can be visualized in terms of a hot wire being drawn through a block of ice.

Since energy deposition occurs throughout the material depth, high depth-to-width ratio weld beads (Fig. 3) can be established compared to the roughly hemispherical weld beads formed by conduction limited weld processes. Detailed discussion of this process is presented in [6, 7].

Processing Energy Requirements. An initial approximation of the energy requirements for laser processing may be obtained from the first law of thermodynamics. This is illustrated in Fig. 4 for welding in which h is the material thickness (weld penetration), w is the weld width, V is the welding speed, t is the interaction time, E is the energy required to fuse the volume of material identified in the figure, C_p is the material specific heat, ρ is the material density, $T_m - T_0$ is the difference between melting and initial temperature, and the last factor

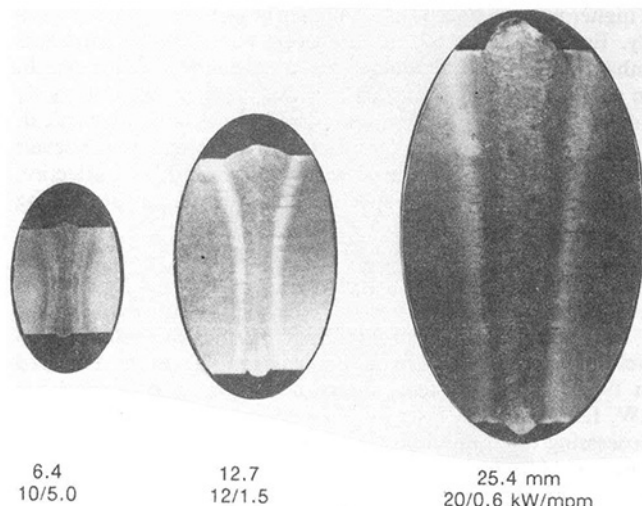
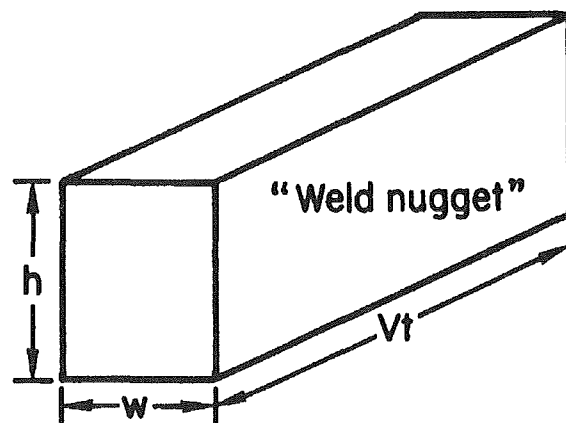


Fig. 3 Laser keyhole welds



$$E = C_p \left[(\rho) (h \times w \times Vt) \right] \left[T_m - T_0 + \frac{H_f}{C_p} \right] = C_p M \Delta T_m$$

Fig. 4 Processing energy balance

represents the temperature equivalence of the heat of fusion. This equation yields the ideal energy requirement, i.e., without any losses due to reflection, radiation, or thermal diffusion into the surrounding material.

Representative thermal process efficiencies obtained by direct calorimetric measurements of welds formed at 5 kW and 2 m/min are shown in Fig. 5 for a range of materials. Absorption is defined as the incident energy less that which is reflected and the melting efficiency represents the fraction of the absorbed energy which effects fusion (the remainder is lost due to thermal diffusion into the surrounding material). Overall process efficiency is the product of these two factors; energy requirements are, therefore, predicted by dividing the energy estimated from Fig. 4 by this product.

Simple consideration of the energy requirements leads to the obvious conclusion that increase in penetration, weld width, and/or speed necessitate increase in laser power. Exact details of the beam interaction with the material, however, hinge on the optical quality of the beam. This, in turn, is characterized by the mode, energy distribution and characteristic beam divergence. In-depth treatment of factors influencing beam focusability may be found in [8].

The consequence of the above is that a lower power laser of excellent optical quality may provide deeper penetration or

a higher welding speed than a higher power one of lesser quality. Energy factors tell us, however, that such performance enhancement can only come with a reduction of weld width. In some instances, this may not only be acceptable but highly desirable; in other applications it may be totally impractical. Claims of "equivalence" of lasers at different power levels should, therefore, be viewed with caution and laser selection should be based upon the specific requirements for the welding process.

Applications

Early History. An early attempt at automotive sheet metal welding is represented by a five axis gantry system delivered in 1973 [9]. This system, shown in Fig. 6, incorporated a 6 kW, fast-axial-flow laser and demonstrated the capability for processing one underbody assembly per minute at a welding speed of 11 m/min. The system was not reduced to production practice because adequate fitup could not be achieved between the mating parts. It is interesting that today, some eighteen years later, part fixturing and fitup remain as the main technical problems for three-dimensional auto body welding.

One of the first (Sept. 1974) high volume production applications of an industrial laser was in the surface treatment

of automotive steering components [10]. In this application, the laser was used to produce hardened wear tracks to improve component durability. Although the initial production application was quite successful, further industrial use of this process developed very slowly. One reason for this has been the significant improvement in the capability of more conventional surface treating equipment, e.g., high frequency induction. One application involving several 5 kW laser systems did evolve, however [11]. This application involved surface transformation hardening of cast iron cylinders of diesel locomotive engines.

Production Welding. Principal application of the multi-kilowatt carbon dioxide laser in the automotive industry has been in the welding of components [12]. These applications have been initially in Italy and the United States. Developments in other European countries have proceeded more slowly and the Japanese auto industry has continued its principal reliance on electron beams for such applications; rapid changes are presently under way, however.

A typical component weld requires a penetration of the order of 5.0 mm, is approximately 375 mm in length, and requires a floor-to-floor processing time of less than ten seconds. If we assume that the required welding time is 5 seconds, we find that the required processing power (Fig. 7) is 6 kW, or more, for a single weld pass. This is adequate for assemblies involving only low carbon steels, which are readily welded. In others, however, one or both of the mating elements may be formed from alloy steels with higher equivalent carbon content. These require careful process development, which may include pre-heat and/or postheat, compatible filler material addition, a tempering weld overpass, etc. In many such applications, laser processing is justified not only by the high processing speed, but by the low specific energy input and resultant minimal thermal distortion of the components.

Multikilowatt lasers have performed admirably in high volume production and have established an enviable durability record. Total production time for machines rated at 5 kW, or above, is measured in millions of hours with individual machines in three-shift service for more than 50,000 hours.

Aerospace Applications

Drilling. Since the first laser production application of drilling diamond wire drawing dies in the mid-60s drilling has

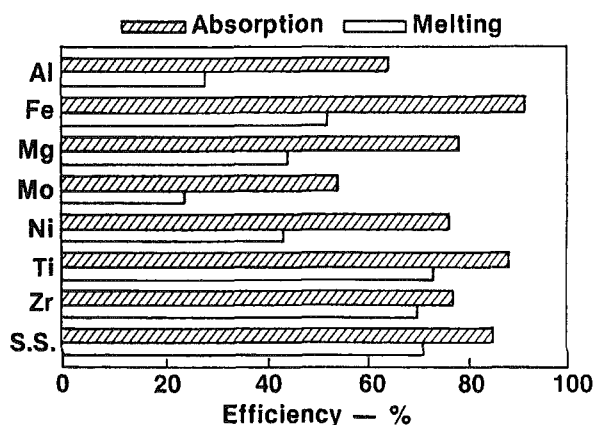


Fig. 5 Welding processing efficiency

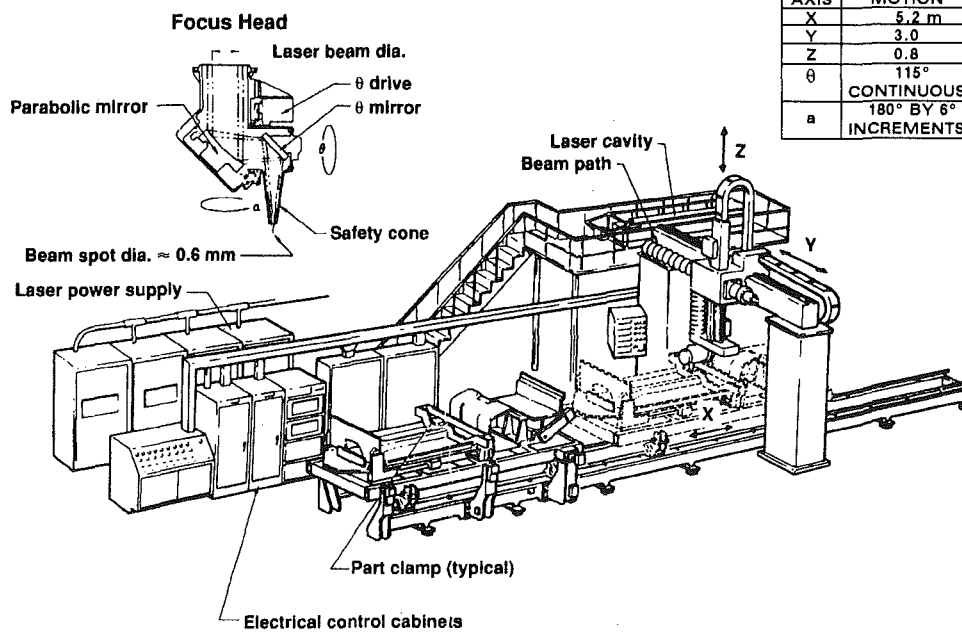


Fig. 6 Auto underbody welding system

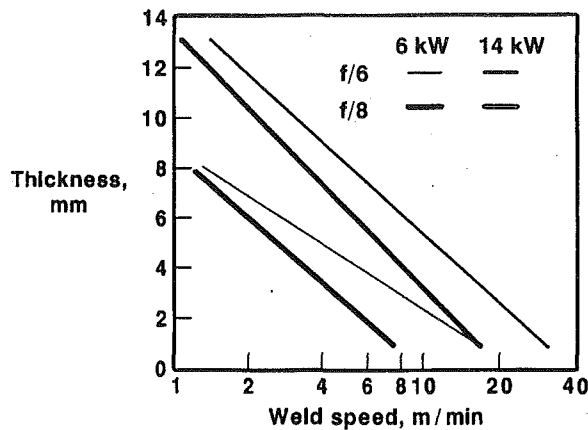


Fig. 7 Multikilowatt laser welding performance

been accomplished by relatively low average power pulsed laser systems. Pulsed YAG systems have found important application in drilling of cooling holes in jet engine turbine vanes. Millions of holes have been cost effectively drilled by the major jet engine manufacturers with pulsed YAG systems having an average output power of 500 W or less. Small diameter (of the order of 0.5 mm) holes are formed with "percussion" drilling in which rapid vaporization of a portion of the molten material results in expulsion of the remainder. Larger diameter holes are formed by trepanning.

Another potential drilling application was formation of cooling holes in a rolled ring jet engine combustor liner as shown in Figs. 8 and 9. As many as 10,000 holes, with typical dimensions of 2 mm diameter and a nominal depth of 3 mm, were required in a single liner. Process requirements were complicated by the tapering section through which the hole passes and the presence of a secondary surface at the base of the hole, which must not be damaged by the beam. Excellent holes were YAG laser trepanned in such combustor liners in 20–30 seconds. Total drilling time for a single liner was, therefore, of the order of 60–90 hours.

Multikilowatt laser piercing was explored as a means for significantly reducing manufacturing time for formation of the required holes. Three possible piercing techniques were examined: (1) use of a focused spot diameter yielding the desired hole diameter in a single exposure, (2) trepanning with a highly focused spot and (3) piercing with a rapidly rotating spot simulating a ring focus. Procedure 3 may be compared to the action of a hole saw in contrast to the circumferential cutting motion in 2.

Results of experimental investigations indicated that approach 1 exhibited difficulty in reproducing hole diameter and approach 2 yielded irregularities in hole shape. Approach 3, which involved slightly off-axis rotation of the focusing mirror, was selected for production. Damage to the material behind the hole was prevented by use of a rotating copper shield. Beam blocking material typically used in turbine vane drilling with YAG systems was ineffective for the multikilowatt, carbon dioxide laser beam. Without either a copper (or tungsten) shield underneath, complete penetration of the lower section occurred under conditions established for effective piercing.

A 6 kW carbon dioxide laser system was selected for production. With this unit, single hole piercing times of 0.2 seconds were easily achieved. With allowance for indexing, this yielded a production capability of two holes per second, which has been demonstrated in more than six years of operation. Piercing time for a complete combustor liner was thereby decreased to the order of 2–3 hours; the 30:1 decrease in required manufacturing time has resulted in a system payback time of the order of 4 months! To this writer's knowledge, this is the only

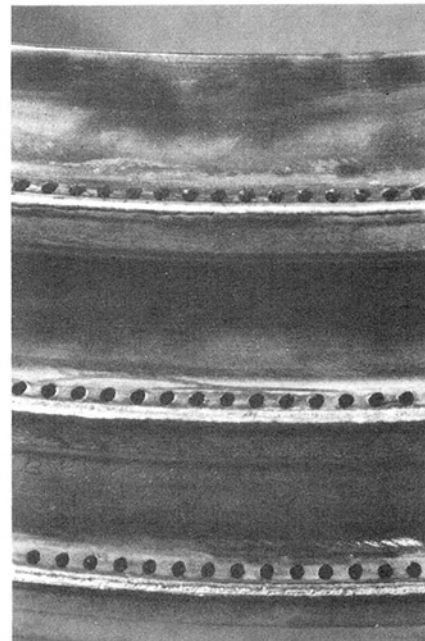


Fig. 8 Combustor liner element

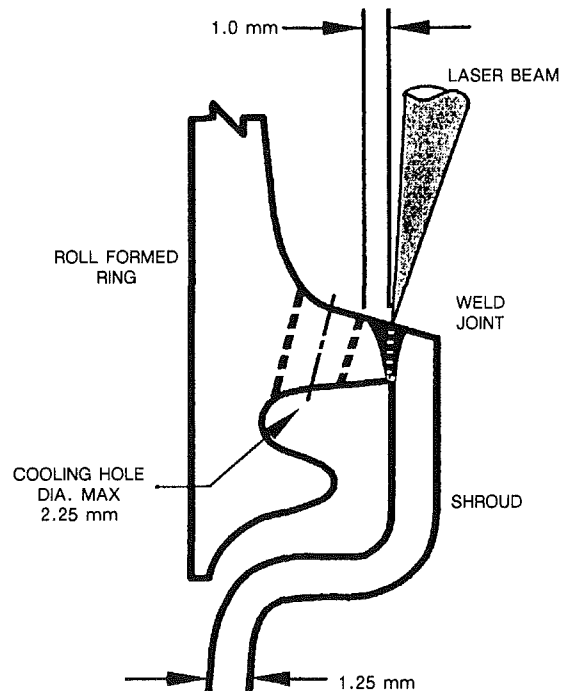


Fig. 9 Combustor liner cross section

current multikilowatt laser piercing (drilling) application in production.

Turbine Blade Notch Hardfacing. Another successful aerospace production application has been laser hardfacing of the outer shroud notch in jet engine turbine blades. Wear due to relative motion between adjacent blade shroud segments results in reduced engine performance. To minimize wear, a cobalt base hardfacing alloy is deposited on the mating surfaces (Fig. 10). Hardfacing was typically accomplished by manual gas tungsten arc; this required highly skilled personnel and was subject to significant rework requirements.

The multikilowatt carbon dioxide laser was explored as a means for more precise energy delivery and control of the notch shroud hardfacing process. Significant process difficulties

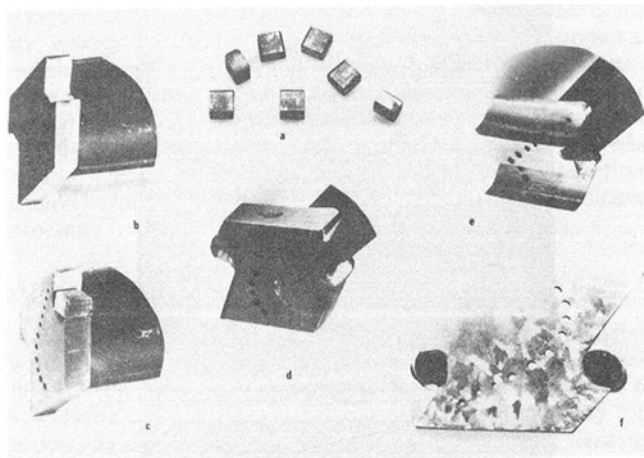


Fig. 10 Blade notch hardfacing sequence

stemmed from the thermal cracking sensitivity of the cast nickel base blade materials used, from requirements of minimal dilution of the hardfacing deposit with base material, and from the specific geometry of the shroud notch.

Preplaced hardfacing powder, dynamic powder addition, and use of a preplaced chip of hardfacing material were explored as means for the laser hardfacing process. A preplaced chip of hardfacing material of appropriate size was selected for initial production. This technique offered the advantages of: (1) precise control of the quantity of the deposit, (2) reduced possibility of hardfacing material contamination in comparison with powder, and (3) minimization of substrate melting resulting in reduced tendency for cracking and dilution. Reasons for the latter were ascertained from high-speed (200 to 5000 frames per second) motion pictures of the hardfacing process. These showed that essentially all of the laser energy at the onset of the process was absorbed by the hardfacing chip. Chip melting occurred prior to any significant heating of the substrate material. On liquefaction of the surface of the substrate, rapid wetting and attachment occurred with desirable results as noted. Typical processing time for an individual notch is 6–8 seconds for the laser process compared to 2–3 minutes for its manual counterpart.

Nearly a million blades have been processed by this means with a rework requirement of less than 1 percent. The success of this program has supported extension of the laser process to a wider range of blades. Widely differing geometry in these blades has prompted re-examination of the dynamic powder hardfacing procedure as a means for facilitating process automation.

Combustor Liner Welding. A third successful multikilowatt laser production aerospace application involves welding of a rolled ring combustor liner (Figs. 8 and 9). In this application, the high-power laser is an extremely effective means for attainment of the required weld characteristics and production speed.

The severe requirements of the welds for this assembly are apparent on examination of the joint details shown in Fig. 9. The weld is formed between the top surface of a rolled ring of 7.5 mm thickness and a thin sheet material shroud. Full weld penetration of the 1.8 mm interface is required with essentially no underbead spatter (a principal disadvantage for electron beam welding of this component). Further, the weld bead must be sufficiently narrow to preclude melt rollover of the outer corner of the shroud (1.25 mm from the weld centerline) and to prevent melting into the previously laser pierced cooling holes (having a minimum possible spacing of 1 mm

from the weld centerline). Further, due to line-of-sight interference of the adjacent components in the assembly, the weld must be formed with the laser beam axis at a slight angle to the weld seam; process conditions were developed to place the intersection point of the beam and interface centerlines at approximately the midpoint of the penetration. With the previously noted constraints on weld width, this necessitated precise location and control of weld bead geometry to avoid a crack starting lack of fusion at the weld root. On a positive note, the liner material is Hastelloy-X, which is readily laser weldable.

The production system used for this welding application encompasses a 12 kW, high-optical-quality, carbon-dioxide laser system with beam switching to two self-contained five-axis tooling stations, each provided with a dedicated CNC. Two stations were implemented to make more effective use of the laser in view of the relatively long setup time for each weld. Since the segments are not exactly circular, active seam tracking is employed to ensure precise placement of the weld beam. Seam tracking is accomplished with a mechanical follower and an LVDT. Signals from the LVDT are conditioned and introduced to the CNC, which has a software program enabling real time corrective motion on two axes of the tooling. Tracking accuracy is within ± 0.05 mm at a welding speed of 7.5 m/min. Two weld schedules have been developed; at 4.5 kW a welding speed of 2.5 m/min is achieved and at 8 kW the welding speed is 6.25 m/min. Single seam welding times for a nominal 1-m-dia. segment are 74 and 30 seconds, respectively. Completed welds are subjected to 100 percent ultrasonic inspection; weld repair, if required, is accomplished by 360 deg rewelding at the same parameters as noted above. This system has been in production operation for more than five years and has demonstrated reliable, cost-effective performance.

Concluding Remarks

The multikilowatt, carbon-dioxide industrial laser has established itself as an effective tool for a variety of joining, surface treating and material removal tasks. Durable, high-uptime performance has been demonstrated and short-term payback has been achieved in appropriate applications. Interactive development among laser, design, and production personnel should lead to expanded utilization of this excitation processing capability.

References

- 1 Belforte, D., and Levitt, M., eds., *The Industrial Laser Handbook*, Pennwell Books, Tulsa, OK, 1986 ed.
- 2 Metzbow, E. A., ed., *Source Book on Applications of the Laser in Metalworking*, ASM, Metals Park, OH 1981.
- 3 Bass, M., ed., *Laser Materials Processing*, North Holland Publishing, Amsterdam, The Netherlands, 1983.
- 4 Arata, Y., *Electron and Laser Beam Technology Development and Use in Materials Processing*, ASM International, Metals Park, OH 1986.
- 5 Breinan, E. M., Kear, B. H., and Banas, C. M., "Processing Materials With Lasers," *Physics Today*, Nov. 1976.
- 6 Tong, H., and Giedt, W. H., "Depth of Penetration During Electron Beam Welding," *ASME Journal of Heat Transfer*, Vol. 93, May 1971, pp. 155–163.
- 7 Klemens, P. G., *Journal of Applied Physics*, Vol. 47, No. 5, May 1976.
- 8 Siegman, A. E., *Lasers*, University Science Books, Mill Valley, CA 1986.
- 9 Ball, W. C., and Banas, C. M., "Welding With a High-Power Carbon Dioxide Laser," SAE Paper No. 740863, Oct. 1974.
- 10 Miller, J. E., and Wineman, J. A., "Laser Hardening at Saginaw Steering Gear," *Metal Progress*, Vol. 111, No. 5, 1977, pp. 38–43.
- 11 Strong, E. J., "How General Motors Decided to Heat Treat With Lasers on the Assembly Line," *Laser Focus*, Vol. 19, No. 11, Nov. 1983.
- 12 Ogle, M., and Gustaferr, D., "Why Laser?" presented at the International Conference on Laser Processing, Welding Institute, Cambridge, United Kingdom, Feb.–Mar. 1989.
- 13 Duhamel, R. F., Banas, C. M., and Kosenski, R. L., "Production Laser Hardfacing of Jet Engine Turbine Blades," *Proceedings of the SPIE*, P. K. Cheo, ed., Vol. 621, 1986, pp. 31–39.

Application of Flash Welding to a Titanium Aluminide Alloy—Microstructural Evaluations

J. E. Gould

T. V. Stotler

Edison Welding Institute,
Columbus, OH 43212

Alpha-two titanium aluminides represent strong candidates for replacing many conventional titanium and nickel-base superalloys for intermediate temperature applications. One potential application of these alloys is turbine engine rings. Nonrotating rings of this type are typically manufactured by flash butt welding. The performance of welds in this alloy is known to be strongly affected by the weld microstructure. Welding processes that result in very slow cooling rates yield relatively coarse Widmanstätten-type microstructure(s), which generally yields acceptable weld performance. Processes that result in intermediate cooling rates, however, result in acicular alpha-two martensite microstructures. These microstructures have very little ductility and lead to reduced weld performance. Finally, for processes where the cooling rate is very rapid, the weld microstructure is a retained ordered beta phase, which apparently results in improved weld properties. In this paper, microstructures of some representative flash welds on Ti-14Al-21Nb were examined. In addition, flash welding conditions were varied to examine the effects of initial die opening and upset distance. In general, it appears that all the welds included in this study contain the ordered HCP martensite in the weld zone. However, both the scale of the microstructure and the weld hardness seem to depend heavily on the particular set of processing conditions used. These results were then used to estimate the relative cooling rates in these welds, and understand the effects of these processing conditions on the developing microstructures.

Introduction

Alpha-two titanium aluminide alloys are now strong candidate materials for replacing conventional titanium alloys and some nickel-base alloys for intermediate temperature engine applications. Advantages of these alloys include higher service temperatures, improved creep resistance, higher moduli, and lower densities as compared to conventional titanium alloys (Lipsitt, 1985). Presently, these alloys are under consideration for many intermediate temperature applications in the engine. Among these applications are nonrotating ring components. Nonrotating rings used in jet engines are typically manufactured by flash-butt welding. However, little or no information is available on the flash butt weldability of such alloys.

In fact, only limited work has been done considering joining these alloys with any joining process. Available work has been restricted to arc and laser welding of these materials (Baeslack et al., 1988, 1989). These works have, however, shown that when these alloys are heated above the beta-transus temperature, the mode of beta decomposition is critical to joint performance. It has been established that welding processes that result in very slow cooling rates ($< 10^\circ\text{C/s}$) yield alpha-two + beta Widmanstätten microstructure results, showing both reasonably low hardness (< 400 KHN) and appreciable ductility

(> 1 percent). However, as the cooling rate increases, the microstructure shows both a reduced level of the beta phase and a progressively more acicular character. As the microstructure becomes more acicular, the hardness appears to increase and the apparent ductility falls. Finally, for very rapid cooling rates (approximately 2000°C/s) it appears that the microstructure is a retained ordered beta phase (Baeslack et al., 1988, 1989; Strychor et al., 1988; Strychor and Williams, 1982). This structure appears to result in lower hardnesses in formed joints (< 350 KHN) and a consequent increase in weld ductility.

This paper reports on work done to characterize microstructures in flash butt welds made on a representative titanium-aluminide alloy. This is an extension of previous work (Stotler et al., 1990) examining relationships between flash weld processing conditions and some representative performance characteristics of the joints. In this work, microstructures of some of these welds were examined in detail. Variations in microstructure associated with two of the process conditions shown in the previous work to have the strongest effect on weld performance (initial die opening and upset distance) are studied. The observed microstructures are used to understand the previously observed mechanical properties results, as well as estimate approximate relative cooling rates in these flash welds.

Experimental

The material used in this program was a Ti-14Al-21Nb alloy,

Contributed by the International Gas Turbine Institute and presented at the 36th International Gas Turbine and Aeroengine Congress and Exposition, Orlando, Florida, June 3-6, 1991. Manuscript received at ASME Headquarters March 4, 1991. Paper No. 91-GT-231. Associate Technical Editor: L. A. Riekert.

Table 1 Nominal composition for the Ti-14Al-21Nb Alloy

Element	Wt. %	Element	Wt. %
Aluminum	13.5-14.5	Carbon	0.10 max.
Niobium	20.0-22.0	Nitrogen	0.05 max.
Iron	0.10 max.	Total Other	0.10 max.
Oxygen	0.08 max.	Titanium	Balance

Table 2 Flashing conditions used in this study

Flashing Distance	6.4 mm
Flashing Velocity	5.4 m/s
Flashing Acceleration	0.0 mm/s ²
Upset Distances	2.5 and 4.6 mm
Initial Die Openings	36 and 42 mm
Flashing Currents	5.7-20.4 kA

Table 3 Process data for the welds used in this study

Sample No.	Recorded Current (kA)	Initial Die Opening (mm)	Upset Distance (mm)
3	11.3	36	2.5
4	--	36	2.5
8	--	42	2.5
9	5.7	42	2.5
13	20.4	36	4.6
14	20.0	36	4.6

supplied as 25-mm-wide by 75-mm-long by 5-mm-thick coupons. The representative chemical composition for this alloy is presented in Table 1.

Flash welding was done on a Precision 200 kVA cam-driven flash-butt welding machine. Flashing conditions are presented in Table 2. In these trials, it was found that by using the flashing velocity given in Table 3 butting occurred during the early stages of flashing even at the highest tap setting. As such, in order to facilitate the initiation of flashing, the samples were beveled on the sides with a 45-deg angle. In this way, the initial contact surface for flashing had a height of only 1.6 mm.

Based on the previous work (Stotler et al., 1990) the effects of two flash welding variables were examined in this study. These include the initial die opening and the upset distance. Initial die opening is defined as the initial spacing of the platens prior to flashing, and upset distance is defined as the distance the platens advance following the termination of flashing. In this study, welds were first made at a nominal set of process conditions. Then, two additional sets of welds were made, one with an increased initial die opening and the other with increased upset distance. Processing conditions for each weld is given in Table 3.

At each set of processing conditions, two welds were made. The first weld of each set had the flash removed and was used for mechanical testing. The second was used for metallographic examination. Mechanical testing was done on a Southwark tensile testing machine, with an extension rate of 0.13 mm/s. Samples for metallographic examination were sectioned along the weld axis, and mounted for examination. Welds were pol-

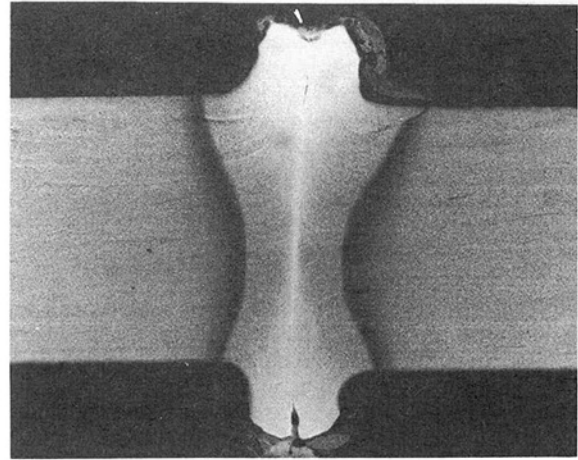


Fig. 1(A) Sample 3, weld made at initial setup conditions (2.5 mm upset distance, 36 mm initial die opening, 10 × magnification)

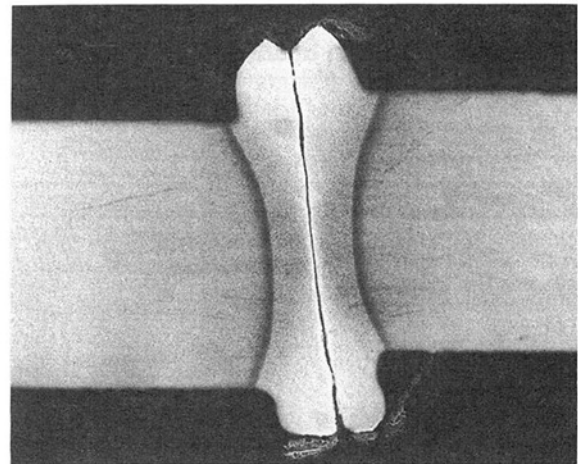


Fig. 1(B) Sample 13, weld made with increased upset distance (4.6 mm upset distance, 36 mm initial die opening, 10 × magnification)

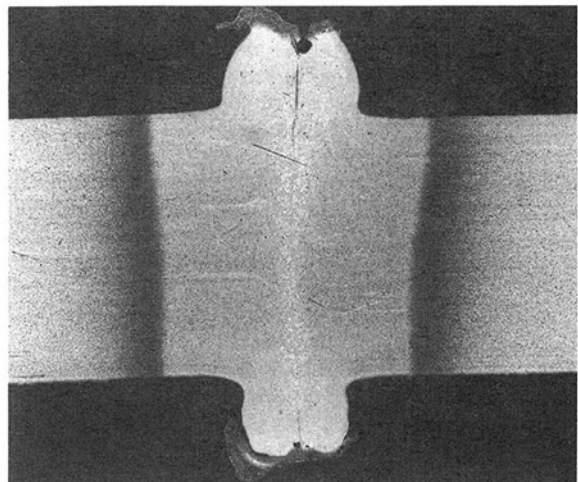


Fig. 1(C) Sample 9, weld made with increased initial die opening (2.5 mm upset distance, 42 mm initial die opening, 10 × magnification)

Fig. 1 Macrostructures for the welds examined in this study

ished using standard metallographic techniques, down to a final polish of 0.05 μm . Samples were then etched in a solution of 10 percent oxalic acid, 1 percent HF, balance H₂O. This solution is very effective for revealing plate structures in titanium alloys (Gould, 1983), and was used here to identify

any martensitic or acicular alpha constituents in the weld structure. Welds were then examined on a Nikon metallograph.

Following metallographic examination, microhardness traverses were also made across these welds. Microhardness testing was done with a Tukon microhardness tester, using a 500-g load and a square pyramid indenter (Vickers microhardness test). In these traverses, microhardness testing was done every 0.3 mm.

Results

Microstructural Results

Weld Macrostructures. Macrostructures of the welds were examined for the three sets of processing conditions and are presented in Figs. 1–3. In general, the microstructure of these welds consist of four zones: the base material, a region of transition from the base material to the fully beta transformed heat-affected zone (HAZ) (far HAZ), the beta transformed HAZ (near HAZ), and the bond region. These welds differ, however, in the distribution and extent of these regions. The weld made at the initial upset and die opening conditions (Fig. 1A) shows a heat-affected area with a convex shape, a well-defined transition region of the far HAZ, and a faintly identifiable bond line. This distribution of structures differs significantly from the weld made with the increased upset distance (Fig. 1B). In this case, the widths of both the heat-affected area and the transition of the far HAZ are restricted. In addition, the residual bond line is considerably more distinct. The weld made with the wider initial die opening (Fig. 1C)

shows a different distribution of structures. In this case, the heat-affected area has both markedly increased in width (by as much as a factor of four compared to the weld shown in Fig. 1A) and has lost its convex shape. In addition, the transition region of the far HAZ is also increased in width. Finally, in the center of the heat-affected area, there is both a lack of an identifiable bond line and apparent substantial prior beta grain growth.

Weld Microstructures. Higher magnification microscopy was used to characterize the microstructures further in each of the four regions of the three welds outlined above. Characteristic microstructures for each of the four regions from the weld made at the initial process conditions (Sample 3, 2.5 mm upset, 36 mm initial die opening) are presented in Fig. 2. Figure 2(A) presents the base material structure for this alloy. This consists of equiaxed alpha-two grains with retained beta particles lying at the alpha-two grain boundary triplepoints. The far HAZ microstructure is presented in Fig. 2(B). This region consists of partially transformed alpha-two grains and regions that have transformed to beta on the thermal cycle, and retransformed to alpha-two on cooling. This zone is actually a microstructural gradient, with increasing fractions of the structure having transformed on the thermal cycle nearer to the bond line. The microstructure of the fully transformed HAZ is presented in Fig. 2(C). In this region, the structure has completely transformed to the beta phase, and decomposed to a fine acicular product on cooling. The morphology is characteristic of martensitic alpha-two observed by other workers (Baeslack, 1988, 1989). In addition, this region of the weld

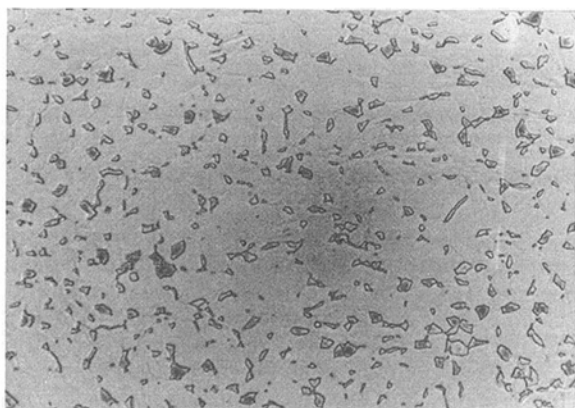


Fig. 2(A) Base metal microstructure, showing equiaxed alpha-two grains and retained beta particles (1000 ×)



Fig. 2(C) Near HAZ, prior beta grains with fine acicular alpha-two martensite plates (1000 ×)

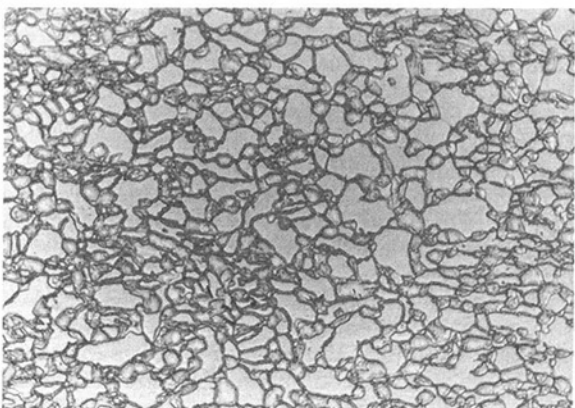


Fig. 2(B) Far HAZ microstructure, showing partially dissolved alpha-two grains (1000 ×)

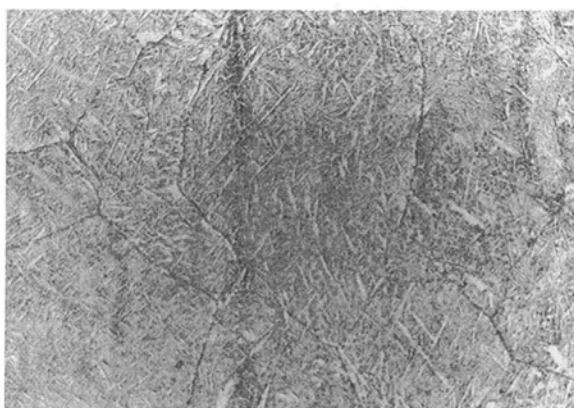


Fig. 2(D) Bond line region, retained beta grains with fine acicular alpha-two martensite plates (1000 ×)

Fig. 2 Microstructures for the weld made at the initial setup conditions (Sample 3, 2.5 mm upset distance, 36 mm initial die opening)

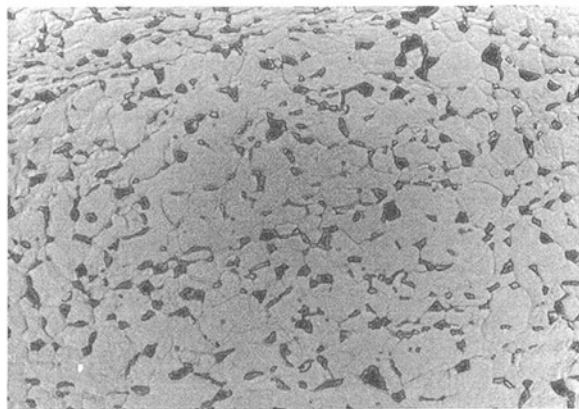


Fig. 3(A) Base metal microstructure, showing equiaxed alpha-two grains and retained beta particles (1000 \times)

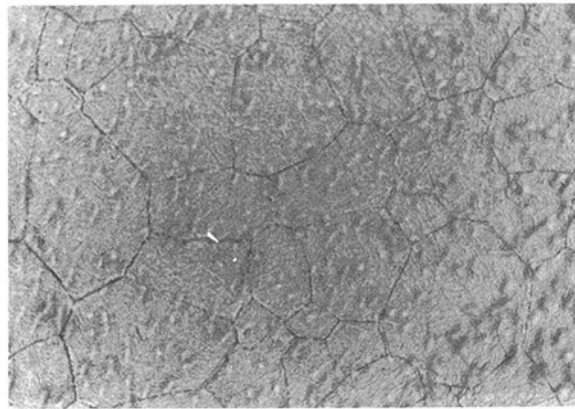


Fig. 3(C) Near HAZ, prior beta grains with fine acicular alpha-two martensite plates (1000 \times)

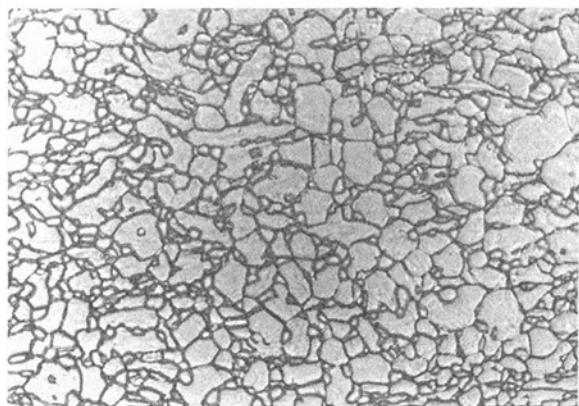


Fig. 3(B) Far HAZ microstructure, showing partially dissolved alpha-two grains (1000 \times)

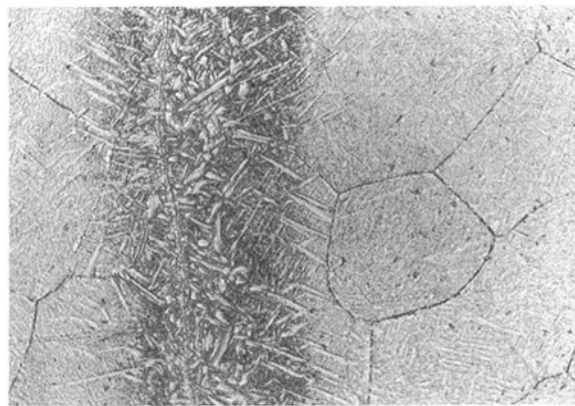


Fig. 3(D) Bond line region, retained beta grains with fine acicular alpha-two martensite plates (1000 \times)

Fig. 3 Microstructures for the weld made with increased upset distance (sample 13, 4.6 mm upset distance, 36 mm initial die opening)

shows some evidence of residual compositional segregation (as evidenced by variations in etching behavior). This segregation is presumably a remnant of the distribution of beta phase in the base material. The microstructure in the area of the bond line is presented in Fig. 2(D). The microstructure is quite similar to that in the bulk of the HAZ, consisting of prior beta grains overlaid with martensitic alpha-two. There is, however, a change in the pattern of the residual segregation. In this region, segregation appears as continuous bands oriented parallel to the bond line. In addition, the heaviest band appears to occur along the bond line itself. This segregation appears to be responsible for the preferential etching of the bond line, and is also noted to have some effect on the scale of the alpha-two plates at the bond line.

Detailed microstructures of the four regions for the weld made with increased upset distance (Sample 13) are shown in Fig. 3. The base material microstructure is shown in Fig. 3(A) and is, of course, identical, to that described in Fig. 2(A). The transition region of the far HAZ is shown in Fig. 3(B). This region is generally quite similar to that described in Fig. 2(B) above, with the notable exception that the gradient in microstructure is so distinct it is easily observable in the micrograph shown. The detailed microstructure of the near HAZ is shown in Fig. 3(C). This structure is in many ways again similar to that described in Fig. 2(C), but with two notable differences. First, the degree of residual segregation from the initial distribution of the beta phase is much greater, and the alpha-two martensite plate size is considerably refined. The microstructure for the bond-line region in this weld is shown in Fig. 3(D).

This microstructure is generally quite similar to that described for the near HAZ (Fig. 3C), although planar composition segregation bands, similar to those described in Fig. 2(C), are noted. This sample also shows a return of very coarse alpha plates in a band along the bond line. It is suspected that this structure is the result of oxygen contamination along the bond line, possibly due to trapped oxides. Dissociation of these oxides would then increase the content of oxygen (an alpha stabilizer) locally at the bond line, resulting in the observed structure.

Detailed microstructures of the four regions taken from the weld with the increased initial die opening (Sample 9) are presented in Fig. 4. The base material microstructure is presented in Fig. 4(A), and is identical to those shown in Figs. 2(A) and 3(A). The far HAZ (transition region) microstructure is shown in Fig. 4(B). In general terms, this microstructure is quite similar to those described in Figs. 2(B) and 3(B). However, as mentioned in Section 3.1.1, this region exists over an extended area compared to the other welds. As such, no gradient in the structure is identifiable in this micrograph. The microstructure for the near HAZ is shown in Fig. 4(C). This microstructure differs from those of comparable location in the other welds (Figs. 2C and 3C) in two ways: There appears to be no residual segregation from the base material and there is a considerable increase in the alpha-two martensite plate size. The detailed microstructure for the bond line region is presented in Fig. 4(D). As suggested in the macrograph (Fig. 1C) this region is characterized by extensive prior beta grain growth, and little notable residual segregation. What little segregation there is

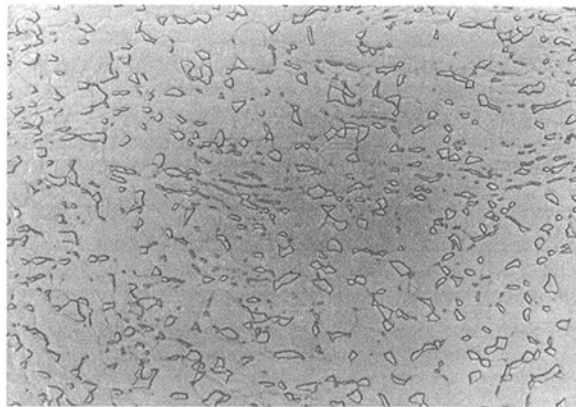


Fig. 4(A) Base metal microstructure, showing equiaxed alpha-two grains and retained beta particles (1000 \times)



Fig. 4(C) Near HAZ, prior beta grains with fine acicular alpha-two martensite plates (1000 \times)

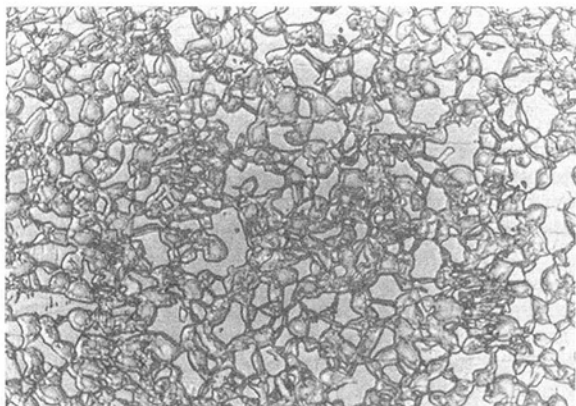


Fig. 4(B) Far HAZ microstructure, showing partially dissolved alpha-two grains (1000 \times)

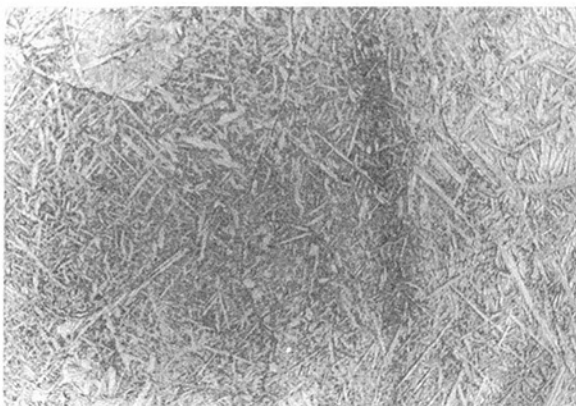


Fig. 4(D) Bond line region, retained beta grains with fine acicular alpha-two martensite plates (1000 \times)

Fig. 4 Microstructures for the weld made with increased initial die opening (Sample 9, 2.5 mm upset distance, 42 mm initial die opening)

appears intermittently along the bond line. Otherwise, the structure is identical to the near HAZ (Fig. 4C).

Microhardness Profiles. Microhardness profiles for the welds made at initial setup conditions with increased upset and with increased initial die opening are presented in Figs. (5A–5C), respectively. In all cases, base metal hardnesses were about 260 VHN. Peak hardnesses in these welds, as well as the apparent width of the hardened zones, appeared to vary with processing conditions. In all cases, however, the width of the measured hard zone widths correlated almost exactly with the fully beta transformed regions shown in Fig. 1.

Results for the sample using the initial setup conditions are shown in Fig. 5(A). This hardness profile indicates a peak hardness of about 485 VHN, and a hard zone width of about 2.1 mm. Hardness results for the weld made with increased upset distance are shown in Fig. 5(B). This weld showed an apparent peak hardness of 515 VHN, and a hard zone width of 1.8 mm. The higher upset distance appeared to result in both an increase in the peak hardness and a reduction in the width of the hard zone. Hardness results for the sample made with increased initial die opening are shown in Fig. 5(C). This weld showed a peak hardness of around 450 VHN and a hard zone width of 5.4 mm. Apparently, the increase in initial die opening resulted in both a reduction in the peak hardness, and a substantial increase in the width of the hardened zone. Peak hardnesses and widths of the measured hardened zones are presented in Table 4.

Mechanical Properties Results. Failure loads, ultimate tensile strengths, and failure locations for each of the welds tested

are given in Table 5. These results indicate that the welds made at both the initial setup conditions and with the increased initial die openings behaved similarly with relatively low strength with fracture noted along the bond line. The sample made with increased upset distance, however, showed both increased strengths and failure locations outside the weld zone.

Discussion

In these welds, there appear to be considerable variations in microstructure, hardness, and mechanical properties. Relationships between processing conditions and the observed microstructures, as well as relationships between microstructures and weld performance, are discussed in the following sections.

Relationships Between Processing Conditions and Weld Microstructures. Weld microstructure in titanium alpha-two aluminide alloys has been well established to be largely defined by the local cooling rate from the beta-transus (Baeslack, 1988, 1989; Strychor et al., 1988; Strychor and Williams, 1982). Certainly, the microstructure observed in these flash welds are similar to those developed under controlled cooling conditions by other workers (Baeslack, 1989). The effect of upset distance can be seen by comparing the microstructural and hardness results presented for the welds made at the initial setup conditions and under conditions of increased upset. Here, it is clear that increasing upset distance increases the cooling rate of the weld. The scale of the microstructure was substantially reduced, and the hardness of the weld was increased. Also, it was noted that homogenization of the beta stabilizing additions

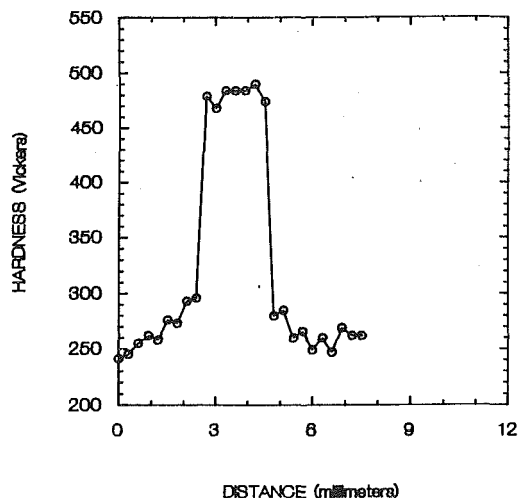


Fig. 5(A) Sample 3, weld made at initial set-up conditions (2.5 mm upset distance, 36 mm initial die opening)

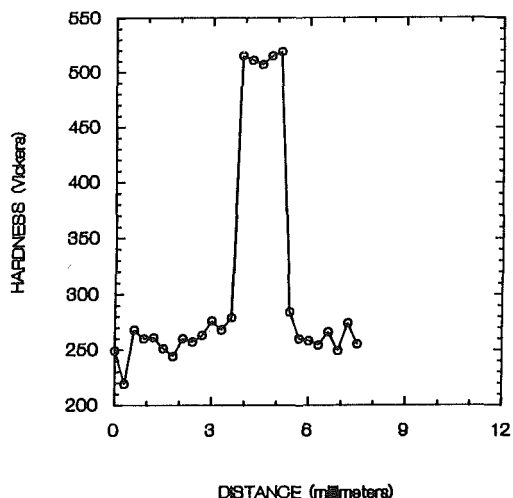


Fig. 5(B) Sample 13, weld made with increased upset distance (4.6 mm upset distance, 36 mm initial die opening)

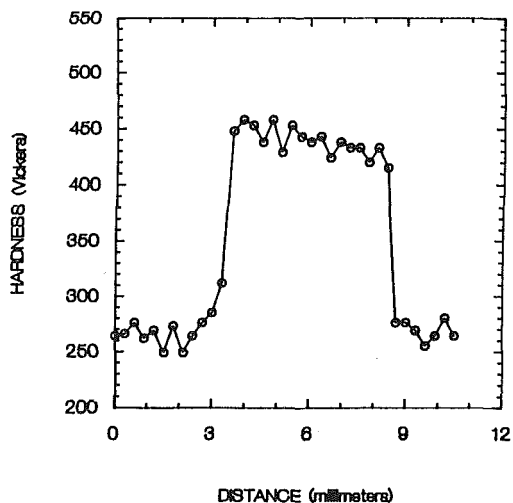


Fig. 5(C) Sample 9, weld made with increased initial die opening (2.5 mm upset distance, 42 mm initial die opening)

Fig. 5 Hardness profiles for the welds examined in this study

Table 4 Peak hardnesses and measured hard zone widths from the hardness traces

Sample No.	Initial Die Opening (mm)	Upset Distance (mm)	Peak Hardness (VHN)	Hard Zone Width (mm)
3	36	2.5	485	2.1
13	42	2.5	515	1.8
9	36	4.6	450	5.4

Table 5 Mechanical properties results

Sample No.	Load (kN)	UTS (N/mm ²)	Failure Location
4	10.3	167	Weld
14	27.9	490	HAZ/Base
8	8.64	158	Weld

was reduced at the higher upset distances, further indicating a rapid thermal cycle. It is believed that the increased upset distance simply brings cold material closer into the weld zone, facilitating rapid heat conduction and increasing the cooling rate.

Increased initial die opening, however, appears to reduce the cooling rate substantially. This can be seen by comparing the microstructural and hardness results for the welds made at the initial setup conditions and at the increased initial die opening. In the latter case, the scale of the alpha-two martensite plates is significantly increased, residual segregation of the beta stabilizers is apparently eliminated, and the hardness is reduced. All, of course, are indicative of slower cooling rates. That increased die openings should reduce the cooling rate of the weld is not surprising. Wider die openings imply longer conduction distances (to the water-cooled dies) and as such slower cooling rates. However, that an increase in the initial die opening of 18 percent should cause the apparent decrease in cooling rate noted here is an indication of the low thermal conductivity of the titanium alpha-two alloy.

Relationships Between Microstructure and Weld Properties. As has been shown previously (Baeslack, 1989), a refinement in the alpha-two plate martensite plate size in these microstructures is an indicator of increased hardness. Consistent with these observations, finer plate sizes in this study led to harder microstructures. Over the three sets of process conditions examined, an order of magnitude plate size reduction (from the wide initial die opening sample to the high upset sample) correlated with an increase in hardness from 450 to 515 VHN.

Interestingly, the apparent effect of weld hardness on the mechanical performance of the joint is contrary to suggestions in other works (Baeslack, 1988, 1989). These other works suggest that increasing hardness correlates with increased brittleness in the weld, and poorer mechanical properties. Here, however, the highest hardness weld showed the best performance by a large margin.

It is worth noting, however, that the weld with the best mechanical properties was that made with the greatest upset distance. It is believed that the apparent improvement in the mechanical properties may be due less to variations in the microstructure and more to the differences in the amount of forging used. It is generally accepted that increased upset distances lead to better overall joint performance. Recent thermal modeling (Nied, 1990; Gould, 1992) of upset welding processes

indicates that the effect of increasing the upset distance is to extend the bond surface, reducing the density of bond-line contaminants and improving joint quality. In these welds, the transformed microstructure is inherently notch sensitive. As such, a local flaw from too low an upset distance could initialize the brittle fractures observed. Where upset is sufficient, and such flaws are minimized, superior performance appears to result.

Conclusions

In this program the effects of upset distance and initial die opening on the underlying microstructures of a titanium alpha-two aluminide alloy were investigated in a preliminary way. The observed microstructures and hardness profiles were used to infer the relative cooling rates in these joints. Also, correlations were made between the underlying microstructures, processing conditions and some preliminary mechanical properties of these joints. From these observations, a number of conclusions were drawn:

1 Increased upset distance led to increased cooling rates in the weld, resulting in a finer scale of alpha-two martensite, higher weld hardness, and increased residual segregation.

2 Increased initial die opening led to significantly reduced cooling rates in the weld, increasing the scale of the alpha-two martensite, reducing weld hardness, and reducing residual segregation.

3 Finer alpha-two martensitic microstructures led to higher hardnesses in these welds.

4 The highest hardness weld also showed the best mechanical properties. The highest hardness weld, however, was also the weld with the greatest upset distance, and it is believed that the improved mechanical properties are the result of the increased forging during upsetting.

5 This limited study has shown microstructural variations in this alloy as a function of thermal history to be consistent with other welds. However, this work is only preliminary, and a detailed understanding of these results will require more detailed study.

Acknowledgments

The authors would like to thank the General Electric Company for their support of this work. Thanks are due to Mr. D. Pallas, Ms. D. Reef, and Mr. J. Hunt for their technical support.

References

- Baerlack, W. A., III, Cieslak, M. J., and Headley, T. J., 1988, "Structure, Properties and Fracture of Pulsed Nd:YAG Laser Welded Ti-14.8wt%Al-21.3wt%Nb Titanium Alloys," *Scripta Metallurgica*, Vol. 22(7), pp. 1155-1160.
- Baerlack, W. A., III, Mascarella, T. J., and Kelly, T. J., 1989, "Weldability of a Titanium Aluminide," *Welding Journal Research Supplement*, Vol. 68(12), pp. 483s-498s.
- Gould, J. E., 1983, "The Effect of Composition and Weld Process on the Structure of Titanium Base Welds," Ph.D. Thesis, Carnegie-Mellon University, Pittsburgh, PA.
- Gould, J. E., 1992, Unpublished Research, Edison Welding Institute, Columbus, OH.
- Lipsitt, H. A., 1985, "Titanium Aluminides, an Overview," *High Temperature Ordered Alloys*, C. C. Koch, C. T. Liu, and N. S. Stoloff, eds., Materials Research Society, Pittsburgh, PA, pp. 351-364.
- Nied, H. A., 1990, "Interface Displacement Characteristics of Upset Welding," *Recent Trends in Welding Science and Technology*, S. A. David and J. M. Vitek, eds., ASM International, Materials Park, OH.
- Stotler, T., Gould, J. E., and English, C., 1990, "Flash Welding Titanium Aluminides," *Advances in Joining Newer Structural Materials*, IIW/Pergamon Press.
- Strychor, R., and Williams, J. C., 1982, "Phase Transformations in Ti-Al-Nb Alloys," *Solid-Solid Phase Transformations*, H. I. Aaronson et al., eds., TMS, Warrendale, PA.
- Strychor, R., Williams, J. C., and Soffa, W. A., 1988, "Phase Transformations and Modulated Microstructures in Ti-Al-Nb Alloys," *Metallurgical Transactions*, Vol. 19A, pp. 225-234.

Finite Element Simulation of the Upset Welding Process

H. A. Nied

General Electric Company,
Research and Development Center,
Schenectady, NY 12301

A finite element model of an elevated temperature upset welding process was developed to simulate the process and to study the role and sensitivity of the major process parameters. Particular attention was focused on the deformation characteristics by studying the displacement and stress fields generated for the purpose of obtaining a better understanding of this solidstate welding process. The paper describes the finite element formulation, the experiments used to validate the modeling, and a selected application for upset welding of a titanium alloy.

Introduction

Solid-state welding is a widely accepted metal joining process used in industry to weld metals together without the inherent problems associated with bulk interface melting. Tylecote [1] describes the history and theory, including the basic fundamentals of solid-state bonding. Solid-state welding includes diffusion-bonding, deformation welding, thermocompression welding, forge welding, roll bonding, and friction welding—all thoroughly described in [2]. For each of these processes the objective is to bring the surfaces into intimate contact by breaking down surface asperities and contaminants in order to have atomic forces provide the bond. In all of these joining methods, the bonding mechanisms at the original interface are extremely complicated depending on the process variables used.

Of all these solid-state joining methods, diffusion-bonding has been studied the most and has been successfully applied to a broad range of metals and alloys including dissimilar materials. The diffusion-bonding process for joining metals and alloys is usually conducted at elevated isothermal temperatures greater than one half the absolute melting temperature ($\geq 1/2 T_m$) for substantially long process times¹ while subjected to moderate interfacial pressures. Various models have been proposed to understand the surface mechanics and grain growth mechanism at the bond interface for diffusion-bonding that do not rely on large interfacial forces nor utilize large upset deformation. References [3–5] describe some of the leading diffusion-bonding theories. The bonding is achieved primarily by grain growth across the original weld interface and the diffusion of any contaminants into the bulk material.

If the materials or alloys to be joined have rapid grain growth characteristics at elevated temperatures for long processing times associated with diffusion-bonding, then this bonding method would be a poor process selection, and the application of upset welding carried out for a short processing time (in the order of seconds) would appear to be more appealing since

grain growth is reduced. Clearly, the mechanism of grain growth across the weld interface would not play a dominant role, and the conditions of high normal interfacial contact stresses would have to be attained to deform plastically the faying surface unevenness, asperities and to break up surface contaminants which could be flushed into the flash. For the case of high upset welding, the mechanisms of interfacial deformation are considerably different from those associated with diffusion-bonding, and they have not been clearly identified nor understood. Experiments have shown that when high deformation upset welding is conducted at elevated temperatures, substantial interfacial deformation can produce local grain deformation, recrystallization, and material displacement.

It is commonly thought in the upset welding industry that the larger the upset deformation, the better the quality of the weld. This is based on the assumption that large deformations will expel all the original interface material into the upset flash and will replace the interfacial surface with bulk virgin material by the flow mechanism. The results of this study clearly show that this does not occur. This investigation has revealed that the original surface material is not replaced by adjacent bulk material, and only a portion of the original surface is expelled into the flash by the process-flushing action. Excessive deformation can severely deform the microstructure and thereby generate planes of weakness. Contact pressure, temperature, and time are the important process variables that have to be controlled to produce high-quality upset welds.

Theory

The mechanism for solid-state welding is not completely understood nor accepted for upset welding or diffusion-bonding. References [3–5] describe the various theories currently used to explain the welding mechanism. In particular, [5] provides an interesting summary of the film, recrystallization, energy, dislocation, electron, and diffusion hypotheses to explain the formation of a solid-state weld. All these references indicate that a combination of time, temperature, and contact stress is the major variable group needed to break down the surface asperities and contaminants in order to produce the

¹Process times on the order of several hours depending on the component size.

Contributed by the International Gas Turbine Institute and presented at the 36th International Gas Turbine and Aeroengine Congress and Exposition, Orlando, Florida, June 3–6, 1991. Manuscript received at ASME Headquarters March 4, 1991. Paper No. 91-GT-230. Associate Technical Editor: L. A. Riekert.

weld. It was not the purpose of this effort to model the interfacial welding mechanism, but to provide a model for determining the macrodeformation, temperature, stress and strain, which together with process test data, can be used to predict weld quality.

Governing Equations. Upset welding is an extremely complicated process involving heat transfer and both the macro/micromechanical deformation considerations. Titanium alloys are allotropic and during the upset welding process a phase change in the microstructure from α to β occurs when the β -transus temperature is exceeded. In this formulation, microstructural aspects are not included directly, but rather implicitly by the temperature-dependent properties used in the model. Elevated temperature upset welding will be treated as a coupled thermomechanical process in the formulation. The coupling occurs not only through the temperature dependent properties, but also by the heat generated in the workpieces due to the dissipation of plastic work. Consequently, the governing equations for the process must describe the temperature distribution and the conservation of mass and momentum.

The temperature distribution is described by the classical transient heat conduction equation:

$$\frac{\partial}{\partial x_i} \left(k \frac{\partial \theta}{\partial x_i} \right) + \dot{Q} = \rho C_p \frac{\partial \theta}{\partial \tau} \quad (1)$$

where θ is the temperature, \dot{Q} is the internal heat generation term, k is the thermal conductivity, ρ is the density, C_p is the specific heat, τ is the time, and x_i is the coordinate written in indicial notation.

In this formulation, the heat generation term \dot{Q} is composed of two components. The heat source may include dissipation of mechanical work in the form of heat, and/or electrical resistance Joule heating. (The electrical resistance capability is needed for analyzing GLEEBLE tests.) This is illustrated in the following equation:

$$\dot{Q} = \dot{Q}_p + \dot{Q}_I \quad (2)$$

If the internal heat generation is due to the dissipation of plastic work, the volumetric heating rate is given by

$$\dot{Q}_p = \sigma'_{ij} d_{ij} \quad (3)$$

where σ'_{ij} is the deviatoric stress tensor and d_{ij} is the deformation rate tensor. The relationship in Eq. (3) assumes that all the plastic work is converted to heat. In reality, a small part of the energy dissipated is stored in the metal as latent heat. If a polycrystalline metal is cold-worked, about 10 percent of the mechanical work goes into internal energy. However, hot working at elevated temperatures reduces the amount of mechanical energy dissipated into internal energy. Consequently, the assumption of complete viscous dissipation used in this formulation is justified because of the high-processing temperatures during upset welding.

If the heat source is due to Joule heating, the heat generation rate is given by

$$\dot{Q}_I = r j_i \cdot j_i \quad (4)$$

where r is the specific resistivity, and j_i is the current density. For Joule heating, the potential distribution must be sought first in order to compute the current density needed in Eq. (4). This potential field can be determined from the solution of the Laplace equation. Accordingly,

$$\frac{\partial}{\partial x_i} \left(\frac{1}{r} \frac{\partial E}{\partial x_i} \right) = 0 \quad (5)$$

applies throughout the continuum with E being the electrical potential and r the specific resistivity. Associated with the Joule heating option either the potential E or the current flux \vec{j} must be specified. For a potential boundary condition, the potential is specified by

$$E = \bar{E} \text{ on } S_E \quad (6)$$

while for the current flux boundary condition,

$$j_i \eta_i = \bar{j} \text{ on } S_j \quad (7)$$

with the vector normal to the surface given by η_i and where S_E and S_j are the boundary conditions for the potential or current flux, respectively. From this potential distribution the local current density vector distribution can be determined from the potential gradients by the relationship:

$$j_i = -\frac{1}{r} \frac{\partial E}{\partial x_i} \quad (8)$$

The capability of Joule heating is needed in this formulation since part of the modeling effort was devoted to analyzing GLEEBLE specimens that are electric resistance heated. Titanium alloys, which have a high specific resistivity when compared to other engineering structural materials, can be easily heated by electric current.

In addition to the various heat sources accounted for in this formulation, it is necessary to impose the boundary conditions for Eq. (1). Neither convective nor radiation heat transfer has been included in this formulation because of the short processing time. Therefore, only two types of boundary conditions are needed for this upset welding formulation; namely, a boundary temperature or a heat flux on the surface. For the temperature boundary condition:

$$\theta = \bar{\theta} \text{ on } S_\theta \quad (9)$$

For the flux boundary condition:

$$q_i \eta_i = \bar{q} \text{ on } S_q \quad (10)$$

with the normal vector given by η_i .

The heat flux vector q_i is related to the temperature gradient and the thermal conductivity by the well-known Fourier relationship:

$$q_i = -k \frac{\partial \theta}{\partial x_i} \quad (11)$$

The mechanical deformation of a viscoplastic solid can be determined by computing the material velocity distribution. Once the velocity field is known, the material displacement can be obtained by time integration. The point of formulating the mechanical behavior in terms of the velocity instead of displacements is a tremendous simplification and yet provides all of the necessary description for large deformation. Accordingly, the flow and deformation of the solid subjected to mechanical loading is described by the conservation of momentum and mass equations. When inertia and body forces are neglected, the equilibrium equation can be written as

$$\frac{\partial \sigma_{ij}}{\partial x_j} = 0 \quad (12)$$

where σ_{ij} is the total stress tensor composed of the deviatoric and hydrostatic stress tensors.

The deformation rate tensor d_{ij} is related to the material velocity gradients by

$$d_{ij} = \frac{1}{2} (v_{i,j} + v_{j,i}) \quad (13)$$

The material incompressibility assumption requires that the trace of the deformation rate tensor vanish, accordingly

$$d_{ii} = v_{i,i} = 0 \quad (14)$$

In this formulation, the mechanical constitutive equation assumes that the elastic material response is small compared to the larger plastic deformation. Consequently, a power law visco-plastic material model is assumed that relates the flow stress to deformation rate for a given temperature. This re-

relationship can be written in terms of the second invariant of the deviatoric stress, as follows:

$$\sigma'_{ij} = C \epsilon_0 \dot{\epsilon}^m d_{ij}^m \quad (15)$$

where C is the activation energy, R the universal gas constant, θ the absolute temperature, and m the strain rate sensitivity factor. The components of the deviatoric stress tensor σ'_{ij} can be obtained from the deformation rate tensor using the associated Levi-Mises flow rule:

$$\sigma'_{ij} = 2\mu^e d_{ij} \quad (15)$$

where effective viscosity μ^e is obtained from Eq. (15).

The mechanical model requires the application of either velocity or force boundary conditions. For the velocity boundary condition:

$$v_i = \bar{v}_i \text{ on } S_v \quad (17)$$

or for tractions T_i on the surface:

$$\sigma_{ij} n_j = \bar{T}_i \text{ on } S_\sigma \quad (18)$$

Equations (1)–(18) can be solved using the powerful finite element method. In this technique, the body is discretized into solid elements by a mesh model. The governing equations are applied to a single element. The global response is then obtained by summation of the contribution from each element.

Finite Element Formulation

The finite element program developed for the upset welding process simulation was based on the 2 dimensional formulation and code called "HICKORY," which was developed by Prof. Paul Dawson of Cornell University. Details of the finite element method used in the formulation are contained in [6, 7]. This code was used as the building block to develop a computer simulation of the upset welding process. Modifications and changes were made to include capabilities needed for analyzing the large upset welding process with the special heat generating features inherent in this process. Each of the governing equations, Eqs. (1), (5), and (12), is solved separately for the temperature, electric potential, and the velocity distributions. The intercoupling is accomplished by successively iterating for the temperature and the flow field until convergence is achieved before updating and taking the next increment in time.

A six-noded isoparametric triangular element was used in Dawson's formulation, which provides the capability to handle the highly nonlinear gradients produced in this process. The six-node triangular finite element is used to determine the potential, velocity, and temperatures at the corner and midpoint nodes. The hydrostatic stress is determined at the corner nodes by using the Lagrangian multiplier method.

The finite element solution for the transient heat conduction (Eq. (1)) can be obtained using Galerkin's method by using a weighted residual formed by the governing equation and a set of weighting functions N_j :

$$R_\theta = \int_V N_j \left[\frac{\partial \theta}{\partial x_i} \left(k \frac{\partial \theta}{\partial x_i} \right) + \dot{Q} - \rho C_p \frac{\partial \theta}{\partial \tau} \right] dV \quad (19)$$

When the first term is integrated by parts and Green's theorem is imposed, the residual is determined to be

$$R_\theta = \int_V \frac{\partial N_j}{\partial x_i} k \frac{\partial \theta}{\partial x_i} dV + \int_V \dot{Q} N_j dV - \int_S \bar{q} N_j dS - \int_V N_j \rho C_p \frac{\partial \theta}{\partial \tau} dV \quad (20)$$

where \bar{q} is the applied heat flux. Equation (20) can be reduced to a matrix equation for each element by using an approximating interpolation function for the temperature and applying the Crank-Nicholson method. Thus, one obtains

$$[[C] + [M]] \{ \theta^{\tau+\Delta\tau} \} = [[C] - [M]] \{ \theta^\tau \} + \{ Q \} \quad (21)$$

where the temperature, heat storage, and thermal conductivity matrices, and the heat force vector are given by

$$\theta = [N] \{ \theta \}_e \quad (22)$$

$$[C] = \int_V [N]^T (\rho C_p) [N] dV \quad (23)$$

$$[M] = \int_V [N']^T [k] [N'] dV \quad (24)$$

$$\{ Q \} = \int_V [N]^T \{ \dot{Q} \} dV + \int_S [N]^T \{ q \} dS \quad (25)$$

The integrals in these relations are obtained using Gaussian quadrature.

The solution for the electric potential field given by Eq. (5) can be easily obtained from the solution of Eq. (1) by noting that the first term in Eq. (1) is Laplace's equation when the heat source term and the transient heat storage term are set equal to zero. Accordingly, the finite element solution for the electric potential field can be obtained by setting the time dependency to zero and applying the appropriate resistivity stiffness matrix in Eq. (24).

The finite element approximation of the momentum equation for the determination of the velocity field is based on the variational statement for virtual rate of work. The functional J is accordingly written as

$$\delta J = \int_V \sigma'_{ij} \delta d_{ij} dV - \delta \int_V p d_{ii} dV - \int_V X_i \delta v_i dV - \int_{S_\sigma} T_i \delta v_i dS \quad (26)$$

where δ denotes variation of function or variable, p is a Lagrangian multiplier having the physical meaning of pressure, X_i is the distributed body force and T_i the applied traction. The velocity and pressure variables are approximated by using the interpolation functions $[N]$ and $[N_p]$. Using the usual matrix notation, these expressions become

$$\{ v \} = [N] \{ V \}_e \quad (27)$$

$$p = [N_p] \{ P \}_e \quad (28)$$

where $\{ V \}_e$ and $\{ P \}_e$ are the velocity and pressures at the nodal points. The matrices $[N']$, $[D]$, $\{ d \}$, and $\{ h \}$ can be defined so that

$$\{ d \} = [N'] \{ V \}_e \quad (29)$$

$$\delta d_{ij} \sigma'_{ij} = \{ \delta d \}^T [D] \{ d \} \quad (30)$$

$$d_{ii} = [h] \{ d \} \quad (31)$$

The variational expression (Eq. (26)) can be written for a single element in the form:

$$\delta J_e = \{ \delta V \}_e^T [K]_e \{ V \}_e - \{ \delta V \}_e^T [G]_e^T \{ P \}_e - \{ \delta P \}_e^T [G]_e \{ V \}_e - \{ \delta V \}_e^T \{ F \}_e \quad (32)$$

where the stiffness matrices are given by

$$[K]_e = \int_{V_e} [N']^T [D] [N'] dV \quad (33)$$

$$[G]_e = \int_{V_e} [N_p]^T [h] [N'] dV \quad (34)$$

and the force vector can be expressed as

$$\{ F_e \} = \int_{V_e} [N]^T \{ X \} dV + \int_{S_e} [N]^T \{ T \} dS \quad (35)$$

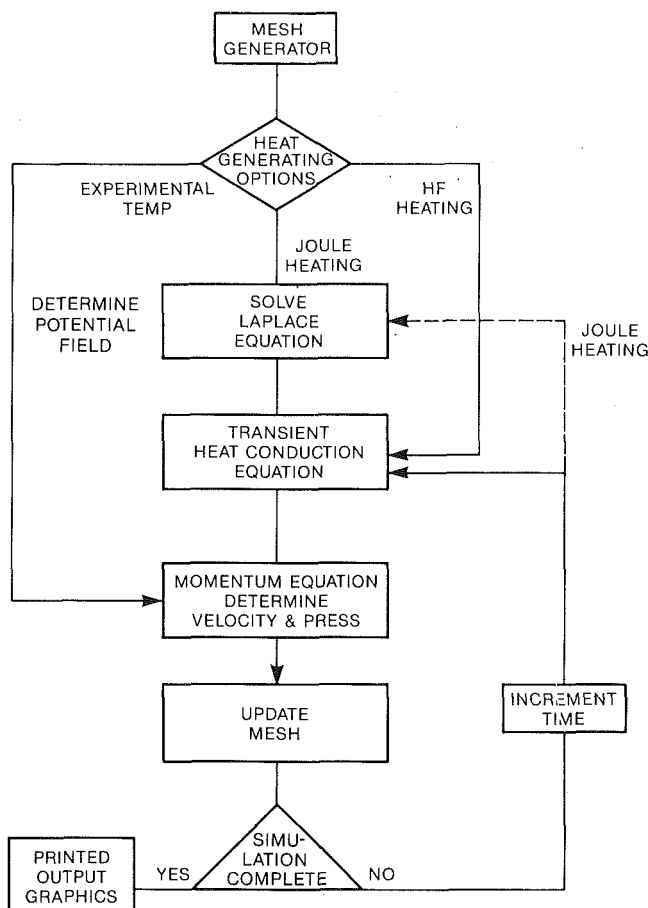


Fig. 1 Flow chart of solution procedure

The finite element method consists of summing the individual element relations (Eqs. (33)–(35)) throughout the discretized volume to obtain the global matrices. When the variation of the functional (Eq. (26)) is taken, the following global set of equations written in matrix form is obtained:

$$\begin{bmatrix} K & G^T \\ G & 0 \end{bmatrix} \begin{Bmatrix} V \\ -P \end{Bmatrix} = \begin{Bmatrix} F \\ 0 \end{Bmatrix} \quad (36)$$

The set of simultaneous equations is solved using the frontal technique to obtain the nodal velocities and pressures. The Newton-Raphson method is used to obtain the nonlinear solution since the stiffness matrix depends on the effective viscosity, which is a function of the deformation rates.

A quasi-Lagrangian reference frame is used in the formulation. An Euler integration scheme is used for each time step to update the mesh in time. The updated mesh is then used as the reference frame for the next time step. In this fashion, the mesh moves with the material. As the FE simulation steps forward in time, the shape of the deformed solid is determined from the nodal velocities that are calculated.

The flow chart of the coupled thermomechanical analysis is shown in Fig. 1. Once the temperature distribution has been established by either reading in experimental test data or using electrical resistance, the transient heat conduction solution is obtained. When the temperature solution converges, the code proceeds to the solution of the momentum equation to obtain the velocity and pressure fields using material properties based on the temperature previously obtained. The code cycles through for each increment in time until the process simulation is complete. For extremely large deformations, a remesh scheme has been included to account for the convective terms of the variables when transforming the variables from the old mesh to the new mesh. A modified algorithm based on the technique

developed by Wang and McLay [8] was used in this code. If the remesh feature is flagged, the code will remesh the model at each time step. It was determined that remeshing at each time step did not produce a significant computation penalty.

During the development of the FE upset weld simulation code, extensive studies were conducted to determine the sensitivity of the program to analyses with and without model remeshing, as well as mesh refinement. It was determined that essentially the same displacements, temperatures, and stresses were obtained whether or not the remesh feature was used up to point of obtaining a negative Jacobian. Since the major interest was focused on interior material deformation, analyses were chiefly conducted without using the remesh capability. The FE mesh used in the examples cited was determined to provide a good simulation of the process for the simple geometries under consideration even though severe triangular mesh distortion occurred. Clearly, other geometries may require a more refined mesh together with the use of the remesh feature when large gradients in the field variables are generated.

When this coupled thermoelectric/mechanical finite element formulation was implemented into a computer code, a program having the following general modeling features and capability was made available to manufacturing engineering:

- 1 Two-dimensional plane strain and axisymmetric geometries.
- 2 Six-node isoparametric triangular element.
- 3 Viscoplastic, strain rate sensitive material model.
- 4 Coupled electric, heat conduction, and mechanical deformation.
- 5 Remesh or no remesh selection.
- 6 Adiabatic heating due to dissipation of mechanical energy.
- 7 Variable velocity or force.
- 8 Joule (electric resistance) heating.
- 9 Weld interface contact stress distribution and total applied load.
- 10 Graphics output:
 - deformation and profile
 - stress contours
 - temperature contours
 - weld interface contact stress plot

Material Model

The simulation of the large deformation upset welding process requires a suitable material model to describe the viscoplastic behavior at elevated temperatures which produce large strain and material displacement. The elevated temperature regime selected for these upset welding studies straddled the superplastic process temperature for titanium alloys. Reference [9]–[11] describe the deformation behavior and microstructural considerations for strain rate sensitive viscoplastic metals. It has been shown [11] that a general empirical model can suitably describe viscoplastic behavior by using the following functional form for the effective flow stress:

$$\sigma_{\text{eff}} = f(\dot{\epsilon}_{\text{eff}}, \theta, S) \quad (37)$$

where $\dot{\epsilon}_{\text{eff}}$ is the viscoplastic strain rate, θ is the absolute temperature, and S is a state variable. The state variable can be related to the microstructure and its evolution during the process history.

This expression can be simplified and specialized for elevated temperature application of this process; see [10, 11]. Because of the short process times associated with the upset process, a power law strain rate sensitive constitutive equation can be effectively used for representing the flow stress response of titanium alloys. The flow stress σ_{eff} can be written in terms of the effective strain rate $\dot{\epsilon}_{\text{eff}}$ and the temperature θ using the familiar Arrhenius relationship:

$$\sigma_{\text{eff}} = C \exp \left(\frac{Q_A}{R\theta} \right) \dot{\epsilon}_{\text{eff}}^m \quad (38)$$

where R is the universal gas constant, Q_A is the activation energy, θ is the absolute temperature, and m is the strain rate sensitivity factor. The coefficient C in this relationship has the dimension of (stress \times time m). Many references are contained in the literature that describe the application of the power law model to titanium α - β alloys. See [9] for an extensive bibliography.

The expression contains three material parameters: C , $\frac{Q_A}{R}$, and m , which can be easily determined from isothermal compression tests. When the natural logarithm is taken of both sides, a linear equation is obtained that can be fitted to material data:

$$\ln \sigma_{\text{eff}} = \ln C + \frac{Q_A}{R\theta} + m \ln \dot{\epsilon} \quad (39)$$

The strain rate sensitivity factor m represents the slope of the curve, while the value of the coefficient C represents the intersection with the ordinate. Test data has shown that the sensitivity factor m is a function of both temperature and strain rate. This factor attains a maximum value at creeping strain rates (10^{-4} to 10^{-3} in./in. s) associated with superplastic forming. For upset welding applications, the strain rates will be in the order of 10^{-1} to 10^{+1} in./in./s. At these strain rates and for the temperature range considered in this study (1700 to 2000°F), the factor m is considered to be a constant material parameter. The data used in these studies were extrapolated from the titanium alloy data cited in [10, 11].

Test Description

Tests were conducted on simple rectangular specimens, which were welded together for different degrees of upset using a GLEEBLE thermomechanical tests machine, which produced the needed temperature distribution by electric resistance Joule heating. This test facility produced a parabolic axial temperature gradient symmetric about the weld interface, thereby simulating many upset welding processes. The process parameters recorded during these test were used as input in the FE model and comparisons between the predictions and deformation response were conducted.

The GLEEBLE 1500 is a universal thermomechanical test facility that has wide applications for establishing and studying process parameters. Ferguson [12] describes several useful applications for determining metalworking process behavior. Figure 2 schematically illustrates how this facility was used for the upset² welding tests conducted on Ti 6Al-4V test specimens. Since this α - β titanium alloy is highly reactive in air at elevated temperatures, all tests were conducted in a vacuum chamber. Figure 3 shows the specimen geometry used for these process tests. The specimen consists of two halves, which are mounted in the water-cooled copper jaws of the test machine. The weld interface is precisely positioned at the midpoint between the two jaws. Electric current is passed between the two copper jaws to heat the specimen up to the desired upset welding temperatures. A thermocouple attached to the specimen near the weld interface provided the sensor data for the closed loop feedback control of the temperatures. The distance used between the watercooled copper jaws determines the temperature gradient used in the test. During the heating cycle, the temperature in both the transverse and axial direction can be monitored by an infrared imaging radiometer system having a silicon CID camera detector developed at GE/CRD. The optical lens attached to the IR camera is focused on the specimen by sighting through a pyrex window of the vacuum chamber. This

²The definition of upset used for this welding process is defined as the ratio of the ram displacement to the original part width.

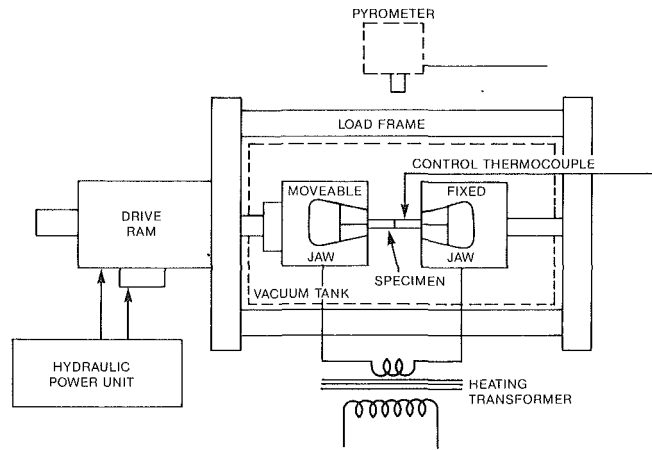


Fig. 2 Schematic of GLEEBLE test configuration

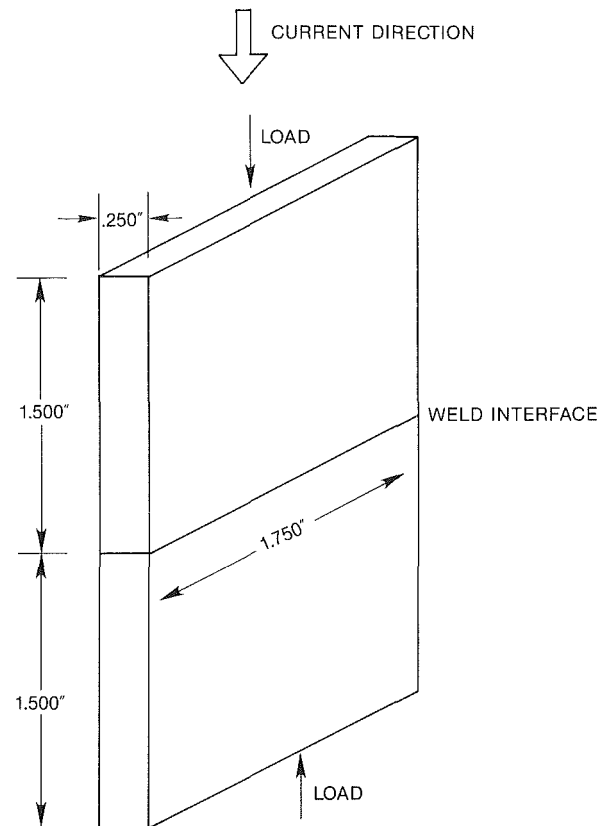


Fig. 3 GLEEBLE specimen geometry

temperature distribution can be observed on a B/W video display monitor as well as being recorded on videotape for future playback. When the temperature distribution is uniform in the transverse direction, the axial temperature gradient is recorded and later analyzed to determine numerical values of the temperature distribution. This axial temperature gradient determined by experiment is used as data input into the upset weld code for the initial temperature distribution.

In order to provide a visual display of the upset welding process, glass specimens containing colored tracers were also included in the test plan. Reference [13] describes the specimen geometry that contained longitudinal, colored filaments, which provided a visual determination of the displacement path near and on the faying surface.

Results

A combination of finite element analyses, evaluation of pho-

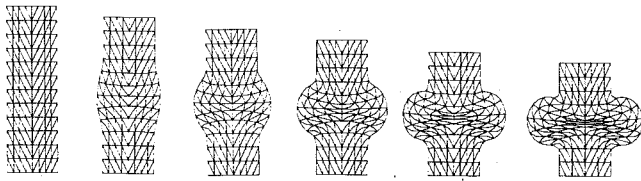


Fig. 4 Weld upset sequence T6-H4D1: 0, 20, 60, 80, 100 percent

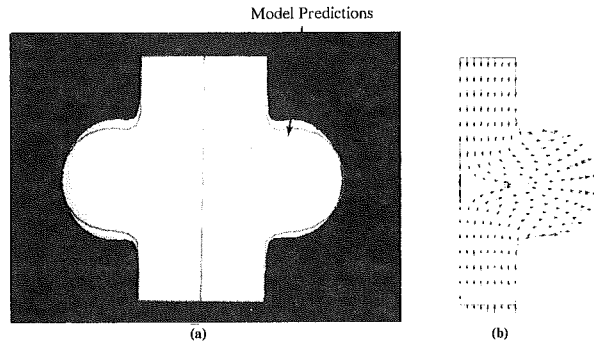


Fig. 5 Specimen T6-H4D1: (a) deformed model overlay on specimen; (b) material velocity field

tomicrographs, and review of certain research papers in the open literature has revealed the basic material deformation and, in particular, the displacement of surface material during upset welding. A series of subscale experiments were conducted on the GLEEBLE for the purposes of understanding the process under precisely controlled test conditions and to validate the finite element code.

Finite element modeling has provided a better understanding of the deformation process in upset welding. Figure 4 shows the results of running the finite element code for a typical test. In this figure, a sequence of deformations is shown up to the final deformation. Since the specimens are mounted in the GLEEBLE jaws with one end fixed, the boundary condition imposed on the model is such that the bottom of the specimen is fixed, and the velocity is applied to the upper surface. The original undeformed mesh model, which consists of 128 finite elements, is shown at the left. The model was subjected to a ram velocity of 1.05 in./s with a weld interface temperature equal to 1956 °F and the temperature gradient corresponding to the actual test data obtained with the IR sensor. Figure 5(a) shows the results of comparing the analytical predictions with the actual test specimen profile. Digitized optical images of this specimen superimposed on the solid line profile predicted by the model. Reasonable agreement was obtained. The differences in the profiles were principally the result of inaccuracies of IR low-temperature measurements near the grips. Nevertheless, the computer simulation provided an excellent prediction of the flash width. Figure 5(b) shows the corresponding material velocity distribution at final instant of 100 percent upset. It is clear that the material velocity at the center on the weld interface is zero, and the velocity increases from that location outward into the flash region. This reveals the characteristic material displacement pattern for a large upset welding process. Some of the bulk material is displaced into the upset region. Figure 6 shows the isotherms at 100 percent upset. Clearly, the highest temperature exists at the center of the specimen along the weld interface. It is desirable to have a uniform temperature in this region to provide the desired microstructural properties. Due to the large deformation, the temperature field becomes distorted because of the displacement of material.

The relationship of element deformation and microstructure at the weld center and in the flash is shown in Fig. 7. Material,

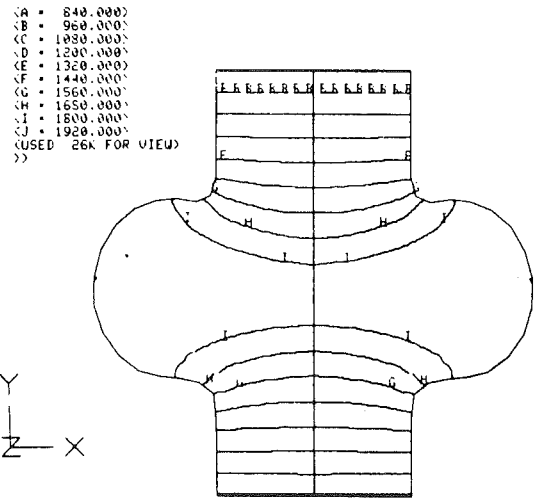


Fig. 6 Temperature distribution at 100 percent upset specimen T6-H4D1

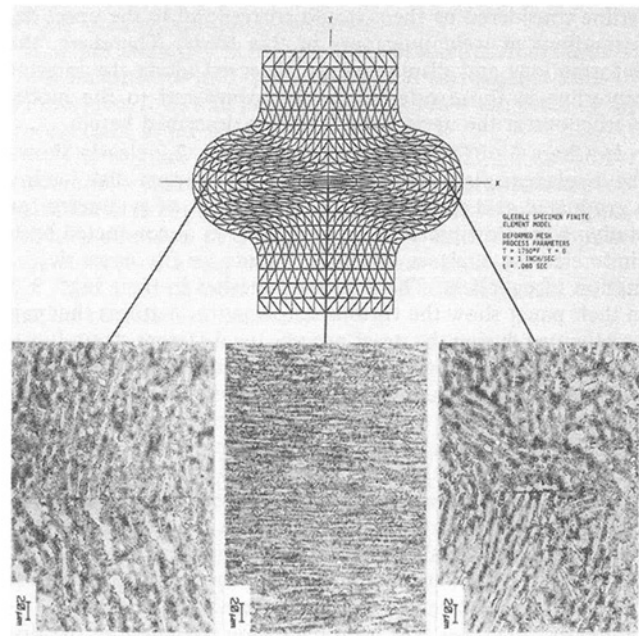


Fig. 7 Upset specimen showing microstructure

which was originally on the sides of the specimen, was displaced into the flash zone without severe distortion of the original microstructure as shown in the two outer photomicrographs. The original weld surfaces can be clearly seen in these micrographs, which reveal defects in the flash zone indicating poor weld structural integrity. However, at the center of the specimen, the material microstructure is subjected to large strain and distortion of the grain structure. The material is compressed in the direction perpendicular to the weld interface and stretched in the direction parallel to the original interface. In this zone, a sound upset weld was made as shown in the photomicrograph and was verified by subsequent mechanical testing.

The results obtained for the deformation distributions are in agreement with the analyses and experiments published in the open literature. Most of the references are concerned with large deformations during the forging process and are too numerous to mention; consequently, only a few pertinent references will be cited. The researchers were mainly interested in the overall deformation pattern associated with forging

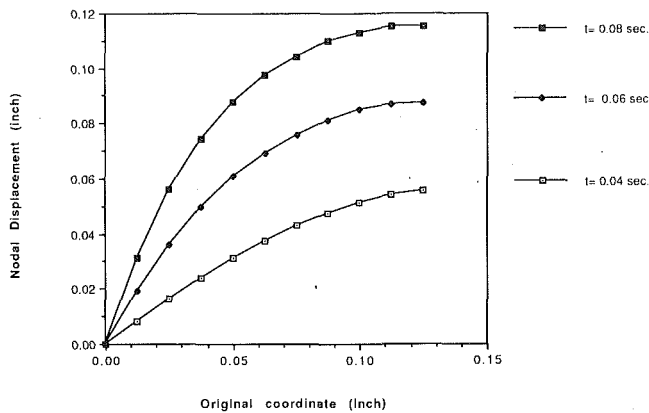


Fig. 8 Weld interface nodal displacements

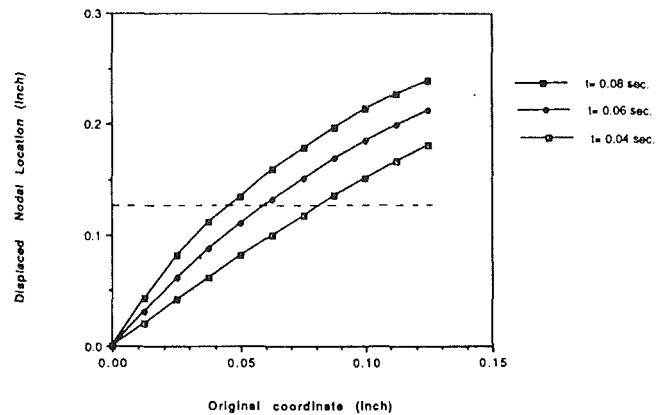


Fig. 9 Weld interface nodal locations

processes and not upset welding deformation. When two similar materials are joined at the same temperature, there will be negligible slip at the interface when subjected to high contact stresses. Consequently, deformations along the forging centerline considered by them would correspond to the upset deformations at weld interfaces in this study. Therefore, the deformations and displacements observed along the interior centerline in those references were compared to the model predictions at the upset weld interface described herein.

In Chap. 2 of [14], entitled forging, Fig. 2.2 clearly shows the displacements produced in an OFHC copper disk having a graduated grid scribed parallel to the axes of symmetry for studying the flow patterns. In [15], Boer et al conducted both finite element analyses and experiments on the upset deformation of cylinders. The deformed meshes in their Figs. 3–5 in their paper show the various deformation patterns that can be obtained during the upset process for different strain-hardening conditions. In their Fig. 6, the authors have overlaid the deformed FEM mesh onto the deformed test specimen showing good agreement for a rigid-plastic material model. In Chap. 20 of [16], Altan et al. conducted analyses simulating forging of titanium alloy disks using the ALPID computer program. Their deformed mesh models show the general characteristics of the local deformation patterns, which have been similarly observed for the analyses conducted during this study.

Just the determination of grid distortion is not sufficient for revealing the displacement behavior at the weld interface. Consequently, emphasis had been placed on determining the displacements and velocities along the interface during the process simulation. Figure 8 is a plot of the nodal displacement as a function of the original coordinate location for three different times during the process. It is immediately apparent that the nodes close to the center of the specimen are displaced very little. The further the node is located from the center, the larger the displacement. A more revealing plot is shown in Fig. 9. Here the X axis is the original nodal location, and the Y axis is the displaced nodal location. One should be aware of the distinction between the nodal displacement, which is the differential between the final and initial location, and the displaced nodal location as measured from the centerline of the specimen. Since the half-width of the specimen is 0.125 in., a horizontal line drawn from the $Y = 0.125$ in. intercept shown as the dotted line will reveal those nodes swept out beyond the original width into the flash zone. From plots such as these, the amount of original surface material flushed into the flash can be precisely estimated for this geometry and upset weld conditions.

The upset welding computer simulation was also applied to larger scale and more complicated geometries. Figure 10–13 show the results of those analyses.

Figure 10 shows the mesh model having 377 node points and

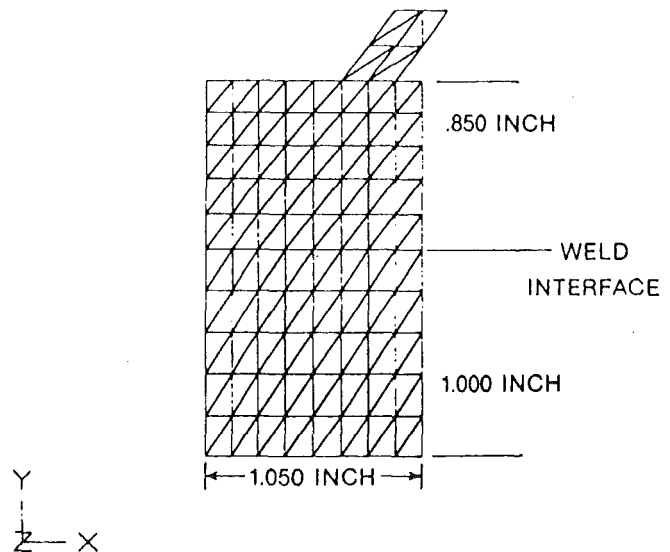


Fig. 10 Prototype joint mesh model

168 elements to represent the weld joint cross section. The width of the Ti 6Al–4V upper and lower weld joint is 1.05 in., while the component heights with respect to the weld interface are 0.85 and 1.00 in. This model was subjected to an initial temperature distribution that was nonsymmetric about the weld interface and a ram velocity of 2 in./s applied to the shoulder of the upper block while the base is fixed. The process velocity was applied to produce a total ram displacement of 0.9 in. for a total process time of 0.45 s. Nine time increments were used during this run with each time step equal to 50 ms. The results of this analysis are given in Figs. 11–13. The deformation of the cross section is shown in Fig. 11. The original weld interface, which was originally flat, becomes distorted during the process. The locus of this interface is no longer flat, but is concave upward. The deformation and strains are greatest in the center of the joint. The deformation process produces a horizontal stretching and vertical compression of elements in this vicinity similar to the smaller scale GLEEBLE specimens. Figure 12 shows the isotherms at the end of the ram stroke. The displacement of the material has produced a redistribution of the temperature field before heat conduction can play a dominant role. The effective stress distribution is shown in Fig. 13. The stress state is essentially an inverse function of the temperature distribution. Accordingly, the stress is lowest in the region straddling the weld interface where the temperature band is the highest. The highest stresses occur on the shoulder near the corners of the blade where the temperature is lowest.

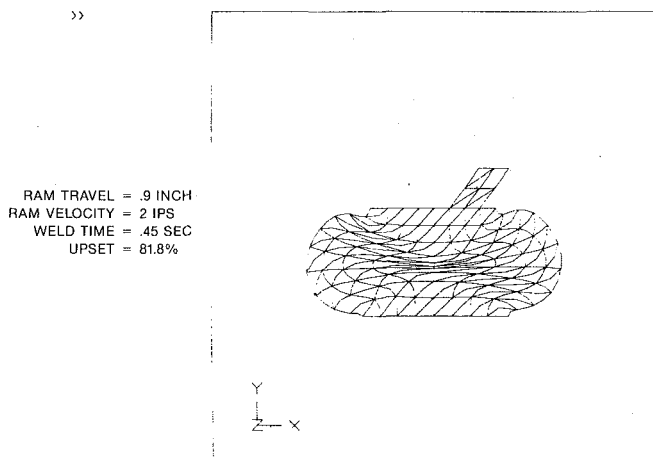


Fig. 11 Upset weld deformation

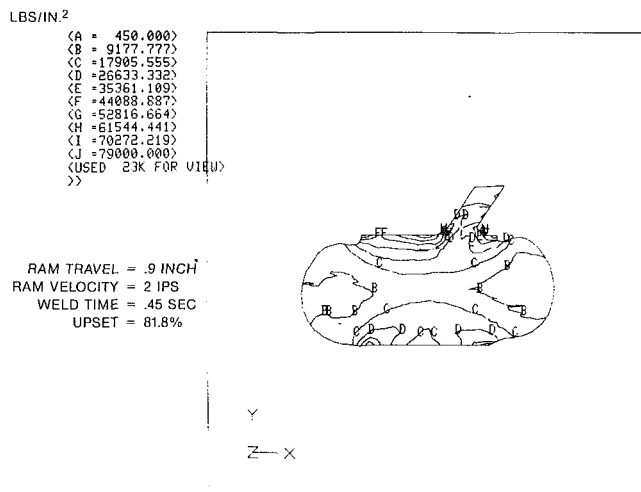


Fig. 13 Upset weld effective stress contours

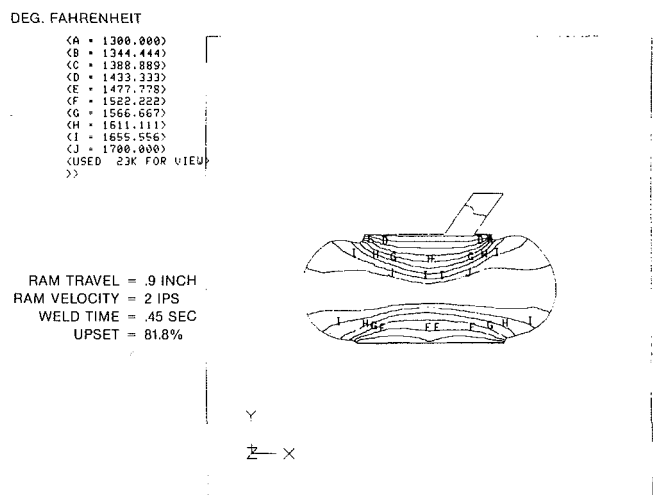


Fig. 12 Upset weld isotherms

The material along the weld interface can be thought of as a rubber membrane, which stretches during the upset process. Material in the vicinity of the stagnation point will not be displaced into the flash region. However, this large stretching mechanism should break up any original surface contaminants, which in the case of highly reactive alloys such as Ti6-4 will be diffused into the bulk material away from the weld interface. It is this sort of surface breakdown that brings the atomic forces into play to produce sound welds. It should be emphasized that material above the weld interfaces does not replace to original surface material as commonly thought by some.

Conclusion

The FEM analyses and experiments of small-scale specimens have shown that indeed a substantial amount of material located on the original interface can be expelled into the flash. However, a substantial portion of the original interfacial material will remain distributed along the weld interface and may be the source of failures if the process parameters are not properly established. For the upset welding process, the combined effect of contact stress, temperature, and time are the important process parameters, which have to be established to produce high-quality welds.

The mechanism of the deformation and the material displacement at the weld faying surface may be characterized in the continuum sense as:

- 1 Material points on the original faying surfaces to be

welded that are located near the centerline are not displaced beyond the original side boundaries.

2 Approximately 32 percent of the original surface material is not flushed out into the flash beyond the original sides of the specimen for a 100 percent upset of Ti6-4 subjected to the process cited in the study.

3 The original interface behaves essentially like a rubber membrane, which stretches during the large deformation process. Material near the stagnation point is under severe compression in a direction perpendicular to the weld line and under large elongation along the weld interface direction.

4 The material near the center region is subjected to the smallest overall displacement.

5 High contact stresses in the large upset process will deform surface asperities; break and disrupt surface contaminants and oxides; and collapse pores and cavities at the surface by plastic deformation.

The two-dimensional finite element method also provides a useful tool to simulate a large-scale upset welding process. This FE process model provides a means to understand better the solid state welding process. The material that is subjected to a temperature range of 1600 to 2000°F will experience significant material displacement during the upset welding process. The geometry of the upset region is dependent on the temperature gradient imposed during the welding. If the gradient near the weld interface is steep, the upset will occur in a narrower band and will have a larger weld width when compared to welding parts subjected to shallower gradients for the same ram displacement. The state of stress is highest in the colder regions and can experience some elastoplastic deformation, which is considerably smaller than the viscoplastic deformation in the hot zone in the vicinity of the weld interface. The deformation along the weld interface is large. Material in the center of the weld will experience large stretch in a direction parallel to the weld interface, while large vertical compressive strains will occur across the weld interface.

Acknowledgments

The major financial support for the development of the finite element code to simulate the upset welding process was provided by John Kelley and Gene Wiggs (GEAE). Their many detailed discussions on the solid-state welding of full-scale components helped furnish information for formulating a realistic model of the process.

The author would also like to acknowledge the help provided by Prof. P. Dawson and J. Eggert during the development of this computer code for an upset welding model, which is based

on their thermomechanical deformation source listing. In addition, the author would like to cite the contributions of E. M. Perry during the validation of the code and the final implementation onto a graphics-driven workstation.

Dr. R. Sundell and S. Godwin of the GE/CRD Process Technology Branch conducted the GLEEBLE tests and compiled the data that were used to run the process model and to conduct the preliminary code validation. The special infrared sensing technique developed by R. Lillquist to obtain precision temperature gradients was vital for conducting the GLEEBLE process model runs and for making a preliminary comparison between test and analysis. He was granted U.S. patent No. 4,687,344 Aug. 18, 1987 for the development of this imaging pyrometer system.

References

- 1 Tylecote, R. F., *The Solid Phase Welding of Metals*, St. Martin's Press, New York, 1968.
- 2 E. F. Nippes, ed., *Metals Handbook, Vol. 6, Welding, Brazing, and Soldering American Society for Metals*, pp. 672-691.
- 3 Fal'chenko, V. M., Larikov, L. N., and Ryabov, V. R., *Diffusion Processes in Solid-Phase Welding of Materials*, Mashinostroenie Publishers, Moscow, 1975, Translated from Russian, Amerind Publishing Co., Ltd., New Delhi, 1984.
- 4 Smith, C. A., "Diffusion Bonding of Titanium Alloys," AMRA CR6-10/1-final report, AD680213, U.S. Army Materials Research Agency, Watertown, MA, June 30, 1968.
- 5 Kazakov, N. F., *Diffusion Bonding of Materials*, translated from Russian, MIR Publishers, Moscow, Pergamon Press, 1985.
- 6 Dawson, P. R., "Viscoplastic Modeling of Upset Welding Using the Finite Element Method," *Process Modeling Tools*, Proc. ASM 1980, pp. 151-172.
- 7 Eggert, G. M., and Dawson, P. R., "Assessment of a Thermoviscoplastic Model of Upset Welding by Comparison to Experiment," *Intl. J. Mech. Sci.*, Vol. 28, No. 9, 1986, pp. 563-589.
- 8 Wang, H. P., and McLay, R. T., "Automatic Remeshing Scheme for Modeling Hot Forming Processes," *Advances in Grid Generation*, K. N. Ghia, ed., ASME FED-Vol. 5, 1983, pp. 151-158.
- 9 Edington, J. W., "Superplasticity," *Progress in Material Science*, Vol. 21, No. 2, Pergamon Press, New York, 1976.
- 10 Gosh, A. K., and Hamilton, C. H., "Influences of Material Parameters and Microstructure on Superplastic Forming," *Met Trans. A*, V-13A, May 1982, pp. 733-742.
- 11 Thomas, J. F., and Srinivasan, X. X., "Constitutive Equations for High Temperature Deformation," presented at Computer Simulation in Materials, 1986 ASM Materials Science Seminar.
- 12 Ferguson, H., "Metalworking Process Simulations Save Production Headaches," *Metal Progress*, Sept. 1986, pp. 37-40.
- 13 Nied, H. A., "Interface Displacement Characteristics of Upset Welding," *Proceedings of the 2nd International Conference on Trends in Welding Research*, S. A. David, and J. M. Vitek, eds., Gatlinburg, TN, May 14-18, 1989, pp. 453-461.
- 14 Avitzur, B., *Handbook of Metal Forming Process*, Wiley, 1983, Chap. 2, pp. 35-39.
- 15 Boer, C. R., et al., *Comparison of Elasto-Plastic FEM. Rigid-Plastic FEM and Experiments for Cylinder Upsetting*, J. F. T. Pitman et al., eds., Pineridge Press, Swansea, United Kingdom, 1982, pp. 217-226.
- 16 Altan, T., et al., *Metal Forming: Fundamentals and Applications*, ASM Press, pp. 32.

P. Lyon

J. F. King

G. A. Fowler

Magnesium Elektron Limited,
Swinton, Manchester M27 2LS,
United Kingdom

Developments in Magnesium-Based Materials and Processes

Recent developments in magnesium alloys, processing techniques, and corrosion protection schemes are reviewed. The casting alloy WE43 is detailed, data being presented showing that it compares favorably with aluminum-based casting alloys on a strength-to-weight basis. In addition its intrinsic corrosion characteristics are shown to be similar to those of aluminum-base alloys. A countergravity casting process, specifically designed to make higher quality, thin-walled magnesium alloy components, is described, together with property data indicating the improvements obtained. Also discussed are the ongoing developments in metal matrix composites and rapid solidification technologies, showing the benefits offered by these processing routes. Finally current corrosion protection schemes are reviewed and their overall cost effectiveness discussed.

Introduction

As aeroengine designers strive for improved efficiencies and performance, the requirement is made of the manufacturers to reduce weight, improve elevated temperature properties, and provide more complex thin-walled castings.

Magnesium alloys have been used for many years, primarily because of their light weight (specific gravity 1.8), only 2/3 as dense as aluminum. Improvements in properties and castability achieved by magnesium in the last 30 years make magnesium alloys a prime choice for further application within the aerospace industry. Their use, however, is inhibited by a reputation for poor corrosion resistance and by the improvements that have been made to aluminum alloys.

To address these problems and increase the use of lightweight magnesium, the following important developments have been made in recent years.

New high corrosion resistant alloys are now available with moderate strength (Mg-Al), for use at low temperatures and high strength alloys (Mg-Y) with usable long term properties to 250°C (482°F). New sand casting processes have been developed that are capable of improving casting quality and complexity (thin walls). Continued development has produced new products such as rapidly solidified material with tensile strengths up to 550 MPa (80 KSI) and metal matrix composites with greatly enhanced stiffness.

The purpose of this paper is to detail some of the advances that have been made and to demonstrate that, with appropriate protection techniques, magnesium offers the aerospace engineer a valuable material choice now and into the 21st century.

1 Cast Alloy Development

Magnesium-based alloys can conveniently be categorized into two groups, namely magnesium-aluminum and magnesium-zirconium alloys.

Contributed by the International Gas Turbine Institute and presented at the 36th International Gas Turbine and Aeroengine Congress and Exposition, Orlando, Florida, June 3-6, 1991. Manuscript received at ASME Headquarters January 25, 1991. Paper No. 91-GT-15. Associate Technical Editor: L. A. Riekert.

1.1 Magnesium-Aluminum (Mg-Al). These are the oldest and lowest cost range of alloys available, the most common example being AZ91C (9 percent Al, 1 percent Zn, 0.2 percent Mn). AZ91C has widespread use in both commercial and aerospace applications where light weight and moderate strength are required.

A hundredfold improvement in the corrosion resistance of this alloy (Fig. 1) has recently been achieved commercially [1] by the reduction in trace element heavy metal impurities such as Fe, Ni, and Cu. The new alloys are designated AZ91E for sand castings and AZ91D for high-pressure die casting.

Although these inherently high corrosion resistant alloys continue to behave similarly to other magnesium alloys in galvanic situations, the greatly improved general corrosion characteristics have generated a significant interest for aerospace and particularly within the US automotive sector.

The Mg-Al group of alloys do however have numerous drawbacks: Above 120°C (248°F) mechanical properties de-

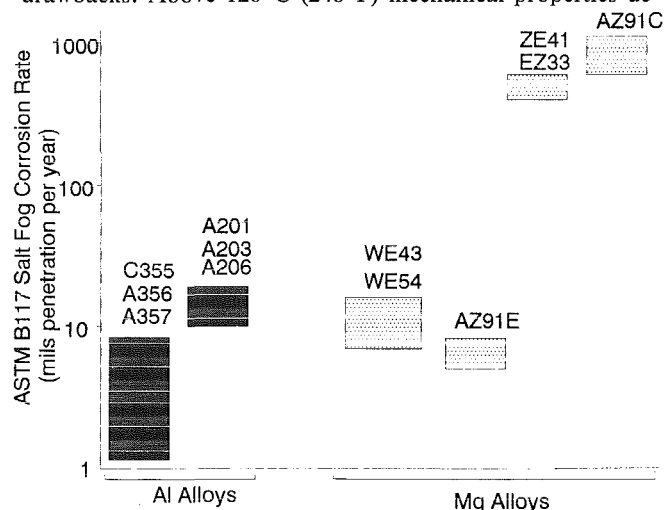


Fig. 1 Corrosion comparison of some magnesium and aluminum casting alloys

Table 1 Tensile properties for some sand cast magnesium alloys

ALLOY	TEMPER	SEPARATELY CAST BARS MPa(KSI)			BARS FROM CASTINGS MPa(KSI)		
		Y.S	T.S	EL%	Y.S	T.S	EL%
AZ91C	T5	130(19)	275(40)	5	100(14)	175(25)	---
ZE41	T5	140(20)	205(30)	5	135(20)	195(28)	2.5
QE22	T6	205(30)	275(40)	4	160(23)	220(32)	---

Nominal Alloy	Suggested Composition(%)	Heat Treatment	Typical RT Tensile Properties *	Typical Tensile Props at 200 °C *	ASTM B117 10 DAY Salt Fog Test Corrosion Rate (mpy)
WE54	Y 5.0-5.5 Nd 1.5-2.0 HRE 1.5-2.0 ***	FULLY HEAT TREATED (T6)	Y.S:200(29) TS: 280(40.5) EL: 4	183(26.5) 241(35) 6.5	10-20
WE43	Y 3.75-4.25 Nd 2.0-2.5 HRE 0.75-1.25 ***	FULLY HEAT TREATED (T6)	Y.S:187(27) TS: 263(38) EL: 8.5	173(25) 257(37.5) 12.5	10 **
WE33	Y 2.5-3.5 Nd2-2.75 HRE 0.5-1 ***	FULLY HEAT TREATED (T6)	YS: 160(23) TS: 245(33.5) EL: 8	_____	10 **

*Strength values in MPa(KSI in brackets).Elongation in%

**Derived from limited data

***Heavy Rare Earths,principally Yb,Er,Dy,Gd

Fig. 2 WE type alloys and properties

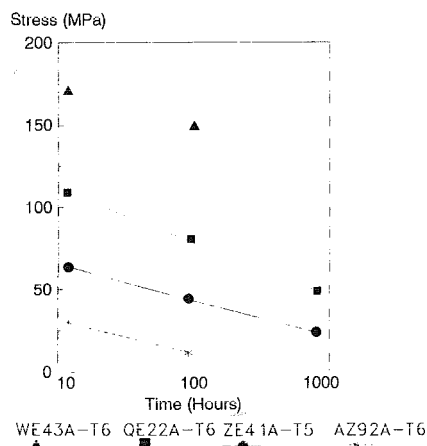


Fig. 3 0.1 percent creep strain of various magnesium alloys at 200°C

teriorate, outcropping microporosity (hence lack of pressure tightness) is often present, and mechanical properties can vary substantially with section thickness. Despite these factors, AZ91C has still found a place in less critical aerospace castings. The availability of the highly corrosion resistant AZ91E offers obvious advantages for direct substitution, to improve corrosion resistance, although no improvements in mechanical properties or castability ensue.

1.2 Magnesium-Zirconium Alloys. Zirconium has an extremely potent grain refining effect upon magnesium that is unavailable to Mg-Al alloys. Consequences of fine equiaxed grain structure are improved mechanical properties, more consistent properties through thin and thick sections, and a lack of outcropping porosity.

A wide range of properties can be achieved by the addition of a range of alloying elements. Although Al is incompatible with Zr, typical additions to Mg-Zr alloys include Zn, Ag, and rare earth elements.

These alloys have so far fulfilled the major requirements of aerospace applications [2]. They have excellent castability, and can be cast into complex shapes virtually free of microporosity.

The most widely used alloy is currently ZE41 (4.2 percent Zn, 1.3 percent Ce, 0.6 percent Zr), which has moderate strength with a simple T5 heat treatment (cast then aged). Strength is maintained up to around 150°C. ZE41 has been the preferred material for helicopter transmission applications for almost 20 years, where its combination of tensile properties, stiffness, and good fatigue resistance are all fully utilized. It is also used in many other aerospace and similar high-quality castings.

More recently, properties have been further increased by the replacement of Zn and Ce with Ag and Nd/Pr, the improved solubility of which permits the alloy to be fully heat treated (T6) by solution, quenching, then precipitation treatment. The higher mechanical properties achieved from these alloys are well maintained to 200°C (392°F).

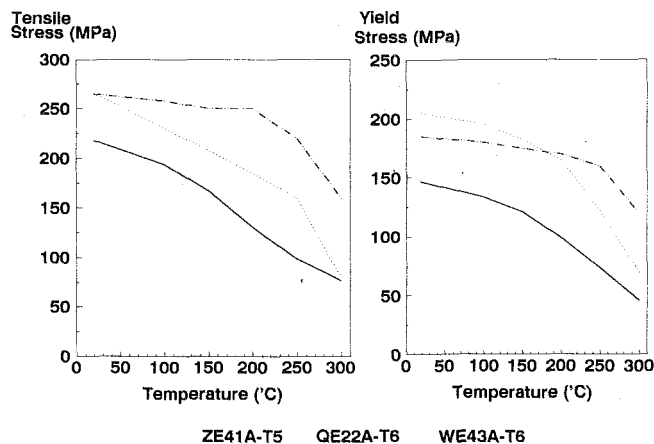
A typical alloy of this type is QE22 (2 percent Ag, 2 percent Nd, 0.6 percent Zr), which has further extended the use of magnesium alloys in aerospace components. A comparison of these alloys is shown in Table 1.

The alloys described have so far satisfied the designers' requirements for lightweight high-performance alloys. It is however recognized that as designers continue to strive for improved power/drive system performance and overall efficiency, the demands on mechanical properties and temperature of application are ever increasing.

In answer to these demands, Magnesium Elektron Ltd. (MEL) has developed a new family of alloys based upon the Mg-Y-Nd RE system (Fig. 2). Due to its combination of superior stability at temperature, and excellent mechanical properties, the alloy considered most suitable for aerospace applications is WE43 (4 percent Y, 2.25 percent Nd, 1 percent HRE,¹ 0.6 percent Zr).

Properties generated from WE43 in the fully heat-treated

¹HRE = Heavy Rare Earths, principally ytterbium, erbium, dysprosium, and gadolinium.



Figs. 4/5 The effect of temperature on the tensile properties of WE43 versus QE22 and ZE41

TEST TEMP (°C)	STRESS REVERSALS/RUNOUT VALUES (MPa)		
	5×10^6	1×10^7	5×10^7
20	87	86	85
150	--	--	80
250	--	--	65

Fig. 6 Fatigue properties of WE43 at various temperatures ($R = -1$ rotating bend)

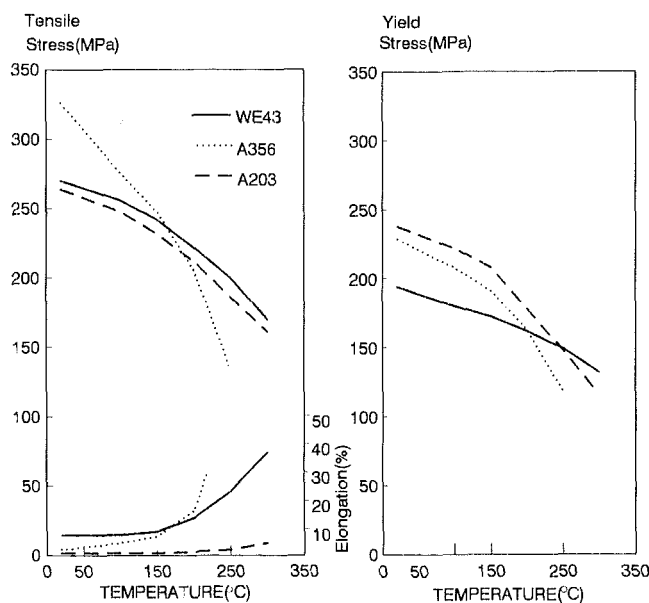


Fig. 7 The effect of temperature on the tensile properties of WE43 versus aluminum alloys A356 and A203

condition (T6) are illustrated in Figs. 3, 4, 5, and 6. It is apparent that WE43 provides consistently improved properties particularly as temperatures increase, when compared to its nearest available magnesium stablemate QE22. The envelope of long-term temperature capabilities has been increased to 250°C (482°F).

When WE43 is compared to commonly used aerospace aluminum-based alloys, such as A356 (Fig. 7) and high-temperature A203, it competes directly on a volume-to-volume basis, and can prove even better at elevated temperatures, with a dramatic potential weight saving of around 30 percent.

After prolonged exposure to elevated temperatures, the ductility of WE43 can be reduced; this effect is seen mostly after exposure at temperatures around 150°C. Exposures for up to

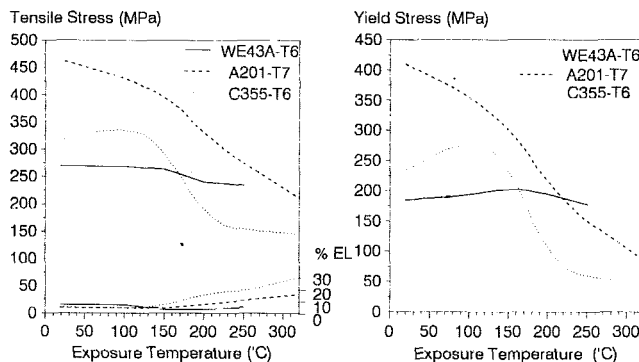


Fig. 8 The effect of 10,000 hour exposure at various temperatures on the room temperature properties of WE43 versus aluminum alloys A201 and C355

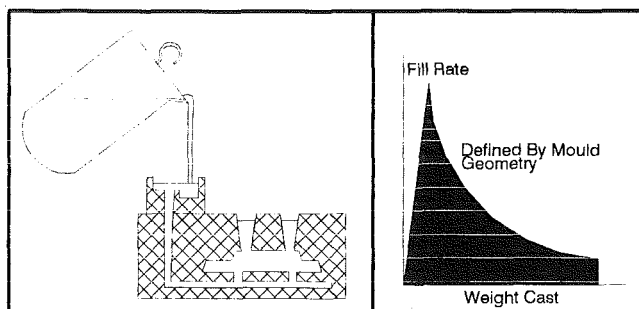


Fig. 9 Conventional gravity pour

10,000 hours at various temperatures up to 250°C have shown no significant reduction in room temperature tensile properties to occur and ductility does not fall below an acceptable 3 percent (Fig. 8). This is not the case for some aluminum alloys such as A201 and C355 where tensile properties can be seen to fall quite drastically after long-term exposure (Fig. 8).

A further major attribute of yttrium-containing alloys is their excellent inherent corrosion resistance. In severe salt water environments WE43 compares favorably with conventional aluminum-based alloys, showing a hundredfold improvement over some other magnesium-based alloys, and similar to the improvement achieved by the high purity AZ91E and AZ91D alloys (Fig. 1).

WE43, although only launched very recently [3], has created great interest in the aerospace industry. Castings have been produced in production foundries throughout the world for evaluation by end users. Alloy property data acquisitions are well advanced and it is expected that aerospace specifications such as AMS and ASTM will be granted during 1991.

In summary, WE43 should be very attractive to designers who wish to uprate current applications, where improved corrosion resistance is required compared to other Mg-Zr alloys and for new applications where all the benefits of high strength, high-temperature capabilities, and corrosion resistance need to be combined with minimum weight.

2 Improved Sand Casting Process

Conventional gravity casting suffers from at least two major drawbacks, both of which are illustrated in Fig. 9:

(a) Turbulent metal flow: Metal must fall by at least the height of the casting and must then turn through 180 deg in several steps to enter the mold cavity. A consequence of this often "turbulent" fill is the opportunity for oxidation and dross formation, particularly in more reactive alloys such as magnesium, which can lead to poor quality castings.

(b) Lack of control over mold fill: The fill rate of the mold is dependent mainly upon the metalostatic head. This leads to

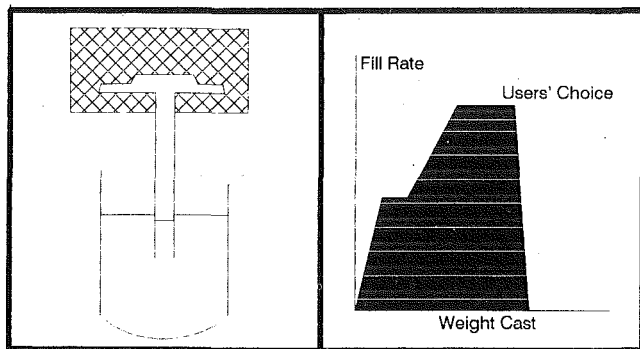


Fig. 10 Countergravity filling

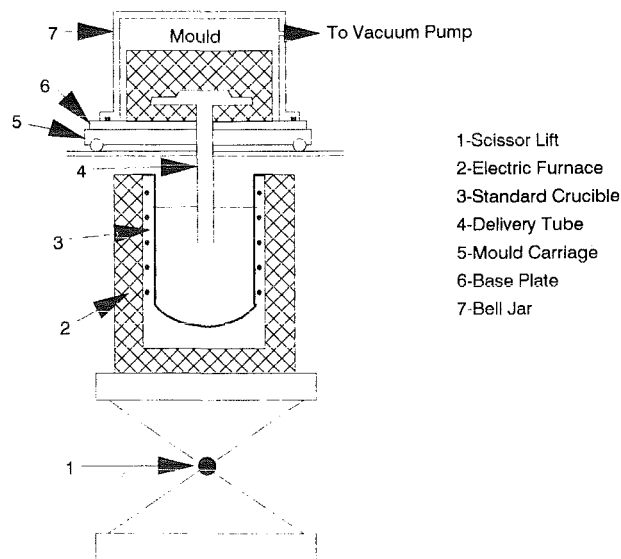


Fig. 11 The MEL* casting process (* registered trade mark)

a reduction in fill rate as metal rises through the casting cavity and metal velocity varies as different thin and thick sections are filled. The result can be too-fast metal flow, allowing turbulence and oxidation at the start of pour and too-slow metal flow to fill thin sections higher in the casting, causing misruns or shortfills at the end of pour.

These problems become more significant as designers demand more complex castings, with thinner walls to achieve weight reductions.

One solution is to fill the mold cavity directly from the bottom, allowing unidirectional filling of the mold, and to control the fill rate by forcing metal into the mold under a controlled pressure (Fig. 10).

Several workers have come to the same conclusions [4-6] and have developed techniques to fulfill the aforementioned requirements. None have been completely suitable for producing high-quality magnesium aerospace castings. Reasons have included difficulty in monitoring melt quality and avoidance of oxide formation [7].

Magnesium Elektron Limited (MEL) has concentrated upon developing a relatively simple system that can be used effectively for small volume batch melting operations typical in light alloy aerospace foundries, as well as for larger bulk melting operations. This process relies on the creation of a differential pressure by evacuating the mold cavity, in contrast to most processes where the melt surface is pressurized.

The process is therefore termed "differential pressure sand casting" (DPSC) (Fig. 11). Principle features are:

(a) A scissor lift raises the crucible until the delivery tube is immersed to the required level.

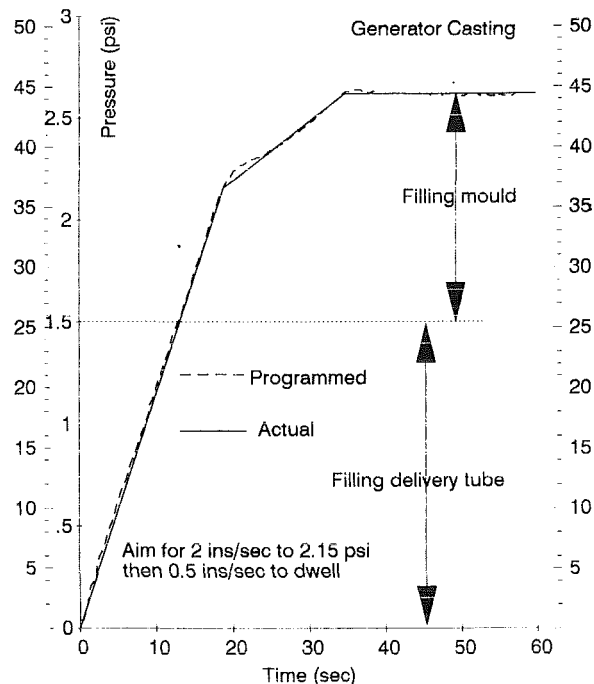


Fig. 12 Controlled filling of test casting

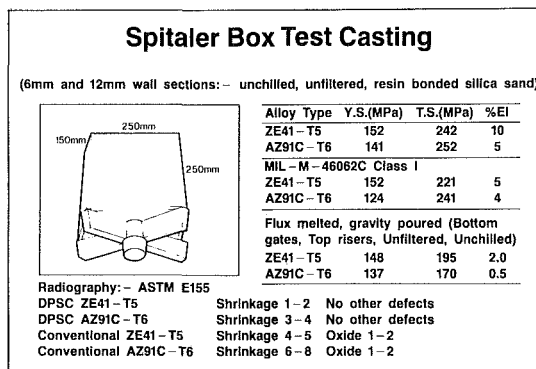


Fig. 13 DPSC versus gravity casting properties

(b) Each mold is provided with its own (recyclable) delivery tube.

(c) The mold can be filled with inert or protective gasses prior to casting.

(d) Differential pressure is applied and controlled automatically under microprocessor control.

Advantages of this process include:

(a) Total control over metal fill rate. Figure 12 illustrates the accuracy achievable. Once the casting parameters have been ascertained, batches of castings can consistently be filled under identical conditions.

(b) Improved metal quality: Figure 13 demonstrates the improvements in both casting integrity and mechanical properties achieved by forcing and maintaining clean metal unidirectionally into the mold.

(c) Thin wall capability: The ability of this process to produce wall thickness in the range 2-4 mm has been shown.

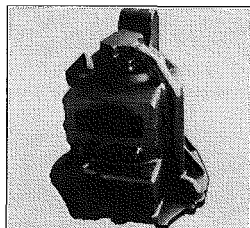
(d) Metal efficiency: Enhanced directional solidification can reduce or eliminate the necessity for risers. This combined with the reduced running system available to the DPSC process allows a reduction in the casting ratio (poured weight:finished weight) (Fig. 14).

The ability to produce consistent high-quality thin-walled sand castings, which DPSC offers, could permit the designer

Table 2 Typical mechanical properties of R.S. magnesium alloy EA55

CONDITION	TENSILE PROPERTIES			HARDNESS(Hv)	FATIGUE STRENGTH (ROTATING BEND) 5 X 10 ⁷ CYCLES MPa	FRACTURE TOUGHNESS Kq(MP m) ^{-1/2}
	YS(MPa)	UTS(MPa)	EL%			
F.I.e.AS EXTRUDED	435	472	13	135	—	10
T4I.e.AS EXTRUDED						
+SOLUTION TREAT +QUENCH	371	425	14	124	195	17

(Localised chills, unrised, unfiltered, resin bonded silica sand)



Typical tensile properties (Av. of 6 results)		
Y.S.(MPa)	T.S.(MPa)	El%
143	227	7
Radiography:— ASTM E155		
Defect	Max. Grade Present	
Microshrinkage	<1 (Plate 2.32)	
Healed microshrinkage	2	
No other defects		

Conventionally poured wt:— 14.6Kg
 DPSC poured wt:— 9.0Kg
 Rough finished wt:— 4.3Kg
 Section thickness:— 5–50mm

Fig. 14 ZE41—T5 production casting: alternator housing

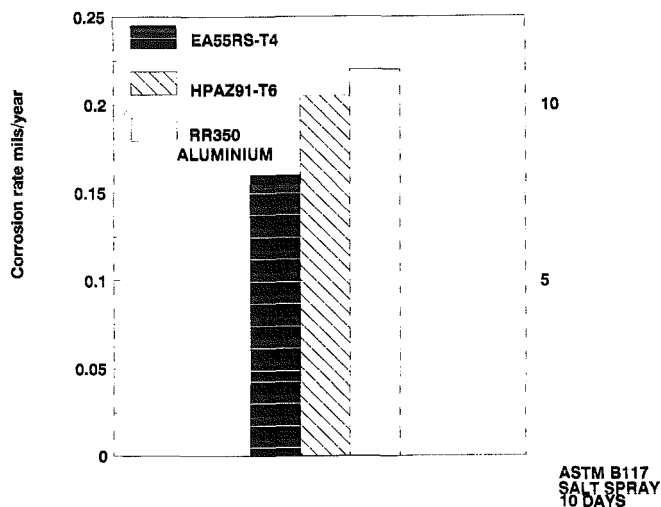


Fig. 15 Corrosion resistance of EA55RS

to lower design factors, which in turn will result in reduced weight of castings.

3 Novel Material Processes

3.1 Rapid Solidification Technology (R.S.T.). Recently, wrought magnesium alloy development has received a new lease on life as a result of the development of R.S.T. Like many other alloy systems, magnesium alloys are amenable to structural refinement and in some instances solid solution extension to give enhanced properties. Development work has been carried out by Lockheed and Allied Signal in North America, MEL/Metalloys/Shell in the United Kingdom, and Norsk-Hydro/Pechiney in Europe. Results to date indicate that tensile strengths in excess of 500 MPa (73 KSI) can be achieved in some alloys [8, 9].

Another important benefit appears to be enhanced corrosion resistance (Fig. 15), offering the prospect of producing alloys

Table 3 Some typical mechanical properties of extruded silicon carbide particulate reinforced magnesium alloys

	%SiC (by volume)	Y.S. (MPa)	T.S. (MPa)	ELONGATION (%)	MODULUS (GPa)
AZM(F)	12	242	310	2.0	60
AZM(F)	UNRF	190	290	18.0	44
ZC7·(T5)	12	283	324	1.3	65
ZC7·(T5)	UNRF	250	312	8.0	44
ZC7·(T6)	12	335	362	1.0	69
ZC7·(T6)	UNRF	320	350	6.0	44
ZM21(F)	12	194	268	2.3	64
ZM21(F)	UNRF	185	263	17.0	44

with equivalent corrosion resistance but higher specific strength than aluminum alloys.

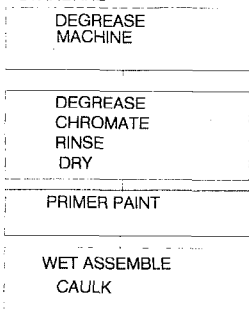
The alloy closest to commercialization is a Mg-5 percent Al-5 percent Zn-5 percent Nd Alloy EA55, developed by Allied Signal [10] and currently being jointly evaluated by Allied and Magnesium Elektron Limited (MEL). Extrusions are produced from hot vacuum pressed billet made from comminuted RS ribbon made by a melt spinning or planar flow casting technique. Tensile strength up to 550 MPa (80 KSI) can be achieved in the as-extruded condition, although fracture toughness is rather low. Fracture toughness is improved by a heat treatment, which redissolves the precipitated $Mg_{17}Al_{12}$ in the structure, although tensile strength is somewhat reduced. Some typical properties are indicated in Table 2. Extruded material up to 80 mm dia has been produced on a development scale. Evaluation quantities are expected to be available in early 1991.

3.2 Metal Matrix Composites (MMC). The demand for reduced weight and increased stiffness in advanced materials applications has generated strong interest in light metal matrix composite components. Since the density of most ceramic reinforcements is higher than either aluminum or magnesium, use of magnesium alloys as matrix materials is particularly beneficial in producing a minimum weight composite.

Development work is progressing on many forms of composite material, and a significant amount of data has been published [11]. Several companies have developed techniques for melt mixing magnesium alloys with particulate SiC or Al_2O_3 to produce material that can be extruded or cast by a range of techniques [11, 12]. Wettability of the ceramic component is less of a problem with magnesium than with aluminum because of the metal's ability to react with any absorbed O_2 or N_2 on the ceramic surface. Yield strength and tensile strength are improved at the expense of ductility compared to the monolithic magnesium alloy, but stiffness can be increased as much as 75 percent. Elevated temperature properties are also significantly enhanced and thermal expansion coefficients reduced.

Magnesium Elektron Limited (MEL) is concentrating upon the liquid metal route of production, employing particulate

PROTECTION SCHEME 1 MINIMUM RECOMMENDED STANDARD



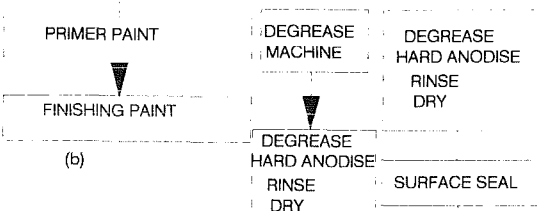
RECOMMENDED PRETREATMENTS FOR AEROSPACE USE CHROMATE PRETREATMENTS

DICHROMATE - MIL-M-3171 TYPE III
CHROME MANGANESE - DTD 911 C BATH V
RAE HOT HALF - DTD 911 C BATH III

ANODIC PRETREATMENTS
DOW - MIL-M-45202
HAE - MIL-M-45202

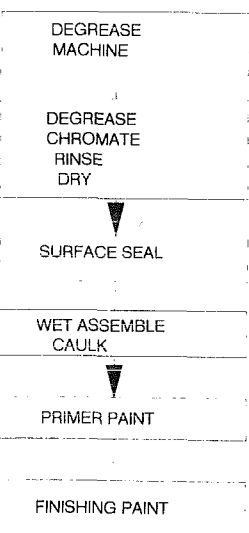
(a)

PROTECTION SCHEME 3 - FOR VERY AGGRESSIVE ENVIRONMENTS



(b)

PROTECTION SCHEME 2 - FOR AGGRESSIVE ENVIRONMENTS



(c)

*HAE retreatment is only possible
if the parts were originally HAE
anodised
(d)

Fig. 16 Protective treatment options for magnesium

SiC. Some typical properties are shown in Table 3. One of the advantages of this is that unlike the powder route, products are not restricted to wrought material but allow castings to be made.

The nearest applications to commercialization are for specialty automotive products such as pistons. It is expected, however, that aerospace applications for these materials will develop, particularly where high stiffness is required, when properties and manufacturing techniques are better developed.

4 Corrosion Protection

Magnesium has a poor reputation for corrosion in commonly found salt-laden atmospheres. This reputation has been exaggerated by uneducated use and improper protection.

New materials such as WE43, AZ91E, and R.S.T. alloys have greatly improved resistance to general corrosion to the level of aluminum base alloys, but protection is still necessary, for aerospace applications.

AREA FAILED FOR COATING SYSTEMS WITH HAE CONVERSION, EPOXY POLYAMIDE PRIMER AND CARC IN 5% SALT SPRAY

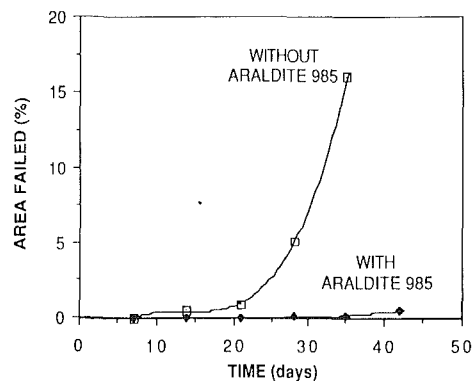


Fig. 17 Advantage of "surface sealing"

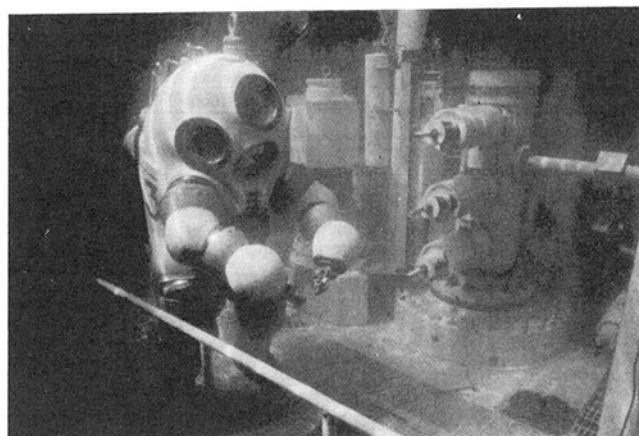


Fig. 18 Magnesium "diving suit"

Two main areas of corrosion protection must be addressed, namely, general surface protection and galvanic protection.

4.1 Surface Protection. Before any surface treatments are applied, contamination (Fe, Ni, Cu, C, etc.) from abrasive cleaning operations such as blasting or peening must be removed. This is particularly important with the new high corrosion resistant alloys, since cathodic surface contamination can completely negate the improved corrosion properties.

Cleaning can be achieved by acid pickling (MIL-M-3171) for rough castings, where losses of up to 50 μ m are acceptable, or by fluoride anodizing [13], where negligible metal is removed for near-finished components.

Having achieved a clean casting, two basic pretreatments are available (Fig. 16a):

(a) Chromate: This treatment is included in US MIL-M-3171 and UK DTD 911C specifications and is the simplest coating to apply.

(b) Anodize: Specified in MIL-M-45202, these coatings offer improved abrasion/damage tolerance and, when used correctly, offer improved protection from corrosion.

The severity of the environment dictates the necessary treatment. For mildly aggressive environments, a simple chromate followed by chromate containing primer and top coat is acceptable (Fig. 16b). Both chromate and anodic pretreatments are porous and, if not sealed before painting, can allow ingress of electrolyte through to the base metal allowing corrosion to spread beneath the coating. A process known as "surface sealing" [14] can successfully fill the pretreatment porosity with a curing epoxy or epoxy phenolic resin subsequent to painting. This treatment uprates the performance of chromate treated material (Fig. 16c) for use in more aggressive environments, e.g., land-based military aircraft.

For very aggressive environments, e.g., sea-based military aircraft, anodic coatings that have been "surface sealed" and painted are suitable (Fig. 16*d*). Because of the increased thickness and porosity of anodic coatings, compared to chromated surfaces, overpainting alone is not acceptable and "surface sealing" becomes essential to achieve successful corrosion protection [15, 16]. Work by the US Army (Fig. 17) confirms this conclusion.

The sealing resins mentioned have good temperature resistance to approximately 200°C (392°F). Recently [17] this has been improved to 250°C (482°F), by the development of a Polyimide sealer, and when combined with DOW 17 anodic pretreatment is very resistant to attack from acid-containing lubricants.

4.2 Galvanic Protection. Magnesium's position in the electrochemical series, coupled with its poor ability to form protective oxide films in salt solution, renders it susceptible to galvanic attack. This is still applicable to the new high corrosion resistant alloys.

Many exposed galvanic couples can be eliminated by good design practices. Examples include the use of studs in blind holes rather than through bolts, cadmium plating and chromate passivation of steel fasteners, and the avoidance of water traps.

Of real practical benefit is the use of "wet assembly" procedures when attaching magnesium to dissimilar metals. This involves the application of sealing compounds (MIL-S-81773) onto mating faces before assembly to prevent ingress of electrolyte and thus prevent galvanic corrosion.

An example of what can be achieved using the types of protection schemes outlined is the magnesium (ZE41) bodied diving suit (Fig. 18), which is used satisfactorily in the most arduous of conditions.

4.3 Commercial Benefits. The cost of employing a satisfactory protection technique must be based upon the expected service life of the component, the cost of maintenance (both in terms of strip down cost and retreatment), and finally the effect of failure upon safety or damage to other components. For aerospace applications, in particular these service "life costs" will be high.

It is reasonable therefore to address the reduction of these

costs by design and specification of good protection systems at an initial stage rather than shortsighted use of low initial cost systems with subsequent higher maintenance or replacement costs.

5 Conclusion

Magnesium alloys and related processes are now available to the designer, offering improved mechanical properties, high corrosion resistance, and high temperature capabilities.

Ongoing developments offer further potential from M.M.C. and R.S.T. materials.

The advancements that have been made will further increase the use of magnesium in the aerospace industry where magnesium's major advantage of light weight continues to be of paramount importance.

References

- 1 Hillis, J. E., *Light Metal Age*, June 1983, pp. 25-29.
- 2 King, J. F., "Development of Magnesium Materials for Advanced Aerospace Components," *Metals Fight Back Conference*, Oct. 1989.
- 3 MEL Data Sheet 467-WE43, May 1989.
- 4 *Foundry Management and Technology*, Sept. 1987, pp. 36-43.
- 5 *Fonderie, Foundeur*, Vol. 29, Nov. 1983, pp. 25-26.
- 6 Broihanne, G., *Proc AGARD Conference*, No. 325, Apr. 1982.
- 7 Fowler, G. A., "Development of New High Strength Corrosion Resistant Magnesium Alloy Castings," *ASM Conference*, Amsterdam, June 1990.
- 8 Gjestland, H., et al., *Proc. 46th World Magnesium Conference (IMA)*, Dearborn, MI, May 1989, p. 72.
- 9 Joshi, A., et al., "Rapidly Solidified Mg-Al-Zn-X Alloys," *Int. J. Rapid Solidification*, to be published.
- 10 Chang, C. F., et al., *Proc. Int. Sampe Metals and Materials Conference*, Dayton, OH., Aug. 1988.
- 11 Albright, D. L., *Proc. 46th World Magnesium Conference (IMA)*, Dearborn, MI, May 1989, p. 33.
- 12 Shook, S. O., et al., *Proc. 43rd World Magnesium Conference (IMA)*, Los Angeles, CA, June 1986, p. 13.
- 13 British Military Specification DTD 911C.
- 14 British Military Specification DTD 935.
- 15 Levy, M., et al., "Assessment of Some Corrosion Protection Schemes for Magnesium Alloy ZE41," *World Magnesium Congress*, Chicago, IL, Sept. 1988.
- 16 Tawil, D. S., "Protection of Magnesium Components in Military Applications," *Paris Airshow*, June 1989.
- 17 Rendu, M., and Tawil, D. S., *SAE Technical Paper* 88-0869, 1988.

The In-Process Dressing Characteristics of Vitrified Bonded CBN Grinding Wheels

J. Williams

H. Yazdzik

Department of Mechanical Engineering,
University of Connecticut,
Storrs, CT 06268

When grinding carbon steels, creep-resistant materials, and other metals such as titanium, cubic boron nitride (CBN) has become recognized as the preferred choice over Al_2O_3 and SiC. The success or failure of the grinding process with CBN lies in the mechanical dressing of the wheel because mechanical dressing is accompanied by very large stresses that distort the grinding wheel and deflect the grinding machine. One recent approach is to true the CBN wheel mechanically and then dress the wheel during the actual grinding manufacturing process. This work observes the dressing of vitrified bonded CBN during the actual like cycle in the production process of steel bearings. Scanning electron micrographs of CBN wheel surfaces are related to surface topography measurements of both wheel and bearing using a Tallysurf machine. In addition, the compositions of the wheel surfaces were checked using the SEM x-ray spectrography facilities. In-process dressing was determined to comprise three distinct stages: the primary or initial dressing, the secondary occurring during steady-state grinding, and finally the tertiary stage after which dimensional tolerance is lost. It was found that the life characteristics of the CBN wheel are quite different than current theories predict. Instead of the limitation of grinding being due to work material loading of the wheel and subsequent dulling of the grains, it was found that the CBN grains remain unchanged and a wear process occurs in the matrix material until the grains fall out and the wheels lose their dimensional tolerance.

Introduction

Grinding is a metal-cutting process using tools with multiple cutting edges provided by randomly bonded abrasive grits of natural or synthetic origin, which remove material at high speed [1]. The abrasive grains are generally of irregular shape [2] and each grain acts as a small cutting tool containing a large negative rake angle. These grains obtain certain characteristics that define their efficiency in removing material, such as crystal hardness, crystal structure, grain shape, the friability or durability of the grain, the chemistry of the abrasive, and the application of any treatment or coating. The types of abrasives available are separated into two categories: (1) conventional, and (2) superabrasive.

The superabrasives are diamond, both natural and synthetic, and cubic boron nitride (CBN). Diamond is used to grind carbide, ceramics, glass, and other refractory nonferrous materials, while CBN is used to grind ferrous materials, particularly hardened steels and alloys of hardness Rc50 and greater [4, 5]. Diamond possesses the properties of high thermal conductivity (two to six times greater than copper) and a chemical affinity to carbon. Owing to these properties, diamond tends to decompose at relatively low temperatures (in the presence

of air at 700°C). When cutting ferrous metals, rapid degeneration of diamond is experienced. In contrast, the chemical nature of cubic boron nitride presents no affinity to low carbon steels and provides it with excellent thermal stability. CBN only shows signs of oxidation above 1000°C with total oxidation taking place at temperatures above 1900°C. The only drawback to CBN is its affinity to water vapor. For this reason, oil-based coolants are preferred when using CBN [4, 6, 7].

There are four basic types of bond used in CBN grinding wheels: resinoid, vitreous, metal, and electroplated. The vitreous bonded wheel, also known as glass or ceramic bonded, is regarded as the most versatile of bonds. It provides higher bonding strength than the resin bond while allowing modifications to the strength and chip clearance capability to vary by altering the wheel porosity and structure. Also, due to the nature of the vitreous bond it is possible to condition the surface of the wheel to achieve a large range of metal removal rates and workpiece surface finishes [8]. The properties of the vitreous bond, with free cutting characteristics and high wear resistance, are deemed the most desirable for the grinding of the bearing rings in a mass production operation. Before the vitreous-bonded CBN grinding wheels can be used to provide the desired metal removal rates and surface finish, proper preparation of the wheel's surface is required. The "conditioning" of the wheel's surface is a two-step process comprised of a truing and dressing operation. Truing is the machining

Contributed by the International Gas Turbine Institute and presented at the ASME Cogen-Turbo V, Budapest, Hungary, September 3-5, 1991. Manuscript received at ASME Headquarters October, 1991. Associate Technical Editor: L. A. Riekert.

of a grinding wheel surface to establish roundness and concentricity to the spindle axis and to produce the desired profile of the wheel [9]. As a result of the high hardness of CBN, diamond is the only practical abrasive used for truing CBN wheels.

There are several methods of truing available. These include stationary tool, brake-controlled, and rotary truing. Truing with stationary tools includes the use of single and multipoint, cluster, and impregnated diamond nibs. The rotary truing devices available include diamond-impregnated disks, cups, and form rollers. Rotary truing devices are best suited for high volume production grinding operations offering a high degree of repeatability. They generally employ metal-bonded or electroplated diamond disks or rolls. The best method of truing vitrified bonded CBN grinding wheels is accomplished using parallel-axis rotary disk, cross-axis rotary disk, and cross-axis rotary cup wheels. However, research has indicated that parallel axis rotary truing with a disk of width 0.060–0.080 in. will yield better results and require lower truing forces. Diamond rolls are generally used when predetermined forms are required to be generated into the wheel's surface [4, 10–12].

Truing leaves the surface of the grinding wheel void of grit protrusions necessary to facilitate chip formation. Once truing has been completed, dressing of the wheel's surface is required to expose the cutting grits, thus providing the protrusion of sharp cutting edges on the wheel surface and providing clearance for chip formation and coolant application. Dressing is accomplished by the careful erosion of the matrix bond material necessary to expose the CBN grains without altering the wheel's form or profile. The methods of dressing vary from manual stick dressing to self or in-process dressing. During manual stick dressing an Al_2O_3 stick is manually fed into the wheel's surface, depending solely on the techniques and skills of the operator. In process dressing occurs during the actual machining of the work material. Once dressed, the grinding wheel will cut more freely with less power required for metal removal [11, 13–15]. Therefore, in-process dressing results in a more controlled and repeatable method of preparing the grinding wheel along with lower production costs due to the elimination of a separate dressing operation. A complete description of the various truing and dressing methods along with recommended applications can be found in [16]. As a result of truing, the matrix material and abrasive grits are on a common plane. Although in-process dressing is successfully applied to vitreous bond CBN grinding wheels, grinding forces are relatively high for the first few parts machined. These higher forces cause a rougher machined surface finish to be generated along with possible geometric discrepancies. Generally, modifications to the cutting process, such as a lower feed rate or lower spindle speed, are required to lower the material removal rate, thereby enhancing the dressing process. Studies have shown that several factors in the truing and cutting operations have an influence on the forces generated during the machining of the initial parts. During truing these include: the truing wheel selection (i.e., mesh size, diamond concentration, bond type, and wheel width), operation parameters (i.e., lead rate, infeed/pass, direction of rotations, speed ratio, overlap, coolant, and workpiece material) and grinding wheel selection (i.e., mesh size, concentration, and bond grade) [4, 7, 10, 12, 13, 17]. Parallel-axis rotary disk truing is the preferred method. The grinding and truing wheel rotations should be unidirectional with a speed ratio in the range of 0.6 to 0.8, a lead/pass of 0.0001–0.0002 in., and as low an overlap factor as possible while still truing the entire wheel surface.

A consequence of the grinding process is the wear of the grinding wheel. The mechanisms of wheel wear are divided into four categories: attritious wear, grain fracture, bond fracture, and bond erosion. Attritious wear is the dulling of the abrasive grains and the generation of wear flats due to rubbing against the workpiece. Grain fracture is the actual breakdown

of the abrasive grain resulting from the high impact stresses incurred during grinding. Bond fracture is the failure of the bond supporting the grains, thus dislodging the grains from the binder. Finally, bond erosion reduces the strength of the bond to hold the abrasive grains in place [18]. Extensive research has been conducted to quantify wear and to understand wear mechanisms as they apply to in-process dressing. Tonshoff [15] generated models for grinding operations employing vitrified bonded CBN wheels. From these models critical grinding parameters can be calculated to aid in optimizing the application of CBN. Ishikawa [14] examined the cause of increased power consumption for the initial parts ground during an in-process dressing operation. Scanning electron microscopy was used to determine physical changes in the CBN crystals and surrounding matrix material for the first few parts machined. Attention was dedicated to the initial stages of an in-process dressing grinding operation. Conclusions generated were that the vitrified CBN wheels should be lightly dressed prior to machining. Finally, Meyer and Sauren [7] studied the suitability of vitrified CBN wheels for in-process dressing. It was recommended that the material removal rate be reduced for the initial 25 parts to enhance the self-dressing process in the case of the internal grinding of bearing rings.

In reviewing previous research, there does not appear to be any documentation of the progressive changes occurring on the surface of a vitrified bonded CBN grinding wheel during the truing, in-process dressing, and mass production process. There exists no overall understanding of the effects grinding has on the surface of the grinding wheel throughout the wheel's life. Therefore, an investigation was conducted to determine the behavior characteristics of a vitreous bonded CBN grinding wheel subjected to machining a type 440C stainless steel bearing ring during an internal grinding process.

Experimental Procedure

This research was conducted during a scheduled production run at The Barden Corp., a precision bearing manufacturer. Work was performed on an internal cylindrical grinder (Bryant Model B). The grinding wheels used were a vitrified bond CBN manufactured by FSK in Japan with the following specification: CBN 325/400 (V10) 200. Prior to efficient machining, conditioning of the grinding wheel's surface was required. The conditioning consisted of a truing process and in-process dressing. Truing was conducted through the use of a Starlite Model 502030 air-driven unit with a 120 grit size, 1/4 in. dia diamond disk. The orientation of the truing device was set up for cross-axis rotary truing. The traverse rate of the grinding wheel across the truing wheel was set at 0.208 in./s and a depth of cut of 0.00005 in. incremented every two passes. A total of five dead passes occurred at the end of the truing sequence. The rotational speed of the grinding wheel was 90,000 rpm throughout the experiment. A total of approximately 0.005 in. was machined off the diameter of the new grinding wheel during truing for a final wheel diameter of 0.220 in. The truing operation was performed dry.

Upon completion of the truing operation the grinding wheel was self-dressed during the actual machining of the production work-pieces. The work-pieces were a standard SR4FF inner bearing ring made of 440C stainless steel (17 percent Cr, 1 percent C, balance Fe) heat treated to a Rockwell hardness of 60–63 Rc with a finished diameter of 0.250 in. and a ground width of 0.166 in. A total of 0.006 in. was machined off the diameter. The rotation of the workpiece and grinding wheel were in the same direction with a workpiece speed of 2750 rpm. A straight oil coolant (international Chemical Co. #1122) was used during the grinding operation.

The grinding process was conducted in two steps. First, a rough grinding cycle with an infeed rate of 0.00052 in./s and then a finishing cycle with an infeed rate of 0.00075 in./s to

Table 1

Test	Parts machined
1	0 (New wheel)
2	0 (Trued wheel)
3	1
4	5
5	10
6	40
7	100
8	200
9	361 (loss of geometry)

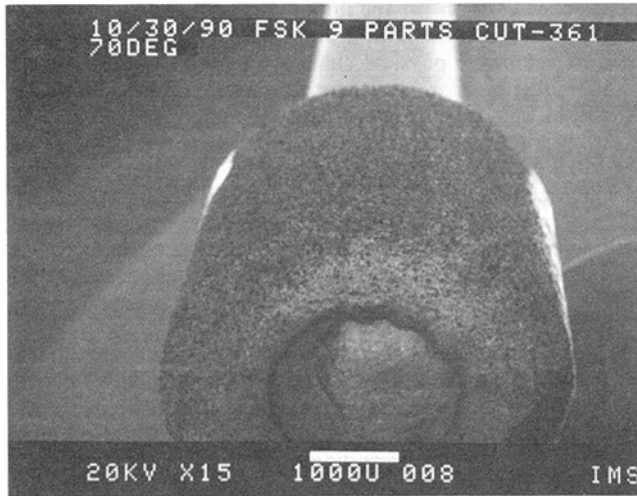


Fig. 1 Orientation of the grinding wheel

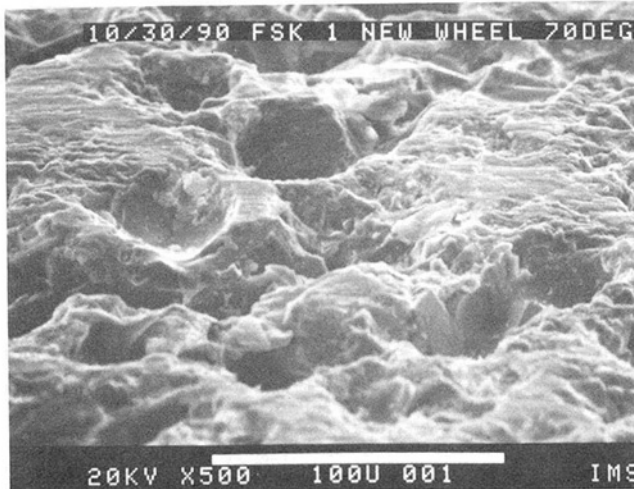


Fig. 2 The excess of matrix covering CBN grains in a new wheel

remove the final 0.0005 in. The oscillation rate of the grinding wheel was 110 strokes/m. To enhance the in-process dressing of the grinding wheel, the rough infeed rate was reduced by 50 percent and incrementally increased for the first 25 parts. A total of eight tests were conducted as outlined in Table 1 with the final test completed with the loss of part geometry.

Surface topography measurements were performed on both the grinding wheel and associated bearing race. The measurements were taken in an axial direction using a Taylor-Hobson Talysurf with a diamond stylus.

Examination of the grinding wheels surface was accomplished through scanning electron microscopy (SEM) and x-ray spectrography analysis on an AMRAY 1000A machine. In order to document surface changes effectively the orientation of the grinding wheel was set as shown in Fig. 1. Special techniques were developed to remove all contaminants from

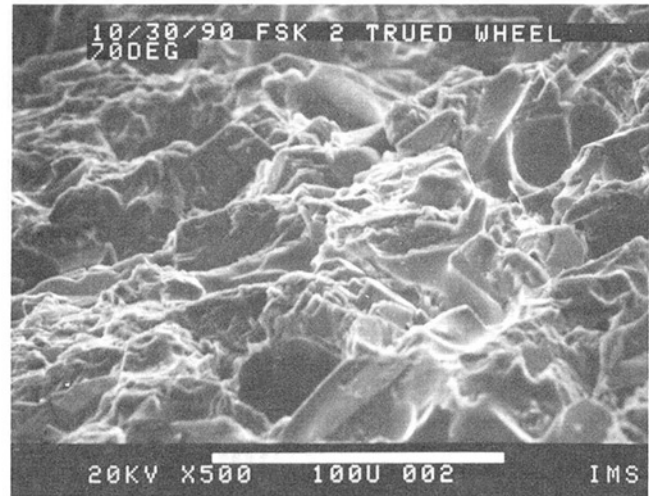


Fig. 3 The trued wheel

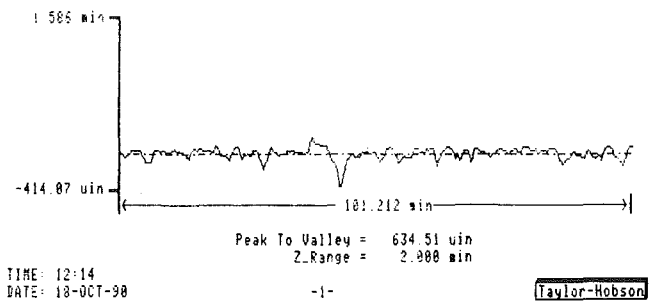


Fig. 4 Talysurf measurements of a trued wheel

the grinding wheel and to prepare the wheels properly for use in the SEM. The wheels were first ultrasonically cleaned with acetone for 5 minutes. Next, a 5 minute ultrasonic rinse using ethanol alcohol was performed to remove the acetone residue. The wheels were then mounted on an aluminum pedestal using a mixture of Duco cement and silver paint. A carbon disk was placed between the grinding wheel and the pedestal to prevent interference from the pedestal during x-ray analysis. Silver paint was then applied to form a conductive path to the base. The wheels were then placed in a vacuum evaporator for 12 hours to remove any residual moisture. Finally a carbon coating 150 Å thick was applied to the wheels using a carbon evaporator to produce a conductive layer for proper electron charging. A carbon coating was used instead of a 60 percent gold 40 percent palladium coating to enhance x-ray analysis.

Results

This experimental work was conducted to examine the characteristics of a vitrified bond CBN grinding wheel throughout its life cycle. Examination of an as-manufactured new wheel showed an excess of matrix material covering the CBN grains (Fig. 2). Truing of the wheel was performed to establish roundness and concentricity of the wheel to the spindle axis and to remove this layer of matrix material, which required the machining of approximately 0.005 in. off the diameter of the wheel. The SEM of the trued wheel (Fig. 3) shows that the matrix material and CBN are on a common plane and there are no cutting edges protruding out of the matrix. A Talysurf roughness measurement (Fig. 4) confirms the smoothness of the wheel with an Ra of 38 μin.

Experience has proven that if grinding were to take place at normal material removal rates directly after truing, when the grinding wheel is blunt with no protrusions of the cutting edges, the grinding wheel will tend to grab the part causing it to spin

Grinding Wheel Roughness FSK Wheels

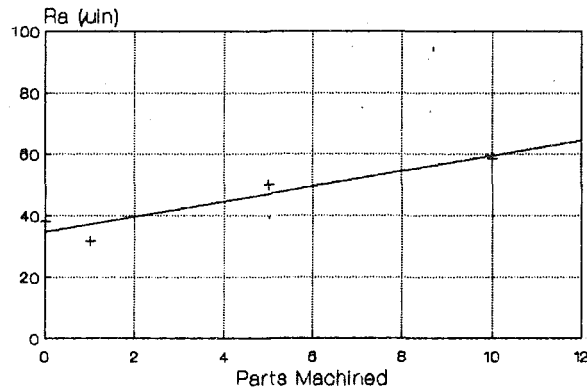


Fig. 5 Surface roughness of wheel during first twelve parts

Grinding Wheel Roughness FSK Wheels

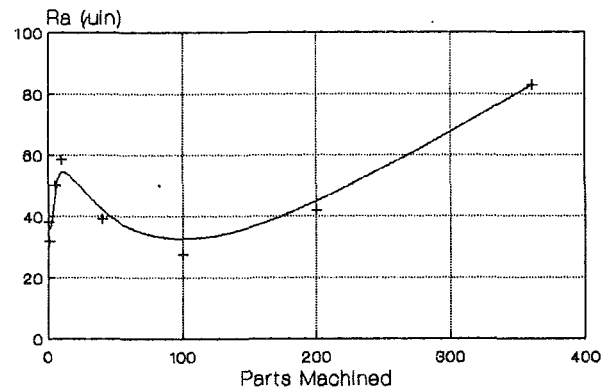


Fig. 7 The change in surface roughness during the wheel life

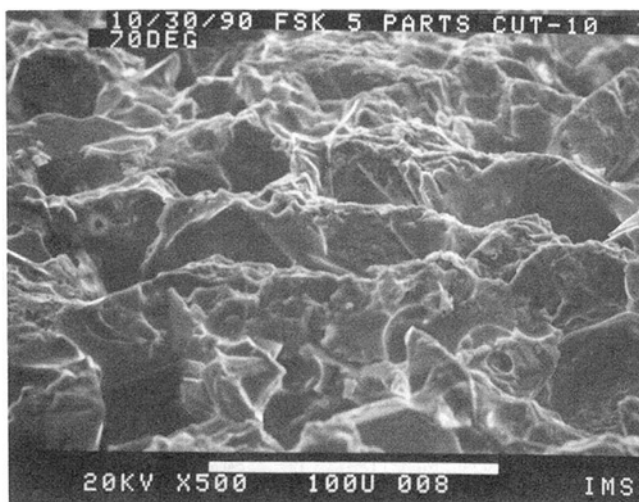


Fig. 6 Erosion of matrix after 10 parts

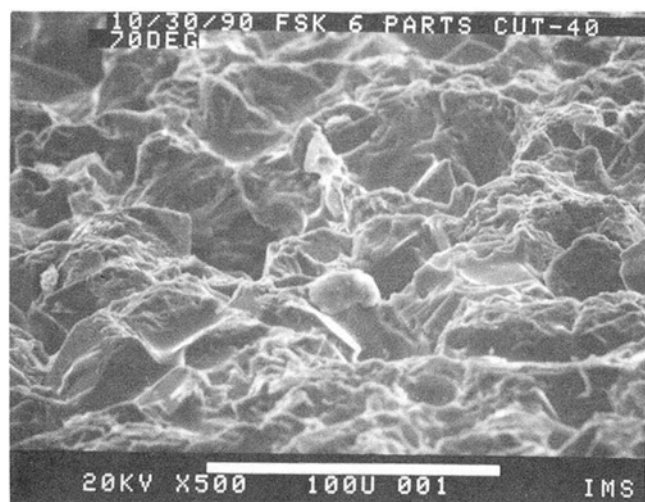


Fig. 8 The exposure of CBN grains after 40 parts

in the fixture. In addition, a very poor surface finish is generated on the workpiece. These findings are consistent with the research reported by Ishikawa [14]. As a result, special compensations to the machining parameters were made to reduce the material removal rate and thus enhance the self-sharpening or in-process dressing of the wheel. For this test the infeed rate was reduced by 50 percent and incrementally increased as the workpiece surface finish improved during the grinding of the first 25 parts. Surface roughness measurements of the wheels show a rapid increase in roughness during this portion of the test (Fig. 5). This is substantiated through SEM analysis in comparing the surface condition of the trued wheel to the wheel after machining ten parts (Fig. 6). It is obvious that an erosion of the matrix material is taking place and the CBN grains are beginning to protrude out of the matrix generating the cutting edges necessary for efficient grinding.

After machining the first 25 parts, the grinding infeed was increased to its full rate. The first observation noted is a sharp decrease in the grinding wheel roughness (Fig. 7).

An SEM comparison between the grinding wheel after 10 parts (Fig. 6) and after 40 parts (Fig. 8) shows that the amount of matrix around the CBN grains has appeared to increase, resulting in less grit protrusion. This is accounted for by concluding that during the primary dressing process when the infeed rate was reduced, the wheel was overdressed and an excess of matrix was eroded away and grit retention by the bond was reduced. Therefore, when the infeed rate was increased, the CBN grains were subjected to higher forces, which

pulled the grains out of the weakened bond resulting in a smoother wheel surface.

As steady-state grinding progressed, the roughness of the wheel's surface continued to increase (Fig. 7). This is a result of the continuous erosion of the matrix material, thereby resolving that in-process dressing is a continuous process. The SEM after 200 parts (Fig. 8) clearly shows that the matrix has been continually eroded and there is dramatic increase in the level of CBN grains protruding, thus increasing the number of active cutting edges and increasing the chip clearance. Finally, the test was completed after grinding 361 parts when geometric tolerances became excessive. This we term the tertiary or final region. Measurements showed that the roughness of the wheel increased sharply. SEM analysis of the wheel after 361 parts (Fig. 9) revealed a dramatic loss of the matrix bond material supporting the CBN grains. In some cases almost the entire grain was protruding from the matrix. This lack of matrix produced an extremely weak bond between the CBN grains and the wheel, resulting in the inability of the bond to hold the grains in place. For this reason, a breakdown of the geometric form of the wheel occurred and retreating or replacement of the wheel was required.

As stated earlier, surface roughness measurements were taken on the ground bearing rings in an axial direction, across the lay. The graphic representation of these measurements is given in Fig. 10. In concurrence with the finding previously defined [14], the roughness value for the first few rings is very high due to grinding with a blunt wheel. As the wheel became more

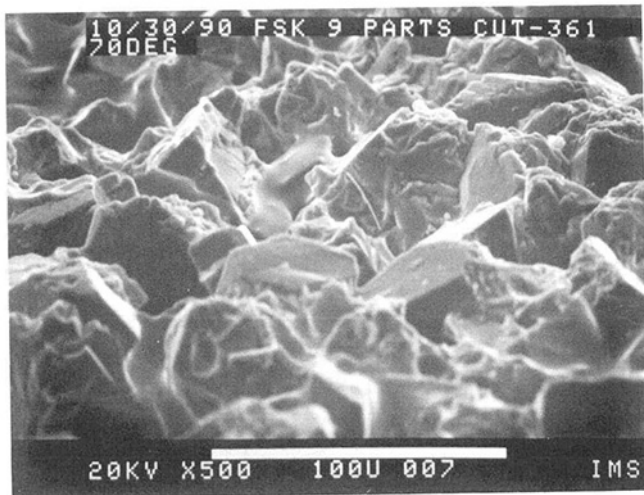


Fig. 9 Extreme exposure of CBN grains at the end of the process

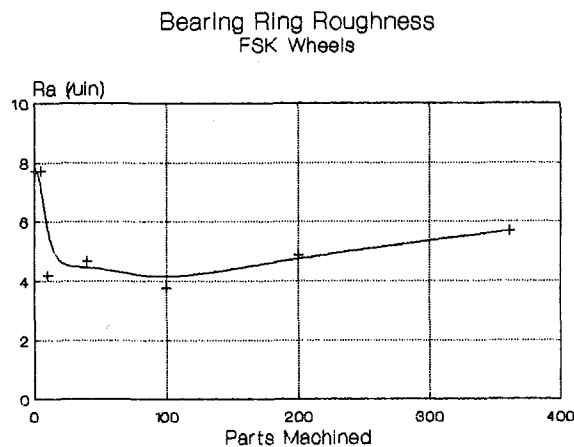


Fig. 10 The roughness of the parts machined during the life of the wheel

dressed and the number of sharp cutting edges in the wheel increased, improvement in the surface finish was noted. Then, as the matrix material continued to erode and the number of active cutting edges increased, there was a gradual degradation of the workpiece surface roughness.

In conducting an SEM examination of the effects of the grinding process on the individual CBN grains it was found that only minor, if any, chipping or wear of the grains occurred. In general, the CBN grains remained passive to this wear with the erosion process affecting only the matrix.

Finally, SEM x-ray spectrography analysis (spectrum analysis) was used to determine if any loading of the workpiece material on the wheel was taking place during the grinding process. It was found that only small traces of chromium and iron were detected. Further analysis revealed that these deposits were random in nature and they were deemed insignificant.

Conclusions

1 Truing is required not only to establish roundness and concentricity to the spindle axis, but also to remove excess matrix material covering the abrasive grains on new wheels.

2 A reduction of the material removal rate for the initial dressing of the wheels is required to prevent damage to the workpiece.

3 The in-process dressing of vitrified bond CBN grinding wheels results in three distinct wear processes: (1) There is a rapid erosion of the matrix material induced by the reduction of the material removal rate for the primary dressing during the first 25 parts, and (2) a steady-state erosion occurs during the normal grinding cycle, which eventually leads to (3) a tertiary or final stage when dimensional tolerance is lost.

4 Excessive primary dressing could result in an overdressed wheel, leading to premature steady state and tertiary wear of the wheel.

5 The wear mechanism is identified as bond erosion, which eventually leads to bond fracture. The CBN abrasive grains remain passive throughout the grinding process with only minimal signs of chipping.

6 In-process dressing is a continuous process throughout the life of the wheel.

7 Although the surface roughness of the workpiece continued to degrade, it remained within acceptable limits. The life of the grinding wheel is determined by the wheel's loss of geometric tolerance resulting from bond fracture and grit release.

8 X-ray spectrographic analysis concluded there was no loading of the workpiece material on the wheel surface.

Acknowledgments

This research was undertaken under the auspices of the Grinding Center, University of Connecticut. The authors wish to thank Pratt & Whitney for their support and Mr. Robert O'Donnell of the Barden Corporation for help in completing the production grinding.

References

- Boothroyd, G., and Knight, W. A., *Fundamentals of Machining and Machine Tools*, 2nd ed., Marcel Dekker, Inc., New York, 1989, p. 49.
- Metzger, J. L., *Superabrasive Grinding*, Butterworth and Co., Ltd., London, 1986, p. 12.
- Boothroyd, G., and Knight, W. A., *Fundamentals of Machining and Machine Tools*, 2nd ed., Marcel Dekker, Inc., New York, 1989, p. 281.
- Edwards, D., "Dressing for CBN," *Modern Machine Shop*, Dec. 1987, pp. 66-74.
- King, R. I., and Hahn, R. S., *Handbook of Modern Grinding Technology*, Chapman and Hall, New York, 1986, pp. 72-75.
- Metzger, J. L., *Superabrasive Grinding*, Butterworth and Co., Ltd., London, 1986, p. 35-36.
- Meyer, H. R., and Sauren, J. K., "Truing and Dressing of CBN Wheels for Production Grinding," *Superabrasives '85 Proceedings*, Chicago, IL, Apr. 22-25, 1985, pp. 11.31-11.47.
- Krar, S. F., and Ratterman, E., *Superabrasives: Grinding and Machining*, McGraw-Hill, New York, 1990, pp. 34-45.
- Metzger, J. L., *Superabrasive Grinding*, Butterworth and Co., Ltd., London, 1986, p. 186.
- Nailor, B., "Truing Parameters for Conditioning Vitrified Bond CBN Wheels," presented at the Abrasive Engineering Conference, Bloomington, IL, Sept. 11-12, 1989.
- Pilbin, L., "Truing and Dressing Devices for Precision Grinding," *Third International Grinding Conference*, Fontana, WI, Oct. 4-6, 1988, MR88-625.
- Subramanian, K., "Vitrified Bonded CBN Wheels—Current Applications and Future Directions," presented at the Industrial Diamond Association Symposium, Japan, Oct. 24-26, 1988.
- Meyer, H. R., and Klocke, F., "New Developments in Dressing of CBN and Conventional Grinding Wheels With Rotary Dressers," *4th International Grinding Conference*, Dearborn, MI, Oct. 9-11, 1990, MR90-527.
- Ishikawa, T., "Dressing of Vitreous Bond CBN Wheel," *4th International Grinding Conference*, Dearborn, MI, Oct. 9-11, 1990, MR90-527.
- Tonshoff, H. K., "Progressive CBN Grinding Using Vitreous Bonded Wheels With Small Diameters," *Third International Grinding Conference*, Fontana, WI, Oct. 4-6, 1988, MR88-597.
- Krar, S. F., and Ratterman, E., *Superabrasives: Grinding and Machining*, McGraw-Hill, New York, 1990, pp. 53-73.
- Subramanian, K., "Diamond/Superabrasives," *Cutting Tool Engineering*, June 1987, pp. 114-117.
- Malkin, S., *Grinding Technology: Theory and Applications of Machining With Abrasives*, Ellis Horwood, Ltd., Chichester, England, 1989, p. 201.

Extension of a Noninteractive Reliability Model for Ceramic Matrix Composites

S. F. Duffy,¹ R. C. Wetherhold,² and L. K. Jain²

Introduction

In the next decade ceramic composites will increasingly be used as high-temperature components in advanced gas turbines. Ceramic components will allow an increase in the operating temperature of the gas stream (measured by the turbine entry temperature), thereby resulting in greater fuel economy in aerospace and automotive turbine applications. Since these materials will be produced from abundant nonstrategic materials, computational structural mechanics methods are evolving to keep pace with this technology. As a result, establishing protocols for sound design methodology, which is the subject of this technical note, is the focus of much current analytical research.

Our objective was to extend a reliability model proposed by Duffy and Manderscheid (1990) for orthotropic ceramic composites. Their approach used tensorial invariant theory to develop an integrity basis from which a subset of invariants was created to incorporate material anisotropy. Herein we propose a different subset of the original integrity basis and construct a more general scalar failure function. The assumption that the failure of a component is governed by its weakest link leads to a formulation that is similar in nature to the principle of independent action (PIA) model for monolithic ceramics. Note that this is a continuum approach to reliability analysis in that it excludes any detailed interaction between individual constituents.

Extension of the Reliability Model

Consider a volume whose failure is assumed to be governed by its weakest link. Under this assumption, events leading to failure of a given link do not affect other links (see, for example, Batdorf and Heinisch (1978), Wetherhold (1983), and

Cassenti (1984)); thus component reliability is given by the following expression:

$$R = \exp \left[- \int_V \psi \, dV \right] \quad (1)$$

Here, $\psi(x_i)$ is the failure function per unit volume at position x_i within the component, and V is the component volume. Note that the lower case Roman letter subscripts denote tensor indices with an implied range from 1 to 3. For orthotropic composites, the failure function must reflect the stress state and the appropriate material symmetry. This requires that

$$\psi = \psi(\sigma_{ij}, a_i, b_i) \quad (2)$$

where a_i and b_i are orthogonal unit vectors that represent the local principal material directions, and σ_{ij} represents the Cauchy stress tensor. The sense of a_i and b_i is immaterial; thus their influence is taken through the products $a_i a_j$ and $b_i b_j$, that is

$$\psi = \psi(\sigma_{ij}, a_i a_j, b_i b_j) \quad (3)$$

Since the stress and local preferred directions may vary from point to point in the component, Eq. (3) implies that the stress field $\sigma_{ij}(x_k)$ and unit vector fields $a_i(x_k)$ and $b_i(x_k)$ must be specified to define ψ .

Because ψ is a scalar function, it must remain form invariant under arbitrary proper orthogonal transformations. Work by Reiner (1945), Rivlin and Smith (1969), Spencer (1971), and others demonstrated that by applying the Cayley-Hamilton theorem and the elementary properties of tensors, a finite set of invariants, known as an integrity basis, can be developed. Form invariance of ψ is ensured if ψ depends on invariants that constitute either the integrity basis or any subset thereof. We are not reporting the first practical application of this approach in formulating models that are functionally dependent on stress and material direction. Others who have used this methodology are the following: Lance and Robinson (1971), who proposed a maximum shear stress plasticity theory for composites; Boehler and Sawczuk (1977), who proposed a plasticity theory for anisotropic cohesive materials; Arnold (1989), who developed a thermoelastic constitutive theory for transversely isotropic materials; and Robinson and Duffy (1990), who developed a viscoplastic constitutive theory for this same class of materials. Clearly, our direction here is not without precedent.

Adapting the previously mentioned work to ψ gives an integrity basis composed of 28 tensor products. Following arguments similar to those of Spencer (1984), we find that several of these tensor products are equal and others are trivial identities such that the final integrity basis for ψ contains only the invariants

$$I_1 = \sigma_{ii} \quad (4)$$

$$I_2 = \sigma_{ij} \sigma_{ji} \quad (5)$$

¹Department of Civil Engineering, Cleveland State University, Cleveland, OH 44115.

²Department of Mechanical and Aerospace Engineering, State University of New York, Buffalo, NY 14260.

Contributed by the International Gas Turbine Institute for publication in the JOURNAL OF ENGINEERING FOR GAS TURBINES AND POWER. Manuscript received by the International Gas Turbine Institute July 31, 1990. Associate Technical Editor: L. A. Riekert.

$$I_3 = \sigma_{ij}\sigma_{jk}\sigma_{ki} \quad (6)$$

$$I_4 = a_i a_j \sigma_{ji} \quad (7)$$

$$I_5 = a_i a_j \sigma_{jk} \sigma_{ki} \quad (8)$$

$$I_6 = b_i b_j \sigma_{ji} \quad (9)$$

and

$$I_7 = b_i b_j \sigma_{jk} \sigma_{ki} \quad (10)$$

From this group we can construct a subset of invariants that corresponds to the stress components oriented to the principal material direction. This new set of invariants includes

$$\hat{I}_1 = I_4 \quad (11)$$

$$\hat{I}_2 = I_6 \quad (12)$$

$$\hat{I}_3 = I_1 - I_4 - I_6 \quad (13)$$

$$\hat{I}_4 = [(2I_5 - \hat{I}_4^2 - \hat{I}_6^2 - I_2 + 2I_7 + \hat{I}_3^2)/2]^{1/2} \quad (14)$$

$$\hat{I}_5 = [(-2I_5 + \hat{I}_4^2 - \hat{I}_6^2 + I_2 - \hat{I}_3^2)/2]^{1/2} \quad (15)$$

and

$$\hat{I}_6 = [(-2I_7 - \hat{I}_4^2 + \hat{I}_6^2 + I_2 - \hat{I}_3^2)/2]^{1/2} \quad (16)$$

For a uniformly stressed unit volume (or in the context of Weibull analysis, a single link) the first three invariants correspond to the magnitudes of the normal stress components. Note that \hat{I}_3 corresponds to the magnitude of the normal stress component in the direction defined by the cross product of vectors a_j and b_k , that is

$$d_i = e_{ijk} a_j b_k \quad (17)$$

where e_{ijk} is the permutation tensor. The last three invariants in the subset correspond to magnitudes of the shear stress components. (Refer to Fig. 1 for a pictorial representation of the invariants.) A fundamental difference between the theory proposed here and that of the original work by Duffy and Manderscheid (1990) lies in the number of invariants derived from the original integrity basis. The previous model employed only five invariants and suppressed the dependence of ψ on invariants I_2 and I_3 . The current formulation uses six invariants and includes I_2 , but it is still independent of I_3 . The additional parameter arises from a different and apparently more consistent set of assumptions. Taking

$$\psi = \psi(\hat{I}_1, \hat{I}_2, \hat{I}_3, \hat{I}_4, \hat{I}_5, \hat{I}_6) \quad (18)$$

ensures ψ is form invariant.

If we assume that compressive stresses associated with normals \hat{I}_1 , \hat{I}_2 , and \hat{I}_3 , do not contribute to failure, then

$$\langle \hat{I}_1 \rangle = \begin{cases} \hat{I}_1 & \hat{I}_1 > 0 \\ 0 & \hat{I}_1 \leq 0 \end{cases} \quad (19)$$

$$\langle \hat{I}_2 \rangle = \begin{cases} \hat{I}_2 & \hat{I}_2 > 0 \\ 0 & \hat{I}_2 \leq 0 \end{cases} \quad (20)$$

$$\langle \hat{I}_3 \rangle = \begin{cases} \hat{I}_3 & \hat{I}_3 > 0 \\ 0 & \hat{I}_3 \leq 0 \end{cases} \quad (21)$$

In addition, the shear stress contribution is sign-insensitive; thus

$$\langle \hat{I}_4 \rangle = |\hat{I}_4| \quad (22)$$

$$\langle \hat{I}_5 \rangle = |\hat{I}_5| \quad (23)$$

$$\langle \hat{I}_6 \rangle = |\hat{I}_6| \quad (24)$$

for all values of \hat{I}_4 , \hat{I}_5 , and \hat{I}_6 . At this point we assume that the stress components identified by the aforementioned invariants act independently in producing failure (i.e., a non-interactive theory). Following reasoning similar to that of Wetherhold (1983), we find that ψ takes the form

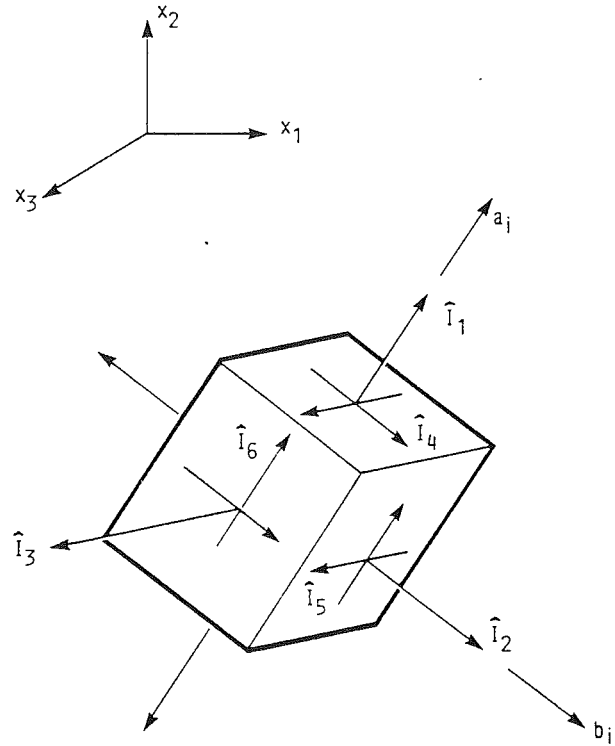


Fig. 1 Physical interpretations of the invariants

$$\psi = \left[\frac{\langle \hat{I}_1 \rangle}{\beta_1} \right]^{\alpha_1} + \left[\frac{\langle \hat{I}_2 \rangle}{\beta_2} \right]^{\alpha_2} + \left[\frac{\langle \hat{I}_3 \rangle}{\beta_3} \right]^{\alpha_3} + \left[\frac{\langle \hat{I}_4 \rangle}{\beta_4} \right]^{\alpha_4} + \left[\frac{\langle \hat{I}_5 \rangle}{\beta_5} \right]^{\alpha_5} + \left[\frac{\langle \hat{I}_6 \rangle}{\beta_6} \right]^{\alpha_6} \quad (25)$$

The α 's associated with each invariant correspond to the Weibull shape parameters, and the β 's correspond to Weibull scale parameters. Inserting Eq. (25) into the volume integration given by Eq. (1), along with Eqs. (19)–(24) yields a reliability model for an orthotropic ceramic composite subject to a three-dimensional state of stress.

Concluding Remarks

In this technical brief we have proposed a more general reliability model for ceramic composites with orthotropic material symmetry. This approach allows material orientation within a component to vary along a family of curves such that the material is locally orthotropic. The model was constructed by using an invariant formulation. Such an approach indicates the maximum number and form of stress invariants necessary to define the failure function ψ . A subset of the integrity basis for ψ was constructed with invariants that correspond to the stress components in the principal material orientation. The result is a model similar in nature, yet different in form, to the PIA theory for monolithic ceramics. This model can be readily integrated with the finite element methods of structural analysis. Using the stress output from a finite element analysis allows component integrity to be computed by calculating element-by-element reliability. On the basis of the weakest link concept the component survivability is simply the product of individual element reliabilities. The model could be easily integrated into a computer algorithm such as SCARE (Structural Ceramics Analysis and Reliability Evaluation, Gyekenyesi (1986)).

References

- Arnold, S. M., 1989, "A Transversely Isotropic Thermoelastic Theory," NASA TM-101302.
- Batdorf, S. B., and Heinisch, H. L., Jr., 1978, "Weakest Link Theory Reformulated for Arbitrary Fracture Criterion," *Journal of the American Ceramic Society*, Vol. 61, No. 7-8, pp. 355-358.
- Boehler, J. P., and Sawczuk, A., 1977, "On Yielding of Oriented Solids," *Acta Mechanica*, Vol. 27, No. 1-4, pp. 185-204.
- Cassenti, B. N., 1984, "Probabilistic Static Failure of Composite Material," *AIAA Journal*, Vol. 22, No. 1, pp. 103-110.
- Duffy, S. F., and Manderscheid, J. M., 1990, "Noninteractive Macroscopic Reliability Model for Ceramic Matrix Composites With Orthotropic Material Symmetry," *AMSE JOURNAL OF ENGINEERING FOR GAS TURBINES AND POWER*, Vol. 113, pp. 507-511; NASA TM-101414.
- Gyekenyesi, J. P., 1986, "SCARE: A Postprocessor Program to MAC/NAS-TRAN for Reliability Analysis of Structural Ceramic Components," *ASME JOURNAL OF ENGINEERING FOR GAS TURBINES AND POWER*, Vol. 108, pp. 540-546.
- Lance, R. H., and Robinson, D. N., 1971, "A Maximum Shear Stress Theory of Plastic Failure of Fiber-Reinforced Materials," *Journal of the Mechanics and Physics of Solids*, Vol. 19, No. 2, pp. 49-60.
- Reiner, M., 1945, "A Mathematical Theory of Dilatancy," *American Journal of Mathematics*, Vol. 67, pp. 350-362.
- Robinson, D. N., and Duffy, S. F., 1990, "Continuum Deformation Theory for High-Temperature Metallic Composites," *Journal of Engineering Mechanics*, Vol. 116, No. 4, pp. 832-844.
- Rivlin, R. S., and Smith, G. F., 1969, "Orthogonal Integrity Basis for N Symmetric Matrices," *Contributions to Mechanics*, D. Abir, ed., Pergamon Press, Oxford, pp. 121-141.
- Spencer, A. J. M., 1971, "Theory of Invariants," *Continuum Physics—Vol. I—Mathematics*, A. C. Eringen, ed., Academic Press, New York, pp. 239-255.
- Spencer, A. J. M., 1984, "Constitutive Theory for Strongly Anisotropic Solids," *Continuum Theory of the Mechanics of Fibre-Reinforced Composites*, A. J. M. Spencer, ed., Springer-Verlag, New York, pp. 1-32.
- Wetherhold, R. C., 1983, "Statistics of Fracture of Composite Materials Under Multiaxial Loading," Ph.D. Thesis, University of Delaware.